

Replicating psychology
experiments pp. 910 & 943

Why it pays to believe
in a punitive god p. 918

Engineering cooperation
among cells pp. 924 & 986

Science

\$10
28 AUGUST 2015
sciencemag.org

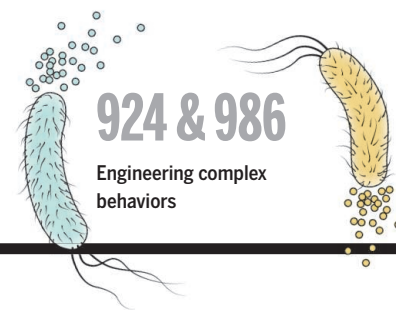
AAAS

Cellular proteins in live action

Pushing the resolution of structured
illumination microscopy p. 944

CONTENTS

28 AUGUST 2015 • VOLUME 349 • ISSUE 6251



918



The faithful are purified of sin at the Kumbh Mela, a vast Hindu gathering.

NEWS

IN BRIEF

906 Roundup of the week's news

IN DEPTH

909 FISCAL CRISIS HAS BRAZILIAN SCIENTISTS SCRAMBLING

Government makes deep cuts in research budgets as economy stumbles
By H. Escobar

910 MANY PSYCHOLOGY PAPERS FAIL REPLICATION TEST

An effort to repeat 100 studies yields sobering results, but many researchers are positive about the process
By J. Bohannon

► RESEARCH ARTICLE P. 943

911 PLUGGED PORES MAY UNDERLIE ALS, DEMENTIA CASES

Multiple groups reveal that “stutter” mutation kills motor nerve cells by clogging channels into the nucleus
By E. Underwood

912 DARK HORSE SCORES A FUSION COUP

California company demonstrates unorthodox approach to trapping superheated plasma
By D. Clery

914 ORCHIDS’ DAZZLING DIVERSITY EXPLAINED

New family tree shows that a series of innovations accelerated speciation
By E. Stokstad

FEATURES

915 THE MISSING MUDBUG

As threats to crayfish mount, researchers push to document the enigmatic crustaceans
By E. DeMarco

918 BIRTH OF THE MORALIZING GODS

A new theory aims to explain why religions with moralizing gods are so successful—but testing it remains a challenge
By L. Wade

922 Turning history into a binary code

By L. Wade

► PODCAST

INSIGHTS

PERSPECTIVES

924 SYNTHETIC COMMUNITIES, THE SUM OF PARTS

Complex behaviors are engineered from cooperating cell communities
By B. P. Teague and R. Weiss
► REPORT P. 986

925 AS SIMPLE AS [2+2]

Iron catalysis transforms readily available commodity olefins into cyclobutane building blocks under thermal conditions
By M. W. Smith and P. S. Baran

► REPORT P. 960

927 SAFEGUARDING GENE DRIVE EXPERIMENTS IN THE LABORATORY

Multiple stringent confinement strategies should be used whenever possible
By O. S. Akbari et al.

929 MICROBIOTA REGULATE INTESTINAL SUPPRESSOR T CELLS

Gut microbes influence the balance of regulatory T cell subtypes to control inflammation
By A. N. Hegazy and F. Powrie

► REPORTS PP. 989 & 993

931 DEFINING THE GENUS HOMO

Early hominin species were as diverse as other mammals
By J. H. Schwartz and I. Tattersall

BOOKS ET AL.

933 FANTASTIC WORLDS

K. van der Veen and D. Dunlop, curators, reviewed by R. Gross

934 SONIC WIND

By C. Ryan, reviewed by L. Vinsel

LETTERS

935 GENE EDITING: ADVISING ADVICE

By C. Addison and S. Taylor-Alexander

935 THE WISDOM OF BABOON DECISIONS

By K. B. Wray

935 RESPONSE

By A. Strandburg-Peshkin et al.

936 TECHNICAL COMMENT ABSTRACTS

DEPARTMENTS

905 EDITORIAL

Preparing for the next Katrina
By Marcia McNutt

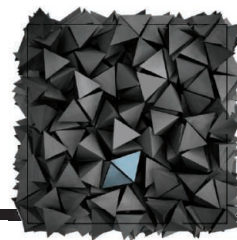
1018 WORKING LIFE

The fungi that ate my house
By Joan W. Bennett



977

How enzymes promote
DNA strand exchange



942

Entropic packing
of pyramids

RESEARCH

IN BRIEF

939 From *Science* and other journals

REVIEW

942 COLLOIDS

Colloidal matter: Packing, geometry, and entropy *V. N. Manoharan*
REVIEW SUMMARY; FOR FULL TEXT:
dx.doi.org/10.1126/science.1253751

RESEARCH ARTICLES

943 PSYCHOLOGY

Estimating the reproducibility of psychological science
Open Science Collaboration
RESEARCH ARTICLE SUMMARY; FOR FULL TEXT:
dx.doi.org/10.1126/science.aac4716
► NEWS STORY P. 910; PODCAST

944 ADVANCED IMAGING

Extended-resolution structured illumination imaging of endocytic and cytoskeletal dynamics *D. Li et al.*
RESEARCH ARTICLE SUMMARY; FOR FULL TEXT:
dx.doi.org/10.1126/science.aab3500



REPORTS

945 SOLID-STATE PHYSICS

Scalable T^2 resistivity in a small single-component Fermi surface *X. Lin et al.*

948 TOPOLOGICAL MATTER

Observation of chiral currents at the magnetic domain boundary of a topological insulator *Y. H. Wang et al.*

952 QUANTUM MECHANICS

Quantum squeezing of motion in a mechanical resonator *E. E. Wollman et al.*

956 NANOPARTICLES

Production of amorphous nanoparticles by supersonic spray-drying with a microfluidic nebulator *E. Amstad et al.*

960 ORGANIC CHEMISTRY

Iron-catalyzed intermolecular [2+2] cycloadditions of unactivated alkenes *J. M. Hoyt et al.*
► PERSPECTIVE P. 925

964 SEXUAL SELECTION

Irrationality in mate choice revealed by túngara frogs *A. M. Lea and M. J. Ryan*

966 LIFE HISTORY

Age-related mortality explains life history strategies of tropical and temperate songbirds *T. E. Martin*

970 FUNGAL SYMBIONTS

Global assessment of arbuscular mycorrhizal fungus diversity reveals very low endemism *J. Davison et al.*

974 NEURONAL DEVELOPMENT

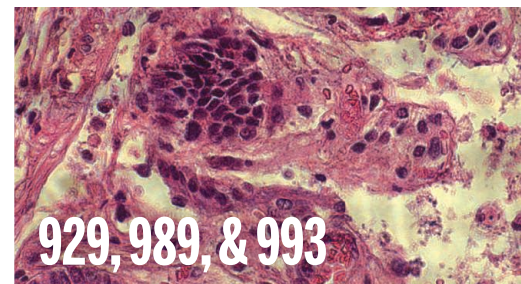
Glycerophospholipid regulation of modality-specific sensory axon guidance in the spinal cord *A. T. Guy et al.*

977 DNA RECOMBINATION

Base triplet stepping by the Rad51/RecA family of recombinases *J. Y. Lee et al.*

982 HEART DISEASE

Titin mutations in iPS cells define sarcomere insufficiency as a cause of dilated cardiomyopathy *J. T. Hinson et al.*



986 SYNTHETIC BIOLOGY

Emergent genetic oscillations in a synthetic microbial consortium *Y. Chen et al.*
► PERSPECTIVE P. 924

MUCOSAL IMMUNOLOGY

989 The microbiota regulates type 2 immunity through ROR γ ⁺ T cells *C. Ohnmacht et al.*

993 Individual intestinal symbionts induce a distinct population of ROR γ ⁺ regulatory T cells *E. Sefik et al.*
► PERSPECTIVE P. 929

ON THE COVER



Single frame from a super-resolution movie of α -actinin (magenta) bundling actin cytoskeletal filaments (green) into thick fibers at the edges of growing membrane ruffles in a living COS-7 cell. The movie was acquired with a new form of nonlinear structured illumination microscopy that achieves 62-nanometer resolution at subsecond acquisition times for dozens of frames. See page 944 and dx.doi.org/10.1126/science.aab3500. *Image: Dong Li and Eric Betzig, Janelia Research Campus/Howard Hughes Medical Institute*

Science Staff	902
AAAS News & Notes	937
New Products	999
Science Careers	1000

SCIENCE (ISSN 0036-8075) is published weekly on Friday, except the last week in December, by the American Association for the Advancement of Science, 1200 New York Avenue, NW, Washington, DC 20005. Periodicals mail postage (publication No. 484460) paid at Washington, DC, and additional mailing offices. Copyright © 2015 by the American Association for the Advancement of Science. The title SCIENCE is a registered trademark of the AAAS. Domestic individual membership and subscription (51 issues): \$153 (\$74 allocated to subscription). Domestic institutional subscription (51 issues): \$1282. Foreign postage extra: Mexico, Caribbean (surface mail) \$55; other countries (air assist delivery) \$85. First class, airmail, student, and emeritus rates on request. Canadian rates with GST available upon request. GST #R1254 88122. Publications Mail Agreement Number 1069624. Printed in the U.S.A. **Change of address:** Allow 4 weeks, giving old and new addresses and 8-digit account number. **Postmaster:** Send change of address to AAAS, P.O. Box 96178, Washington, DC 20090-6178. **Single-copy sales:** \$10.00 current issue, \$15.00 back issue prepaid includes surface postage; bulk rates on request. **Authorization to photocopy** material for internal or personal use under circumstances not falling within the fair use provisions of the Copyright Act is granted by AAAS to libraries and other users registered with the Copyright Clearance Center (CCC) Transactional Reporting Service, provided that \$30.00 per article is paid directly to CCC, 222 Rosewood Drive, Danvers, MA 01923. The identification code for Science is 0036-8075. Science is indexed in the Reader's Guide to Periodical Literature and in several specialized indexes.

Editor-in-Chief Marcia McNutt

Executive Editor Monica M. Bradford **News Editor** Tim Appenzeller

Managing Editor, Research Journals Katrina L. Kelnor

Deputy Editors Barbara R. Jasny, Andrew M. Sugden(UK), Valda J. Vinson, Jake S. Yeston

Research and Insights

SR. EDITORS Caroline Ash(UK), Gilbert J. Chin, Lisa D. Chong, Julia Fahrenkamp-Uppenbrink(UK), Pamela J. Hines, Stella M. Hurlty(UK), Paula A. Kiberstis, Marc S. Lavine(Canada), Kristen L. Mueller, Ian S. Osborne(UK), Beverly A. Purnell, L. Bryan Ray, Guy Riddihough, H. Jesse Smith, Jelena Stajic, Peter Stern(UK), Phillip D. Szurmi, Brad Wible, Nicholas S. Wigginton, Laura M. Zahn **ASSOCIATE EDITORS** Brent Grocholski, Keith T. Smith, Sacha Vignieri **ASSOCIATE BOOK REVIEW EDITOR** Valerie B. Thompson **ASSOCIATE LETTERS EDITOR** Jennifer Sills **CHIEF CONTENT PRODUCTION EDITOR** Cara Tate **SR. CONTENT PRODUCTION EDITOR** Harry Jack **CONTENT PRODUCTION EDITORS** Jeffrey E. Cook, Chris Filiatreau, Cynthia Howe, Lauren Kmcac, Barbara P. Ordway, Catherine Wolner **SR. EDITORIAL COORDINATORS** Carolyn Kyle, Beverly Shields **EDITORIAL COORDINATORS** Ramatoulaye Diop, Joi S. Granger, Lisa Johnson, Anita Wynn **PUBLICATIONS ASSISTANTS** Aneera Dobbins, Jeffrey Hearn, Dona Mathieu, Le-Toya Mayne Flood, Shannon McMahon, Scott Miller, Jerry Richardson, Rachel Roberts(UK), Alice Whaley(UK), Brian White **EXECUTIVE ASSISTANT** Anna Bashkirova **ADMINISTRATIVE SUPPORT** Janet Clements(UK), Lizanne Newton(UK), Maryrose Madrid, Laura-Nadine Schuhmacher (UK, Intern), Alix Welch (Intern), John Wood(UK)

News

NEWS MANAGING EDITOR John Travis **INTERNATIONAL EDITOR** Richard Stone **DEPUTY NEWS EDITORS** Daniel Clery(UK), Robert Coontz, Elizabeth Culotta, David Grimm, David Malakoff, Leslie Roberts **CONTRIBUTING EDITOR** Martin Enserink(Europe) **SR. CORRESPONDENTS** Jeffrey Mervis, Elizabeth Pennisi **NEWS WRITERS** Adrian Cho, Jon Cohen, Jennifer Couzin-Frankel, Carolyn Gramling, Eric Hand, Jocelyn Kaiser, Catherine Matacic, Kelly Servick, Robert F. Service, Erik Stokstad(Cambridge, UK), Emily Underwood **INTERNS** Hanae Armitage, Emily DeMarco, Annick Laurent, Laura Olivieri, Juan David Romero **CONTRIBUTING CORRESPONDENTS** Michael Balter(Paris), John Bohannon, Ann Gibbons, Mara Hvistendahl, Sam Kean, Eli Kintisch, Kai Kupferschmidt(Berlin), Andrew Lawler, Christina Larson(Beijing), Mitch Leslie, Charles C. Mann, Eliot Marshall, Virginia Morell, Dennis Normile(Tokyo), Heather Pringle, Tania Rabesandratana(London), Gretchen Vogel(Berlin), Lizzie Wade(Mexico City) **CAREERS** Donisha Adams, Rachel Bernstein **COPY EDITORS** Julia Cole, Jennifer Levin (Chief) **ADMINISTRATIVE SUPPORT** Jessica Williams

Executive Publisher Rush D. Holt

Publisher Kent R. Anderson **Chief Digital Media Officer** Rob Covey

BUSINESS OPERATIONS AND PORTFOLIO MANAGEMENT DIRECTOR Sarah Whalen **BUSINESS SYSTEMS AND FINANCIAL ANALYSIS DIRECTOR** Randy Yi **MANAGER OF FULFILLMENT SYSTEMS** Neal Hawkins **SYSTEMS ANALYST** Nicole Mehmedovic **ASSISTANT DIRECTOR, BUSINESS OPERATIONS** Eric Knott **MANAGER, BUSINESS OPERATIONS** Jessica Tierney **BUSINESS ANALYSTS** Cory Lipman, Cooper Tilton, Celeste Troxler **FINANCIAL ANALYST** Robert Clark **RIGHTS AND PERMISSIONS ASSISTANT DIRECTOR** Emilie David **PERMISSIONS ASSOCIATE** Elizabeth Sandler **RIGHTS, CONTRACTS, AND LICENSING ASSOCIATE** Lili Kiser

MARKETING DIRECTOR Ian King **MARKETING MANAGER** Julianne Wielga **MARKETING ASSOCIATE** Elizabeth Sattler **SR. MARKETING EXECUTIVE** Jennifer Reeves **SR. ART ASSOCIATE, PROJECT MANAGER** Tzeitel Sorrosra **ART ASSOCIATE** Seil Lee **SR. ART ASSOCIATE** Kim Huynh **ASSISTANT COMMERCIAL EDITOR** Selby Frame **MARKETING PROJECT MANAGER** Angelissa McArthur **PROGRAM DIRECTOR, AAAS MEMBER CENTRAL** Peggy Mihelich **FULFILLMENT SYSTEMS AND OPERATIONS** membership@aaas.org **MANAGER, MEMBER SERVICES** Pat Butler **SPECIALISTS** LaToya Casteel, Terrance Morrison, Latasha Russell **MANAGER, DATA ENTRY** Mickie Napoleoni **DATA ENTRY SPECIALISTS** JJ Regan, Brenden Aquilino, Fiona Giblin

DIRECTOR, SITE LICENSING Tom Ryan **DIRECTOR, CORPORATE RELATIONS** Eileen Bernadette Moran **SR. PUBLISHER RELATIONS SPECIALIST** Kiki Forsyth **PUBLISHER RELATIONS MANAGER** Catherine Holland **PUBLISHER RELATIONS, EASTERN REGION** Keith Layson **PUBLISHER RELATIONS, WESTERN REGION** Ryan Rexroth **SALES RESEARCH COORDINATOR** Aiesha Marshall **MANAGER, SITE LICENSE OPERATIONS** Iquo Edim **SENIOR PRODUCTION SPECIALIST** Robert Koepke **SENIOR OPERATIONS ANALYST** Lana Guz **FULFILLMENT ASSISTANT** Judy Lillibridge **ASSOCIATE DIRECTOR, MARKETING** Christina Schlecht **MARKETING ASSOCIATES** Thomas Landreth, Isa Sesay-Bah

DIRECTOR OF WEB TECHNOLOGIES Ahmed Khadr **SR. DEVELOPER** Chris Coleman **DEVELOPERS** Dan Berger, Jimmy Marks **SR. PROJECT MANAGER** Trista Smith **SYSTEMS ENGINEER** Luke Johnson

CREATIVE DIRECTOR, MULTIMEDIA Martyn Green **DIRECTOR OF ANALYTICS** Enrique Gonzales **SR. WEB PRODUCER** Sarah Crespi **WEB PRODUCER** Alison Crawford **VIDEO PRODUCER** Nguyen Nguyen **SOCIAL MEDIA PRODUCER** Meghna Sachdev

DIRECTOR OF OPERATIONS PRINT AND ONLINE Elizabeth Harman **DIGITAL/PRINT STRATEGY MANAGER** Jason Hillman **QUALITY TECHNICAL MANAGER** Marcus Spiegler **PROJECT ACCOUNT MANAGER** Tara Kelly **DIGITAL PRODUCTION MANAGER** Lisa Stanford **ASSISTANT MANAGER DIGITAL/PRINT** Rebecca Doshi **SENIOR CONTENT SPECIALISTS** Steve Forrester, Antoinette Hodal, Lori Murphy, Anthony Rosen **CONTENT SPECIALISTS** Jacob Hedrick, Kimberley Oster

DESIGN DIRECTOR Beth Rakouskas **DESIGN EDITOR** Marcy Atarod **SENIOR DESIGNER** Garvin Grullón **DESIGNER** Chrystal Smith **GRAPHICS MANAGING EDITOR** Alberto Cuadra **SENIOR SCIENTIFIC ILLUSTRATORS** Chris Bickel, Katharine Sutliff **SCIENTIFIC ILLUSTRATOR** Valerie Altounian **SENIOR ART ASSOCIATES** Holly Bishop, Preston Huey **SENIOR PHOTO EDITOR** William Douthitt **PHOTO EDITORS** Leslie Bilzard, Christy Steele

DIRECTOR, GLOBAL COLLABORATION, CUSTOM PUBLICATIONS, ADVERTISING Bill Moran **EDITOR, CUSTOM PUBLISHING** Sean Sanders: 202-326-6430 **ASSISTANT EDITOR, CUSTOM PUBLISHING** Tianna Hicklin: 202-326-6463 **ADVERTISING MARKETING MANAGER** Justin Sawyers: 202-326-7061 **science.advertising@aaas.org** **ADVERTISING MARKETING ASSOCIATE** Javia Flemmings **ADVERTISING SUPPORT MANAGER** Karen Foote: 202-326-6740 **ADVERTISING PRODUCTION OPERATIONS MANAGER** Deborah Tompkins **SR. PRODUCTION SPECIALIST/GRAPHIC DESIGNER** Amy Hardcastle **PRODUCTION SPECIALIST** Yuse Lajiminnuh **SR. TRAFFIC ASSOCIATE** Christine Hall **SALES COORDINATOR** Shirley Young **ASSOCIATE DIRECTOR, COLLABORATION, CUSTOM PUBLICATIONS/CHINA/TAIWAN/KOREA/SINGAPORE** Ruolei Wu: +86-186 0082 9345, rwu@aaas.org **COLLABORATION/ CUSTOM PUBLICATIONS/JAPAN** Adarsh Sandhu + 81532-81-5142 asandhu@aaas.org **EAST COAST/E. CANADA** Laurie Faraday: 508-747-9395, FAX 617-507-8189 **WEST COAST/W. CANADA** Lynne Stickrod: 415-931-9782, FAX 415-520-6940 **MIDWEST** Jeffrey Dembski: 847-498-4520 x3005, Steven Loerch: 847-498-4520 x3006 **UK EUROPE/ASIA** Roger Gonçalves: TEL/FAX +41 43 243 1358 **JAPAN** Katsuyoshi Fukamizu(Tokyo): +81-3-3219-2773 kfukamizu@aaas.org **CHINA/TAIWAN** Ruolei Wu: +86-186 0082 9345, rwu@aaas.org

WORLDWIDE ASSOCIATE DIRECTOR OF SCIENCE CAREERS Tracy Holmes: +44 (0) 1223 326525, FAX +44 (0) 1223 326532 tholmes@science-int.co.uk **CLASSIFIED** advertise@sciencecareers.org **U.S. SALES** Tina Burks: 202-326-6577 **Nancy Toema**: 202-326-6578 **SALES ADMINISTRATOR** Marci Gallun **EUROPE/ROW SALES** Axel Gesatzki, Sarah Lelange **SALES ASSISTANT** Kelly Grace **JAPAN** Hiroyuki Mashiki(Kyoto): +81-75-823-1109 hmashiki@aaas.org **CHINA/TAIWAN** Ruolei Wu: +86-186 0082 9345, rwu@aaas.org **MARKETING MANAGER** Allison Pritchard **MARKETING ASSOCIATE** Aimee Aponte

AAAS BOARD OF DIRECTORS **RETIRING PRESIDENT, CHAIR** Gerald R. Fink **PRESIDENT** Geraldine (Geri) Richmond **PRESIDENT-ELECT** Barbara A. Schaaf **TREASURER** David Evans **SHAW CHIEF EXECUTIVE OFFICER** Rush D. Holt **BOARD** Bonnie L. Bassler, May R. Berenbaum, Carlos J. Bustamante, Stephen P.A. Fodor, Claire M. Fraser, Michael S. Gazzaniga, Laura H. Greene, Elizabeth Loftus, Mercedes Pascual

SUBSCRIPTION SERVICES For change of address, missing issues, new orders and renewals, and payment questions: 866-434-AAAS (2227) or 202-326-6417, FAX 202-842-1065. Mailing addresses: AAAS, P.O. Box 96178, Washington, DC 20090-6178 or AAAS Member Services, 1200 New York Avenue, NW, Washington, DC 20005

INSTITUTIONAL SITE LICENSES 202-326-6755 **REPRINTS:** Author Inquiries 800-635-7181 **COMMERCIAL INQUIRIES** 803-359-4578 **PERMISSIONS** 202-326-6765, permissions@aaas.org **AAAS Member Services** 202-326-6417 or http://membercentral.aaas.org/discounts

Science serves as a forum for discussion of important issues related to the advancement of science by publishing material on which a consensus has been reached as well as including the presentation of minority of conflicting points of view. Accordingly, all articles published in Science—including editorials, news and comment, and books reviews—are signed and reflect the individual views of the authors and not official points of view adopted by AAAS or the institutions with which the authors are affiliated.

INFORMATION FOR AUTHORS See pages 678 and 679 of the 6 February 2015 issue or access www.sciencemag.org/about/authors

SENIOR EDITORIAL BOARD

Robert H. Grubbs, *California Institute of Technology*, Gary King, *Harvard University*
Susan M. Rosenberg, *Baylor College of Medicine*, Ali Shalatifard, *Northwestern University*
Feinberg School of Medicine, Michael S. Turner, *U. of Chicago*

BOARD OF REVIEWING EDITORS (Statistics board members indicated with \$)

Adriano Aguzzi, *U. Hospital Zürich*
Takuzo Aida, *U. of Tokyo*
Leslie Aiello, *Wenner-Gren Foundation*
Judith Allen, *U. of Edinburgh*
Sonia Altizer, *U. of Georgia*
Sebastian Amigorena, *Institut Curie*
Kathryn Anderson, *Memorial Sloan-Kettering Cancer Center*
Meinrat O. Andreae, *Max-Planck Inst. Mainz*
Paola Arlotta, *Harvard U.*
Johan Auwerx, *EPFL*
David Awschalom, *U. of Chicago*
Jordi Bascompte, *Estación Biológica de Doñana CSIC*
Facundo Batista, *Londón Research Inst.*
Ray H. Baughman, *U. of Texas, Dallas*
David Baum, *U. of Wisconsin*
Carlo Beenakker, *Leiden U.*
Kamran Behnia, *ESPCI-ParisTech*
Yasmine Belkaid, *NIH/NIH*
Philip Benfey, *Duke U.*
Stephen J. Benkovic, *Penn State U.*
May Berenbaum, *U. of Illinois*
Gabriele Bergers, *U. of California, San Francisco*
Bradley Bernstein, *Massachusetts General Hospital*
Peer Bork, *EMBL*
Bernard Bourdon, *Ecole Normale Supérieure de Lyon*
Chris Bowler, *Ecole Normale Supérieure*
Ian Boyd, *U. of St. Andrews*
Emily Brodsky, *U. of California, Santa Cruz*
Ron Brookmeyer, *U. of California Los Angeles (\$)*
Christian Büchel, *Hamburg-Eppendorf*
Joseph A. Burns, *Cornell U.*
Gyorgy Buzsáki, *New York U. School of Medicine*
Blanche Capel, *Duke U.*
Mats Carlsson, *U. of Oslo*
David Clapham, *Children's Hospital Boston*
David Clary, *U. of Oxford*
Joel Cohen, *Rockefeller U., Columbia U.*
James Collins, *Boston U.*
Robert Cook-Deegan, *Duke U.*
Alan Cowman, *Walter & Eliza Hall Inst.*
Robert H. Crabtree, *Yale U.*
Roberta Croce, *Vrije Universiteit*
Janet Currie, *Princeton U.*
Jeff L. Dangl, *U. of North Carolina*
Tom Daniel, *U. of Washington*
Frans de Waal, *Emory U.*
Stanislas Dehaene, *Collège de France*
Robert Desimone, *MIT*
Claude Desplan, *New York U.*
Ap Dijksterhuis, *Radboud U. of Nijmegen*
Dennis Discher, *U. of Pennsylvania*
Gerald W. Dorn II, *Washington U. School of Medicine*
Jennifer A. Doudna, *U. of California, Berkeley*
Bruce Dunn, *U. of California, Los Angeles*
Christopher Dye, *WHO*
Todd Ehlers, *U. of Tuebingen*
David Ehrhardt, *Carnegie Inst. of Washington*
Tim Elston, *U. of North Carolina at Chapel Hill*
Gerhard Ertl, *Fritz-Haber-Institut, Berlin*
Barry Everitt, *U. of Cambridge*
Ernst Fehr, *U. of Zurich*
Anne C. Ferguson-Smith, *U. of Cambridge*
Michael Feuer, *The George Washington U.*
Toren Finkel, *NHLBI, NIH*
Kate Fitzgerald, *U. of Massachusetts*
Peter Fratzl, *Max-Planck Inst.*
Elaine Fuchs, *Rockefeller U.*
Daniel Geschwind, *UCLA*
Andrew Gewirth, *U. of Illinois*
Karl-Heinz Glassmeier, *TU Braunschweig*
Ramon Gonzalez, *Rice U.*
Julia R. Greer, *Caltech*
Elizabeth Grove, *U. of Chicago*
Nicolas Gruber, *ETH Zurich*
Kip Guy, *St. Jude's Children's Research Hospital*
Taekjip Ha, *U. of Illinois at Urbana-Champaign*
Christian Haass, *Ludwig Maximilians U.*
Steven Hahn, *Fred Hutchinson Cancer Research Center*
Michael Hasselmo, *Boston U.*
Martin Heimann, *Max-Planck Inst. Jena*
Yka Helariutta, *U. of Cambridge*
James A. Hendler, *Rensselaer Polytechnic Inst.*
Janet C. Hering, *Swiss Fed. Inst. of Aquatic Science & Technology*
Kai-Uwe Hinrichs, *U. of Bremen*
Kei Hirose, *Tokyo Inst. of Technology*
David Hodell, *U. of Cambridge*
David Holden, *Imperial College*
Laura Hooper, *UT Southwestern Medical Ctr. at Dallas*
Raymond Huey, *U. of Washington*
Steven Jacobson, *U. of California, Los Angeles*
Kai Johnsson, *EPFL Lausanne*
Peter Jonas, *Inst. of Science & Technology (IST) Austria*
Matt Kaeblerlein, *U. of Washington*
William Kaelin Jr., *Dana-Farber Cancer Inst.*
Daniel Kahne, *Harvard U.*
Daniel Kammen, *U. of California, Berkeley*
Masashi Kawasaki, *U. of Tokyo*
Y. Narry Kim, *Seoul National U.*
Joel Kingsolver, *U. of North Carolina at Chapel Hill*
Robert Kingston, *Harvard Medical School*
Etienne Kochlin, *Ecole Normale Supérieure*
Alexander Koldkin, *Johns Hopkins U.*
Alberto R. Kornblitt, *U. of Buenos Aires*
Leonid Kruglyak, *UCLA*
Thomas Langer, *U. of Cologne*
Mitchell A. Lazar, *U. of Pennsylvania*
David Lazer, *Harvard U.*
Thomas Lecuit, *IBDM*
Virginia Lee, *U. of Pennsylvania*
Stanley Lemon, *U. of North Carolina at Chapel Hill*
Ottoline Leyser, *Cambridge U.*
Marcia C. Linn, *U. of California, Berkeley*
Jianguo Liu, *Michigan State U.*
Luis Liz-Marzan, *CSIC biomagUNE*
Jonathan Losos, *Columbia U.*
Ke Lu, *Chinese Acad. of Sciences*
Christian Lüscher, *U. of Geneva*
Laura Machesky, *CRUK Beatson Inst. for Cancer Research*
Anne Magurran, *U. of St. Andrews*
Oscar Marin, *CSIC & U. Miguel Hernández*
Charles Marshall, *U. of California, Berkeley*
C. Robertson McClung, *Dartmouth College*
Graham Medley, *U. of Warwick*
Tom Misteli, *NCI*
Yasushi Miyashita, *U. of Tokyo*
Mary Ann Moran, *U. of Georgia*
Richard Morris, *U. of Edinburgh*
Alison Moutser-Reif, *NC State U. (\$)*
Sean Munro, *MRC Lab. of Molecular Biology*
Thomas Murray, *The Hastings Center*
James Nelson, *Stanford U. School of Med.*
Daniel Neumark, *U. of California, Berkeley*
Kitty Nijmeijer, *U. of Twente*
Pär Nordlund, *Karolinska Inst.*
Helga Nowotny, *European Research Advisory Board*
Ben Olken, *MIT*
Joe Orenstein, *U. of California*
Berkeley & Lawrence Berkeley National Lab
Harry Orr, *U. of Minnesota*
Andrew Oswald, *U. of Warwick*
Steve Palumbi, *Stanford U.*
Jane Parker, *Max-Planck Inst. of Plant Breeding Research*
Giovanni Parmigiani, *Dana-Farber Cancer Inst. (\$)*
Donald R. Paul, *U. of Texas, Austin*
John H. J. Petrini, *Memorial Sloan-Kettering Cancer Center*
Joshua Plotkin, *U. of Pennsylvania*
Albert Pollman, *FOM Institute AMOLF*
Philipp Poulin, *CNRS*
Jonathan Prichard, *Stanford U.*
David Randall, *Colorado State U.*
Colin Renfrew, *U. of Cambridge*
Felix Rey, *Institut Pasteur*
Trevor Robbins, *U. of Cambridge*
Jim Roberts, *Fred Hutchinson Cancer Research Ctr.*
Barbara A. Romanowicz, *U. of California, Berkeley*
Jens Rostrup-Nielsen, *Haldor Topsøe*
Mike Ryan, *U. of Texas, Austin*
Mittori Saitou, *Kyoto U.*
Shimon Sakaguchi, *Kyoto U.*
Miguel Salmeron, *Lawrence Berkeley National Lab*
Jürgen Sandkühner, *Medical U. of Vienna*
Alexander Schlier, *Harvard U.*
Randy Seeley, *U. of Cincinnati*
Vladimir Shalay, *Purdue U.*
Robert Siliciano, *Johns Hopkins School of Medicine*
Denis Simon, *Arizona State U.*
Alison Smith, *Johns Innes Centre*
Richard Smith, *U. of North Carolina (\$)*
John Speakman, *U. of Aberdeen*
Allan C. Spradling, *Carnegie Institution of Washington*
Jonathan Sprent, *Garvan Inst. of Medical Research*
Eric Steig, *U. of Washington*
Paula Stephan, *Georgia State U. and National Bureau of Economic Research*
Molly Stevens, *Imperial College London*
V. S. Subrahmanian, *U. of Maryland*
Ira Tabas, *Columbia U.*
Sarah Teichmann, *Cambridge U.*
John Thomsen, *North Carolina State U.*
Shubha Tole, *Tata Institute of Fundamental Research*
Christopher Tyler-Smith, *The Wellcome Trust Sanger Inst.*
Herbert Virgin, *Washington U.*
Berth Vogelstein, *Johns Hopkins U.*
Cynthia Volkert, *U. of Göttingen*
Douglas Wallace, *Dalhousie U.*
David Wallace, *Weizmann Inst. of Science*
Ian Walmsley, *U. of Oxford*
Jane-Ling Wang, *U. of California, Davis*
David A. Wardle, *Swedish U. of Agric. Sciences*
David Waxman, *Fudan U.*
Jonathan Weissman, *U. of California, San Francisco*
Chris Wikle, *U. of Missouri (\$)*
Ian A. Wilson, *The Scripps Res. Inst. (\$)*
Timothy D. Wilson, *U. of Virginia*
Rosemary Wyse, *Johns Hopkins U.*
Jan Zaenen, *Leiden U.*
Kenneth Zaret, *U. of Pennsylvania School of Medicine*
Jonathan Zehr, *U. of California, Santa Cruz*
Len Zon, *Children's Hospital Boston*
Maria Zuber, *MIT*

BOOK REVIEW BOARD

David Bloom, *Harvard U.*, Samuel Bowring, *MIT*, Angela Creager, *Princeton U.*, Richard Swedner, *U. of Chicago*, Ed Wasserman, *DuPont*

Preparing for the next Katrina

Ten years ago, Katrina, a category 5 hurricane at peak strength, slammed into New Orleans. Its associated storm surge breached the extensive levee system that had protected the city. Nearly 2000 residents died, and damages exceeded \$100 billion. The storm remains the costliest natural disaster in U.S. history, and the resulting economic, social, and environmental turmoil led to the largest mass migration since the U.S. Civil War. A distinguished panel* of scientists and engineers who had been on the scene of Katrina was convened on the eve of the 10th anniversary of this event to address the question: Are American cities better prepared for the next major hurricane?

The good news is that cities are better prepared, according to the panelists. Today, it is routine for agencies such as the U.S. Army Corps of Engineers to apply a systems-based approach for managing disaster: a strategy that recognizes that communication is just as important as a seawall, and that applies appropriate risk management to system operation. The growth in the use of social media to broadcast timely and authoritative information to the public and to receive situational reports from the public has been phenomenal. During the Tulsa flooding this past June, public engagement with the Army Corps of Engineers' social media outlet grew from 5 million to 65 million hits.

Nevertheless, there is much more that can be done to prepare cities for the inevitable. Communities need to be thinking beyond seawalls for future flood and hurricane protection. Alternative routes to resilience include restoring salt marshes and oyster flats or installing more modular structures that "stage" as a disaster unfolds.

The human dimension of hurricanes also needs attention, such as collecting behavioral data on the factors that influence decisions on whether to evacuate or stay put, rebuild or relocate, etc. Many residents refused to

evacuate in the face of Katrina because shelters would not accept pets, for example. A sensible recommendation (from the Select Bipartisan Committee to Investigate the Preparation for and Response to Hurricane Katrina) was to turn the 9th Ward of New Orleans into green space, because it is below sea level. However, residents insisted on returning to that region—their home. Indeed, community members want to decide where they will live and

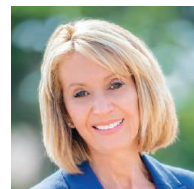
how much they are willing to invest to live there. The challenge is to provide the science and engineering information in a transparent way, along with concepts of resilience and risk, so that people are clearly aware of all the relevant factors when they make up their minds about where they will live.

The hurricane panelists frequently used the earthquake community as a role model to emulate. Annual events such as the "Great ShakeOut" convince people worldwide that they are vulnerable to seismic events, prepare them mentally to take action, and show them how to survive. Another promotion has been for residents in earthquake country to keep prepackaged

earthquake survival kits handy. Both ideas are readily transferable to the many at risk from hurricanes. U.S. earthquake resilience benefitted greatly from international collaboration with Japan, Chile, China, and other partners, who shared their knowledge of how engineered structures respond to various ground shaking, and their successes with early warning systems during rare seismic events. By comparison, hurricane resilience research has lacked an international perspective, despite the large number of nations that experience typhoons and similar severe coastal storms.

Like all other natural disasters, it is not a question of if, but when. We know which U.S. cities are the most at risk. Everyone must work together to make them the most prepared.

— Marcia McNutt



Marcia McNutt
Editor-in-Chief
Science Journals



"Communities need to be thinking beyond seawalls for future flood and hurricane protection."

*The panel consisted of Gregory Baecher, University of Maryland; Thomas Bostick, U.S. Army Corps of Engineers; Wayne Clough, former secretary of the Smithsonian Institution; Reginald DesRoches, Georgia Institute of Technology; Alton Romig Jr., National Academy of Engineering; and Lauren Sauer, Johns Hopkins School of Medicine.

“I’d like for the last guinea worm to die before I do.”

Former U.S. President Jimmy Carter, at a press conference on his cancer diagnosis. Since its creation in 1986, the Carter Center has helped reduce guinea worm disease incidence from 3.6 million to 11 known cases globally.

IN BRIEF

IS group destroys ancient temple



Palmyra's Temple of Baalshamin (here in 2008) was destroyed by the IS group.

Fighters from the Islamic State (IS) group have blown up the 2000-year-old Temple of Baalshamin (above) in the ancient trade route city of Palmyra, Syria. The IS group has held Palmyra since May, when its military commanders had promised to “destroy idols” but spare historic buildings (*Science*, 5 June, p. 1064). The temple, which mixed elements of local and Greco-Roman architecture, was among the best-preserved buildings in the old city and declared a UNESCO World Heritage Site in 1980. News of its destruction—which may have taken place as far back as July—came 1 week after IS group militants beheaded archaeologist and historian Khaled al-Asaad, Palmyra’s director of antiquities for 40 years. The researcher was accused of apostasy and representing Syria at “infidel” conferences. “The systemic destruction of cultural symbols embodying Syrian cultural diversity reveals the true intent of such attacks, which is to deprive the Syrian people of its knowledge, its identity, and history,” UNESCO Director-General Irina Bokova said in a statement on Monday. IS group fighters have destroyed other ruins across Syria and Iraq, including the ancient Assyrian city of Nimrud in March.

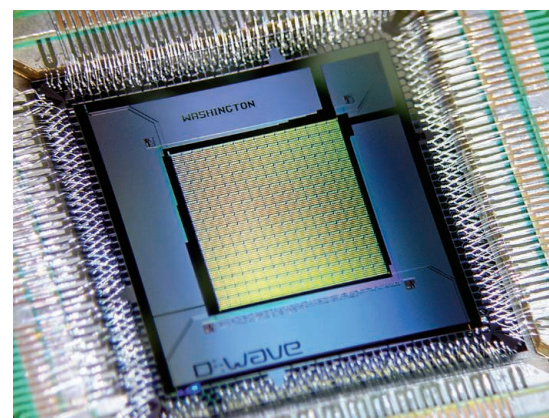
AROUND THE WORLD

More Hawaiian telescope arrests

MAUNA KEA, HAWAII | The construction of Hawaii’s Thirty Meter Telescope (TMT) on the summit of Mauna Kea—which many Hawaiians consider to be sacred land—has drawn hundreds of protestors and national headlines (*Science*, 3 July, p. 8). But another telescope project on another sacred mountain is increasingly drawing protestors’ ire. On 20 August, eight people—including a leader of the TMT protests—were arrested as they attempted to block construction of the Daniel K. Inouye Solar Telescope atop Haleakala volcano on Maui; another 20 had been arrested at the end of July. That project has been under construction since November 2012 and is about 80% complete.

Quantum chip doubles the qubits

BURNABY, CANADA | D-Wave Systems, which calls itself “the quantum computing company,” released a new processor this week. Ordinary computers flip bits that can be set to 0 or 1; quantum computers use qubits that can be set to 0, 1, or—thanks to quantum weirdness—0 and 1 simultaneously. In the D-Wave machine, each qubit is a tiny ring of superconductor in which electricity can run one way, the other, or both ways at once. The previous chip had 512 qubits; the new one has 1152. The processor works by finding the



D-Wave’s newest quantum processor breaks the “1000-qubit barrier,” with 1152 qubits.

lowest energy state of the qubits as various interactions between them are ramped up to encode a problem to be solved. D-Wave also reported tests in which the improved chip outpaced ordinary computers. But the tests were all different versions of randomly assigned interactions between qubits. How well the chip handles realistic computing challenges such as search algorithms remains to be seen.

'Female Viagra' company bought

WASHINGTON, D.C. | The U.S. Food and Drug Administration (FDA) gave its stamp of approval on 18 August to the first-ever sex drive enhancement drug for women, called Addyi. Just 2 days later, Valeant Pharmaceuticals announced their acquisition of Addyi and its former parent company Sprout Pharmaceuticals, for \$1 billion. It's been a long road for Addyi: FDA rejected it twice on grounds of statistically insignificant effectiveness and potentially harmful side effects. But results from a reformatted, third clinical trial proved significant, and FDA waved the drug forward. Scientists have shown Addyi regulates neurotransmitters that are thought to kindle desire, but the exact mechanisms remain unclear. Along with its approval, FDA also mandated that follow-up trials for Addyi be conducted to better understand the potential side effects, especially among consumers of alcohol. http://scim.ag/_Addyi

Coca-Cola responds to critics

ATLANTA | Coca-Cola has come under fire for its support of a nonprofit organization that has used medical journals and social media to promote the message that exercise, not diet, is primarily to blame for America's obesity epidemic. According to a report in *The New York Times* earlier this month, the company donated \$1.5 million last year to help start the Global Energy Balance Network, and provided another \$4 million in funding to two of its founding members. Some scientists have suggested that the nonprofit's message is intended to deflect attention from research supporting links between sugary drinks and obesity and type 2 diabetes. The company has scrambled to respond; a statement by Coca-Cola Co. Chairman and CEO Muhtar Kent published 19 August in *The Wall Street Journal* expressed disappointment that the company's actions "to fund scientific research and health and well-being programs have served only to create more confusion and mistrust," and pledged more transparency in its research efforts.



A dead fin whale calf in May (top). Bears feed on a fin whale carcass in June (bottom).

Unexplained whale deaths in the Gulf of Alaska

The deaths of 30 large whales in the Gulf of Alaska represent an "unusual mortality event" (UME), the National Oceanic and Atmospheric Administration (NOAA) announced last week. Such a designation triggers a focused investigation into the cause of the deaths, which now number more than three times the normal annual average, NOAA Fisheries lead marine mammal scientist Teri Rowles said at a press conference 20 August. It's the 61st UME since the Marine Mammal Protection Act was established in 1991; scientists have determined the cause of only 29 of those. The current event is the "most difficult" type, Rowles said, because most of the carcasses are floating in the ocean rather than washed up on beaches, making samples difficult to obtain. Furthermore, accessing the beached whales can be tricky, she said, because of "predator competition for samples"—from bears, for example. One possible explanation for the UME is biotoxins from harmful algal blooms, but there is now no conclusive evidence linking such blooms to the whale deaths. Other possible causes of death could include an infectious disease or human interactions.



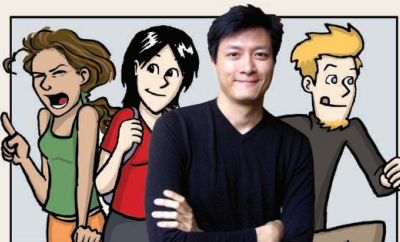
Status: **In a Relationship**

With: My thesis

And: *It's complicated.*

Ph.D. woes earn cinematic sequel

Four years ago, former engineer Jorge Cham took his popular online comic *Piled Higher and Deeper* (or *PHD*) to the big screen. An ensemble of California Institute of Technology researchers, including Alexandra Lockwood (above, in *PHD2*), produced and starred in a movie version of the comic, which depicts the trials and tribulations of being a graduate student in the sciences. Next month, *The PHD Movie 2: Still in Grad School* hits theaters. *Science* and Cham exchanged emails about the upcoming sequel. <http://scim.ag/JorgeCham>



Q: Why go through this insanity again?

A: The main catalyst was the increasing number of fans who would approach me at events and ask if there was going to be a sequel. ... The first movie was produced, directed and acted by mostly all grad students and academics. One of the themes of the second movie is collaboration ... we brought in a professional director (Iram Parveen Bilal), crew, and also professional actors to up the game.

Q: Does the sequel tackle any newly emerging career issues?

A: I tried to incorporate a lot of the things that people are talking about these days: how hard it is to get funding, the lack of representation of women in academia, the limited number of academic jobs available, ethical boundaries in research, among others. I think mostly I tried to reflect the general feeling of self-assessment that I'm sensing from grad students and administrators about what is a Ph.D., and what it is for, and what it entails.

Q: Does your sequel have more characters and explosions?

A: There aren't any explosions, but ... our cast list for this movie had over 50 characters!

FINDINGS

Early breast lesions overtreated?

One of the biggest puzzles in cancer treatment is how to define and tackle early-stage disease. A provocative study published last week in *JAMA Oncology* suggests that for women with a very early form of breast cancer, ductal carcinoma in situ (DCIS), doctors may be urging aggressive therapy that doesn't affect long-term mortality, regardless of treatment type (such as mastectomy or radiation).

There are about 60,000 DCIS diagnoses each year in the United States, making up more than 20% of breast cancer diagnoses (*Science*, 28 March 2014, p. 1454). The new observational study of more than 108,000 women with DCIS found that their chance of dying from breast cancer was 1.1% after 10 years and 3.3% after 20 years—similar to the risk for an average woman for the same time frames. Still, some cases of DCIS—for example, in younger women and in African-Americans—are much higher risk.

BY THE NUMBERS

1379

Minimum estimate of how many minerals on Earth remain undiscovered, based on an analysis of 4831 known minerals from 135,415 locations (*American Mineralogist*).

64

Tally of papers withdrawn last week by Springer from 10 of its journals, after an internal investigation revealed fake peer-review reports linked to the articles.

108

Age in years of the world's oldest message in a bottle, found last week on a North Sea island. The bottle was one of 1020 released between 1904 and 1906 by George Parker Bidder, former president of the Marine Biological Association in Plymouth, U.K.

Self-medicating ants

They may not keep it in a medicine cabinet, but ants dose themselves with hydrogen peroxide to stave off infection. Insects that live in dense social colonies like ants and bees are vulnerable to fungal diseases. Now, for the first time, scientists have observed ants self-medicating with hydrogen peroxide-laden food to prevent fungal infections. In a series of experiments, researchers showed that ants infected with a dangerous fungus had a higher survival rate if they were fed a solution spiked with hydrogen peroxide—and that the infected ants chose this diet, in seemingly careful dosages, over an innocuous solution laced with honey. In the wild, the animals could feed on aphids or decaying dead ants, which contain reactive chemicals similar to those in hydrogen peroxide to achieve the same effect, the researchers report in *Evolution*.



Researchers worry budget cuts could threaten the operation of Brazil's new Amazon Tall Tower Observatory, which makes atmospheric measurements.

BRAZIL

Fiscal crisis has Brazilian scientists scrambling

Government makes deep cuts in research budgets as economy stumbles

By **Herton Escobar**, in São Paulo, Brazil

Brazilian neuroscientist Suzana Herculano-Houzel spent years studying the brains of mammals, including mice, whales, and humans, to understand the forces that shape their intricate folds. The effort paid off last month, when the Federal University of Rio de Janeiro professor co-authored a high-profile paper showing that the folding is governed by a relatively straightforward mathematical relationship (*Science*, 3 July, p. 74). But even as Herculano-Houzel's research soared, she was struggling to solve a much more pragmatic equation: how to pay her laboratory bills amid one of the worst science funding crises to strike Brazil in decades.

Battling a slumping economy and debt, Brazil's federal government has taken an ax to spending, and it isn't sparing science. President Dilma Rousseff's administration has cut by 25% the Ministry of Science's projected 2015 budget of

7.3 billion reais (\$2 billion), and sliced 9% from the 48.8 billion real (\$13.7 billion) budget of the Ministry of Education, which plays an important role in funding graduate students. Research agencies are delaying payments for grants that have already been awarded, and have canceled or postponed new calls for proposals. And Rousseff is re-

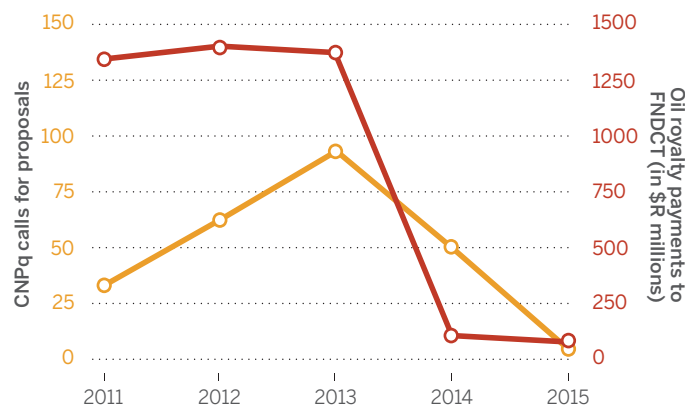
directing funds once earmarked largely for research to send Brazilian students abroad to study.

The funding climate is "the worst in 20 years," says Helena Nader, president of the Brazilian Society for the Advancement of Science (SBPC). Herculano-Houzel is even more pessimistic: "Brazilian science is bankrupt."

At the root of the problem are changes in how Brazil's government spends the royalties generated by the nation's lucrative offshore oil fields, which have been a major source of funding for science and technology development. As recently as 2013, oil royalties helped pump some 1.4 billion reais (roughly \$600 million at the time) into the country's National Fund for Scientific and Technological Development (FNDCT), which provides federal research agencies with the bulk of their funds. More recently, however, policy changes redirected much of the oil revenue from FNDCT into a new fund primarily focused on education and health.

Falling fortunes

As Brazil's government has reduced the flow of oil revenue into a national fund that supports research (red), the country's main science funding agency has cut back on calls for proposals (orange).



The results have been disastrous for Brazil's science ministry and its main funding agency, the National Council for Scientific and Technological Development (CNPq), which receives from FNDCT a large share of the money it hands out as grants. This year, the council expected to receive 1.2 billion reais (\$350 million) from the fund; it has gotten just 27% of that amount. As a result, CNPq has not announced some of its usual granting programs, including the Universal Call open to all research fields, and canceled others. Officials have also delayed announcing awards in a major competition to establish new virtual research institutes; the winners were supposed to be announced this past March. And CNPq is withholding payments on some 5500 existing grants it awarded in 2014's Universal Call. "The money just wasn't there," says Glaucius Oliva, a researcher at the Physics Institute of São Carlos and a former president of CNPq.

Herculano-Houzel is among the scientists waiting for payments. She holds a CNPq grant for 50,000 reais, but has gotten just 6500. That's better, however, than the zero payout she's received on another grant, awarded by a state funding agency. To keep her lab operating, she's loaning her own money to her project. "I owe myself some 15,000 reais already," she says.

Paulo Artaxo, a University of São Paulo physicist, worries the cuts will hamper one of Brazil's newest research efforts. Just last week, officials celebrated the opening of the 325-meter-high Amazon Tall Tower Observatory, which will collect atmospheric data deep in the Amazon (*Science*, 6 March, p. 1051). But the funding crisis is threatening "our ability to secure funds for its operation and long-term measurements," Artaxo says.

Scientists blame some of the cuts in FNDCT grants on the Rousseff administration's determination to protect one of its flagship programs, Science Without Borders, which is sending 100,000 students (mostly undergraduates) to study abroad. Last year, the program received 1 billion reais from the fund, and it may get the same sum this year. Science Without Borders "is important" but shouldn't come "at the expense of the entire scientific community," Nader says.

The Brazilian Academy of Sciences and SBPC are pleading with Rousseff to find new sources of funding—but so far to no avail. In the meantime, the science ministry officials have negotiated a \$2.5 billion loan from the Inter-American Development Bank to help researchers through the crisis, but Brazilian officials and lawmakers have yet to approve the deal. ■

REPRODUCIBILITY

Many psychology papers fail replication test

An effort to repeat 100 studies yields sobering results, but many researchers are positive about the process

By John Bohannon

The largest effort yet to replicate psychology studies has yielded both good and bad news. On the down side, of the 100 prominent papers analyzed, only 39% could be repli-

cated unambiguously, as a group of 270 researchers describes on page 943. On the up side, despite the sobering results, the effort seems to have drawn little of the animosity that greeted a similar replication effort last year (*Science*, 23 May 2014, p. 788). This time around, many of the original authors are praising the replications as a useful addition to their own research.

"This is how science works," says Joshua Correll, a psychologist at the University of Colorado, Boulder, and one of the authors whose results could not be replicated. "How else will we converge on the truth? Really, the surprising thing is that this kind of systematic attempt at replication is not more common."

That's encouraging news to Brian Nosek, a psychologist at the University of Virginia in Charlottesville who led the effort. "I don't know if replication is 'entirely ordinary' yet, but it is certainly more ordinary than it was [a few] years ago," he says. In that time, major psychology journals have started publishing replications alongside original research. "The change is pretty remarkable."

The mass replication effort began in 2011 with the goal of putting psychological science on more rigorous

experimental footing. The strategy was to replicate a sample of published studies using an approach that Nosek has popularized through the Center for Open Science, a nonprofit he founded in 2013: publish your experimental design first, receive open peer review on it, and only then carry out

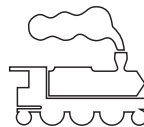
the experiment and share the results, no matter the outcome. That should reduce the number of papers that report statistically significant results that are actually false positives.

In the Open Science Collaboration, 270 psychologists from around the world signed up to replicate studies; they did not receive any funding. The group selected the studies to be replicated based on the feasibility of the experiment, choosing from those published in 2008 in three journals: *Psychological Science*, the *Journal of Personality and Social Psychology* (JPSP), and the *Journal of Experimental Psychology: Learning, Memory, and Cognition*. Not only were all 100 replications preregistered, but the authors of the original studies were invited to collaborate in the design of the replication.

The results lend support to the idea that scientists and journal editors are biased—consciously or not—in what they publish. For example, even in studies that could be replicated, the size of the effect—a measure of how much of a difference there was between the experiment groups—was on average only half as big as the original studies. The bias could be due to scientists throwing out negative

Real effect?

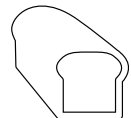
A 2008 study found that people were slower to correctly name an object when shown the names of similar objects. A replication of this study failed to find that effect.



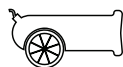
Carriage



Ankle



Cracker



Pistol



Ferry



Clam

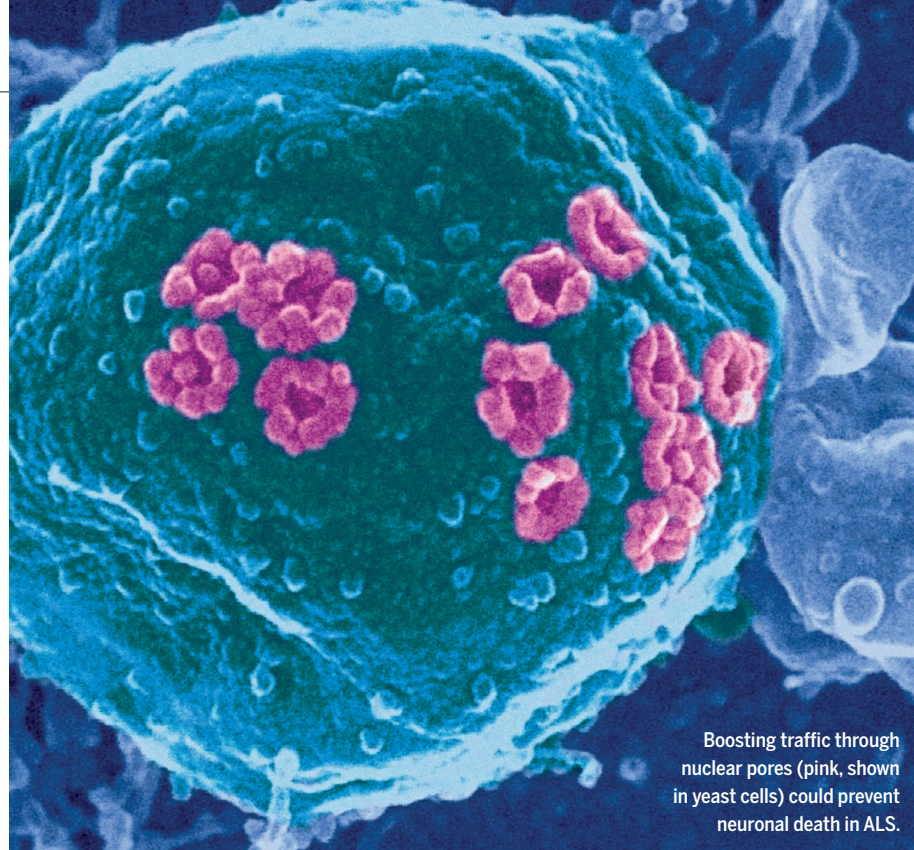
results, for example, or journal editors preferentially accepting papers with bigger effects. Some of the replications even found the opposite effect compared with the original paper. “This very well done study shows that psychology has nothing to be proud of when it comes to replication,” says Charles Gallistel, president of the Association for Psychological Science.

“Their data are sobering and present a clear challenge to the field,” says Lynne Cooper, a psychologist at the University of Missouri, Columbia, who became one of the editors of *JPSP* in January. Already, she says, the journal is instituting reforms. In order to encourage researchers to test published results, *JPSP* will publish more replications, Cooper says. The journal is also launching new policies that will encourage “authors, editors, and reviewers ... to reexamine and recalibrate basic notions about what constitutes good scholarship,” she says. The details have not yet been announced.

“Some will be tempted to conclude that psychology is a bad apple,” says Charles Carver, a psychologist at the University of Miami who was one of the editors of *JPSP* in 2008. He insists this is not the case. “This is a problem of science, medical science no less than behavioral science.” Replication efforts in other fields are equally low, says John Ioannidis, a biologist at Stanford University in Palo Alto, California, who suspects the true proportion of psychology papers that are not false positive is “something like 25% ... [which] seems to be in the same ballpark as what we see in many biomedical disciplines.”

Like most researchers contacted by *Science*, Correll says the exercise was “worth the effort,” no matter the outcome. That’s not to say Correll is disavowing his earlier results. In his 2008 *JPSP* study, his team asked subjects to identify images of weapons while simultaneously showing them images of people of different races. The goal was to test the idea that differences in the reaction times indicate a person’s implicit racial bias. They found that the variation in people’s response times had a nonrandom signature known as 1/f noise that predicted their bias.

But when Etienne LeBel’s lab at the University of Western Ontario in Canada repeated the experiment, they found 1/f noise, but the prediction did not hold. Correll says the failure “does not convince me that my original effects were [a] fluke. I know that other researchers have found similar patterns ... and my lab has additional data that supports our basic claim.” He is already working on the follow-up study. ■



Boosting traffic through nuclear pores (pink, shown in yeast cells) could prevent neuronal death in ALS.

NEUROSCIENCE

Plugged pores may underlie some ALS, dementia cases

Multiple groups reveal that “stutter” mutation kills nerve cells by clogging channels into the nucleus

By Emily Underwood

It is famous for robbing Lou Gehrig of his life and Stephen Hawking of his mobility and voice, but just how amyotrophic lateral sclerosis (ALS) destroys motor neurons in the brain and spinal cord remains a mystery. Now, scientists are converging on an explanation, at least for a fraction of the ALS cases caused by a specific mutation. In cells with the mutation, the new work shows, pores in the membrane separating the nucleus and cytoplasm become clogged, preventing vital molecules from passing through and creating a fatal cellular traffic jam.

For now, the work applies only to the mutation dubbed C9orf72—a DNA stutter in which a short nucleotide sequence, GGGGCC, is repeated hundreds to thousands of times in a gene on chromosome 9. Nor do the multiple labs reporting results this week agree on exactly what plugs those nuclear pores and how the cells die. Still, the work is “a major breakthrough”

in ALS research, says Amelie Gubitza, program director of the neurodegeneration division at the National Institute of Neurological Disorders in Bethesda, Maryland. The groups worked independently, starting with different hypotheses and experimental designs, yet reached similar conclusions, making the finding more convincing. And it suggests that boosting traffic through nuclear pores could be a new strategy for treating some cases of ALS and frontotemporal dementia (FTD), another neurodegenerative condition C9orf72 can cause.

Based on past work by their own and other groups, neuroscientists Jeff Rothstein and Tom Lloyd at Johns Hopkins University in Baltimore, Maryland, suspected that the long strands of excess RNA produced by C9orf72 cause neurodegeneration by binding to, and thus sequestering, key cellular proteins. The team tested the idea in fruit flies with the mutation, which display damage in the nerve cells of their eyes and in motor neurons.

They boosted the activity of 400 genes that encode candidate proteins. Increased amounts of one of them, RanGAP, which helps shuttle molecules through the nuclear pore, completely prevented neuronal degradation in the flies, the group reports in *Nature* this week. In neurons taken from flies as well as derived from stem cells from people with the C9orf72 mutation, increasing RanGAP improved nuclear traffic in the cells, clearing up abnormally distributed protein aggregations, the team also found.

Those findings are compelling in light of two “gorgeous” papers by other groups, says Steven McKnight, a biochemist at the University of Texas Southwestern Medical Center in Dallas. Unlike Rothstein and Lloyd, neither group started with preconceptions about which genes might counteract C9orf72’s toxicity, he notes. A group led by molecular biologist Paul Taylor of St. Jude Children’s Research Hospital in Memphis, Tennessee, and neuroscientist Fen-Biao Gao of the University of Massachusetts Medical School in Worcester, for example, performed an unbiased screen of more than 9000 fruit fly genes, looking for DNA variants that either suppressed or exaggerated the mutation’s deleterious effects. The team reports in *Nature* a very high hit rate among genes involved with nuclear pore transport, in line with the RanGAP findings.

Rothstein and Lloyd believe that what plugs the nuclear pores in C9orf72 carriers is the abnormal RNA itself, interacting with RanGAP and other cellular proteins. They found, for example, that they could counteract the toxic effects of the mutation by neutralizing the RNA with complementary nucleotide strands. But a third study, in *Nature Neuroscience*, points to a different villain.

Stanford University geneticist Aaron Gitler, in Palo Alto, California, and his team performed an unbiased genetic screen of their own. They genetically engineered yeast to make Pro-Arg, one of the proteins encoded by the C9orf72 mutation, but not to make long repetitive strands of RNA. Pro-Arg is

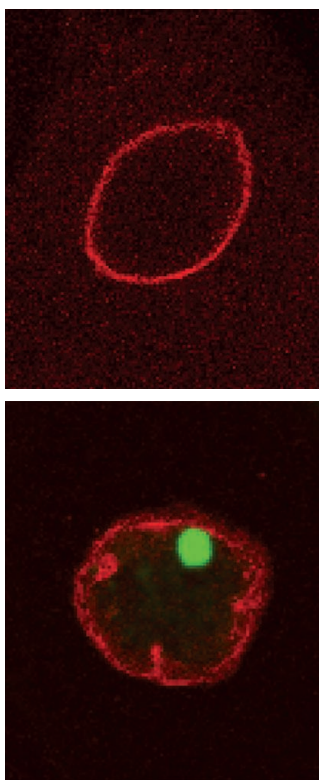
found in small concentrations in the post-mortem brain tissue of people with ALS, and previous studies have shown that protein alone is toxic to neurons as well as to yeast. Gitler’s study, like the other studies, showed that boosting nuclear transport helped the cells survive. The fact that the typical C9orf72 RNA was not present, however, persuades Gitler that Pro-Arg, and perhaps the other C9orf72-spawned proteins, are what block the nuclear pores—and would be the best targets of any therapeutic strategy.

Taylor believes “a case is building” for those proteins as the pore plugs, but he notes that his own results provide some support for both the RNA and protein hypotheses. “What’s really intriguing is that three different groups coming from different directions” all now agree that blockage of the nuclear pore is the central problem caused by the C9orf72 mutation, he says. Given that nuclear pores are known to degrade even in normal aging, “it is enticing to speculate” that their blockage or breakdown could play a role in a range of neurodegenerative processes, Rothstein’s group adds.

Because fewer than 10% of ALS cases are linked to the C9orf72 mutation, Gubitza says, the new results may not explain how other forms of ALS kill nerve cells, or why the mutation sometimes causes FTD instead. Still, she says, the abnormal buildup of proteins in the cell nucleus or cy-

toplasm—particularly of a protein called TDP-43—is a “unifying theme” across ALS and FTD cases.

An important next step, Gubitza adds, is to study cases of ALS and FTD without a known mutation to see whether those people have defects in genes governing nuclear transport. An answer could come from a new collaboration announced this month: The pharmaceutical company Biogen, the ALS Association, and Columbia University Medical Center plan to perform whole-genome sequencing of 1500 people with both inherited and sporadic forms of the disease. ■



Compared with the nucleus of a normal fly neuron (above), one from a fly with a common ALS mutation (below) has choppy clusters of nuclear pore protein (red) around its edges. In green, an abnormal cluster of the protein poly(GP).

ENERGY

Dark horse scores a fusion coup

California company shows new approach to trapping hot plasma

By Daniel Clery, in Foothill Ranch, California

Nuclear fusion has always required titanic machines and billions of dollars in public money—and success is always decades away. Now, a privately funded company here has taken what some physicists say is a significant step toward mastering fusion energy with a smaller, cheaper, faster approach. Tri Alpha Energy announced this week that it has built a machine that forms a ball of gas—superheated to about 10 million degrees Celsius—and holds it steady for 5 milliseconds without decaying.

Those conditions are well short of what is needed for fusion, but the feat shows for the first time that Tri Alpha’s unorthodox approach can trap hot fusion gas, or plasma, in a steady state. “Until you learn to control and tame [plasma], it’s never going to work,” says Jaeyoung Park, head of the rival fusion startup Energy/Matter Conversion Corporation in San Diego, California. “In that regard, it’s a big deal. They seem to have found a way to tame it.” The claims have not yet been peer-reviewed, but the company says a paper is in preparation.

Now, the scientists hope to scale up the technique toward times and temperatures sufficient to cause atomic nuclei in the gas to fuse together, releasing energy.

The burgeoning cost and complexity of huge government-funded projects—including the \$20 billion ITER reactor, under construction in France, and the U.S. Department of Energy’s \$4 billion National Ignition Facility (NIF) in Livermore, California—have raised doubts that they will ever produce plants that generate affordable energy. Tri Alpha and a handful of other startups take a different approach, which promises simpler, cheaper machines that can be developed more quickly (*Science*, 25 July 2014, p. 370). Tri Alpha also aims to use a different fuel—a mix of hydrogen and boron—in place of the usual



hydrogen isotopes. Hydrogen-boron is harder to react, but Tri Alpha researchers say it would not produce the destructive floods of neutrons that are likely to plague conventional fusion power plants. For investors and outside experts, that has been a major draw, says plasma physicist David Hammer of Cornell University, also a Tri Alpha adviser. “They are where they are because people are able to believe they can get a [hydrogen-boron] reactor to work.”

Like other fusion techniques, Tri Alpha’s device aims to confine a superhot mixture of electrons and ions known as plasma and force the ions to fuse, converting some of their mass into energy. That requires temperatures of at least 100 million degrees Celsius with conventional fuel. To keep the plasma from melting the reactor vessel, facilities like NIF rapidly implode it, relying on its inward inertia to hold it for long enough for a burst of fusion reactions. In the other large-scale approach, at ITER and similar machines, powerful magnetic fields hold the plasma steady inside a doughnut-shaped chamber, known as a tokamak.

Tri Alpha’s machine also produces a doughnutlike blob of plasma, but it is shaped to generate its own confining magnetic field. This approach, known as a field-reversed configuration (FRC), has been known since the 1960s. Despite decades of work, however, researchers could get the blobs of plasma to last only about 0.3 milliseconds before they broke up or melted away. In 1998, physicist Norman Rostoker of the University of California, Irvine, and colleagues set up Tri Alpha to try a new approach, which would add beams of high-energy particles to the recipe. By last year the company, based

in an unremarkable—and unlabeled—industrial unit about 75 kilometers south of Los Angeles, employed 150 people and was working with C-2, a 23-meter-long tube ringed by magnets and bristling with equipment. The machine forms two smoke rings of plasma and fires them at nearly a million kilometers per hour toward its center, where they merge and transform their kinetic energy into heat.

The team also had to tame the turbulence and instability that plagued previous attempts at long-lasting FRCs. Rostoker, a theorist, believed the solution lay in firing beams of high-speed particles into the edge of the plasma. The fast-moving incomers would follow wide orbits in the plasma’s magnetic field, forming a sort of protective shell that would stiffen the plasma against both turbulence and instability.

To make it work, the Tri Alpha team needed to precisely control the magnetic conditions around the edge of the cigar-shaped FRC, which is a cylinder as much as 3 meters long and 40 centimeters across.

Clouds of particles will slam together in this reaction chamber, creating superhot gas.

They did it by penning in the plasma with magnetic fields generated by electrodes and magnets at each end of the long tube.

In experiments last year, C-2 produced FRCs that lasted 5 milliseconds, more than 10 times the previous record. “In 8 years, they went from an empty room to an FRC lasting 5 milliseconds. That’s pretty good progress,” Hammer says. But the FRCs still decayed. Last autumn the researchers dismantled C-2. In collaboration with Russia’s Budker Institute of Nuclear Physics in Akademgorodok, they upgraded the particle beam system, increasing its power from 2 megawatts to 10 megawatts and angling the beams to make better use of their power.

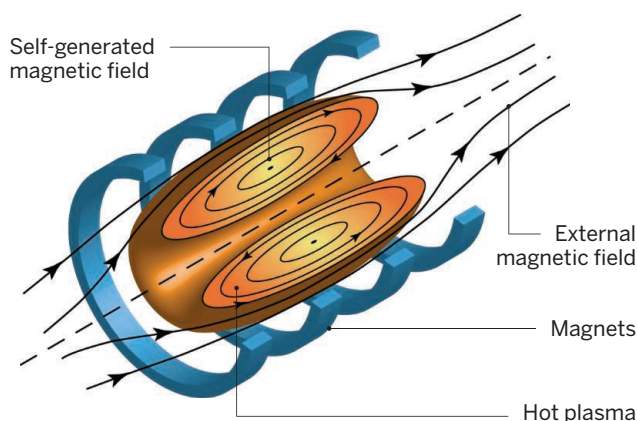
The upgraded C-2U was back in operation by March. At a symposium held this week in memory of Rostoker, who died in December, Tri Alpha’s chief technology officer Michl Binderbauer announced that by June the new machine was producing FRCs lasting 5 milliseconds with no sign of decay.

Binderbauer says that next year the team will build C-2W, an almost entirely new machine designed to achieve longer FRCs and higher temperature. A 10-fold increase in temperature would make their plasma hot enough to spark reactions in conventional fusion fuel, a mixture of the hydrogen isotopes deuterium and tritium, known as D-T. Tri Alpha’s goal—hydrogen-boron fusion—will require ion temperatures above 3 billion degrees Celsius. Plasma physicist Jon Menard of the Princeton Plasma Physics Laboratory in New Jersey, who was not involved in the project, says that would be “very challenging.”

At first glance, hydrogen-boron fuel doesn’t look promising. “It takes 30 times as much energy to cook, and you get half as much energy out per particle,” Binderbauer says. But boron is abundant, and the reaction produces no neutrons, just three alpha particles (helium nuclei)—hence the company’s name. Banishing the neutrons is an alluring prospect, because many researchers see them as a dealbreaker for D-T fusion in commercial reactors. Particle physicist Burton Richter of Stanford University in Palo Alto, California, is one of them. “I wouldn’t have spent 10 years on [Tri Alpha’s advisory] committee if it was working on a D-T system,” Richter says. ■

Control yourself!

Plasma “doughnuts” in Tri Alpha’s machine hold together thanks to their own self-generated magnetic fields.



BOTANY

Orchids' dazzling diversity explained

New family tree shows that a series of innovations accelerated speciation

By Erik Stokstad

What did Charles Darwin write to follow up *On the Origin of Species*? A treatise on the pollination of orchids. Darwin had marveled at the diversity of these plants, and he saw the myriad ways in which the flowers and pollinating insects have adapted to each other as an extended case study in natural selection. "The contrivances for insect fertilization in Orchids are multiform & truly wonderful & beautiful," he wrote to a horticulturist who had sent him specimens.

Evolutionary biologists never lost their fascination with orchids. With more than 25,000 species, they're the biggest group within the plant kingdom, comprising roughly 8% of all vascular plant species. Biologists have proposed various explanations for this extraordinary diversity, but it has been impossible to nail down their relative importance.

Now, a new family tree of the orchids is a major step in that direction. "For the first time, they have a well-supported phylogeny for all main branches," says orchidologist Barbara Gravendeel of the Naturalis Biodiversity Center in Leiden, the Netherlands, who was not involved in the work. "It's a great study," Gravendeel says, and it shows how orchids owe their diversity to a series of innovations—above all, the ability to grow in tropical mountains—that individually or jointly touched off explosions of new species.

Previous orchid phylogenies had compared just a few genes found in chloroplasts, the organelles that turn water and CO₂ into sugars. (Chloroplast genes evolve slowly, which helps reveal distant evolutionary relationships.) By using new gene sequencing methods, a team led by Thomas Givnish, a plant ecologist at the University of Wisconsin, Madison, created a phylogeny of orchids with an unprecedented 75 chloroplast genes from 39 species, representing almost all major groups of orchids, as well as from 96 distant relatives among

all flowering plants. Using the estimated ages of fossils of 17 flowering plants, including the few known orchid specimens, they were able to date the main branches in the phylogeny and calculate the rate at which new species appeared.

The team's new evolutionary timeline begins 112 million years ago, when the first orchids appeared. About 90 million years ago, the major living lineages started to split from each other. Then, sometime before 64 million years ago, a key innovation occurred: Orchids developed a way to

colonize new environmental conditions; the rate of net diversification increased 8.8% for epiphytes. To make up for having their roots exposed, some lineages adopted a kind of water-saving photosynthesis called crassulacean acid metabolism that likely helped them survive only on fog and rain; it increased their diversification rate by a remarkable 20.3%.

The biggest boost, however, came in lineages that moved into tropical mountains such as the Andes and the New Guinea highlands, where they found many new opportunities for diversification.

The rate of speciation among these cloud forest dwellers rose 24.9% compared with lineages that stayed in the lowlands. Givnish says it's difficult to disentangle the effect of mountain-climbing from tree-climbing, because the vast majority of mountain species are also epiphytes.

Scientists say these traits are all plausible drivers of diversification. But many puzzle at one result. One-third of all orchids deceive pollinators by luring them with structures or scents that resemble food, nesting sites, or even mates. Yet this trickery, another important evolutionary novelty, apparently didn't speed up the evolution of new species. "It was a big surprise," says Givnish, who is stumped. Gravendeel thinks that this deceit probably did accelerate

speciation, but that researchers have either misidentified or missed anatomical details in many tropical orchids.

Other experts say even more robust family trees will come from studying DNA in the cell nucleus, in part because it contains far more genes than chloroplasts do. "The only way to get a real story, the closest we can get, is to sequence nuclear genomes from orchids," says Victor Albert, a plant geneticist at the State University of New York at Buffalo. This past November researchers published the first orchid genome, for the tropical epiphyte *Phalaenopsis equestris*. More genomes will follow, and they are bound to shed more light on the evolution of traits that so delighted Darwin. ■



A bumblebee emerges from an orchid with a package of pollen (yellow) stuck to its head.

lump their pollen into sticky balls, called pollinia, so that pollinators would not lose any grains before reaching other orchids. As flowers evolved intricate structures to attach pollinia—some orchids stick them smack between the eyes of their favorite insect species, for instance—reproductive barriers likely formed, giving birth to new species. Indeed, in lineages that have pollinia, the speciation rate was 5.1% higher than in lineages that don't, Givnish and colleagues report this week in the *Proceedings of the Royal Society B*.

Next, some orchids evolved an aerial lifestyle. By 35 million years ago, many had become epiphytes, plants that cling to trees. This shift opened up many new areas

THE MISSING MUDBUG



As threats to crayfish mount, researchers push to document the enigmatic crustaceans

By **Emily DeMarco**, in Pineville, West Virginia

One morning this past May, biologist Zachary Loughman waded into Pinnacle Creek, a tumbling stream tucked high into the central Appalachian Mountains here. Loughman, who works at West Liberty University in West Virginia, pointed to a large, flat boulder submerged in the knee-deep water. “That’s the one,” he said. “That’s where we found it the last time.”

Six years ago, Loughman flipped that rock and made a rare catch: a Guyandotte River crayfish (*Cambarus veteranus*), a small olive-brown crustacean with menacing claws and striking orange-red antennae. Now, he was back, sent by the U.S. Fish and Wildlife Service (FWS) to see whether the crayfish—a candidate for protection under the federal Endangered Species Act (ESA)—had lost its clawhold in its last known holdout. “Hopefully,” he said, “we’ll find that’s not true.”

Loughman isn’t the only scientist out searching for the creatures some call mudbugs or crawdaddies. Spurred by growing concerns that pollution, habitat destruction, and other threats are imperiling many crayfish species, federal officials are taking a hard look at whether to give legal protection to the Guyandotte River crayfish and another known as the Big Sandy. And they plan to evaluate some 70 additional species over the next several years. If the listings go through, a broad range of economically important activities that affect crayfish, including mining, logging, and recreation, could feel an impact. So government officials are proceeding with care, seeking to learn as much as possible about the enigmatic invertebrates before making

decisions—and they are asking researchers for help.

It’s a big task: In North America, crayfish have diversified into roughly 400 species, two-thirds of the world’s total. But biologists lack even basic information about the biology and range of more than half of them. And new species are still coming to light, hidden in isolated waterbodies, creating headaches for wildlife officials but exciting biologists. “Crayfish tend to be lumped together, ... [but]

we’re just on the verge of learning how different these animals can be,” says ecologist Jim



A Big Sandy River crayfish defends its ground (above). Until recently, biologists believed the Big Sandy and the Guyandotte River crayfish (left) were a single species. Both are imperiled.

Stoeckel of Auburn University in Alabama. “There’s a huge range of behaviors.”

The result has been an “explosion of interest in crayfish research,” says ecologist Susan Adams with the U.S. Forest Service’s Southern Research Station in Oxford, Mississippi. “People are realizing that there’s a tremendous need to study them if we’re going to conserve them.”

DRAB EXCEPT FOR the occasional dash of color, “crayfish aren’t cute; they’re not warm and fuzzy,” says biologist Robert DiStefano of the Missouri Department of Conservation in Columbia, who has studied the animals for more than 20 years. “They can be vicious and territorial,” he adds, especially when facing off against their own relatives. But he sees them as “the ultimate survivalists.”

Researchers believe they’ve been around some 300 million years, having evolved from clawed lobsters—their saltwater doppelgängers. They have since spread widely into temperate regions (see map, p. 917), adapting to life in clear, cold mountain creeks, turbid lakes, sluggish swamps, and even pitch-black caves. They have also colonized land, digging carefully engineered burrows in moist earth or mud. (Burrowers sometimes build mud chimneys, and recent research suggests they might serve as signal towers, spreading chemical cues that guide young crayfish from the nearby streams where they were born to good habitat.)

Crayfish have a wide diet, including rotting leaves and wood, snails, and small fish. In turn, they are a key prey of many fish, birds, and other animals. “They’re kind of like chickens in that everything likes to eat them,” Stoeckel says. When threatened, the creatures can dart away backward with a flick of their fan-shaped tail—or rear up on legs that end in dainty points and wave sharp claws that look like oversized mittens.

Researchers are still describing new species—two or three a year from the United States; globally, it’s five to 10. In part, that’s because genetic and morphological studies have revealed that some similar-looking crayfish thought to be members of the same species are actually from different species. The Guyandotte River crayfish, for instance, was until last year lumped with the Big Sandy crayfish (*C. callainus*), another imperiled species that lives in a nearby watershed. Researchers are also discovering that

many species have relatively small ranges. In the United States, for instance, many species occur only within a single watershed or state. (In contrast, just 16% of freshwater fish have such limited territories.) “People think you’ve got to go to the deepest Amazon to find new species,” says Guenter Schuster, a retired crayfish biologist from Eastern Kentucky University in Richmond. “But that’s just not so.”

Even as new species turn up, others are vanishing. Globally, about one-third of crayfish species are at risk of extinction, concluded a January survey of 590 species published in the *Philosophical Transactions of the Royal Society B*. Threats include pollution, dams, development,



Biologist Zachary Loughman has been surveying crayfish across West Virginia, helping federal officials determine whether some species should be declared endangered.

climate change, and, sometimes, invasive crayfish. In Europe, the introduction of several North American species has devastated two of the continent’s five native species; the invaders carry a funguslike protist that causes a disease commonly called “crayfish plague.” Worldwide, at least four known species have already gone extinct, the survey concluded.

In the United States, biologists estimate that nearly half of crayfish species are imperiled. Those living in the heart of the southeast, the world’s center of crayfish diversity, are most vulnerable, DiStefano says. “Those are probably the places where we’re losing crayfishes before we even hardly know we have them,” he says.

One big threat is sediment that erodes from unpaved roads, mines, and construction and logging sites. The muck clogs the crevices between and under rocks where crayfish hide and lay eggs. Another problem in Appalachia is acidic, metal-contaminated wastewater from coal mines. The region where the Guyandotte River and

Big Sandy crayfish are found, for instance, had nearly 200 active surface and underground coal mines in 2012. And in 2000, a waste impoundment at one area mine failed, releasing nearly 1 billion liters of polluted water into the Big Sandy River, devastating nearly 180 kilometers of stream.

In the United States, states now recognize at least 66 crayfish species as imperiled. Just four are protected under federal law, but that number could rise as the result of a 2010 petition filed with FWS by conservation groups, led by the Center for Biological Diversity of Tucson, Arizona. The groups called on the agency to consider using the ESA to protect more than 400 species found in the southeastern United States, including about 80 kinds of crayfish.

For FWS officials, the petition—and some subsequent litigation—was a wake-up call. They needed a scientist who knew the native mudbugs and could help assess their biological status. West Liberty’s Loughman got the call.

WHITE MOUNTAIN laurel flowers speckled the mountainsides earlier this year as Loughman steered his silver research van toward Pinnacle Creek. The road twisted past scattered houses and the occasional coal mine, tucked into hollows and hugging creeks. A resolute box turtle in the middle of the road brought the van to an abrupt

halt. With a mad sprint, Loughman ferried the creature to safety.

Originally, Loughman had dreamed of studying turtles and other reptiles—of becoming a herpetologist. But as a graduate student at Marshall University in Huntington, West Virginia, he reconsidered. A labmate kept losing the salamanders she was studying to crayfish that fell into her traps and got hungry. “She slammed a bucket [of crayfish] onto my desk and said: ‘Figure out what those damned things are,’” Loughman recalls.

He discovered that he relished identifying crayfish. And he “realized that West Virginia didn’t really have a crayfish person, and that I could be that person.”

In the summer of 2007, Loughman and a colleague, Stuart Welsh of West Virginia University in Morgantown, began an unprecedented survey of the state’s crayfish. For five summers, he splashed through streams and tramped into muddy backyards, sometimes dangling bait in crayfish burrows to coax out the residents. He once

lost his wedding ring in a burrow and had to dig it out.

The surveys produced detailed range maps—and revealed some good news about the crustacean now called the Guyandotte River crayfish. Decades ago, when it was still known as the Big Sandy, researchers had documented it at 15 sites in the upper Guyandotte River watershed. Around 2000, however, researchers reexamined those sites, found none, and concluded they were gone for good. But in 2009, Loughman decided to look again for the missing mudbug. He searched for days without success. Then he flipped that boulder in Pinnacle Creek and discovered two of the elusive creatures. In 2011, he found five more in the same spot.

For crayfish biologists, such discoveries come with the territory. Experts estimate that as many as 60% of U.S. and Canadian crayfish lack basic biological and current distributional information. And a 2013 study found researchers have published life histories of just 12% of North American species.

The push to federally protect some crayfish is catalyzing studies that are helping fill the gaps. Last year, FWS gave DiStefano a small grant to see if he could find a little-studied crayfish known only from one cave in southern Missouri. On one visit, he found about eight of the albino creatures—more than had ever been observed at one time. “I thought: ‘Holy smokes, this might be the only population on Earth,’” he says. “I went home and emailed my mom and dad like I used to do in junior high.”

Other recent studies have revealed that some crayfish aren’t in as bad shape as feared. Three species from Alabama and Mississippi named in ESA petitions appear to be flourishing, biologists found last year. Despite Loughman’s 2009 find, however, it appeared the Guyandotte River crayfish was in trouble. Surveys suggested Pinnacle Creek was its last refuge, and earlier this year FWS proposed listing the new species, and the nearby Big Sandy crayfish, as endangered.

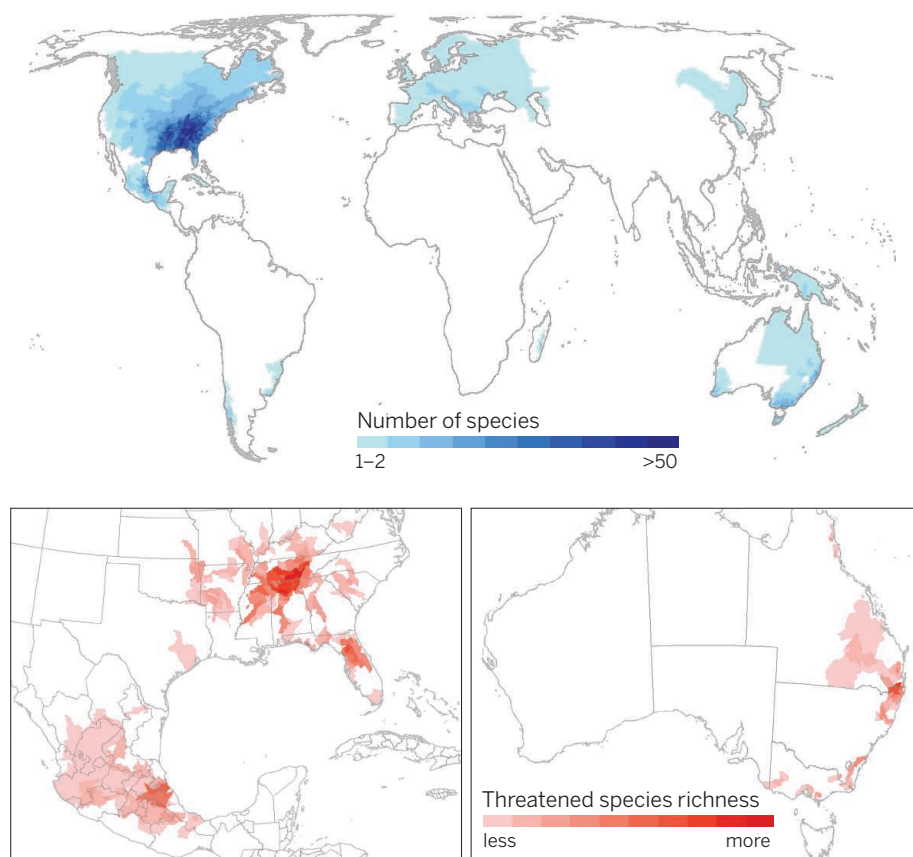
Still, Loughman’s work wasn’t done. This year, at the agency’s request, he and several students returned to Pinnacle Creek and other streams to make sure the crayfish was still around.

It didn’t take him long to find the lucky boulder. As he tried to get a grip on the slippery rock, his students readied a large net downstream. Nearby, an angler—a recently retired coal miner with a grizzled beard—watched with amusement. “Y’all find a bunch,” he shouted, “and we’ll have a crawfish boil!”

After some huffing and a few expletives, however, it was clear that no crayfish would be found under the rock. It was stuck fast in the sediment.

Where the crayfish are

North America is home to some 400 crayfish species—two-thirds of the world’s total—with the greatest diversity found in the southern United States (dark blue). Biologists estimate a third of the world’s crayfish are imperiled. The threat of species loss is especially acute in major centers of diversity, including the southern United States and eastern Australia (dark red).



IF FWS FINALIZES THE LISTINGS (it is expected to decide next year), the Guyandotte River and Big Sandy crayfish would be the first in their watersheds to gain ESA protection. That could ultimately lead to new controls on some activities in the area, including logging, drilling for gas, and the use of nearby roads and trails by recreational all-terrain vehicles.

The bigger question is whether the presence of endangered crayfish will affect one of the region’s biggest economic and environmental forces: coal mining. A 1996 FWS policy statement, known as a “biological opinion,” appears to protect miners from the impact of a listing. The opinion stipulates that mining won’t be considered a threat to endangered species as long as mine operators comply with the requirements of a law called the Surface Mining Control and Reclamation Act. But some environmental groups have challenged the opinion in court, so the issue isn’t resolved.

In the meantime, Loughman is aware that his work could have ripple effects. “The last

thing I want is everyone angry at the crayfish and viewing it as this nasty creature that’s going to eliminate jobs,” he says. “But if the crayfish is going away, there’s a reason. It could be a message to the community that something’s wrong with the water, and we need to fix it.”

AFTER A REST, Loughman wades downstream from the stubborn boulder. This time, he and a student are able to tip a submerged slab. They use their feet to stir up a sediment plume, letting sand and detritus drift into the billowing net. They raise the net, and there’s a moment of silence as everyone peers in. There are pebbles, leaves, some wood—and a Guyandotte River crayfish. Before it can scurry away, Loughman makes the snatch.

Since then, there has been more good news. Although Loughman’s team found no Guyandotte River crayfish at about 60 sites they visited, they caught a few at other spots, including in two streams never before sampled. “It’s still here,” he says. “Thank God.” ■



Big gods demand costly displays of faith, like Abraham's willingness to sacrifice his son Isaac. In Rembrandt's painting, God sends an angel to stay the knife.

BIRTH OF THE MORALIZING GODS

A new theory aims to explain the success of world religions—but testing it remains a challenge

By Lizzie Wade

An ancient Egyptian spent her whole life preparing for the moment when her heart would be weighed. After death, she was escorted before a divine scale. In one pan rested an ostrich feather belonging to Maat, the goddess of social order. The other pan held her heart. The deceased had been buried with a list of her virtues: “I have not uttered lies.” “I have not slain men and women.” “I have not stopped the flow of water [of the Nile.]” Any sins would weigh down her heart. When the scale settled, her fate would be clear: If her heart weighed no more than Maat’s feather, she was escorted to paradise. If her heart was too heavy, the crocodile demon Amemet reared up and devoured it, obliterating her soul.

Although much of Egyptian cosmology is alien today, some is strikingly familiar: The gods of today’s major religions are also moralizing gods, who encourage virtue and punish selfish and cruel people after death. But for most of human history, moralizing gods have been the exception. If today’s hunter-gatherers are any guide, for thousands of years our ancestors conceived of deities as utterly indifferent to the human realm, and to whether we behaved well or badly.

To crack the mystery of why and how people around the world came to believe in moralizing gods, researchers are using a novel tool in religious studies: the scientific method. By combining laboratory experiments, cross-cultural fieldwork, and analysis of the historical record, an interdisciplinary team has put forward a hypothesis that has

the small community of researchers who study the evolution of religion abuzz. A culture like ancient Egypt didn’t just stumble on the idea of moralizing gods, says psychologist Ara Norenzayan of the University of British Columbia (UBC), Vancouver, in Canada, who synthesized the new idea in his 2013 book *Big Gods: How Religion Transformed Cooperation and Conflict*. Instead, belief in those judgmental deities, or “big gods,” was key to the cooperation needed to build and sustain Egyptians’ large, complex society.

In this view, without supernatural enforcement of cooperative, “moral” behavior, ancient Egypt—as well as nearly every other large-scale society in history—wouldn’t have been able to get off the ground. All-knowing big gods are “crazily effective” at enforcing social norms, says Norenzayan’s collaborator Edward Slingerland, a historian at UBC Vancouver. “Not only can they see you everywhere you are, but they can actually look inside your mind.” And once big gods and big societies existed, the moralizing gods helped religions as dissimilar as Islam and Mormonism spread by making groups of the faithful more cooperative, and therefore more successful.

It’s a sweeping theory, grander in scale than much of the scholarship by religious studies experts, who usually examine one tradition at a time. “They’ve done a great service by bringing together a lot of important findings in the field,” says Richard Sosis, a human behavioral ecologist at the University of Connecticut, Storrs. Now, they’re embarking on new experiments and analysis to test

it—a challenging task given the scope of the theory. “It’s easy to say” that moralizing religions spread through cultural evolution, says Dominic Johnson, an evolutionary biologist at the University of Oxford in the United Kingdom who studies religion and cooperation. “But it’s quite hard to demonstrate.”

WHEN NORENZAYAN was growing up in Lebanon in the 1970s and 1980s, “it was very hard to miss religion,” he remembers. Faith was the defining fact of people’s lives, and it fueled the sectarian war that consumed the country. After moving to the United States for a Ph.D., Norenzayan

became fascinated with scientific efforts to explain belief, many of them rooted in cognitive sciences. A series of studies had shown that both children and adults eagerly ascribe humanlike intentions and

actions to inanimate objects like rocks and the sun. For example, British and American children repeatedly told scientists that rocks are sharp so animals won’t sit on them, rather than because they are made up of smaller pieces of material (*Science*, 6 November 2009, p. 784). Such studies contributed to a growing scientific consensus that belief in the supernatural is an evolutionary byproduct of the quirks of the human brain, piggybacking on abilities that evolved for different purposes.

But Norenzayan was not satisfied. The byproduct model doesn’t explain the particular nature of religions in complex societies—the presence of moralizing gods who prescribe human behavior. Nor does it

PODCAST

To hear a podcast with author Lizzie Wade, see http://scim.ag/6251_Pod

explain why a handful of those faiths have proved so successful.

In an effort to answer these questions, Norenzayan began making forays into the psychology of religion. In one study, published in 2007 in *Psychological Science*, he and a colleague gave \$10 to participants, who could then decide how much to give to a stranger and how much to keep for themselves. When primed with religious words, participants gave away an average of \$4.22, whereas a control group gave away only \$1.84.

A few years later, human evolutionary biologist Joseph Henrich (then at UBC Vancouver, now at Harvard University) and his colleagues asked people in 15 societies, ranging from tribal farmers in Papua New Guinea to wageworkers in Missouri, to play a similar economic game. The researchers found that across these cultures, people who participated in a moralizing world religion, particularly Christianity and Islam, gave as much as 10% more to strangers than did unbelievers or practitioners of animism. Their results were published in *Science* in 2010.

Norenzayan thinks this connection between moralizing deities and “prosocial” behavior—curbing self-interest for the good of others—could help explain how religion evolved. In small-scale societies, prosocial behavior does not depend on religion. The Hadza, a group of African hunter-gatherers, do not believe in an afterlife, for example, and their gods of the sun and moon are indif-



When Kenya's Orma people converted to Islam, they gained advantageous economic ties and new customs like this Muslim ceremony.

ferent to the paltry actions of people. Yet the Hadza are very cooperative when it comes to hunting and daily life. They don't need a supernatural force to encourage this, because everyone knows everyone else in their small bands. If you steal or lie, everyone will find out—and they might not want to cooperate with you anymore, Norenzayan says. The danger of a damaged reputation keeps people living up to the community's standards.

As societies grow larger, such intensive social monitoring becomes impossible. So there's nothing stopping you from taking advantage of the work and goodwill of others and giving nothing in return. Reneging on a payment or shirking a shared responsibility have no consequences if you'll never see the injured party again and state institutions like police forces haven't been invented yet. But if everyone did that, nascent large-scale societies would collapse. Economists call this

paradox the free rider problem. How did the earliest large-scale societies overcome it?

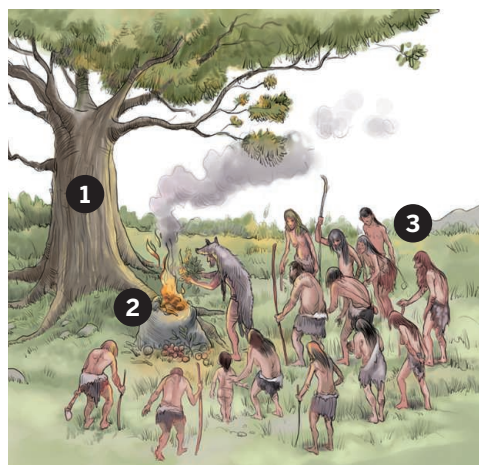
In some societies, belief in a watchful, punishing god or gods could have been the key, Norenzayan believes. As he wrote in *Big Gods*, “Watched people are nice people.” Belief in karma—which Norenzayan calls “supernatural punishment in action”—could have had a similar psychological effect in the absence of actual gods, a proposition his colleagues are investigating in Asia.

History and archaeology offer hints that religion really did shape the earliest complex societies. Conventional wisdom says that the key to settling down in big groups was agriculture. But “agriculture itself is a wildly improbable cooperative activity,” notes Slingerland, who studies ancient China. “Especially in places where you can't get agriculture off the ground without large-scale irrigation or water control projects, the cooperation problem has to get solved before you can even get the agriculture ramped up.” That's where religion came in, he and Norenzayan think.

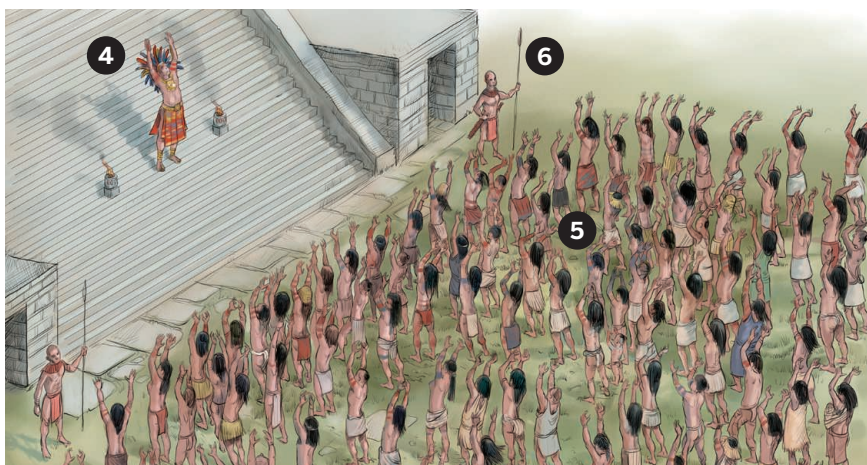
A case in point, they say, is Göbekli Tepe, an archaeological site in southeastern Turkey. Huge stone obelisks carved with evocative half-human, half-animal figures dot the 11,500-year-old site, which the late Klaus Schmidt of the German Archaeological Institute, who excavated there, called “the first manmade holy place” (*Science*, 18 January 2008, p. 278). Moving and decorating the

As societies grow bigger, so do their gods

Small tribes worship spirits that pay little heed to human behavior, whereas moralizing “big” gods may help societies scale up to full-blown states.



The gods of small-scale societies, such as nature spirits (1), may demand offerings (2) or enforce taboos. But villagers watch each other (3) and enforce social norms without any supernatural help.



Big gods help bring big societies together. Omniscient, moralizing deities (4) keep a close eye on human behavior and punish those who are selfish or cruel. Rituals (5) and other costly displays of faith prove who is a trustworthy true believer. Increased cooperation helps societies grow into complex states with other prosocial institutions, like police forces (6).

great obelisks must have required a huge community effort. But signs of agriculture don't appear nearby until 500 years later, meaning that the builders of Göbekli Tepe were likely hunter-gatherers who had come together to practice shared religious beliefs, Slingerland says. As Schmidt has said, "First came the temple, then the city."

The big gods hypothesis also helps explain why a handful of religions spread widely: They offer new adherents expanded opportunities for economic and social cooperation. The Orma herders of East Africa, for example, maintained their animist beliefs for centuries while living in close contact with Muslim friends and business partners. Then, in the latter half of the 19th century, war ruined the Orma's local institutions and weakened their control of the regional ivory and livestock trades. Within a few decades, the entire Orma society had converted to Islam. And once they did, they were inducted into a worldwide network of long-distance traders, bound together by the trust that a shared faith in a moralizing god provides.

The Orma had to do more than profess their newfound faith. They had to show they meant it by giving up pork, eschewing alcohol, reforming their rules about polygamy, and praying five times a day. These "costly displays of faith" are "markers that you're a true believer in Islam" and therefore are likely to keep your word, especially to your fellow Muslims, Henrich explains. Whether they take the form of generous donations to the church or painful body modifications like circumcision or scarification, these displays prove to others that you are truly committed to your religion and thus can function as a shorthand for trustworthiness.

After their conversion, the Orma "missed their days of drunken bashes," an aspect of many earlier local rituals, says economist Jean Ensminger of the California Institute of Technology in Pasadena, who spent several years with them doing fieldwork. But a religion that opened up access to economic and social networks all over the world, while ensuring everyone in that network adhered to the same standards of behavior, was "a pretty good package," she says.

Islam's spread to the Orma is an example of a broader pattern, Norenzayan says. Groups with "moralizing, interventionist deities or spirits ... expand because all things being equal, they do better than the noncooperative groups," he says. "And then the beliefs expand" alongside them. "Take this idea to its extreme and we get world religions," he says, such as Islam, Christianity, Buddhism, and Hinduism.

Many scientists are impressed by the careful combination of laboratory experi-

ments and suggestive evidence from the ethnographic and historical records that Norenzayan and his team have marshaled. But others question whether moralizing high gods require a special explanation beyond the cognitive byproduct model. "In the same way you don't need any adaptation for people to believe in supernatural agents, you don't need any adaptation to explain why people believe in moralizing religion," says Nicolas Baumard, a psychologist who studies the evolution of religion at the École Normale Supérieure in Paris. All you need, he argues, is a sufficiently affluent society in which people can afford to prioritize long-term goals (like the afterlife) over short-term needs. Studying Eurasian societies between 500 B.C.E. and 300 B.C.E., Baumard recently found that moralizing religions were much more likely to emerge in societies where people had access to more than 20,000 kilocalories in total

community. The researchers expect to publish the first results this fall.

They are also seeking more evidence for the claim that moralizing religion lays the foundation for large-scale societies. Slingerland is appealing to his historian colleagues to contribute to a new database that will assemble quantitative data about social complexity and religion (see sidebar, p. 922). "If we find there's a systematic pattern where most societies in the world scaled up without religion, I would worry," Norenzayan says. "I would say that's a falsification of the hypothesis."

Other scientists say some historical evidence already challenges it. This spring, a study in the *Proceedings of the Royal Society B* reported that out of 96 traditional Austronesian societies spread throughout the Pacific, six had moralizing high gods—and they emerged after the societies became politi-



In Buddhism, the concept of karma may play the role of a moralizing god, enforcing selfless behavior.

energy resources each day, from food, fuel, and draft animals, for example.

TO PROVE THAT MORALIZING religion is an adaptive tool to increase cooperation, the big gods team needs to confirm that belief in prosocial deities actually causes followers to be nicer to each other. To that end, Norenzayan and Henrich have expanded their experimental work on religion and generosity to societies around the world. They hope to show that the more omniscient and punitive the gods that people worship, the more money they are willing to give to strangers in their own religious

cally complex, not before, apparently contradicting the big gods idea. Norenzayan points out, however, that the complexity of most of the cultures analyzed is limited—they are small-scale chiefdoms, not large agricultural societies. "You see moralizing gods when you get to a state-level society," he says. "But there could be lots of intermediate cases"—nature spirits that enforce taboos protecting shared resources, for example.

A third test of the big gods hypothesis is whether it accurately predicts which religions spread. The Mormons, for example, have had spectacular success spreading a faith focused on a judgmental god with strict moral rules,

a strong cooperative ethic, and costly signs of devotion like avoiding caffeine and spending 2 years as a missionary. “It almost seems like Joseph Smith [founder of the faith] read our article” on big gods, Slingerland jokes. The team plans to use Mormonism as a template for identifying other highly prosocial religions throughout history, quantitatively recording its features and systematically searching for them in other faiths. If many of those religions also prove to have spread rapidly, that could point to a deep pattern.

Critics complain that the definition of a “moralizing” religion can be slippery. Baumard quibbles with Norenzayan’s interpretation of ancient Egyptian beliefs, in which “stopping the flow of water” appears to be a sin. To Baumard, this is clearly not a moral concern, but some kind of taboo. The big gods team is “projecting a moralizing aspect onto gods that don’t care about morality,” he says.

Slingerland disagrees. Ancient Egypt’s agriculture was exquisitely calibrated to the

Nile’s annual flood. If someone tampered with the irrigation system for short-term personal gain, the whole society would suffer. In the context of that society, religious injunctions against interfering with the Nile “are absolutely moral,” he says.

Only Maat may have the insight to resolve that debate once and for all. In the meantime, these researchers may have found a new way to get closer to a fuller understanding of religion, from ancient Egypt to today: Hypothesize, test, and repeat. ■

Turning history into a binary code

By Lizzie Wade

In January of this year, Anders Petersen folded his nearly 2-meter frame into an airplane seat for a flight from Copenhagen to

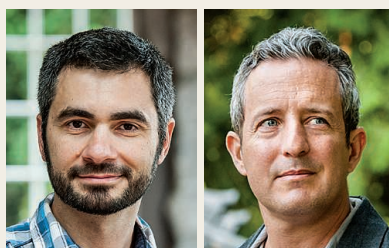
Vancouver, Canada, crossing two continents on his way to check boxes on a computer screen. It would be a new experience for the religious studies scholar from Aarhus University in Denmark, who, like many in the humanities, has made a career out of “sitting in a room and writing my books and my articles” alone, eschewing even a cellphone. Now, he had agreed to help test a burgeoning new theory about the origins of religion (see main story, p. 918) by translating the nuanced knowledge in his head into the kind of data that scientists need: a database’s binary code of yes/no answers.

Petersen, who studies the religious movements—including early Christianity—that sprang up across the Mediterranean about 2000 years ago, was creating an entry for the Database of Religious History (DRH), the brainchild of a multidisciplinary team investigating the evolution of religion. They’re attempting to bridge the gulf between humanistic and scientific scholarship, but success hinges on enticing leading scholars like Petersen to join them.

Many are reluctant. Cross-cultural databases like the DRH “are going to make the humanities a lot more powerful than they are now,” says Yale University historian Joseph Manning, who has written a DRH entry on ancient Egypt. But “a lot of my colleagues think the opposite.” Since the rise of postmodernism in the 1960s, the

humanities have strenuously rejected the idea of a single “truth” in favor of understanding the world as an endless series of cultural “texts” whose meanings constantly shift. Comparing one culture with another came to be seen as meaningless at best, racist at worst.

Yet historical, cross-cultural information is what psychologist Ara Norenzayan of the University of British Columbia (UBC), Vancouver, needs to test his “big gods” hypothesis. Did moralizing gods, community-wide



Ara Norenzayan (left) and Edward Slingerland are recruiting historians to help test the big gods hypothesis.

rituals, and supernatural punishment emerge before or after societies became politically complex? Has any large-scale society succeeded without prosocial religion? And what does “moralizing” really mean in different cultures and at different times?

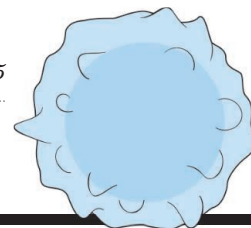
To answer these questions in a way that goes “beyond cherry-picking and anecdote,” scientists need an unbiased, scientific survey of religions, says Edward Slingerland, a historian at UBC Vancouver who is heading up the DRH. And the only way to get that is to “force historians to do what historians hate to do”—turn their qualitative knowledge

into black-and-white quantitative data.

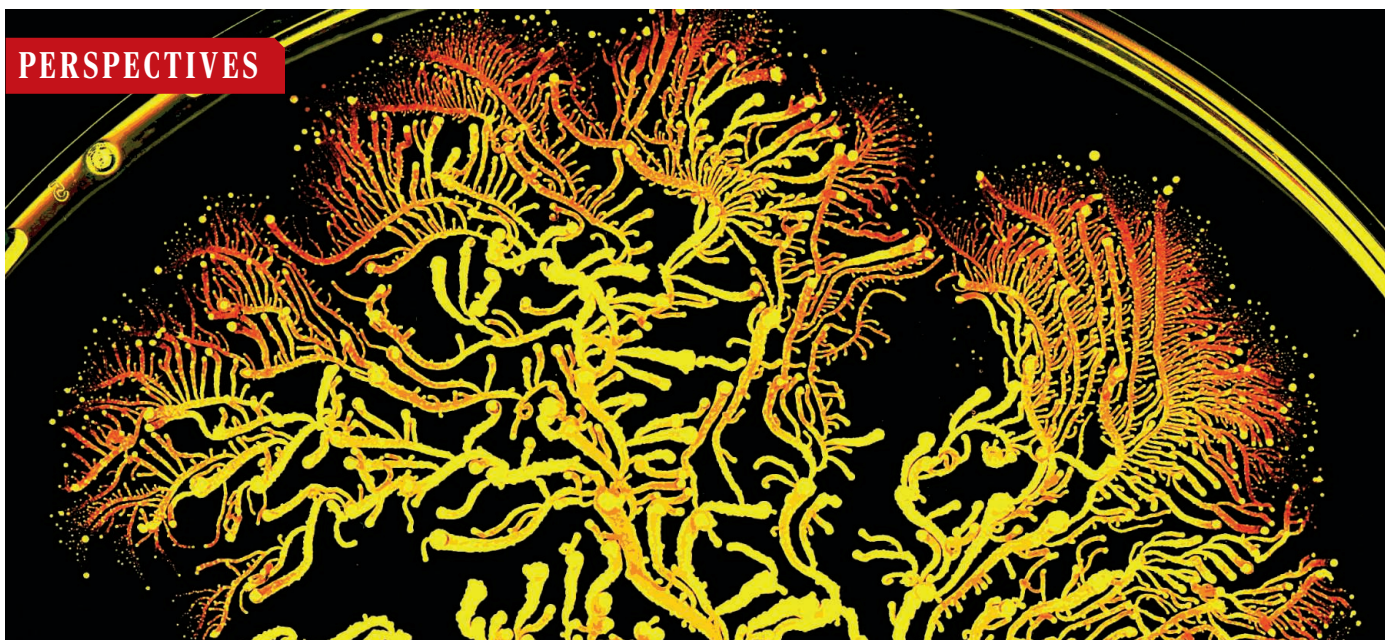
Petersen, the Danish religious scholar, was one of the first to agree to try it. When he arrived in Vancouver, Slingerland and several grad students were on hand to guide him through hundreds of yes/no questions. Petersen chose one sect to focus on: Pauline Christianity, as expressed in texts written by the apostle Paul between 48 C.E. and 56 C.E. Some of the questions were easy. Is a supreme high god present? (Yes.) Does that god care about murder? (Yes.) Gossiping? (Yes.) Disrespecting elders? (No.)

Others stumped him. For example, it’s impossible to tell how many adherents Pauline Christianity had based solely on Paul’s writings, and Christianity left no archaeological record until later. It’s even possible that Paul was writing only for himself, Petersen says. But the DRH doesn’t leave much room for that kind of uncertainty, so when confronted with questions about community size and structure, Petersen checked “Field doesn’t know” and moved on. All told, it took him 2.5 exhausting hours to turn the knowledge in his head into check marks on a computer screen.

Now up to about 60 entries, the DRH is still in its infancy. Recruiting is slow going and depends heavily on Slingerland’s personal connections. He’s not above showing up to colleagues’ houses bearing gifts; Petersen admits that his participation was helped along by their “shared love of Italian red wine.” Slingerland believes going directly to top experts shows “we take humanistic scholarship seriously,” and that once enough high-profile scholars participate, it will create a snowball effect. Reaching that critical mass, however, will take a lot of work—and wine. ■



PERSPECTIVES



Social structure. The social behavior of *Paenibacillus vortex* bacteria underlies their elaborate 8-cm-diameter colony, created to forage for nutrients.

SYNTHETIC BIOLOGY

Synthetic communities, the sum of parts

Complex behaviors are engineered from cooperating cell communities

By **Brian P. Teague** and **Ron Weiss**

Cooperation between cells is one of evolution's fundamental innovations. It allows cells to specialize: Different members of a consortium assume different responsibilities, increasing overall productivity and allowing for more complex behavior than is possible with a single cell or a monoculture (1). These features of natural systems have attracted the attention of synthetic biologists, who have made engineering of cooperation between cells a long-standing goal. On page 986 of this issue, Chen *et al.* (2) report the creation of a synthetic consortium of cooperating *Escherichia coli* bacteria. The design principles they demonstrate have important implications for the construction of multicellular synthetic systems.

Cooperation between specialized cell types is a hallmark of complex multicellular organisms, but even unicellular prokary-

otes are found primarily in consortia such as biofilms, whose community structure provides for sharing of metabolites and resistance to environmental perturbations (3). Specialization is key to productive cooperation because it allows for spatial segregation of function (1). For example, one species in a biofilm might be responsible for adhesion, while another synthesizes an energetically expensive metabolic product.

As synthetic biology begins to address problems that span from bioremediation to medicine (4), engineered multicellular behavior is emerging as a key tool for building advanced synthetic systems that robustly perform complex behaviors. Recent work (5) has ranged from density-dependent population control to synchronized behavior in spatially separate populations. However, most studies describe a single isogenic strain of cells or two cell types where dedicated senders control the behavior of a dedicated receiver population.

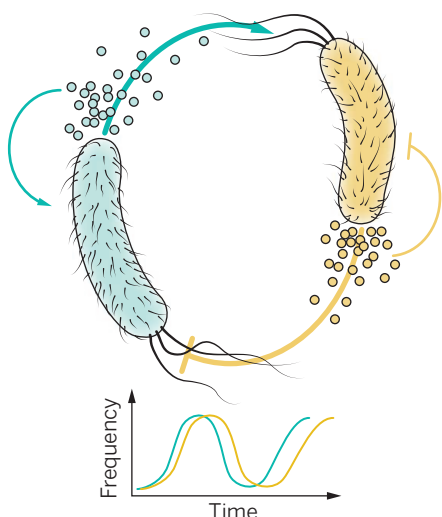
Chen *et al.* took a different approach. Rather than gene circuits controlling transcription in independent cells, they built a gene circuit spanning two nonisogenic populations of *E. coli*, comprising an "activator" strain and a "repressor" strain that communicate through a pair of intercellular signaling molecules. Each strain implements half of a dual-relaxation oscillator, and when they are cultured together, the transcriptional output of the gene circuit oscillates synchronously in both populations (see the figure). The oscillatory behavior of the consortium is mutually obligatory: The two populations together display an emergent behavior that neither constituent is capable of alone.

The "division of labor" approach has broad implications for designing synthetic multicellular systems. For example, observations of

Department of Biological Engineering and Department of Electrical Engineering and Computer Science, NE47-223, Massachusetts Institute of Technology, Cambridge, MA 02139-4307, USA. E-mail: rweiss@mit.edu

natural systems suggest that such consortia are robust to perturbations (3), as confirmed by Chen *et al.* They found that interlocking feedback loops supported robust and persistent oscillations, even as they varied gene circuit topologies, promoter strengths, and population ratios of the two strains. Such robustness is important for industrial applications of synthetic biology, including bioprocessing and bioremediation (6).

Specialization of subpopulations also allows for the engineering of consortium-wide



Work with me. A dual-feedback oscillator gene circuit across two strains of *E. coli* involves quorum-sensing molecules. The gene circuit only oscillates when both strains are present.

behavior that would be difficult to achieve with a monogenic strain. Previous examples include complex boolean computation based on the spatial arrangement of bacterial colonies encoding simpler logic gates (7), with colonies communicating via chemical “wires” composed of diffusing quorum-sensing molecules. As with Chen *et al.*, implementation of the desired behavior is divided among cell types, allowing for scalability and control over consortium behavior.

The construction of synthetic multicellular consortia also has implications for understanding and manipulating natural communities of cells. Of key importance are the molecular mechanisms that stabilize social interactions (8): How are intercellular signals sensed, processed, and integrated? How are cheaters punished and cooperators rewarded? Such questions have direct relevance to health and human disease, such as understanding the gut microbiome (9). This “virtual organ” (10) of microbes has roles in metabolism, inflammation, immunity, and even neurochemistry, but the structure and dynamics of the microbial community remain unclear. Such knowledge is crucial

for manipulating the microbiome for better health outcomes.

More broadly, understanding cells’ social context presents therapeutic opportunities. For example, antibiotic resistance in pathogens may arise from bacterial “charity work” (11), and dysregulation in social interaction in immune cells can lead to autoimmunity (8). Particularly intriguing is the notion of cancers as cooperating communities of clonal populations (12). The emerging story is familiar: Diversity and heterogeneity give rise to specificity, cooperation, and robustness against therapeutic assault. A deeper understanding of community dynamics may point the way to approaches that target intratumor ecology instead of specific cell subpopulations, and synthetic models of such communities may advance our understanding of these dynamics.

Synthetic communities of cooperating cells have broad potential impact, but key challenges remain. For example, the number of orthogonal cell-cell communication channels remains limited. Intercellular communication modules imported from other kingdoms of life will continue to be useful, such as a communication channel in yeast based on a plant hormone (13). Further, even though a small number of parameters can produce a broad range of behaviors (14), many synthetic systems are still based on traditional cell density-dependent quorum sensing. A larger palette of reliable, robust design motifs would expand the impact of our limited communication channels substantially. Moreover, interspecies (and interkingdom) communication has only been explored to a limited extent (15), despite abundant evidence in natural systems (1).

Chen *et al.* demonstrate the fundamental power of cell specialization and cooperation, recapitulating a strategy employed by many natural systems. It is a powerful reminder that such communities are frequently more than the sum of their parts. ■

REFERENCES

1. E. H. Wintermute, P. A. Silver, *Genes Dev.* **24**, 2603 (2010).
2. Y. Chen *et al.*, *Science* **349**, 986 (2015).
3. K. Brenner *et al.*, *Trends Biotechnol.* **26**, 483 (2008).
4. A. L. Slusarczyk *et al.*, *Nat. Rev. Genet.* **13**, 406 (2012).
5. W. Bacchus, M. Fussenegeger, *Metab. Eng.* **16**, 33 (2013).
6. J. Shong, M. R. Jimenez Diaz, C. H. Collins, *Curr. Opin. Biotechnol.* **23**, 798 (2012).
7. A. Tamsir, J. J. Tabor, C. A. Voigt, *Nature* **469**, 212 (2011).
8. J. B. Xavier, *Mol. Syst. Biol.* **7**, 483 (2011).
9. Human Microbiome Project Consortium, *Nature* **486**, 207 (2012).
10. J. M. Evans *et al.*, *J. Endocrinol.* **218**, R37 (2013).
11. H. H. Lee *et al.*, *Nature* **467**, 82 (2010).
12. D. P. Tabassum, K. Polyak, *Nat. Rev. Cancer* **15**, 473 (2015).
13. A. Khakhar, N. J. Bolten, J. Nemhauser, E. Klavins, *ACS Synth. Biol.* **10**, 1021/acssynbio.5b00064 (2015).
14. H. Youk, W. A. Lim, *Science* **343**, 6171 (2014).
15. W. Weber *et al.*, *Proc. Natl. Acad. Sci. U.S.A.* **104**, 10435 (2007).

10.1126/science.aad0876

ORGANIC CHEMISTRY

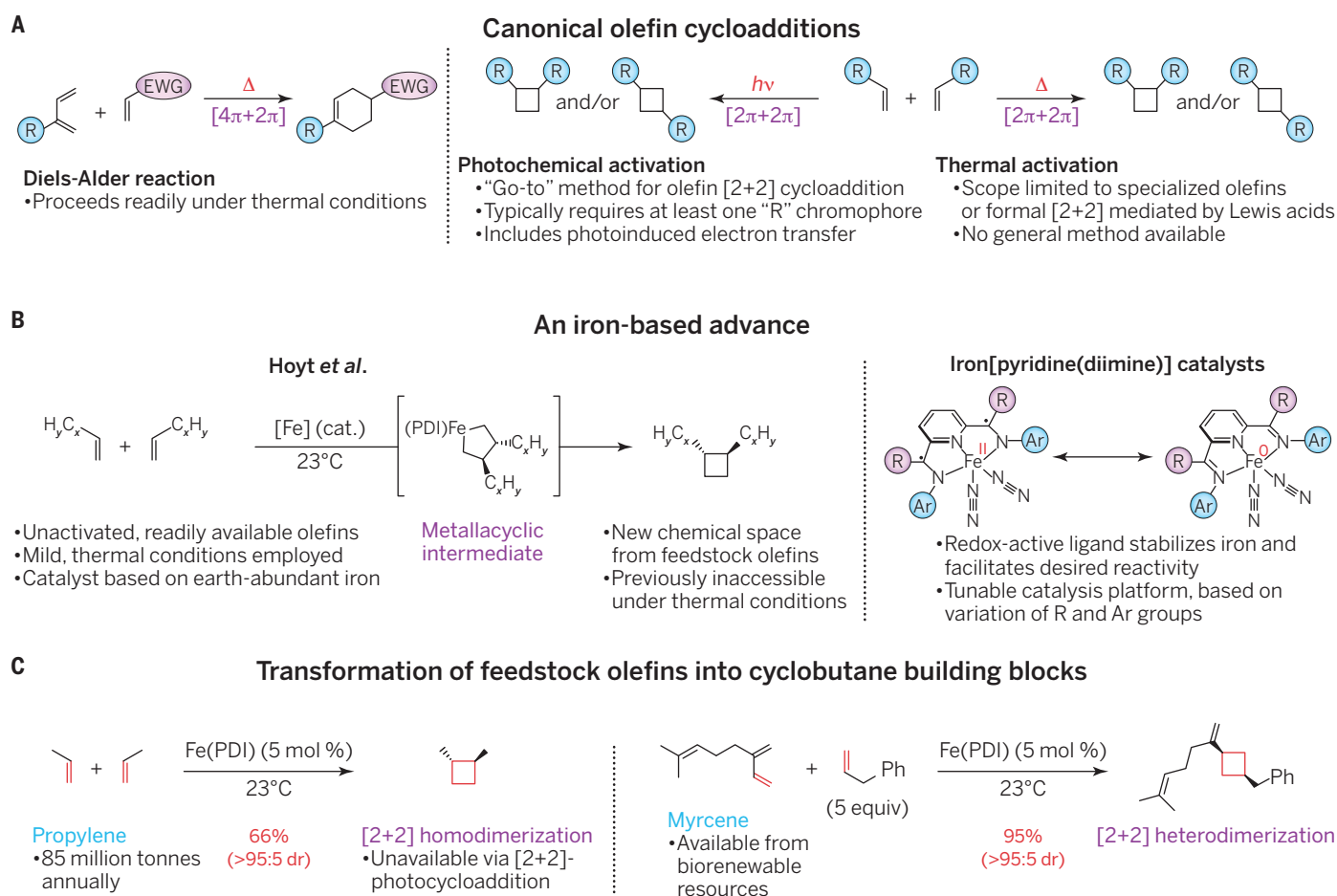
As simple as [2+2]

Iron catalysis transforms readily available commodity olefins into cyclobutane building blocks under thermal conditions

By Myles W. Smith and Phil S. Baran

Olefin cycloadditions, pericyclic reactions in which the relatively weak π bonds of these unsaturated species are swapped out for stronger σ bonds, are among the most widely exploited transformations in organic synthesis (1). Indeed, the Diels-Alder reaction—a $[4\pi+2\pi]$ cycloaddition (a $[4+2]$ cycloaddition for short) that forms six-membered rings from a diene (the 4π component) and an olefin (the 2π component)—has a storied history in the many branches of synthetic chemistry and proceeds readily under thermal conditions (see the figure, panel A) (2). However, a similarly fundamental pericyclic reaction—the corresponding $[2+2]$ cycloaddition of two olefins, leading to cyclobutane rings—usually requires photochemical conditions to proceed efficiently, a fact enforced by the constraints of orbital symmetry (3). On page 960 of this issue, Hoyt *et al.* (4) report the development of catalysts based on iron that transform simple feedstock olefins into cyclobutanes through $[2+2]$ cycloadditions under mild, thermal conditions.

Thermal $[2+2]$ cycloadditions are relatively rare, and those that do proceed typically require activated olefins such as allenes or ketenes, or special diolefin substrates that can form the corresponding cyclobutane products under the influence of a Lewis acid (see the figure, panel A) (3). The $[2+2]$ cycloaddition of simple, unfunctionalized olefins—many of which are available industrially on multiton scales—requires a conceptually different approach, such as one that uses transition metal catalysis. Efforts along these lines date back to the 1960s, but the existing methods (encompassing a range of different metals) are only able to achieve the conversion of specific types of olefins, typically ones that are activated by strain. Systems that can accommodate simple olefins do so with very narrow scope and moderate levels of efficiency (5).



Hot routes to cyclobutanes. (A) Canonical olefin cycloadditions, [4+2] and [2+2], are compared. EWG is an electron-withdrawing group; R is an alkyl group. (B) A rationally designed iron catalyst enables the thermally forbidden [2+2] reaction of unactivated olefins; Ar is an aryl group. (C) The iron-catalyzed [2+2] can convert abundant natural resources into high-value cyclobutanes; dr is diastereomeric ratio, a measure of the purity of the chiral product.

The method of Hoyt *et al.* brings unprecedented scope to this ostensibly simple yet deceptively challenging transformation. Crucial to this success has been the use of well-defined iron catalysts based on a set of structurally tunable pyridine(diimine) (PDI) ligands (see the figure, panel B) (6). These ligands bind to the metal and modulate not only the steric environment around this reactive center, but also the oxidation state of the metal itself through a give-and-take of electrons via their π frameworks. Using a loading of 5 mol % of these catalysts, Hoyt *et al.* were able to dimerize a range of terminal olefins at room temperature. Commodity olefins such as propylene were converted selectively to 1,2-trans-substituted cyclobutanes, likely via metallacyclic intermediates (see the figure, panel C). In fact, favoring the desired transformation among the known alternative pathways (e.g., hydrovinylolation) hinged entirely on subtle changes to the ligand structure, and careful

fine-tuning was required to coax out the desired reactivity. Similarly, through rational adjustment to the PDI ligand, the authors extended the process by using a slight excess of the olefin partner to achieve selective cross-dimerization of 1,3-dienes with olefins. Notably, barring a few exceptions, all of the cyclobutanes produced have been previously inaccessible through direct olefin [2+2] dimerization.

With respect to substrate scope, Hoyt *et al.* wisely focused on the use of feedstock olefins and dienes—abundant compounds whose production is expected to only increase further, given the development of processes that use natural gas-derived resources. With access to these “commodity cyclobutanes,” creative uses of these building blocks will no doubt proliferate. Further, as the method is developed in the future to tolerate more functional groups, applications in medicinal, agricultural, and materials science will emerge, given the utility that these ring systems hold in such fields. Ideally, this work will provide the end user with a low-cost, generally applicable tool with which to

explore the cyclobutane chemical space via nonphotochemical means. Apparent, too, is the potential for the design of chiral ligands based on (or related to) the modular PDI framework, which might confer asymmetry to resulting cyclobutane products.

In light of this clear potential, as well as its demonstrated utility, the work of Hoyt *et al.* constitutes an impressive first step in facilitating the archetypal [2+2] cycloadditions of simple olefins under thermal conditions. This compelling discovery will no doubt spur the development of more robust and versatile catalyst platforms for the [2+2] cycloadditions of commodity olefins and beyond. ■

REFERENCES

1. W. Carruthers, *Cycloaddition Reactions in Organic Synthesis* (Pergamon, Oxford, 1990).
2. K. C. Nicolaou, S. A. Snyder, T. Montagnon, G. E. Vassilikogiannakis, *Angew. Chem. Int. Ed.* **41**, 1668 (2002).
3. E. Lee-Ruff, G. Mladenova, *Chem. Rev.* **103**, 1449 (2003).
4. J. M. Hoyt, V. A. Schmidt, A. M. Tondreau, P. J. Chirik, *Science* **349**, 960 (2015).
5. P. Heimbach, *Angew. Chem. Int. Ed. Engl.* **12**, 975 (1973).
6. B. L. Small, M. Brookhart, A. M. A. Bennett, *J. Am. Chem. Soc.* **120**, 4049 (1998).

Scripps Research Institute, La Jolla, CA, USA.
E-mail: pbaran@scripps.edu

10.1126/science.aac9883

Safeguarding gene drive experiments in the laboratory

Multiple stringent confinement strategies should be used whenever possible

By Omar S. Akbari^{1,2}, Hugo J. Bellen^{3,4}, Ethan Bier^{5,*}, Simon L. Bullock⁶, Austin Burt⁷, George M. Church^{8,9}, Kevin R. Cook¹⁰, Peter Duchek¹¹, Owain R. Edwards¹², Kevin M. Esvelt^{3,*}, Valentino M. Gantz⁵, Kent G. Golic¹³, Scott J. Gratz¹⁴, Melissa M. Harrison¹⁵, Keith R. Hayes¹⁶, Anthony A. James¹⁷, Thomas C. Kaufman¹⁰, Juergen Knoblich¹¹, Harmit S. Malik^{18,19}, Kathy A. Matthews¹⁰, Kate M. O'Connor-Giles^{14,20}, Annette L. Parks¹⁰, Norbert Perrimon^{9,21}, Phillip Port⁶, Steven Russell²², Ryu Ueda^{23,24}, Jill Wildonger²⁵

Gene drive systems promote the spread of genetic elements through populations by assuring they are inherited more often than Mendelian segregation would predict (see the figure). Natural examples of gene drive from *Drosophila* include sex-ratio meiotic drive, segregation distortion, and replicative transposition. Synthetic drive systems based on selective embryonic lethality or homing endonucleases have been described

previously in *Drosophila melanogaster* (1–3), but they are difficult to build or are limited to transgenic populations. In contrast, RNA-guided gene drives based on the CRISPR/Cas9 nuclease can, in principle, be constructed by any laboratory capable of making transgenic organisms (4). They have tremendous potential to address global problems in health, agriculture, and conservation, but their capacity to alter wild populations outside the laboratory demands caution (4–7). Just as researchers working with self-propagating pathogens must ensure that these agents do not escape to the outside world, scientists working in the laboratory with gene drive constructs are responsible for keeping them confined (4, 6, 7).

Two of us recently used a CRISPR/Cas9-based gene drive system to generate a *Drosophila* strain homozygous for a loss-of-function mutation [the mutagenic chain reaction (6)] (see the figure). Even though *D. melanogaster* ordinarily poses no threat to human health or agriculture, the accidental release of flies carrying gene drive constructs from the laboratory could have unpredictable ecological consequences. This study there-

fore used institutionally approved stringent barrier methods. Only one experimenter handled the flies, inside an Arthropod Containment Level 2 insectary suitable for work with mosquitoes carrying human pathogens. Because barrier protocols can be vulnerable to human error (8), these authors suggested (6) that additional molecular confinement methods described (4) and used by others of us in budding yeast (9) could further reduce risks. That these studies documented highly efficient RNA-guided gene drive in flies and yeast underscores the potential of the technology and the risk resulting from an accidental release.

As concerned scientists working in related areas, we engaged in collective discussions to identify and publicize interim safety recommendations for laboratory

research involving potential gene drive systems while formal national guidelines are developed. Although we cannot claim to represent all researchers, we share a commitment to the safe and responsible development of gene drive technology. Although we differ in our assessments of the types of precaution needed, we recognize that any single confinement strategy could fail. We therefore unanimously recommend that future studies use a combination of stringent confinement strategies (see the table) whenever possible and always use safeguards adequate for preventing the unintentional release of synthetic gene drive systems into natural populations.

RECOMMENDATIONS. RNA-guided gene drive systems are created by delivering into the germline a DNA cassette encoding Cas9 and a single synthetic guide RNA (sgRNA) that is flanked by sequences matching those on either side of the sgRNA target site (4). Cas9 nuclease-stimulated copying of the cassette into the target allele leads to continued Cas9+sgRNA expression and subsequent copying of the cassette into the other allele (6, 9). The recurrent conversion of heterozygotes into homozygotes permits spread through populations (see the figure).

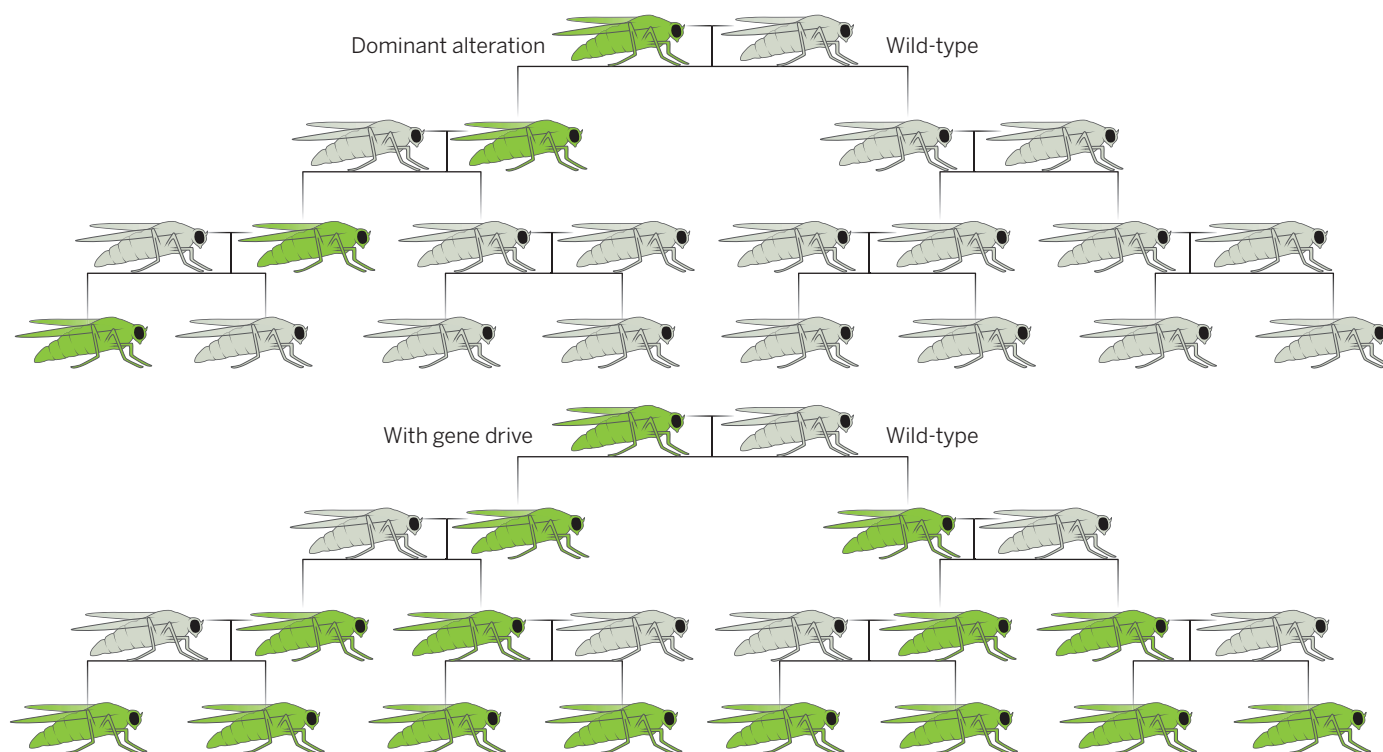
The vast majority of recent genome engineering approaches developed in model organisms neither involve nor risk the creation of gene drive systems. For example, *Drosophila* mutants can be readily generated by injecting sgRNAs or sgRNA-encoding plasmids into transgenic embryos expressing Cas9 (10–13) or by crossing

Potentially stringent confinement strategies for gene drive research

Multiple stringent confinement strategies should be used whenever possible.

TYPE	STRINGENT CONFINEMENT STRATEGY	EXAMPLES
Molecular	Separate components required for genetic drive Target synthetic sequences absent from wild organisms	sgRNA and Cas9 in separate loci (8) Drive targets a sequence unique to laboratory organisms (3,4,8)
Ecological	Perform experiments outside the habitable range of the organism Perform experiments in areas without potential wild mates	<i>Anopheles</i> mosquitoes in Boston <i>Anopheles</i> mosquitoes in Los Angeles
Reproductive	Use a laboratory strain that cannot reproduce with wild organisms	<i>Drosophila</i> with compound autosomes*
Barrier	Physical barriers between organisms and the environment • Remove barriers only when organisms are inactive • Impose environmental constraints • Take precautions to minimize breaches due to human error	Triply nested containers, >3 doors (6) Anesthetize before opening (6) Low-temperature room, air-blast fans Keep careful records of organisms, one investigator performs all experiments (6)

*An example of reproductive confinement would be *Drosophila* laboratory strains with a compound autosome, where both copies of a large autosome are conjoined at a single centromere. These strains are fertile when crossed inter se but are sterile when outcrossed to any normal or wild-type strain because all progeny are monosomic or trisomic and die early in development.



The spread of RNA-guided gene drive systems. Unlike the population dynamics of normal genomic alterations, gene drive systems can spread changes through wild populations by converting heterozygotes into homozygotes in each generation.

sgRNA-expressing strains to Cas9-expressing strains (12–14). These approaches do not risk creating a gene drive system because cassettes encoding Cas9 and sgRNA are not inserted into the cut site or located adjacent to one another in the genome and can thus be safely used by researchers without additional precautions. Given the availability of efficient alternatives and the potential risks, we recommend that gene drive approaches to genome engineering be strictly reserved for cases that require their use.

The safest approach for using gene drives creates biallelic mutations with an sgRNA-only cassette that can spread only when combined with an unlinked Cas9 transgene (4). In such a “split gene drive system,” homozygous individuals lacking the Cas9 gene can be easily isolated in subsequent generations. The efficiency of gene drive exhibited by a split system in yeast is equivalent to that of a construct encoding both Cas9 and sgRNA (9). Split drive systems present a much lower

risk if organisms are accidentally released because the population frequency of the Cas9 gene will be determined by normal, nondrive dynamics, consequently limiting the spread of the sgRNA cassette.

Nevertheless, any mutational event that moves the Cas9 gene into or directly adjacent to the sgRNA cassette could create an autonomous Cas9+sgRNA drive system by allowing the Cas9 gene to be copied into the target locus along with the sgRNA cassette upon repair of Cas9-induced DNA cleavage. Although the probability of such an event is extremely low, we recommend that at least one additional form of stringent confinement be used (see the table) and that the strains be continually monitored.

Other forms of stringent confinement include performing experiments in an area lacking wild populations (4) and, when the goal is to study gene drive systems in the laboratory, exclusively targeting synthetic sequences not found in natural populations

(3, 4, 9). Because these strategies suffer from independent vulnerabilities, the safety improvements afforded by combining them will be multiplicative. Thus, the great majority of gene drive experiments can be performed with minimal risk of altering wild populations. Accordingly, we strongly recommend that

1) All work involving potential gene drive systems should be preceded by a thorough assessment by the relevant biosafety authorities of the risk of unwanted release from the laboratory. We encourage these authorities to seek guidance from external experts and make their evaluation available to others.

2) All laboratory gene drive experiments should employ at least two stringent confinement strategies (see the table) whenever possible to minimize the risk of altering wild populations. Using one form of confinement may be justified only if relevant biosafety authorities determine that

¹Department of Entomology, Univ. of California, Riverside, CA 92507, USA. ²Center for Disease Vector Research, Institute for Integrative Genome Biology, Univ. of California, Riverside, CA 92507, USA.

³Department of Molecular and Human Genetics, Baylor College of Medicine, Houston, TX 77030, USA. ⁴Howard Hughes Medical Institute, Baylor College of Medicine, Houston, TX 77030, USA. ⁵Section of Cell and Developmental Biology, Univ. of California, San Diego, La Jolla, CA 92095, USA. ⁶Division of Cell Biology, Medical Research Council Laboratory of Molecular Biology, Cambridge CB2 0QH, UK.

⁷Department of Life Sciences, Imperial College London, Silwood Park, Ascot, Berks SL5 7PY, UK. ⁸Wyss Institute for Biologically Inspired Engineering, Harvard Medical School, Boston, MA 02115, USA.

⁹Department of Genetics, Harvard Medical School, Boston, MA 02115, USA. ¹⁰Bloomington Drosophila Stock Center, Department of Biology, Indiana Univ., Bloomington, IN 47405, USA. ¹¹Institute of Molecular Biotechnology of the Austrian Academy of Sciences, 1030 Vienna, Austria. ¹²CSIRO Centre for Environment and Life Sciences, Underwood Avenue, Floreat, WA 6014, Australia. ¹³Department of Biology, Univ. of Utah, Salt Lake City, UT 84112, USA. ¹⁴Laboratory of Genetics, Univ. of Wisconsin-Madison, Madison, WI 53706, USA. ¹⁵Department of Biomolecular Chemistry, Univ. of Wisconsin-Madison, Madison, WI 53706, USA. ¹⁶CSIRO Biosecurity Flagship, General Post Office Box 1538, Hobart, Tasmania, 7001, Australia. ¹⁷Departments of Microbiology & Molecular Genetics and Molecular Biology & Biochemistry, Univ. of California at Irvine, Irvine, CA 92697, USA. ¹⁸Division of Basic Sciences, Fred Hutchinson Cancer Research Center, Seattle, WA 98109, USA. ¹⁹Howard Hughes Medical Institute, Fred Hutchinson Cancer Research Center, Seattle, WA 98109, USA. ²⁰Laboratory of Cell and Molecular Biology, Univ. of Wisconsin-Madison, Madison, WI 53706, USA. ²¹Howard Hughes Medical Institute, Harvard Medical School, Boston, MA 02115, USA. ²²Department of Genetics, Univ. of Cambridge, Cambridge, Cambridgeshire CB2 3EH, UK. ²³Department of Genetics, Graduate Univ. for Advanced Studies, Mishima, Shizuoka 411-8540, Japan. ²⁴NIG-Fly Stock Center, National Institute of Genetics, Mishima, Shizuoka 411-8540, Japan. ²⁵Department of Biochemistry, Univ. of Wisconsin-Madison, Madison, WI 53706, USA. *Corresponding author. E-mail: kevin.esvelt@wyss.harvard.edu (K.E.); ebier@ucsd.edu (E.B.)

it will reduce the probability of release to a level that is acceptably low. This probability must be defined on a case-by-case basis. The analyses necessary to confidently predict the efficacy of confinement strategies for gene drive systems are in a nascent form. Therefore, any proposal to use one rather than multiple forms of confinement requires even greater scrutiny and extensive deliberation between regulatory authorities and scientists.

3) Organisms carrying gene drive constructs that could spread if the reproductively capable life stages were to escape in transit should not be distributed to other institutions until formal biosafety guidelines are established. Whenever possible, laboratories should instead send DNA constructs or information sufficient to reconstruct the gene drive. Protocols for distributing materials should be established in discussion with the wider research community and other relevant stakeholders.

Broadly inclusive and ongoing discussions among diverse groups concerning safeguards, transparency, proper use, and public involvement should inform expert bodies as they develop formal research guidelines for gene drive research in the laboratory and potential transitions to open field trials. We applaud the U.S. National Academy of Sciences for committing to provide recommendations for responsible gene drive research (15). By recommending strong safeguards and encouraging discussion of this technology, we hope to build a foundation of public trust for potential future applications in public health, sustainable agriculture, and ecological conservation. ■

REFERENCES AND NOTES

1. C.-H. Chen *et al.*, *Science* **316**, 597 (2007).
2. O. S. Akbari *et al.*, *Curr. Biol.* **23**, 671 (2013).
3. Y.-S. Chan, D. A. Naujoks, D. S. Huen, S. Russell, *Genetics* **188**, 33 (2011).
4. K. M. Esvelt, A. L. Smidler, F. Catteruccia, G. M. Church, *eLife* **2014**, e03401 (2014).
5. K. A. Oye *et al.*, *Science* **345**, 626 (2014).
6. V. M. Gantz, E. Bier, *Science* **348**, 442 (2015).
7. A. Burt, *Proc. R. Soc. London Ser. B* **270**, 921 (2003).
8. R. D. Henkel *et al.*, *Appl. Biosaf.* **18**, 171 (2012).
9. J. E. DiCarlo *et al.*, *bioRxiv* 013896 (2015).
10. X. Ren *et al.*, *Proc. Natl. Acad. Sci. U.S.A.* **110**, 19012 (2013).
11. S. J. Gratz *et al.*, *Genetics* **196**, 961 (2014).
12. F. Port, H.-M. Chen, T. Lee, S. L. Bullock, *Proc. Natl. Acad. Sci. U.S.A.* **111**, E2967 (2014).
13. F. Port *et al.*, *G3 (Bethesda)* **5**, 1493 (2015).
14. S. Kondo, R. Ueda, *Genetics* **195**, 715 (2013).
15. National Research Council, *Gene Drive Research in Non-Human Organisms: Recommendations for Responsible Conduct* (DELS-BLS-15-06, National Academy of Sciences, Washington, DC, 2015); <http://bit.ly/CurrProjects-regul>.

ACKNOWLEDGMENTS

The authors are grateful for conversations with T. Wu, J. Lunshof, and A. Birnbaum. V.M.G., E.B., G.M.C., and K.M.E. are inventors on relevant provisional and nonprovisional patents filed by the University of California and Harvard University.

Published online 30 July 2015

10.1126/science.aac7932

MICROBIOME

Microbiota RORγt Regulates intestinal suppressor T cells

Gut microbes influence the balance of regulatory T cell subtypes to control inflammation

By Ahmed N. Hegazy^{1,2} and Fiona Powrie^{1,2}

The immune system in the intestine is highly adapted to resist invading pathogens while residing peacefully with the abundant and diverse commensal bacteria that colonize the gastrointestinal tract. In turn, bacterial signals shape immunity in the intestine, promoting intestinal homeostasis in part by inducing and expanding specialized regulatory T (T_{reg}) cells that prevent aberrant inflammatory responses to self and environmental stimuli (1). On pages 989 and 993 of this issue, Ohnmacht *et al.* (2) and Sefik *et al.* (3), respectively, report the development and function of a subpopulation of T_{reg} cells found primarily in the large intestine, and characterized by expression of the nuclear hormone receptor retinoic acid receptor-related orphan receptor γt (RORγt). This is surprising because RORγt classically promotes the differentiation of T helper 17 (T_H17) cells, a population associated with tissue inflammation in many inflammatory diseases (4). Both studies show that microbiota-derived signals induce the expression of RORγt in T_{reg} cells that control intestinal inflammation (see the figure). These findings highlight the diversity of colonic T_{reg} cells, their complex transcriptional programs, and their important role in the intestine.

T_{reg} cells express the forkhead transcription factor Foxp3, which promotes their differentiation, maintenance, and function (5). Alongside anti-inflammatory functions, they control nonimmunological processes including tissue repair and metabolism in the parenchyma (6). T_{reg} cells also adapt to environmental cues by expressing canonical effector T cell-associated transcription factors to control pathogenic immune responses (7).

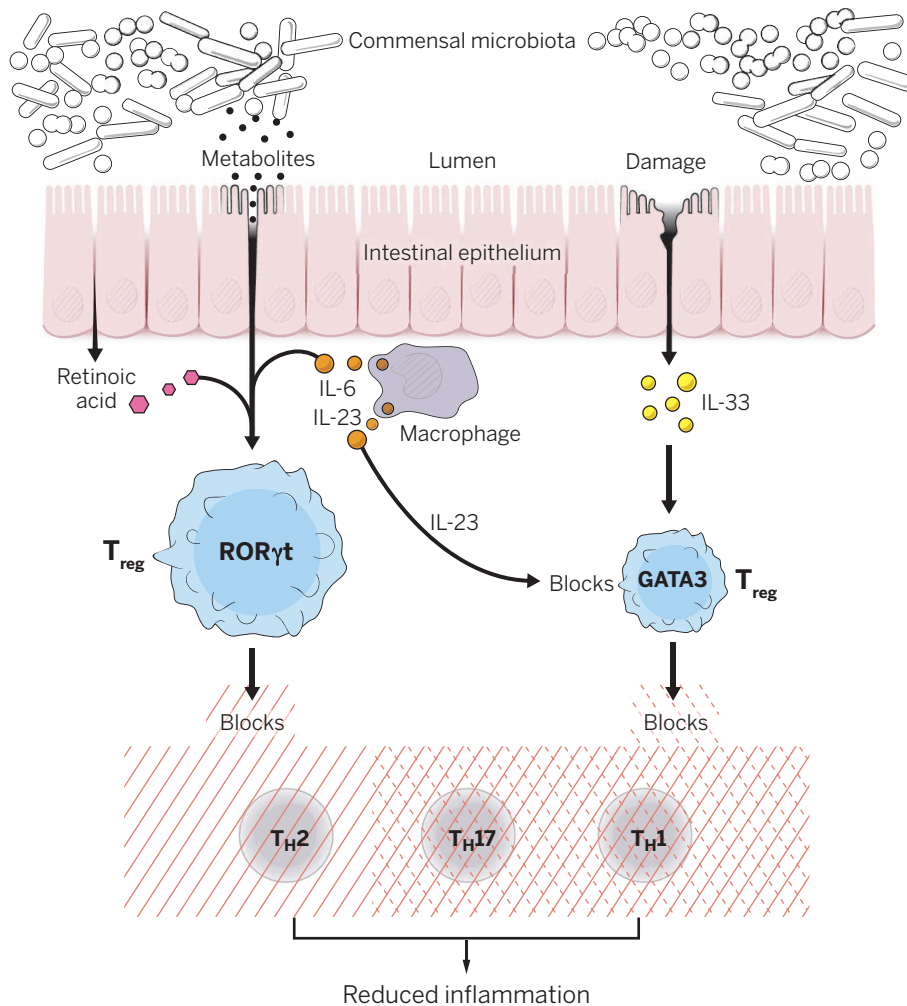
Both Ohnmacht *et al.* and Sefik *et al.* found that in mice, a large fraction of intestinal T_{reg} cells express RORγt. These cells were distinct from colonic T_{reg} cells that express the transcription factor GATA3 and are poised to respond to the cytokine interleukin (IL)-33 after tissue damage (8, 9). However, RORγt-expressing T_{reg} cells had an activated phenotype similar to that of GATA3-expressing T_{reg} cells, and bore markers related to T_{reg} cells

residing in lymphoid and non-lymphoid tissues (6). Strikingly, the microbiota was an absolute requirement for the induction and maintenance of RORγt-expressing T_{reg} cells in these animals. This T_{reg} cell population was markedly reduced in germ-free mice, and colonization with a diverse microbiota or consortia of symbionts was sufficient for the induction of RORγt-expressing T_{reg} cells. Sefik *et al.* went further and recolonized germ-free mice with 22 different bacterial species, and showed that a number of them (not belonging to any specific phylum or genus) elicited RORγt-expressing T_{reg} cells at comparable frequencies to a diverse microbiota. Short-chain fatty acids, which are common bacterial metabolites, can selectively expand intestinal T_{reg} cells (10). Ohnmacht *et al.* could increase RORγt-expressing T_{reg} cells by feeding mice a diet rich in the short-chain fatty acid butyrate.

“These studies...are an important stepping stone to deciphering the complex dynamics of different tissue-resident T_{reg} cell subsets...”

Which signals promote RORγt expression in T_{reg} cells? The T_H17-favoring cytokines IL-6 and IL-23 were required for accumulation of RORγt-expressing T_{reg} cells, which raises the question of what tips the balance toward these T cells rather than T_H17 cells. The vitamin A metabolite retinoic acid promotes T_{reg} cell generation in vivo and RORγt-expressing T_{reg} cells in vitro (11, 12). Consistent with this, Ohnmacht *et al.* show that vitamin A metabolism influences the differentiation equilibrium by favoring the development of RORγt-expressing T_{reg} cells in vivo. Although both T_{reg} cells and T_H17 cells express RORγt, analysis of all the transcripts expressed by each population revealed marked differences, suggesting that the transcriptional footprint of RORγt is context-dependent in different T cells.

What is the function of RORγt-expressing



Fine-tuning intestinal homeostasis. Microbiota and tissue-derived factors regulate the balance between RORγt-expressing and GATA3-expressing T_{reg} cells in the mouse intestine. The microbiota promotes RORγt expression in intestinal T_{reg} cells through multiple factors including bacterial metabolites, retinoic acid, and cytokines. Tissue-resident T_{reg} cells control effector T cell responses to promote intestinal homeostasis.

T_{reg} cells in health and disease? Ohnmacht *et al.* and Sefik *et al.* addressed this question by conditional deletion of the *Rorc* gene in T cells expressing Foxp3, producing mice specifically deficient in RORγt-expressing T_{reg} cells. The results were, however, ambiguous, perhaps reflecting differences in experimental models, animal housing, or the indigenous microbiota. Ohnmacht *et al.* observed a pronounced increase in type 2 cytokines under steady-state conditions, with consequent resistance to helminth infection. Inflammatory outcomes differed according to the chemically induced colitis model used. In oxazolone-induced colitis (a type 2 cytokine-driven model), mice developed severe and

lethal colitis accompanied by an increase in type 2 cytokines, whereas no alteration in pathology or T_H1 and T_H17 cell responses was observed in dextran sulfate sodium-induced colitis (a type 1 and type 17 cytokine-dependent model). Sefik *et al.* chemically blocked RORγt function and found that colonic T_{reg} cell frequency decreased, and interferon-γ and IL-17 production by effector T cells increased, under steady-state conditions. These mice developed severe colitis in another chemically induced (trinitrobenzenesulfonic acid) colitis model.

The findings of Ohnmacht *et al.* and Sefik *et al.* show that microbe-induced expression of RORγt by T_{reg} cells contributes to the control of intestinal inflammation. But what is the role of distinct colonic T_{reg} cell subsets (RORγt and GATA3) in intestinal homeostasis? Is there functional redundancy or division of labor? It may be that RORγt-expressing T_{reg} cells, which produce increased amounts of cytotoxic T lymphocyte

antigen 4 (CTLA4) and IL-10 (both of which dampen immune responses), decrease inflammation, whereas GATA3-expressing T_{reg} cells, which produce the tissue-remodeling factor amphiregulin and respond to the alarm signal (“alarmin”) IL-33, mediate tissue repair. It is certainly possible that locally produced inflammatory and tissue-derived factors might activate or antagonize different T_{reg} cell subpopulations to coordinate the anti-inflammatory and healing processes.

Another issue raised by these studies is whether T_{reg} cell subsets are specialized in controlling particular effector T cell responses. Ohnmacht *et al.* propose that RORγt-expressing T_{reg} cells are critical in controlling aberrant type 2 responses and that deficiencies in these microbiota-driven T_{reg} cells may contribute to increases in allergic disease. However, Sefik *et al.* observed control of T_H1 and T_H17 cells by RORγt-expressing T_{reg} cells. It seems highly likely that the relative activity and function of distinct colonic T_{reg} cell populations will be highly context-dependent and influenced by the microbiota. It is important to understand the ontogeny of RORγt-expressing T_{reg} cells and GATA3-expressing T_{reg} cells and whether they represent distinct lineages or can interconvert. Inducible labeling and tracking of T_{reg} cell subsets would provide valuable insights into their interplay and stability under steady-state and inflammatory conditions. It remains to be established why only certain bacterial species induce RORγt expression in T_{reg} cells and whether we can identify similar T_{reg} cell subsets in humans and manipulate them *in vivo*. The studies by Ohnmacht *et al.* and Sefik *et al.* are an important stepping stone to deciphering the complex dynamics of different tissue-resident T_{reg} cell subsets toward the understanding of how their dysregulation precipitates human disease. ■

REFERENCES AND NOTES

1. Y. Belkaid, T. W. Hand, *Cell* **157**, 121 (2014).
2. C. Ohnmacht *et al.*, *Science* **349**, 989 (2015).
3. E. Sefik *et al.*, *Science* **349**, 993 (2015).
4. T. Korn, E. Bettelli, M. Oukka, V. K. Kuchroo, *Annu. Rev. Immunol.* **27**, 485 (2009).
5. S. Z. Josefowicz, L.-F. Lu, A. Y. Rudensky, *Annu. Rev. Immunol.* **30**, 531 (2012).
6. D. Burzyn *et al.*, *Nat. Immunol.* **14**, 1007 (2013).
7. D. J. Campbell, M. A. Koch, *Nat. Rev. Immunol.* **11**, 119 (2011).
8. E. A. Wohlfert *et al.*, *J. Clin. Invest.* **121**, 4503 (2011).
9. C. Schiering *et al.*, *Nature* **513**, 564 (2014).
10. P. M. Smith *et al.*, *Science* **341**, 569 (2013).
11. D. Mucida *et al.*, *Science* **317**, 256 (2007).
12. M. Lochner *et al.*, *J. Exp. Med.* **205**, 1381 (2008).

ACKNOWLEDGMENTS

A.N.H. was supported by a European Molecular Biology Organization fellowship (ALTF 116-2012) and currently is a Marie Curie fellow (FP7-PEOPLE-2012-IEF, Proposal 330621). F.P. is supported by a Wellcome Trust Investigator Award.

¹Kennedy Institute of Rheumatology, Nuffield Department of Orthopaedics, Rheumatology and Musculoskeletal Sciences, University of Oxford, Headington, Oxford OX3 7FY, UK.

²Translational Gastroenterology Unit, Nuffield Department of Clinical Medicine, Experimental Medicine Division, John Radcliffe Hospital, University of Oxford, Oxford OX3 9DU, UK. E-mail: fiona.powrie@kennedy.ox.ac.uk

Defining the genus *Homo*

Early hominin species were as diverse as other mammals

By Jeffrey H. Schwartz¹ and Ian Tattersall²

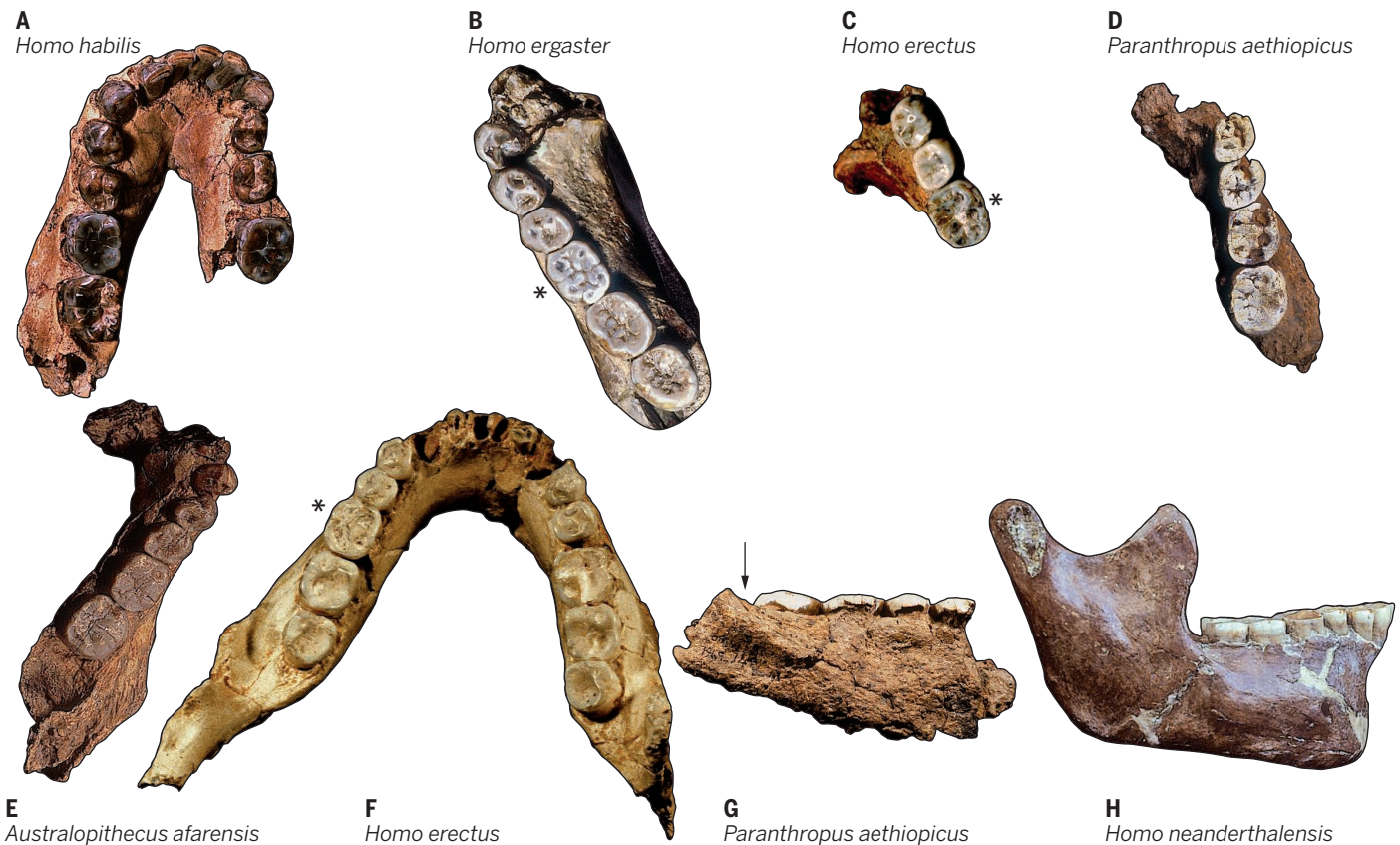
Almost 300 years ago, Linnaeus defined our genus *Homo* (and its species *Homo sapiens*) with the noncommittal words *nosce te ipsum* (know thyself) (1). Since then, fossil and molecular biology studies have provided insights into its evolution, yet the boundaries of both the species and the genus remain as fuzzy as ever, new fossils having been rather haphazardly assigned to species of *Homo*, with minimal attention to details of morphology.

In the late 18th century, Blumenbach attempted to distinguish *H. sapiens*—and by implication the genus *Homo*—from other

mammals, citing morphological features such as small canines not separated from small incisors, a chin, a short mandible and face, a large rounded skull atop a vertically oriented spine, a bowl-shaped pelvis, and erect posture (2). Some of these features turned out to characterize only living humans, but others are found in all hominins. The 1856 discovery of the Feldhofer Grotte Neandertal provoked heated debate about human antiquity (3). At one extreme, Thomas Huxley saw the Neandertals as extending a continuum of living races into the past; at the other, William King argued that its distinctive morphology warranted a separate species, *Homo neanderthalensis*, for the first time expanding our genus be-

yond *H. sapiens*. Once Eugene Dubois had assigned human-like fossils from Java to *Pithecanthropus erectus* (now regarded as *Homo erectus*) in 1894, the human family rapidly accumulated new members, taking on the appearance of typically mammalian diversity.

But in the mid-20th century, the view of *Homo* changed dramatically. First, Dobzhansky (4) proclaimed that because culture allows hominins to adapt to any ecosystem, speciation in the human lineage was impossible. Then, Mayr (5) declared that as all known hominids were upright bipeds, all belonged to the single genus *Homo*. Further, his definition of *Homo* included only three *Homo* species—*H. transvaalensis* (the early hominids now known as australopiths), *H. erectus*, and *H. sapiens*—that were held to have transformed in sequence with time. The inclusion of the australopiths was rapidly rejected (6), but otherwise Mayr's extended concept of *Homo*, defined by adaptation rather than morphology, became rapidly entrenched in paleoanthropology (7).



What is “early *Homo*”? (A to C, F, H) Specimens attributed to *Homo* with dental and mandibular features that resemble those of australopiths [e.g., posteriorly narrow, tapered molars; notch between cheek-facing/buccal cusps (*); anteriorly tall mandible], and (D, E, G) australopiths with features claimed to be specific to *Homo* [e.g., anteriorly narrow molars; no buccal-cusp notch; last molar not entirely masked by the ascending portion of the mandible (arrow)]. (A) OH7 (*H. habilis*); (B) KNM-ER 992 (*H. ergaster*); (C) Sangiran 6 (*H. erectus*); (D and G) Omo 75-1969-14A (australopith, *Paranthropus aethiopicus*); (D) occlusal, (G) lateral; (E) A.L.128-23 (*A. afarensis*); (F) Tighenif 1 (*H. erectus*); (H) Tabun II (*H. neanderthalensis*). The OH7, KNM-ER 992, Sangiran 6, and Tighenif 1 molars narrow posteriorly (A, B, C, and F), but in Omo 75-1969-14A and A.L.128-23 they are narrower anteriorly (D and E). A buccal notch (*) is present in KNM-ER 992 (B), Sangiran 6 (C), and Tighenif (F), but not in Omo 75-1969-14A (D) and A.L.128-23 (E). The last molar of Omo 75-1969-14A (G) would have been partially exposed in front of the ramus (arrow). The Tabun II mandible (H) is tall anteriorly. The fossils are not to scale.

In 1964, Leakey and colleagues (8) attributed the newly discovered ~1.8-million-year-old partial mandible, skullcap and hand (OH7) and foot (OH8), plus other materials from Olduvai Gorge, to the new species *Homo habilis*. This species replaced the very roughly contemporaneous South African australopiths in Mayr's transformationist scenario, although there was scant morphological justification for including any of this very ancient material in *Homo*. Indeed, the main motivation appears to have been Leakey's desire to identify this hominid as the maker of the simple stone tools found in the lower layers of the Gorge, following the dictum of *Man the Toolmaker* (9). This association has subsequently proven highly dubious (10). The inclusion in *Homo* of the *H. habilis* fossils so broadened the morphology of the genus that further hominids from other sites could be shoehorned into it almost without regard to their physical appearance. As a result, the largely unexamined definition of *Homo* became even murkier.

One strains to identify any derived features that would describe all or even most of this morass of specimens. Yet, subsequent attempts to define *Homo* have typically accepted the expanded genus (7, 11, 12). For example, Antón *et al.* recently united disparate East African, Georgian, and Asian fossils in *H. erectus*, prior to delineating two groups of "early *Homo*" (7). They excluded the *H. habilis* fossils from Olduvai from consideration because the OH7 mandible is distorted. One of their early *Homo* groups is exemplified by the Koobi Fora KNM-ER 1470 cranium and is derived in its tall, flat face and anteriorly straight-across maxilla that corners at the second premolar. The other, typified by the KNM-ER 1813 cranium, is distinguished by primitive (hence undiagnostic) features of its anteriorly rounded, narrow, and roughly parallel-sided maxilla. Had the authors not assigned the KNM-WT 15000 Nariokotome skull and skeleton to *H. erectus* (a species that is actually defined by younger, highly distinctive materials from Trinil and Sangiran, Java), an alternative might have been to note the striking facial, maxillary, and dental resemblances between KNM-ER 1813 and the Nariokotome individual. But either way, the ineluctable conclusion was that multiple species existed within "early *Homo*."

Shortly thereafter, Spoor *et al.* (11) virtually reconstructed the OH7 mandible, additionally extrapolating maxillary shape. As previously reported for the mandible (13),

they found that the resulting jaws resembled those of australopiths and apes in being long, narrow, and roughly parallel-sided. Whereas Antón *et al.* had rejected brain size as a defining feature of their "early *Homo*" groups, Spoor *et al.* inferred from their reconstruction of the OH7 cranial vault that in early *Homo*, the jaws remained primitive, but the brain was enlarged. Noting dissimilarities both between *H. habilis* and other "early *Homo*," and among the latter, Spoor *et al.* also argued that "early *Homo*" included multiple species.

Concurrently, Villmoare *et al.* (12) identified a ~2.8-million-year-old mandible with some teeth (LD350-1) from Ethiopia's Ledi-Geraru as the earliest member of *Homo*. Their reasons were that, unlike *Australopithecus afarensis* especially, its mandible is shallow anteriorly; its tooth rows are divergent; its ramus arises opposite the last,

"If we want to be objective, we shall almost certainly have to scrap the iconic list of names in which hominin fossil specimens have historically been trapped..."

not second, molar; and its preserved M2 and M3 are narrower anteriorly, shallowly notched between the buccal cusps, and rounded posteriorly rather than tapering. They thus concluded that *Homo* had ancient roots and was diverse early on.

These studies clearly raise issues that will have to be clarified in any satisfactory morphological definition of the genus *Homo* and the species within it (see the figure). For example, mandibular shape is australopith-like in OH7 (panel A), KNM-ER 992 (panel B), and Lantian 1; the mandible is deep anteriorly in relatively recent *Homo* KRM1B/AP6222, Tabun II (panel H), and Qafzeh 9; the ramus arises opposite M2 in *H. sapiens* and such australopiths as SK55b and Omo 75-1969-14A (panels D and G); and, as in australopiths, the molars are notched buccally in KNM-ER 992 and *H. erectus* Sangiran 6 (panel C), while being broad anteriorly with tapered last molars in the temporally separated KNM-ER 992, Tighenif 1 and 2 (panel F), Qafzeh 2, and KRM/AP6222-6230, all assigned to *Homo*. Conversely, in some undoubted australopiths, such as SK25, SKW5, and Omo 75-1969-14A, the preserved molars are LD350-1-like in being narrow anteriorly and/or flat buccally, as in Omo 75-1969-14A and Hadar A.L.128-23 (panel E) (13).

Recent analyses (7, 11, 12) agree in recognizing that the term "early *Homo*" masks taxonomic diversity. But they produce inconsistent results. Wood and Collard (14), for example, suggest that the species *H. habilis* and *Homo rudolfensis* be excluded from *Homo* for adaptive reasons, whereas Antón *et al.* (7) claim that an adaptive shift unites these species. Spoor *et al.* (11) stress the australopith-like shape of the *H. habilis* OH7 mandible, whereas Villmoare *et al.* (12) assert that the more derived features of LD350 warrant its inclusion in *Homo*. Nonetheless, all make clear how sorely both our concept of *Homo*, and the number of its known species, require reassessment.

The fact that detail has often been overshadowed by generalization in the study of the hominin fossil record is a product of paleoanthropology's unique history (3). But tradition alone cannot justify maintaining the status quo. Perhaps it is time to forget parochial habit and to begin approaching hominid systematics as students of other organisms do, especially in undertaking broader and morphologically more detailed comparisons than have been customary, and in revisiting morphological criteria for species recognition. If we want to be objective, we shall almost certainly have to scrap the iconic list of names in which hominin fossil specimens have historically been trapped, and start from the beginning by hypothesizing morphs, building testable theories of relatedness, and rethinking genera and species. In contrast to Mayr's austere linearity, we may find that human evolution rivaled that of other mammals in its evolutionary experimentation and luxuriant diversity. ■

REFERENCES

1. C. Linnaeus, *Systema naturae per regna tria naturae, secundum classes, ordines, genera, species cum characteribus, differentiis, synonymis, locis* (Laurentii Salvii, Stockholm, 1735).
2. J. F. Blumenbach, *On the Natural Varieties of Mankind (De Generis Humani Varietate Nativa)* (Bergman, New York, 1969), vol. 1775 and 1795 treatises.
3. I. Tattersall, J. H. Schwartz, *Extinct Humans* (Westview, Boulder, CO, 2000).
4. T. Dobzhansky, *Am. J. Phys. Anthropol.* **2**, 251 (1944).
5. E. Mayr, *Cold Spring Harb. Symp. Quant. Biol.* **15**, 109 (1950).
6. J. T. Robinson, *Am. J. Phys. Anthropol.* **12**, 181 (1954).
7. S. C. Antón, R. Potts, L. C. Aiello, *Science* **345**, 1236828 (2014).
8. L. S. B. Leakey, P. V. T. Tobias, J. R. Napier, *Nature* **202**, 7 (1964).
9. K. Oakley, *Man the Toolmaker* [British Museum (Natural History), London, 1949].
10. J. de Heinzelin *et al.*, *Nature* **284**, 625 (1999).
11. F. Spoor *et al.*, *Nature* **519**, 83 (2015).
12. B. Villmoare *et al.*, *Science* **347**, 1352 (2015).
13. J. H. Schwartz, I. Tattersall, *The Human Fossil Record*, vol. 4: *Craniodental Morphology of Australopithecus, Paranthropus, and Orrorin* (Wiley-Liss, New York, 2005).
14. B. Wood, M. Collard, *Science* **284**, 65 (1999).

¹Department of Anthropology, University of Pittsburgh, Pittsburgh, PA 15260, USA. ²Division of Anthropology, American Museum of Natural History, New York, NY 10024, USA. E-mail: jhs@pitt.edu; iant@amnh.org



Louis Figuier's *La Terre Avant le Déluge*
[*The World Before the Deluge*], 1863

EXHIBITION

Fact meets fiction

Science and fantasy collide in the newly refurbished Smithsonian Libraries Exhibition Gallery

By Rachel Gross

In 1835, readers of *The New York Sun* learned of an astounding discovery: life on the moon. Among the luxuriant forests, oceans, and volcanoes that carpeted our humble satellite lived fantastical creatures: bluish goat-unicorns, bipedal beavers, and fur-covered men who flapped around with bat-like wings. The *Sun*'s series of "scientific articles" would ultimately be revealed as history's most elaborate practical joke, known today as the Great Moon Hoax.

It's easy to poke fun at those who fell for such absurdities, but consider the atmosphere of the time: Scientists were beginning to plumb the depths of the ocean, explorers had just mapped the last unknown corners of the Earth, and physicists were developing the means to harness electricity. As Earth began to yield up the last of her remaining mysteries, our understanding of the universe and our place in it went through a sea change. Were bat-people really so much of a stretch?

This is the atmosphere of scientific possibility and wonder that the Smithsonian Museum of American History strives to cap-

ture in its new exhibition, *Fantastic Worlds: Science and Fiction 1780–1910*. Relying on nearly 70 rare books drawn from 21 library collections, *Fantastic Worlds* chronicles the era of rapid scientific discovery and innovation that gave birth to a burgeoning new literary genre: science fiction.

"We wanted to tell the story of 19th-century science through the lens of literature and the popular press," says Doug Dunlop, co-curator of the exhibit and a metadata librarian at Smithsonian Libraries.

Ocean explorations and fossil discoveries during the 1800s provided material for the works of Jules Verne, the star of this exhibition. *Twenty Thousand Leagues Under the Sea*, *Journey to the Center of the Earth*, and *Around the World in 80 Days* all gained richness, realism, and detail from Verne's meticulous research into the latest news and scientific articles. "I have invented nothing," he is quoted as saying. Yet his books are fanciful and didactic, chock-full of both imagination and facts about the real world.

By the 1800s, scientists had begun to investigate the powerful new force known as electricity and had developed inklings that it might be a critical element of life. Research that sought to draw connections between electricity and the life sciences had a deep impact on novelists of the day, including the young Mary Shelley, who had read up on the

Fantastic Worlds

Science and Fiction
1780–1910

Kirsten van der Veen and
Doug Dunlop, curators

National Museum of
American History,

Washington, DC, USA

1 July 2015–October 2016



animation of matter and electricity's effect on dead bodies when she penned *Frankenstein; or, the Modern Prometheus* in 1816.

Frankenstein, considered by many to be the first true work of science fiction, captures technology's possibilities both great and terrible. Quite unlike a Vernian tale of unabashed wonder, it is the haunting moral tale of a scientist who pushes the boundaries of nature and the consequences that befall him—a natural outgrowth of an era of exploration that seemed to be crossing many of man's frontiers and taboos.

In *Fantastic Worlds*, art and fact are presented as equal strands in a single, grand tapestry: An Inuit stone knife is displayed beside a print of fantastical Arctic landscapes; a blown-up microscope slide of the ocean floor is overlaid on an enlarged print from *Twenty Thousand Leagues*; scientific manuscripts chronicling "animal electricity" are displayed next to Frankenstein-like images of a corpse coming to life. Standing before each display, one feels the same thrill of wonder and discovery at the historical science as toward the ideas presented in the science fiction. Perhaps, the exhibition suggests, the two are not such strange bedfellows after all.

One weakness of the exhibition is that it implies that groundbreaking ideas followed a unidirectional path from science to fiction. Yet, in reality, many of the ideas that cropped up for the first time in science fiction ended up inspiring real scientific leaps. For instance, Verne has been credited as the inspiration for a wealth of scientific innovations, from submarine design, to the concept of the helicopter, to the Hubble telescope. (The exhibit does mention in passing that Verne foreshadowed the launch of a NASA rocket from Florida.)

Which brings us back to the Great Moon Hoax. The winged moonman reminds us of a time when all was possible, a time when the only thing the public could expect was to have their expectations upended. In the end, the hoax deftly captures the merging of two frontiers, two fantastic worlds: the one outside our heads and the one within.

The reviewer is a writer at Slate magazine in Washington, DC.
E-mail: rachelegross@gmail.com

10.1126/science.aac7812

HISTORY OF SCIENCE

The daring doctor

John Paul Stapp and the biophysical boundaries of the human body

By Lee Vinsel

On 10 December 1954, Col. John Stapp shot across the grounds of Holloman Air Force Base on a rocket sled, reaching 639 miles per hour and coming to a complete halt in less than 1.37 seconds. During his short trip, he experienced forces of 46.2 g. Stapp survived the experiment, leading *Time* magazine to call him “the fastest man on Earth.” The hogs that had been subjected to the harrowing trip before Stapp were not so lucky. They were eaten at base picnics, dubbed “Operation Barbecue.”

The feat was not a publicity stunt. Stapp, a biophysicist and medical doctor, was conducting an experiment in the emerging scientific field of biomechanics. His work in this arena ultimately played a major role in aviation and automobile safety, space flight, and other fields. Stapp has deserved a good biography for years. Craig Ryan's new book, *Sonic Wind*, partly answers that need, although it will leave many readers desiring more.

In smooth, novelistic prose, Ryan recounts how Stapp, a child of Baptist missionaries, spent much of his youth in Brazil before moving to the United States as a teenager. He went on to receive a Ph.D. in biophysics from the University of Texas at Austin and an M.D. from the University of Minnesota, Twin Cities. Stapp joined the Army Medical Corps in October 1944 and quickly became involved in cutting-edge research in aviation medicine, particularly projects focused on the extreme forces, temperatures, and other hardships faced by jet pilots, astronauts, and motor vehicle operators.

First at Muroc (later renamed Edwards) Air Force Base and later at Holloman, Stapp conducted a series of experiments involving rocket sleds that were designed to test how much force the human body could withstand. His findings—and his willingness to serve as a test subject in his own experi-

ments—won Stapp fame and came to influence safety protocols in a number of areas.

Early in his career, Stapp took an interest in automobile accidents, and in 1955, he organized the first conference on crash safety. The community of researchers that Stapp brought together came to play a fundamental role in reforming automotive safety when Ralph Nader and others used their ideas to create federal automotive safety standards in the 1960s.

Ryan humanizes Stapp wonderfully. We learn about his upbringing, his love life,



Colonel John Stapp endures the effects of acceleration and deceleration in a rocket-propelled research sled.

his personal tragedies and insecurities, and his regular battles with depression. Stapp comes across as a truly entrepreneurial spirit who had a knack for winning others to his cause and would stop at nothing to reach his goals.

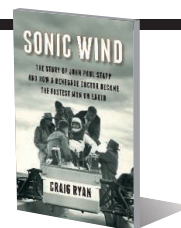
Two problems undermine Ryan's fine work. First, he does little to place Stapp in historical context. For example, Ryan mentions that Stapp worked in biophysics and industrial medicine, but he does not describe these two young disciplinary subfields or how they shaped Stapp's later work. Moreover, Ryan rarely mentions the Cold War and never examines how it pro-

Sonic Wind

The Story of John Paul Stapp and How a Renegade Doctor Became the Fastest Man on Earth

Craig Ryan

Liveright, 2015. 411 pp.



vided a rich environment for the creation and reception of Stapp's ideas.

The book's second problem is more fundamental. Ryan's brief biography on the book jacket refers to him as “the author of two acclaimed books on extreme adventure and scientific discovery,” and throughout the work, it is obvious that extremity is what interests him. He recounts Stapp's truly extreme experiments in loving detail. Unfortunately, this approach fails to

answer the key question raised by the book's title, namely, how Stapp became “the fastest man on Earth.”

At least since Bruno Latour's *The Pasteurization of France* was published in English in 1988, historians of science and technology have regarded stories of lone geniuses skeptically. In *Pasteurization*, Latour argues that Louis Pasteur's ideas about the germ theory of disease thrived in the 19th century, not because of his scientific genius but because a whole network of individuals came to accept and promote them. The same premise holds true for science that requires military bases, rocket sleds built by military contractors, and “zoos” full of test animals. Stapp succeeded because he built networks. His accomplishments in auto safety, for example, mostly came about as a result of his efforts to unite and support researchers who had already been working on the topic for years, and yet the reader gets no sense of this in *Sonic Wind*.

Ryan's approach translates to a problem of sources. He relies heavily on Stapp's unpublished memoir and personal correspondence. But many important questions can only be answered by other sources. For instance, what did Stapp's superiors think of him, and why did they allow journalists to cover his work when so many other Cold War projects were kept secret? It was this openness, after all, that enabled *Time* to name Stapp “the fastest man on Earth.” To truly live up to the book's subtitle, Ryan would have needed to cast a much broader net.

The reviewer is at the College of Arts and Letters, Stevens Institute of Technology, Hoboken, NJ 07030, USA.
E-mail: lee.vinsel@gmail.com

10.1126/science.aac8111

LETTERS

Edited by Jennifer Sills

Gene editing: Advising advice

IN RESPONSE TO recent forays into gene editing, the National Academies of Sciences and Medicine have established an advisory group and resolved to hold an international summit (1, 2). There has been much discussion of whether we should ("Germline gene therapy: We're ready," H. I. Miller. Letters, 19 June, p. 1325) or should not ("Eugenics lurk in the shadow of CRISPR," R. Pollack, Letters, 22 May, p. 871) move ahead with gene-editing technologies, but little discussion of how the decision and those that follow it will be made. We see two key problems with the proposed advisory group.

First, the group risks marginalizing key stakeholders. The named advisory group has 14 members: 13 are scientists and/or physicians; 1 is a law/bioethics scholar (1). Incorporating lay insights into biomedical and ethical decision-making fosters social consensus at and after times of controversy (3). Patients and their families will be the first to encounter gene editing. Their views could be included through focus groups. Participants (patients, family, and carriers) could be readily sampled from existing disease registries. Moreover, forays into the human genome theoretically implicate everyone. The public should thus also be consulted. Randomly distributed questionnaires could achieve this with relative ease. Social scientists are well equipped to design and implement such research.

Second, current ways of evaluating the ethics of emergent techniques like CRISPR tend to presume that science proceeds in a linear fashion. The challenge, Williams (4) notes, is to accommodate "the serendipity of innovation processes" without reductionism. Enduring partnerships between the natural and social sciences would promote nuanced exploration of gene editing and germline research by weaving ethical evaluation throughout research projects, rather than concentrating it at the outset. This could enrich how we think about ethics; the anthropology of ethics, for example, empirically examines how ethics manifest in routine work and interactions. Funding sources and publishing forums for interdisciplinary work are important long-term objectives, and would encourage constructive scholarly dialogue. The present moment is an opportunity to develop truly useful evaluative mechanisms. The resulting



systems should be diverse (disciplinarily, geographically, socially) and self-appraising (while committed to receiving external input). It is essential now to set a precedent for proceeding with CRISPR, germline interventions, and the cascade of innovations that will follow.

Courtney Addison^{1*} and Samuel Taylor-Alexander²

¹Department for Food and Resource Economics, The University of Copenhagen, Copenhagen, 1958, Denmark. ²Mason Institute for Medicine, Life Science and the Law, School of Law, University of Edinburgh, Edinburgh, EH8 9YL, UK.

*Corresponding author. E-mail: cpa@ifro.ku.dk

REFERENCES

1. The National Academies, "Advisory group for human gene editing initiative named" (15 June 2015); <http://www8.nationalacademies.org/onpinews/newsitem.aspx?RecordID=06152015>.
2. D. Baltimore *et al.*, *Science* **348**, 36 (2015).
3. K. Saha, J. B. Hurlbut, *Nature* **478**, 312 (2011).
4. R. Williams, *Sci. Cult.* **15**, 327 (2006).

The wisdom of baboon decisions

IN THEIR REPORT "Shared decision-making drives collective movement in wild baboons" (Reports, 19 June, p. 1358), A. Strandburg-Peshkin *et al.* argue that "the decision-making process driving day-to-day movement patterns in baboons is fundamentally shared." Their data show that, contrary to what one might expect, dominant individuals in the group do not determine the movement patterns of the group. However,

the data do not support their conclusion that the decisions of the group "emerge from a shared democratic process."

Strandburg-Peshkin *et al.* observed that some portion of the group initiates movement in one direction or another, and the remaining members of the group respond in various ways to how the initiators behaved. If the initiators go in roughly the same direction, the group tends to follow a path between the paths taken by the initiators. If the initiators deviate substantially from each other, the group tends to follow one set of initiators, rather than follow the path between the two sets of initiators. There is no basis for claiming that a democratic process explains these behaviors. Rather, the collective behavior seems to support a hypothesis of the "wisdom of the crowds," where a solution emerges from the many uncoordinated decisions of the various individuals involved (1).

K. Brad Wray

REFERENCE

1. J. Surowiecki, *Wisdom of Crowds* (Doubleday, New York, 2004).

Response

WE THANK K. B. Wray for his Letter, but we disagree with his interpretation of the terminology he uses. Wray presents a false dichotomy between "wisdom of the crowds" and "democratic decision-making." In the study of collective animal behavior, "shared consensus" (also referred to as "democratic consensus") means that each individual contributes to the decision-making process approximately equally [see (1–4)]. "Wisdom

of the crowds” refers to the enhancement in decision-making accuracy that can be achieved by aggregating information or preferences across many individuals (5) and can be an outcome of shared decision-making processes (2). Our data provide evidence that when the angle between initiated directions is above a critical angle, as predicted by the theory of shared decision-making (6), baboons tend to follow the majority, thus potentially benefiting from the “wisdom of the crowds.”

Ariana Strandburg-Peshkin,^{1*} Damien R. Farine,^{2,3,4*} Iain D. Couzin,^{1,5,6} Margaret C. Crofoot^{2,3*}

¹Department of Ecology and Evolutionary Biology, Princeton University, Princeton, NJ 08544, USA.

²Department of Anthropology, University of California, Davis, Davis, CA 95616, USA. ³Smithsonian Tropical Research Institute, Panama. ⁴Edward Grey Institute of Field Ornithology, Department of Zoology, University of Oxford, Oxford, OX1 3PS, UK. ⁵Department of Collective Behaviour, Max Planck Institute for Ornithology, Konstanz, D-78457, Germany. ⁶Chair of Biodiversity and Collective Behaviour, Department of Biology, University of Konstanz, Konstanz, D-78457, Germany.

*Corresponding author. E-mail: astrandb@princeton.edu (A.S.-P.); damien.farine@zoo.ox.ac.uk (D.R.F.); mccrofoot@ucdavis.edu (M.C.C.)

REFERENCES

1. L. Conradt, T. J. Roper, *Nature* **421**, 155 (2003).
2. L. Conradt, T. J. Roper, *Trends Ecol. Evol.* **20**, 449 (2005).
3. I. D. Couzin *et al.*, *Science* **334**, 1578 (2011).
4. C. Sueur, O. Petit, *Behav. Process* **78**, 84 (2008).
5. J. Surowiecki, *Wisdom of Crowds* (Doubleday, New York, 2004).
6. I. D. Couzin, J. Krause, N. R. Frants, S. A. Levin, *Nature* **433**, 513 (2005).

TECHNICAL COMMENT ABSTRACTS

Comment on “Extreme electric fields power catalysis in the active site of ketosteroid isomerase”

Aditya Natarajan, Filip Yabukarski, Vandana Lamba, Jason P. Schwans, Fanny Sunden, Daniel Herschlag

Fried *et al.* (Reports, 19 December 2014, p. 1510) demonstrated a strong correlation between reaction rate and the carbonyl stretching frequency of a product analog bound to ketosteroid isomerase (KSI) oxyanion hole mutants and concluded that the active-site electric field provides 70% of catalysis. Alternative comparisons suggest a smaller contribution, relative to the corresponding solution reaction, and highlight the importance of atomic-level descriptions.

Full text at <http://dx.doi.org/10.1126/science.aab1584>

Comment on “Extreme electric fields power catalysis in the active site of ketosteroid isomerase”

Deliang Chen and Tor Savidge

Fried *et al.* (Reports, 19 December 2014, p. 1510), demonstrate electric field-dependent acceleration of biological catalysis using ketosteroid isomerase as a prototypic example. These findings were not extended to aqueous solution because water by itself has field fluctuations that are too large and fast to provide a catalytic effect. Given physiological context, when water electrostatic interactions are considered, electric fields play a less important role in the catalysis.

Full text at <http://dx.doi.org/10.1126/science.aab0095>

Response to Comments on “Extreme electric fields power catalysis in the active site of ketosteroid isomerase”

Stephen D. Fried and Steven G. Boxer

Natarajan *et al.* and Chen and Savidge comment that comparing the electric field in ketosteroid isomerase’s (KSI’s) active site to zero overestimates the catalytic effect of KSI’s electric field because the reference reaction occurs in water, which itself exerts a sizable electrostatic field. To compensate, Natarajan *et al.* argue that additional catalytic weight arises from positioning of the general base, whereas Chen and Savidge propose a separate contribution from desolvation of the general base. We note that the former claim is not well supported by published results, and the latter claim is intriguing but lacks experimental basis. We also take the opportunity to clarify some of the more conceptually subtle aspects of electrostatic catalysis.

Full text at <http://dx.doi.org/10.1126/science.aab1627>

Response to Comment on “Global diversity and geography of soil fungi”

Leho Tedersoo, Mohammad Bahram, Sergei Põlme, Sten Anslan, Taavi Riit, Urmas Kõljalg, R. Henrik Nilsson, Falk Hildebrand, Kessy Abarenkov

Schadt and Rosling (Technical Comment, 26 June 2015, p. 1438) argue that primer-template mismatches neglected the fungal class Archaeorhizomycetes in a global soil survey. Amplicon-based metabarcoding of nine barcode-primer pair combinations and polymerase chain reaction (PCR)-free shotgun metagenomics revealed that barcode and primer choice and PCR bias drive the diversity and composition of microorganisms in general, but the Archaeorhizomycetes were little affected in the global study. We urge that careful choice of DNA markers and primers is essential for ecological studies using high-throughput sequencing for identification.

Full text at <http://dx.doi.org/10.1126/science.aaa5594>

TECHNICAL COMMENT

BIOPHYSICS

Comment on “Extreme electric fields power catalysis in the active site of ketosteroid isomerase”

Aditya Natarajan,¹ Filip Yabukarski,¹ Vandana Lamba,¹ Jason P. Schwans,²
Fanny Sunden,¹ Daniel Herschlag^{1*}

Fried *et al.* (Reports, 19 December 2014, p. 1510) demonstrated a strong correlation between reaction rate and the carbonyl stretching frequency of a product analog bound to ketosteroid isomerase oxyanion hole mutants and concluded that the active-site electric field provides 70% of catalysis. Alternative comparisons suggest a smaller contribution, relative to the corresponding solution reaction, and highlight the importance of atomic-level descriptions.

We were excited to see the data of Fried *et al.* (1) demonstrating a strong correlation between reaction rate and the stretching frequency of the carbonyl group of a product analog bound to a series of ketosteroid isomerase (KSI) oxyanion hole mu-

nants. These data were interpreted in terms of a model, calibrated using vibrational data and molecular dynamics simulations in a series of solvents, which led to the conclusion that the active-site electric field generated by the oxyanion hole and surrounding groups accounts for

10⁵-fold rate enhancement and 70% of the observed catalysis. Based on these findings, it was suggested that electrostatic forces are the dominant contributor to catalysis.

Below, we note that the conclusion of a dominant contribution to KSI catalysis relies on comparison to a hypothetical enzyme that provides zero electric field at the position of the carbonyl group and would not hold for a comparison to the corresponding reaction in aqueous solution. The accompanying analysis leading to an estimate of the rate advantage from positioning of KSI's general base is similarly affected. Finally, we note that electrostatic stabilization requires and is linked to positioning of the groups responsible for that stabilization.

Conservative mutations, such as the Tyr¹⁶Phe mutation in the construct employed by Fried *et al.*, often transmute a polar group to a nonpolar group and generate an apolar or hydrophobic environment that is less favorable toward charge accumulation than the polar environment in aqueous solution, and are inhibitory as a result (2). Thus, a “conservative” mutation of the dominant

¹Department of Biochemistry, Stanford University School of Medicine, Stanford, CA 94305, USA. ²Department of Chemistry and Biochemistry, California State University Long Beach, Long Beach, CA 90840, USA.
*Corresponding author. E-mail: herschla@stanford.edu

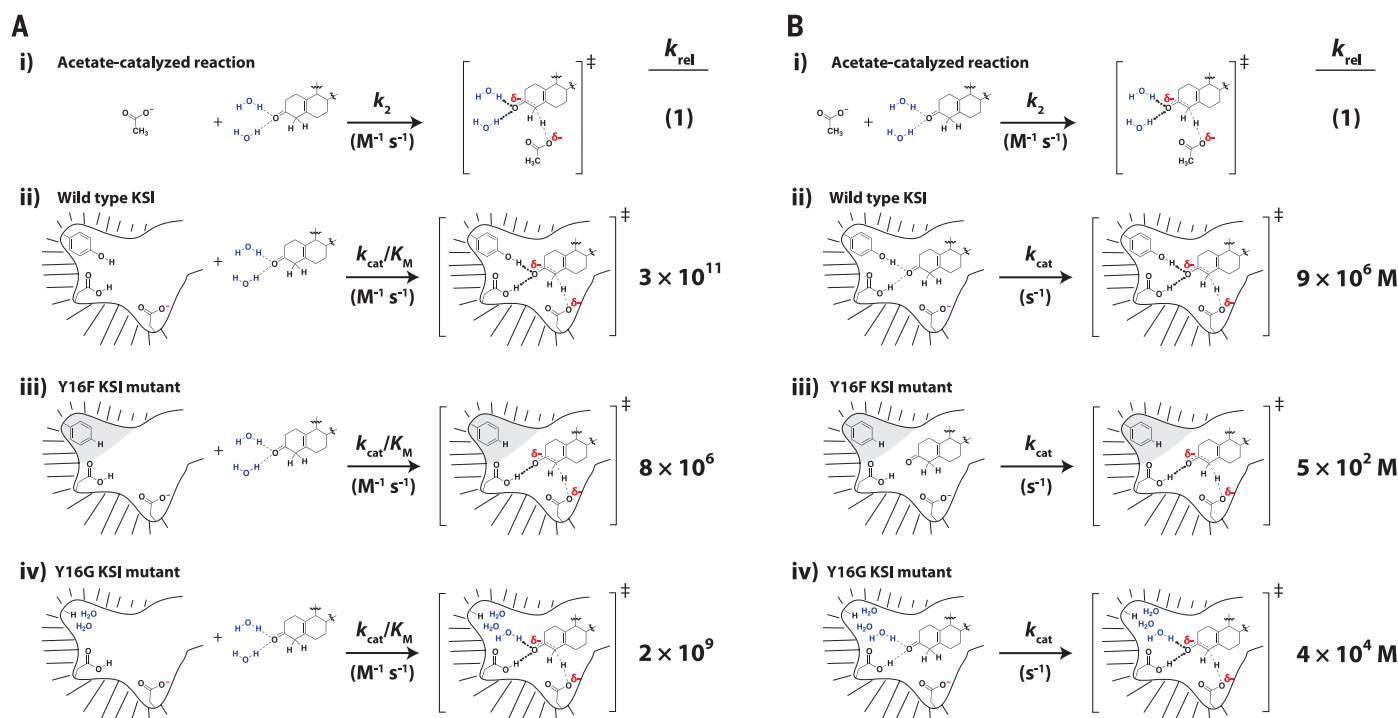


Fig. 1. Rate enhancement provided by different KSI variants relative to the rate of the acetate-catalyzed reaction. Rate enhancement provided by different KSI variants relative to the rate of the acetate-catalyzed reaction under (A) subsaturating and (B) saturating conditions. (i) Reaction between substrate and acetate in aqueous solution. (ii) Reaction between substrate and wild-type KSI. (iii) Reaction between substrate and KSI with a conservative Tyr¹⁶Phe mutation that replaces the oxyanion hole hydrogen-bond donor Tyr¹⁶ with a hydrophobic environment. (iv) Reaction between substrate and KSI with a Tyr¹⁶Gly

mutation, more drastic than the Tyr¹⁶Phe mutation above. The units of each rate constant are shown in parentheses under the corresponding reaction arrow. Values were computed from rate constants for variants of KSI from *Pseudomonas putida* tabulated in table S2 in Kraut *et al.* (2) and correspond to the substrate 5(10)-estren-3,17-dione, because a chemical step is rate-limiting for reaction of this substrate (9). Similar rate enhancements are provided for reactions with the substrate 5-androstene-3,17-dione referred to by Fried *et al.*, although a nonchemical step is partially rate limiting for this substrate (9, 10).

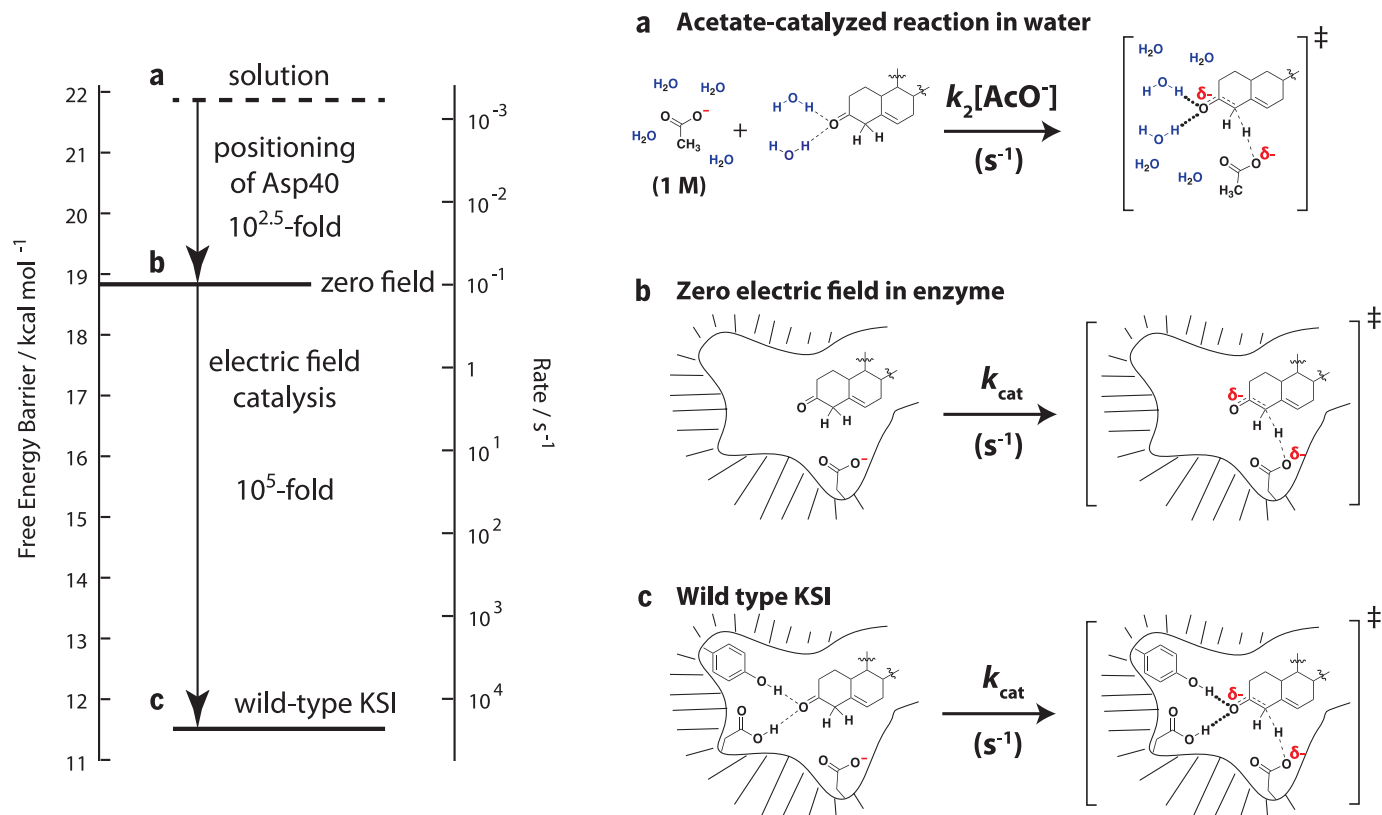


Fig. 2. Reactions used by Fried *et al.* to estimate the fraction of the overall catalytic power from the electric field on the carbonyl group.

The left side of the figure is reproduced from Fried *et al.* with the reactions annotated by the lowercase letters and a schematic of each corresponding reaction shown on the right. The reactions are depicted schematically on the right and are as follows: (a) Nonenzymatic reaction between acetate and substrate in aqueous solution. Because this is a second-order process

whose reaction rate depends on acetate concentration, Fried *et al.* used the observed rate constant at 1 M acetate (so that the calculated rate enhancement of $10^{2.5}$ is unitless but will vary with different concentrations of acetate used as the reference reaction). (b) Reaction with substrate bound to an enzyme that provides zero electric field at the carbonyl (and the same contribution from the general base as in wild-type KSI). (c) Reaction with substrate bound to wild-type KSI.

KSI oxyanion-stabilizing residue (3), such as Tyr¹⁶Phe, can exaggerate the catalytic contribution of active-site hydrogen-bonding groups relative to aqueous solution (Fig. 1A, reaction iii). Indeed, KSI variants with more extreme ablation of Tyr¹⁶ (e.g., Tyr¹⁶Ser, Ala, or Gly) are two orders of magnitude more active than the Tyr¹⁶Phe variant (Fig. 1A, reaction iv) (2), suggesting that replacing the hydrophobic Phe residue with what seems to be a relatively disordered water molecule is much less deleterious (2). In this mutant, only ~20% (log scale) of the catalytic power is lost and ~ 10^9 -fold catalysis remains, suggesting that the oxyanion hole may not be the dominant contributor to KSI catalysis.

Below, we lay out more explicitly the comparisons used by Fried *et al.* and demonstrate that there is likely more catalysis from the positioned general base than estimated by these authors, thereby helping to clarify the relative contributions of catalytic mechanisms and the underlying comparisons used to derive them.

Figure 3C from Fried *et al.* proposes a full accounting of catalysis, assigning a modest catalytic contribution from general base positioning and a dominant contribution from the enzyme's electric field. Figure 2 reproduces figure 3C in

Fried *et al.*, annotated with the corresponding reactions that were used by these authors to estimate the catalytic contributions. Three reactions were considered:

- Nonenzymatic reaction in aqueous solution between 1 M acetate and substrate.
- Substrate bound to a hypothetical enzyme that provides zero electric field at the position of the carbonyl group.
- Substrate bound to wild-type enzyme.

Fried *et al.* estimated the contribution from the positioned general base from comparison of reactions **a** and **b**, but these reactions have two differences, and thus, the comparison does not isolate the contribution from the positioned general base. Specifically, reaction **a** takes place with free general base (acetate ion) in aqueous solution, whereas reaction **b** takes place with positioned general base in an enzyme with a zero electric field at the oxyanion hole (Fig. 2). As noted above, a hydrophobic or zero-field oxyanion hole environment would be inhibitory relative to an aqueous environment, as also implied by the comparisons of figure 3, A and B, of Fried *et al.* Stated another way, charge localization is more difficult upon removal of the aqueous surroundings and placement in a zero field or hydrophobic

environment. Thus, the effect from the positioned general base appears to be underestimated by the comparison of reactions **a** and **b**. Correspondingly, this result implies an overestimation of the catalytic effect from the oxyanion hole.

In addition, Fried *et al.* use the assumption that the oxyanion hole and general base contributions are independent to parse the catalytic contributions, although, as they note, there is no experimental evidence to support this assumption. The additivity of the catalytic features remains to be tested.

Fried *et al.* consider effects of positioning and electrostatics and state that “contrary to earlier views [(4, 5)], electrostatic stabilization can be the more important of the two (Fig. 3C).” We emphasize that positioning is also important for electrostatic catalysis. As Fried *et al.* note elsewhere, “the active site achieves this large field by restricting H-bond conformations to those that are associated with the largest electric fields.” If there were no positioning of the active site groups giving rise to the electric field, the fields would be lower, and if positioning of the oxyanion hole and surrounding residues were incorrect (e.g., backward with respect to substrate), the fields could even be inhibitory. The field is a consequence of

both the functional groups that are present and their positioning. This positioning arises from the folding of the protein, using favorable folding energy to orient and restrict the conformational mobility of these groups, and from binding of the substrate, in a pocket also formed due to folding of the protein (6–8). Turning to the substrate, if there were no pocket or if the substrate were sterically restricted from approaching the oxyanion hole, then there would be less or no catalysis; if the substrate were bound but positioned such that its carbonyl group faced away from the oxyanion hole, then the oxyanion hole and its surroundings would not contribute to catalysis. In summary, electrostatic catalysis, to be effective, requires positioning—proper positioning of the substrate via binding interactions into a pocket that is created via protein folding as well as proper positioning of enzymatic groups, again via protein folding and substrate binding, to make favorable electrostatic interactions in the reaction's transition state. Thus, catalytic contributions from electrostatics and positioning appear to be inextricably linked. Understanding this linkage, and catalysis, will likely require descriptions that extend beyond measures of apparent electric fields to atomic-level descriptions and models, including the multiple states present in the ensemble of an enzyme-substrate

complex and the reaction probability from each state.

Another future challenge will be to understand the extent to which functional groups near and far from the active site contribute to the electric field perceived at the substrate carbonyl and how much they contribute to catalysis. Fried *et al.* (7) cite the observation of a nonzero field in the Tyr¹⁶Phe mutant to conclude that “a substantial electrostatic field contribution also arises from the environment fashioned by the enzyme scaffold.” An alternative model that remains to be tested is that the nonzero field in this mutant arises largely from Asp¹⁰³, the other oxyanion hole hydrogen-bond donor. The observation of a negligible electrostatic field effect from mutation of the Asp⁴⁰ general base to Asn suggests a limited propagation distance (7).

Vibrational measurements, like those elegantly presented by Fried *et al.*, provide a powerful means to compare enzyme variants, and the observed vibrational properties can be compared to predictions from computation to assess those models. For example, Fried *et al.* note that molecular dynamics simulations with KSI did not reproduce the electric fields calculated from the experimentally observed vibrational frequencies [supplementary text 4 of (7)], providing a strong indication of features or factors lacking in the

computation model, in its implementation, or in its underlying physical forces. Analogously, whether hydrogen-bond interactions can be quantitatively and accurately modeled as field effects or correlate with field effects and require more sophisticated atomic-level models remains to be determined. Regardless, vibrational data, as obtained by Fried *et al.* and others, provide an incisive window into the active site that will help test, develop, and refine increasingly accurate and predictive models for enzymatic catalysis.

REFERENCES

1. S. D. Fried, S. Bagchi, S. G. Boxer, *Science* **346**, 1510–1514 (2014).
2. D. A. Kraut, P. A. Sigala, T. D. Fenn, D. Herschlag, *Proc. Natl. Acad. Sci. U.S.A.* **107**, 1960–1965 (2010).
3. G. Choi *et al.*, *Biochemistry* **40**, 6828–6835 (2001).
4. M. I. Page, W. P. Jencks, *Proc. Natl. Acad. Sci. U.S.A.* **68**, 1678–1683 (1971).
5. J. R. Knowles, *Nature* **350**, 121–124 (1991).
6. D. A. Kraut, K. S. Carroll, D. Herschlag, *Annu. Rev. Biochem.* **72**, 517–571 (2003).
7. W. P. Jencks, *Adv. Enzymol. Relat. Areas Mol. Biol.* **43**, 219–410 (1975).
8. D. Blow, *Structure* **8**, R77–R81 (2000).
9. R. M. Pollack, S. Bantia, P. L. Bounds, B. M. Koffman, *Biochemistry* **25**, 1905–1911 (1986).
10. D. C. Hawkinson, T. C. M. Eames, R. M. Pollack, *Biochemistry* **30**, 10849–10858 (1991).

19 March 2015; accepted 24 July 2015
10.1126/science.aab1584

This copy is for your personal, non-commercial use only.

If you wish to distribute this article to others, you can order high-quality copies for your colleagues, clients, or customers by [clicking here](#).

Permission to republish or repurpose articles or portions of articles can be obtained by following the guidelines [here](#).

The following resources related to this article are available online at www.sciencemag.org (this information is current as of September 3, 2015):

Updated information and services, including high-resolution figures, can be found in the online version of this article at:

<http://www.sciencemag.org/content/349/6251/936.1.full.html>

A list of selected additional articles on the Science Web sites **related to this article** can be found at:

<http://www.sciencemag.org/content/349/6251/936.1.full.html#related>

This article **cites 10 articles**, 3 of which can be accessed free:

<http://www.sciencemag.org/content/349/6251/936.1.full.html#ref-list-1>

This article has been **cited by** 1 articles hosted by HighWire Press; see:

<http://www.sciencemag.org/content/349/6251/936.1.full.html#related-urls>

This article appears in the following **subject collections**:

Biochemistry

<http://www.sciencemag.org/cgi/collection/biochem>

TECHNICAL COMMENT

BIOPHYSICS

Comment on “Extreme electric fields power catalysis in the active site of ketosteroid isomerase”

Deliang Chen¹ and Tor Savidge^{2,3*}

Fried *et al.* (Reports, 19 December 2014, p. 1510) demonstrate electric field-dependent acceleration of biological catalysis using ketosteroid isomerase as a prototypic example. These findings were not extended to aqueous solution because water by itself has field fluctuations that are too large and fast to provide a catalytic effect. Given physiological context, when water electrostatic interactions are considered, electric fields play a less important role in the catalysis.

Fried *et al.* (1) report that the isomerization of 5-androstene-3,17-dione by ketosteroid isomerase (KSI) has a markedly higher (4×10^7 M) rate constant (k_{cat}) than in aqueous solution (k^{AcO}). The free-energy barrier for the reaction catalyzed by KSI is much lower because (i) the difference in effective acetate (COO^-) concentration (ΔG_{S}) is higher for KSI than for k^{AcO} ; (ii) different electric-field contributions on the C=O bond ($\Delta G_{\text{C=O}}$); and (iii) hydrogen abstraction by the carboxyl group (ΔG_{H}), as shown in Fig. 1. Thus,

$$\Delta G_{\text{S}} + \Delta G_{\text{C=O}} + \Delta G_{\text{H}} = -RT \ln(4 \times 10^7) = -10.5 \text{ kcal mol}^{-1} \quad (1)$$

Fried *et al.* also report that the free-energy barrier for the rate-limiting enolate transition catalyzed by KSI is $11.5 \text{ kcal mol}^{-1}$, compared with $18.8 \text{ kcal mol}^{-1}$ in a nonpolar environment where the electric field is 0. On this premise, KSI contributes an electric field of $7.3 \text{ kcal mol}^{-1}$ to its free-energy-barrier reduction when compared with the nonpolar environment. This model assumes that bulk water confers no electric power toward catalysis because it has field fluctuations that are too wide and fast compared with the narrow infrared shifts that are evident in KSI and its active-site mutants. Thus, $\Delta G_{\text{C=O}}$ is $-7.3 \text{ kcal mol}^{-1}$, ΔG_{S} is approximately $-3.2 \text{ kcal mol}^{-1}$, and ΔG_{H} is 0, because the model does not take into account the effect of hydrogen abstraction on the free-energy barrier.

Life on earth depends on water and the hydrogen bonds that it forms in biological systems. Water can accelerate reactions by more than 10^{10} -fold ($>13.8 \text{ kcal mol}^{-1}$ of free-energy-barrier

reduction) when atoms in transition states become more charged than in ground states (Fig. 1). Such hydrogen bonds potentiate catalysis in a number of ways that are also directly relevant to the isomerization of 5-androstene-3,17-dione by KSI mutants that contain active-site cavities sufficiently large for water to interact with C=O, as suggested by Kraut *et al.* (2). For example, because water forms electrostatic interactions with the negatively charged oxygen atom of the C=O group in 5-androstene-3,17-dione, these forces stabilize transition states as the oxygen atom is more negatively charged and reduce the free-energy barrier of the isomerization reaction by $\sim 4.0 \text{ kcal mol}^{-1}$.

The broad line width of C=O in 19-nortestosterone measured in aqueous solution indicates that electrostatic interactions between water and C=O adopt diverse conformations. A thermodynamic cycle shows to what extent broad electric fields of water can reduce the free-energy barrier for the isomerization reaction of 5-androstene-3,17-dione (Fig. 2). ΔG_{rig} represents the free-energy-barrier reduction by well-oriented active-site-associated water, which is expected to contribute a larger C=O spectral shift than in aqueous solution. Thus, ΔG_{rig} is less than -4 kcal mol^{-1} , based on the infrared spectra for C=O in nonpolar solvent, water, and KSI. A more accurate calculation of ΔG_{rig} ($-4.8 \text{ kcal mol}^{-1}$) is derived from the analysis of free-energy barriers during the isomerization of 5-androstene-3,17-dione by the KSI Tyr¹⁶Ser mutant, where water can interact with C=O ($13.6 \text{ kcal mol}^{-1}$), versus Tyr¹⁶Phe ($16.0 \text{ kcal mol}^{-1}$), where water interactions are absent (1, 2). This is supported by the observation that the infrared spectral shift of 19-nortestosterone bound to the Tyr¹⁶Ser mutation is narrow (1). From this, ΔG_{sol} is the free-energy-barrier reduction by water C=O interactions and can be obtained by

$$\Delta G_{\text{sol}} = -4.8 + \Delta G_1 - \Delta G_2 \quad (2)$$

Both ΔG_1 and ΔG_2 are greater than 0 at room temperature, just as ΔG for the transition from

water to ice is greater than 0. Because exact values for ΔG_1 and ΔG_2 are not available, we estimated ΔG_1 by assuming that water-C=O and water-water interactions are comparable. ΔG_1 is the maximum free energy of reorganization for the reference reaction and is close to the free-energy change of the process in which one hydrogen bond of a water molecule is fixed and the water molecule can still rotate freely around the hydrogen bond. At 273.2 K , ΔG , ΔH , and ΔS from water to ice are 0, $-1.44 \text{ kcal mol}^{-1}$, and $-5.26 \text{ cal mol}^{-1} \text{ K}^{-1}$, respectively. As one mole of water molecules in ice contains two moles of hydrogen bonds, and constrained water in the cycle can rotate in one direction, ΔH_1 and ΔS_1 are $-0.72 \text{ kcal mol}^{-1}$ and $-4.38 \text{ cal mol K}^{-1}$. $\Delta G_1 = 2 \times [-0.72 - 298 \times (-4.38)/1000] = 1.17 \text{ kcal mol}^{-1}$. Thus, the free-energy-barrier reduction by water is $\Delta G_2 + 3.63 \text{ kcal mol}^{-1}$. Because ΔG_2 is similar to ΔG_1 , ΔG_{sol} is closer to $-4.0 \text{ kcal mol}^{-1}$, which is estimated based on the C=O spectral shift in aqueous solution. Electrostatic interactions between the C=O group and water therefore contribute $\sim 4.0 \text{ kcal mol}^{-1}$ to the free-energy-barrier reduction for the reference reaction in water. Thus, the electrostatic contribution of the C=O group to free-energy-barrier reduction for the reaction catalyzed by KSI versus the reaction in water is $3.3 \text{ kcal mol}^{-1}$ (Fig. 2).

The origin of ΔG_{H} is desolvation of active-site Asp⁴⁰. In aqueous solution, the COO^- group is completely solvated and at least one water molecule is removed for COO^- to abstract the α -hydrogen atom, whereas in KSI, no water molecules are removed for Asp⁴⁰ to abstract the hydrogen atom (Fig. 1). The crystal structure of *Pseudomonas putida* KSI mutant Asp⁴⁰Asn complexed with androsten-3 β -ol-17-one (3) shows that the oxygen atom involved in abstracting the α -hydrogen is desolvated and surrounded by hydrophobic groups (Fig. 2), indicating that the desolvation process does not occur from the ground to transition state catalyzed by KSI. Rather, desolvation of Asp⁴⁰ occurs during substrate binding to KSI, supported by the observation that analog binding affinity increases by ~ 2 orders of magnitude for the Asp⁴⁰Ala mutation compared with wild-type (4). Moreover, electrostatic interactions with the COO^- group decrease as the reaction proceeds because the oxygen atoms of COO^- become less negatively charged, thereby increasing the free-energy barrier. This free-energy-barrier increment for the reference reaction—in which the COO^- group interacts with three water molecules (Fig. 1)—is larger than that for the reaction in KSI, in which the COO^- group interacts with Trp¹²⁰ (Fig. 2). Thus, desolvation of Asp⁴⁰ can reduce the free-energy barrier to a meaningful extent. Similar cases exist in organic reactions in which the desolvation of anions can accelerate reactions dramatically (Fig. 1).

In summary, the relative free-energy contribution of KSI's catalytic power includes electric-field and desolvation effects, as well as general base positioning. The contribution of the electric-field effect compared to that in water is $3.3 \text{ kcal mol}^{-1}$ and accounts for $\sim 31.4\%$ of KSI's catalytic speed-up relative to the uncatalyzed reference reaction

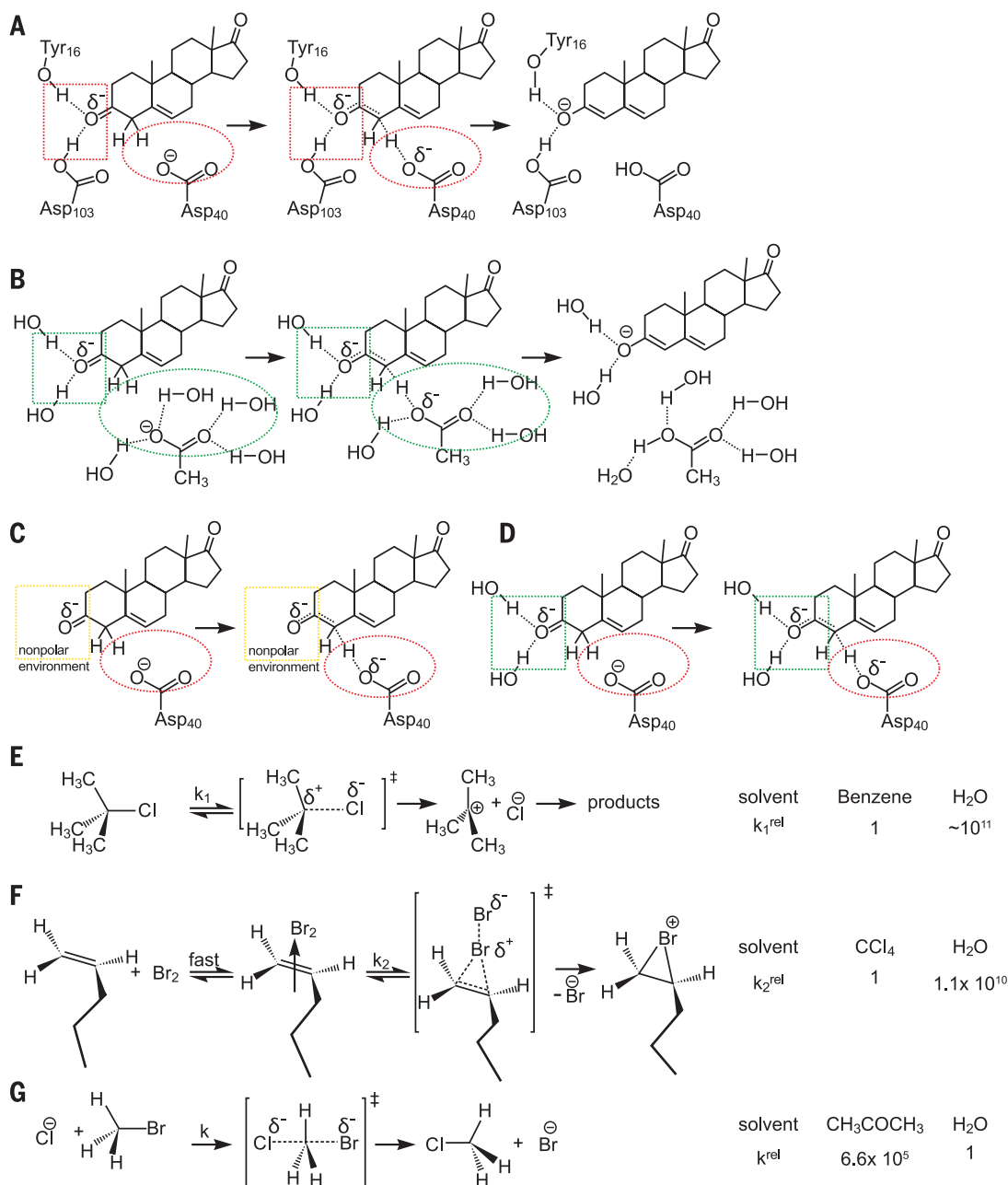
¹Jiangxi Key Laboratory of Organo-Pharmaceutical Chemistry, Gannan Normal University, Jiangxi 341000, China.

²Department of Pathology and Immunology, Baylor College of Medicine, Houston, TX 77030, USA. ³Department of Pathology, Texas Children's Hospital, Houston, TX 77030, USA.

*Corresponding author. E-mail: tor.savidge@bcm.edu

Fig. 1. Isomerization of 5-androstene-3,17-dione and the effects of water on free-energy barriers. The chemical mechanism for the first step of the isomerization reaction catalyzed by KSI

(A) and the uncatalyzed reaction in aqueous solution (B). The two reactions differ in (i) electrostatic interactions of the C=O group (squares) and (ii) the carboxyl group abstracting the α -hydrogen (circles). (C) Ground and transition states for the isomerization reaction in which the electric field exerted on the C=O bond is zero (nonpolar environment), whereas the carboxyl group abstracting the α -hydrogen is similar to (A). (D) Ground and transition states for the isomerization reaction in which the electric field exerted on the C=O bond is the similar to that of aqueous solution in (B), whereas the carboxyl group abstracting the α -hydrogen is similar to (A). (E and F) Water accelerates reactions in which the atoms are more charged in transition than ground states (5). (G) Desolvation accelerates reactions in which the atoms are less charged in transition than ground states (5, 6).



in aqueous solution. However, it is worthwhile emphasizing that the overall energy gain of the reaction is distinct from that contributed by electrostatic interactions of C=O. Regardless of the overall gain for the reaction in aqueous versus hydrophobic environments, electrostatic interaction of C=O with water for the reference reaction contributes toward the free-energy-barrier reduction. Exact contributions of desolvation (ΔG_{H}) and general base positioning (ΔG_{S}) to free-energy-

barrier reduction cannot be calculated based on the information provided in this paper.

REFERENCES AND NOTES

- S. D. Fried, S. Bagchi, S. G. Boxer, *Science* **346**, 1510–1514 (2014).
- D. A. Kraut, P. A. Sigala, T. D. Fenn, D. Herschlag, *Proc. Natl. Acad. Sci. U.S.A.* **107**, 1960–1965 (2010).
- N. C. Ha, M. S. Kim, W. Lee, K. Y. Choi, B. H. Oh, *J. Biol. Chem.* **275**, 41100–41106 (2000).
- E. A. Ruben *et al.*, *Biochemistry* **52**, 1074–1081 (2013).

- C. Reichardt, *Solvents and Solvent Effects in Organic Chemistry* (Wiley-VCH, Weinheim, Germany, ed. 3, 2003).
- W. R. Cannon, S. J. Benkovic, *J. Biol. Chem.* **273**, 26257–26260 (1998).

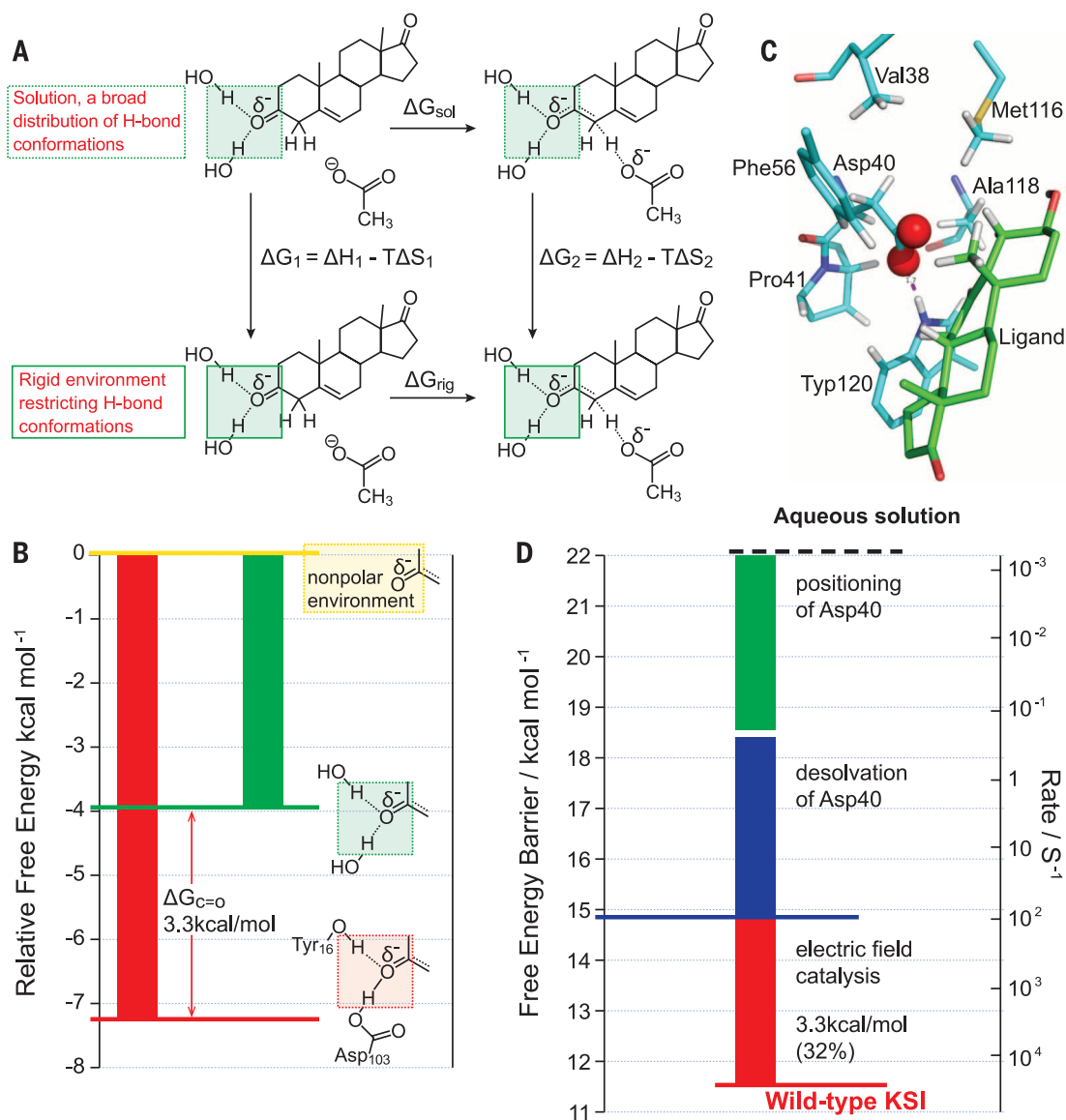
ACKNOWLEDGMENTS

This work was supported by grants from the National Science Foundation of China (21473041) and A1100914, DK096323, P30 DK56338, and Clinical and Translational Science Award UL1TR000071 from the National Institutes of Health.

27 February 2015; accepted 24 July 2015
10.1126/science.aab0095

Fig. 2. Contribution of active-site electric fields and desolvation of Asp⁴⁰ to KSI's catalytic power.

(A) Thermodynamic cycle showing the electrostatic contributions of the C=O group to the free-energy-barrier reduction (ΔG_{sol}) for the isomerization of 5-androstene-3,17-dione in water solution. **(B)** Relative electrostatic contributions of the C=O group to free-energy-barrier reduction in a nonpolar environment, in water and KSI. The free-energy-barrier reduction in KSI is 3.3 kcal mol⁻¹ more than that in aqueous solution. This represents the contribution of electric fields to the catalytic power of KSI because the catalytic power of KSI is estimated based on the uncatalyzed reaction in aqueous solution. **(C)** Crystal structure of KSI mutant Asp⁴⁰Asn complexed with androsten-3 β -ol-17-one (Protein Data Bank, 1E3R) (3). The nitrogen atom of Asn⁴⁰ is changed to an oxygen atom. Red spheres represent oxygen atoms of the carboxyl group. Hydrogen atoms that affect solvent-accessible areas of the oxygen atoms are shown. The oxygen atom abstracting α -hydrogen is surrounded by hydrophobic groups. The other oxygen atom forms a hydrogen bond with Trp¹²⁰. **(D)** The relative contribution of KSI's catalytic power. The electric field contributes ~32%, which is markedly less than the combined base positioning and desolvation of Asp⁴⁰, which contribute approximately 68%.



This copy is for your personal, non-commercial use only.

If you wish to distribute this article to others, you can order high-quality copies for your colleagues, clients, or customers by [clicking here](#).

Permission to republish or repurpose articles or portions of articles can be obtained by following the guidelines [here](#).

The following resources related to this article are available online at www.sciencemag.org (this information is current as of September 3, 2015):

Updated information and services, including high-resolution figures, can be found in the online version of this article at:

<http://www.sciencemag.org/content/349/6251/936.2.full.html>

A list of selected additional articles on the Science Web sites **related to this article** can be found at:

<http://www.sciencemag.org/content/349/6251/936.2.full.html#related>

This article **cites 5 articles**, 4 of which can be accessed free:

<http://www.sciencemag.org/content/349/6251/936.2.full.html#ref-list-1>

This article has been **cited by** 1 articles hosted by HighWire Press; see:

<http://www.sciencemag.org/content/349/6251/936.2.full.html#related-urls>

This article appears in the following **subject collections**:

Biochemistry

<http://www.sciencemag.org/cgi/collection/biochem>

TECHNICAL RESPONSE

BIOPHYSICS

Response to Comments on “Extreme electric fields power catalysis in the active site of ketosteroid isomerase”

Stephen D. Fried* and Steven G. Boxer†

Natarajan *et al.* and Chen and Savidge comment that comparing the electric field in ketosteroid isomerase's (KSI's) active site to zero overestimates the catalytic effect of KSI's electric field because the reference reaction occurs in water, which itself exerts a sizable electrostatic field. To compensate, Natarajan *et al.* argue that additional catalytic weight arises from positioning of the general base, whereas Chen and Savidge propose a separate contribution from desolvation of the general base. We note that the former claim is not well supported by published results, and the latter claim is intriguing but lacks experimental basis. We also take the opportunity to clarify some of the more conceptually subtle aspects of electrostatic catalysis.

Although the active site of ketosteroid isomerase (KSI) exerts a very large electric field (magnitude close to 150 MV/cm) onto its bound substrate, the substrate experiences a rather large electric field (magnitude 80 MV/cm, on average) when interacting with water in aqueous solution. A key point raised by Natarajan *et al.* (1) and Chen and Savidge (2) in their Comments is that bulk water would exert a catalytic effect on KSI's reaction proportional to its electric field. Chen and Savidge further imply that polar reactions are always accelerated by a polar medium. These suggestions reflect fundamental misunderstandings. Marcus theory teaches us that in reactions (such as KSI's) during which dipoles reorient and charges move, a polar solvent can actually have an inhibitory effect because there is an energetic cost (the reorganization energy) imposed by the requirement for the solvent sphere to forfeit the conformation that stabilizes the reactant's charge configuration to adopt a conformation that stabilizes the transition state's (TS's) charge configuration (3). An electric field (regardless of magnitude) can only have a catalytic effect by the model in figure 1B of our paper [Fried *et al.* (4)], if it adopts an orientation that specifically stabilizes the TS—that is, it is preorganized (5). The observation of narrow C=O bands in all the KSI active sites studied suggests that KSI's active-site electric field is fixed and preorganized [see also (6)] and therefore capable of producing a catalytic effect proportional to field magnitude. Solvent reaction fields (such as in bulk water) are not preorganized because they stabilize the reac-

tant's (and not the TS's) charge configuration and have large fluctuations. The importance of this distinction is evidenced by the fact that several fundamental polar reactions are faster in the gas phase than in aqueous solution (7). Therefore, we do not think a priori that water itself will provide a catalytic effect due to its electric field relative to the gas phase, and for this reason, we counted the electric field of the KSI active site in full to estimate its contribution to catalysis.

Natarajan *et al.* are correct to emphasize that the electric field C=O experiences is the result of both the residues that create the field and those that position the steroid ligand within it; indeed, the “electric field picture” (8) illuminates why key hydrogen-bond-donating residues cooperate with positioning residues to confer maximal catalytic effect. To be clear, we reserve the term “chemical positioning” to refer to the positions of components that participate in chemistry (i.e., breaking and forming of bonds); this should be largely separable from electrostatic catalysis, which depends on the positions of atoms that define the environment in which the reaction occurs but do not necessarily participate in the reaction. Natarajan *et al.* suggest that chemical positioning provides the majority of KSI's catalytic effect. This suggestion seems unlikely to us, since several experiments conducted by Herschlag and colleagues that directly examined the effect of positioning Asp⁴⁰ are consistent with our 10^{2.5}-fold assignment: The introduction of mutations that misposition Asp⁴⁰ (9, 10) reduces activity by a factor of 10^{1.5} to 10³. It would be very interesting to conduct “chemical rescue” studies (11) in which activity is restored to an Asp⁴⁰Gly mutant of KSI with exogenous acetate. Our assignment for the contribution of chemical positioning [figure 3C in (4)] could be tested by measuring the effective acetate concentration that provides an equivalent rate as wild-type KSI.

Natarajan *et al.* emphasize experiments on a collection of mutants of KSI in which the oxyanion hole and its environs are removed and partially replaced with small residues, leaving a water-filled cavity in its wake (part of which gets displaced by the substrate). These mutants reduce KSI's catalytic effect by 10³-fold, and the authors take this to imply that electrostatic stabilization of C=O by KSI's active site provides a 10³-fold effect relative to water. We disagree with this claim because, first, the active-site electric field arises not only from the oxyanion hole but also from the enzyme scaffold as a whole (so removing the oxyanion hole side chains would not remove all contributions to the active-site electric field). Second, it is unlikely that the water molecules trapped in the active site are analogous to bulk water, because they will be (partially) preorganized by the same enzyme scaffold that would otherwise organize Tyr¹⁶ and Asp¹⁰³. Enzyme design efforts have demonstrated that active-site waters (much like amino acid residues) can assist or impede catalysis depending on their positions, orientations, and dynamics (12, 13). Specifically in the case of KSI, water dynamics in the active-site cleft near a substrate analog were found to be substantially different from those of bulk water, even for a rather exposed region of the cleft (14).

Chen and Savidge suggest the existence of an important third catalytic contribution from the placement of Asp⁴⁰ in a nonpolar environment. Rephrasing their idea as we understand it, the concept is that just as C=O becomes more polar in the TS, and so would be stabilized by an active-site environment that exerts larger electric fields than water, the carboxyl group of Asp⁴⁰ becomes less polar in the TS, and so would be less destabilized by an environment that exerts smaller electric fields than water. Such proposals would have to be tested by measuring the electric field on the carboxyl group across several mutants and seeing if it bears any relationship to rate. We would hesitate to assign this hypothetical effect a specific catalytic weight in the absence of experimental evidence, although in any event, it should still qualify under the heading of electrostatic catalysis.

REFERENCES

1. A. Natarajan *et al.*, *Science* **349**, 936 (2015).
2. D. Chen, T. Savidge, *Science* **349**, 936 (2015).
3. R. A. Marcus, *J. Chem. Phys.* **24**, 966 (1956).
4. S. D. Fried, S. Bagchi, S. G. Boxer, *Science* **346**, 1510–1514 (2014).
5. A. Warshel *et al.*, *Chem. Rev.* **106**, 3210–3235 (2006).
6. S. K. Jha, M. Ji, K. J. Gaffney, S. G. Boxer, *Proc. Natl. Acad. Sci. U.S.A.* **108**, 16612–16617 (2011).
7. M. J. S. Dewar, D. M. Storch, *Proc. Natl. Acad. Sci. U.S.A.* **82**, 2225–2229 (1985).
8. S. D. Fried, S. G. Boxer, *Acc. Chem. Res.* **48**, 998–1006 (2015).
9. J. P. Schwans *et al.*, *Proc. Natl. Acad. Sci. U.S.A.* **110**, 11308–11313 (2013).
10. J. P. Schwans *et al.*, *Biochemistry* **53**, 2541–2555 (2014).
11. M. D. Toney, J. F. Kirsch, *Science* **243**, 1485–1488 (1989).
12. E. W. Debler, R. Müller, D. Hilvert, I. A. Wilson, *Proc. Natl. Acad. Sci. U.S.A.* **106**, 18539–18544 (2009).
13. H. K. Privett *et al.*, *Proc. Natl. Acad. Sci. U.S.A.* **109**, 3790–3795 (2012).
14. S. K. Jha, M. Ji, K. J. Gaffney, S. G. Boxer, *J. Phys. Chem. B* **116**, 11414–11421 (2012).

20 April 2015; accepted 24 July 2015
10.1126/science.aab1627

Department of Chemistry, Stanford University, Stanford, CA 94305-5080, USA.

*Present address: Protein and Nucleic Acid Chemistry Division, Medical Research Council Laboratory of Molecular Biology, Cambridge CB2 0QH, UK. †Corresponding author. E-mail: sboxer@stanford.edu

This copy is for your personal, non-commercial use only.

If you wish to distribute this article to others, you can order high-quality copies for your colleagues, clients, or customers by [clicking here](#).

Permission to republish or repurpose articles or portions of articles can be obtained by following the guidelines [here](#).

The following resources related to this article are available online at www.sciencemag.org (this information is current as of September 3, 2015):

Updated information and services, including high-resolution figures, can be found in the online version of this article at:

<http://www.sciencemag.org/content/349/6251/936.3.full.html>

A list of selected additional articles on the Science Web sites **related to this article** can be found at:

<http://www.sciencemag.org/content/349/6251/936.3.full.html#related>

This article **cites 14 articles**, 9 of which can be accessed free:

<http://www.sciencemag.org/content/349/6251/936.3.full.html#ref-list-1>

This article appears in the following **subject collections**:

Biochemistry

<http://www.sciencemag.org/cgi/collection/biochem>

TECHNICAL RESPONSE

FUNGAL BIOGEOGRAPHY

Response to Comment on “Global diversity and geography of soil fungi”

Leho Tedersoo,^{1*} Mohammad Bahram,^{2,3} Sergei Pölme,¹ Sten Anslan,² Taavi Riit,² Urmas Kõljalg,² R. Henrik Nilsson,⁴ Falk Hildebrand,⁵ Kessy Abarenkov¹

Schadt and Rosling (Technical Comment, 26 June 2015, p. 1438) argue that primer-template mismatches neglected the fungal class Archaeorhizomycetes in a global soil survey. Amplicon-based metabarcoding of nine barcode-primer pair combinations and polymerase chain reaction (PCR)-free shotgun metagenomics revealed that barcode and primer choice and PCR bias drive the diversity and composition of microorganisms in general, but the Archaeorhizomycetes were little affected in the global study. We urge that careful choice of DNA markers and primers is essential for ecological studies using high-throughput sequencing for identification.

Schadt and Rosling (1) argue that primer-template mismatches neglected the fungal class Archaeorhizomycetes in a global soil survey. Fungi are the dominant eukaryote kingdom in soil (2). The recently described fungal class Archaeorhizomycetes accounts for a high proportion of soil fungal communities around the world (3, 4), ranging from 0 to 20% in our recent global study (5). Schadt and Rosling argue that the relative importance of this group has been substantially underestimated in our study because our molecular identification approach may have involved a primer bias—i.e., distorted taxon distribution as a result of imperfect primer matches with some templates. We decided not to account for two unique mismatches of the ITS4ngs primer to Archaeorhizomycetes (2, 3), owing to its relatively low taxonomic diversity with two described species (0.002% of all described taxa) and a few hundred species-level taxa based on DNA sequences recovered from the soil environment (4, 6).

To gain insight into the magnitude of this primer bias, we generated a data set comprising amplicon-based sequencing of nine barcode-primer pair combinations (Fig. 1A) and polymerase chain reaction (PCR)-free shotgun metagenomics for a subset of the samples from Papua New Guinea (2, 5). Although differences in taxonomic richness and relative abundance of all fungal classes were highly significant (Fig. 1, B and C), there was no evidence for specific discrimination against Archaeorhizomycetes by one or two central mismatches in the primers SSU515ngs, ITS4ngs, or LR0Rngs (2). However, mismatches near the 3' end of a primer reduced the perceived abundance of particular taxa (for example, the primers ITS1ngs in

Sordariomycetes, ITS1Fngs in Mucoromycetes, ITS2 in Tremellomycetes and Glomeromycetes, and LF402 in Chytridiomycetes). Introns within barcodes accounted for another potential source of bias in Geoglossomycetes (the ITS1ngs-ITS2 and LR3R-LR5 primer pairs). In addition, a greater proportion of G and C nucleotides and greater barcode length reduce the chances of successful amplification and/or emulsion PCR of DNA molecules (7–9). Despite all these PCR and primer biases, the median amplicon-based abundance of fungal classes was strongly correlated with abundance estimates based on the shotgun metagenomics approach ($F_{1,37} = 111.9$; $R_{\text{Pearson}} = 0.867$; $P < 0.001$). Furthermore, the metagenomics data analysis confirmed that Archaeorhizomycetes, as well as arbuscular mycorrhizal Glomeromycetes, exhibit low relative abundance in these tropical forest soils (5). The extreme dominance of Archaeorhizomycetes in some previous studies may have derived from a cloning bias favoring relatively

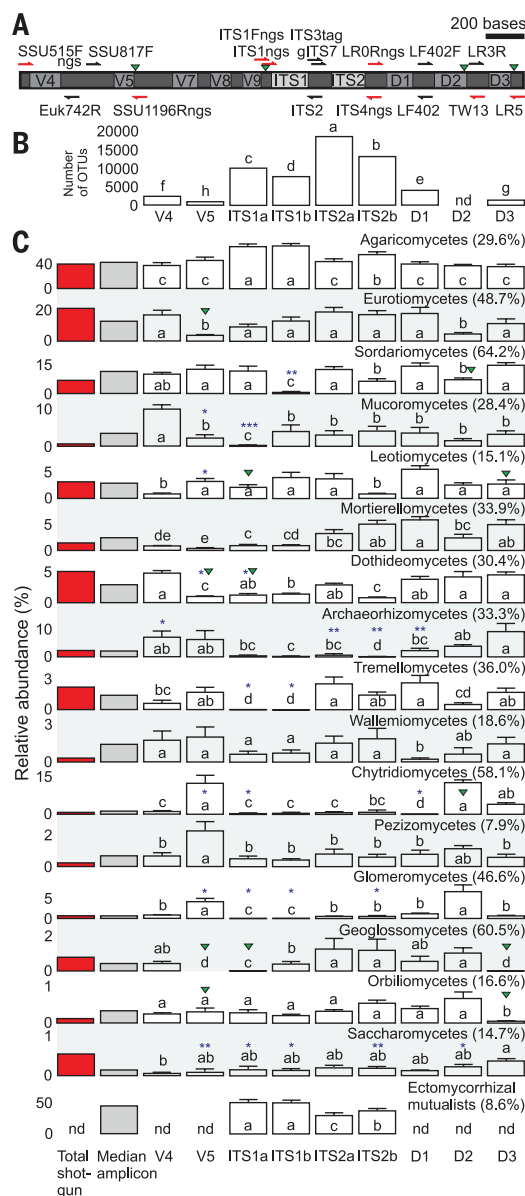


Fig. 1. Overview of barcode-primer pair combinations. (A) Primer map indicating variable domains, position of primers (identifier-tagged primers in red), and intron sites within barcodes (triangles). (B) Total taxonomic richness based on samples rarefied to 8609 sequences, with different letters indicating significantly different groups. (C) Proportion of sequences corresponding to the 16 most common fungal classes (median amplicon-based abundance >0.1% sequences; shaded columns) as based on the average values of amplicons (open columns) and shotgun metagenomes (red columns). Error bars, letters, asterisks, and triangles indicate standard error, significantly different groups, primer-template mismatches, and introns within barcodes, respectively. Numbers behind class names indicate variation (R^2_{adj}) explained by the choice of primers. ITS1a, primer pair ITS1Fngs-ITS2; ITS1b, ITS1ngs-ITS2; ITS2a, ITS3mixtag-ITS4ngs; ITS2b, gITS7-ITS4ngs (5).

¹Natural History Museum, University of Tartu, Tartu, Estonia.

²Institute of Ecology and Earth Sciences, University of Tartu, Tartu, Estonia. ³Department of Organismal Biology, Uppsala University, Uppsala, Sweden. ⁴Department of Biological and Environmental Sciences, University of Gothenburg, Göteborg, Sweden. ⁵European Molecular Biology Laboratory, Heidelberg, Germany.

*Corresponding author. E-mail: leho.tedersoo@ut.ee

short internal transcribed spacer (ITS) amplicons characteristic of this fungal class (2).

Schadt and Rosling also argue that the primer discrimination against Archaeorhizomycetes affects the perceived proportion of functional groups. Indeed, our results showed that the choice of primers explains 8.6 and 62.0% of variation in the proportion of ectomycorrhizal (ITS data set: $F_{3,72} = 70.14$; $P < 0.001$) and arbuscular mycorrhizal (full data set: $F_{8,205} = 90.64$; $P < 0.001$) symbionts, respectively. However, the disparity in ectomycorrhizal fungi is ascribed to the overestimation of relative abundance of Agaricomycetes, which comprise ~95% of all ectomycorrhizal fungal species (10, 11), by the ITS1 barcode. Because the class-level abundance of fungi based on

ITS3tagmix-ITS4nsgs primer pair (4) had the strongest correlation among all nine primer pairs to the respective median values ($F_{1,37} = 827.4$; $R_{\text{Pearson}} = 0.978$; $P < 0.001$), we reckon that the abundance estimates of functional groups were relatively little biased in our global study. Furthermore, these primers recovered the greatest species- and class-level diversity of all primer pairs tested (Fig. 1B), which encourages their use in future studies (2).

In conclusion, thorough consideration of primers and barcodes is clearly essential for the highly sensitive metabarcoding analyses. Similarly, anticipating unaccounted biases is of utmost importance in molecular studies of plant, animal, and microbial community ecology.

REFERENCES

1. C. W. Schadt, A. Rosling, *Science* **348**, 1438 (2015).
2. L. Tedersoo *et al.*, *MycKeys* **10**, 1–43 (2015).
3. A. Rosling *et al.*, *Science* **333**, 876–879 (2011).
4. A. Menkis, H. Urbina, T. Y. James, A. Rosling, *Fungal Biol.* **118**, 943–955 (2014).
5. L. Tedersoo *et al.*, *Science* **234**, 1078 (2014).
6. U. Kõljalg *et al.*, *Mol. Ecol.* **22**, 5271–5277 (2013).
7. K. Ihrmark *et al.*, *FEMS Microbiol. Ecol.* **82**, 666–677 (2012).
8. A. J. Pinto, L. Raskin, *PLOS ONE* **7**, e43093 (2012).
9. B. D. Lindahl *et al.*, *New Phytol.* **199**, 288–299 (2013).
10. A. Rinaldi, O. Comandini, T. W. Kuyper, *Fung. Div.* **33**, 1–45 (2008).
11. L. Tedersoo, M. E. Smith, *Fungal Biol. Rev.* **27**, 83–99 (2013).

9 January 2015; accepted 29 July 2015
10.1126/science.aaa5594

This copy is for your personal, non-commercial use only.

If you wish to distribute this article to others, you can order high-quality copies for your colleagues, clients, or customers by [clicking here](#).

Permission to republish or repurpose articles or portions of articles can be obtained by following the guidelines [here](#).

The following resources related to this article are available online at www.sciencemag.org (this information is current as of September 3, 2015):

Updated information and services, including high-resolution figures, can be found in the online version of this article at:

<http://www.sciencemag.org/content/349/6251/936.4.full.html>

A list of selected additional articles on the Science Web sites **related to this article** can be found at:

<http://www.sciencemag.org/content/349/6251/936.4.full.html#related>

This article **cites 11 articles**, 3 of which can be accessed free:

<http://www.sciencemag.org/content/349/6251/936.4.full.html#ref-list-1>

This article appears in the following **subject collections**:

Ecology

<http://www.sciencemag.org/cgi/collection/ecology>



The 2015 GIST Tech-I competition finalists hailed from 23 developing countries.

Global competition propels innovation “snowball”

In Nairobi, GIST Tech-I finalists transformed their ideas into business plans for great social impact

By **Michaela Jarvis**

Late this summer, young entrepreneur Tendekayi Katsiga traveled from his home in Gaborone, Botswana, to a village in the Kalahari Desert to talk to schoolchildren about innovation. He was fresh off a victory at the Global Innovation through Science and Technology (GIST) Tech-I competition—organized this year by AAAS in Nairobi, Kenya—where he won an award in the category of Most Potential for Societal Impact. Katsiga's start-up company, for which he was recognized, makes low-cost solar-powered hearing aids, a promising idea in the developing world, where hearing impairment is especially common and hearing aid batteries are unaffordable.

Katsiga's trip to the Kalahari, however, showed that his impact on society goes even beyond hope for the poor who are hearing-impaired. The 39-year-old innovator is a living example in his community, with firsthand experience of the power of scientific and technological innovation.

“When you think about the snowball effect, the impact of the GIST Tech-I competition could be huge,” said David Ireland, who was recruited by AAAS to be a mentor to the competitors. Ireland is the general manager of International & Innovation Systems for Australia's Commonwealth Scientific and Industrial Research Organisation. “GIST Tech-I directly supports 30 teams to build innovative businesses that can help them and their communities overcome challenges, create jobs, and make more money. The really exciting part is that we hopefully inspire these people to go

back into their communities and inspire and support others to be entrepreneurial, to then go on and build their own businesses.”

Begun in 2011, the GIST Tech-I competition, which is administered by AAAS, represents an initiative by the U.S. Department of State to support scientific and technological innovation in the developing world. Participants apply for the program and are named finalists through an extremely competitive multistep selection process. This year's finals, held 22 to 26 July and orchestrated by the AAAS International and Security Affairs Office and other AAAS staff, brought together 30 young entrepreneurs from 23 developing countries. Thirteen winners took home nearly \$140,000 in cash prizes, double the amount from the 2014 competition. The finals are hosted as part of the annual Global Entrepreneurship Summit, which this year drew a visit from President Barack Obama.

AAAS plays a principal role in the GIST Tech-I because the competition's goals align closely with those of the Association, said Edward Derrick. Derrick is the chief program director for the AAAS Center of Science, Policy, and Society Programs and attended the competition finals in Nairobi.

“It's there in our mission—to support science, engineering, and innovation, throughout the world, for the benefit of all people,” Derrick said. “These young entrepreneurs are trying to do just that—we're helping give them the tools to be successful, and drawing attention to the important role innovators play in connecting science and technology to people's lives.”

GIST alumni have generated \$110 million in revenue by commercializing their innovations, according to U.S. State Department figures.

For this year's competition, Ireland and nine other mentors—recruited by AAAS from industry, research, funding agencies, and science and technology advancement organizations—provided a training ground and ongoing support network for the young innovators. At the competition finals, company start-up experts Itzam De Gortari, CEO of the TechBA Program in Seattle, and Matthew

Graham Dyor, CEO at Payboard, walked the young innovators through 2 days of instruction in how to validate their products, know their potential customers and business competitors, build a team, and pitch their business propositions to investors.

"I think the training is essential for most candidates, who have a minimum understanding of developing a product and pitching it as an entrepreneur seeking further funding support," said mentor Wael Al-Delaimy, head of the Division of Global Health at the University of California, San Diego. "A few of the candidates are already well versed in many aspects of this approach, but they still benefit from the input of mentors with different backgrounds and experiences," he said.

As explained by Ireland, South African contestant Rudi Cooke, who won first place in the Idea and Best in Energy categories, had a sound idea for providing drinking water to communities in need. What Cooke realized was lacking was "a viable business model," Ireland said. "He has solved this, and I'm sure will be able to very quickly help these communities get access to safe and clean drinking water.

The skills to bring scientific and technological innovations to

market are incorporated into the message that Tech-I competitors carry back to their communities, said Mojisola Ojebode, a nutritional and industrial biochemist from Nigeria. Ojebode's product, which is derived from lemongrass and protects stored food crops from insects, earned her three awards: second place in the Idea category, Best Female, and Best in Agriculture.

"I have become a mentor to young people in my institution [University of Ibadan, Nigeria], especially to females," Ojebode said. "I have received messages from people who want to become entrepreneurs based on their research findings and skills but have been having problems taking the next step."

Mexican competitor Carlos Francisco Bernal Velazquez is equally determined to pass on his experience to others. Bernal won first place in the Start-Up category at GIST with his urine glucose monitor—which operates from inside diabetics' toilet bowls and can connect to the Internet—and he and his team are moving closer to commercializing the product. "I really want to be able to talk to students," Bernal said, "and tell them, 'If I can do it, you can do it, too.'"

EntryPoint! places students with disabilities on STEM tracks

By Becky Ham

In the 10 weeks that Rose Buchmann worked at The Mayo Clinic this summer, the college junior got a chance to try out new lab techniques and learn more about what a full-time career in science looks like. The internship, arranged by AAAS's EntryPoint! program, also gave Buchmann a chance to make lasting connections with the people she hopes will be her future colleagues.

"It was good to meet people in my field and people related to what I'll actually be doing in my career," said Buchmann, who is studying biomedical engineering at the Milwaukee School of Engineering. "Having an opportunity to get an internship like this, it really gets your name out there and you get to network a little bit."



Rose Buchmann

Buchmann is one of 27 students who worked as 2015 EntryPoint! interns at places like NASA, Georgia Tech, and Johns Hopkins University. Launched in 1996, the historic AAAS program has recruited students with disabilities who are studying science, technology, engineering, and mathematics (STEM) to work in industry, universities, and government agencies.

As EntryPoint! approaches its 20th anniversary, it stands as a singularly successful career launching pad. There are more than 580 alumni in the program, "and out of that number, we know that over 80% are now working in STEM fields," said Laureen Summers, the program's coordinator. Other programs such as the federal Workforce Recruitment Program help college students with disabilities enter the workforce, but Summers said that EntryPoint! is the only such program to focus on STEM jobs.

The program is planning a luncheon and panel at the 2016 AAAS Annual Meeting to celebrate its two decades' of work, coinciding with new efforts to bring together alumni who can act as mentors to the new cohorts of EntryPoint! applicants.

Buchmann has vascular Ehlers-Danlos syndrome, a rare genetic disorder that weakens connective tissues and major blood vessels. She said that the Mayo Clinic's Office of Diversity was very supportive of her throughout her internship. "It was great for me to meet everyone and do the research, but it wasn't just the work that I liked," she recalled. "Just getting out and having something productive to do with your summer is so much fun."

AAAS annual election: Preliminary announcement

The 2015 AAAS election of general and section officers is scheduled to begin in October. All members will receive a ballot for election of the president-elect, members of the Board of Directors, and members of the Committee on Nominations. Additionally, members registered in sections (up to three) will receive ballots for the specified section elections. Biographical information for the candidates will be provided along with ballots. The list of section candidates can be viewed at www.aaas.org/annual-election. The general election slate of candidates will be published in AAAS News & Notes in the 25 September issue of *Science*.

Additional names may be placed in nomination for any office by petition submitted to the Chief Executive Officer no later than 25 September 2015. Petitions nominating candidates for president-elect, members of the Board, or members of the Committee on Nominations must bear the signatures of at least 100 members of the association. Petitions nominating candidates for any section office must bear the signatures of at least 50 members of the section. A petition to place an additional name in nomination for any office must be accompanied by the nominee's curriculum vitae as well as a statement of acceptance of nomination.

RESEARCH

Wing growth rates drive songbird selection

Martin et al., p. 966



IN SCIENCE JOURNALS

Edited by Nick Wigginton

SEXUAL SELECTION

A third option leads to poor mates

A “decoy” effect decreases rational decision-making in humans. Irrational decisions in this case are a result of a choice between two options being affected by the introduction of a suboptimal third choice. Lea and Ryan show that tungara frogs are also subject to a decoy effect, choosing a male with a less appealing call when presented with a third, inferior calling male. These results suggest that the choice of mates by animals may be context dependent. It appears that rational choice may not always drive sexual selection. — SNV

Science, this issue p. 964



Tungara frogs are subject to a “decoy” effect when choosing potential mates

QUANTUM MECHANICS

Manipulation of a quantum squeeze

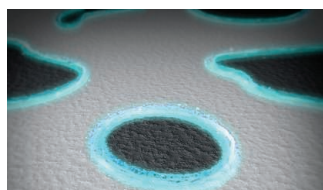
The uncertainty principle of quantum mechanics dictates that even when a system is cooled to its ground state, there are still fluctuations. This zero-point motion is unavoidable but can be manipulated. Wollman *et al.* demonstrate such manipulation with the motion of a micrometer-sized mechanical system. By driving up the fluctuations in one of the variables of the system, they are able to squeeze the other related variable below the expected zero-point limit. Quantum squeezing will be important for realizing ultrasensitive sensors and detectors. — ISO

Science, this issue p. 952

TOPOLOGICAL MATTER

Magnetizing a topological insulator

Inducing magnetism in a topological insulator can lead to exotic effects. The usual experimental route is to introduce magnetic dopants into the material, but that approach is intricate and creates unwanted disorder. Wang *et al.* used a simpler technique: They fabricated



Edge current (blue) flows at the boundaries of magnetic domains on a topological insulator

a bilayer consisting of Bi_2Se_3 , a topological insulator, and EuS, a magnet. The physical proximity of EuS induced magnetism on the surface of Bi_2Se_3 . This approach allowed for the creation of magnetic domains at will and the detection of characteristic current flowing along the domains' edges. — JS

Science, this issue p. 948

SYNTHETIC BIOLOGY

Engineering cell population behavior

Attaining the full promise of synthetic biology will require designing population-level behaviors of multiple interacting cell types. As a start, Chen *et al.* engineered two strains of the bacterium *Escherichia coli*

to produce signaling molecules that regulate transcription in the complementary strain (see the Perspective by Teague and Weiss). The signaling circuit was successfully designed to produce feedback loops that produce synchronous oscillations in transcription between the two strains. A mathematical model helped determine how to modulate the oscillations and control their robustness to perturbations. — LBR

Science, this issue p. 986; see also p. 924

NANOPARTICLES

Crystal nuclei beaten to the punch

Amorphous nanoparticles often dissolve more rapidly than their

crystalline counterparts, which can be useful in applications such as drug delivery. Amstad *et al.* made amorphous nanoparticles from organic and inorganic compounds—even table salt—using droplets of dissolved compounds created with a microfluidic nebulator. The solvent evaporates fast enough that nanoparticles form before crystal nuclei can develop. The small particle size inhibits crystallization for periods of months — PDS

Science, this issue p. 956

FUNGAL SYMBIONTS

Cosmopolitan plant root symbionts

The aboveground lives of plants are only sustainable because of the symbiotic soil fungi that encase their roots. These fungi swap nutrients with plants, defend them from attack, and help them withstand abrupt environmental changes. Out of necessity, fungal symbionts in the soil would appear to be restricted and local to certain plant species. Davison *et al.*, however, discovered that some taxa are globally distributed. How these underground fungi have dispersed so widely remains a mystery; perhaps human farmers have had something to do with it. — CA

Science, this issue p. 970

MUCOSAL IMMUNOLOGY

Gut microbes make T cells keep the peace

Our guts harbor trillions of microbial inhabitants, some of which regulate the types of immune cells that are present in the gut. For instance, *Clostridium* species of bacteria induce a type of T cell that promotes tolerance between the host and its microbial contents. Ohnmacht *et al.* and Sefik *et al.* characterized a population of gut regulatory T cells in mice, which required gut microbiota to survive. Multiple bacterial species of the microbiota could induce transcription factor-expressing regulatory T cells that helped maintain immune

homeostasis. Mice engineered to lack these transcription factors exhibited enhanced susceptibility to colonic inflammation and had elevated amounts of proinflammatory molecules associated with allergies (see the Perspective by Hegazy and Powrie). — KLM

Science, this issue pp. 989 and 993

CLIMATE SCIENCE

How to melt the Antarctic Ice Sheet

Computer simulations suggest that it is possible to entirely eliminate the Antarctic Ice Sheet, Earth's largest reservoir of fresh water. Winkelmann *et al.* explored the fate of the Antarctic Ice Sheet over 10,000 years into the future, showing that global warming related to massive carbon emissions would not only lead to complete melting of the ice sheet, but a global sea-level rise of more than 50 m. The global demand for energy derived from fossil fuels, if left unchecked, is likely to have devastating impacts on coastal populations and polar ecosystems. — KVH

Sci. Adv. 10.1126/sciadv.1500589 (2015).

CANCER

Not just another Notch for treatment

Pulmonary neuroendocrine tumors, such as small-cell lung cancer, are among the most difficult cancers to treat. The healing effects of standard chemotherapy regimens are only transient, and the tumors typically acquire drug resistance quickly. Saunders *et al.* discovered that DLL3, a ligand in the Notch signaling pathway, is associated with the neuroendocrine cancer phenotype. An antibody conjugated to a cytotoxic drug targeted DLL3, which proved to be much more effective than standard chemotherapy for treating patient-derived tumor xenografts. Unlike chemotherapy, the anti-DLL3 treatment was particularly effective against tumor-initiating cells. — YN

Sci. Transl. Med. 7, 302ra136 (2015).

IN OTHER JOURNALS

Edited by **Kristen Mueller**
and **Jesse Smith**



Pesticides affect earthworms in a variety of ways

PESTICIDES

The effects of pesticides run deep

Many pesticides negatively affect pollinators, such as bees, but how do they affect soil-dwelling organisms such as earthworms, which help enhance the nutrient availability of soil? Gaupp-Berghausen *et al.* addressed this by testing the effects of a commonly used glyphosate-containing herbicide on two species of earthworms in a greenhouse experiment. They found that herbicide treatment reduced an activity called casting that promotes soil health in one species and decreased the ability of the other species to reproduce by nearly 50%. Soil concentrations of nitrate and phosphate, which can negatively affect the surrounding environment, also increased. These results emphasize that pesticides probably have effects on ecosystems that go well beyond what we might predict or recognize. — SNV

Sci. Rep. 5, 12886 (2015).

APPLIED OPTICS

Adding communication to light harvesting

Solar cells are often thought of as passive devices sitting on a rooftop, benignly soaking up sunlight and converting it into useful electricity. On the smaller scale, they can be integrated into electrical devices, removing the need for a battery. Zhang *et al.* now show that solar cells can also function as data detectors. Using visible light communication, a wireless medium in which information can be encoded and transferred as an optical signal piggybacking on the light from an LED source, they demonstrate high-speed data communication. The flexibility and relatively low cost of organic solar cells provide the possibility of integrating such self-powered devices into the "Internet of things." — ISO

Optica **2**, 607 (2015).

ORGANIC CHEMISTRY

An E-Z route to photobases

Although many stable photoactivated acids are known, there are fewer examples of photoactivated Lewis bases, most of which form by the liberation of protecting or blocking groups. He *et al.* report that a molecule with a conjugated nitrogen framework, a triazabutadiene, becomes more basic in water (by almost one pH unit) when the absorption of ultraviolet light rotates a double bond and converts the *E* isomer to the *Z* form. An organic-soluble derivative was used to catalyze a condensation reaction, the Henry reaction between nitroethane and *p*-nitrobenzaldehyde. — PDS

J. Am. Chem. Soc. **10.1021/jacs.5b04367** (2015).

GEOCHEMISTRY

Core composition gets nebular

The composition of Earth's core is a key piece of evidence needed to determine how and from what sources



Fat, like sweetness, sourness, bitterness, and saltiness, may be a distinct taste

TASTE

Does this taste fatty to you?

Just as food can be too salty or too sweet, we also complain if food is too oily or fatty. But is that judgement based on the distinct taste of fat, or is it just a mix of other basic tastes and textures? Running *et al.* now report that our primary taste senses have a previously unknown sibling, dubbed "oleogustus." They asked 48 volunteers to sort 15 taste samples by quality, and most of them could distinguish long-chained nonesterified fatty acids (NEFAs) such as oleic acid from sweet, sour, salty, bitter, and umami substances, whereas short-chained NEFAs such as citric acid tasted sour. The results may be important to the food industry, such as when selecting fat replacers. — LNS

Chem. Senses **10.1093/chemse/bjv036** (2015).

it was formed. The core is composed mainly of a mixture of iron and nickel but also contains unknown amounts of other elements, including silicon. Dauphas *et al.* find that the isotopic composition of silicon in a particular class of meteorites called Angrites is identical to that of Earth's mantle and probably was inherited from the solar nebula. This unexpected observation suggests that there is less silicon in the core than previously thought, and in general muddies the use of its isotopes to constrain the amount of silicon in planetary cores. — BG

Earth Planet. Sci. Lett. **10.1016/j.epsl.2015.07.008** (2015).



HEART DISEASE

A cadherin gene enters MVP territory

The average human heart beats about 100,000 times daily. With each beat, the heart's four valves open and close tightly in a synchronized fashion, ensuring that blood flows in only one direction. For the 1 in 40 people with mitral valve prolapse (MVP), the valve between the heart's two left chambers does not close properly, which can cause blood to leak backward, reducing the heart's efficiency. Durst *et al.* studied three families predisposed to MVP and found mutations in a gene coding for a specific cadherin, a group of proteins that help cells adhere to one another. Studies in mice revealed that the mutations disrupt how cells move and organize themselves during heart valve morphogenesis. — PAK

Nature **10.1038/nature14670** (2015).

Piece of a rare
angrite meteorite

COMPUTATIONAL BIOLOGY

Deciphering function from single-cell data

Given their wide range of duties, cells must make tradeoffs between optimal performance and the ability to multitask. Scientists have proposed that groups of cells do this by arranging themselves in the shape of a polygon, in which cells at the vertices express distinct genes optimized for different tasks. Korem *et al.* analyzed single-cell measurements of gene expression in various mouse and human tissues and confirmed that cells do organize themselves in this manner. Some tissues showed distinct clusters or well-separated cell types, whereas other tissues had cells with a continuum of gene expression profiles. Examining the gene expression patterns in the cells closest to the vertices may reveal unknown functions for such cells. — LBR

PLOS Comput. Biol. **11**, e1004224 (2015).

ALSO IN SCIENCE JOURNALS

Edited by Nick Wigginton

COLLOIDS

Learning from the packing of particles

Colloidal particles, which consist of clusters of hundreds or thousands of atoms, can still resemble atomic systems. In particular, colloids have been used to study the packing of spheres and the influence of short-range interactions on crystallization and melting. Manoharan reviews these similarities, as well as the cases in which colloidal particles show behavior not seen in atomic systems. For example, the packing of nonspherical objects, where geometry or topology may matter, can give insights into the role of entropy in packing. — MSL

Science, this issue p. 942

PSYCHOLOGY

Empirically analyzing empirical evidence

One of the central goals in any scientific endeavor is to understand causality. Experiments that seek to demonstrate a cause/effect relation most often manipulate the postulated causal factor. Aarts *et al.* describe the replication of 100 experiments reported in papers published in 2008 in three high-ranking psychology journals. Assessing whether the replication and the original experiment yielded the same result according to several criteria, they find that about one-third to one-half of the original findings were also observed in the replication study. — GJC

Science, this issue p. 943

ADVANCED IMAGING

Adding to the super-resolution arsenal

Structured illumination microscopy (SIM) uses light intensities that are orders of magnitude lower than other super-resolution methods. SIM is also far faster over cellular-sized

fields of view. Li *et al.* used two approaches to improve the resolution of SIM to allow live cell imaging of dynamic cellular processes, including endocytosis and cytoskeleton remodeling. The contrast in performance between SIM and other techniques is due to a few key differences. Defining the practical resolution at the limited signal-to-noise ratios necessary for live cell imaging will require better imaging metrics. — SMH

Science, this issue p. 944

ORGANIC CHEMISTRY

Iron plays matchmaker to pair up olefins

In theory, shining the right wavelength of light onto carbon-carbon double bonds should pair them up into four-membered cyclobutane rings. In practice, however, this route can prove finicky and inefficient, particularly if the necessary wavelength lies deep in the ultraviolet region. Hoyt *et al.* report an iron catalyst that coaxes a wide variety of simple olefins into such rings without the need for photoexcitation (see the Perspective by Smith and Baran). Systematic optimization of the ligand coordinated to iron effectively eliminated competing pathways to alternative products. — JSY

Science, this issue p. 960;
see also p. 925

LIFE HISTORY

Wing growth drives songbird selection

Nesting birds are particularly vulnerable to predation, providing pressure for individuals to grow and leave the nest as quickly as possible. In contrast to temperate songbirds, tropical birds appear to grow more slowly despite high rates of nest predation. Martin shows that overall rates of growth are similar across this latitudinal gradient, but tropical birds become mobile more rapidly

due to faster wing growth. This trajectory is facilitated by higher provisioning of fewer offspring, providing an example of how life history responds to divergent selection pressures. — SNV

Science, this issue p. 966

IMMUNOLOGY

New targets to treat inflammation

Some members of the mitogen-activated protein kinase (MAPK) family promote the production of proinflammatory cytokines. As such, these kinases have been targeted for the treatment of inflammatory diseases. Disappointing clinical trials with such drugs, however, have spurred the search for other candidate targets. Wilhelmsen *et al.* found that MAPK family member ERK5 promoted inflammatory responses to microbial products in human endothelial and immune cells. Inhibitors of ERK5 and its upstream activating kinase reduced systemic inflammation in mice with microbial infections or tissue injury. — JFF

Sci. Signal. **8**, ra86 (2015).

PALEONTOLOGY

Species diversity in human evolution

Early *Homo* species were long thought to have evolved from one into the next, culminating in *Homo sapiens*. In a Perspective, Schwartz and Tattersall highlight recent studies that argue against this linear transformative view. Many studies do not pay enough attention to morphological differences, shoe-horning fossils into *Homo* without properly defining what characterizes the genus or the species within it. Recent research suggests that in the past, *Homo* was as diverse as other mammals. Acknowledging this diversity will help us better understand how humans evolved. — JFU

Science, this issue p. 931

NEURONAL DEVELOPMENT

Axon paths in developing spinal cords

Sensory neurons entering the spinal cord take different paths as inputs for pain and proprioception diverge. Working with chick and mouse embryos, Guy *et al.* found that glycerophospholipids produced by radial glial cells guide these neural fibers, or axons, in the developing spinal cord. A soluble glycerophospholipid released by the cells provided an inhibitory signal to the pain-sensitive axons, keeping them on their own unique pathway. — PJH

Science, this issue p. 974

HEART DISEASE

A giant disruption of the heart

Certain forms of heart failure originate from genetic mutations. Understanding how the culprit mutant proteins alter normal heart function could lead to more effective treatments. One candidate is the giant protein tintin, which is mutated in a subset of patients with dilated cardiomyopathy. Through a combination of patient-derived stem cells, tissue engineering, and gene editing, Hinson *et al.* found that disease-associated titin mutations disrupt the function of the contractile unit in heart muscle. As a result, the heart does not respond properly to mechanical and other forms of stress. — PAK

Science, this issue p. 982

DNA RECOMBINATION

Matching DNA three bases at a time

The exchange of genetic information between DNA strands is vital for accurate DNA repair and effective meiotic cell division. Using single-molecule methods and molecular dynamics simulations, Lee *et al.* show that

members of the family of recombinase enzymes responsible for these strand exchange reactions search for and recognize matching DNA strands three bases at a time. A single mismatch abolishes triplet recognition, except for the meiosis-specific recombinase. This enzyme can stabilize a partially mismatched triplet, reflecting the partial homology of the DNA substrates in meiosis. — GR

Science, this issue p. 977

SOLID-STATE PHYSICS

Trying to break a stubborn law

The electrical resistivity of most metals at low temperatures has a characteristic quadratic dependence on temperature. This law is typically ascribed to the scattering of electrons off each other in the presence of a crystal lattice. By measuring the resistivity of SrTiO_3 with varying dopant concentrations, Lin *et al.* test the applicability of the law for metals with low carrier densities. The law persists down to the lowest carrier concentrations, into the regime where the conditions for this behavior were previously thought to break down. — JS

Science, this issue p. 945

REVIEW SUMMARY

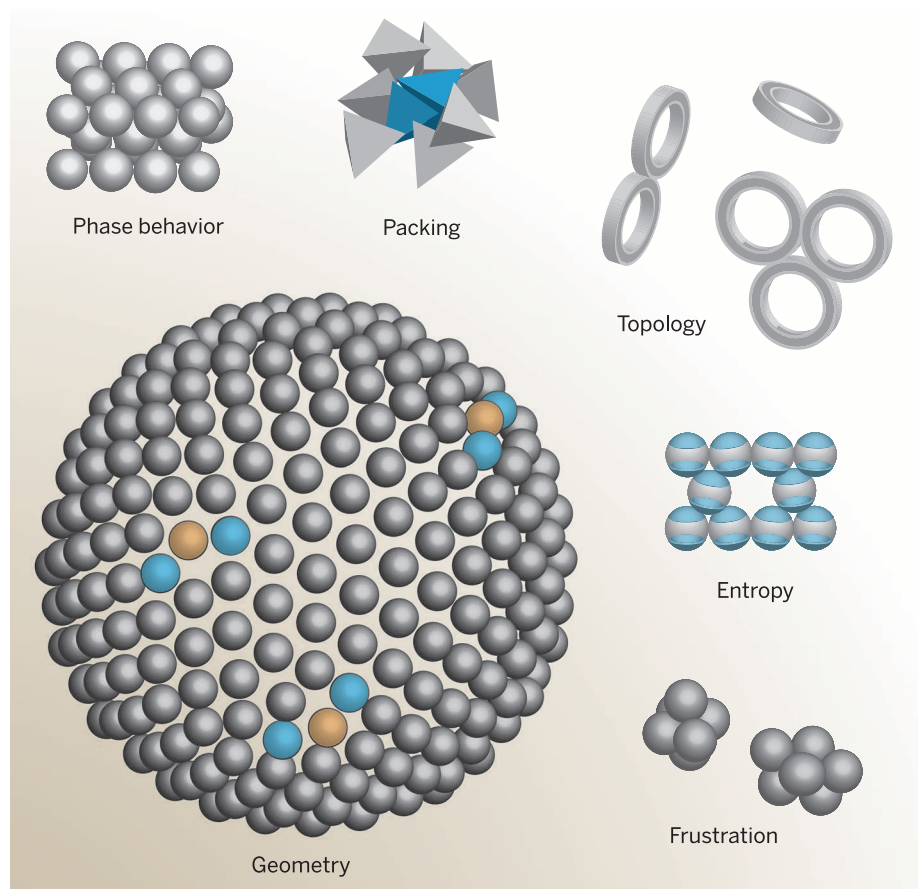
COLLOIDS

Colloidal matter: Packing, geometry, and entropy

Vinothan N. Manoharan*

BACKGROUND: Colloids consist of solid or liquid particles, each about a few hundred nanometers in size, dispersed in a fluid and kept suspended by thermal fluctuations. Whereas natural colloids are the stuff of paint, milk, and glue, synthetic colloids with well-controlled size distributions and interactions are a model system for understanding phase transitions. These colloids can form crystals and other phases of matter seen in atomic and molecular systems, but because the particles are large

enough to be seen under an optical microscope, the microscopic mechanisms of phase transitions can be directly observed. Furthermore, their ability to spontaneously form phases that are ordered on the scale of visible wavelengths makes colloids useful building blocks for optical materials such as photonic crystals. Because the interactions between particles can be altered and the effects on structure directly observed, experiments on colloids offer a controlled approach toward understanding and harnessing



The many dimensions of colloidal matter. The self-assembly of colloids can be controlled by changing the shape, topology, or patchiness of the particles, by introducing attractions between particles or by constraining them to a curved surface. All of the assembly phenomena illustrated here can be understood from the interplay between entropy and geometrical constraints.

self-assembly, a fundamental topic in materials science, condensed-matter physics, and biophysics.

ADVANCES: In the past decade, our understanding of colloidal self-assembly has been

ON OUR WEB SITE

Read the full article at <http://dx.doi.org/10.1126/science.1253751>

transformed by experiments and simulations that subject colloids to geometrical or topological constraints, such as curved surfaces, fields, or the shapes of the particles themselves. In particular, advances in the synthesis of nonspherical particles with controlled shape and directional interactions have led to the discovery of structural transitions that do not occur in atoms or molecules. As a result, colloids are no longer seen as a proxy for atomic systems but as a form of matter in their own right. The wide range of self-assembled structures seen in colloidal matter can be understood in terms of the interplay between packing constraints, interactions, and the freedom of the particles to move—in other words, their entropy. Ongoing research attempts to use geometry and entropy to explain not only structure but dynamics as well. Central to this goal is the question of how entropy favors certain local packings. The incompatibility of these locally favored structures with the globally favored packing can be linked to the assembly of disordered, arrested structures such as gels and glasses.

OUTLOOK: We are just beginning to explore the collective effects that are possible in colloidal matter. The experimentalist can now control interactions, shapes, and confinement, and this vast parameter space is still expanding. Active colloidal systems, dispersions of particles driven by intrinsic or extrinsic energy sources rather than thermal fluctuations, can show nonequilibrium self-organization with a complexity rivaling that of biological systems. We can also expect new structural transitions to emerge in “polygamous” DNA-functionalized colloids, which have no equivalent at the molecular scale. New frameworks are needed to predict how all of these variables—confinement, activity, and specific interactions—interact with packing constraints to govern both structure and dynamics. Such frameworks would not only reveal general principles of self-assembly but would also allow us to design colloidal particles that pack in prescribed ways, both locally and globally, thereby enabling the robust self-assembly of new materials. ■

Harvard John A. Paulson School of Engineering and Applied Sciences and Department of Physics, Harvard University, Cambridge, MA 02138, USA.

*Corresponding author. E-mail: vnman@seas.harvard.edu
Cite this article as V. N. Manoharan, *Science* 349, 1253751 (2015). DOI: 10.1126/science.1253751

REVIEW

COLLOIDS

Colloidal matter: Packing, geometry, and entropy

Vinothan N. Manoharan*

Colloidal particles with well-controlled shapes and interactions are an ideal experimental system for exploring how matter organizes itself. Like atoms and molecules, these particles form bulk phases such as liquids and crystals. But they are more than just crude analogs of atoms; they are a form of matter in their own right, with complex and interesting collective behavior not seen at the atomic scale. Their behavior is affected by geometrical or topological constraints, such as curved surfaces or the shapes of the particles. Because the interactions between the particles are often short-ranged, we can understand the effects of these constraints using geometrical concepts such as packing. The geometrical viewpoint gives us a window into how entropy affects not only the structure of matter, but also the dynamics of how it forms.

A colloid is a dispersion of microscopic particles that are individually unremarkable but collectively interesting. More traditionally, one might say that a colloid is a fluid dispersion, like fog, milk, paint, or glue, where the particles are larger than a molecule but small enough to stay dispersed for days or longer. But defining colloids in the traditional way is a bit like defining puppies as young dogs; though technically accurate, it doesn't quite capture their appeal. The feature of colloids that drives much current research is their collective behavior—their ability to form complex structures and show unusual dynamical transitions. By exploring how these collective effects emerge, we gain insights into general questions of how matter organizes itself, questions that are fundamental to condensed-matter physics, materials science, and even our understanding of life itself.

Many of the things that used to be called colloidal particles are now more often called nanoparticles, the “nano-” prefix highlighting a size scale where unusual electronic, magnetic, or optical properties reside. Meanwhile, the term “colloid” (1) has come to refer to a dispersion of larger particles, perhaps hundreds of nanometers or so, with uniform shapes and a controlled size distribution. Compared to a nanoparticle, an individual colloidal particle (in this narrower definition of the term) has no remarkable material properties. From the perspective of quantum mechanics, it is a blob of macroscopic matter, no more interesting than a baseball.

It is precisely because there is nothing exciting about an individual particle that the collective behavior of colloids is worth studying. Each particle is classical, and its interaction with other

particles is generally related to its shape. Yet each is big enough so that we can resolve it from its neighbors under an optical microscope. So when we see these well-characterized, mundane classical particles doing something collectively unexpected—like forming a crystal—it tells us something about the fundamental physics governing that same phenomenon in more complex systems. Indeed, colloids do form crystals, as well as other phases of matter found in atomic and molecular systems, and because the structural length scales of these phases are on the order of visible light, they serve as useful model systems for observing the microscopic mechanisms of phase transitions.

But colloids are more than just crude models for atomic systems; they are themselves a form of matter, with interesting collective behavior not seen at the atomic scale. By observing how that behavior is modified by geometrical or topological constraints, such as surfaces, fields, or the shapes of the particles themselves, we garner clues about how order arises in condensed phases and how it might be disrupted. An enduring mystery of biological systems is how they harness stochastic motion at the molecular level to build ordered structures. Experiments on colloids constitute perhaps the most carefully controlled approach toward understanding the statistical physics underlying this process, which is called self-assembly. The self-assembly of colloidal particles is well worth studying on its own merits, since it can be used to make photonic crystals and macroporous materials (2, 3), although that is not the focus of this Review.

The discussion will focus on the general principles concerning the structure and dynamics of colloidal matter, and how this behavior can be understood in terms of geometry and topology. Two themes emerge. The first is that entropy, an abstract thermodynamic quantity colloquially associated with “disorder,” makes its presence felt

in unexpected ways, including driving the formation of ordered phases. The second is the relation between packing constraints, which are imposed by the shapes of the particles, and structure and structural transitions. These two themes intersect at one of the frontiers of the field: understanding how entropy and geometry govern not only the structure of matter, but also the dynamics of how it forms.

From atoms to model atoms

To understand why entropy is so important in colloidal dispersions, we first consider a single colloidal particle in a liquid. As Robert Brown showed in 1827 (4), it moves about randomly and incessantly. This Brownian motion, as we now call it, was quantified by Jean Perrin (5), who used Einstein's theory (6) to extract Avogadro's number from the slope of the mean-squared particle displacements as a function of time. Perrin's result proved that matter must be discretized at some scale. The random forces imparted by its discrete units—atoms and molecules—give rise to the movement of the particle (Fig. 1A).

As a consequence of these random forces, a colloidal particle changes its direction and velocity on time scales smaller than a microsecond. This means that over longer times, it can explore its container (Fig. 1B) and—in the language of mechanics—its phase space (momentum and position). If the dispersion is kept free of contaminants that might cause the particles to aggregate, it can reach a state of thermal and chemical equilibrium in perhaps hours or days, reasonable time scales for an experiment.

We can therefore bring the apparatus of statistical thermodynamics to bear on understanding the collective behavior of the particles. In equilibrium at constant temperature, the colloid minimizes its free energy $F = U - TS$, where S is the entropy and T the temperature. The internal energy U is the sum of the kinetic energy, which is constant and can be ignored, and an “effective” potential that accounts for interactions between the solvent molecules and the particle and between the particles themselves (7). If we are given a model or measurement of the effective potential, we can sweep the details of molecules under the rug.

The role of the entropy S , and how it relates to the organization of matter, is best illustrated by hard spheres, where the potential energy U is a constant for all configurations. Computer simulations in the 1950s (8, 9) showed that hard spheres spontaneously form a face-centered cubic (fcc) lattice at volume fractions of about 0.50. In 1986, Pusey and van Megen (10) showed that a colloidal dispersion of particles that closely approximated hard spheres showed a fluid-to-crystal transition. Their colloid contained on the order of 10^{14} particles, which, in contrast to the simulations, was unambiguously in the thermodynamic limit.

It is perhaps surprising that hard spheres should show a freezing transition. Because the potential energy U is a constant (taken to be zero), we must conclude that the crystallization is driven

Harvard John A. Paulson School of Engineering and Applied Sciences and Department of Physics, Harvard University, Cambridge, MA 02138, USA.

*Corresponding author. E-mail: vnm@seas.harvard.edu

by an increase in entropy. A simple packing argument (11) shows how. The densest packing of spheres in three dimensions (3D) is the fcc lattice (12, 13), with a volume fraction of 74%, whereas the densest disordered packing of spheres occurs at about 64% volume fraction, as observed in experiments on ball bearings (14). The exact volume fraction of the disordered state depends on the packing protocol (15), but it is always well below the maximum density of the solid. Therefore, at some volume fraction lower than about 64%, a crystalline solid should have higher vibrational entropy than the fluid. If arranged in an fcc lattice at 64% volume fraction, the particles have room to rattle around their lattice sites, whereas in a disordered arrangement, they are jammed (Fig. 1C). A more quantitative argument for the phase boundary requires a numerical analysis (16), but the packing argument makes clear that there is an upper bound at which the solid phase must be entropically favored.

The hard-sphere freezing transition shows that entropy should be thought of not as “disorder” but rather as a measure of the configuration space of the particles. The ordering influence of entropy was first predicted in the 1940s by Onsager, who showed that hard rods at high density should orient themselves in the same direction to maximize their freedom to translate (17). This entropic alignment is the origin of the isotropic-nematic transition in a liquid crystal. Since the discovery of hard sphere

crystallization, other experiments and simulations on variously shaped hard particles have revealed many entropy-driven transitions from disorder to order (18–21).

The observation that colloids can replicate fundamental phase transitions, as shown in hard spheres (10) and earlier in charged repulsive particles (22, 23), has resulted in more than three decades of experiments in which colloids have been used as “model atoms” (24) or “big atoms” (25) for exploring longstanding questions in condensed-matter physics and materials science. Experiments on colloids have examined the formation of defects in crystals under stress (26, 27), the dynamics of crystal melting (28, 29), the nucleation and growth of crystals (30, 31), the role of thermal capillary waves in interfacial phenomena (32), and the glass transition (33). By replacing traditional liquids and crystals by their colloidal counterparts, the experimentalist can image and quantify the motions of individual particles in “real space,” as opposed to the less direct “reciprocal space” picture given by scattering techniques. Real-space studies were essential in demonstrating that supercooled liquids showed dynamical heterogeneities (34, 35), a precursor to the glass transition.

From model atoms to colloidal matter

However, there are differences between colloids and atoms, and these differences result in some of the more interesting features of colloidal

matter. The attractions between colloidal particles can be made much shorter ranged (in proportion to the particle size) than those of atoms, and when this is the case, the rates of transitions between structures depend on entropy and hydrodynamics, in contrast to the energy barriers that govern dynamics of atomic systems. Also, because the particles are purely classical objects, vibrational and rotational entropy can stabilize the equilibrium phases, which does not happen in atomic systems at low temperatures.

Ganapathy *et al.* (36) examined how the range of attractive forces affects the growth of crystals. They created colloidal crystal “islands” on a lithographically patterned surface by introducing a depletion attraction between the particles. The depletion interaction, which is induced by smaller, noninteracting, nanoscale particles, is fundamentally entropic: When two larger particles come together, they create more space for the smaller particles to move, increasing the total entropy of the system. Although the interaction strength in the Ganapathy experiments was large enough to drive crystallization, the range of the attraction was short, only about 0.5% of the particle diameter.

The short range of the attraction creates a free-energy barrier for particles to move across the corners and edges of islands. Each particle must break a “bond” (depletion interaction) with one or more particles and then diffuse to reach its new lattice site (Fig. 2A). By contrast, in epitaxial growth of atomic crystals, such step-edge barriers arise from the long-ranged interactions between atoms; as the particle crosses the edge, it still “feels” the attractions from next-nearest neighbors in the crystal. Ganapathy *et al.* found that, surprisingly, the bond-breakage-plus-diffusion process in the colloid leads to growth rates that are quantitatively similar to those in atomic epitaxy. The diffusion process slows down the kinetics, much as the long-range potential barrier does in an atomic system.

However, the similarity between colloidal- and atomic-scale kinetics need not always hold. For a general transition between two states, we must consider how the free energy varies as a function of the configuration of all the particles. Typical models for kinetics in atomic, molecular, and biological systems calculate transition rates from the pathways and barriers between basins on this “free-energy landscape” (37) (Fig. 2B). But for colloidal particles, this framework breaks down, owing to the short range of the attraction and hydrodynamic drag.

Recent theories of colloidal dynamics take both of these effects into account. Holmes-Cerfon *et al.* (38) considered structural transitions in clusters of spherical particles with short-range attractive interactions. They considered transitions that are conceptually similar to those observed by Ganapathy *et al.*, but generalized: After a bond is broken, particles can diffuse individually or in concert along “soft modes” (Fig. 2B). In the limit of an infinitesimally short-ranged (or “sticky”) attraction—a reasonable approximation for depletion or DNA-mediated (39, 40)

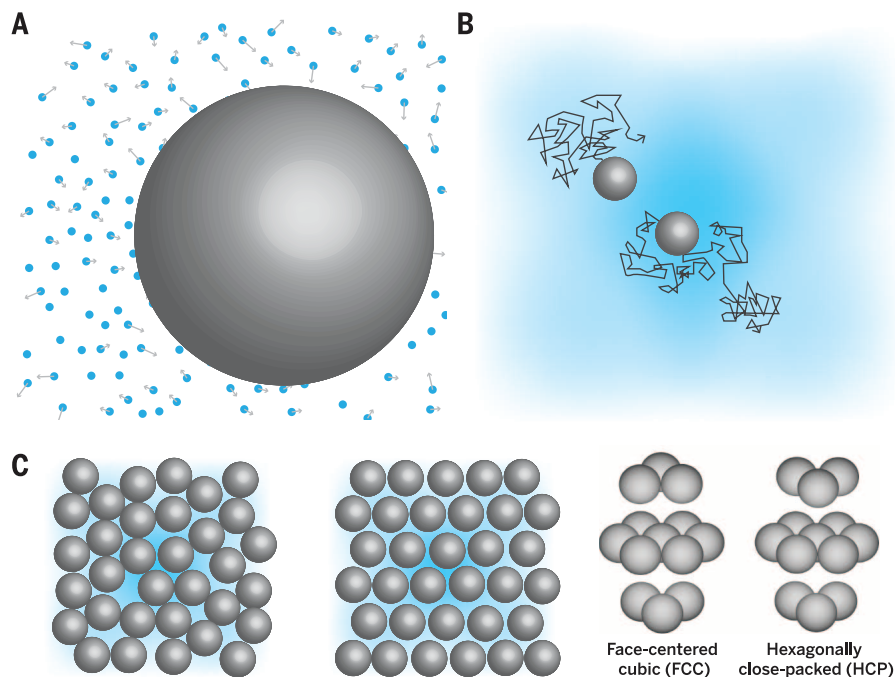


Fig. 1. Colloids are a model system for understanding phase transitions. (A) Collisions with solvent molecules (blue) lead to fluctuating, random forces on a particle (gray). (B) On larger time scales, the particles execute a random walk. We can use statistical mechanics to understand the collective behavior because the particles explore their container and interact with each other. (C) Hard spherical particles at a sufficiently high density have less room to move in a fluid phase (left) than in a crystal (right). In 3D, they spontaneously crystallize into a face-centered cubic lattice (right) at 50% volume fraction. A hexagonally close-packed lattice is shown for contrast.

attractions—only two parameters, both easily measured in experiment, are needed to predict the transition rates: a diffusion coefficient and the probability of two spheres binding. The rest of the model is pure geometry: The entropy can be calculated as a function of the particle positions along the pathway. Similar models, incorporating not only the effects of drag on individual particles, but also the effects of hydrodynamic interactions between particles, have recently been used to explain nonequilibrium solid-solid transitions in colloidal crystals (41).

Another key difference between colloidal and atomic matter is that colloidal particles are purely classical objects. If we constrain some of the degrees of freedom, others can stabilize new equilibrium phases. Chen *et al.* (42) found that colloidal spheres with attractive patches centered on two poles can form a stable Kagome lattice—an “open” lattice with a low volume fraction (Fig. 2C). The Kagome structure is favored over other lattices with equivalent potential energy, some having higher density. Mao *et al.* (43) later showed that open lattices like the Kagome are favored by the entropy associated with both vibration and rotation of the particles around their lattice sites (Fig. 2C). Because these entropic terms can be increased by increasing the patch size, many different phases, including the three-dimensional (3D) diamond lattice and even liquid phases (44), might be stabilized by changing patch size and geometry.

This work illustrates the critical role that entropy plays in the organization of colloidal matter, even in the presence of strong attractive interactions. In atomic-scale systems, the vibrational and rotational modes—which in spin systems are better known by the names of their respective quasi-particles, phonons and magnons—also play a role in determining the equilibrium crystal structures, but these modes can be quantized even at room temperature. In contrast, colloidal systems are purely classical, so there is a continuous spectrum of energies for each mode. No modes can be “frozen out” by reducing the temperature, and all contribute simultaneously to the free energy.

Anisotropic and patchy particles

The “patchy particles” of Chen *et al.* (42), which interact preferentially along certain directions, are part of a new generation of colloidal particles that break orientational isotropy (45–47). The phase behavior of these particles is potentially much richer than that of spheres. For instance, tetrahedrally coordinated patchy particles (48) might crystallize into a diamond lattice, and mixtures of patchy particles might form exotic phases such as an “empty liquid” (49), a liquid phase that persists to vanishingly small densities.

For hard particles, changes in shape dramatically alter the equilibrium phases. This point has been examined most thoroughly in simulations. Damasceno *et al.* (21) explored how the densest equilibrium phase varies as a function of shape in families of convex polyhedra. These polyhedra formed a variety of crystals, liquid crystals, and

glasses. In many cases, the phase behavior agreed with expectations. For example, nearly spherical polyhedra formed fcc plastic crystals, a configuration that makes intuitive sense: The lattice allows the particles to maximize their vibrational entropy while maintaining their freedom to rotate. But other transitions were counterintuitive. Some polyhedra formed more complex phases than expected, and still others failed to crystallize, even though their densest phase is known to be ordered. Although Damasceno *et al.* could not predict the densest equilibrium phase directly from the shape, they were able to correlate the observed phase behavior to two geometrical parameters, the sphericity of the particles and their average coordination number in the fluid phase (Fig. 3A). The connection between global phase behavior and local structure was later explained by van Anders *et al.* (50) in terms of “directional entropic interactions”: When two particles orient their faces toward one another, they increase the free volume available to the rest of the particles (Fig. 3B). The predictions of Damasceno *et al.* have not yet been tested in experiments at the colloidal scale, owing to the difficulty of synthesizing hard polyhedra. Inorganic nanoparticles with such shapes have been assembled by using depletion interactions or sedimentation (51, 52), but experiments on hard colloidal particles would make it possible to visualize the dynamics governing the solid-solid and glass transitions.

An experimentally simpler way to control colloidal assembly is through the topography of the particles. The depletion attraction between two surfaces can be modulated by roughness comparable to the size of the small depleting particles (53). In particles with rough and smooth

spots, the smooth parts act as attractive patches. Kraft *et al.* (54) exploited this effect to assemble analogs of surfactant micelles from sphere doublets comprising one large, rough sphere and one small, smooth sphere (Fig. 3C). Another way to control the depletion interaction is to imprint a concave region on an otherwise spherical particle (55). This topographical feature acts as a “lock” for another particle (the “key”) having a convex surface that closely matches the contour of the lock. The lock particles can be made by buckling spheres or by growing a spherical particle on a nonspherical seed and then removing the seed (56), leaving a dimple. Such particles can assemble into dimers, chains, and networks (Fig. 3D).

All of these colloidal particles, whether spherical or polyhedral, convex or concave, rough or smooth, have a common feature: They are topologically equivalent, or “homeomorphic.” That is, they can all be continuously deformed into one another. It is easiest to understand this if we imagine a colloidal particle as a lump of clay. We can knead it into many different shapes, but unless we punch a hole in it, or roll it into a cylinder and glue the ends together, there is no way to turn it into a torus. So, in terms of topology, even the “nonspherical” particles we have seen are spherical! Both the shape and topology of a particle determine the interactions between particles inserted into a medium that is partially ordered, such as a nematic liquid crystal. Defects in the medium can be created by controlling the anchoring conditions or by moving the particles around to make defect lines and even knots (57). Smalyukh and co-workers (58, 59) showed that new classes of defect structures could be stabilized by particles with “handles” (Fig. 3D) or knots (59). Handles are a topological feature: A

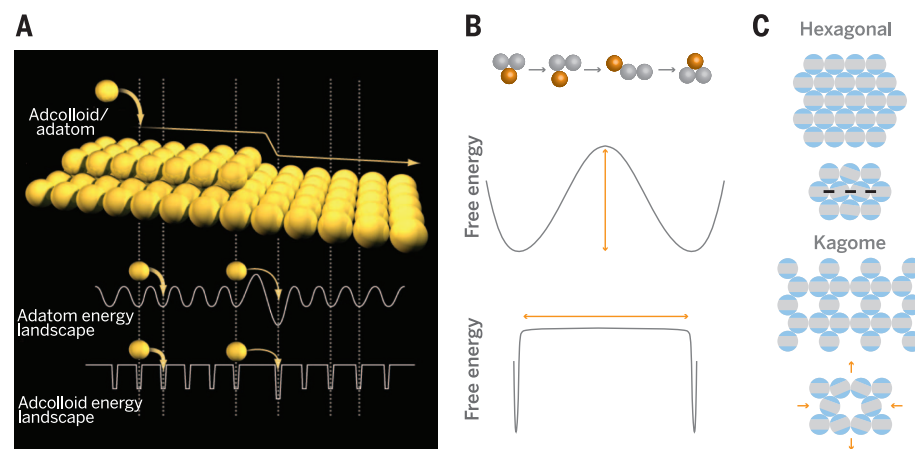


Fig. 2. Colloidal matter reveals structural and dynamical features not seen at the atomic scale.

(A) Crystals grow through the motion of particles across step edges (top). Short-range interactions between colloidal particles give rise to a different energy landscape for adatoms (middle) than for adcolloids (bottom). [Figure adapted from (105). Reprinted with permission from AAAS.] (B) For atoms, the rate of a transition (top) is set by the energy barrier (middle); for colloidal particles, one must consider the rate of diffusion after the bond is broken (bottom). The x axis indicates the coordinate along the transition path. (C) Janus particles with two attractive patches (blue) assemble into an open Kagome lattice rather than the more dense hexagonal lattice. Both lattices have the same number of contacting patches, but the constraints in the hexagonal lattice (black lines) do not allow the vibrational and rotational degrees of freedom (orange arrows) seen in the Kagome (bottom).

sphere has none, a ring or coffee mug has one, and two or more rings glued together in the plane have multiple handles. Ultimately, these topologically distinct particles may be able to self-assemble into novel structures, owing to the effective interactions that emerge as the liquid crystal minimizes the elastic energy associated with the defects (60, 61).

Colloidal matter on curved surfaces

Geometry allows us to rationalize, and in some cases predict, how colloidal matter organizes, and even how its dynamics emerge. But what if we could change the rules of geometry itself?

We can do this by curving the space that the colloid inhabits. Imagine that we put hard spheres on a spherical surface. At high density, the system favors a triangular lattice, which corresponds to the densest packing of spheres in 2D (62). Each particle in the lattice has six nearest neighbors arranged in a hexagon, so that each component triangle of the hexagon subtends an angle of $\pi/3$. But on a sphere, the sum of the interior angles of a

triangle must exceed π (Fig. 4A), which means that the hexagon is strained.

How does the system accommodate this curvature-induced strain? Part of the answer comes from mathematics. We can break down any 2D arrangement of points on the sphere into a network of (not necessarily regular) triangles that form a closed polyhedron. A famous result from Euler relates the number of vertices V , edges E , and faces F of the polyhedron: $V - E + F = 2$. The number 2, called the Euler characteristic, indicates that some particles must have fewer than six nearest neighbors; otherwise, we would have $V - E + F = 0$.

The simplest way to satisfy Euler's theorem is to add 12 defects in which a particle is coordinated by five, rather than six, nearest neighbors. These 12 fivefold disclinations, as they are called, can be seen in an old-style, hand-stitched soccer ball (or a “football,” as it is known in most places), which contains exactly 12 pentagonal panels, the rest being hexagonal. The 12 pentagons allow the otherwise hexagonal tiling to

make up for the angular surplus imposed by the Gaussian curvature. More generally, we can assign each fivefold disclination a topological “charge” of +1, and each sevenfold defect a charge of -1. The total disclination charge must be six times the Euler characteristic, which varies for different topologies.

Geometry does not entirely dictate the structure, though. The potential between the particles also matters (63). Bausch *et al.* (64) observed nearly hard-sphere colloidal particles bound to the surface of a spherical droplet and found that although the total disclination charge was exactly 12, in agreement with Euler's theorem, there

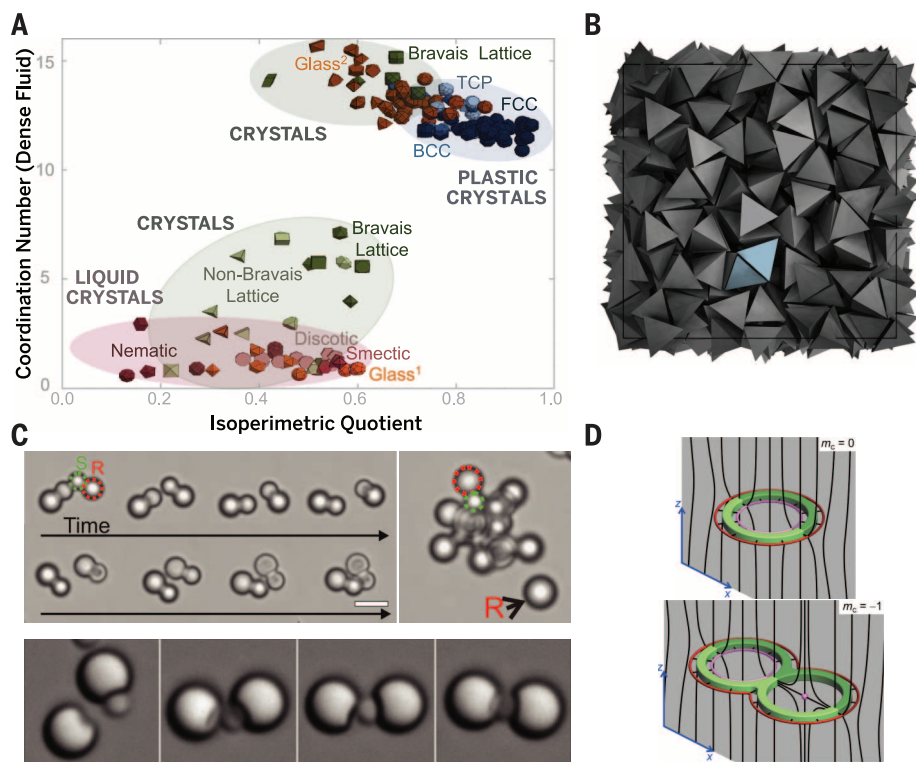


Fig. 3. The shape, topography, and topology of nonspherical particles can be used to control assembly. (A) Equilibrium phases found in simulations of hard convex polyhedral correlate with the coordination number in the fluid and the degree of sphericity of the particles. [Adapted from (21). Reprinted with permission from AAAS.] (B) To maximize the entropy of the system, the particles tend to orient with their faces parallel and close to one another. The tendency can be viewed as a “directional entropic force” [adapted from (50)]. (C) Topographical features control assembly in the presence of depletion forces. Top: time series of micrographs showing dimers of rough (“R”) and smooth (“S”) particles assembling into analogs of micelles. Scale bar, 5 μm [adapted from (54)]. Bottom: time series of micrographs showing 2- μm -diameter particles with concave dimples attracting convex particles and assembling into chains. [Adapted by permission from Macmillan Publishers Ltd: (55), copyright 2010.] (D) Particles with different numbers of topological handles affect the director field (black lines) in a liquid crystal. The interactions between such particles can be controlled by the anchoring conditions and the number of handles. [Adapted by permission from Macmillan Publishers Ltd: (58), copyright 2013.]

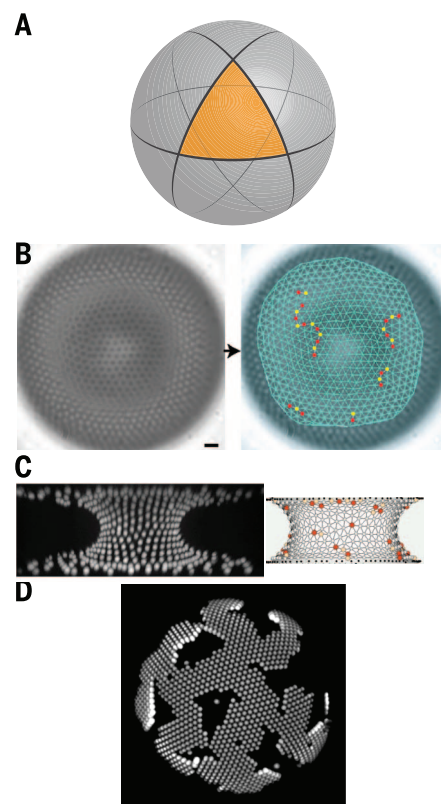


Fig. 4. Curvature controls defects and growth in colloidal crystals. (A) The sum of the interior angles of an equilateral triangle on a sphere must exceed π . As a consequence, a hexagonal lattice on the sphere is strained. (B) To minimize the elastic strain caused by the curvature, hard-sphere crystals on a spherical surface (left) form chains of disclinations known as grain-boundary scars (right; red: fivefold disclination; yellow: sevenfold disclination). [From (64). Reprinted with permission from AAAS.] (C) Polarized disclination pairs form in crystals on a capillary bridge (left). These “pleats” minimize the elastic strain associated with the gradient in curvature (yellow: fivefold disclination; red: sevenfold disclination). [Adapted by permission from Macmillan Publishers Ltd: (65), copyright 2010.] (D) Attractive particles on a sphere form ribbon-like domains, which allow the crystal to minimize its elastic energy while still covering a large surface area. [image from Guangnan Meng]

were more than 12 defects. The excess defects consisted of pairs of fivefold and sevenfold disclinations aligned in chains that Bausch *et al.* termed “grain boundary scars” (Fig. 4B). They argued that the scars minimize the elastic energy associated with the required disclinations (note that in theoretical models of the free energy, one treats the crystal as a continuous elastic medium and then calculates the deformation arising from the curvature-induced strain and the defects). The elastic energy implicitly includes an entropic contribution; indeed, for hard spheres, this is the only contribution. Bausch *et al.*’s elastic model showed that a single isolated fivefold disclination would incur a large local elastic strain, resulting in a large elastic energy penalty. To avoid the penalty, the crystal creates chains of defects, which gradually reduce the strain while keeping the total disclination charge constant.

Different defect motifs emerge to accommodate gradients in curvature like those found in a capillary bridge. Topologically such bridges are equivalent to cylinders, which have an Euler characteristic of zero—meaning that no defects are required. The curvature, however, can vary across the bridge: It is zero near the top or bottom plates, and positive or negative at the center, depending on the distance between the plates. Irvine *et al.* (65) examined defects in a colloidal suspension confined to a capillary bridge and found that as they pulled the surfaces apart, chains of dislocations formed with their sevenfold disclinations closer to the center of the bridge (Fig. 4C). The total disclination charge remained zero, as required by topology. These polarized dislocations allow the crystal to minimize the elastic energy associated with the gradient in curvature, much as pleats allow a pair of trousers to accommodate the different curvatures of the wearer’s waist and hips.

More recent experimental work has examined how curvature can affect the mobility of defects (66) and the growth of crystals (67). Meng and co-workers (67) found that particles with short-ranged depletion interactions on a spherical droplet formed crystals consisting of connected “ribbons,” anisotropic domains with widths much smaller than their lengths (Fig. 4D). The ribbon-like growth is a consequence of elastic considerations. When the attraction between particles is short-ranged, the crystal is brittle, and trying to wrap it around the sphere is like trying to gift-wrap a basketball: The wrapping paper can’t stretch, and if we are not allowed to wrinkle it, our only option is to tear it into strips. Multiple strips of the same width allow the crystal to cover a large area with minimal strain.

We still do not have a full picture of how curvature and the interparticle potential affect the kinetics of phase transitions. Simulations (68, 69) of crystal growth on curved surfaces usually employ long-range attractive potentials, which give rise to dislocations, grain boundary scars, or pleats in the growing crystal, depending on the curvature and its gradient. But in colloidal matter, where attractions are short-ranged, it could well be difficult to reach the ground states, which must (by Euler’s theorem) include topological de-

fects. It will therefore be interesting to see if biological systems on curved surfaces, such as viral capsids and lipid vesicles, follow the same growth pattern shown by colloidal crystals on curved surfaces.

Geometrical frustration in three dimensions

Taken together, the results of the previous section show that curvature “frustrates” the growth of 2D colloidal crystals of spherical particles. It makes the locally favored packing of particles incompatible with the space-filling packing, resulting in disorder. Theories of geometrical frustration reason in the opposite direction to understand 3D disorder: Given a particular 3D system, can we understand its propensity for disorder in terms of a competition between locally and globally favorable structures?

There are many 3D disordered systems; indeed, most colloids form glasses or gels. The origins of these nonequilibrium phases, whether in colloidal matter or condensed matter as a whole, remain poorly understood. One body of work (70, 71) attempts to connect the slowdown of dynamics near the glass or gel transition to a

growing structural length scale, perhaps associated with locally favored structures.

The challenge, then, is to determine the locally favored structures. This problem has a long history in materials science and condensed-matter physics, beginning with a 1952 paper by Frank (72) showing that an icosahedron of 13 spheres interacting through a Lennard-Jones 6-12 potential has an 8.4% lower energy than arrangements that occur in the fcc or hexagonally close-packed (hcp) lattices (Fig. 5A). Frank hypothesized that these stable icosahedral arrangements might be common in liquids and, furthermore, that they might allow certain liquids to be supercooled well below their freezing point, since the fivefold symmetry of icosahedra is incompatible with crystalline order. Later calculations found that fivefold symmetric structures, though not necessarily icosahedra, are more stable than lattice-like clusters for other model potentials and for larger numbers of spheres (73). The statistical mechanics of such finite systems has become a field of its own (37, 74). In the last decade, Frank’s hypothesis was verified by x-ray experiments that revealed structures with fivefold symmetry in metallic liquids (75).

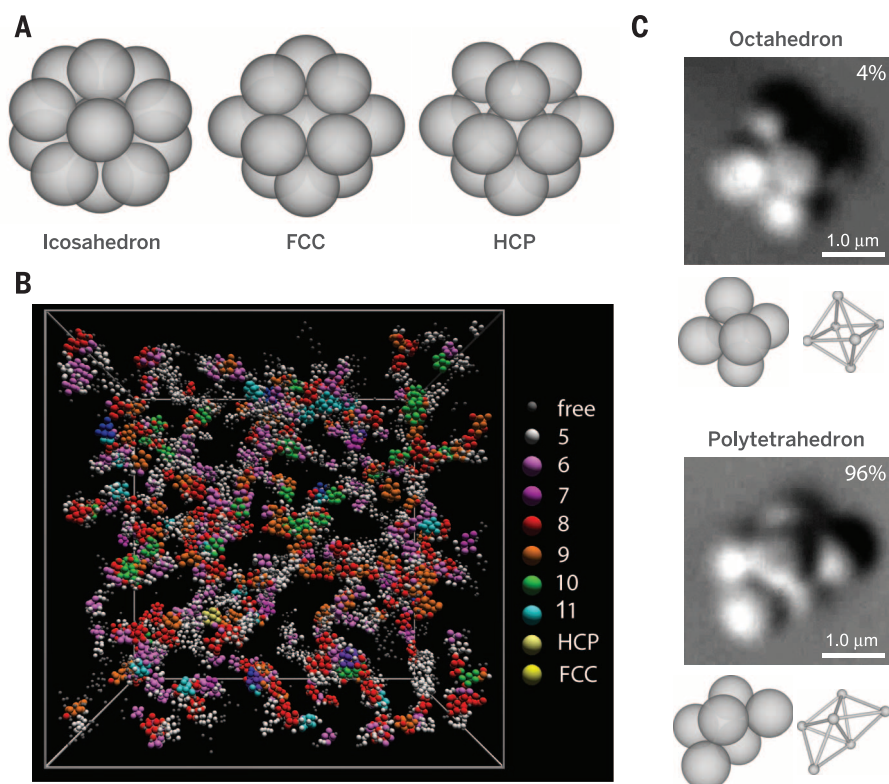


Fig. 5. The tension between locally and globally favored structures leads to frustration. (A) The lowest potential-energy configuration of 13 spheres interacting through a Lennard-Jones potential is an icosahedron. Unlike the fcc or hcp clusters, icosahedra cannot tile space. **(B)** Particles interacting through short-range attractions form a gel. The minimal-energy clusters of such particles (shown in colors) form a percolating network. [Adapted by permission from Macmillan Publishers Ltd: (87), copyright 2008.] **(C)** Entropy favors asymmetry in local structure. Six particles with short-range attractions form an asymmetric configuration (the polytetrahedron) more than 24 times as often as they form a symmetric structure (the octahedron) in equilibrium. Both structures have the same potential energy. The difference in probabilities is primarily due to the higher rotational entropy for the asymmetric structure.

However, we must be careful when applying Frank's hypothesis to colloidal matter. The Lennard-Jones 6-12 and related potentials are reasonable approximations for certain nanoparticles (76) but are poor models for colloids, which have much shorter-range attractions. Moreover, entropy must play a role in structuring colloids, even when the potential is attractive.

In hard spheres, where the only structuring influence is entropy, the locally favored structures do not appear to be icosahedra, except when the particles are confined (77). Colloidal hard spheres in 3D show a glass transition at a volume fraction of about 0.60 or higher, depending on the polydispersity (78). "Supercooled" fluids of such particles—that is, dispersions that remain fluid although they have been concentrated to volume fractions above the freezing transition—show structural and dynamical features similar to those of atomic-scale liquids (79). Yet, experiments show that the local structure of supercooled colloidal fluids differs qualitatively from that of metallic liquids. Gasser *et al.* found few true icosahedra in the bulk of supercooled hard-sphere fluids (80). Simulations by Royall *et al.* at larger supercooling (higher volume fraction) also did not find icosahedra to be favored, although 10-membered clusters that are fragments of icosahedra were a common motif (81). However, the same study suggests that even deeper supercooling is necessary to resolve the connection between locally favored structures and the glass transition.

Experiments on random packings of hard macroscopic spheres, beginning with Stephen Hales's examination of pea packings in 1727 (82), and continuing to Bernal and Finney's studies of ball-bearing packings (14, 83) and more recent work on x-ray tomography of spherical beads (84), have found fivefold local packings but also many other local structures that are incompatible with crystalline order. As van Meel and co-workers noted (85), "Bernal and many after him have indeed observed just about any small polyhedron in hard-sphere fluids." It is still not clear which locally favored structures we should be looking for in hard-sphere fluids.

When the particles attract one another, locally favored structures can be found by using energetic calculations or cluster lifetimes (86). Royall *et al.* (87) found that icosahedral, deltahedral, and bipyramidal clusters minimize the potential energy of a Morse potential with a short-range parameter, which approximates a depletion interaction between spherical particles. Using confocal microscopy, they looked for these clusters inside a colloidal gel and found that they occurred in long-lived percolating networks (Fig. 5B). These networks might contribute to the slowdown of dynamics near the gel transition.

The stability of such clusters is also influenced by entropy (88, 89). One entropic effect that must be considered is the huge number of competing structures at any given cluster size: for example, for a 10-sphere cluster, there are nearly 400 potential-energy minima, most of which are degenerate (90, 91). A second entropic effect

involves the number of ways in which each cluster can form. Meng *et al.* found that clusters of attractive spherical particles formed asymmetric structures in equilibrium (89). This tendency, which arises because lower-symmetry clusters have more permutations of particles that result in the same structure, strongly selects against the icosahedron and fivefold symmetry, while favoring polytetrahedral clusters (Fig. 5C). This case shows yet another way in which short-range attractions and entropy in colloidal matter conspire to produce results different from (and, in this case, almost exactly the opposite of) those of atomic systems.

There is still no direct correlation between the stability of certain clusters and a growing structural length scale in arrested colloidal phases. But perhaps this has more to do with the system than the model (92). Spherical particles may be one of the simpler experimental systems to examine, but they are also one of the trickiest to think about geometrically. Thus, some experiments have begun to examine slow dynamics in dispersions of anisotropic particles (93).

Hard tetrahedra may be a better system for testing theories of geometrical frustration because they "prefer" higher dimensions: Although they cannot fill 3D Euclidean space, they can perfectly tile the surface of a 4D hypersphere (94). Just as putting hard spheres on the surface of a sphere leads to disclinations, so does putting densely packed tetrahedra in flat (Euclidean) space (95, 96); both systems are subject to a curvature-induced elastic strain. Simulations have found that hard tetrahedra form a disordered, quasicrystal phase that persists to high densities, even though a denser ordered phase can form (97). It is interesting to consider whether the stability of this quasicrystal might be traced to locally favored structures that—like the ribbons we saw in crystals of attractive spheres on a sphere (67)—minimize the curvature-induced elastic strain.

Looking forward

Perhaps it should not be surprising that geometry and packing arguments can be used to understand the organization of colloidal matter. The earliest incarnations of colloidal particles were nanoscale objects with haphazard arrangements of charges and uncontrolled polydispersity. Advances in synthesis and fabrication have transformed colloids into their modern form: highly symmetric shapes with well-controlled size distributions, surface chemistry, topography, and topology. In other words, colloidal matter is designed to obey geometrical rules.

What is surprising is the richness of the phenomena that emerge when we combine these well-controlled particles with simple constraints. These phenomena occur because thermodynamic quantities such as the elastic energy depend sensitively on the interaction potential, and the entropy on how the particles are allowed to fluctuate. When we constrain the dominant degrees of freedom (by, for example, introducing patchy attractions), the other degrees of freedom that we previously neglected come to the fore, stabilizing new structures.

In most cases, however, geometrical arguments remain post hoc explanations for the collective behavior we discover in experiment or simulation. Steps toward predictive frameworks have been made in the geometrical model of the free-energy landscape of Holmes-Cerfon *et al.* (38) and the directional entropic forces of van Anders *et al.* (50). But many other transitions and structural motifs remain to be discovered in the vast parameter space now accessible to the experimentalist—a space spanned by shape, topography, topology, and curvature.

Dynamics offers yet another dimension of control, one that is difficult to vary in atomic systems but that in colloidal matter emerges naturally from the interactions between particles and fluid. Even at the single-particle level, the thermally driven motion of nonspherical particles (98) and of particles in anisotropic fluids (99) continues to reveal surprises, nearly 100 years after Perrin's experiments. The hydrodynamic interactions between these particles can not only select for certain phases (41), but can also result in different collective phenomena when the driving forces are intrinsic or extrinsic energy sources rather than thermal fluctuations (100). Such active colloidal systems show nonequilibrium self-organization with complexity rivaling that of biological systems such as living cells, bacterial baths, and animal flocks.

Another variable is specificity. DNA-functionalized colloidal particles have effective attractions that are both short-ranged and specific (101), and each particle can carry more than 40 different strands of DNA (102). It is therefore possible to explore systems in which the number of independent pair interactions is comparable to the number of particles. Collective effects should emerge from the interplay between specificity and packing constraints in such "polygamous" systems, which have no equivalent at the molecular scale.

Understanding the effects of specificity, dynamics, and the many other dimensions of colloidal matter will require new experiments and theoretical models. But with such understanding, we might resolve long-standing challenges, such as the "inverse" problem of creating a colloidal system that will self-assemble into a prescribed structure. Optical materials are a prime application, since the scale of colloidal particles is on the order of visible light. The optimal structures for materials that show structural colors (103) and photonic band gaps (104) are not crystals, but disordered materials with short-range correlations. Thus, the framework of geometrical frustration, which has been used to explain disordered systems, could be used to design new ones instead, through specific choices for the shapes or interactions of the particles.

Future discoveries in colloidal matter will continue to come from systematic and iterative collaborations between those who synthesize particles, those who measure their structure and dynamics, and those who construct models explaining the phenomena. Colloidal matter is, and will continue to be, where geometry, chemistry, and physics meet.

REFERENCES AND NOTES

- In another semantic shift, the word "colloid" is increasingly used to refer to an individual colloidal particle. In this article, I use the traditional definition, where "colloid" means "colloidal dispersion."
- F. Li, D. P. Josephson, A. Stein, Colloidal assembly: The road from particles to colloidal molecules and crystals. *Angew. Chem. Int. Ed.* **50**, 360–388 (2011). doi: [10.1002/anie.201001451](#); pmid: [21038335](#)
- O. Kruglova, P.-J. Demeyer, K. Zhong, Y. Zhou, K. Clays, Wonders of colloidal assembly. *Soft Matter* **9**, 9072–9087 (2013). doi: [10.1039/c3sm50845e](#)
- R. Brown, A brief account of microscopical observations made in the months of June, July and August 1827, on the particles contained in the pollen of plants; and on the general existence of active molecules in organic and inorganic bodies. *Philos. Mag. Ser. 2* **4**, 161–173 (1828). doi: [10.1080/14786442808674769](#)
- J. Perrin, Mouvement brownien et réalité moléculaire. *Ann. Chim. Phys.* **18**, 5–104 (1909).
- A. Einstein, Über die von der molekularkinetischen Theorie der Wärme geforderte Bewegung von in ruhenden Flüssigkeiten suspendierten Teilchen. *Ann. Phys.* **322**, 549–560 (1905). doi: [10.1002/andp.19053220806](#)
- D. Frenkel, in *Soft Condensed Matter Physics in Molecular and Cell Biology*, W. C. K. Poon, D. Andelman, Eds. (CRC Press, Boca Raton, FL, 2006), *Scottish Graduate Series*, pp. 19–48.
- W. W. Wood, J. D. Jacobson, Preliminary results from a recalculation of the Monte Carlo equation of state of hard spheres. *J. Chem. Phys.* **27**, 1207–1208 (1957). doi: [10.1063/1.1743956](#)
- B. J. Alder, T. E. Wainwright, Phase transition for a hard sphere system. *J. Chem. Phys.* **27**, 1208–1209 (1957). doi: [10.1063/1.1743957](#)
- P. N. Pusey, W. van Meegen, Phase behaviour of concentrated suspensions of nearly hard colloidal spheres. *Nature* **320**, 340–342 (1986). doi: [10.1038/320340a0](#)
- T. C. Lubensky, Soft condensed matter physics. *Solid State Commun.* **102**, 187–197 (1997). doi: [10.1016/S0038-1098\(96\)00718-1](#)
- T. C. Hales, Sphere packings, I. *Discrete Comput. Geom.* **17**, 1–51 (1997). doi: [10.1007/BF02770863](#)
- T. C. Hales, Sphere packings, II. *Discrete Comput. Geom.* **18**, 135–149 (1997). doi: [10.1007/PL00009312](#)
- J. D. Bernal, J. Mason, Packing of spheres: Co-ordination of randomly packed spheres. *Nature* **188**, 910–911 (1960). doi: [10.1038/188910a0](#)
- S. Torquato, T. M. Truskett, P. G. Debenedetti, Is random close packing of spheres well defined? *Phys. Rev. Lett.* **84**, 2064–2067 (2000). doi: [10.1103/PhysRevLett.84.2064](#); pmid: [11017210](#)
- A. D. Dinsmore, A. G. Yodh, D. J. Pine, Phase diagrams of nearly-hard-sphere binary colloids. *Phys. Rev. E Stat. Phys. Plasmas Fluids Relat. Interdiscip. Topics* **52**, 4045–4057 (1995). doi: [10.1103/PhysRevE.52.4045](#); pmid: [9963877](#)
- L. Onsager, The effects of shape on the interaction of colloidal particles. *Ann. N.Y. Acad. Sci.* **51**, 627–659 (1949). doi: [10.1111/j.1749-6632.1949.tb27296.x](#)
- D. Frenkel, H. N. W. Lekkerkerker, A. Stroobants, Thermodynamic stability of a smectic phase in a system of hard rods. *Nature* **332**, 822–823 (1988). doi: [10.1038/332822a0](#)
- D. Frenkel, Entropy-driven phase transitions. *Phys. Stat. Mech. Its Appl.* **263**, 26–38 (1999). doi: [10.1016/S0378-4371\(98\)00501-9](#)
- Z. Dogic, S. Fraden, Ordered phases of filamentous viruses. *Curr. Opin. Colloid Interface Sci.* **11**, 47–55 (2006). doi: [10.1016/j.cocis.2005.10.004](#)
- P. F. Damasceno, M. Engel, S. C. Glotzer, Predictive self-assembly of polyhedra into complex structures. *Science* **337**, 453–457 (2012). doi: [10.1126/science.1220869](#); pmid: [22837525](#)
- D. W. Schaefer, B. J. Ackerson, Melting of colloidal crystals. *Phys. Rev. Lett.* **35**, 1448–1451 (1975). doi: [10.1103/PhysRevLett.35.1448](#)
- H. M. Lindsay, P. M. Chaikin, Elastic properties of colloidal crystals and glasses. *J. Chem. Phys.* **76**, 3774–3781 (1982). doi: [10.1063/1.443417](#)
- V. J. Anderson, H. N. W. Lekkerkerker, Insights into phase transition kinetics from colloid science. *Nature* **416**, 811–815 (2002). doi: [10.1038/416811a](#); pmid: [11976674](#)
- W. Poon, Physics: Colloids as big atoms. *Science* **304**, 830–831 (2004). doi: [10.1126/science.1097964](#); pmid: [15131294](#)
- P. Schall, I. Cohen, D. A. Weitz, F. Spaepen, Visualization of dislocation dynamics in colloidal crystals. *Science* **305**, 1944–1948 (2004). doi: [10.1126/science.1102186](#); pmid: [15448265](#)
- P. Schall, I. Cohen, D. A. Weitz, F. Spaepen, Visualizing dislocation nucleation by indenting colloidal crystals. *Nature* **440**, 319–323 (2006). doi: [10.1038/nature04557](#); pmid: [16541069](#)
- A. M. Alsayed, M. F. Islam, J. Zhang, P. J. Collings, A. G. Yodh, Premelting at defects within bulk colloidal crystals. *Science* **309**, 1207–1210 (2005). doi: [10.1126/science.1112399](#); pmid: [15994377](#)
- Z. Wang, F. Wang, Y. Peng, Z. Zheng, Y. Han, Imaging the homogeneous nucleation during the melting of superheated colloidal crystals. *Science* **338**, 87–90 (2012). doi: [10.1126/science.1224763](#); pmid: [23042889](#)
- U. Gasser, E. R. Weeks, A. Schofield, P. N. Pusey, D. A. Weitz, Real-space imaging of nucleation and growth in colloidal crystallization. *Science* **292**, 258–262 (2001). doi: [10.1126/science.1058457](#); pmid: [11303095](#)
- J. Russo, H. Tanaka, The microscopic pathway to crystallization in supercooled liquids. *Sci. Rep.* **2**, 505 (2012). doi: [10.1038/srep00505](#); pmid: [22792437](#)
- D. G. A. Aarts, M. Schmidt, H. N. W. Lekkerkerker, Direct visual observation of thermal capillary waves. *Science* **304**, 847–850 (2004). doi: [10.1126/science.1097116](#); pmid: [15131300](#)
- P. N. Pusey, W. van Meegen, Observation of a glass transition in suspensions of spherical colloidal particles. *Phys. Rev. Lett.* **59**, 2083–2086 (1987). doi: [10.1103/PhysRevLett.59.2083](#); pmid: [10035413](#)
- W. K. Kegel, A. van Blaaderen, Direct observation of dynamical heterogeneities in colloidal hard-sphere suspensions. *Science* **287**, 290–293 (2000). doi: [10.1126/science.287.5451.290](#); pmid: [10634780](#)
- E. R. Weeks, J. C. Crocker, A. C. Levitt, A. Schofield, D. A. Weitz, Three-dimensional direct imaging of structural relaxation near the colloidal glass transition. *Science* **287**, 627–631 (2000). doi: [10.1126/science.287.5453.627](#); pmid: [10649991](#)
- R. Ganapathy, M. R. Buckley, S. J. Gerbode, I. Cohen, Direct measurements of island growth and step-edge barriers in colloidal epitaxy. *Science* **327**, 445–448 (2010). doi: [10.1126/science.1179947](#); pmid: [20093469](#)
- D. Wales, *Energy Landscapes: Applications to Clusters, Biomolecules and Glasses* (Cambridge Univ. Press, Cambridge, 2004).
- M. Holmes-Cerfon, S. J. Gortler, M. P. Brenner, A geometrical approach to computing free-energy landscapes from short-ranged potentials. *Proc. Natl. Acad. Sci. U.S.A.* **110**, E5–E14 (2013). doi: [10.1073/pnas.1211720110](#); pmid: [23248296](#)
- W. B. Rogers, J. C. Crocker, Direct measurements of DNA-mediated colloidal interactions and their quantitative modeling. *Proc. Natl. Acad. Sci. U.S.A.* **108**, 15687–15692 (2011). doi: [10.1073/pnas.1109853108](#); pmid: [21896714](#)
- P. Varilly, S. Angioletti-Uberti, B. M. Mognetti, D. Frenkel, A general theory of DNA-mediated and other valence-limited colloidal interactions. *J. Chem. Phys.* **137**, 094108, 094108–094115 (2012). doi: [10.1063/1.4748100](#); pmid: [22957556](#)
- I. C. Jenkins, M. T. Casey, J. T. McGinley, J. C. Crocker, T. Sinno, Hydrodynamics selects the pathway for displacive transformations in DNA-linked colloidal crystallites. *Proc. Natl. Acad. Sci. U.S.A.* **111**, 4803–4808 (2014). doi: [10.1073/pnas.1318012111](#); pmid: [24639545](#)
- Q. Chen, S. C. Bae, S. Granick, Directed self-assembly of a colloidal kagome lattice. *Nature* **469**, 381–384 (2011). doi: [10.1038/nature09713](#); pmid: [21248847](#)
- X. Mao, Q. Chen, S. Granick, Entropy favours open colloidal lattices. *Nat. Mater.* **12**, 217–222 (2013). doi: [10.1038/nmat3496](#); pmid: [23314105](#)
- F. Smallenburg, F. Sciortino, Liquids more stable than crystals in particles with limited valence and flexible bonds. *Nat. Phys.* **9**, 554–558 (2013). doi: [10.1038/nphys2693](#)
- S. C. Glotzer, M. J. Solomon, Anisotropy of building blocks and their assembly into complex structures. *Nat. Mater.* **6**, 557–562 (2007). doi: [10.1038/nmat1949](#); pmid: [17667968](#)
- E. Duguet, A. Désert, P. Perro, S. Ravaine, Design and elaboration of colloidal molecules: An overview. *Chem. Soc. Rev.* **40**, 941–960 (2011). doi: [10.1039/c0cs00048e](#); pmid: [21212874](#)
- S. Sacanna, D. J. Pine, G.-R. Yi, Engineering shape: The novel geometries of colloidal self-assembly. *Soft Matter* **9**, 8096–8106 (2013). doi: [10.1039/c3sm50500f](#)
- Y. Wang *et al.*, Colloids with valence and specific directional bonding. *Nature* **491**, 51–55 (2012). doi: [10.1038/nature11564](#); pmid: [23128225](#)
- E. Bianchi, J. Largo, P. Tartaglia, E. Zaccarelli, F. Sciortino, Phase diagram of patchy colloids: Towards empty liquids. *Phys. Rev. Lett.* **97**, 168301 (2006). doi: [10.1103/PhysRevLett.97.168301](#); pmid: [17155440](#)
- G. van Anders, D. Klotsa, N. K. Ahmed, M. Engel, S. C. Glotzer, Understanding shape entropy through local dense packing. *Proc. Natl. Acad. Sci. U.S.A.* **111**, E4812–E4821 (2014). doi: [10.1073/pnas.1418159111](#); pmid: [25344532](#)
- K. L. Young *et al.*, A directional entropic force approach to assemble anisotropic nanoparticles into superlattices. *Angew. Chem. Int. Ed.* **52**, 13980–13984 (2013). doi: [10.1002/anie.201306009](#); pmid: [24353226](#)
- J. Henzie, S. C. Andrews, X. Y. Ling, Z. Li, P. Yang, Oriented assembly of polyhedral plasmonic nanoparticle clusters. *Proc. Natl. Acad. Sci. U.S.A.* **110**, 6640–6645 (2013). doi: [10.1073/pnas.1218616110](#); pmid: [23569275](#)
- K. Zhao, T. G. Mason, Directing colloidal self-assembly through roughness-controlled depletion attractions. *Phys. Rev. Lett.* **99**, 268301 (2007). doi: [10.1103/PhysRevLett.99.268301](#); pmid: [18233607](#)
- D. J. Kraft *et al.*, Surface roughness directed self-assembly of patchy particles into colloidal micelles. *Proc. Natl. Acad. Sci. U.S.A.* **109**, 10787–10792 (2012). doi: [10.1073/pnas.1116820109](#); pmid: [22715288](#)
- S. Sacanna, W. T. M. Irvine, P. M. Chaikin, D. J. Pine, Lock and key colloids. *Nature* **464**, 575–578 (2010). doi: [10.1038/nature08906](#); pmid: [20336142](#)
- S. Sacanna *et al.*, Shaping colloids for self-assembly. *Nat. Commun.* **4**, 1688 (2013). doi: [10.1038/ncomms2694](#); pmid: [23575692](#)
- U. Tkalec, M. Ravnik, S. Čopar, S. Žumer, I. Mušević, Reconfigurable knots and links in chiral nematic colloids. *Science* **333**, 62–65 (2011). doi: [10.1126/science.1205705](#); pmid: [21719671](#)
- B. Senyuk *et al.*, Topological colloids. *Nature* **493**, 200–205 (2013). doi: [10.1038/nature11710](#); pmid: [23263182](#)
- A. Martinez *et al.*, Mutually tangled colloidal knots and induced defect loops in nematic fields. *Nat. Mater.* **13**, 258–263 (2014). doi: [10.1038/nmat3840](#); pmid: [24390381](#)
- P. Poulin, H. Stark, T. C. Lubensky, D. A. Weitz, Novel colloidal interactions in anisotropic fluids. *Science* **275**, 1770–1773 (1997). doi: [10.1126/science.275.5307.1770](#); pmid: [9065396](#)
- I. Mušević, Nematic colloids, topology and photonics. *Philos. Trans. A Math. Phys. Eng. Sci.* **371**, 20120266 (2013). doi: [10.1098/rsta.2012.0266](#); pmid: [23459967](#)
- A. Thue, Om nagle geometrisk-taltheoretiske Theoremer. *Forh Ved Skand. Naturforskere*, 352–353 (1892).
- M. J. Bowick, L. Giomi, Two-dimensional matter: Order, curvature and defects. *Adv. Phys.* **58**, 449–563 (2009). doi: [10.1080/00018730903043166](#)
- A. R. Bausch *et al.*, Grain boundary scars and spherical crystallography. *Science* **299**, 1716–1718 (2003). doi: [10.1126/science.1081160](#); pmid: [12637740](#)
- W. T. M. Irvine, V. Vitelli, P. M. Chaikin, Pleats in crystals on curved surfaces. *Nature* **468**, 947–951 (2010). doi: [10.1038/nature09620](#); pmid: [21164482](#)
- W. T. M. Irvine, M. J. Bowick, P. M. Chaikin, Fractionalization of interstitials in curved colloidal crystals. *Nat. Mater.* **11**, 948–951 (2012). doi: [10.1038/nmat3429](#); pmid: [23023553](#)
- G. Meng, J. Paulose, D. R. Nelson, V. N. Manoharan, Elastic instability of a crystal growing on a curved surface. *Science* **343**, 634–637 (2014). doi: [10.1126/science.1244827](#); pmid: [24503849](#)
- R. Backofen, A. Voigt, T. Witkowski, Particles on curved surfaces: A dynamic approach by a phase-field-crystal model. *Phys. Rev. E Stat. Nonlin. Soft Matter Phys.* **81**, 025701 (2010). doi: [10.1103/PhysRevE.81.025701](#); pmid: [20365624](#)
- A. Luque, D. Reguera, A. Morozov, J. Rudnick, R. Bruinsma, Physics of shell assembly: Line tension, hole implosion, and closure catastrophe. *J. Chem. Phys.* **136**, 184507 (2012). doi: [10.1063/1.4712304](#); pmid: [22583300](#)
- S. Karmakar, C. Dasgupta, S. Sastry, Growing length scales and their relation to timescales in glass-forming liquids. *Annu. Rev. Condens. Matter Phys.* **5**, 255–284 (2014). doi: [10.1146/annurev-conmatphys-031113-133848](#)
- C. P. Royall, S. R. Williams, The role of local structure in dynamical arrest. *Phys. Rep.* **560**, 1–75 (2014). doi: [10.1016/j.physrep.2014.11.004](#)
- F. C. Frank, Supercooling of Liquids. *Proc. R. Soc. Lond. A* **215**, 43–46 (1952).

73. J. P. K. Doye, D. J. Wales, Structural consequences of the range of the interatomic potential - A menagerie of clusters. *J. Chem. Soc. Faraday Trans.* **93**, 4233–4243 (1997). doi: [10.1039/a706221d](https://doi.org/10.1039/a706221d)
74. F. H. Stillinger, T. A. Weber, Packing structures and transitions in liquids and solids. *Science* **225**, 983–989 (1984). doi: [10.1126/science.225.4666.983](https://doi.org/10.1126/science.225.4666.983); pmid: [17783020](https://pubmed.ncbi.nlm.nih.gov/17783020/)
75. H. Reichert *et al.*, Observation of five-fold local symmetry in liquid lead. *Nature* **408**, 839–841 (2000). doi: [10.1038/35048537](https://doi.org/10.1038/35048537); pmid: [11130718](https://pubmed.ncbi.nlm.nih.gov/11130718/)
76. J. Lacava, P. Born, T. Kraus, Nanoparticle clusters with Lennard-Jones geometries. *Nano Lett.* **12**, 3279–3282 (2012). doi: [10.1021/nl3013659](https://doi.org/10.1021/nl3013659); pmid: [22575027](https://pubmed.ncbi.nlm.nih.gov/22575027/)
77. B. de Nijs *et al.*, Entropy-driven formation of large icosahedral colloidal clusters by spherical confinement. *Nat. Mater.* **14**, 56–60 (2015). doi: [10.1038/nmat4072](https://doi.org/10.1038/nmat4072); pmid: [25173580](https://pubmed.ncbi.nlm.nih.gov/25173580/)
78. G. Brambilla *et al.*, Probing the equilibrium dynamics of colloidal hard spheres above the mode-coupling glass transition. *Phys. Rev. Lett.* **102**, 085703 (2009). doi: [10.1103/PhysRevLett.102.085703](https://doi.org/10.1103/PhysRevLett.102.085703); pmid: [19257755](https://pubmed.ncbi.nlm.nih.gov/19257755/)
79. G. L. Hunter, E. R. Weeks, The physics of the colloidal glass transition. *Rep. Prog. Phys.* **75**, 066501 (2012). doi: [10.1088/0034-4885/75/6/066501](https://doi.org/10.1088/0034-4885/75/6/066501); pmid: [22790649](https://pubmed.ncbi.nlm.nih.gov/22790649/)
80. U. Gasser, A. Schofield, D. A. Weitz, Local order in a supercooled colloidal fluid observed by confocal microscopy. *J. Phys. Condens. Matter* **15**, S375–S380 (2003). doi: [10.1088/0953-8984/15/1/351](https://doi.org/10.1088/0953-8984/15/1/351)
81. C. P. Royall, A. Malins, A. J. Dunleavy, R. Pinney, Strong geometric frustration in model glassformers. *J. Non-Cryst. Solids* **407**, 34–43 (2015).
82. S. Hales, *Vegetable staticks: or, an account of some statical experiments on the sap in vegetables: being an essay towards a natural history of vegetation. Also, a specimen of an attempt to analyse the air, By a great Variety of Chymio-Statical Experiments; Which were read at several Meetings before the Royal Society* (printed for W. and J. Innys, T. Woodward, London, 1727).
83. J. L. Finney, Fine structure in randomly packed, dense clusters of hard spheres. *Mater. Sci. Eng.* **23**, 199–205 (1976). doi: [10.1016/0025-5416\(76\)90194-4](https://doi.org/10.1016/0025-5416(76)90194-4)
84. N. Francois, M. Saadatfar, R. Cruikshank, A. Sheppard, Geometrical frustration in amorphous and partially crystallized packings of spheres. *Phys. Rev. Lett.* **111**, 148001 (2013). doi: [10.1103/PhysRevLett.111.148001](https://doi.org/10.1103/PhysRevLett.111.148001); pmid: [24138272](https://pubmed.ncbi.nlm.nih.gov/24138272/)
85. J. A. van Meel, B. Charbonneau, A. Fortini, P. Charbonneau, Hard-sphere crystallization gets rarer with increasing dimension. *Phys. Rev. E Stat. Nonlin. Soft Matter Phys.* **80**, 061110 (2009). doi: [10.1103/PhysRevE.80.061110](https://doi.org/10.1103/PhysRevE.80.061110); pmid: [20365121](https://pubmed.ncbi.nlm.nih.gov/20365121/)
86. A. Malins, J. Eggers, H. Tanaka, C. P. Royall, Lifetimes and length scales of structural motifs in a model glassformer. *Faraday Discuss.* **167**, 405–423 (2013). doi: [10.1039/c3fd000078h](https://doi.org/10.1039/c3fd000078h); pmid: [24640503](https://pubmed.ncbi.nlm.nih.gov/24640503/)
87. C. Patrick Royall, S. R. Williams, T. Ohtsuka, H. Tanaka, Direct observation of a local structural mechanism for dynamic arrest. *Nat. Mater.* **7**, 556–561 (2008). doi: [10.1038/nmat2219](https://doi.org/10.1038/nmat2219); pmid: [18568032](https://pubmed.ncbi.nlm.nih.gov/18568032/)
88. A. Malins, S. R. Williams, J. Eggers, H. Tanaka, C. P. Royall, Geometric frustration in small colloidal clusters. *J. Phys. Condens. Matter* **21**, 425103 (2009). doi: [10.1088/0953-8984/21/42/425103](https://doi.org/10.1088/0953-8984/21/42/425103); pmid: [21715858](https://pubmed.ncbi.nlm.nih.gov/21715858/)
89. G. Meng, N. Arkus, M. P. Brenner, V. N. Manoharan, The free-energy landscape of clusters of attractive hard spheres. *Science* **327**, 560–563 (2010). pmid: [20110500](https://pubmed.ncbi.nlm.nih.gov/20110500/)
90. N. Arkus, V. N. Manoharan, M. P. Brenner, Minimal energy clusters of hard spheres with short range attractions. *Phys. Rev. Lett.* **103**, 118303–118304 (2009). doi: [10.1103/PhysRevLett.103.118303](https://doi.org/10.1103/PhysRevLett.103.118303); pmid: [19792406](https://pubmed.ncbi.nlm.nih.gov/19792406/)
91. R. S. Hoy, J. Harwayne-Gidansky, C. S. O'Hern, Structure of finite sphere packings via exact enumeration: Implications for colloidal crystal nucleation. *Phys. Rev. E Stat. Nonlin. Soft Matter Phys.* **85**, 051403 (2012). doi: [10.1103/PhysRevE.85.051403](https://doi.org/10.1103/PhysRevE.85.051403); pmid: [23004757](https://pubmed.ncbi.nlm.nih.gov/23004757/)
92. B. Charbonneau, P. Charbonneau, G. Tarjus, Geometrical frustration and static correlations in hard-sphere glass formers. *J. Chem. Phys.* **138**, 12A515 (2013). doi: [10.1063/1.4770498](https://doi.org/10.1063/1.4770498); pmid: [23556766](https://pubmed.ncbi.nlm.nih.gov/23556766/)
93. K. V. Edmond, M. T. Elsesser, G. L. Hunter, D. J. Pine, E. R. Weeks, Decoupling of rotational and translational diffusion in supercooled colloidal fluids. *Proc. Natl. Acad. Sci. U.S.A.* **109**, 17891–17896 (2012). doi: [10.1073/pnas.1203328109](https://doi.org/10.1073/pnas.1203328109); pmid: [23071311](https://pubmed.ncbi.nlm.nih.gov/23071311/)
94. H. S. M. Coxeter, Close-packing and froth. *III. J. Math.* **2**, 746–758 (1958).
95. M. Kléman, J. F. Sadoc, A tentative description of the crystallography of amorphous solids. *J. Phys. Lett.* **40**, 569–574 (1979). doi: [10.1051/physlet:019790040021056900](https://doi.org/10.1051/physlet:019790040021056900)
96. D. R. Nelson, F. Spaepen, in *Solid State Physics*, H. Ehrenreich, D. Turnbull, Eds. (Academic Press, New York, 1989), vol. 42, pp. 1–90; www.sciencedirect.com/science/article/pii/S008119470860079X.
97. A. Haji-Akbari *et al.*, Disordered, quasicrystalline and crystalline phases of densely packed tetrahedra. *Nature* **462**, 773–777 (2009). doi: [10.1038/nature08641](https://doi.org/10.1038/nature08641); pmid: [20010683](https://pubmed.ncbi.nlm.nih.gov/20010683/)
98. A. Chakrabarty *et al.*, Brownian motion of boomerang colloidal particles. *Phys. Rev. Lett.* **111**, 160603 (2013). doi: [10.1103/PhysRevLett.111.160603](https://doi.org/10.1103/PhysRevLett.111.160603); pmid: [24182246](https://pubmed.ncbi.nlm.nih.gov/24182246/)
99. T. Turiv *et al.*, Effect of collective molecular reorientations on Brownian motion of colloids in nematic liquid crystal. *Science* **342**, 1351–1354 (2013). doi: [10.1126/science.1240591](https://doi.org/10.1126/science.1240591); pmid: [24337292](https://pubmed.ncbi.nlm.nih.gov/24337292/)
100. M. C. Marchetti *et al.*, Hydrodynamics of soft active matter. *Rev. Mod. Phys.* **85**, 1143–1189 (2013). doi: [10.1103/RevModPhys.85.1143](https://doi.org/10.1103/RevModPhys.85.1143)
101. L. Di Michele, E. Eiser, Developments in understanding and controlling self assembly of DNA-functionalized colloids. *Phys. Chem. Chem. Phys.* **15**, 3115–3129 (2013). doi: [10.1039/c3cp43841d](https://doi.org/10.1039/c3cp43841d); pmid: [23340793](https://pubmed.ncbi.nlm.nih.gov/23340793/)
102. K.-T. Wu *et al.*, Polyamorous particles. *Proc. Natl. Acad. Sci. U.S.A.* **109**, 18731–18736 (2012). doi: [10.1073/pnas.1207356109](https://doi.org/10.1073/pnas.1207356109); pmid: [23100534](https://pubmed.ncbi.nlm.nih.gov/23100534/)
103. J. D. Forster *et al.*, Biomimetic isotropic nanostructures for structural coloration. *Adv. Mater.* **22**, 2939–2944 (2010). doi: [10.1002/adma.200903693](https://doi.org/10.1002/adma.200903693); pmid: [20414884](https://pubmed.ncbi.nlm.nih.gov/20414884/)
104. M. Florescu, S. Torquato, P. J. Steinhardt, Designer disordered materials with large, complete photonic band gaps. *Proc. Natl. Acad. Sci. U.S.A.* **106**, 20658–20663 (2009). doi: [10.1073/pnas.0907744106](https://doi.org/10.1073/pnas.0907744106); pmid: [19918087](https://pubmed.ncbi.nlm.nih.gov/19918087/)
105. T. L. Einstein, T. J. Stasevich, Epitaxial growth writ large. *Science* **327**, 423–424 (2010). doi: [10.1126/science.1184947](https://doi.org/10.1126/science.1184947); pmid: [20093465](https://pubmed.ncbi.nlm.nih.gov/20093465/)

ACKNOWLEDGMENTS

I thank P. Chaikin, D. Grier, D. Pine, M. Wyart, S. Glotzer, M. Holmes-Cerfon, J. Crocker, and P. Royall for helpful discussions. Research discussed from my own group is funded by the National Science Foundation through grant numbers DMR-1306410 and DMR-1420570.

10.1126/science.1253751

This copy is for your personal, non-commercial use only.

If you wish to distribute this article to others, you can order high-quality copies for your colleagues, clients, or customers by [clicking here](#).

Permission to republish or repurpose articles or portions of articles can be obtained by following the guidelines [here](#).

The following resources related to this article are available online at www.sciencemag.org (this information is current as of September 2, 2015):

Updated information and services, including high-resolution figures, can be found in the online version of this article at:

<http://www.sciencemag.org/content/349/6251/1253751.full.html>

This article **cites 98 articles**, 28 of which can be accessed free:

<http://www.sciencemag.org/content/349/6251/1253751.full.html#ref-list-1>

This article appears in the following **subject collections**:

Materials Science

http://www.sciencemag.org/cgi/collection/mat_sci

RESEARCH ARTICLE SUMMARY

PSYCHOLOGY

Estimating the reproducibility of psychological science

Open Science Collaboration*

INTRODUCTION: Reproducibility is a defining feature of science, but the extent to which it characterizes current research is unknown. Scientific claims should not gain credence because of the status or authority of their originator but by the replicability of their supporting evidence. Even research of exemplary quality may have irreproducible empirical findings because of random or systematic error.

RATIONALE: There is concern about the rate and predictors of reproducibility, but limited evidence. Potentially problematic practices include selective reporting, selective analysis, and insufficient specification of the conditions necessary or sufficient to obtain the results. Direct replication is the attempt to recreate the conditions believed sufficient for obtaining a pre-

viously observed finding and is the means of establishing reproducibility of a finding with new data. We conducted a large-scale, collaborative effort to obtain an initial estimate of the reproducibility of psychological science.

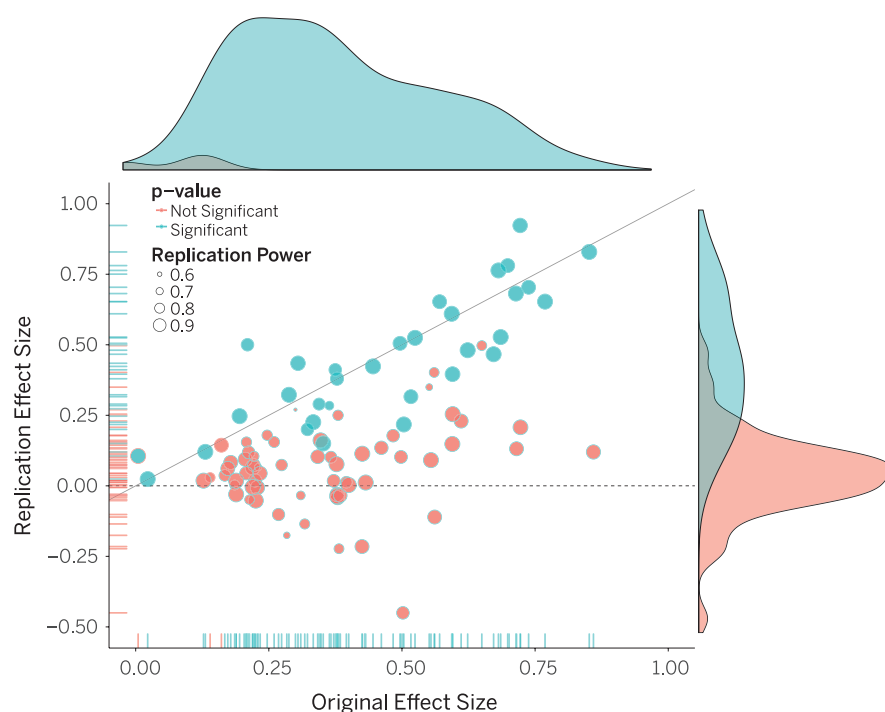
RESULTS: We conducted replications of 100 experimental and correlational studies published in three psychology journals using high-powered designs and original materials when available. There is no single standard for evaluating replication success. Here, we evaluated reproducibility using significance and *P* values, effect sizes, subjective assessments of replication teams, and meta-analysis of effect sizes. The mean effect size (*r*) of the replication effects ($M_r = 0.197$, $SD = 0.257$) was half the magnitude of the mean effect size of the original effects ($M_o = 0.403$, $SD = 0.188$), representing a

substantial decline. Ninety-seven percent of original studies had significant results ($P < .05$). Thirty-six percent of replications had significant results; 47% of original effect sizes were in the 95% confidence interval of the replication effect size; 39% of effects were subjectively rated to have replicated the original result; and if no bias in original results is assumed, combining original and replication results left 68% with statistically significant effects. Correlational tests suggest that replication success was better predicted by the strength of original evidence than by characteristics of the original and replication teams.

CONCLUSION: No single indicator sufficiently describes replication success, and the five indicators examined here are not the only ways to evaluate reproducibility. Nonetheless, collectively these results offer a clear conclusion: A large portion of replications produced weaker evidence for the original findings despite using materials provided by the original authors, review in advance for methodological fidelity, and high statistical power to detect the original effect sizes. Moreover, correlational evidence is consistent with the conclusion that variation in the strength of initial evidence (such as original *P* value) was more predictive of replication success than variation in the characteristics of the teams conducting the research (such as experience and expertise). The latter factors certainly can influence replication success, but they did not appear to do so here.

Reproducibility is not well understood because the incentives for individual scientists prioritize novelty over replication. Innovation is the engine of discovery and is vital for a productive, effective scientific enterprise. However, innovative ideas become old news fast. Journal reviewers and editors may dismiss a new test of a published idea as unoriginal. The claim that “we already know this” belies the uncertainty of scientific evidence. Innovation points out paths that are possible; replication points out paths that are likely; progress relies on both. Replication can increase certainty when findings are reproduced and promote innovation when they are not. This project provides accumulating evidence for many findings in psychological research and suggests that there is still more work to do to verify whether we know what we think we know. ■

The list of author affiliations is available in the full article online.
*Corresponding author. E-mail: nosek@virginia.edu
Cite this article as Open Science Collaboration, *Science* 349, aac4716 (2015). DOI: 10.1126/science.aac4716



Original study effect size versus replication effect size (correlation coefficients). Diagonal line represents replication effect size equal to original effect size. Dotted line represents replication effect size of 0. Points below the dotted line were effects in the opposite direction of the original. Density plots are separated by significant (blue) and nonsignificant (red) effects.

RESEARCH ARTICLE

PSYCHOLOGY

Estimating the reproducibility of psychological science

Open Science Collaboration*†

Reproducibility is a defining feature of science, but the extent to which it characterizes current research is unknown. We conducted replications of 100 experimental and correlational studies published in three psychology journals using high-powered designs and original materials when available. Replication effects were half the magnitude of original effects, representing a substantial decline. Ninety-seven percent of original studies had statistically significant results. Thirty-six percent of replications had statistically significant results; 47% of original effect sizes were in the 95% confidence interval of the replication effect size; 39% of effects were subjectively rated to have replicated the original result; and if no bias in original results is assumed, combining original and replication results left 68% with statistically significant effects. Correlational tests suggest that replication success was better predicted by the strength of original evidence than by characteristics of the original and replication teams.

Reproducibility is a core principle of scientific progress (1–6). Scientific claims should not gain credence because of the status or authority of their originator but by the replicability of their supporting evidence. Scientists attempt to transparently describe the methodology and resulting evidence used to support their claims. Other scientists agree or disagree whether the evidence supports the claims, citing theoretical or methodological reasons or by collecting new evidence. Such debates are meaningless, however, if the evidence being debated is not reproducible.

Even research of exemplary quality may have irreproducible empirical findings because of random or systematic error. Direct replication is the attempt to recreate the conditions believed sufficient for obtaining a previously observed finding (7, 8) and is the means of establishing reproducibility of a finding with new data. A direct replication may not obtain the original result for a variety of reasons: Known or unknown differences between the replication and original study may moderate the size of an observed effect, the original result could have been a false positive, or the replication could produce a false negative. False positives and false negatives provide misleading information about effects, and failure to identify the necessary and sufficient conditions to reproduce a finding indicates an incomplete theoretical understanding. Direct replication provides the opportunity to assess and improve reproducibility.

There is plenty of concern (9–13) about the rate and predictors of reproducibility but limited evidence. In a theoretical analysis, Ioannidis estimated that publishing and analytic practices make it likely that more than half of research

results are false and therefore irreproducible (9). Some empirical evidence supports this analysis. In cell biology, two industrial laboratories reported success replicating the original results of landmark findings in only 11 and 25% of the attempted cases, respectively (10, 11). These numbers are stunning but also difficult to interpret because no details are available about the studies, methodology, or results. With no transparency, the reasons for low reproducibility cannot be evaluated.

Other investigations point to practices and incentives that may inflate the likelihood of obtaining false-positive results in particular or irreproducible results more generally. Potentially problematic practices include selective reporting, selective analysis, and insufficient specification of the conditions necessary or sufficient to obtain the results (12–23). We were inspired to address the gap in direct empirical evidence about reproducibility. In this Research Article, we report a large-scale, collaborative effort to obtain an initial estimate of the reproducibility of psychological science.

Method

Starting in November 2011, we constructed a protocol for selecting and conducting high-quality replications (24). Collaborators joined the project, selected a study for replication from the available studies in the sampling frame, and were guided through the replication protocol. The replication protocol articulated the process of selecting the study and key effect from the available articles, contacting the original authors for study materials, preparing a study protocol and analysis plan, obtaining review of the protocol by the original authors and other members within the present project, registering the protocol publicly, conducting the replication, writing the final report, and auditing the process and analysis for quality control. Project coordinators

facilitated each step of the process and maintained the protocol and project resources. Replication materials and data were required to be archived publicly in order to maximize transparency, accountability, and reproducibility of the project (<https://osf.io/ezcuq>).

In total, 100 replications were completed by 270 contributing authors. There were many different research designs and analysis strategies in the original research. Through consultation with original authors, obtaining original materials, and internal review, replications maintained high fidelity to the original designs. Analyses converted results to a common effect size metric [correlation coefficient (r)] with confidence intervals (CIs). The units of analysis for inferences about reproducibility were the original and replication study effect sizes. The resulting open data set provides an initial estimate of the reproducibility of psychology and correlational data to support development of hypotheses about the causes of reproducibility.

Sampling frame and study selection

We constructed a sampling frame and selection process to minimize selection biases and maximize generalizability of the accumulated evidence. Simultaneously, to maintain high quality, within this sampling frame we matched individual replication projects with teams that had relevant interests and expertise. We pursued a quasi-random sample by defining the sampling frame as 2008 articles of three important psychology journals: *Psychological Science* (PSC), *Journal of Personality and Social Psychology* (JPSP), and *Journal of Experimental Psychology: Learning, Memory, and Cognition* (JEP: LMC). The first is a premier outlet for all psychological research; the second and third are leading disciplinary-specific journals for social psychology and cognitive psychology, respectively [more information is available in (24)]. These were selected a priori in order to (i) provide a tractable sampling frame that would not plausibly bias reproducibility estimates, (ii) enable comparisons across journal types and sub-disciplines, (iii) fit with the range of expertise available in the initial collaborative team, (iv) be recent enough to obtain original materials, (v) be old enough to obtain meaningful indicators of citation impact, and (vi) represent psychology sub-disciplines that have a high frequency of studies that are feasible to conduct at relatively low cost.

The first replication teams could select from a pool of the first 20 articles from each journal, starting with the first article published in the first 2008 issue. Project coordinators facilitated matching articles with replication teams by interests and expertise until the remaining articles were difficult to match. If there were still interested teams, then another 10 articles from one or more of the three journals were made available from the sampling frame. Further, project coordinators actively recruited teams from the community with relevant experience for particular articles. This approach balanced competing goals: minimizing selection bias by

*All authors with their affiliations appear at the end of this paper.

†Corresponding author. E-mail: nosek@virginia.edu

having only a small set of articles available at a time and matching studies with replication teams' interests, resources, and expertise.

By default, the last experiment reported in each article was the subject of replication. This decision established an objective standard for study selection within an article and was based on the intuition that the first study in a multiple-study article (the obvious alternative selection strategy) was more frequently a preliminary demonstration. Deviations from selecting the last experiment were made occasionally on the basis of feasibility or recommendations of the original authors. Justifications for deviations were reported in the replication reports, which were made available on the Open Science Framework (OSF) (<http://osf.io/ezcu1>). In total, 84 of the 100 completed replications (84%) were of the last reported study in the article. On average, the to-be-replicated articles contained 2.99 studies ($SD = 1.78$) with the following distribution: 24 single study, 24 two studies, 18 three studies, 13 four studies, 12 five studies, 9 six or more studies. All following summary statistics refer to the 100 completed replications.

For the purposes of aggregating results across studies to estimate reproducibility, a key result from the selected experiment was identified as the focus of replication. The key result had to be represented as a single statistical inference test or an effect size. In most cases, that test was a t test, F test, or correlation coefficient. This effect was identified before data collection or analysis and was presented to the original authors as part of the design protocol for critique. Original authors occasionally suggested that a different effect be used, and by default, replication teams deferred to original authors' judgments. Nonetheless, because the single effect came from a single study, it is not necessarily the case that the identified effect was central to the overall aims of the article. In the individual replication reports and subjective assessments of replication outcomes, more than a single result could be examined, but only the result of the single effect was considered in the aggregate analyses [additional details of the general protocol and individual study methods are provided in the supplementary materials and (25)].

In total, there were 488 articles in the 2008 issues of the three journals. One hundred fifty-eight of these (32%) became eligible for selection for replication during the project period, between November 2011 and December 2014. From those, 111 articles (70%) were selected by a replication team, producing 113 replications. Two articles had two replications each (supplementary materials). And 100 of those (88%) replications were completed by the project deadline for inclusion in this aggregate report. After being claimed, some studies were not completed because the replication teams ran out of time or could not devote sufficient resources to completing the study. By journal, replications were completed for 39 of 64 (61%) articles from *PSCI*, 31 of 55 (56%) articles from *JPSP*, and 28 of 39 (72%) articles from *JEP:LMC*.

The most common reasons for failure to match an article with a team were feasibility constraints for conducting the research. Of the 47 articles from the eligible pool that were not claimed, six (13%) had been deemed infeasible to replicate because of time, resources, instrumentation, dependence on historical events, or hard-to-access samples. The remaining 41 (87%) were eligible but not claimed. These often required specialized samples (such as macaques or people with autism), resources (such as eye tracking machines or functional magnetic resonance imaging), or knowledge making them difficult to match with teams.

Aggregate data preparation

Each replication team conducted the study, analyzed their data, wrote their summary report, and completed a checklist of requirements for sharing the materials and data. Then, independent reviewers and analysts conducted a project-wide audit of all individual projects, materials, data, and reports. A description of this review is available on the OSF (<https://osf.io/xtine>). Moreover, to maximize reproducibility and accuracy, the analyses for every replication study were reproduced by another analyst independent of the replication team using the R statistical programming language and a standardized analytic format. A controller R script was created to regenerate the entire analysis of every study and recreate the master data file. This R script, available at <https://osf.io/fkmwg>, can be executed to reproduce the results of the individual studies. A comprehensive description of this reanalysis process is available publicly (<https://osf.io/a2eyg>).

Measures and moderators

We assessed features of the original study and replication as possible correlates of reproducibility and conducted exploratory analyses to inspire further investigation. These included characteristics of the original study such as the publishing journal; original effect size, P value, and sample size; experience and expertise of the original research team; importance of the effect, with indicators such as the citation impact of the article; and rated surprisingness of the effect. We also assessed characteristics of the replication such as statistical power and sample size, experience and expertise of the replication team, independently assessed challenge of conducting an effective replication, and self-assessed quality of the replication effort. Variables such as the P value indicate the statistical strength of evidence given the null hypothesis, and variables such as "effect surprisingness" and "expertise of the team" indicate qualities of the topic of study and the teams studying it, respectively. The master data file, containing these and other variables, is available for exploratory analysis (<https://osf.io/5wup8>).

It is possible to derive a variety of hypotheses about predictors of reproducibility. To reduce the likelihood of false positives due to many tests, we aggregated some variables into summary indicators: experience and expertise of original team, experience and expertise of replication team, challenge of replication, self-assessed quality of repli-

cation, and importance of the effect. We had no a priori justification to give some indicators stronger weighting over others, so aggregates were created by standardizing [mean (M) = 0, $SD = 1$] the individual variables and then averaging to create a single index. In addition to the publishing journal and subdiscipline, potential moderators included six characteristics of the original study and five characteristics of the replication (supplementary materials).

Publishing journal and subdiscipline

Journals' different publishing practices may result in a selection bias that covaries with reproducibility. Articles from three journals were made available for selection: *JPSP* ($n = 59$ articles), *JEP:LMC* ($n = 40$ articles), and *PSCI* ($n = 68$ articles). From this pool of available studies, replications were selected and completed from *JPSP* ($n = 32$ studies), *JEP:LMC* ($n = 28$ studies), and *PSCI* ($n = 40$ studies) and were coded as representing cognitive ($n = 43$ studies) or social-personality ($n = 57$ studies) subdisciplines. Four studies that would ordinarily be understood as "developmental psychology" because of studying children or infants were coded as having a cognitive or social emphasis. Reproducibility may vary by subdiscipline in psychology because of differing practices. For example, within-subjects designs are more common in cognitive than social psychology, and these designs often have greater power to detect effects with the same number of participants.

Statistical analyses

There is no single standard for evaluating replication success (25). We evaluated reproducibility using significance and P values, effect sizes, subjective assessments of replication teams, and meta-analyses of effect sizes. All five of these indicators contribute information about the relations between the replication and original finding and the cumulative evidence about the effect and were positively correlated with one another (r ranged from 0.22 to 0.96, median $r = 0.57$). Results are summarized in Table 1, and full details of analyses are in the supplementary materials.

Significance and P values

Assuming a two-tailed test and significance or α level of 0.05, all test results of original and replication studies were classified as statistically significant ($P \leq 0.05$) and nonsignificant ($P > 0.05$). However, original studies that interpreted nonsignificant P values as significant were coded as significant (four cases, all with P values < 0.06). Using only the nonsignificant P values of the replication studies and applying Fisher's method (26), we tested the hypothesis that these studies had "no evidential value" (the null hypothesis of zero-effect holds for all these studies). We tested the hypothesis that the proportions of statistically significant results in the original and replication studies are equal using the McNemar test for paired nominal data and calculated a CI of the reproducibility parameter. Second, we compared the central tendency of the distribution of P values of original and

Table 1. Summary of reproducibility rates and effect sizes for original and replication studies overall and by journal/discipline. *df/N* refers to the information on which the test of the effect was based (for example, *df* of *t* test, denominator *df* of *F* test, sample size –3 of correlation, and sample size for *z* and χ^2). Four original results had *P* values slightly higher than 0.05 but were considered positive results in the original article and are treated that way here. Exclusions (explanation provided in supplementary materials, A3) are “replications $P < 0.05$ ” (3 original nulls excluded; *n* = 97 studies); “mean original and replication effect sizes” (3 excluded; *n* = 97 studies); “meta-analytic mean estimates” (27 excluded; *n* = 73 studies); “percent meta-analytic ($P < 0.05$)” (25 excluded; *n* = 75 studies); and, “percent original effect size within replication 95% CI” (5 excluded, *n* = 95 studies).

	Effect size comparison						Original and replication combined				
	Replications <i>P</i> < 0.05 in original direction	Percent	Mean (SD) original effect size	Median original <i>df/N</i>	Mean (SD) replication effect size	Median replication <i>df/N</i>	Average replication power	Meta- analytic mean (SD) estimate	Percent meta- analytic (<i>P</i> < 0.05)	Percent original effect size within replication 95% CI	Percent subjective “yes” to “Did it replicate?”
Overall	35/97	36	0.403 (0.188)	54	0.197 (0.257)	68	0.92	0.309 (0.223)	68	47	39
<i>JPSP</i> , social	7/31	23	0.29 (0.10)	73	0.07 (0.11)	120	0.91	0.138 (0.087)	43	34	25
<i>JEP:LMC</i> , cognitive	13/27	48	0.47 (0.18)	36.5	0.27 (0.24)	43	0.93	0.393 (0.209)	86	62	54
<i>PSCI</i> , social	7/24	29	0.39 (0.20)	76	0.21 (0.30)	122	0.92	0.286 (0.228)	58	40	32
<i>PSCI</i> , cognitive	8/15	53	0.53 (0.2)	23	0.29 (0.35)	21	0.94	0.464 (0.221)	92	60	53

Table 2. Spearman’s rank-order correlations of reproducibility indicators with summary original and replication study characteristics. Effect size difference computed after converting *r* to Fisher’s *z*. *df/N* refers to the information on which the test of the effect was based (for example, *df* of *t* test, denominator *df* of *F* test, sample size –3 of correlation, and sample size for *z* and χ^2). Four original results had *P* values slightly higher than 0.05 but were considered positive results in the original article and are treated that way here. Exclusions (explanation provided in supplementary materials, A3) are “replications $P < .05$ ” (3 original nulls excluded; *n* = 97 studies), “effect size difference” (3 excluded; *n* = 97 studies); “meta-analytic mean estimates” (27 excluded; *n* = 73 studies); and, “percent original effect size within replication 95% CI” (5 excluded, *n* = 95 studies).

	Replications <i>P</i> < 0.05 in original direction	Effect size difference	Meta-analytic estimate	Original effect size within replication 95% CI	Subjective “yes” to “Did it replicate?”
Original study characteristics					
Original <i>P</i> value	–0.327	–0.057	–0.468	0.032	–0.260
Original effect size	0.304	0.279	0.793	0.121	0.277
Original <i>df/N</i>	–0.150	–0.194	–0.502	–0.221	–0.185
Importance of original result	–0.105	0.038	–0.205	–0.133	–0.074
Surprising original result	–0.244	0.102	–0.181	–0.113	–0.241
Experience and expertise of original team	–0.072	–0.033	–0.059	–0.103	–0.044
Replication characteristics					
Replication <i>P</i> value	–0.828	0.621	–0.614	–0.562	–0.738
Replication effect size	0.731	–0.586	0.850	0.611	0.710
Replication power	0.368	–0.053	0.142	–0.056	0.285
Replication <i>df/N</i>	–0.085	–0.224	–0.692	–0.257	–0.164
Challenge of conducting replication	–0.219	0.085	–0.301	–0.109	–0.151
Experience and expertise of replication team	–0.096	0.133	0.017	–0.053	–0.068
Self-assessed quality of replication	–0.069	0.017	0.054	–0.088	–0.055

replication studies using the Wilcoxon signed-rank test and the *t* test for dependent samples. For both tests, we only used study-pairs for which both *P* values were available.

Effect sizes

We transformed effect sizes into correlation coefficients whenever possible. Correlation coefficients have several advantages over other effect size measures, such as Cohen’s *d*. Correlation coefficients are bounded, well known, and therefore more readily interpretable. Most important for our purposes, analysis of correlation coefficients is straightforward because, after ap-

plying the Fisher transformation, their standard error is only a function of sample size. Formulas and code for converting test statistics *z*, *F*, *t*, and χ^2 into correlation coefficients are provided in the appendices at <http://osf.io/ezum7>. To be able to compare and analyze correlations across study-pairs, the original study’s effect size was coded as positive; the replication study’s effect size was coded as negative if the replication study’s effect was opposite to that of the original study.

We compared effect sizes using four tests. We compared the central tendency of the effect size distributions of original and replication studies using both a paired two-sample *t* test and the

Wilcoxon signed-rank test. Third, we computed the proportion of study-pairs in which the effect of the original study was stronger than in the replication study and tested the hypothesis that this proportion is 0.5. For this test, we included findings for which effect size measures were available but no correlation coefficient could be computed (for example, if a regression coefficient was reported but not its test statistic). Fourth, we calculated “coverage,” or the proportion of study-pairs in which the effect of the original study was in the CI of the effect of the replication study, and compared this with the expected proportion using a goodness-of-fit χ^2 test. We carried

out this test on the subset of study pairs in which both the correlation coefficient and its standard error could be computed [we refer to this data set as the meta-analytic (MA) subset]. Standard errors could only be computed if test statistics were r , t , or $F(1, df_2)$. The expected proportion is the sum over expected probabilities across study-pairs. The test assumes the same population effect size for original and replication study in the same study-pair. For those studies that tested the effect with $F(df_1 > 1, df_2)$ or χ^2 , we verified coverage using other statistical procedures (computational details are provided in the supplementary materials).

Meta-analysis combining original and replication effects

We conducted fixed-effect meta-analyses using the R package metafor (27) on Fisher-transformed correlations for all study-pairs in subset MA and on study-pairs with the odds ratio as the dependent variable. The number of times the CI of all these meta-analyses contained 0 was calculated. For studies in the MA subset, estimated effect sizes were averaged and analyzed by discipline.

Subjective assessment of “Did it replicate?”

In addition to the quantitative assessments of replication and effect estimation, we collected subjective assessments of whether the replication provided evidence of replicating the original result. In some cases, the quantitative data anticipate a straightforward subjective assessment of replication. For more complex designs, such as multivariate interaction effects, the quantitative analysis may not provide a simple interpretation. For subjective assessment, replication teams answered “yes” or “no” to the question, “Did your results replicate the original effect?” Additional subjective variables are available for analysis in the full data set.

Analysis of moderators

We correlated the five indicators evaluating reproducibility with six indicators of the origi-

nal study (original P value, original effect size, original sample size, importance of the effect, surprising effect, and experience and expertise of original team) and seven indicators of the replication study (replication P value, replication effect size, replication power based on original effect size, replication sample size, challenge of conducting replication, experience and expertise of replication team, and self-assessed quality of replication) (Table 2). As follow-up, we did the same with the individual indicators comprising the moderator variables (tables S3 and S4).

Results

Evaluating replication effect against null hypothesis of no effect

A straightforward method for evaluating replication is to test whether the replication shows a statistically significant effect ($P < 0.05$) with the same direction as the original study. This dichotomous vote-counting method is intuitively appealing and consistent with common heuristics used to decide whether original studies “worked.” Ninety-seven of 100 (97%) effects from original studies were positive results (four had P values falling a bit short of the 0.05 criterion— $P = 0.0508, 0.0514, 0.0516$, and 0.0567 —but all of these were interpreted as positive effects). On the basis of only the average replication power of the 97 original, significant effects [$M = 0.92$, median (Mdn) = 0.95], we would expect approximately 89 positive results in the replications if all original effects were true and accurately estimated; however, there were just 35 [36.1%; 95% CI = (26.6%, 46.2%)], a significant reduction [McNemar test, $\chi^2(1) = 59.1, P < 0.001$].

A key weakness of this method is that it treats the 0.05 threshold as a bright-line criterion between replication success and failure (28). It could be that many of the replications fell just short of the 0.05 criterion. The density plots of P values for original studies (mean P value = 0.028) and replications (mean P value = 0.302) are shown in Fig. 1, left. The 64 nonsignificant

P values for replications were distributed widely. When there is no effect to detect, the null distribution of P values is uniform. This distribution deviated slightly from uniform with positive skew, however, suggesting that at least one replication could be a false negative, $\chi^2(128) = 155.83, P = 0.048$. Nonetheless, the wide distribution of P values suggests against insufficient power as the only explanation for failures to replicate. A scatterplot of original compared with replication study P values is shown in Fig. 2.

Evaluating replication effect against original effect size

A complementary method for evaluating replication is to test whether the original effect size is within the 95% CI of the effect size estimate from the replication. For the subset of 73 studies in which the standard error of the correlation could be computed, 30 (41.1%) of the replication CIs contained the original effect size (significantly lower than the expected value of 78.5%, $P < 0.001$) (supplementary materials). For 22 studies using other test statistics [$F(df_1 > 1, df_2)$ and χ^2], 68.2% of CIs contained the effect size of the original study. Overall, this analysis suggests a 47.4% replication success rate.

This method addresses the weakness of the first test that a replication in the same direction and a P value of 0.06 may not be significantly different from the original result. However, the method will also indicate that a replication “fails” when the direction of the effect is the same but the replication effect size is significantly smaller than the original effect size (29). Also, the replication “succeeds” when the result is near zero but not estimated with sufficiently high precision to be distinguished from the original effect size.

Comparing original and replication effect sizes

Comparing the magnitude of the original and replication effect sizes avoids special emphasis on P values. Overall, original study effect sizes

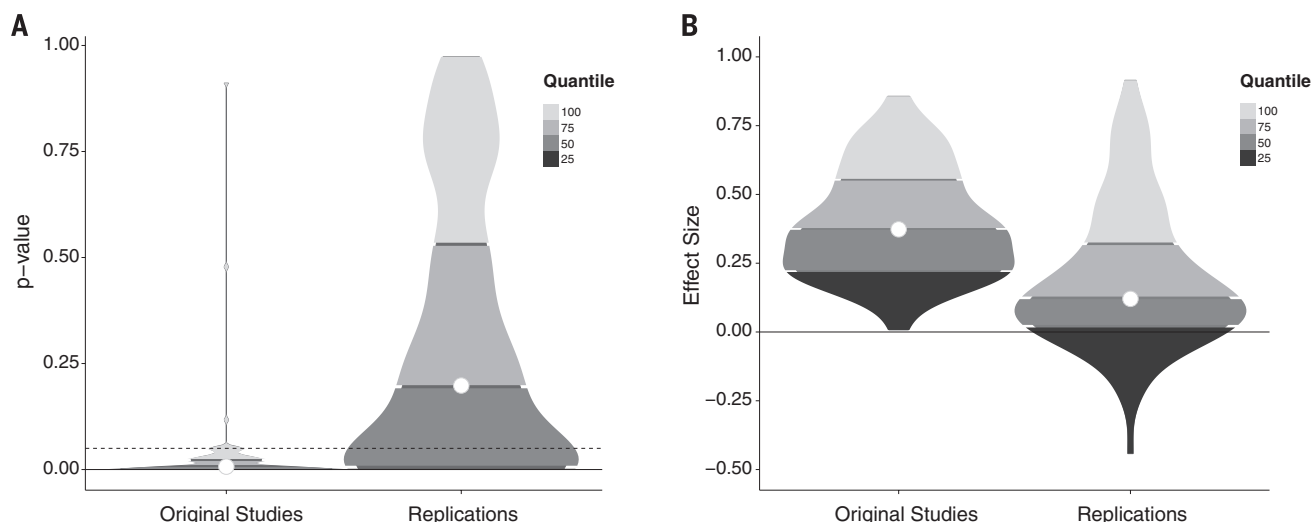


Fig. 1. Density plots of original and replication P values and effect sizes. (A) P values. (B) Effect sizes (correlation coefficients). Lowest quantiles of P values are not visible because they are clustered near zero.

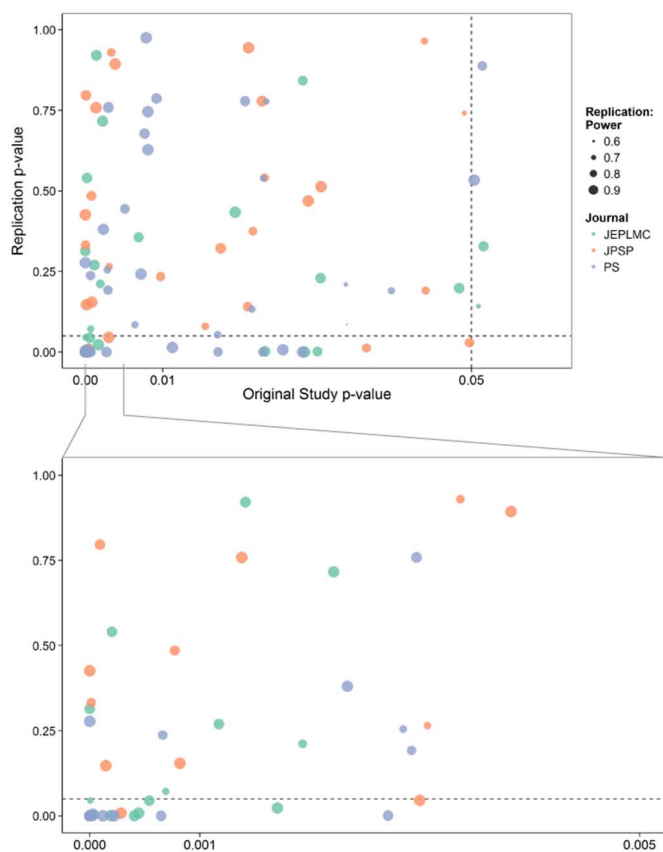


Fig. 2. Scatterplots of original study and replication P values for three psychology journals.

Data points scaled by power of the replication based on original study effect size. Dotted red lines indicate $P = 0.05$ criterion. Subplot below shows P values from the range between the gray lines ($P = 0$ to 0.005) in the main plot above.

($M = 0.403$, $SD = 0.188$) were reliably larger than replication effect sizes ($M = 0.197$, $SD = 0.257$), Wilcoxon's $W = 7137$, $P < 0.001$. Of the 99 studies for which an effect size in both the original and replication study could be calculated (30), 82 showed a stronger effect size in the original study (82.8%; $P < 0.001$, binomial test) (Fig. 1, right). Original and replication effect sizes were positively correlated (Spearman's $r = 0.51$, $P < 0.001$). A scatterplot of the original and replication effect sizes is presented in Fig. 3.

Combining original and replication effect sizes for cumulative evidence

The disadvantage of the descriptive comparison of effect sizes is that it does not provide information about the precision of either estimate or resolution of the cumulative evidence for the effect. This is often addressed by computing a meta-analytic estimate of the effect sizes by combining the original and replication studies (28). This approach weights each study by the inverse of its variance and uses these weighted estimates of effect size to estimate cumulative evidence and precision of the effect. Using a fixed-effect model, 51 of the 75 (68%) effects for which a meta-analytic estimate could be computed had 95% CIs that did not include 0.

One qualification about this result is the possibility that the original studies have inflated effect sizes due to publication, selection, reporting, or other biases (9, 12–23). In a discipline with low-powered research designs and an emphasis on positive results for publication, effect sizes will be systematically overestimated in the published literature. There is no publication bias in the replication studies because all results are reported. Also, there are no selection or reporting biases because all were confirmatory tests based on pre-analysis plans. This maximizes the interpretability of the replication P values and effect estimates. If publication, selection, and reporting biases completely explain the effect differences, then the replication estimates would be a better estimate of the effect size than would the meta-analytic and original results. However, to the extent that there are other influences, such as moderation by sample, setting, or quality of replication, the relative bias influencing original and replication effect size estimation is unknown.

Subjective assessment of “Did it replicate?”

In addition to the quantitative assessments of replication and effect estimation, replication teams

provided a subjective assessment of replication success of the study they conducted. Subjective assessments of replication success were very similar to significance testing results (39 of 100 successful replications), including evaluating “success” for two null replications when the original study reported a null result and “failure” for a $P < 0.05$ replication when the original result was a null.

Correlates of reproducibility

The overall replication evidence is summarized in Table 1 across the criteria described above and then separately by journal/discipline. Considering significance testing, reproducibility was stronger in studies and journals representing cognitive psychology than social psychology topics. For example, combining across journals, 14 of 55 (25%) of social psychology effects replicated by the $P < 0.05$ criterion, whereas 21 of 42 (50%) of cognitive psychology effects did so. Simultaneously, all journals and disciplines showed substantial and similar [$\chi^2(3) = 2.45$, $P = 0.48$] declines in effect size in the replications compared with the original studies. The difference in significance testing results between fields appears to be partly a function of weaker original effects in social psychology studies, particularly in *JPSP*, and perhaps of the greater frequency of high-powered within-subjects manipulations and repeated measurement designs in cognitive psychology as suggested by high power despite relatively small participant samples. Further, the type of test was associated with replication success. Among original, significant effects, 23 of the 49 (47%) that tested main or simple effects replicated at $P < 0.05$, but just 8 of the 37 (22%) that tested interaction effects did.

Correlations between reproducibility indicators and characteristics of replication and original studies are provided in Table 2. A negative correlation of replication success with the original study P value indicates that the initial strength of evidence is predictive of reproducibility. For example, 26 of 63 (41%) original studies with $P < 0.02$ achieved $P < 0.05$ in the replication, whereas 6 of 23 (26%) that had a P value between $0.02 < P < 0.04$ and 2 of 11 (18%) that had a P value > 0.04 did so (Fig. 2). Almost two thirds (20 of 32, 63%) of original studies with $P < 0.001$ had a significant P value in the replication.

Larger original effect sizes were associated with greater likelihood of achieving $P < 0.05$ ($r = 0.304$) and a greater effect size difference between original and replication ($r = 0.279$). Moreover, replication power was related to replication success via significance testing ($r = 0.368$) but not with the effect size difference between original and replication ($r = -0.053$). Comparing effect sizes across indicators, surprisingness of the original effect, and the challenge of conducting the replication were related to replication success for some indicators. Surprising effects were less reproducible, as were effects for which it was more challenging to conduct the replication. Last, there was little evidence that perceived importance of the effect, expertise of the original or replication teams, or self-assessed quality of the replication accounted for meaningful variation

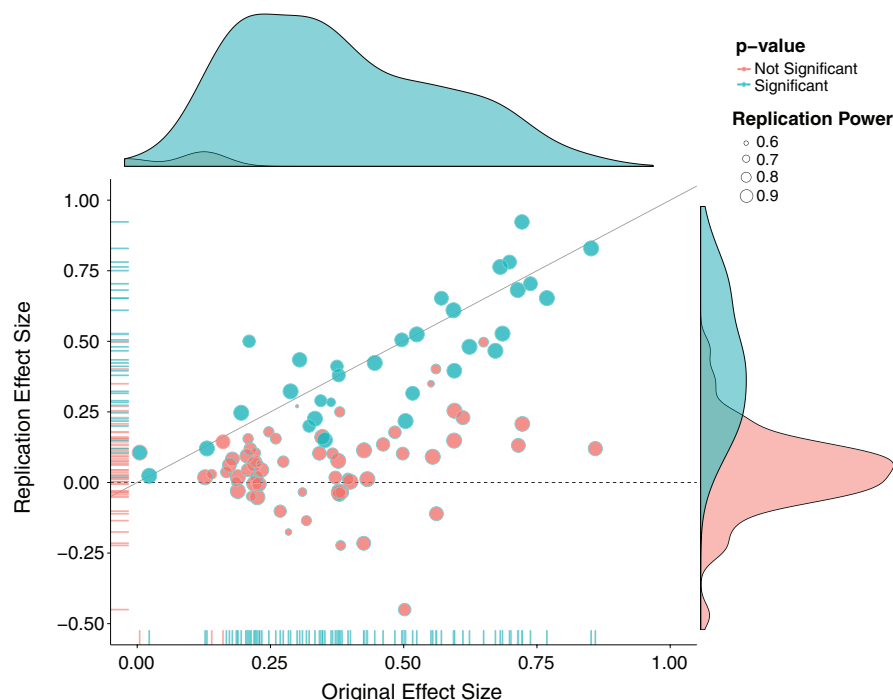


Fig. 3. Original study effect size versus replication effect size (correlation coefficients). Diagonal line represents replication effect size equal to original effect size. Dotted line represents replication effect size of 0. Points below the dotted line were effects in the opposite direction of the original. Density plots are separated by significant (blue) and nonsignificant (red) effects.

in reproducibility across indicators. Replication success was more consistently related to the original strength of evidence (such as original *P* value, effect size, and effect tested) than to characteristics of the teams and implementation of the replication (such as expertise, quality, or challenge of conducting study) (tables S3 and S4).

Discussion

No single indicator sufficiently describes replication success, and the five indicators examined here are not the only ways to evaluate reproducibility. Nonetheless, collectively, these results offer a clear conclusion: A large portion of replications produced weaker evidence for the original findings (31) despite using materials provided by the original authors, review in advance for methodological fidelity, and high statistical power to detect the original effect sizes. Moreover, correlational evidence is consistent with the conclusion that variation in the strength of initial evidence (such as original *P* value) was more predictive of replication success than was variation in the characteristics of the teams conducting the research (such as experience and expertise). The latter factors certainly can influence replication success, but the evidence is that they did not systematically do so here. Other investigators may develop alternative indicators to explore further the role of expertise and quality in reproducibility on this open data set.

Insights on reproducibility

It is too easy to conclude that successful replication means that the theoretical understanding of

the original finding is correct. Direct replication mainly provides evidence for the reliability of a result. If there are alternative explanations for the original finding, those alternatives could likewise account for the replication. Understanding is achieved through multiple, diverse investigations that provide converging support for a theoretical interpretation and rule out alternative explanations.

It is also too easy to conclude that a failure to replicate a result means that the original evidence was a false positive. Replications can fail if the replication methodology differs from the original in ways that interfere with observing the effect. We conducted replications designed to minimize a priori reasons to expect a different result by using original materials, engaging original authors for review of the designs, and conducting internal reviews. Nonetheless, unanticipated factors in the sample, setting, or procedure could still have altered the observed effect magnitudes (32).

More generally, there are indications of cultural practices in scientific communication that may be responsible for the observed results. Low-power research designs combined with publication bias favoring positive results together produce a literature with upwardly biased effect sizes (14, 16, 33, 34). This anticipates that replication effect sizes would be smaller than original studies on a routine basis—not because of differences in implementation but because the original study effect sizes are affected by publication and reporting bias, and the replications are not. Consistent with this expectation, most replication effects were

smaller than original results, and reproducibility success was correlated with indicators of the strength of initial evidence, such as lower original *P* values and larger effect sizes. This suggests publication, selection, and reporting biases as plausible explanations for the difference between original and replication effects. The replication studies significantly reduced these biases because replication preregistration and pre-analysis plans ensured confirmatory tests and reporting of all results.

The observed variation in replication and original results may reduce certainty about the statistical inferences from the original studies but also provides an opportunity for theoretical innovation to explain differing outcomes, and then new research to test those hypothesized explanations. The correlational evidence, for example, suggests that procedures that are more challenging to execute may result in less reproducible results, and that more surprising original effects may be less reproducible than less surprising original effects. Further, systematic, repeated replication efforts that fail to identify conditions under which the original finding can be observed reliably may reduce confidence in the original finding.

Implications and limitations

The present study provides the first open, systematic evidence of reproducibility from a sample of studies in psychology. We sought to maximize generalizability of the results with a structured process for selecting studies for replication. However, it is unknown the extent to which these findings extend to the rest of psychology or other disciplines. In the sampling frame itself, not all articles were replicated; in each article, only one study was replicated; and in each study, only one statistical result was subject to replication. More resource-intensive studies were less likely to be included than were less resource-intensive studies. Although study selection bias was reduced by the sampling frame and selection strategy, the impact of selection bias is unknown.

We investigated the reproducibility rate of psychology not because there is something special about psychology, but because it is our discipline. Concerns about reproducibility are widespread across disciplines (9–21). Reproducibility is not well understood because the incentives for individual scientists prioritize novelty over replication (20). If nothing else, this project demonstrates that it is possible to conduct a large-scale examination of reproducibility despite the incentive barriers. Here, we conducted single-replication attempts of many effects obtaining broad-and-shallow evidence. These data provide information about reproducibility in general but little precision about individual effects in particular. A complementary narrow-and-deep approach is characterized by the Many Labs replication projects (32). In those, many replications of single effects allow precise estimates of effect size but result in generalizability that is circumscribed to those individual effects. Pursuing both strategies across disciplines, such as the ongoing effort in cancer biology (35), would yield insight about common and distinct

challenges and may cross-fertilize strategies so as to improve reproducibility.

Because reproducibility is a hallmark of credible scientific evidence, it is tempting to think that maximum reproducibility of original results is important from the onset of a line of inquiry through its maturation. This is a mistake. If initial ideas were always correct, then there would hardly be a reason to conduct research in the first place. A healthy discipline will have many false starts as it confronts the limits of present understanding.

Innovation is the engine of discovery and is vital for a productive, effective scientific enterprise. However, innovative ideas become old news fast. Journal reviewers and editors may dismiss a new test of a published idea as unoriginal. The claim that “we already know this” belies the uncertainty of scientific evidence. Deciding the ideal balance of resourcing innovation versus verification is a question of research efficiency. How can we maximize the rate of research progress? Innovation points out paths that are possible; replication points out paths that are likely; progress relies on both. The ideal balance is a topic for investigation itself. Scientific incentives—funding, publication, or awards—can be tuned to encourage an optimal balance in the collective effort of discovery (36, 37).

Progress occurs when existing expectations are violated and a surprising result spurs a new investigation. Replication can increase certainty when findings are reproduced and promote innovation when they are not. This project provides accumulating evidence for many findings in psychological research and suggests that there is still more work to do to verify whether we know what we think we know.

Conclusion

After this intensive effort to reproduce a sample of published psychological findings, how many of the effects have we established are true? Zero. And how many of the effects have we established are false? Zero. Is this a limitation of the project design? No. It is the reality of doing science, even if it is not appreciated in daily practice. Humans desire certainty, and science infrequently provides it. As much as we might wish it to be otherwise, a single study almost never provides definitive resolution for or against an effect and its explanation. The original studies examined here offered tentative evidence; the replications we conducted offered additional, confirmatory evidence. In some cases, the replications increase confidence in the reliability of the original results; in other cases, the replications suggest that more investigation is needed to establish the validity of the original findings. Scientific progress is a cumulative process of uncertainty reduction that can only succeed if science itself remains the greatest skeptic of its explanatory claims.

The present results suggest that there is room to improve reproducibility in psychology. Any temptation to interpret these results as a defeat for psychology, or science more generally, must contend with the fact that this project demon-

strates science behaving as it should. Hypotheses abound that the present culture in science may be negatively affecting the reproducibility of findings. An ideological response would discount the arguments, discredit the sources, and proceed merrily along. The scientific process is not ideological. Science does not always provide comfort for what we wish to be; it confronts us with what is. Moreover, as illustrated by the Transparency and Openness Promotion (TOP) Guidelines (<http://cos.io/top>) (37), the research community is taking action already to improve the quality and credibility of the scientific literature.

We conducted this project because we care deeply about the health of our discipline and believe in its promise for accumulating knowledge about human behavior that can advance the quality of the human condition. Reproducibility is central to that aim. Accumulating evidence is the scientific community's method of self-correction and is the best available option for achieving that ultimate goal: truth.

REFERENCES AND NOTES

- C. Hempel, Maximal specificity and lawlikeness in probabilistic explanation. *Philos. Sci.* **35**, 116–133 (1968). doi: [10.1086/288197](https://doi.org/10.1086/288197)
- C. Hempel, P. Oppenheim, Studies in the logic of explanation. *Philos. Sci.* **15**, 135–175 (1948). doi: [10.1086/286983](https://doi.org/10.1086/286983)
- I. Lakatos, in *Criticism and the Growth of Knowledge*, I. Lakatos, A. Musgrave, Eds. (Cambridge Univ. Press, London, 1970), pp. 170–196.
- P. E. Meehl, Appraising and amending theories: The strategy of Lakatosian defense and two principles that warrant it. *Psychol. Inq.* **1**, 108–141 (1990). doi: [10.1207/s15327965pli0102_1](https://doi.org/10.1207/s15327965pli0102_1)
- J. R. Platt, Strong Inference: Certain systematic methods of scientific thinking may produce much more rapid progress than others. *Science* **146**, 347–353 (1964). doi: [10.1126/science.146.3642.347](https://doi.org/10.1126/science.146.3642.347); pmid: [17739513](https://pubmed.ncbi.nlm.nih.gov/17739513/)
- W. C. Salmon, in *Introduction to the Philosophy of Science*, M. H. Salmon Ed. (Hackett Publishing Company, Indianapolis, 1999), pp. 7–41.
- B. A. Nosek, D. Lakens, Registered reports: A method to increase the credibility of published results. *Soc. Psychol.* **45**, 137–141 (2014). doi: [10.1027/1864-9335/a000192](https://doi.org/10.1027/1864-9335/a000192)
- S. Schmidt, Shall we really do it again? The powerful concept of replication is neglected in the social sciences. *Rev. Gen. Psychol.* **13**, 90–100 (2009). doi: [10.1037/a0015108](https://doi.org/10.1037/a0015108)
- J. P. A. Ioannidis, Why most published research findings are false. *PLoS Med.* **2**, e124 (2005). doi: [10.1371/journal.pmed.0020124](https://doi.org/10.1371/journal.pmed.0020124); pmid: [16060722](https://pubmed.ncbi.nlm.nih.gov/16060722/)
- C. G. Begley, L. M. Ellis, Drug development: Raise standards for preclinical cancer research. *Nature* **483**, 531–533 (2012). doi: [10.1038/483531a](https://doi.org/10.1038/483531a); pmid: [22460880](https://pubmed.ncbi.nlm.nih.gov/22460880/)
- F. Prinz, T. Schlange, K. Asadullah, Believe it or not: How much can we rely on published data on potential drug targets? *Nat. Rev. Drug Discov.* **10**, 712–713 (2011). doi: [10.1038/nrd3439-cl](https://doi.org/10.1038/nrd3439-cl); pmid: [21892149](https://pubmed.ncbi.nlm.nih.gov/21892149/)
- M. McNutt, Reproducibility. *Science* **343**, 229 (2014). doi: [10.1126/science.1250475](https://doi.org/10.1126/science.1250475); pmid: [24436391](https://pubmed.ncbi.nlm.nih.gov/24436391/)
- H. Pashler, E.-J. Wagenmakers, Editors' introduction to the special section on replicability in psychological science: A crisis of confidence? *Perspect. Psychol. Sci.* **7**, 528–530 (2012). doi: [10.1177/1745691612465253](https://doi.org/10.1177/1745691612465253); pmid: [26168108](https://pubmed.ncbi.nlm.nih.gov/26168108/)
- K. S. Button *et al.*, Power failure: Why small sample size undermines the reliability of neuroscience. *Nat. Rev. Neurosci.* **14**, 365–376 (2013). doi: [10.1038/nrn3475](https://doi.org/10.1038/nrn3475); pmid: [23571845](https://pubmed.ncbi.nlm.nih.gov/23571845/)
- D. Fanelli, “Positive” results increase down the hierarchy of the sciences. *PLOS ONE* **5**, e10068 (2010). doi: [10.1371/journal.pone.0010068](https://doi.org/10.1371/journal.pone.0010068); pmid: [20383332](https://pubmed.ncbi.nlm.nih.gov/20383332/)
- A. G. Greenwald, Consequences of prejudice against the null hypothesis. *Psychol. Bull.* **82**, 1–20 (1975). doi: [10.1037/h0076157](https://doi.org/10.1037/h0076157)
- G. S. Howard *et al.*, Do research literatures give correct answers? *Rev. Gen. Psychol.* **13**, 116–121 (2009). doi: [10.1037/a0015468](https://doi.org/10.1037/a0015468)
- J. P. A. Ioannidis, M. R. Munaf, P. Fusar-Poli, B. A. Nosek, S. P. David, Publication and other reporting biases in cognitive sciences: Detection, prevalence, and prevention. *Trends Cogn. Sci.* **18**, 235–241 (2014). doi: [10.1016/j.tics.2014.02.010](https://doi.org/10.1016/j.tics.2014.02.010); pmid: [24656991](https://pubmed.ncbi.nlm.nih.gov/24656991/)
- L. K. John, G. Loewenstein, D. Prelec, Measuring the prevalence of questionable research practices with incentives for truth telling. *Psychol. Sci.* **23**, 524–532 (2012). doi: [10.1177/0956797611430953](https://doi.org/10.1177/0956797611430953); pmid: [22508865](https://pubmed.ncbi.nlm.nih.gov/22508865/)
- B. A. Nosek, J. R. Spies, M. Motyl, Scientific utopia: II. Restructuring incentives and practices to promote truth over publishability. *Perspect. Psychol. Sci.* **7**, 615–631 (2012). doi: [10.1177/1745691612459058](https://doi.org/10.1177/1745691612459058); pmid: [26168121](https://pubmed.ncbi.nlm.nih.gov/26168121/)
- R. Rosenthal, The file drawer problem and tolerance for null results. *Psychol. Bull.* **86**, 638–641 (1979). doi: [10.1037/0033-2909.86.3.638](https://doi.org/10.1037/0033-2909.86.3.638)
- P. Rozin, What kind of empirical research should we publish, fund, and reward?: A different perspective. *Perspect. Psychol. Sci.* **4**, 435–439 (2009). doi: [10.1111/j.1745-6924.2009.01151.x](https://doi.org/10.1111/j.1745-6924.2009.01151.x); pmid: [26158991](https://pubmed.ncbi.nlm.nih.gov/26158991/)
- J. P. Simmons, L. D. Nelson, U. Simonsohn, False-positive psychology: Undisclosed flexibility in data collection and analysis allows presenting anything as significant. *Psychol. Sci.* **22**, 1359–1366 (2011). doi: [10.1177/0956797611417632](https://doi.org/10.1177/0956797611417632); pmid: [22006061](https://pubmed.ncbi.nlm.nih.gov/22006061/)
- Open Science Collaboration, An open, large-scale, collaborative effort to estimate the reproducibility of psychological science. *Perspect. Psychol. Sci.* **7**, 657–660 (2012). doi: [10.1177/1745691612462588](https://doi.org/10.1177/1745691612462588); pmid: [26168127](https://pubmed.ncbi.nlm.nih.gov/26168127/)
- Open Science Collaboration, in *Implementing Reproducible Computational Research (A Volume in The R Series)*, V. Stodden, F. Leisch, R. Peng, Eds. (Taylor & Francis, New York, 2014), pp. 299–323.
- R. A. Fisher, Theory of statistical estimation. *Math. Proc. Camb. Philos. Soc.* **22**, 700–725 (1925). doi: [10.1017/S0305004100009580](https://doi.org/10.1017/S0305004100009580)
- W. Viechtbauer, Conducting meta-analyses in R with the metafor package. *J. Stat. Softw.* **36**, 1–48 (2010).
- S. L. Braver, F. J. Thoemmes, R. Rosenthal, Continuously cumulating meta-analysis and replicability. *Perspect. Psychol. Sci.* **9**, 333–342 (2014). doi: [10.1177/1745691614529796](https://doi.org/10.1177/1745691614529796); pmid: [26173268](https://pubmed.ncbi.nlm.nih.gov/26173268/)
- U. Simonsohn, Small telescopes: Detectability and the evaluation of replication results. *Psychol. Sci.* **26**, 559–569 (2015). doi: [10.1177/0956797614567341](https://doi.org/10.1177/0956797614567341); pmid: [25800521](https://pubmed.ncbi.nlm.nih.gov/25800521/)
- D. Lakens, Calculating and reporting effect sizes to facilitate cumulative science: A practical primer for t-tests and ANOVAs. *Front. Psychol.* **4**, 863 (2013). doi: [10.3389/fpsyg.2013.00863](https://doi.org/10.3389/fpsyg.2013.00863); pmid: [24324449](https://pubmed.ncbi.nlm.nih.gov/24324449/)
- J. Lehrer, The truth wears off: Is there something wrong with the scientific method? *The New Yorker*, 52–57 (2010).
- R. Klein *et al.*, Investigating variation in replicability: A “many labs” replication project. *Soc. Psychol.* **45**, 142–152 (2014). doi: [10.1027/1864-9335/a000178](https://doi.org/10.1027/1864-9335/a000178)
- J. Cohen, The statistical power of abnormal-social psychological research: A review. *J. Abnorm. Soc. Psychol.* **65**, 145–153 (1962). doi: [10.1037/h0045186](https://doi.org/10.1037/h0045186); pmid: [13880271](https://pubmed.ncbi.nlm.nih.gov/13880271/)
- T. D. Sterling, Publication decisions and their possible effects on inferences drawn from tests of significance—or vice versa. *J. Am. Stat. Assoc.* **54**, 30–34 (1959).
- T. M. Errington *et al.*, An open investigation of the reproducibility of cancer biology research. *eLife* **3**, e04333 (2014). doi: [10.7554/eLife.04333](https://doi.org/10.7554/eLife.04333); pmid: [25490932](https://pubmed.ncbi.nlm.nih.gov/25490932/)
- J. K. Hartshorne, A. Schachner, Tracking replicability as a method of post-publication open evaluation. *Front. Comput. Neurosci.* **6**, 8 (2012). doi: [10.3389/fncom.2012.00008](https://doi.org/10.3389/fncom.2012.00008); pmid: [22403538](https://pubmed.ncbi.nlm.nih.gov/22403538/)
- B. A. Nosek *et al.*, Promoting an open research culture. *Science* **348**, 1422–1425 (2015). doi: [10.1126/science.aab2374](https://doi.org/10.1126/science.aab2374); pmid: [26113702](https://pubmed.ncbi.nlm.nih.gov/26113702/)

ACKNOWLEDGMENTS

In addition to the coauthors of this manuscript, there were many volunteers who contributed to project success. We thank D. Acup, J. Anderson, S. Anzellotti, R. Araujo, J. D. Arnal, T. Bates, R. Battleday, R. Bauchwitz, M. Bernstein, B. Blohowiak, M. Boffo, E. Bruneau, B. Chabot-Hanowell, J. Chan, P. Chu, A. Dalla Rosa, B. Deen, P. DiGiacomo, C. Dogulu, N. Dufour, C. Fitzgerald, A. Foote, A. Garcia, E. Garcia, C. Gautreau, L. Germinet, T. Gill, L. Goldberg, S. D. Goldinger, H. Gweon, D. Haile, K. Hart, F. Hjorth, J. Hoening, A. Innes-Ker, B. Jansen, R. Jersakova, Y. Jie, Z. Kaldy, W. K. Kong, A. Kenney, J. Kingston, J. Koster-Hale, A. Lam, R. LeDonne, D. Luman, E. Luong, S. Man-pui, J. Martin, A. Mauk, T. McElroy, K. McRae, T. Miller, K. Moser, M. Mullarkey, A. R. Munoz, J. Ong, C. Parks, D. S. Pate, D. Patron, H. J. M. Pennings, M. Penuliar, A. Pfammatter, J. P. Shanoltz, E. Stevenson, E. Pichler, H. Raudszus, H. Richardson, N. Rothstein, T. Scherndl, S. Schrager, S. Shah, Y. S. Tai, A. Skerry, M. Steinberg, J. Stoeterrau, H. Tibboel, A. Tooley, A. Tullett, C. Vaccaro, E. Vergauwe, A. Watanabe, I. Weiss, M. H. White II,

P. Whitehead, C. Widmann, D. K. Williams, K. M. Williams, and H. Yi. Also, we thank the authors of the original research that was the subject of replication in this project. These authors were generous with their time, materials, and advice for improving the quality of each replication and identifying the strengths and limits of the outcomes. The authors of this work are listed alphabetically. This project was supported by the Center for Open Science and the Laura and John Arnold Foundation. The authors declare no financial conflict of interest with the reported research.

The Open Science Collaboration

Alexander A. Aarts,¹ Joanna E. Anderson,² Christopher J. Anderson,³ Peter R. Attridge,^{4,5} Angela Attwood,⁶ Jordan Axt,⁷ Molly Babel,⁸ Štěpán Bahnik,⁹ Erica Baranski,¹⁰ Michael Barnett-Cowan,¹¹ Elizabeth Bartmess,¹² Jennifer Beer,¹³ Raoul Bell,¹⁴ Heather Bentley,⁵ Leah Beyan,⁵ Grace Binion,^{5,15} Denny Borsboom,¹⁶ Annick Bosch,¹⁷ Frank A. Bosco,¹⁸ Sara D. Bowman,¹⁹ Mark J. Brandt,²⁰ Erin Braswell,¹⁹ Hilmar Brohmer,²⁰ Benjamin T. Brown,⁵ Kristina Brown,⁵ Jovita Bruning,^{21,22} Ann Calhoun-Sauls,²³ Shannon P. Callahan,²⁴ Elizabeth Chagnon,²⁵ Jesse Chandler,^{26,27} Christopher R. Chartier,²⁸ Felix Cheung,^{29,30} Cody D. Christopherson,³¹ Linda Cillessen,¹⁷ Russ Clay,³² Hayley Cleary,¹⁸ Mark D. Cloud,³³ Michael Cohn,¹² Johanna Cohoon,¹⁹ Simon Columbus,¹⁵ Andreas Cordes,³⁴ Giulio Costantini,³⁵ Leslie D. Cramblet Alvarez,³⁶ Ed Cremata,³⁷ Jan Crusius,³⁸ Jamie DeCoster,⁷ Michelle A. DeGaetano,⁵ Nicolás Della Penna,³⁹ Bobby den Bezemer,¹⁶ Marie K. Deserno,¹⁶ Olivia Devitt,⁵ Laura Dewitte,⁴⁰ David G. Dobolyi,⁷ Geneva T. Dodson,⁷ M. Brent Donnellan,⁴¹ Ryan Donohue,⁴² Rebecca A. Dore,⁷ Angela Dorrrough,^{43,44} Anna Dreber,⁴⁵ Michelle Dugas,²⁵ Elizabeth W. Dunn,⁸ Kayleigh Easey,⁶ Sylvia Eoibge,⁵ Casey Eggleston,⁷ Jo Embley,⁴⁶ Sacha Epskamp,¹⁶ Timothy M. Errington,¹⁹ Vivien Estel,⁴⁷ Frank J. Fara,^{48,49} Jenelle Feather,⁵⁰ Anna Fedor,⁵¹ Belén Fernández-Castilla,⁵² Susann Fiedler,⁴⁴ James G. Field,¹⁸ Stanka A. Fitneva,⁵³ Taru Flagan,¹³ Amanda L. Forest,⁵⁴ Eskil Forsell,⁴⁵ Joshua D. Foster,⁵⁵ Michael C. Frank,⁵⁶ Rebecca S. Frazier,⁷ Heather Fuchs,³⁸ Philip Gable,⁵⁷ Jeff Galak,⁵⁸ Elisa Maria Galliani,⁵⁹ Anup Gampa,⁷ Sara Garcia,⁶⁰ Douglas Gazarian,⁶¹ Elizabeth Gilbert,⁷ Roger Giner-Sorolla,⁴⁶ Andreas Glöckner,^{34,44} Lars Goellner,⁴³ Jin X. Goh,⁶² Rebecca Goldberg,⁶³ Patrick T. Goodbourn,⁶⁴ Shauna Gordon-McKeon,⁶⁵ Bryan Gorges,¹⁹ Jessie Gorges,¹⁹ Justin Goss,⁶⁶ Jesse Graham,³⁷ James A. Grange,⁶⁷ Jeremy Gray,²⁹ Chris Hartgering,²⁰ Joshua Hartshorne,⁶⁸ Fred Hasselmann,^{17,68} Timothy Hayes,³⁷ Emma Heikensten,⁴⁵ Felix Henninger,^{69,44} John Hodsoll,^{70,71} Taylor Holubar,⁵⁶ Gea Hoogendoorn,²⁰ Denise J. Humphries,⁵ Cathy O.-Y. Hung,³⁰ Nathali Immelman,⁷² Vanessa C. Irsik,⁷³ Georg Jahn,⁷⁴ Frank Jäkel,⁷⁵ Marc Jekel,³⁴ Magnus Johannesson,⁴⁵ Larissa G. Johnson,⁷⁶ David J. Johnson,²⁹ Kate M. Johnson,³⁷ William J. Johnston,⁷⁷ Kai Jonas,¹⁶ Jennifer A. Joy-Gaba,¹⁸ Heather Barry Kappes,⁷⁸ Kim Kelso,³⁶ Mallory C. Kidwell,¹⁹ Seung Kyung Kim,⁵⁶ Matthew Kirkhart,⁷⁹ Bennett Kleinberg,^{16,80} Goran Knežević,⁸¹ Franziska Maria Kolarz,¹⁷ Jolanda J. Kossakowski,¹⁶ Robert Wilhelm Krause,¹⁷ Job Krijnen,²⁰ Tim Kuhlmann,⁸² Yoram K. Kunkels,¹⁶ Megan M. Kyc,³³ Calvin K. Lai,⁷ Aamir Laique,⁸³ Daniel Lakens,⁸⁴ Kristin A. Lane,⁶¹ Bethany Lassetter,⁸⁵ Lijlana B. Lazarevic,⁸¹ Etienne P. LeBel,⁸⁶ Key Jung Lee,⁵⁶ Minha Lee,⁷ Kristi Lemm,⁸⁷ Carmel A. Levitan,⁸⁸ Melissa Lewis,⁸⁹ Lin Lin,³⁰ Stephanie Lin,⁵⁶ Matthias Lippold,³⁴ Darren Loureiro,²⁵ Ilse Luteijn,¹⁷ Sean Mackinnon,⁹⁰ Heather N. Mainard,⁵ Denise C. Marigold,⁹¹ Daniel P. Martin,⁷ Tylar Martinez,³⁶ E.J. Masicampo,⁹² Josh Matacotta,⁹³ Maya Mathur,⁹⁶ Michael May,^{44,94} Nicole Mechin,⁵⁷ Pranjal Mehta,¹⁵ Johannes Meixner,^{21,95} Alissa Melinger,⁹⁶ Jeremy K. Miller,⁹⁷ Mallorie Miller,⁸³ Katherine Moore,^{42,98} Marcus Möschl,⁹⁹ Matt Motyl,¹⁰⁰ Stephanie M. Müller,⁴⁷ Marcus Munafo,⁶ Koen I. Neijenhuijs,¹⁷ Taylor Nervi,²⁸ Gandalf Nicolas,¹⁰¹ Gustav Nilssonne,^{102,103} Brian A. Nosek,^{73,104} Michèle B. Nuijten,²⁰ Catherine Olsson,^{50,104} Colleen Osborne,⁷ Lutz Ostkamp,⁷⁵ Misha Pavel,⁶² Ian S. Penton-Voak,⁶⁵ Olivia Perna,²⁸ Cyril Pernet,¹⁰⁵ Marco Perugini,³⁵ R. Nathan Pipitone,³⁶ Michael Pitts,⁸⁹ Franziska Plessow,^{99,106} Jason M. Prenoveau,⁷⁹ Rima-Maria Rahal,^{44,16} Kate A. Ratliff,¹⁰⁷ David Reinhard,⁷ Frank Renkewitz,⁴⁷ Ashley A. Ricker,¹⁰ Anastasia Rigney,¹³ Andrew M. Rivers,²⁴ Mark Roebke,¹⁰⁸ Abraham M. Rutnick,¹⁰⁹ Robert S. Ryan,¹¹⁰ Onur Sahin,¹⁶ Anondah Saide,¹⁰ Gillian M. Sandstrom,⁶⁹ David Santos,^{111,112} Rebecca Saxe,⁵⁰ René Schlegelmilch,^{44,47} Kathleen Schmidt,¹¹³ Sabine Scholz,¹¹⁴ Larissa Seibel,¹⁷ Dylan Faulkner Selterman,²⁵ Samuel Shaki,¹¹⁵ William B. Simpson,⁷ H. Colleen Sinclair,⁶³ Jeanine L. M. Skorinko,¹¹⁶ Agnieszka Slowik,¹¹⁷ Joel S. Snyder,⁷³ Courtney Soderberg,¹⁹ Carina Sonnleitner,¹¹⁷ Nick Spencer,³⁶ Jeffrey R. Spies,¹⁹

Sara Steegen,⁴⁰ Stefan Stieger,⁸² Nina Strohminger,¹¹⁸ Gavin B. Sullivan,¹¹⁹ Thomas Talhelm,¹¹⁹ Megan Tapia,¹⁶ Annieke Te Dorsthorst,¹⁷ Manuela Thomas,^{72,120} Sarah L. Thomas,⁷ Pia Tio,¹⁶ Frits Traets,⁴⁰ Steve Tsang,¹²¹ Francis Tuerlinckx,⁴⁰ Paul Turchan,¹²² Milan Valášek,¹⁰⁵ Anna E. van 't Veer,^{20,123} Robbie Van Aert,²⁰ Marcel van Assen,²⁰ Riet van Bork,¹⁶ Mathijs van de Ven,¹⁷ Don van den Bergh,¹⁶ Marije van der Hulst,¹⁷ Roel van Dooren,¹⁷ Johnny van Doorn,⁴⁰ Daan R. van Renswoude,¹⁶ Hedderik van Rijn,¹¹⁴ Wolf Vanpaemel,⁴⁰ Alejandro Vázquez Echeverría,¹²⁴ Melissa Vazquez,⁵ Natalia Velez,⁵⁶ Marieke Vermue,¹⁷ Mark Verschoor,²⁰ Michelangelo Vianello,⁵⁹ Martin Voracek,¹¹⁷ Gina Vuu,⁷ Eric-Jan Wagenmakers,¹⁵ Joanneke Weerdmeester,¹⁷ Ashlee Welsh,³⁶ Erin C. Westgate,⁷ Joeri Wissink,²⁰ Michael Wood,⁷² Andy Woods,^{125,6} Emily Wright,³⁶ Sining Wu,⁶³ Marcel Zeelenberg,²⁰ Kellylynn Zuni³⁶

¹Open Science Collaboration, Nuenen, Netherlands. ²Defense Research and Development Canada, Ottawa, ON, Canada. ³Department of Psychology, Southern New Hampshire University, Schenectady, NY 12305, USA. ⁴Merced School of Medicine, Macon, GA 31207, USA. ⁵Georgia Gwinnett College, Lawrenceville, GA 30043, USA. ⁶School of Experimental Psychology, University of Bristol, Bristol BS8 1TH, UK. ⁷University of Virginia, Charlottesville, VA 22904, USA. ⁸University of British Columbia, Vancouver, BC V6T 1Z4 Canada. ⁹Department of Psychology II, University of Würzburg, Würzburg, Germany. ¹⁰Department of Psychology, University of California, Riverside, Riverside, CA 92521, USA. ¹¹University of Waterloo, Waterloo, ON N2L 3G1, Canada. ¹²University of California, San Francisco, San Francisco, CA 94118, USA. ¹³Department of Psychology, University of Texas at Austin, Austin, TX 78712, USA. ¹⁴Department of Experimental Psychology, Heinrich Heine University Düsseldorf, Düsseldorf, Germany. ¹⁵Department of Psychology, University of Oregon, Eugene, OR 97403, USA. ¹⁶Department of Psychology, University of Amsterdam, Amsterdam, Netherlands. ¹⁷Radboud University Nijmegen, Nijmegen, Netherlands. ¹⁸Virginia Commonwealth University, Richmond, VA 23284, USA. ¹⁹Center for Open Science, Charlottesville, VA 22902, USA. ²⁰Department of Social Psychology, Tilburg University, Tilburg, Netherlands. ²¹Humboldt University of Berlin, Berlin, Germany. ²²Charité—Universitätsmedizin Berlin, Berlin, Germany. ²³Belmont Abbey College, Belmont, NC 28012, USA. ²⁴Department of Psychology, University of California, Davis, Davis, CA 95616, USA. ²⁵University of Maryland, Washington, DC 20012, USA. ²⁶Institute for Social Research, University of Michigan, Ann Arbor, MI 48104, USA. ²⁷Mathematica Policy Research, Washington, DC 20002, USA. ²⁸Ashland University, Ashland, OH 44805, USA. ²⁹Michigan State University, East Lansing, MI 48824, USA. ³⁰Department of Psychology, University of Hong Kong, Pok Fu Lam, Hong Kong. ³¹Department of Psychology, Southern Oregon University, Ashland, OR 97520, USA. ³²College of Staten Island, City University of New York, Staten Island, NY 10314, USA. ³³Department of Psychology, Lock Haven University, Lock Haven, PA 17745, USA. ³⁴University of Göttingen, Göttingen, Germany. ³⁵University of Milan-Bicocca, Milan, Italy. ³⁶Department of Psychology, Adams State University, Alamosa, CO 81101, USA. ³⁷University of Southern California, Los Angeles, CA 90089, USA. ³⁸University of Cologne, Cologne, Germany. ³⁹Australian National University, Canberra, Australia. ⁴⁰University of Leuven, Leuven, Belgium. ⁴¹Texas A & M University, College Station, TX 77845, USA. ⁴²Elmhurst College, Elmhurst, IL 60126, USA. ⁴³Department of Social Psychology, University of Siegen, Siegen, Germany. ⁴⁴Max Planck Institute for Research on Collective Goods, Bonn, Germany. ⁴⁵Department of Economics, Stockholm School of Economics, Stockholm, Sweden. ⁴⁶School of Psychology, University of Kent, Canterbury, Kent, UK. ⁴⁷University of Erfurt, Erfurt, Germany. ⁴⁸University of Washington, Seattle, WA 98195, USA. ⁴⁹Prometheus Research, New Haven, CT 06510, USA. ⁵⁰Department of Brain and Cognitive Sciences, Massachusetts Institute of Technology, Cambridge, MA 02139, USA. ⁵¹Parmenides Center for the Study of Thinking, Munich, Germany. ⁵²Universidad Complutense de Madrid, Madrid, Spain. ⁵³Department of Psychology, Queen's University, Kingston, ON, Canada. ⁵⁴Department of Psychology, University of Pittsburgh, Pittsburgh, PA 15260, USA. ⁵⁵Department of Psychology, University of South Alabama, Mobile, AL 36688, USA. ⁵⁶Stanford University, Stanford, CA 94305, USA. ⁵⁷Department of Psychology, University of Alabama, Tuscaloosa, AL 35487, USA. ⁵⁸Carnegie Mellon University, Pittsburgh, PA 15213, USA. ⁵⁹Department FISPPA—Applied Psychology Unit, University of Padua, Padova, Italy. ⁶⁰Universidad Nacional De Asunción, Asunción, Paraguay. ⁶¹Bard College, Providence, RI 02906, USA. ⁶²Northeastern University, Boston, MA 02115, USA. ⁶³Department of Counseling and Educational Psychology, Mississippi State University,

Mississippi State, MS 39762, USA. ⁶⁴School of Psychology, University of Sydney, Sydney, Australia. ⁶⁵Hampshire College, Amherst, MA 01002, USA. ⁶⁶Colorado State University-Pueblo, Pueblo, CO 81001, USA. ⁶⁷School of Psychology, Keele University, Keele, Staffordshire, UK. ⁶⁸Behavioral Science Institute, Nijmegen, Netherlands. ⁶⁹University of Koblenz-Landau, Landau, Germany. ⁷⁰Department of Biostatistics, Institute of Psychiatry, Psychology, and Neuroscience, IHR Biomedical Research Centre for Mental Health, South London, London, UK. ⁷¹Maudsley NHS Foundation Trust, King's College London, London, UK. ⁷²Department of Psychology, University of Winchester, Winchester, UK. ⁷³University of Nevada, Las Vegas, Las Vegas, NV 89154, USA. ⁷⁴Institute for Multimedia and Interactive Systems, University of Lubeck, Lubeck, Germany. ⁷⁵Institute of Cognitive Science, University of Osnabrück, Osnabrück, Germany. ⁷⁶University of Birmingham, Northampton, Northamptonshire NN1 3NB, UK. ⁷⁷University of Chicago, Chicago, IL 60615, USA. ⁷⁸London School of Economics and Political Science, London WC2A 2AE, UK. ⁷⁹Loyola University Maryland, Baltimore, MD 21210, USA. ⁸⁰Department of Security and Crime Science, University College London, London WC1H 9EZ, UK. ⁸¹Department of Psychology, University of Belgrade, Belgrade, Serbia. ⁸²Department of Psychology, University of Konstanz, Konstanz, Germany. ⁸³Open Science Collaboration, Saratoga, CA, USA. ⁸⁴School of Innovation Sciences, Eindhoven University of Technology, Eindhoven, Netherlands. ⁸⁵Department of Psychology, University of Iowa, Iowa City, IA 52242, USA. ⁸⁶Department of Psychology, Western University, London, ON N6A 5C2, Canada. ⁸⁷Department of Psychology, Western Washington University, Bellingham, WA 98225, USA. ⁸⁸Department of Cognitive Science, Occidental College, Los Angeles, CA 90041, USA. ⁸⁹Department of Psychology, Reed College, Portland, OR 97202, USA. ⁹⁰Department of Psychology and Neuroscience, Dalhousie University, Halifax, NS, Canada. ⁹¹Renison University College at University of Waterloo, Waterloo, ON N2L 3G4, Canada. ⁹²Department of Psychology, Wake Forest University, Winston-Salem, NC 27109, USA. ⁹³Counseling and Psychological Services, California State University, Fullerton, Fullerton, CA 92831, USA. ⁹⁴University of Bonn, Bonn, Germany. ⁹⁵University of Potsdam, Potsdam, Germany. ⁹⁶School of Psychology, University of Dundee, Dundee, Scotland. ⁹⁷Willamette University, Salem, OR 97301, USA. ⁹⁸Arcadia University, Glenside, PA 19038, USA. ⁹⁹Department of Psychology, Technische Universität Dresden, Dresden, Germany. ¹⁰⁰Department of Psychology, University of Illinois at Chicago, Chicago, IL 60607, USA. ¹⁰¹William and Mary, Williamsburg, VA 23185, USA. ¹⁰²Stockholm University, Stockholm, Sweden. ¹⁰³Karolinska Institute, Stockholm, Sweden. ¹⁰⁴Center for Neural Science, New York University, New York, NY 10003, USA. ¹⁰⁵Centre for Clinical Brain Sciences, The University of Edinburgh, Edinburgh EH16 4SB, UK. ¹⁰⁶Department of Neurology, Beth Israel Deaconess Medical Center, Harvard Medical School, Boston, MA 02215, USA. ¹⁰⁷Department of Psychology, University of Florida, Gainesville, FL 32611, USA. ¹⁰⁸Department of Psychology, Wright State University, Dayton, OH 45435, USA. ¹⁰⁹California State University, Northridge, Northridge, CA 91330, USA. ¹¹⁰Kutztown University of Pennsylvania, Kutztown, PA 19530, USA. ¹¹¹Department of Psychology, Universidad Autónoma de Madrid, Madrid, Spain. ¹¹²IE Business School, Madrid, Spain. ¹¹³Department of Social Sciences, University of Virginia's College at Wise, Wise, VA 24230, USA. ¹¹⁴University of Groningen, Groningen, Netherlands. ¹¹⁵Department of Behavioral Sciences, Ariel University, Ariel, 40700 Israel. ¹¹⁶Department of Social Science, Worcester Polytechnic Institute, Worcester, MA 01609, USA. ¹¹⁷Department of Basic Psychological Research and Research Methods, University of Vienna, Vienna, Austria. ¹¹⁸Duke University, Durham, NC 27708, USA. ¹¹⁹Centre for Research in Psychology, Behavior and Achievement, Coventry University, Coventry CV1 5FB, UK. ¹²⁰The Open University, Buckinghamshire MK7 6AA, UK. ¹²¹City University of Hong Kong, Shamsuipo, KLN, Hong Kong. ¹²²Jacksonville University, Jacksonville, FL 32211, USA. ¹²³TIBER (Tilburg Institute for Behavioral Economics Research), Tilburg, Netherlands. ¹²⁴Universidad de la República Uruguay, Montevideo 11200, Uruguay. ¹²⁵University of Oxford, Oxford, UK.

SUPPLEMENTARY MATERIALS

www.sciencemag.org/content/349/6251/aac4716/suppl/DC1
Materials and Methods

Figs. S1 to S7

Tables S1 to S4

References (38–41)

29 April 2015; accepted 28 July 2015
10.1126/science.aac4716

This copy is for your personal, non-commercial use only.

If you wish to distribute this article to others, you can order high-quality copies for your colleagues, clients, or customers by [clicking here](#).

Permission to republish or repurpose articles or portions of articles can be obtained by following the guidelines [here](#).

The following resources related to this article are available online at www.sciencemag.org (this information is current as of August 28, 2015):

Updated information and services, including high-resolution figures, can be found in the online version of this article at:

<http://www.sciencemag.org/content/349/6251/aac4716.full.html>

Supporting Online Material can be found at:

<http://www.sciencemag.org/content/suppl/2015/08/26/349.6251.aac4716.DC1.html>

A list of selected additional articles on the Science Web sites **related to this article** can be found at:

<http://www.sciencemag.org/content/349/6251/aac4716.full.html#related>

This article **cites 37 articles**, 13 of which can be accessed free:

<http://www.sciencemag.org/content/349/6251/aac4716.full.html#ref-list-1>

This article appears in the following **subject collections**:

Psychology

<http://www.sciencemag.org/cgi/collection/psychology>

RESEARCH ARTICLE SUMMARY

ADVANCED IMAGING

Extended-resolution structured illumination imaging of endocytic and cytoskeletal dynamics

Dong Li, Lin Shao, Bi-Chang Chen, Xi Zhang, Mingshu Zhang, Brian Moses, Daniel E. Milkie, Jordan R. Beach, John A. Hammer III, Mithun Pasham, Tomas Kirchhausen, Michelle A. Baird, Michael W. Davidson, Pingyong Xu, Eric Betzig*

INTRODUCTION: Various methods of super-resolution (SR) fluorescence microscopy have the potential to follow the dynamic nanoscale interactions of specific macromolecular assemblies in living cells. However, this potential is often left unfulfilled, either owing to the method's inability to follow these processes at the speeds dictated by nature or because they require intense light that can substantially perturb the very physiology one hopes to study. An exception is structured illumination microscopy (SIM), which can image live cells far faster and with orders of magnitude less light than required for other SR approaches. However, SIM's resolution is usually limited to only a twofold gain beyond conventional optical microscopes, or ~100 nm with visible light.

RATIONALE: We endeavored to find ways to extend SIM to the sub-100-nm regime while retaining, to the greatest extent possible, the advantages that make it the preferred SR method for live-cell imaging. Our first solution used an ultrahigh numerical aperture (NA) lens and total internal reflection fluorescence (TIRF) to achieve 84-nm resolution at subsecond acquisition speeds over hundreds of time points in multiple colors near the basal plasma membrane. Our second exploited the spatially patterned activation of a recently developed, reversibly photoswitchable fluorescent protein to reach 45- to 62-nm resolution, also at subsecond acquisition, over ~10 to 40 time points.

RESULTS: We used high-NA TIRF-SIM to image the dynamic associations of cortical fila-

mentous actin with myosin IIA, paxillin, or clathrin, as well as paxillin with vinculin and clathrin with transferrin receptors. Thanks to the combination of high spatial and temporal resolution, we were able to measure the sizes of individual clathrin-coated pits through their initiation, growth, and internalization. We were

ON OUR WEB SITE

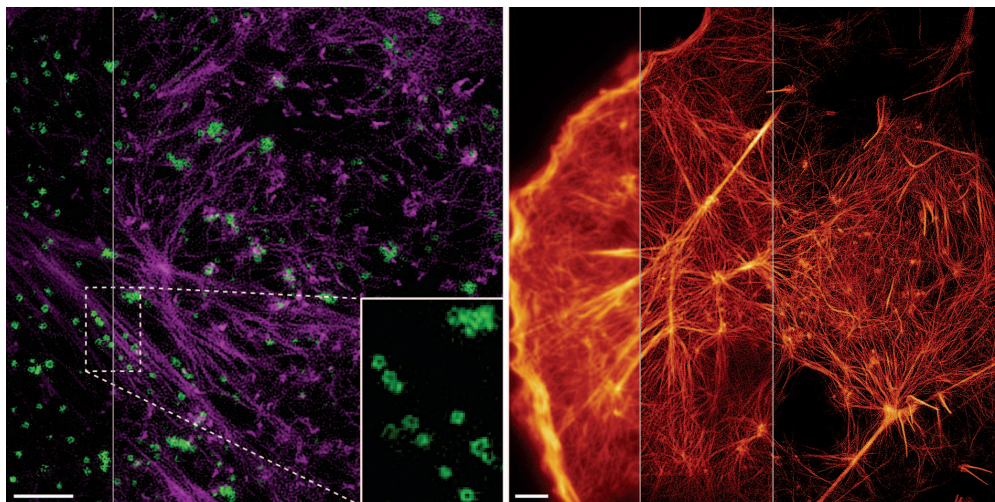
Read the full article at <http://dx.doi.org/10.1126/science.aab3500>

also able to relate pit size to lifetime, identify and characterize localized hot spots of pit generation, and describe the interaction of actin with clathrin

and its role in accelerating endocytosis. With nonlinear SIM by use of patterned activation (PA NL-SIM), we monitored the remodeling of the actin cytoskeleton and the dynamics of caveolae at the cell surface. By combining TIRF-SIM and PA NL-SIM for two-color imaging, we followed the dynamic association of actin with α -actinin in expanding filopodia and membrane ruffles and characterized shape changes in and the transport of early endosomes. Last, by combining PA NL-SIM with lattice light sheet microscopy, we observed, in three dimensions and across the entire volume of whole cells, the dynamics of the actin cytoskeleton, the fusion and fission of mitochondria, and the trafficking of vesicles to and from the Golgi apparatus, each at axial resolution fivefold better than that of conventional widefield microscopy.

In addition, through direct experimental comparisons, we demonstrated that the resolution for our methods is comparable with or better than other SR approaches yet allowed us to image at far higher speeds, and for far longer durations. To understand why this is so, we developed a detailed theoretical model showing that our methods transmit the information encoded in spatial frequencies beyond the diffraction limit with much greater strength than do other alternatives and hence require far fewer photons emitted from the specimen, using far less intense light.

CONCLUSION: High-NA TIRF-SIM and PA NL-SIM fill an unmet need for minimally invasive tools to image live cells in the gap between the 100-nm resolution traditionally associated with SIM and the sub-60-nm regime of protein-specific structural imaging served by single-molecule localization microscopy. ■



Two approaches for improved live-cell imaging at sub-100-nm resolution. (Left) Association of cortical actin (purple) with clathrin-coated pits (green), the latter seen as rings (*inset*) at 84-nm resolution via a combination of total internal reflection fluorescence and structured illumination microscopy at ultrahigh numerical aperture (high-NA TIRF-SIM). **(Right)** Progression of resolution improvement across the actin cytoskeleton of a COS-7 cell, from conventional, diffraction-limited TIRF (220-nm resolution), to TIRF-SIM (97-nm resolution), and nonlinear SIM based on the patterned activation of a reversibly photoswitchable fluorescent protein (PA NL-SIM, 62 nm resolution). (Left and right represent single frames from time-lapse movies over 91 and 30 frames, respectively. Scale bars, 2 μ m (left); 3 μ m (right).

The list of author affiliations is available in the full article online.

*Corresponding author. E-mail: betzig@janelia.hhmi.org

Cite this article as Li *et al.*, *Science* 349, aab3500 (2015). DOI: 10.1126/science.aab3500

RESEARCH ARTICLE

ADVANCED IMAGING

Extended-resolution structured illumination imaging of endocytic and cytoskeletal dynamics

Dong Li,¹ Lin Shao,¹ Bi-Chang Chen,^{1*} Xi Zhang,^{2,3} Mingshu Zhang,² Brian Moses,⁴ Daniel E. Milkie,⁴ Jordan R. Beach,⁵ John A. Hammer III,⁵ Mithun Pasham,⁶ Tomas Kirchhausen,⁶ Michelle A. Baird,^{5,7} Michael W. Davidson,⁷ Pingyong Xu,² Eric Betzig^{1†}

Super-resolution fluorescence microscopy is distinct among nanoscale imaging tools in its ability to image protein dynamics in living cells. Structured illumination microscopy (SIM) stands out in this regard because of its high speed and low illumination intensities, but typically offers only a twofold resolution gain. We extended the resolution of live-cell SIM through two approaches: ultrahigh numerical aperture SIM at 84-nanometer lateral resolution for more than 100 multicolor frames, and nonlinear SIM with patterned activation at 45- to 62-nanometer resolution for approximately 20 to 40 frames. We applied these approaches to image dynamics near the plasma membrane of spatially resolved assemblies of clathrin and caveolin, Rab5a in early endosomes, and α -actinin, often in relationship to cortical actin. In addition, we examined mitochondria, actin, and the Golgi apparatus dynamics in three dimensions.

Fluorescence microscopy continues to play a key role in elucidating structure and function of living systems, thanks to its ability to image specific proteins with single-molecule sensitivity, as well as its capacity to study in vivo dynamics in a minimally invasive manner. Its power has grown with the introduction of super-resolution (SR) techniques (1) that extend its diffraction-limited spatial resolution [~ 200 nm for green fluorescent protein (GFP)] by as much as an order of magnitude. However, although the SR imaging of fixed specimens, the most common modality, offers the highest resolution, it does so at the considerable risk of altering the very ultrastructure it hopes to reveal because of both the fixation process itself (fig. S1) (2) and the extremely high density of fluorescent markers required to achieve such resolution (3). Furthermore, with the advent of genetically encoded markers for electron microscopy (EM) (4, 5), the

continued preeminence of SR microscopy for protein-specific structural imaging at the nanoscale is no longer assured.

A different situation emerges for in vivo imaging, in which EM is too destructive and fixation is not involved. However, although this would appear to be the ideal niche of SR microscopy, SR techniques such as localization microscopy (6, 7), stimulated emission depletion (STED) microscopy (8, 9), and reversible saturable optical fluorescence transitions (RESOLFT) microscopy (10, 11) place extraordinary demands on the photon budget, represented by the product of the number of fluorescent molecules in the specimen and the number of photons each can emit before bleaching irreversibly (fig. S2) (12). They also require specialized photoswitchable labels and excitation intensities of 10^3 to 10^8 W/cm², which are orders of magnitude greater than the 0.1 W/cm² under which life evolved (fig. S3). As a result, time-lapse measurements with these techniques rarely consist of more than a few frames, and phototoxic changes to cellular physiology can set in quickly even at the lower end of this range (movie S1). In addition, typical SR acquisition speeds of ~ 1 s to several minutes per frame are too slow to follow processes that move faster than ~ 1 to 50 nm/s without introducing motion-induced artifacts (fig. S4), whereas common resolution metrics such as the Nyquist criterion for labeling density (6, 7) or the width of an isolated feature (8–11) tend to substantially overestimate the true spatial resolution (figs. S5 and S6).

A notable exception is structured illumination microscopy (SIM), which in vivo (13–15) can image in multiple colors using conventional flu-

orescent labels as fast as 11 frames/s (13) at intensities of only 1 to 100 W/cm². Its primary limitation is that its resolution in vivo has been limited to ~ 100 nm for GFP, or only twice beyond the diffraction limit. This has provided the motivation for the development of other in vivo-compatible SR methods, but to date, all suffer from substantial limitations as noted above.

Extending SIM resolution via high-numerical-aperture optics

We extended the resolution of live-cell SIM by two independent means. In the first, we used the higher numerical aperture (NA) afforded by a commercially available 1.7-NA objective to image at 84-nm resolution (for GFP) (fig. S7). Although the total internal reflection fluorescence (TIRF) condition at this NA confines observations to within ~ 50 to 200 nm of the basal plasma membrane (fig. S8), it also restricts the excitation to only a small fraction of the cellular volume, further reducing phototoxicity, eliminating out-of-focus background, and leaving unaffected a potential reservoir of cytosolic target molecules that might be recruited to the plasma membrane at later time points. With this approach, termed high-NA TIRF-SIM, we could image dynamic associations between proteins in a variety of systems at sub-100-nm resolution, often for 80 to 100 time points, including filamentous actin (mApple-F-actin) and enhanced GFP (EGFP)-myosin IIA (Fig. 1, A and B; Movie 1; and fig. S9); mApple-F-actin and mEmerald-paxillin (Fig. 1, C and D, and movie S2); mEmerald-paxillin and mTagRFP-vinculin (RFP, red fluorescent protein) (Fig. 1, E and F; Movie 2; and fig. S10); mEmerald-clathrin light chain b (CLTB) and Alexa 568-tagged transferrin (fig. S11 and movie S3); and mEmerald-CLTB and mCherry-Lifeact (Fig. 2, E to G) (16). Acquisition times were typically less than 1 s per color per frame, although the time interval between frames was adjusted in each case in order to match the dynamics of interest and to give the cell time to recover from the effects of the excitation applied during the acquisition.

In the case of mEmerald-paxillin and mTagRFP-vinculin, we found that both proteins expanded inward for those focal adhesions near the periphery of an HFF-1 cell (Movie 2 and fig. S12). mEmerald-paxillin dominated in the peripheral-facing end of these adhesions, whereas mTagRFP-vinculin increased in concentration toward the interior (Fig. 1, E and F, and fig. S10C). In contrast, for adhesions located far away from the periphery, mTagRFP-vinculin dominated (fig. S10A), and there was little change in the distribution of either protein over time. The resolution of our data was comparable with that demonstrated by means of live-cell localization microscopy (fig. S13) (6). However, we could image in two colors at intensities of only 30 to 100 W/cm² in a total acquisition time of 1.67 s, versus a single color acquired at 1 kW/cm² in 25 s in the localization case. This represents a 90 to 97% decrease in excitation intensity and a 15-fold increase in imaging speed.

¹Janelia Research Campus, Howard Hughes Medical Institute, Ashburn, VA 20147, USA. ²Key Laboratory of RNA Biology and Beijing Key Laboratory of Noncoding RNA, Institute of Biophysics, Chinese Academy of Sciences, Beijing 100101, China. ³College of Life Sciences, Central China Normal University, Wuhan 430079, Hubei, China. ⁴Coleman Technologies, 5131 West Chester Pike, Newtown Square, PA 19073, USA. ⁵Cell Biology and Physiology Center, National Heart, Lung, and Blood Institute, National Institutes of Health, Bethesda, MD 20892, USA. ⁶Department of Cell Biology and Pediatrics, Harvard Medical School and Program in Cellular and Molecular Medicine, Boston Children's Hospital, Boston, MA 02115, USA. ⁷National High Magnetic Field Laboratory and Department of Biological Science, Florida State University, Tallahassee, FL 32310, USA.

*Present address: Research Center for Applied Sciences, Academia Sinica, Taipei 11529, Taiwan. †Corresponding author. E-mail: betzig@janelia.hhmi.org

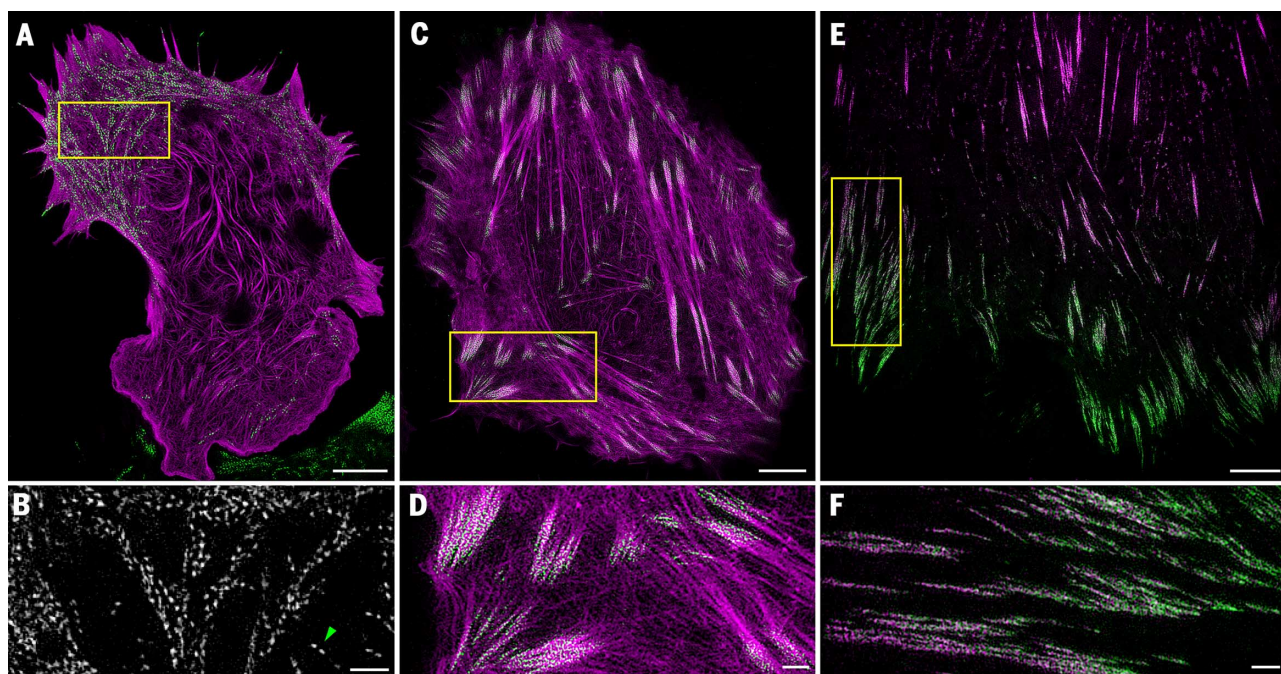


Fig. 1. High-speed live-cell imaging at 37°C of associations between proteins at sub-100-nm resolution. (A) Cytoskeletal proteins mApple-F-tractin (purple) and EGFP-myosin IIA (green) in a mouse embryonic fibroblast cell (Movie 1 and fig. S9). (B) Magnified view of the boxed region in (A), showing bipolar myosin IIA filaments with clearly resolved opposed head groups (for example, green arrowhead). (C) mApple-F-tractin (purple) and the focal adhesion protein mEmerald-paxillin (green) in a U2OS cell (movie S2).

(D) Magnified view of the boxed region in (C), showing association of paxillin with smaller actin fibers fanning out from the ends of larger stress fiber cables. (E) Focal adhesion proteins mTagRFP-vinculin (purple) and mEmerald-paxillin (green) in a HFF-1 cell (Movie 2 and figs. S10 and S13). (F) Magnified view of the boxed region in (E), showing a gradient of increased paxillin concentration toward the cell periphery. Scale bars, 5 μm (A), (C), and (E); 1 μm (B), (D), and (F).

For clathrin (Fig. 2), we saw that mature clathrin-coated pits (CCPs) were resolved as rings (fig. S14 and movie S4), presumably because the distal end of each resides outside the evanescent excitation field. When imaged at 37°C, CCPs large and stable enough to be resolved as a ring at one or more time points grew to a ~152-nm median maximum diameter (Fig. 2B) (17) in BSC-1 cells expressing EGFP-CLTA (Fig. 2A and fig. S14), with similar results in COS-7 cells expressing mEmerald-CLTB (Fig. 2F and fig. S15B), and persisted for on the order of 1 min (Movie 3 and fig. S15A). Linear regression revealed a positive correlation of 0.20 nm/s between maximum ring diameter and lifetime (Fig. 2C), which is consistent with previously observed correlations between lifetime and clathrin intensity or cargo size (18).

In BSC-1 cells, most CCPs were isolated at any given time, but the sites of their initiation did not follow a Poisson distribution (fig. S16). Instead, when the 1297 initiation events over the course of Movie 3 were binned into 0.32- by 0.32- μm sites, corresponding to a mean density of 0.29 events per site, 36.5% of all events occurred at sites of one or more additional events, compared with 13.5% expected if they were Poisson distributed at this mean density. Indeed, at 3.6% of the sites, five or more CCPs were generated sequentially (for example, one marked by green arrows at different time points in Fig. 2D), which would otherwise be a very rare event (0.0053%) assuming Poisson statistics. Although such “hot spots” have been observed previously (19, 20), in our case

we found that these consisted of single, persistent, subdiffractive patches of clathrin, from which multiple CCPs emerged (Movie 4) like bubbles.

In COS-7 cells, mEmerald-CLTB appeared as both isolated rings and larger structures (Fig. 2F, Movie 5, figs. S17 and S18, and movie S5), the latter consisting of aggregates of rings (fig. S19). They may be related to clathrin plaques made of extended clathrin lattices of low curvature (20), also referred to elsewhere as flat clathrin lattices (21). Although they persisted far longer than isolated CCPs, individual rings would occasionally detach from these aggregates (fig. S19). In no instance did we observe large, homogenous patches of clathrin, as we might expect for the flat clathrin lattices common in EM images (22).

The role of actin in clathrin-mediated endocytosis in mammalian cells remains an area of some debate (17, 23–26). Our two-color imaging of COS-7 cells by means of high-NA TIRF-SIM revealed that all aggregates of mEmerald-CLTB rings were associated with mCherry-Lifeact over at least part of their areas at all times (fig. S19). In contrast, approximately equal populations of individual CCPs completed endocytosis either with (Fig. 2E and fig. S20, A and B) or without (fig. S20, C and D) recruitment of Lifeact in the final five frames (20 s) before internalization of the pit. In both cases, histograms of CCP lifetimes were well described by single exponential fits, indicating constant probabilities of internalization per unit time (fig. S15A). The $1/e$ lifetimes of 56.4 ± 3.0 s for the Lifeact-associated CCPs and

67.2 ± 1.9 s for CCPs without Lifeact indicate that actin, when present, indeed increases the internalization probability. Consistent with this, the median maximum clathrin ring diameter for rings persisting over at least five frames was slightly smaller with than without associated Lifeact (160 versus 168 nm) (fig. S15B).

Lifeact associated with CCPs usually approached in a wave or filament (Fig. 2E and fig. S20A). We also observed rings of Lifeact (COS-7 cells) (Fig. 2G and fig. S21, C and D) or F-tractin (U2OS cell) (fig. S21, A and B) similar in size to the clathrin ones and having lifetimes of several minutes (fig. S17B). However, Lifeact rings were not as numerous as clathrin ones and were coincident with them in only a few instances (fig. S22). Although they might be associated with other forms of clathrin-independent endocytosis, their role remains unclear.

Live-cell nonlinear SIM via patterned activation of photoswitchable fluorophores

To achieve even higher resolution than that of high-NA TIRF-SIM, we turned to nonlinear SIM (NL-SIM). The nonlinearity inherent in either the patterned saturation of fluorescence excitation at high intensity (27, 28) or the patterned depletion of photoswitchable fluorophores (fig. S23) (29) introduces additional harmonics H , which permit resolution extension at wavelength λ via SIM to $\sim \lambda/[2NA(H+1)]$ with $H \geq 2$, compared with $H = 1$ for the traditional linear form of SIM and $H = 0$ for diffraction-limited widefield

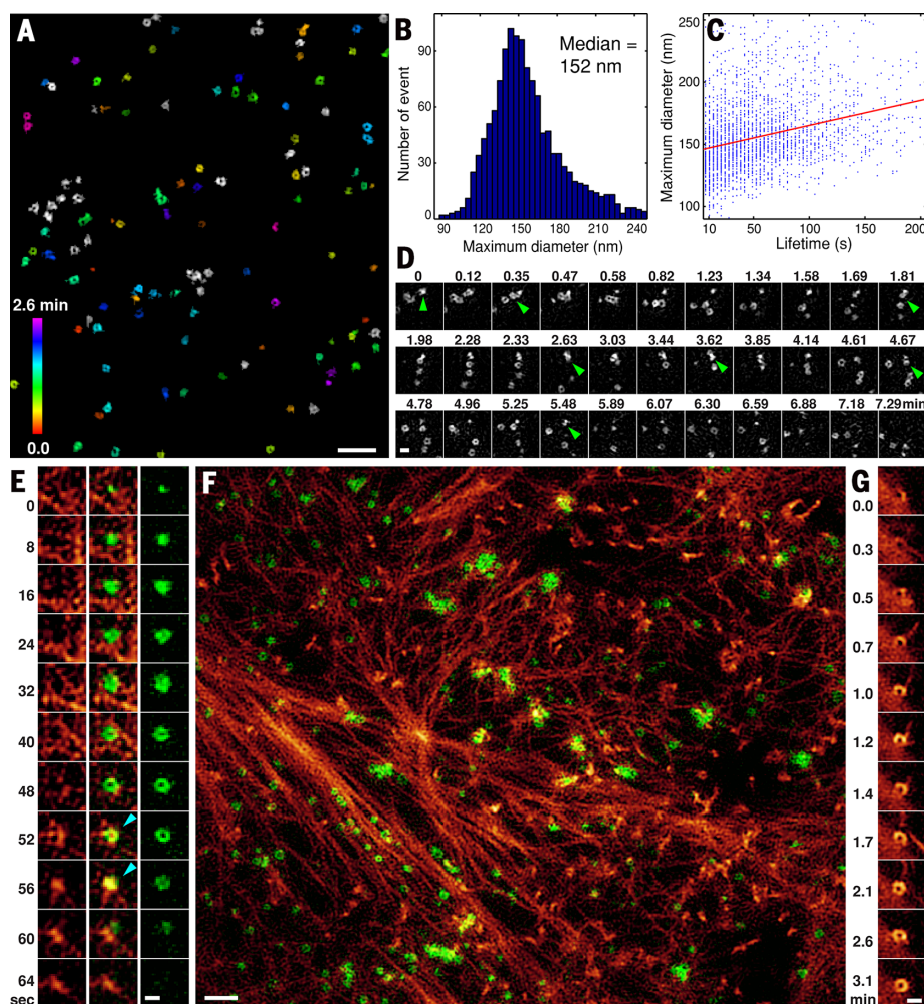


Fig. 2. Dynamics of clathrin-mediated endocytosis and the cortical actin cytoskeleton. (A) CCPs, resolved as rings (fig. S14 and movie S4) and color-coded according to their age since initial formation, at one time point from a movie of CCP dynamics in a BSC-1 cell at 37°C stably expressing EGFP-clathrin light chain a (Movie 3). (B) Histogram of maximum diameter of each CCP over its lifetime. (C) Plot of CCP overall lifetime versus CCP maximum diameter. (D) Sequential production of multiple CCPs at a CCP-generating “hot spot,” identified with green arrowheads (Movie 4 and fig. S16). (E) Formation, growth, and dissolution of a single CCP (right) and its relationship to cortical f-actin (left) in a COS-7 cell at 37°C transfected with mEmerald-clathrin light chain b and mCherry-Lifeact. Light blue arrowheads mark time points at which f-actin associates with the CCP. (F) Individual CCPs and clathrin plaques (green) and cortical f-actin (red) at one time point during their evolution in a COS-7 cell (Movie 5, figs. S17 and S18, and movie S5). (G) Formation of a nanoscale ring of f-actin (fig. S17B). Scale bars, 1 μ m (A) and (F); and 200 nm (D), (E), and (G).

imaging with uniform illumination (fig. S24, A and B). Resolution of ~ 50 nm has been demonstrated with both approaches, although not on living cells; saturated excitation was used to image densely labeled fluorescent beads at the likely phototoxic peak intensity of 8 MW/cm² (28), whereas saturated depletion (SD) imaged single fixed cells at 945 s/frame (29)—far too slow to follow most cellular processes.

SD provides the basis of resolution enhancement in STED and RESOLFT as well as SD NL-SIM. The degree of enhancement depends on the degree of saturation (figs. S23 and S25 and movie S6, part 3), defined in multiples of the saturation factor (SF) for which $1/e$ of the irradiated mol-

ecules remain in the original activated or excited state. However, high SFs are very photon inefficient; only a fraction of the photobleaching-dictated number of switching cycles for any given molecule then contributes useful signal (figs. S25 to S27). Furthermore, high SFs require high intensities and/or long exposures (fig. S28), neither of which is compatible with fast, non-invasive live-cell imaging.

We addressed these issues by using patterned activation (PA) followed with patterned excitation and readout of the green photoswitchable FP Skytan-NS (fig. S29 and movie S6, part 1) (30), rather than SD, to generate $H = 2$ harmonics yielding 62-nm resolution and subsecond acqui-

sition times in TIRF for live cells (Fig. 3). This approach, termed PA NL-SIM, allowed us to achieve large amplitudes in both the first and second harmonics of the emission pattern (fig. S29, G and H), leading to SR images of high signal-to-noise ratio (SNR), even at low activation and excitation saturation factors SF_{act} and SF_{exc} obtained with low intensities and short exposures (table S1). Furthermore, by keeping SF_{act} low, only a small fraction of the total molecular population needed to be activated for every raw image, and with $H = 2$, only $N = (2H + 1)^2 = 25$ such raw images needed to be acquired to reconstruct each SIM image frame (fig. S30). Consequently, we could acquire substantially more frames at substantially higher SNR (fig. S26) in far less time (table S1) by means of PA NL-SIM (Movie 6) than SD NL-SIM (movie S7).

PA NL-SIM of Skytan-NS-Lifeact (Fig. 3, A and B; Movie 6; and movies S8 to S10) in living COS-7 cells revealed considerably more detail than did TIRF-SIM (Fig. 3B) in dense, peripheral actin arcs and star-like junctions of single actin filaments. We were also able to resolve individual Lifeact rings once again, including rings too small to see clearly with high-NA TIRF-SIM (fig. S21, C and D, and movie S8). Furthermore, we could follow the dynamics of the Lifeact-decorated actin cytoskeleton for 30 image frames acquired in 1.2 s each (Movie 6). This is 1250 \times faster and used 20 \times lower intensity (100 W/cm²) than was required for an image of phalloidin-labeled actin at the ventral surface of a fixed BSC-1 cell obtained by means of dual-objective localization microscopy (31), yet the level of detail seen by the two methods was comparable (fig. S31), even though our 62-nm resolution was threefold coarser than that reported in the localization image.

We also used PA NL-SIM to image keratin (fig. S6 and movie S11) and caveolin (Fig. 3, C to F; Movie 7; figs. S32 and S33; and movie S12) in living COS-7 cells, each with Skytan-NS, at a resolution of 59 nm. In the latter case, this was sufficient to resolve numerous caveolae moving by less than their radii during the acquisition time as rings, which is consistent with their invaginated appearance by means of EM (32). Such rings were not observed at caveolae in a HeLa cell imaged with RESOLFT (fig. S34) (33), despite a similar reported resolution. Rings of Skytan-NS-caveolin were somewhat more abundant than CCPs (figs. S17 and S18), and although most were below 100 nm in size, their distribution was broader (Fig. 3D) than the 60 to 80 nm range observed with EM. However, some of the larger rings (Fig. 3E) may represent multiple caveolae clustered around surface-docked vesicles (34). Caveolae also tended to loosely cluster in long narrow ribbons, although we saw tighter aggregations of rings (Fig. 3F) as well, similar to those we saw in clathrin plaques (fig. S19).

Our time-lapse imaging showed that most caveolae moved only a fraction of their size during the acquisition time, although more met this condition when slowed (35) by operating at 23°C (Movie 7 and fig. S32) than when imaged at 37°C

Fig. 3. Live-cell non-linear structured illumination microscopy based on patterned photoactivation. (A)

Single time point from a movie of the evolution of cortical f-actin in a COS-7 cell at 23°C transfected with Skylan-NS-Lifeact, seen at 62-nm resolution (Movie 6, fig. S31, and movie S8). **(B)** Magnified view from a different cell at 37°C, comparing diffraction-limited TIRF microscopy (top left), TIRF with deconvolution (top right), TIRF-SIM (bottom left), and non-linear TIRF-SIM with patterned activation (PA NL-SIM, bottom right) (movies S9 and S10). **(C)** Caveolae in a COS-7 cell at 23°C transfected with Skylan-NS-caveolin, comparing TIRF with deconvolution (top left, 220-nm resolution), TIRF SIM (top right, 97-nm resolution), PA NL-SIM (bottom left, 62-nm resolution), and saturated PA NL-SIM (bottom right, 45-nm resolution). (Insets) A single caveolae pit eventually resolved as a ring by saturated PA NL-SIM (Movie 7, figs. S34 to S37, and movie S13).

(D) Diversity of caveolae ring diameters as seen by means of PA NL-SIM. **(E)** Larger rings that may represent surface-docked vesicles. **(F)** Clusters of caveolae reminiscent of clathrin plaques. (D) to (F) are from a different cell at 37°C (fig. S33 and movie S12). Scale bars, 3 μm (A); 1 μm (B); 200 nm (C); and 100 nm (D), (E), (F), and (C), inset.

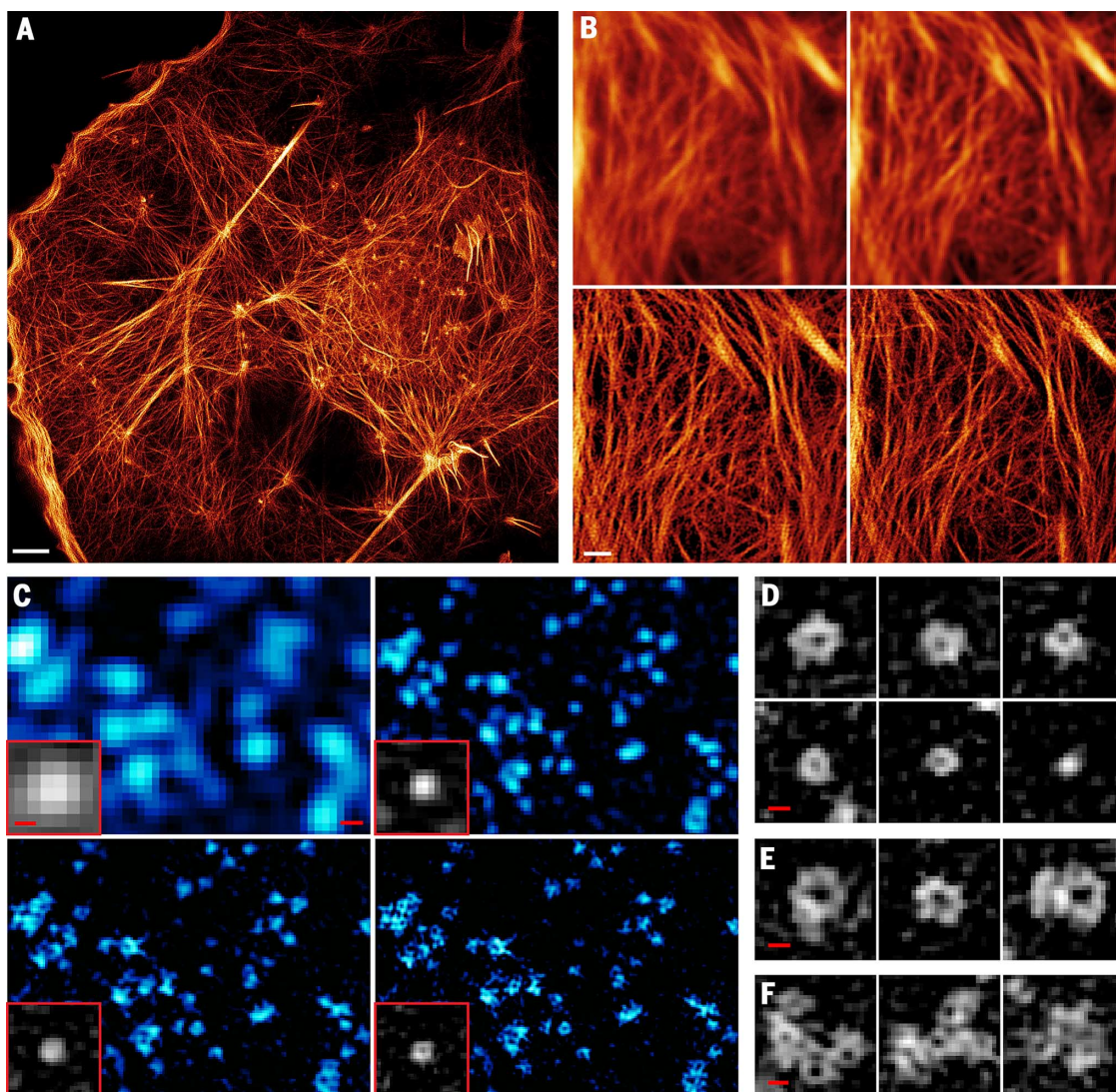


(fig. S33 and movie S12). The smaller, laterally mobile fraction in each case appeared as distorted, discontinuous rings or quasiperiodic patches (fig. S35). These morphologies are indicative of motion-induced artifacts and underscore the difficulty of live-cell SR imaging, by any method: Higher resolution must be accompanied by proportionally faster acquisition times to follow dynamic events of a given velocity, yet higher resolution also requires a quadratically increasing number of raw measurements for each two-dimensional (2D) image frame. Even the comparatively brief 0.35 s we needed to acquire $N = 25$ raw images for each PA NL-SIM image was insufficient to accurately depict caveolae moving by much more than our 59-nm resolution in this time.

Nevertheless, by further increasing SF_{act} we were able to saturate the fraction of molecules in the activated state near the maxima of the patterned activation light (movie S6, part 2). Saturated

PA NL-SIM generates an additional harmonic ($H = 3$) strong enough (fig. S29) to further extend the resolution to 45 nm (figs. S36 and S37) and allowed us to identify even smaller Skylan-NS-caveolin rings unresolvable without the extra harmonic (Fig. 3C). Using $N = 35$ rather than $N = 49$ raw images per frame, we balanced the resulting anisotropic resolution (fig. S30) against the needs for rapid acquisition (0.49 s/frame) and parsimonious use of the photon budget to image caveolin rings over 12 frames at 3 s intervals (movie S13).

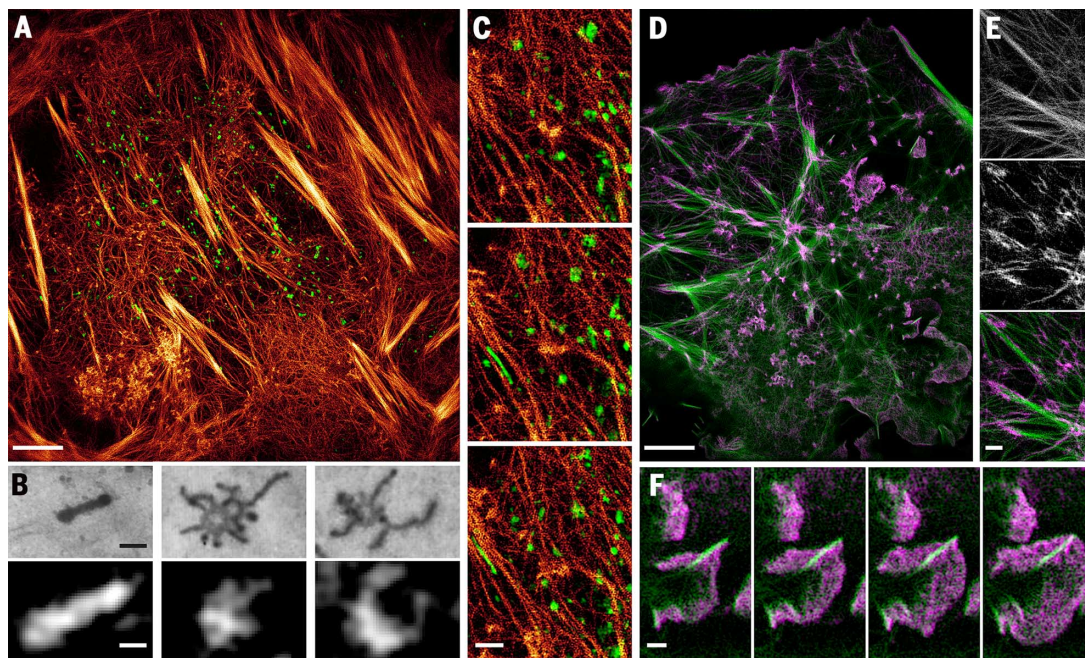
Two-color live imaging via combined TIRF-SIM and PA NL-SIM

By combining linear SIM and PA NL-SIM, both in TIRF, we could study associations between fluorescent proteins, one conventional and one photoswitchable, in two colors at higher resolution than by means of linear TIRF-SIM alone. Images (Fig. 4, A to C, and figs. S38 and S39) and

movies (Movie 8 and movie S14) of mCherry-Rab5a—a regulator of the formation, fusion, and transport of early endosomes (EEs) (36)—revealed irregularly shaped, dynamically remodeling patches of Rab5a (fig. S39, A and B) consistent with the tubular/vesicular architecture of EEs seen in EM (Fig. 4B) (37). Numerous patches also featured dark spots (fig. S39C) perhaps indicative of cargo or internal vacuoles depleted of Rab5a. Most patches moved randomly between successive 20-s time intervals at velocities slow enough to avoid motion artifacts during each 0.34-s acquisition. We also observed a subpopulation of slowly growing Skylan-NS-Lifeact-associated Rab5a patches that were constrained for minutes at a time (fig. S39D, arrows). At the other extreme, we occasionally observed streaks of Rab5a moving parallel to nearby actin filaments at velocities of 3 to 5 $\mu\text{m/s}$ (Fig. 4C and fig. S39E). These may represent EEs actively transported along microtubules (38) parallel to the filaments.

Fig. 4. Combined TIRF-SIM and PA NL-SIM of protein-pair dynamics in living cells.

(A) Sky lantern-NS-Lifect (orange, PA NL-SIM) and mCherry-Rab5a, a marker of early endosomes (green, TIRF-SIM) in a COS-7 cell at 23°C (Movie 8, figs. S38 and S39, and movie S14). (B) Comparison of EM images of early endosomes (37) with similarly shaped Rab5a patches seen in (A). (C) Magnified view at three successive time points, showing rapid transport of a Rab5a streak parallel to the cytoskeleton. (D) Sky lantern-NS-Lifect (green, PA NL-SIM) and mCherry- α -actinin (purple, TIRF-SIM) in a COS-7 cell at 23°C (Movie 9, figs. S40 and S41, and movie S15). (E) Magnified view from (D), with Lifect (top), α -actinin (middle), and overlay (bottom) showing paired association at focal adhesions and along the sides of large stress fibers. (F) Evolution of a membrane ruffle, showing α -actinin concentrated at the leading edge. Scale bars, 5 μ m (A), (D); 200 nm (B); 1 μ m (C) and (E); and 500 nm (F).



We also used PA NL-SIM and TIRF-SIM, respectively, to study the association of Sky lantern-NS-Lifect with mCherry- α -actinin (Fig. 4, D to F, and fig. S40). Consistent with its role as an actin-bundling protein (39), in COS-7 cells we found α -actinin at the treadmilling edge of the lamellipodium and at the basal surface in both filopodia and the leading edges of growing membrane ruffles (Fig. 4F, Movie 9, and movie S15). We also observed concentrations of α -actinin along the sides (Fig. 4E) and at the branching ends of stress fibers that likely attach to cell-substrate adhesions (40). Last, α -actinin was present at dense junctions of Lifect-decorated filaments, and Sky lantern-NS-Lifect rings as described above were colocalized in every instance with a mCherry- α -actinin ring of similar size (fig. S41). Septins, another class of actin-bundling proteins, have been shown (41) to produce f-actin rings in vitro (albeit of larger size than here), so perhaps α -actinin not only aids in bundling actin filaments in nanometric rings but also contributes to their extreme curvature.

3D live-cell imaging with combined PA NL-SIM and lattice light sheet microscopy

Although the ~50- to 200-nm extent of the evanescent excitation field we used in the examples above eliminated out-of-focus background and confined potentially phototoxic exposure to a minute fraction of the cellular volume, it also limited our observations to this subvolume and severely restricted the total photon budget available for those targets unable to be replenished from the cytosol during the imaging interval.

To extend our observations to the entire cell, we turned to live-cell 3D-SIM (14, 15). Unfortunately, traditional 3D-SIM with linear, widefield excitation brings limitations of its own: It is slow

(~20 s acquisition for whole adherent HeLa cells), limited to thin specimens (because of out-of-focus background), and requires high SNR for accurate image reconstruction. It is also potentially phototoxic and bleaches specimens rapidly because of continuous whole-cell illumination. These problems would all be greatly magnified in its direct extension to PA NL-SIM.

Thus, to apply PA NL-SIM to living cells in three dimensions (Fig. 5), we used lattice light sheet microscopy (42). In this technique, an excitation objective (fig. S42A) projects a thin sheet of light (fig. S42A, blue) through a specimen (fig. S42A, orange), and the fluorescence generated in the illuminated plane is collected by a detection objective and imaged onto a camera. Repeating this process plane-by-plane through the specimen produces a 3D image. Restriction of the light to the detection focal plane eliminates out-of-focus background, increases the z axis resolution and greatly reduces photobleaching and phototoxicity.

In cross-section, the light sheet has the 2D periodic structure of an optical lattice (fig. S42B). Sweeping the sheet back and forth along the x axis produces time-averaged uniform illumination, offering high speed and diffraction-limited xyz resolution of 230 by 230 by 370 nm, as seen in a volume-rendered image of the actin cytoskeleton (fig. S43A) and its corresponding overall optical transfer function (OTF) (fig. S43D). Stepping the sheet in x in five equal fractions of the lattice period and applying the algorithms of 3D-SIM to the resulting five raw images per plane extends the xyz resolution to 150 by 230 by 280 nm (fig. S43, B and E), but at the cost of at least 5 \times longer acquisition times (42).

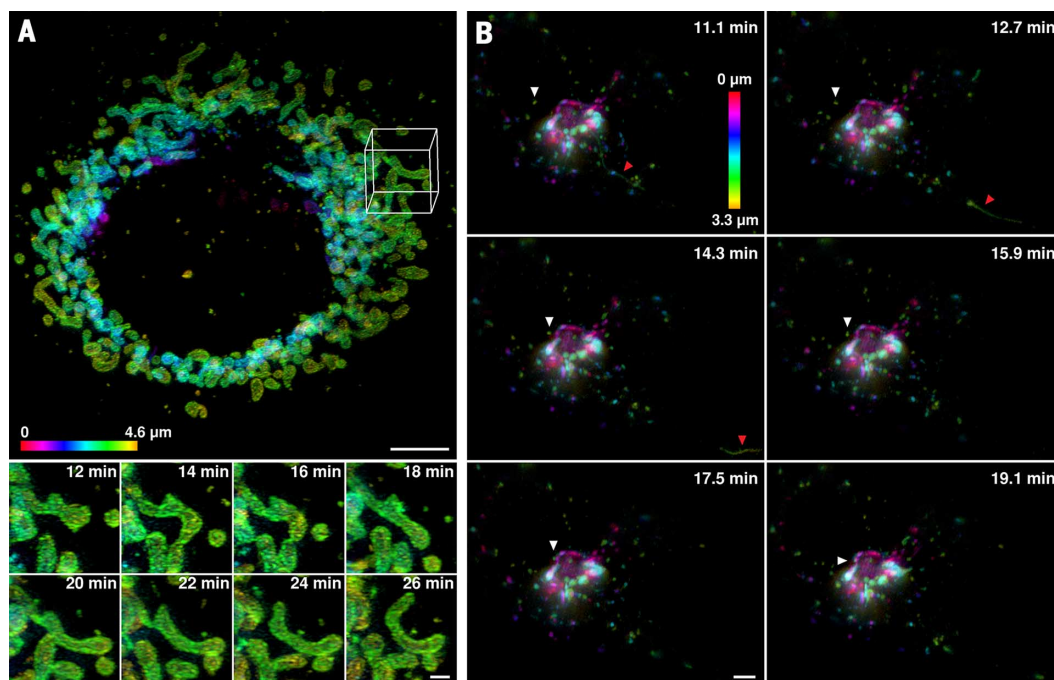
To further extend the 3D resolution via PA NL-SIM, we first photoactivated target molecules

fused to Sky lantern-NS using a hexagonal lattice light sheet of $\lambda = 405$ nm wavelength having $H = 2$ harmonics (fig. S43E). We then imaged the fluorescence from the activated region, exciting the fluorescence with a lattice light sheet of $\lambda = 488$ nm wavelength having the same hexagonal symmetry and period (fig. S42B, bottom) as the activation lattice. For activation well below saturation, the product of the activation and excitation patterns creates a fluorescence emission pattern within the specimen having $H = 4$ harmonics (fig. S43F). Thus, we stepped the sheet in x in $2H + 1 = 9$ equal fractions of the lattice period while recording nine images. Repeating this process for every plane within the specimen, we then reconstructed a 3D PA NL-SIM volume-rendered image (fig. S43C), with resolution extended to 118 by 230 by 170 nm.

We used this approach to image mitochondria in COS-7 cells (Fig. 5A) as well as the actin cytoskeleton (fig. S43, A to C, and movie S16) and the Golgi apparatus (Fig. 5B) in U2OS cells, all at 23°C so as to simplify the overlap of the activation and excitation patterns. Time-lapse 3D images (Fig. 5A, bottom) and movies (Movie 10) of Sky lantern-NS-tagged translocase of outer mitochondrial membrane 20 (TOM20) revealed the migration, constriction before fission, and fusion of individual mitochondria (43, 44), each clearly resolved as a hollow tubular structure. The 3D volume rendering and the widths of mitochondrial membranes in individual xy orthoslices were both comparable with similar data from a fixed cell imaged with 3D localization microscopy (45) at a reported xyz resolution of ~20 by 20 by 60 nm (fig. S44).

A volume-rendered movie (movie S17) of the Golgi-resident enzyme Mannosidase II (MannII)

Fig. 5. Live-cell 3D PA NL-SIM via lattice light sheet microscopy. (A) (Top) Membrane marker Skyran-NS-TOM20 showing mitochondria in a COS-7 cell at 23°C, color-coded for distance from the substrate. (Bottom) Evolution of individual mitochondria, showing fission and fusion events, the former preceded by mitochondrial constriction (Movie 10 and fig. S44). (B) Time-lapse distribution of Golgi-resident enzyme Skyran-NS-Mann II in a U2OS cell at 23°C, showing centralized cisternae surrounded by vesicles. White arrowheads indicate a docking vesicle, and red arrowheads highlight rapid export of a long tubular vesicle (movies S17 and S18). Scale bars, 5 μm (A), top; 1 μm (A), bottom; and 3 μm (B).



tagged with Skyran-NS in a U2OS cell as seen looking into the cis-face from the nucleus showed Mann II concentrated in a hollow sphere of cisternae having a cis-facing void. Time-lapse 3D data (Fig. 5B and movie S18) color-coded for height showed the docking of small vesicles (Fig. 5B, white arrows) that may represent pre-Golgi intermediates (46) as well as the rapid export of Mann II in long, tubular post-Golgi carriers (Fig. 5B, red arrows) (47).

The volumetric resolution of 3D lattice light sheet PA NL-SIM at the 0.6-NA excitation and 1.1-NA detection we used here is comparable with the 105- by 105- by 369-nm xyz resolution of widefield 3D-SIM at 1.2 NA. However, the lattice approach has twofold higher axial resolution and fourfold better than traditional diffraction-limited microscopy. It is therefore better suited to problems in which its superior optical sectioning is essential, such as in resolving heterogeneities in nuclear architecture, distinguishing events occurring at the dorsal or ventral plasma membrane, or as above, tracking vesicles through the secretory pathway. Whole-cell acquisition times (70.5 and 32.7 s in Fig. 5, A and B, respectively) are slow compared with PA NL-SIM in TIRF but similar to widefield 3D-SIM. However, thanks to the oblique imaging geometry (fig. S42), restricted xy fields of view can be imaged at proportionally faster speed through the entire thickness of the cell.

Discussion

The above results provide but a brief glimpse of the biology that might be uncovered with the live-cell-compatible SR methods of high-NA TIRF-SIM and PA NL-SIM. We have measured and correlated the diameters and lifetimes of CCPs, observed at high resolution different forms of CCP initiation, and shown that CCP internaliza-

tion is aided by actin filaments in about half of all cases. We have seen that caveolin localizes not only to the 60- to 80-nm invaginated caveolae common in EM images, but also to much larger ring-like structures, and have followed dynamic changes in the shapes of early endosomes. Last, we have observed the nanoscale remodeling of the actin cytoskeleton in relation to clathrin and Rab5a, as well as cytoskeletal-related proteins such as myosin IIA, α -actinin, and paxillin.

However, the above results also amply illustrate the trade-offs inherent in live SR imaging: With high-NA TIRF-SIM at 1.7 NA, we could acquire up to 200 image frames in <0.5 s each at intensities of 20 to 100 W/cm² and a resolution of 84 nm (for GFP), whereas extending the resolution to 62 nm with PA NL-SIM restricted us to no more than 40 frames, and further extension to 45 nm with saturated PA NL-SIM required 490 W/cm² and produced only 12 frames at useful SNR.

In short, even modest gains in resolution come at substantial cost in terms of the other metrics important for live-cell imaging. These tradeoffs are not specific to SIM. In fact, our extensions of SIM are far more compatible with live imaging than any other form of SR fluorescence microscopy of comparable resolution demonstrated to date. In part, this is because the OTF, which defines the degree to which different sample spatial frequencies (representing differently sized structures) are passed to the image, is far stronger in the 100-nm regime (fig. S24B) for high-NA TIRF-SIM at 1.7 NA than other linear methods such as confocal or image scanning microscopy (ISM) (48–50), and far stronger in the 50- to 100-nm regime (fig. S24C) for PA NL-SIM than other nonlinear methods such as STED (8, 9), point-scanning (PS) RESOLFT (10), or array-based widefield (WF) RESOLFT (17). As a result, far fewer

photons need to be collected (fig. S2), and far less light (fig. S3) needs to be applied to the specimen to see features in these regimes at acceptable SNR. Localization microscopy is also photon inefficient, in that the density of localized molecules is nearly always more limiting to the resolution than is the number of photons emitted per switching cycle, which dictates the localization precision. For example, simulations (12) based on the theoretical OTFs suggest that to resolve an 85-nm grating, PA NL-SIM requires ~80× fewer photons from the specimen per unit area than localization microscopy, ~200× fewer than WF-RESOLFT, and ~15× fewer than PS-RESOLFT or STED, each at a depletion saturation factor of $SF_{\text{depletion}} = 10$ (fig. S2).

Another reason for the greater compatibility of high-NA TIRF-SIM and PA NL-SIM with living cells is that they require much lower peak intensities of applied light. High resolution with STED or RESOLFT demands high factors of saturated depletion (fig. S25, A and C) that are wasteful of the photon budget (fig. S25, B and D) and require enormous intensities and/or long exposures for activation (fig. S45), depletion (fig. S28), and read-out of the final signal (fig. S3). Localization microscopy also requires high intensities to achieve high photon emission and photoswitching rates from single molecules. For example, extrapolating from reported experimental values for live-cell imaging (table S1), the 0.8- to 3.5-W/cm² activation intensity used over the 45- by 45- μm field of view in Fig. 3A in 1.2 s by means of PA NL-SIM is 960,000 times weaker than that which would be required to image the same area in the same acquisition time by means of PS-RESOLFT (10). Similarly, under the same parameters, the 100-W/cm² read-out intensity used for PA NL-SIM shown in Fig. 3A is 200 times weaker than that which would be required for localization

microscopy (6, 7) and 640,000 times less than PS-RESOLFT (10). Furthermore, STED and RESOLFT require an additional depletion step not needed in PA NL-SIM, which would further expose the sample to peak intensities of 807 MW/cm² for STED (8), 1.7 MW/cm² for PS-RESOLFT (10), and 3 kW/cm² for WF-RESOLFT (11). Even over small image fields, nanoscopy with focused light such as PS-RESOLFT and STED uses intensities 10⁵- to 10¹⁰-fold larger than that of terrestrial solar flux and is thus ill-equipped to study live-cell dynamics noninvasively.

Of course, despite these gains, no method of live-cell fluorescence microscopy, including high-NA TIRF-SIM and PA NL-SIM, can claim to be completely noninvasive, owing to possible photo-induced physiological changes, protein overexpression, and/or label-induced perturbations. For example, the gradual development of curved filopodia and membrane ruffles after the start of imaging are shown in Movies 5 and 6 and movie S2. These may reflect a response to the illumination, although we have also commonly seen such structures under initial conditions when imaging with diffraction-limited TIRF (fig. S46). Another caveat is that all the cells except BSC-1 in this work were transiently transfected, and hence, expression levels of the target proteins were uncontrolled. This could affect either morphologies, such as the sizes of Rab5a-labeled endosomes (Fig. 4, A to C, and figs. S38 and S39) (51), or dynamic phenotypes, such as the growth rate of membrane ruffles in mCherry- α -actinin-expressing cells (Fig. 4E, Movie 9, and movie S15). Although endogenous expression levels can be achieved with genome editing (52), even more light or longer exposures would be needed for cases in which these levels are lower than those used here. Thus, the biological findings described in this work should not be considered definitive. More extensive measurements across multiple cell lines with careful controls and targeted perturbation experiments will be needed to reach conclusive insights.

The lesson is that when addressing any biological question by means of live-cell imaging, it is prudent to start with less invasive, lower-resolution methods such as widefield, spinning disk confocal, or lattice light sheet microscopy and move progressively only as needed to more invasive, higher-resolution methods such as 3D-SIM, TIRF-SIM, PA NL-SIM, and last, localization microscopy. Seen from this perspective, the two extended-resolution methods of high-NA TIRF-SIM and PA NL-SIM we introduce here fill an important gap between the 100-nm limit of traditional SIM and the macromolecular level of localization microscopy. Together, they open the door to high-resolution, minimally invasive studies of dynamic processes, including endocytosis, exocytosis, signal transduction, protein diffusion, vesicle trafficking, viral entry, cytoskeletal remodeling, interactions with the extracellular matrix, and the evolution of lipid rafts.

Materials and methods

Optical path of the TIRF-SIM system

The schematic of TIRF-SIM system is presented in fig. S47A. The beam from a laser combiner

equipped with 405 nm (250 mW, RPMC, Oxixus LBX-405-300-CIR-PP), 488 nm (500mW, Coherent, SAPPHIRE 488-500), and 560 nm (1W, MPB Communications, 2RU-VFL-P-1000-560-BIR) lasers is passed through an acousto-optic tunable filter (AOTF; AA Quanta Tech, AOTFnc-400.650-TN). The beam is then expanded to a $1/e^2$ diameter of 12 mm and sent to a phase-only modulator (13) consisting of a polarizing beam splitter, a achromatic half-wave plate (HWP; Bolder Vision Optik, BVO AHWP3), and a ferroelectric spatial light modulator (SLM; Forth Dimension Displays, SXGA-3DM). Light diffracted by the grating pattern displayed on SLM passes through a polarization rotator (15) consisting of a liquid crystal cell (LC; Meadowlark, SWIFT) and an achromatic quarter-wave plate (QWP; Bolder Vision Optik, BVO AQWP3), which rotates the linear polarization of the diffracted light so as to maintain the *s*-polarization necessary to maximize the pattern contrast for all pattern orientations. A mask consisting of a hollow barrel with slots for different pattern orientations (15) is driven by a galvanometric scanner (Cambridge Technology, 6230HB) to filter out all diffraction orders created by the binary and pixelated nature of the SLM except for the desired ± 1 diffraction orders. These are then imaged at the back focal plane of the objective (Olympus APON 100XHOTIRF 1.7 NA for high-NA TIRF-SIM, Olympus, UAPON 100XOTIRF 1.49 NA for PA NL-SIM at 23°C, or Zeiss Plan-Apochromat 100X Oil-HI 1.57 NA for high-NA PA-NL-SIM at 37°C) as two spots at opposite sides of the pupil. After passage through the objective, the two beams intersect at the interface between the coverslip and the sample at an angle exceeding the critical angle for total internal reflection. An evanescent standing wave penetrating ~ 100 nm into the sample is thereby generated, consisting of a sinusoidal pattern of excitation intensity that is a low-pass filtered image of the SLM pattern. The period, orientation, and relative phase of this excitation pattern can be finely tuned by altering the corresponding pattern displayed on SLM. For each orientation and phase of the applied excitation pattern, the resulting fluorescence is collected by the objective, focused by a tube lens at an intermediate image plane, separated from excitation light by a dichroic mirror (Chroma, ZT405/488/560 tpc. 22.5deg) placed between two relay lenses, and reimaged onto a sCMOS camera (Hamamatsu, Orca Flash 4.0 v2 sCMOS), where the structured fluorescence emission pattern is recorded.

Calibration of pattern overlap for PA NL-SIM

In order to maximize the amplitudes of the nonlinear harmonics for PA NL-SIM to work efficiently, the sinusoidal patterns of 405 nm activation light and 488 nm excitation and deactivation light must be aligned to precisely overlap one another. As noted above, these patterns at the sample plane are created by displaying corresponding binary grating patterns on an SLM at a corresponding optically conjugate plane. In this case,

the period p_s at the specimen is related to the period p_{SLM} at the SLM by

$$p_s = M_\lambda \cdot p_{\text{SLM}} \quad (1)$$

where M is the demagnification factor between the two conjugate planes and is dictated to be the focal lengths of the relay lenses between the two planes. Unfortunately, chromatic aberration leads to slightly different focal lengths for even achromatic relay lenses for different wavelengths of light. In particular, in our system, M_{405} and M_{488} vary by $\sim 2\%$. Considering that the sinusoidal interference pattern is composed of hundreds of periods across our 45- by 45- μm^2 field-of-view (FOV), even this 2% difference results in substantial drift in the relative phases of the 405- and 488-nm excitation patterns across the FOV (fig. S48, A to C), leading to spatially variable amplitudes for the nonlinear harmonics and corresponding spatially variable errors in the resulting SIM reconstructions.

A straightforward way to compensate for chromatic aberration and achieve identical periods $p_{s,405} = p_{s,488}$ at the sample (fig. S47B) is to introduce a period difference Δp_{SLM} between the two corresponding patterns at the SLM (fig. S47C). In fact, in order to compensate completely and achieve well-overlapped 405- and 488-nm excitation patterns over the whole FOV, we need to measure two parameters: the initial period difference at the sample, $\Delta p_s^i = \Delta p_{s,488}^i - \Delta p_{s,405}^i$, when p_{SLM} is the same for both wavelengths; and the phase difference, $\Delta \phi_s^i = \Delta \phi_{s,488}^i - \Delta \phi_{s,405}^i$, when p_s is the same. Do to so, we used a sample consisting of a dense but submonolayer spread of green fluorescent beads excitable at both 405 and 488 nm and proceeded as follows.

Step 1

Keeping p_{SLM} constant, we acquired five images each of the sample under 405- and 488-nm sinusoidal excitation, with the phase shifted by $p_{\text{SLM}}/5$ for each image at a given wavelength. We then applied the structured illumination (SI) reconstruction algorithm (53) to each set of five images, from which $p_{s,405}^i$ and $p_{s,488}^i$ emerged as measured outputs. For a given period $p_{\text{SLM},488}$ used at the SLM for 488-nm excitation, the corresponding period $p_{\text{SLM},405}$ needed at the SLM for 405-nm excitation to produce the same period p_s at the sample for both wavelengths is then given by

$$p_{\text{SLM},405} = \left(\frac{p_{s,488}^i}{p_{s,405}^i} \right) p_{\text{SLM},488} \quad (2)$$

Step 2

After adjusting $p_{\text{SLM},405}$ and $p_{\text{SLM},488}$ to obtain the same period p_s at the sample for both wavelengths, a constant phase offset exists between the two sinusoidal illumination patterns across the FOV (fig. S48, D and E). We measured the phase ϕ for each wavelength by applying the sinusoidal illumination for that wavelength and then recorded the position x_n along the modulation direction and intensity I_n for each of N beads scattered across the FOV. We then fit the

function $I(x) = I_{\max}[1 + \sin(2\pi x/p_s + \phi)]/2$ to this data to find ϕ (fig. S48F). A phase shift $\Delta\phi = \phi_{488} - \phi_{405}$ was then applied the SLM pattern for the 405-nm illumination so as to bring it into phase with the 488-nm illumination at the specimen (figs. S48, G to I).

Step 3

Last, we confirmed that both the period and phase of the sinusoidal illumination patterns at the two wavelengths match across the entire FOV by remeasuring the periods $p_{s,488}$, $p_{s,405}$ and the phases ϕ_{488} , ϕ_{405} as described above and confirming that they are identical.

SLM pattern generation

We generated the sinusoidal illumination patterns using a binary ferroelectric SLM (Forth Dimension Displays, SXGA-3DM) because it has the submillisecond switching times needed to acquire the nine (TIRF-SIM), 25 (PA NL-SIM), or more (saturated PA NL-SIM) raw images of different phase and orientation required to reconstruct a single SIM image in as fast as 100 to 400 ms. However, care must be taken to account for the finite pixel size of the SLM, especially considering that subpixel adjustment accuracy is necessary to achieve precise pattern overlap at 405 and 488 nm, as described in the previous section. The SLM pattern-generation algorithms used in previous work (13–15) do not provide such subpixel accuracy. Thus, in this work, we developed a new algorithm that matches the two pattern periods to 0.02% precision, leading to a phase error no greater than 1.8° over the $45\text{-}\mu\text{m}$ FOV.

In detail, a set of radial vectors $\{\mathbf{A}_n\}$ define the desired orientations of the grating pattern at the SLM. The angular orientation of this radial set relative to the x and y axes defined by pixel rows and columns of the SLM is chosen so that each vector is at least 4° away from either axis. This is essential to achieve subpixel precision in the adjustment of the period. For each orientation represented by \mathbf{A}_n , we define a vector \mathbf{B}_n that is orthogonal to \mathbf{A}_n (fig. S49). Likewise, for every pixel of the SLM we define a pixel vector (such as $\mathbf{C1}$ or $\mathbf{C2}$ in fig. S49) from the point O at the intersection of \mathbf{A}_n and \mathbf{B}_n to the pixel. We then calculate $F = [(\mathbf{C} \cdot \mathbf{B}) \bmod p]/p$, the fraction of the period p by which the pixel extends beyond an integral number of periods on the SLM. For a pattern with a desired off fraction D per period ($D = 0.5$ in 2D SIM), the pixel is set to 0 if $F < D$ and set to 1 otherwise. Last, to define the pixel patterns required for the other $N - 1$ phases of the illumination for a given orientation, the point O is translated along \mathbf{B}_n in steps of p/N , and this process is repeated with the new vector \mathbf{C} for each pixel. Unlike the pixel assignment algorithm used previously for SIM (15), this approach does not rely on unit-cell repetition and therefore does not succumb to error accumulation over the entire span of the SLM.

Lattice light sheet PA NL-SIM system

To extend PA NL-SIM to three dimensions, it is essential to minimize out-of-focus fluorescence

emission that can cause the shot noise in the DC harmonic to completely overwhelm the weak signals in the nonlinear harmonics. To accomplish this, we turned to the SIM mode of lattice light sheet microscopy (42). Just as in the case of 2D-SIM, and for the same reasons, we choose to introduce the nonlinear harmonics through patterned activation of SkyScan-NS. The excitation objective (Special Optics, 0.65 NA, 3.74 mm WD) is placed perpendicular to the detection objective (Nikon, CFI Apo LWD 25XW, 1.1 NA, 2 mm WD) to confine the illumination to the proximity of the latter's focal plane (fig. S42A). The lattice pattern projected on the SLM (Forth Dimension Displays, SXGA-3DM) is imaged onto the focal plane of the excitation objective, after the excitation is first spatially filtered by an annular mask (Photo-Science) and relayed by a pair of galvanometers (Cambridge Technology, 6215H) that phase step the pattern in the x direction and scan the light sheet in z . Also as in 2D PA NL-SIM, we match the periods and phases of the 405- and 488-nm lattices to exactly match by measuring their excitation profiles across the FOV using fluorescent beads (fig. S42B) and adjusting accordingly. The fluorescence emission is collected by the detection objective and imaged by a tube lens onto a sCMOS camera (Hamamatsu Orca Flash 4.0 v2). A 3D image is formed by repeating this process as the sample is translated through the light sheet with a piezoelectric stage (Physik Instrumente, P-621.1CD) along an axis s in the plane of the cover slip, and a 3D super-resolution NL-SIM image is reconstructed as described below.

Data acquisition

High-NA TIRF SIM

All high-NA TIRF-SIM images were acquired with the Olympus 1.7-NA objective under the physiological conditions of 37°C and 5% CO_2 . At each time point, we acquired three raw images at successive phase steps of 0, $1/3$, and $2/3$ of the illumination period. We then repeated this process with the standing wave excitation pattern rotated $\pm 120^\circ$ with respect to the first orientation, for a total of nine raw images. The phase stepping and pattern rotation were accomplished by rotating or translating the binary grating pattern displayed on the SLM. For multicolor imaging, we acquired nine raw images at each excitation wavelength before moving to the next and then repeated this series at successive time points. We could adjust the excitation NA for each wavelength by changing the period of the grating pattern at the SLM. This allowed us to control penetration depth of the evanescent wave (fig. S8) in order to balance the number of excitable fluorescent molecules against the background fluorescence and possible physiological effects of the excitation.

PA NL-SIM and saturated PA NL-SIM

The high refractive index immersion oil required for the Olympus 1.7-NA objective strongly absorbs 405-nm light, leading to a substantial reduction in the modulation depth we could achieve in the activation pattern at this wavelength. Conse-

quently, for NL-SIM we first turned to the Olympus 1.49-NA TIRF objective and imaged at room temperature (23°C) with LI5 medium, without phenol red having 10% fetal bovine serum (Life Technologies). With this objective, we were able to achieve high modulation contrast while stably and precisely overlapping the 405- and 488-nm standing waves over the whole FOV. An excitation NA of 1.44 was used for both 488- and 560-nm light in this case, leading to 62-nm resolution for PA NL-SIM when using green-emitting FPs. Recently, however, we found that the high refractive index immersion oil used for the Zeiss 1.57-NA objective did not absorb 405-nm light strongly and therefore could be used to maintain precisely overlapped 405- and 488-nm standing waves with high modulation contrast at 37°C and 5% CO_2 . The excitation NA in this case was 1.52 for 488-nm light, leading to 59-nm resolution for PA NL-SIM when using green-emitting FPs.

The exposure procedure for a single phase step in NL-SIM consists of (i) 405-nm patterned illumination for 1 ms to activate the fluorescent molecules; (ii) 488-nm patterned illumination for 5 to ~ 30 ms to read-out the activated molecules; and (iii) 488-nm uniform illumination for 2 to ~ 10 ms to read-out the remaining activated molecules and return the sample back to the original unactivated state. We collected the fluorescence from both steps (ii) and (iii) to reconstruct the SR image. Depending on the number of modulation harmonics H of non-negligible amplitude in the image ($H = 2$ for PA-NL-SIM and $H = 3$ or possibly more for saturated PA NL-SIM), we repeated this sequence for $2H + 1$ raw images at each of $2H + 1$ angular orientations equally spaced around 360° for a total of $(2H + 1)^2$ raw images at each NL-SIM time point. An exception was saturated PA-NL-SIM, for which to reduce the acquisition time, we often used only five orientations rather than seven.

In two-color imaging combining linear TIRF-SIM and PA NL-SIM (Fig. 4), at each time point we acquired the PA NL-SIM image as discussed above. However, we acquired the TIRF-SIM image with five instead of three orientations (15 raw images for the TIRF-SIM channel at every time point) in order to match the orientations of the five-slot, galvanometer-driven barrel mask used to pick out the desired diffraction orders for the PA NL-SIM acquisition.

3D PA NL-SIM with lattice light sheet microscopy

Here, we used a hexagonal lattice having a period large enough to contain two harmonics for each of the 405-nm activation and the 488-nm excitation (42)—one harmonic just below the Abbe limit of the 0.65-NA excitation objective, and the other at twice this period. The product of these patterns created a fluorescence emission pattern containing $H = 4$ harmonics (fig. S43F). However, with a single excitation objective, we were limited to producing this pattern at only one orientation. Therefore, at each plane of the 3D stack, we acquired $2H + 1 = 9$ images, resulting in improved resolution (Fig. 5)

in both the lateral and axial directions of the pattern.

Reconstruction of SIM images

The raw image frames with patterned excitation were processed and reconstructed into the super-resolved images by means of a previously described algorithm (53). In brief, for each pattern orientation with H modulation harmonics, $2H + 1$ raw images are collected and Fourier transformed into $2H + 1$ information components. These components are assembled by initially translating each in Fourier space by a distance equal to the amplitude of the illumination pattern vector $n\mathbf{k}_0$, where \mathbf{k}_0 is the spatial frequency of the illumination pattern and $n = -H$ to H . The pattern vector of each information component is then fine-tuned by finding the vector that maximizes the complex cross-correlation in the overlap region between successive components. The modulation amplitude of the harmonic and its starting phase are found through complex linear regression. In line with previous work (28), the modulation amplitudes for the highest harmonics are generally too low for this empirical approach to work well, so for these, the theoretical values of their complex amplitudes are used. After fine-tuning the positions and complex amplitudes of the information components in the overlap regions, a generalized Wiener filter is applied to this expanded transfer function to balance the amplitudes of the various spatial frequencies against the underlying noise. Next, an apodization function is applied to minimize ringing artifacts when the result is Fourier-transformed back to real space. However, rather than the triangle apodization $A(k) = 1 - k/k_{\max}$ normally used (53), we applied a γ apodization $A(k) = 1 - (k/k_{\max})^\gamma$, usually with $\gamma = 0.4$, so that the higher spatial frequencies are not suppressed more than necessary. Furthermore, we strictly followed the azimuthally dependent support $k_{\max}(\theta)$ of the expanded OTF (figs. S7 and S30) to define the endpoint of the apodization function. This provides additional suppression of ringing artifacts. For the time series data, we independently implement this reconstruction process for each time point.

Cell culture, transfection, staining, and fixation

BSC-1, COS-7, U2OS, and mouse embryonic fibroblast (MEF) cells (American Type Culture Collection) were grown to ~60 to 80% confluency in Dulbecco's modified eagle medium (DMEM) with high glucose and no phenol red supplemented with 15% fetal bovine serum (Life Technologies). BSC-1 cells stably expressed EGFP-CLTA. Other cells were transiently transfected with an Amara Nucleofector 96-well shuttle system (Lonza) with 1 μ g DNA per 400,000 cells with nucleofection solution and a program optimized for each cell line per the manufactures instructions. Before imaging, 25-mm or 5-mm coverslips were coated with 10 μ g/ml fibronectin (Millipore, FC010) for 24 hours before plating transfected cells. Imaging was performed in DMEM with HEPES if there is no CO₂ control containing no phenol red at temperatures specifically stated in each case.

In two-color imaging of CCPs and transferrin receptors (TfRs) by means of high-NA TIRF-SIM, MEF cells expressing clathrin light chain B fused to the C terminal of mEmerald were incubated with DMEM medium containing 250 μ g/mL TfR bound to human transferrin conjugated with Alexa 568 (T23365, Life Technologies) for 15 min.

Fixed cells were treated for 15 min with fixation buffer containing 4% paraformaldehyde, 0.1% glutaraldehyde in PHEM buffer (25 mM HEPES, 10 mM EGTA, 2 mM MgCl₂, and 120 mM PIPES in pH 7.3).

Tracking analysis of CCPs

For each image frame, we segmented the CCPs using a watershed algorithm written in Matlab (MathWorks, 2014a) and measured their centroids individually. Subsequently, the centroid position was linked between time points using u-track 2.1 (54). This linking operation collected successive position information for each pit over the entire endocytic process (Fig. 2E) from initiation to final internalization. It was then straightforward to determine the lifetime (Fig. 2A) for each endocytic event.

In order to precisely measure the pit diameter (Fig. 2, B and C), we first measured the system magnification to the camera by imaging a standard fine counting grid (2280-32, Ted Pella). The SIM image of each CCP was then deconvolved with the equivalent PSF of the SIM system to compensate for the broadening due to the finite resolution of the instrument. Last, we measured the diameter of each deconvolved pit using an intensity-weighted average radius relative to the centroid of the pit. In certain cases (Fig. 2A and Movie 3), pits were color-coded at each time point based on the time since their initiation to the current time point.

One challenge in this analysis was how to identify isolated pits rather than aggregates and how to be sure that these represented true pits rather than noise or disorganized patches of nonassembled clathrin. To accomplish this, we set some conditions during the analysis, such as that a pit must start as a spot and then evolve into a ring at at least one time point. When analyzing the correlation between pit lifetime and maximum diameter, we added the further constraint of including only those pits formed after the first frame in order to insure that we could accurately measure the entire lifetime.

When measuring the associations of actin with clathrin, we first implemented the tracking algorithm above to obtain time-lapse CCP images for each endocytic event. We then created a mask for each CCP identified in each frame, equal to the CCP size plus an additional boundary of one pixel. We then applied these masks to each frame of Lifeact data and integrated the actin fluorescence within each CCP-derived mask. If the actin signal integrated over the area of a given mask increased during the final five frames of the life of the associated CCP, it was decided that actin was recruited to the CCP during the final stage of endocytosis.

REFERENCES AND NOTES

1. L. Schermelleh, R. Heintzmann, H. Leonhardt, A guide to super-resolution fluorescence microscopy. *J. Cell Biol.* **190**, 165–175 (2010). doi: [10.1083/jcb.201002018](https://doi.org/10.1083/jcb.201002018); pmid: [20643879](https://pubmed.ncbi.nlm.nih.gov/20643879/)
2. U. Schnell, F. Dijk, K. A. Sjollema, B. N. Giepmans, Immunolabeling artifacts and the need for live-cell imaging. *Nat. Methods* **9**, 152–158 (2012). doi: [10.1038/nmeth.1855](https://doi.org/10.1038/nmeth.1855); pmid: [22290187](https://pubmed.ncbi.nlm.nih.gov/22290187/)
3. R. P. Nieuwenhuizen et al., Measuring image resolution in optical nanoscopy. *Nat. Methods* **10**, 557–562 (2013). doi: [10.1038/nmeth.2448](https://doi.org/10.1038/nmeth.2448); pmid: [23624665](https://pubmed.ncbi.nlm.nih.gov/23624665/)
4. X. Shu et al., A genetically encoded tag for correlated light and electron microscopy of intact cells, tissues, and organisms. *PLoS Biol.* **9**, e1001041 (2011). doi: [10.1371/journal.pbio.1001041](https://doi.org/10.1371/journal.pbio.1001041); pmid: [21483721](https://pubmed.ncbi.nlm.nih.gov/21483721/)
5. J. D. Martell et al., Engineered ascorbate peroxidase as a genetically encoded reporter for electron microscopy. *Nat. Biotechnol.* **30**, 1143–1148 (2012). doi: [10.1038/nbt.2375](https://doi.org/10.1038/nbt.2375); pmid: [23086203](https://pubmed.ncbi.nlm.nih.gov/23086203/)
6. H. Shroff, C. G. Galbraith, J. A. Galbraith, E. Betzig, Live-cell photoactivated localization microscopy of nanoscale adhesion dynamics. *Nat. Methods* **5**, 417–423 (2008). doi: [10.1038/nmeth.1202](https://doi.org/10.1038/nmeth.1202); pmid: [18408726](https://pubmed.ncbi.nlm.nih.gov/18408726/)
7. S. H. Shim et al., Super-resolution fluorescence imaging of organelles in live cells with photoswitchable membrane probes. *Proc. Natl. Acad. Sci. U.S.A.* **109**, 13978–13983 (2012). doi: [10.1073/pnas.1201882109](https://doi.org/10.1073/pnas.1201882109); pmid: [22891300](https://pubmed.ncbi.nlm.nih.gov/22891300/)
8. B. Hein, K. I. Willig, S. W. Hell, Stimulated emission depletion (STED) nanoscopy of a fluorescent protein-labeled organelle inside a living cell. *Proc. Natl. Acad. Sci. U.S.A.* **105**, 14271–14276 (2008). doi: [10.1073/pnas.0807705105](https://doi.org/10.1073/pnas.0807705105); pmid: [18796604](https://pubmed.ncbi.nlm.nih.gov/18796604/)
9. V. Westphal et al., Video-rate far-field optical nanoscopy dissects synaptic vesicle movement. *Science* **320**, 246–249 (2008). doi: [10.1126/science.1154228](https://doi.org/10.1126/science.1154228); pmid: [18292304](https://pubmed.ncbi.nlm.nih.gov/18292304/)
10. T. Grotjohann et al., rsEGFP2 enables fast RESOLFT nanoscopy of living cells. *eLife* **1**, e00248 (2012). doi: [10.7554/eLife.00248](https://doi.org/10.7554/eLife.00248); pmid: [23330067](https://pubmed.ncbi.nlm.nih.gov/23330067/)
11. A. Chmyrov et al., Nanoscopy with more than 100,000 'doughnuts'. *Nat. Methods* **10**, 737–740 (2013). doi: [10.1038/nmeth.2556](https://doi.org/10.1038/nmeth.2556); pmid: [23832150](https://pubmed.ncbi.nlm.nih.gov/23832150/)
12. Materials and methods are available as supplementary materials on Science Online.
13. P. Kner, B. B. Chhun, E. R. Griffis, L. Winoto, M. G. Gustafsson, Super-resolution video microscopy of live cells by structured illumination. *Nat. Methods* **6**, 339–342 (2009). doi: [10.1038/nmeth.1324](https://doi.org/10.1038/nmeth.1324); pmid: [19404253](https://pubmed.ncbi.nlm.nih.gov/19404253/)
14. L. Shao, P. Kner, E. H. Rego, M. G. Gustafsson, Super-resolution 3D microscopy of live whole cells using structured illumination. *Nat. Methods* **8**, 1044–1046 (2011). doi: [10.1038/nmeth.1734](https://doi.org/10.1038/nmeth.1734); pmid: [22002026](https://pubmed.ncbi.nlm.nih.gov/22002026/)
15. R. Fiolka, L. Shao, E. H. Rego, M. W. Davidson, M. G. Gustafsson, Time-lapse two-color 3D imaging of live cells with doubled resolution using structured illumination. *Proc. Natl. Acad. Sci. U.S.A.* **109**, 5311–5315 (2012). doi: [10.1073/pnas.1119262109](https://doi.org/10.1073/pnas.1119262109); pmid: [22431626](https://pubmed.ncbi.nlm.nih.gov/22431626/)
16. J. Riedl et al., Lifeact: A versatile marker to visualize F-actin. *Nat. Methods* **5**, 605–607 (2008). doi: [10.1038/nmeth.1220](https://doi.org/10.1038/nmeth.1220); pmid: [18536722](https://pubmed.ncbi.nlm.nih.gov/18536722/)
17. H. T. McMahon, E. Boucrot, Molecular mechanism and physiological functions of clathrin-mediated endocytosis. *Nat. Rev. Mol. Cell Biol.* **12**, 517–533 (2011). doi: [10.1038/nrm3151](https://doi.org/10.1038/nrm3151); pmid: [21779028](https://pubmed.ncbi.nlm.nih.gov/21779028/)
18. M. Ehrlich et al., Endocytosis by random initiation and stabilization of clathrin-coated pits. *Cell* **118**, 591–605 (2004). doi: [10.1016/j.cell.2004.08.017](https://doi.org/10.1016/j.cell.2004.08.017); pmid: [15339664](https://pubmed.ncbi.nlm.nih.gov/15339664/)
19. I. Gaidarov, F. Santini, R. A. Warren, J. H. Keen, Spatial control of coated-pit dynamics in living cells. *Nat. Cell Biol.* **1**, 1–7 (1999). pmid: [10559856](https://pubmed.ncbi.nlm.nih.gov/10559856/)
20. S. Saffarian, E. Cocucci, T. Kirchhausen, Distinct dynamics of endocytic clathrin-coated pits and coated plaques. *PLoS Biol.* **7**, e1000191 (2009). doi: [10.1371/journal.pbio.1000191](https://doi.org/10.1371/journal.pbio.1000191); pmid: [19809571](https://pubmed.ncbi.nlm.nih.gov/19809571/)
21. J. Grove et al., Flat clathrin lattices: Stable features of the plasma membrane. *Mol. Biol. Cell* **25**, 3581–3594 (2014). doi: [10.1091/mbc.E14-06-1154](https://doi.org/10.1091/mbc.E14-06-1154); pmid: [25165141](https://pubmed.ncbi.nlm.nih.gov/25165141/)
22. J. Heuser, Effects of cytoplasmic acidification on clathrin lattice morphology. *J. Cell Biol.* **108**, 401–411 (1989). doi: [10.1083/jcb.108.2.401](https://doi.org/10.1083/jcb.108.2.401); pmid: [2563729](https://pubmed.ncbi.nlm.nih.gov/2563729/)
23. M. Kaksonen, C. P. Toret, D. G. Drubin, Harnessing actin dynamics for clathrin-mediated endocytosis. *Nat. Rev. Mol. Cell Biol.* **7**, 404–414 (2006). doi: [10.1038/nrm1940](https://doi.org/10.1038/nrm1940); pmid: [16723976](https://pubmed.ncbi.nlm.nih.gov/16723976/)

24. D. K. Cureton, R. H. Massol, S. Saffarian, T. L. Kirchhausen, S. P. Whelan, Vesicular stomatitis virus enters cells through vesicles incompletely coated with clathrin that depend upon actin for internalization. *PLOS Pathog.* **5**, e1000394 (2009). doi: [10.1371/journal.ppat.1000394](https://doi.org/10.1371/journal.ppat.1000394); pmid: [19390604](https://pubmed.ncbi.nlm.nih.gov/19390604/)
25. S. Boulant, C. Kural, J. C. Zeeh, F. Ubelmann, T. Kirchhausen, Actin dynamics counteract membrane tension during clathrin-mediated endocytosis. *Nat. Cell Biol.* **13**, 1124–1131 (2011). doi: [10.1038/ncb2307](https://doi.org/10.1038/ncb2307); pmid: [21841790](https://pubmed.ncbi.nlm.nih.gov/21841790/)
26. A. I. Shevchuk *et al.*, An alternative mechanism of clathrin-coated pit closure revealed by ion conductance microscopy. *J. Cell Biol.* **197**, 499–508 (2012). doi: [10.1083/jcb.201109130](https://doi.org/10.1083/jcb.201109130); pmid: [22564416](https://pubmed.ncbi.nlm.nih.gov/22564416/)
27. R. Heintzmann, T. M. Jovin, C. Cremer, Saturated patterned excitation microscopy—a concept for optical resolution improvement. *J. Opt. Soc. Am. A Opt. Image Sci. Vis.* **19**, 1599–1609 (2002). doi: [10.1364/JOSAA.19.001599](https://doi.org/10.1364/JOSAA.19.001599); pmid: [12152701](https://pubmed.ncbi.nlm.nih.gov/12152701/)
28. M. G. Gustafsson, Nonlinear structured-illumination microscopy: Wide-field fluorescence imaging with theoretically unlimited resolution. *Proc. Natl. Acad. Sci. U.S.A.* **102**, 13081–13086 (2005). doi: [10.1073/pnas.0406877102](https://doi.org/10.1073/pnas.0406877102); pmid: [16141335](https://pubmed.ncbi.nlm.nih.gov/16141335/)
29. E. H. Rego *et al.*, Nonlinear structured-illumination microscopy with a photoswitchable protein reveals cellular structures at 50-nm resolution. *Proc. Natl. Acad. Sci. U.S.A.* **109**, E135–E143 (2012). doi: [10.1073/pnas.1107547108](https://doi.org/10.1073/pnas.1107547108); pmid: [22160683](https://pubmed.ncbi.nlm.nih.gov/22160683/)
30. X. Zhang *et al.*, Development of a reversibly switchable fluorescent protein for super-resolution optical fluctuation imaging (SOFI). *ACS Nano* **9**, 2659–2667 (2015). doi: [10.1021/nn5064387](https://doi.org/10.1021/nn5064387); pmid: [25695314](https://pubmed.ncbi.nlm.nih.gov/25695314/)
31. K. Xu, H. P. Babcock, X. Zhuang, Dual-objective STORM reveals three-dimensional filament organization in the actin cytoskeleton. *Nat. Methods* **9**, 185–188 (2012). doi: [10.1038/nmeth.1841](https://doi.org/10.1038/nmeth.1841); pmid: [22231642](https://pubmed.ncbi.nlm.nih.gov/22231642/)
32. R. G. Parton, K. Simons, The multiple faces of caveolae. *Nat. Rev. Mol. Cell Biol.* **8**, 185–194 (2007). doi: [10.1038/nrm2122](https://doi.org/10.1038/nrm2122); pmid: [17318224](https://pubmed.ncbi.nlm.nih.gov/17318224/)
33. F. Lavoie-Cardinal *et al.*, Two-color RESOLFT nanoscopy with green and red fluorescent photochromic proteins. *ChemPhysChem* **15**, 655–663 (2014). doi: [10.1002/cphc.201301016](https://doi.org/10.1002/cphc.201301016); pmid: [24449030](https://pubmed.ncbi.nlm.nih.gov/24449030/)
34. R. G. Parton, M. Hanzal-Bayer, J. F. Hancock, Biogenesis of caveolae: A structural model for caveolin-induced domain formation. *J. Cell Sci.* **119**, 787–796 (2006). doi: [10.1242/jcs.02853](https://doi.org/10.1242/jcs.02853); pmid: [16495479](https://pubmed.ncbi.nlm.nih.gov/16495479/)
35. E. Boucrot, M. T. Howes, T. Kirchhausen, R. G. Parton, Redistribution of caveolae during mitosis. *J. Cell Sci.* **124**, 1965–1972 (2011). doi: [10.1242/jcs.076570](https://doi.org/10.1242/jcs.076570); pmid: [21625007](https://pubmed.ncbi.nlm.nih.gov/21625007/)
36. M. Jovic, M. Sharma, J. Rahajeng, S. Caplan, The early endosome: A busy sorting station for proteins at the crossroads. *Histol. Histopathol.* **25**, 99–112 (2010). pmid: [19924646](https://pubmed.ncbi.nlm.nih.gov/19924646/)
37. J. Tooze, M. Hollinshead, In AtT20 and HeLa cells brefeldin A induces the fusion of tubular endosomes and changes their distribution and some of their endocytic properties. *J. Cell Biol.* **118**, 813–830 (1992). doi: [10.1083/jcb.118.4.813](https://doi.org/10.1083/jcb.118.4.813); pmid: [1500425](https://pubmed.ncbi.nlm.nih.gov/1500425/)
38. E. Nielsen, F. Severin, J. M. Backer, A. A. Hyman, M. Zerial, Rab5 regulates motility of early endosomes on microtubules. *Nat. Cell Biol.* **1**, 376–382 (1999). doi: [10.1038/14075](https://doi.org/10.1038/14075); pmid: [10559966](https://pubmed.ncbi.nlm.nih.gov/10559966/)
39. C. A. Otey, O. Carpen, Alpha-actinin revisited: A fresh look at an old player. *Cell Motil. Cytoskeleton* **58**, 104–111 (2004). doi: [10.1002/cm.20007](https://doi.org/10.1002/cm.20007); pmid: [15083532](https://pubmed.ncbi.nlm.nih.gov/15083532/)
40. C. K. Choi *et al.*, Actin and alpha-actinin orchestrate the assembly and maturation of nascent adhesions in a myosin II motor-independent manner. *Nat. Cell Biol.* **10**, 1039–1050 (2008). doi: [10.1038/ncb1763](https://doi.org/10.1038/ncb1763); pmid: [19160484](https://pubmed.ncbi.nlm.nih.gov/19160484/)
41. M. Mavrakakis *et al.*, Septins promote F-actin ring formation by crosslinking actin filaments into curved bundles. *Nat. Cell Biol.* **16**, 322–334 (2014). doi: [10.1038/ncb2921](https://doi.org/10.1038/ncb2921); pmid: [24633326](https://pubmed.ncbi.nlm.nih.gov/24633326/)
42. B. C. Chen *et al.*, Lattice light-sheet microscopy: Imaging molecules to embryos at high spatiotemporal resolution. *Science* **346**, 1257998 (2014). doi: [10.1126/science.1257998](https://doi.org/10.1126/science.1257998); pmid: [25342811](https://pubmed.ncbi.nlm.nih.gov/25342811/)
43. A. Legesse-Miller, R. H. Massol, T. Kirchhausen, Constriction and Dnm1p recruitment are distinct processes in mitochondrial fission. *Mol. Biol. Cell* **14**, 1953–1963 (2003). doi: [10.1091/mbc.E02-10-0657](https://doi.org/10.1091/mbc.E02-10-0657); pmid: [12802067](https://pubmed.ncbi.nlm.nih.gov/12802067/)
44. J. R. Friedman *et al.*, ER tubules mark sites of mitochondrial division. *Science* **334**, 358–362 (2011). doi: [10.1126/science.1207385](https://doi.org/10.1126/science.1207385); pmid: [21885730](https://pubmed.ncbi.nlm.nih.gov/21885730/)
45. B. Huang, S. A. Jones, B. Brandenburg, X. Zhuang, Whole-cell 3D STORM reveals interactions between cellular structures with nanometer-scale resolution. *Nat. Methods* **5**, 1047–1052 (2008). doi: [10.1038/nmeth.1274](https://doi.org/10.1038/nmeth.1274); pmid: [19029906](https://pubmed.ncbi.nlm.nih.gov/19029906/)
46. J. F. Presley *et al.*, ER-to-Golgi transport visualized in living cells. *Nature* **389**, 81–85 (1997). doi: [10.1038/38891](https://doi.org/10.1038/38891); pmid: [9288971](https://pubmed.ncbi.nlm.nih.gov/9288971/)
47. K. Hirschberg *et al.*, Kinetic analysis of secretory protein traffic and characterization of golgi to plasma membrane transport intermediates in living cells. *J. Cell Biol.* **143**, 1485–1503 (1998). doi: [10.1083/jcb.143.6.1485](https://doi.org/10.1083/jcb.143.6.1485); pmid: [9852146](https://pubmed.ncbi.nlm.nih.gov/9852146/)
48. C. J. R. Sheppard, Super-resolution in confocal imaging. *Optik (Stuttg.)* **80**, 53 (1988).
49. C. B. Müller, J. Enderlein, Image scanning microscopy. *Phys. Rev. Lett.* **104**, 198101 (2010). doi: [10.1103/PhysRevLett.104.198101](https://doi.org/10.1103/PhysRevLett.104.198101); pmid: [20867000](https://pubmed.ncbi.nlm.nih.gov/20867000/)
50. A. G. York *et al.*, Resolution doubling in live, multicellular organisms via multifocal structured illumination microscopy. *Nat. Methods* **9**, 749–754 (2012). doi: [10.1038/nmeth.2025](https://doi.org/10.1038/nmeth.2025); pmid: [22581372](https://pubmed.ncbi.nlm.nih.gov/22581372/)
51. R. L. Roberts *et al.*, Endosome fusion in living cells overexpressing GFP-rab5. *J. Cell Sci.* **112**, 3667–3675 (1999). pmid: [10523503](https://pubmed.ncbi.nlm.nih.gov/10523503/)
52. J. D. Sander, J. K. Joung, CRISPR-Cas systems for editing, regulating and targeting genomes. *Nat. Biotechnol.* **32**, 347–355 (2014). doi: [10.1038/nbt.2842](https://doi.org/10.1038/nbt.2842); pmid: [24584096](https://pubmed.ncbi.nlm.nih.gov/24584096/)
53. M. G. L. Gustafsson *et al.*, Three-dimensional resolution doubling in wide-field fluorescence microscopy by structured illumination. *Biophys. J.* **94**, 4957–4970 (2008). doi: [10.1529/biophysj.107.120345](https://doi.org/10.1529/biophysj.107.120345); pmid: [18326650](https://pubmed.ncbi.nlm.nih.gov/18326650/)
54. K. Jaqaman *et al.*, Robust single-particle tracking in live-cell time-lapse sequences. *Nat. Methods* **5**, 695–702 (2008). doi: [10.1038/nmeth.1237](https://doi.org/10.1038/nmeth.1237); pmid: [18641657](https://pubmed.ncbi.nlm.nih.gov/18641657/)

ACKNOWLEDGMENTS

We thank the Shared Resource teams at Janelia for their skill and dedication in specimen handling and preparation and the Instrument Design and Fabrication team for their manufacturing expertise. D.L., L.S., B.-C.C., and E.B. are funded by the Howard Hughes Medical Institute (HHMI). X.Z., M.Z., and P.X. are funded by the National Basic Research Program (973 Program) of China (2013CB910103), the National Natural Science Foundation of China (31370851), and the Beijing Natural Science Foundation, China (7131011). M.P. and T.K. were funded in part by NIH grant GM-075252. Skylar-NS is available from P.X. upon execution of a materials transfer agreement with the Institute of Biophysics. Other fluorescent protein constructs used in this work are from the Michael Davidson Collection and are available, along with sequence information, from Addgene (www.addgene.org/fluorescent-proteins/davidson). Researchers can apply to access the microscope as visitors through the Advanced Imaging Center at Janelia (www.janelia.org/open-science/advanced-imaging-center). Technical information for the construction of a copy of the microscope is available to nonprofit entities upon execution of a no-cost Research License with HHMI. Nonlinear SIM with patterned activation, in two or three dimensions, as described here is covered within U.S. provisional patent application 62/057,220 filed by E.B. and D.L. and assigned to HHMI.

SUPPLEMENTARY MATERIALS

www.sciencemag.org/content/349/6251/aab3500/suppl/DC1
Supplementary Text
Figs. S1 to S55
Table S1 and S2
References (55–68)
Movies S1 to S18

15 April 2015; accepted 20 July 2015
10.1126/science.aab3500

This copy is for your personal, non-commercial use only.

If you wish to distribute this article to others, you can order high-quality copies for your colleagues, clients, or customers by [clicking here](#).

Permission to republish or repurpose articles or portions of articles can be obtained by following the guidelines [here](#).

The following resources related to this article are available online at www.sciencemag.org (this information is current as of September 2, 2015):

Updated information and services, including high-resolution figures, can be found in the online version of this article at:

<http://www.sciencemag.org/content/349/6251/aab3500.full.html>

Supporting Online Material can be found at:

<http://www.sciencemag.org/content/suppl/2015/08/26/349.6251.aab3500.DC1.html>

A list of selected additional articles on the Science Web sites **related to this article** can be found at:

<http://www.sciencemag.org/content/349/6251/aab3500.full.html#related>

This article **cites 62 articles**, 20 of which can be accessed free:

<http://www.sciencemag.org/content/349/6251/aab3500.full.html#ref-list-1>

This article appears in the following **subject collections**:

Cell Biology

http://www.sciencemag.org/cgi/collection/cell_biol

REPORTS

SOLID-STATE PHYSICS

Scalable T^2 resistivity in a small single-component Fermi surface

Xiao Lin, Benoît Fauqué, Kamran Behnia*

Scattering among electrons generates a distinct contribution to electrical resistivity that follows a quadratic temperature (T) dependence. In strongly correlated electron systems, the prefactor A of this T^2 resistivity scales with the magnitude of the electronic specific heat, γ . Here we show that one can change the magnitude of A by four orders of magnitude in metallic strontium titanate (SrTiO_3) by tuning the concentration of the carriers and, consequently, the Fermi energy. The T^2 behavior persists in the single-band dilute limit despite the absence of two known mechanisms for T^2 behavior: distinct electron reservoirs and Umklapp processes. The results highlight the absence of a microscopic theory for momentum decay through electron-electron scattering in various Fermi liquids.

Warming a metal enhances its resistivity because scattering events along the trajectory of a charge-carrying electron become more frequent with increasing temperature (T). In most simple metals, the dominant mechanism is scattering by phonons, leading to a T^5 dependence of resistivity. In

1937, Baber identified electron-electron scattering as the origin of T^2 resistivity observed in many transition metals (1). During the past few decades, it has been firmly established that, at low temperatures, resistivity (ρ) in a Fermi liquid follows a quadratic temperature dependence expressed as $\rho = \rho_0 + AT^2$ (where A is the prefactor

of the T^2 resistivity) and that correlations among electrons enhance both A and the electronic specific heat, γ . This is often expressed through the Kadowaki-Woods ratio ($R_{\text{KW}} = A/\gamma^2$) ($2-6$), which links two distinct properties of a Fermi liquid, each set by the same material-dependent Fermi energy, E_F .

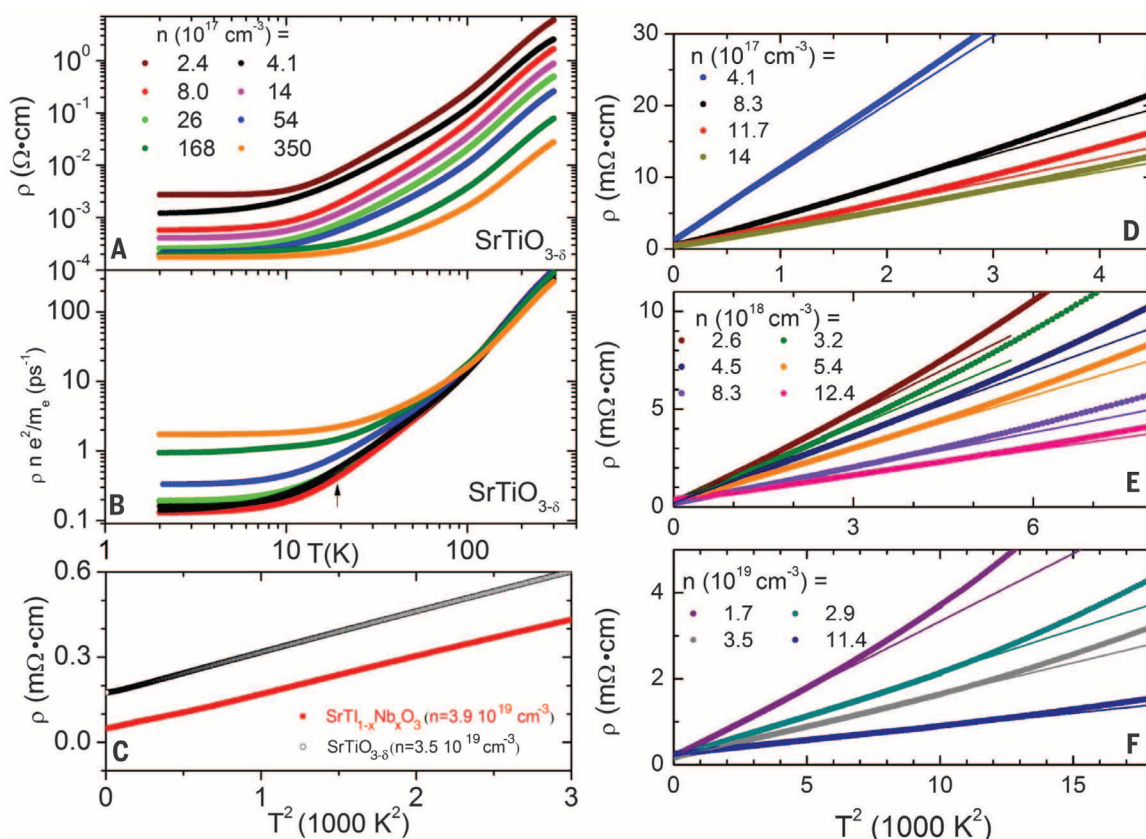
The Pauli exclusion principle is the ultimate reason behind both the T -linear specific heat and T -square resistivity in Fermi liquids. Electrons that give rise to both properties are those confined to a width of $k_B T/E_F$, where k_B is the Boltzmann constant. In the case of resistivity, this is true of both electrons participating in the scattering event, hence the exponent of two. However, electron-electron scattering alone does not generate a finite contribution to resistivity, because such a scattering event would conserve momentum with no decay in the charge current. The presence of an underlying lattice is required in any scenario for generating T^2 resistivity from electron-electron scattering. Dimensional considerations imply

$$A = \frac{\hbar}{e^2} \left(\frac{k_B}{E_F} \right)^2 \ell_{\text{quad}} \quad (1)$$

Laboratoire de Physique et Etude des Matériaux (CNRS/UPMC), Ecole Supérieure de Physique et de Chimie Industrielles, 10 Rue Vauquelin, F-75005 Paris, France.
*Corresponding author. E-mail: kamran.behnia@espci.fr

Fig. 1. Doping and temperature dependence of resistivity in n-doped SrTiO_3 .

(A) Evolution of resistivity in $\text{SrTiO}_{3-\delta}$ with doping across two orders of carrier density. (B) The product of resistivity and carrier density yields the scattering rate, which does not depend on carrier concentration above 100 K. (C) Resistivity plotted as a function of T^2 in oxygen-deficient and Nb-doped SrTiO_3 samples of comparable carrier concentration displays the same slope but different intercepts. (D to F) Resistivity versus T^2 in $\text{SrTiO}_{3-\delta}$ as the carrier density changes by two orders of magnitude. Straight solid lines represent the best fits to low-temperature data. As doping increases, the slope gradually decreases, and the upward deviation toward the phonon-dominated regime shifts to higher temperatures. Note the change in the vertical and horizontal scales with increasing carrier density.



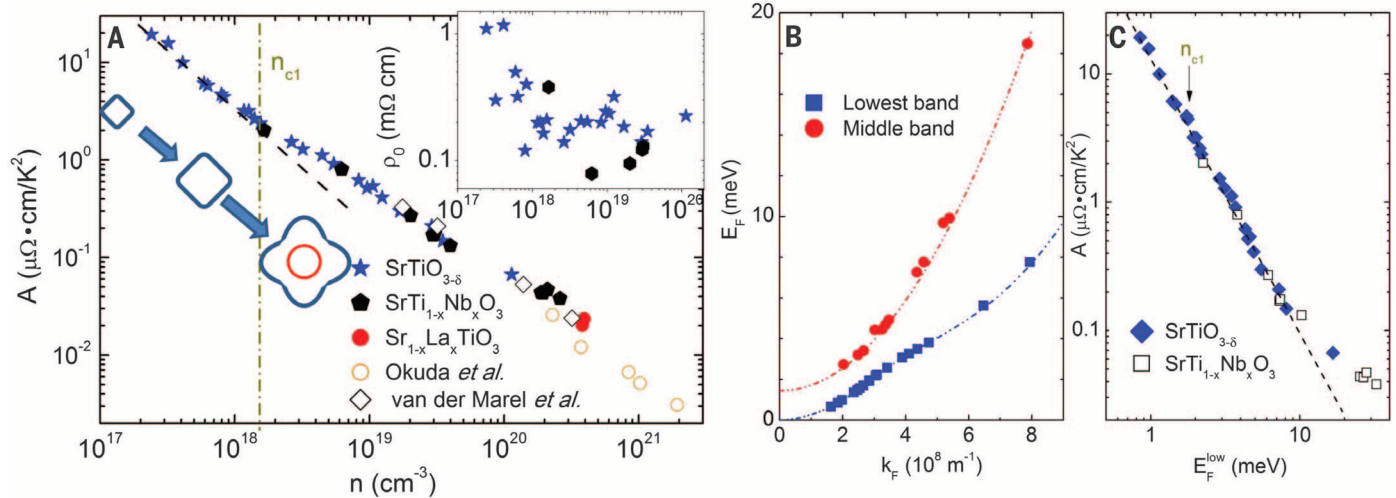


Fig. 2. Variation of A with carrier concentration and Fermi energy. (A) The prefactor A of T^2 resistivity as a function of carrier concentration on a log-log scale. The data represented by empty circles and diamonds are from (12) and (13), respectively. A dash-dot vertical line marks the first critical doping, above which a second band begins to be filled (13, 16). The evolution of the Fermi surface with increasing concentration is also depicted here. Below n_{c1} , the Fermi

surface is a simple squeezed ellipsoid, whereas above n_{c1} it has two concentric components with growing outer lobes. (Inset) Residual resistivity ρ_0 extracted from $\rho = \rho_0 + AT^2$ fits. (B) Dispersion of the two bands extracted from quantum-oscillation measurements (16). (C) Dependence of the prefactor A on the Fermi energy measured from the bottom of the lower band. Its dependence is close to E_F^{-2} across n_{c1} , with a deviation emerging at higher energies.

Here, \hbar is Planck's constant \hbar divided by 2π ; e is the electron charge; and ℓ_{quad} is a material-dependent length scale, which can be set by the Fermi wavelength of electrons, the interatomic distance, or a combination of both. Mott argued that the average distance between two scattering events is proportional to the concentration and the collision cross section of electrons (σ_{cs}) (7). Therefore

$$A = \frac{\hbar}{e^2} \left(\frac{k_B}{E_F} \right)^2 k_F \sigma_{\text{cs}} \quad (2)$$

Here, k_F is the Fermi wave vector, and σ_{cs} is set by the specific process governing the decay in charge current due to the presence of a lattice.

There are several types of theoretical proposals for generating T^2 resistivity from electron-electron scattering in the presence of a lattice. The first (1) invokes a multiband system with two different electron masses. Momentum transfer between these two distinct electron reservoirs sets the temperature dependence of resistivity, and the mass mismatch leads to a leak of momentum toward the lattice thermal bath. The second invokes Umklapp scattering and the fact that momentum conservation does not prohibit the transfer of a unit vector of the reciprocal lattice (8, 9). In addition to these theories, Pal *et al.* have recently argued that Fermi liquids lacking Galilean invariance can display T -square resistivity, even in the absence of any Umklapp process (10), due to electron-impurity scattering. In addition to these semiclassical scenarios, quantum interference can also generate a resistivity proportional to $T^2 \ln T$ (10, 11). The relevance of these ideas to the ubiquitous T^2 resistivity observed in a wide variety of Fermi liquids has not been settled experimentally.

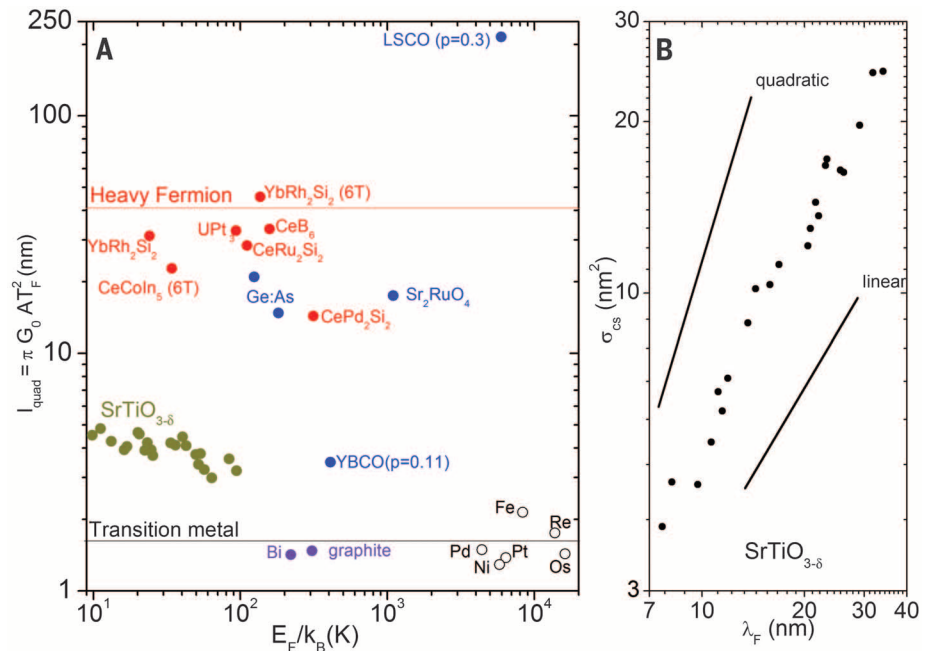


Fig. 3. Characteristic length scale of electron-electron scattering in $\text{SrTiO}_{3-\delta}$ compared with other Fermi liquids. (A) The length scale shown here is defined in Eq. 1 and extracted from A and T_F ($\ell_{\text{quad}} = \pi G_0 A T_F^2$, where $G_0 = 2e^2/h$) in $\text{SrTiO}_{3-\delta}$, as well as a number of other Fermi liquids (see tables S3 and S4 for details and references). The two horizontal solid lines correspond to the Kadowaki-Woods A/γ^2 ratio in heavy fermions ($10 \text{ microhm}\cdot\text{cm mol}^2 \text{ K}^2 \text{ J}^{-2}$; red) and transition metals ($0.4 \text{ microhm}\cdot\text{cm mol}^2 \text{ K}^2 \text{ J}^{-2}$; black) (2, 3, 6). LSCO, $\text{La}_{2-x}\text{Sr}_x\text{CuO}_4$; YBCO, $\text{YBa}_2\text{Cu}_3\text{O}_y$. (B) The extracted collision cross section of electrons (see Eq. 2) as a function of Fermi wavelength follows a dependence close to $\lambda_F^{-1.2}$.

It has been known for two decades that n-doped SrTiO_3 with a carrier density exceeding 0.01 electrons per formula unit follows a T^2 resistivity (12). This T^2 resistivity provided input for the analysis of the Kadowaki-Woods ratio in low-density Fermi liquids (5) and the Landau quasi-

particles of the polaron Fermi liquid (13). More recently, it has been reported that because of its exceptionally long Bohr radius, SrTiO_3 keeps a robust metallic resistivity down to very low doping levels (14). Moreover, both oxygen-deficient (15, 16) and La-doped SrTiO_3 (17) host a well-defined

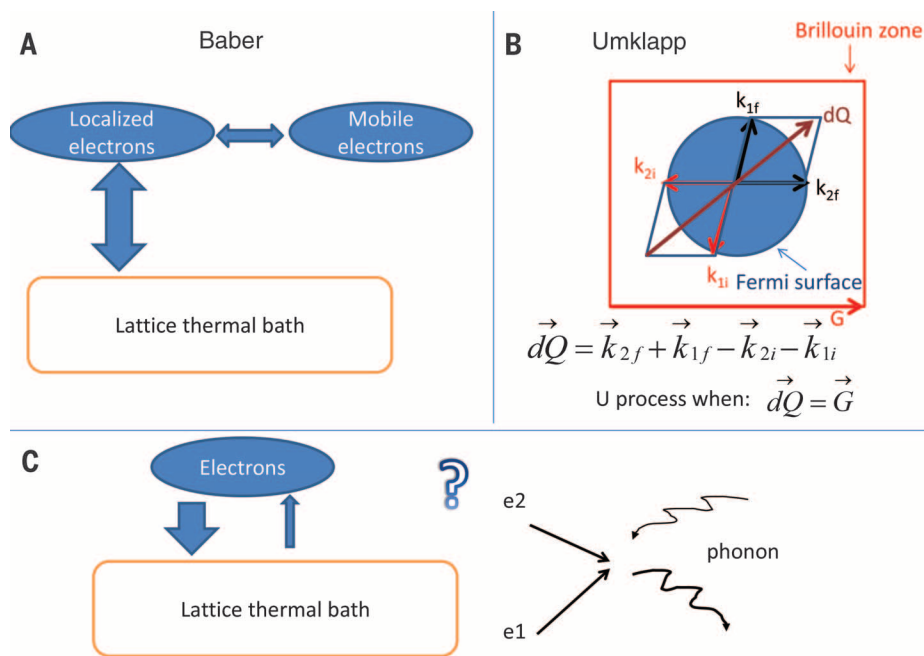


Fig. 4. Theoretical models for T^2 resistivity. (A) The original mechanism (1) requires two distinct reservoirs of electrons with different strengths of coupling to the lattice. (B) Umklapp scattering in which the momentum balance between incoming and outgoing electrons differs by a unit vector (k_{1i}, k_{2i}) of the reciprocal lattice. Such events are possible only when the Fermi wave vector (k_{1f}, k_{2f}) is equal to or larger than one-fourth the width of the Brillouin zone. \vec{G} , reciprocal lattice vector; \vec{dQ} , wave-vector imbalance between initial and final states. (C) Neither of these scenarios can explain the persistence of T^2 resistivity in the case of dilute $\text{SrTiO}_{3-\delta}$, in which there is a single tiny Fermi surface at the center of the Brillouin zone. A scenario is required in which (at least some) scattering events between electrons are accompanied by an asymmetric exchange of momentum with the lattice.

Fermi surface down to carrier densities as low as $3 \times 10^{17} \text{ cm}^{-3}$ (which corresponds to 2×10^{-5} electrons per formula unit). Such a context provides an opportunity to test the relevance of different theoretical pictures for the origin of T^2 resistivity.

Here we present resistivity measurements showing that the T^2 resistivity persists when the carrier density becomes two orders of magnitude lower than previously reported values (12, 13). The magnitude of A varies smoothly as a function of E_F and becomes comparable to what has been seen in a heavy-fermion metal. The most important finding is the persistence of T^2 behavior in the single-band regime, where there is only a single electron reservoir with a Fermi wave vector much too small for any Umklapp process. This severely restrains possible origins of the observed T^2 resistivity. The experimental determination of the collision cross section of electrons in a Fermi liquid with a simple and well-documented Fermi surface topology provides a quantitative challenge for theory. Comparing the data obtained on n-doped SrTiO_3 with other Fermi liquids, we argue that ℓ_{quad} , the characteristic length scale of electron-electron scattering in each Fermi liquid, is a source of information regarding the microscopic origin of momentum decay.

The evolution of resistivity as carrier density changes from between 10^{17} and 10^{20} cm^{-3} is presented in Fig. 1 [see (18) for details on all 35 sam-

ples studied]. In agreement with previous reports (14–17, 19), SrTiO_3 in this doping range is found to be a dilute metal whose resistivity drops by several orders of magnitude as it is cooled from room temperature to liquid helium temperatures.

Above 100 K, the scattering rate extracted from resistivity and carrier concentration [$\tau^{-1} = \frac{\rho n e^2}{m_e}$ (n , carrier density; m_e , free electron mass) in Fig. 1B] does not vary with doping and roughly follows a T^9 dependence (we are neglecting the mass renormalization, which would lead to a correction between 1.8 and 5 in this doping window). Below 100 K, inelastic resistivity evolves with carrier concentration. Both electron-phonon and electron-electron scattering mechanisms can depend on the size of the Fermi surface. In the case of acoustic phonons, as documented in graphene (20), the Bloch-Grüneisen temperature ($\Theta_{\text{BG}} = \frac{2\hbar v_s k_F}{k_B}$, where v_s is the sound velocity) separates two regimes. In a degenerate three-dimensional Fermi liquid, the inelastic resistivity caused by phonon scattering is expected to follow T^5 below Θ_{BG} and become T -linear above Θ_{BG} . In our case, Θ_{BG} and the Fermi degeneracy temperature are of the same order of magnitude. Therefore, at high temperatures, electrons scattered by phonons are obeying Boltzmann statistics. Here we focus on the T^2 inelastic resistivity emerging at low temperatures, which has been attributed to the scattering of electrons off of each other (5, 12, 13).

As seen in Fig. 1, D to F, the slope of the ρ -versus- T^2 plots for $\text{SrTiO}_{3-\delta}$ (δ quantifies the departure from stoichiometry due to the introduction of oxygen vacancies) smoothly decreases with increasing carrier concentration. In all cases, there is a deviation upward from the T^2 behavior toward a regime with a higher exponent. This is in contrast to the case of Fermi liquids with strong correlation, in which quasi-particles are destroyed by warming well below the degeneracy temperature. In SrTiO_3 , the temperature at which the deviation occurs increases with doping. We found similar behavior in Nb-doped and La-doped SrTiO_3 (18). Fig. 2A shows the magnitude of A as a function of carrier concentration. Our data are compatible with those previously reported for higher carrier concentrations (12, 13). Thus, decreasing carrier concentration is concomitant with a monotonous and uninterrupted increase in the magnitude of A across several orders of magnitude, as expected from Eq. 1. The residual resistivity ρ_0 (inset) varies much less with carrier concentration. Figure 1C shows that the magnitude of A is quasi-identical in two samples with identical carrier densities but different residual resistivities. Therefore, the magnitude of A is set by n and not by ρ_0 .

In a Fermi liquid, the Fermi energy is reduced when the Fermi surface shrinks or when the effective mass is enhanced. In both cases, the magnitude of A is expected to increase, according to Eq. 1. Mass enhancement is the origin of the large A in heavy-fermion metals. Our results show that a large A can also be achieved by reducing the sheer size of the Fermi surface. In the extreme dilute limit, A becomes an order of magnitude larger than what is found in heavy-fermion UPt_3 (21).

Figure 2A reveals a hump in $A(n)$ near $n = 1.2 \times 10^{18} \text{ cm}^{-3}$. According to an extensive study of quantum oscillations (16), at this carrier density (dubbed n_{cl}), a second band begins to be filled and the cyclotron mass of the lowest band suddenly enhances. Figure 2B shows the energy dispersion in the two bands constructed from the frequency and effective mass obtained by quantum oscillations (18). The deviation from parabolicity in the lowest band occurs at $k = 0.4 \text{ nm}^{-1}$, close to the expectations from the theoretical band structure, according to which anticrossing between bands generates a downward deviation of the lowest band near this wave vector (13).

The dispersion map of Fig. 2B allows us to determine the Fermi energy of each sample from its carrier density, leading to Fig. 2C, which shows A as a function of the Fermi energy of the lowest band with no visible anomaly near n_{cl} . The dependence remains close to E_F^{-2} over a wide range. This is a strong indication that the n_{cl} anomaly seen in Fig. 1A is almost entirely caused by deviation from parabolic dispersion in the lowest band, which hosts most of carriers.

As seen in fig. S1 (18), one can clearly detect a correlation between large A and small E_F across different materials by comparing the variation of A with Fermi energy in $\text{SrTiO}_{3-\delta}$ and in other Fermi liquids. The inclusion of dilute Fermi liquids in which the electronic specific heat is set by

the ratio of carrier density to Fermi energy is an extension of the Kadowaki-Woods approach.

Using Eq. 1, one can extract ℓ_{quad} , the characteristic length scale associated with electron-electron scattering in $\text{SrTiO}_{3-\delta}$. The extracted length (Fig. 3A) shows only a very slight decrease with doping and is not proportional to the Fermi wavelength (λ_F). A proportional relation between ℓ_{quad} and λ_F would have led to a $n^{-5/3}$ dependence of A in conformity with the simplest available treatments of electron-electron scattering (22, 23).

Figure 3A compares the magnitude of ℓ_{quad} in $\text{SrTiO}_{3-\delta}$ with that of other Fermi liquids (see tables S3 and S4 for details). In a multi-component Fermi surface, a complication arises because there is a multiplicity of Fermi energies. When the Fermi surface occupies a large fraction of the Brillouin zone, one can assume that there is roughly one electron per formula unit, and it is possible to extract the Fermi energy from γ . Thus, one can estimate the order of magnitude of ℓ_{quad} in dense heavy-fermion and transition metals. In Fig. 3A, these metal types lie close to the horizontal lines that represent the Kadowaki-Woods ratios in the two families (2–6). Figure 3A also includes data for the Fermi-liquid unconventional superconductor Sr_2RuO_4 (24), the heavily doped nonsuperconducting compound $\text{La}_{2-x}\text{Sr}_x\text{CuO}_4$ (25), and the $\text{YBa}_2\text{Cu}_3\text{O}_y$ cuprate at a doping level of $p = 0.11$ [in which resistivity is T^2 (26, 27) and the Fermi energy of the small pocket seen by quantum oscillation has been quantified (28)]. We have also included reported data on bismuth (29), graphite (30), and arsenic-doped germanium (31). Figure 3A shows that ℓ_{quad} lies mostly between 1 and 40 nm. Its magnitude can be linked to the microscopic details of momentum decay by scattering in each system.

Using Eq. 2, we have also extracted the collision cross section of electrons in $\text{SrTiO}_{3-\delta}$ from the magnitude of A and the measured radius of the Fermi surface. Figure 3B shows variation of the collision cross section as a function of their Fermi wavelength. If the electrons were classical objects bouncing off of each other, σ_{cs} would have been $2\pi\lambda_F^2$. Our data are inconsistent with that classical picture; Fig. 3B shows that σ_{cs} is much smaller than $2\pi\lambda_F^2$ and does not follow λ_F^2 . Hence, the theoretical challenge of providing a quantitative explanation for this observation remains.

The mechanism by which electron-electron scattering in Fermi liquids causes T^2 resistivity is not well understood. Previously, T^2 resistivity in Fermi liquids was observed in systems with a large single-component Fermi surface (such as $\text{La}_{1.7}\text{Sr}_{0.3}\text{CuO}_4$) or those with small multi-component surfaces (such as bismuth or graphite). In each case, one of the scenarios shown in Fig. 4 could be ruled out, but one could still invoke either the multiplicity of reservoirs or the relevance of Umklapp processes. However, in the case of extremely dilute $\text{SrTiO}_{3-\delta}$, no room is left for either of the two. An Umklapp event cannot occur unless the largest available Fermi wave vector is one-fourth the size of the smallest vector of the reciprocal lattice, G . By a rough estima-

tion, this corresponds to a carrier density of $2 \times 10^{20} \text{ cm}^{-3}$, and Umklapp scattering may cause the hump in the energy dependence of $A(E_F)$ near 10 meV (see Fig. 2C), which corresponds to this carrier concentration. However, we find that A is still growing when k_F becomes 30 times smaller than G .

In the specific case of doped SrTiO_3 , an explanation of the T^2 resistivity may invoke the polaronic nature of the quasi-particles (13) or the distorted structure of the Fermi surface (17). Beyond this particular case, our results highlight the absence of a microscopic theory for momentum decay through electron-electron scattering in different Fermi liquids. The magnitude of ℓ_{quad} can be experimentally quantified in each Fermi liquid. A potentially important role of phonon-assisted (32) electron-electron scattering should be reconsidered.

REFERENCES AND NOTES

- W. G. Baber, *Proc. R. Soc. London Ser. A* **158**, 383–396 (1937).
- M. J. Rice, *Phys. Rev. Lett.* **20**, 1439–1441 (1968).
- K. Kadowaki, S. B. Woods, *Solid State Commun.* **58**, 507–509 (1986).
- K. Miyake, T. Matsuura, C. M. Varma, *Solid State Commun.* **71**, 1149–1153 (1989).
- N. E. Hussey, *J. Phys. Soc. Jpn.* **74**, 1107–1110 (2005).
- A. C. Jacko, J. O. Fjaerestad, B. J. Powell, *Nat. Phys.* **5**, 422–425 (2009).
- N. F. Mott, in *Metal-Insulator Transitions* (Taylor and Francis, London, ed. 2, 1990), pp. 72–73.
- K. Yamada, K. Yosida, *Prog. Theor. Phys.* **76**, 621–638 (1986).
- H. Maebashi, H. Fukuyama, *J. Phys. Soc. Jpn.* **67**, 242–251 (1998).
- H. K. Pal, V. I. Yudson, D. L. Maslov, *Lith. J. Phys.* **52**, 142–164 (2012).
- I. Paul, *Phys. Rev. B* **77**, 224418 (2008).

- T. Okuda, K. Nakanishi, S. Miyasaka, T. Tokura, *Phys. Rev. B* **63**, 113104 (2001).
- D. van der Marel, J. L. M. van Mechelen, I. I. Mazin, *Phys. Rev. B* **84**, 205111 (2011).
- A. Spinelli, M. A. Torija, C. Liu, C. Jan, C. Leighton, *Phys. Rev. B* **81**, 155110 (2010).
- X. Lin, Z. Zhu, B. Fauqué, K. Behnia, *Phys. Rev. X* **3**, 021002 (2013).
- X. Lin et al., *Phys. Rev. Lett.* **112**, 207002 (2014).
- S. J. Allen et al., *Phys. Rev. B* **88**, 045114 (2013).
- See supplementary materials on Science Online.
- A. Verma, A. P. Kajdos, T. A. Cain, S. Stemmer, D. Jena, *Phys. Rev. Lett.* **112**, 216601 (2014).
- D. K. Efetov, P. Kim, *Phys. Rev. Lett.* **105**, 256805 (2010).
- R. Joynt, L. Taillefer, *Rev. Mod. Phys.* **74**, 235–294 (2002).
- W. E. Lawrence, J. W. Wilkins, *Phys. Rev. B* **7**, 2317–2332 (1973).
- A. H. Thompson, *Phys. Rev. Lett.* **35**, 1786–1789 (1975).
- A. P. Mackenzie, Y. Maeno, *Rev. Mod. Phys.* **75**, 657–712 (2003).
- S. Nakamae et al., *Phys. Rev. B* **68**, 100502(R) (2003).
- D. LeBoeuf et al., *Phys. Rev. B* **83**, 054506 (2011).
- N. Barišić et al., *Proc. Natl. Acad. Sci. U.S.A.* **110**, 12235–12240 (2013).
- J. Chang et al., *Phys. Rev. Lett.* **104**, 057005 (2010).
- R. Hartman, *Phys. Rev.* **181**, 1070–1086 (1969).
- D. T. Morelli, C. Uher, *Phys. Rev. B* **30**, 1080(R) (1984).
- M. J. Katz, S. H. Koenig, A. A. Lopez, *Phys. Rev. Lett.* **15**, 828–830 (1965).
- A. H. MacDonald, *Phys. Rev. Lett.* **44**, 489–493 (1980).

ACKNOWLEDGMENTS

We thank H. Maebashi, D. Maslov, and K. Miyake for stimulating discussions. This work was supported by Agence Nationale de Recherche through the SUPERFIELD and QUANTUM LIMIT projects and by a grant from the Ile de France region.

SUPPLEMENTARY MATERIALS

www.sciencemag.org/content/349/6251/945/suppl/DC1
Materials and Methods
Supplementary Text
Figs. S1 and S2
Tables S1 to S4
References (33–60)

6 February 2015; accepted 29 July 2015
10.1126/science.aaa8655

TOPOLOGICAL MATTER

Observation of chiral currents at the magnetic domain boundary of a topological insulator

Y. H. Wang,^{1,2*} J. R. Kirtley,¹ F. Katmis,^{3,4} P. Jarillo-Herrero,⁴
J. S. Moodera,^{3,4} K. A. Moler^{1,2*}

A magnetic domain boundary on the surface of a three-dimensional topological insulator is predicted to host a chiral edge state, but direct demonstration is challenging. We used a scanning superconducting quantum interference device to show that current in a magnetized topological insulator heterostructure ($\text{EuS}/\text{Bi}_2\text{Se}_3$) flows at the edge when the Fermi level is gate-tuned to the surface band gap. We further induced micrometer-scale magnetic structures on the heterostructure and detected a chiral edge current at the magnetic domain boundary. The chirality of the current was determined by magnetization of the surrounding domain, and its magnitude by the local chemical potential rather than the applied current. Such magnetic structures provide a platform for detecting topological magnetoelectric effects and may enable progress in quantum information processing and spintronics.

The metallic surface of a three-dimensional topological insulator (3D-TI) is protected by time-reversal symmetry (TRS). Breaking TRS opens a band gap on the surface Dirac cone and transforms it into a Chern insu-

lator (1–4). TRS-broken surface states are predicted to exhibit topological magneto-electric effects (1) and, when coupled with a superconductor, Majorana fermions (5–7). Just as the surface Dirac cone is a signature of the nontrivial

topological bulk band structure of a time-reversal invariant 3D-TI, bulk-boundary correspondence dictates that the TRS-broken surface states with a nonzero Chern number manifest as a gapless chiral edge state (CES) at its boundary (1).

In the special case where the boundary is the edge of the sample surface, a CES along the edge leads to a quantized Hall conductance equal to e^2/h , where e is the electron charge and h is the Planck constant, even at zero magnetic field. This quantized anomalous Hall conductance was observed only in a 3D-TI doped with a high concentration of magnetic impurities to break TRS, with the measurements performed at very low temperatures to achieve ballistic transport between contacts (8, 9). More generally, a CES theoretically should exist at a magnetic domain boundary (1, 10), which does not need to be the physical boundary of the system. In this case, the presence of a CES changes only the local conductivity and therefore does not contribute to the conductance of the system (11). The CES at a magnetic domain boundary can be used to investigate 1D quantum transport without edge effects (12–14), to induce a parity anomaly (4), or to realize magnetically defined quantum bits (15).

Inducing magnetism on the surface of a TI through proximity to a ferromagnet provides an alternative strategy for breaking the TRS on the surface states without disrupting the bulk. Previous bulk magnetic and transport measurements (16) revealed some evidence of enhanced magnetization at the interface of a heterostructure composed of EuS, a known ferromagnetic insulator (FMI) (17–19), and Bi₂Se₃, a prototypical TI (20–23) (Fig. 1A). For our experiments, a Hall bar was etched through the bilayer using a shadow mask (Fig. 1B) for transport measurements. The Curie temperature of the EuS (10 nm)/Bi₂Se₃ (5 nm) heterostructure was previously found by magnetoresistance and bulk magnetic measurement to be approximately 15 K (16, 24), comparable to that of bulk EuS (17).

We employed scanning superconducting quantum interference device (SQUID) microscopy (Fig. 1A), a sensitive probe for detecting magnetic flux from magnetic domains or current on the mesoscopic scale (25, 26), to search for the chiral edge states in a EuS/Bi₂Se₃ heterostructure (Fig. 1B). The pickup loop (Fig. 1A) was integrated into a two-junction SQUID that converts the flux through the loop (Φ) into a voltage signal (27–29). Flowing a current (I_F) through the field coil (Fig. 1A) provided a local magnetic field for either susceptometry measurement ($d\Phi/dI_F$) or to manipulate magnetic domain structures in our bilayers (Fig. 1A). Current magnetometry (Φ_1/I_{AC}) was per-

formed simultaneously with direct current (DC) magnetometry by measuring the component of the flux through the pickup loop that is locked to the frequency and in phase (Φ') with the alternating current (AC) source-drain bias current (I_{AC}).

A typical magnetometry micrograph (Fig. 1C) of the sample under zero field cooling displayed micrometer-scale patches of magnetic domains at the base temperature of 4 K. Such magnetic features disappeared at 19 K (Fig. 1C, inset), consistent with the Curie temperature of these samples (16, 24). The etched area of the Hall bar showed zero magnetization (Fig. 1C) and susceptibility (Fig. 1D). The much-reduced susceptibility of the film at 21 K (Fig. 1D, inset) was also consistent with its ferromagnetic nature. To break the TRS at the EuS/Bi₂Se₃ interface with magnetization, we applied a uniform out-of-plane magnetic field of 30 G while cooling the sample from 18 K to 5 K (30). After field cooling, the magnetic structure close to the edge of the Hall bar, as determined from scanning susceptometry (Fig. 2A), showed a change of magnetization from the film side to the substrate side; this indicated that the out-of-plane magnetic field induced, on average, a mixture of out-of-plane and in-plane remnant magnetization (31). The lateral variation of magnetization along the edge may be caused by the inhomogeneity of the film and some domain structure (31). The magnetic field from the magnetization is less than 1 G (31) and is too small to induce any observable Landau levels (32) at 4 K.

To determine how current flows around the edge of a Hall bar when it is magnetized, we

simultaneously performed magnetometry (measurement of the static magnetic field) and current magnetometry (lock-in measurement of the magnetic field produced by the applied current) at various back-gate voltages V_G (Fig. 2). Although the magnetometry images did not change as a function of V_G (Fig. 2, A to C), current magnetometry images strongly depended on V_G (Fig. 2, D to F). We found a current magnetometry pattern with both positive and negative polarity developing along the edge as the back-gate voltage was tuned to be more negative (Fig. 2D). The current magnetometry pattern reached a maximum at $V_G = -220$ V (Fig. 2E). The pattern became weaker with decreasing V_G and completely disappeared at $V_G = -350$ V (Fig. 2F). The cross sections normal to the edge from these images (Fig. 2G) clearly exhibited a field profile consistent with an edge current developing when the Fermi level is gate-tuned to the surface band gap induced by magnetism (25). The extracted current density from the flux image at $V_G = -220$ V indicates that the edge current appears to be confined to the edge with a full width at half maximum (FWHM) width of 4.1 μm (Fig. 2H), which is likely resolution-limited for the 3- μm -diameter pickup loop at a scan height of $\sim 1 \mu\text{m}$ in this particular measurement (31).

Having demonstrated the existence of edge states at the physical boundary of the heterostructure, we investigated whether there were any CESs at a magnetic domain boundary. We applied DC to the field coil at 12 K while scanning the field coil in a square (Fig. 3A) to write a magnetic structure with two opposite out-of-plane

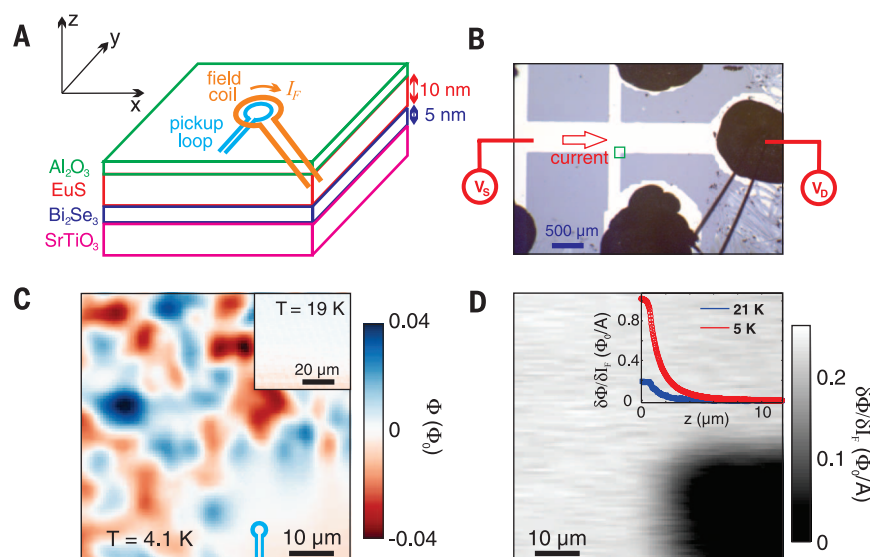
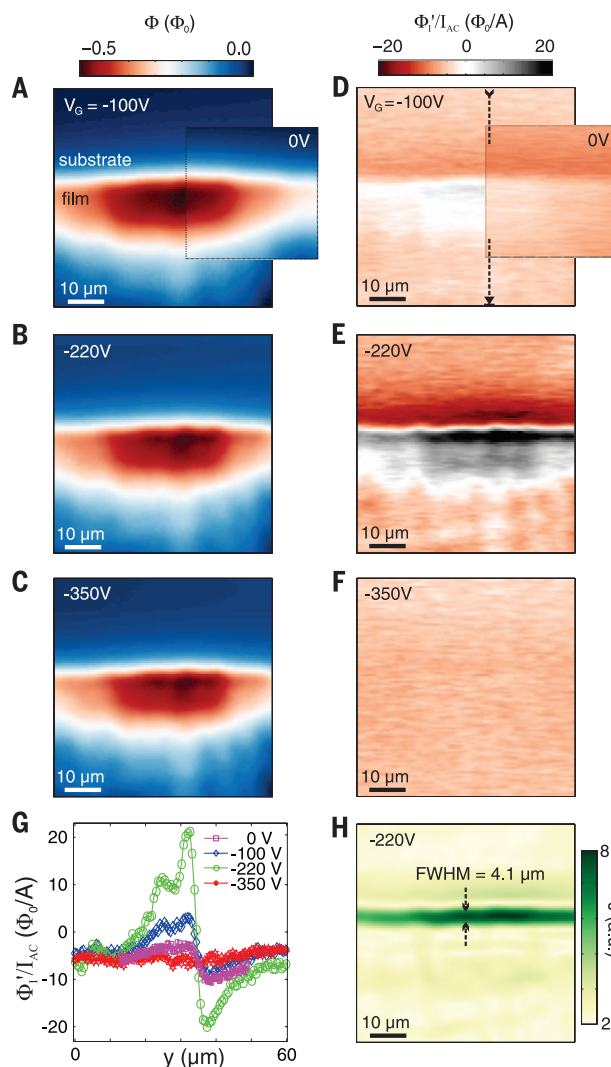


Fig. 1. Scanning SQUID microscopy of a TI-FMI heterostructure shows micrometer-scale magnetic domains. (A) Schematic of the EuS/Bi₂Se₃ bilayer nanostructure on the SrTiO₃ substrate under the pickup loop and field coil of a SQUID. (B) Optical image of the patterned bilayer film. The Hall bar has all the layers shown in (A), and the etched area has only the SrTiO₃ substrate. (C) Scanning SQUID flux (Φ) image of the green square area in (B) at 4.1 K after zero-field cooling and at 19 K (inset). The pickup loop (cyan) is shown to scale. Φ_0 is the flux quantum. (D) Susceptometry ($d\Phi/dI_F$) micrograph of the area in (C). (Inset) Susceptibility as a function of distance from the surface of the film at 5 K (red) and 21 K (blue). The lower right corner of (C) and (D), which corresponds to an etched area, shows small flux and susceptibility.

¹Department of Physics and Applied Physics, Stanford University, Stanford, CA 94305, USA. ²Stanford Institute for Materials and Energy Sciences, SLAC National Accelerator Laboratory, Menlo Park, CA 94025, USA. ³Francis Bitter Magnet Laboratory and Plasma Science and Fusion Center, Massachusetts Institute of Technology, Cambridge, MA 02139, USA. ⁴Department of Physics, Massachusetts Institute of Technology, Cambridge, MA 02139, USA. *Corresponding author. E-mail: wangyhw@stanford.edu (Y.H.W.); kmoler@stanford.edu (K.A.M.)

Fig. 2. Edge current in a magnetized topological insulator appears by tuning the back gate. (A to C)

Magnetometry images along the sample edge after cooling in a uniform 30 G out-of-plane magnetic field at various back-gate voltages V_G . (D to F) are the corresponding current magnetometry (Φ'_I/I_{AC}) images. The 0-V images [(A) and (D) insets] were taken in a slightly shifted area. (G) Cross sections of the current magnetometry images [(D), (E), and (F)] along the direction and position shown along the arrows in (D). (H) Current density for the current magnetometry image in (E), extracted by fast Fourier transform. The arrows indicate the FWHM width of the edge current, which is likely resolution-limited.



magnetizations next to each other and away from the edge (31).

To investigate the current around this magnetic structure, we performed current magnetometry with source-drain voltage biased both ways (Fig. 3). The reversal of the bias voltage does not cause any change to the induced magnetic structure (Fig. 3, A and B). For the current flowing in a conventional metal, the direction of the current and therefore its magnetic field reverses sign when the source-drain bias is reversed (fig. S4). Such nonchiral current is present in our TI-FMI heterostructure: On the left side of the images in Fig. 3, C and D, in which average magnetization is zero (Fig. 3A), as well as in the image with $V_G = 0$ V (Fig. 3E), there is a linear background that switches sign when the bias current is switched. This is consistent with the out-of-plane magnetic field from a uniform plane current flowing horizontally (fig. S5A) and likely comes from the bottom surface or the bulk. The background current is caused by the gradient of chemical potential across the thickness of the Bi_2Se_3 layer, even when the chemical potential on the top is tuned to inside the energy gap of the surface states by the back-gate voltage (33), as is also known to happen in 2D quantum spin Hall systems (25).

In addition, sharp current flux features appeared that, in contrast to the background current, did not switch sign as the voltage bias was reversed (Fig. 3, C and D). These features, reminiscent of the flux generated by an edge current (Fig. 2E), appeared along the magnetic domain wall at $V_G = -220$ V (Fig. 3, C and D) but were absent at $V_G = 0$ V (Fig. 3E), which is consistent with the gate dependence of the edge current (Fig. 2) and suggests their common origin from the states in the surface gap. The sign of these features is opposite (Fig. 3, C and D) along the left edges of the top

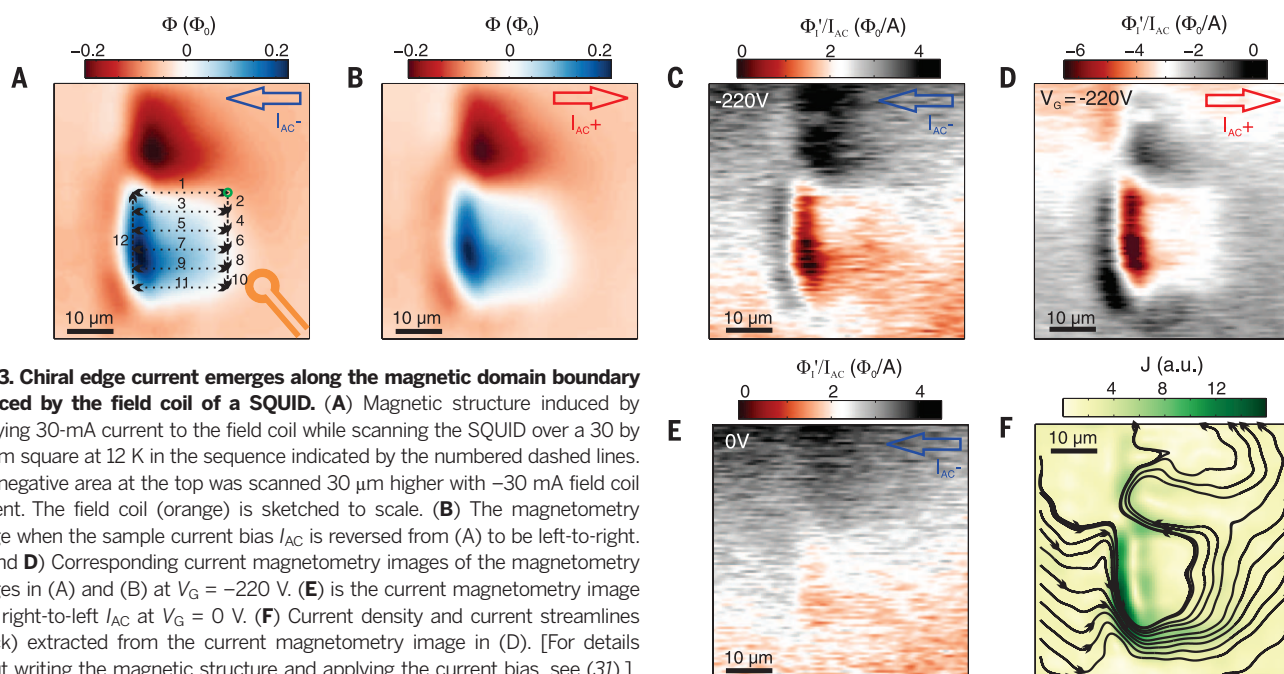


Fig. 3. Chiral edge current emerges along the magnetic domain boundary induced by the field coil of a SQUID. (A) Magnetic structure induced by applying 30-mA current to the field coil while scanning the SQUID over a 30 by 30 μm square at 12 K in the sequence indicated by the numbered dashed lines. The negative area at the top was scanned 30 μm higher with -30 mA field coil current. The field coil (orange) is sketched to scale. (B) The magnetometry image when the sample current bias I_{AC} is reversed from (A) to be left-to-right. (C and D) Corresponding current magnetometry images of the magnetometry images in (A) and (B) at $V_G = -220$ V. (E) is the current magnetometry image with right-to-left I_{AC} at $V_G = 0$ V. (F) Current density and current streamlines (black) extracted from the current magnetometry image in (D). [For details about writing the magnetic structure and applying the current bias, see (31).]

and bottom domains with reversed magnetizations (Fig. 3A), indicating the chiral nature of the edge current. These chiral features in current magnetometry disappeared when the temperature was increased to 12 K, whereas the magnetization became weaker but was still present (fig. S6). This observation suggests that a strong magnetization is essential to the chiral current features and therefore only the top surface of Bi_2Se_3 is contributing to such features, because exchange coupling from the FMI layer is short range (34, 35). In stark contrast, current magnetometry on a trivial semimetal-FMI bilayer showed no such chiral features around a magnetic structure at base temperature, regardless of gating (fig. S4).

The average of the current magnetometry images with opposite source-drain bias canceled out the nonchiral background current and clearly reveals the chiral features along the magnetic domain boundary in the shape of a square (fig. S3B). We find that the peaks in current magnetometry were approximately described using the out-of-plane magnetic field generated by thin current wires with finite width (31). The current density (Fig. 3F) extracted from the current magnetometry image (Fig. 3D) (25) confirmed this picture of chiral edge current surrounding the magnetic domain boundary with chirality deter-

mined by magnetization of the domain. Because the magnetization that we induced with the field coil was below the saturation magnetization of similar films (16), there could be domains beyond the resolution of the pickup loop inside the magnetic structures (Fig. 3A). However, the chiral current from these smaller domains only reduces the average intensity of chiral features in current magnetometry in a similar fashion that these domains reduce the average magnitude of magnetization detected by the pickup loop (31).

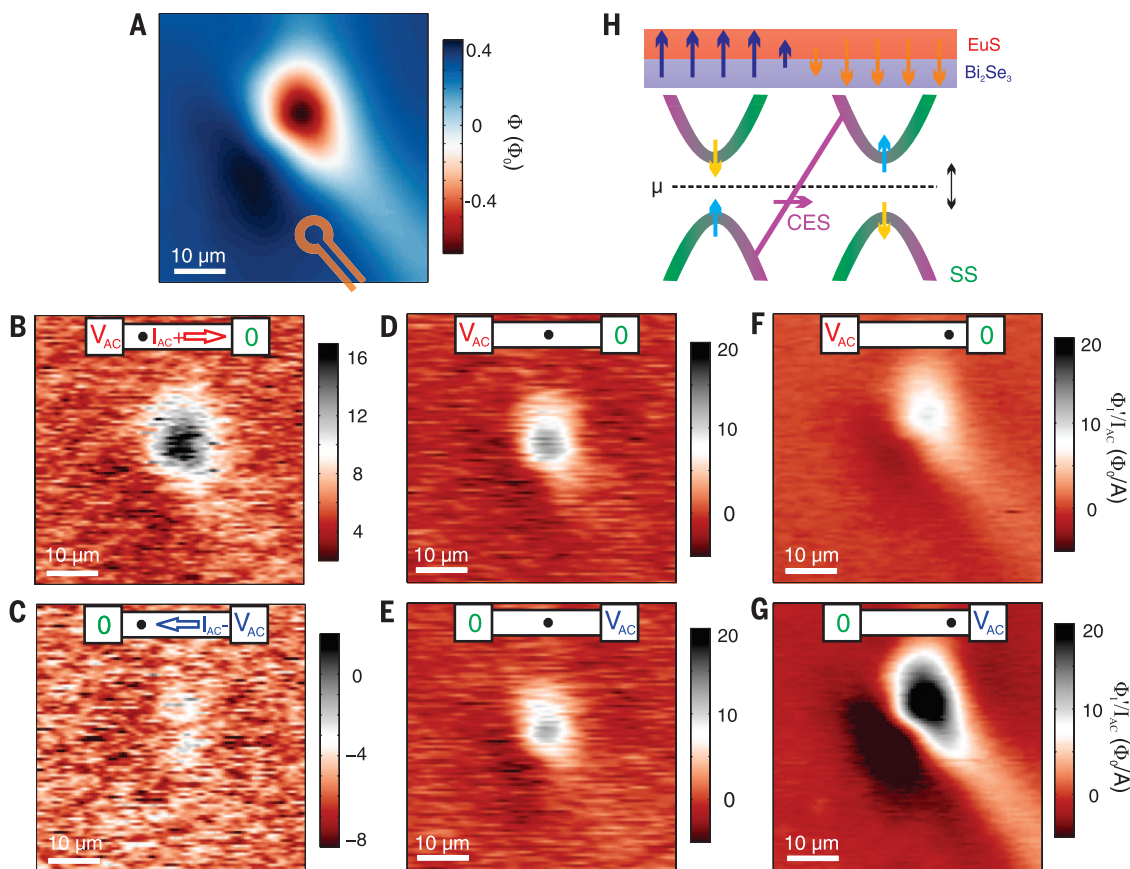
To identify what determines chiral current intensity, we performed current magnetometry on the magnetic structures induced at various positions along the Hall bar, where the electrochemical potentials (μ) differ (Fig. 4). Magnetic structures were induced at different locations along the Hall bar (Fig. 4A and fig. S12) by cooling the sample from 15 K while applying DC current to the field coil (31). The current magnetometry images (Fig. 4, B to G) correspond to such structures induced on the left of the Hall bar close to the source contact (Fig. 4, B and C), in the middle of the Hall bar (Fig. 4, D and E), and on the right of the Hall bar close to the drain contact (Fig. 4, F and G). Although the sign of the current features was the same for all configurations (at $V_G = -200$ V) (Fig. 4, B to G), as expected from a chiral effect, the intensity was strongly

position-dependent. For the magnetic structure close to the source, the intensity of the current features was stronger when the voltage bias was on the source (Fig. 4B) than when the bias was on the drain (Fig. 4C). This behavior was reversed for the magnetic structure close to the drain (Fig. 4, F and G), whereas the middle structure displayed approximately equal intensity when the voltage bias was switched (Fig. 4, D and E).

Because the location of the application of the voltage bias does not change the total current flowing through the Hall bar, the position-dependent current flux intensity suggests that μ rather than the bias current I_{AC} determined the chiral current intensity. μ at each location was linearly proportional to the position along the Hall bar because the Hall bar's length is much longer than the typical electron mean free path (Fig. 1B and fig. S12D). This dependence on μ is reminiscent of the chiral edge current in a quantum Hall state, where the domain boundary is the edge of the sample (34). Current flowing along each edge is proportional to the μ of the contact from which the charge is emitted. Meanwhile, the total bias current depends on the difference in μ between the source and drain contacts. If the voltages on the contacts are equal, then there will be no net current, but there will be a circulating edge current with a magnitude dependent on

Fig. 4. Chiral current intensity depends on electrochemical potential.

(A) Magnetic structure induced by the field coil when applying 30 mA of current and cooled from 15 K. The field coil (orange) is sketched to scale. **(B to G)** Current magnetometry images when the left side of the Hall bar is attached to a voltage lead and the right side is grounded [(B), (D), and (F)] versus the opposite lead configuration [(C), (E), and (G)]. (B) and (C), (D) and (E), and (F) and (G) are from the magnetic structures on the left, middle, and right of the Hall bar, respectively (as indicated on the sketch at the top of each panel). When the magnetic structure is closer to V_{AC} than to the ground, the modulation of μ is larger, yielding the stronger chiral feature in current magnetometry. **(H)** Band structure of the surface states (SS) and the CES around a magnetic domain boundary. Arrows indicate the direction of spin polarization, and the color coding of the surface states indicates how their momentum-dependent spin texture is modified by the magnetization of the top EuS layer from in-plane (green and magenta) to out-of-plane (blue and yellow). The AC biased source-drain voltage $V_{AC} = V_0 \sin(\omega t)$ modulates the electrochemical potential μ , which is proportional to the magnitude of the edge current.



the source-drain voltage relative to the back-gate voltage (*II*).

In our TI-FMI heterostructure, the drop of μ across the magnetic structure was small compared with the drop of μ across source and drain (due to the ratio of their lengths), and therefore the local μ determined the magnitude of the chiral edge current. Because current magnetometry is a lock-in measurement (*3I*), the measured magnetic response from the chiral current is proportional to the modulation of the local μ when the Fermi level is in the surface gap. When the domain boundary is close to the alternating AC voltage bias (Fig. 4, B and G), μ is more strongly modulated than when it is close to the ground (Fig. 4, C and F), yielding a stronger chiral current intensity in current magnetometry (Fig. 4H). The magnitude of the extracted current *I* (fig. S5B) along the magnetic domain boundary (*3I*) is in agreement with calculations of the current carried by one spin-polarized edge mode in the ballistic transport regime $I = e\mu/h$ (*11, 35, 36*).

Our results not only demonstrate the existence of CES at the magnetic domain boundary of a TI but also establish a versatile platform in scanning SQUID microscopy for imaging and manipulating broken TRS TI surface states on the mesoscopic scale. The broken TRS state and its chiral edge will be a playground for exploring interaction between TIs and FMIs (*37–40*).

REFERENCES AND NOTES

- X.-L. Qi, S.-C. Zhang, *Rev. Mod. Phys.* **83**, 1057–1110 (2011).
- M. Z. Hasan, C. L. Kane, *Rev. Mod. Phys.* **82**, 3045–3067 (2010).
- Y. H. Wang, H. Steinberg, P. Jarillo-Herrero, N. Gedik, *Science* **342**, 453–457 (2013).
- O. Pankratov, *Phys. Lett. A* **121**, 360–366 (1987).
- A. Y. Kitaev, *Physics-Uspekhi* **44** (10S), 131–136 (2001).
- L. Fu, C. L. Kane, *Phys. Rev. Lett.* **100**, 096407 (2008).
- A. R. Akhmerov, J. Nilsson, C. W. Beenakker, *Phys. Rev. Lett.* **102**, 216404 (2009).
- C. Z. Chang et al., *Science* **340**, 167–170 (2013).
- X. Kou et al., *Phys. Rev. Lett.* **113**, 137201 (2014).
- R. Yu et al., *Science* **329**, 61–64 (2010).
- S. Datta, *Electronic Transport in Mesoscopic Systems* (Cambridge Univ. Press, Cambridge, 1995).
- Q. Meng, S. Vishveshwara, T. L. Hughes, *Phys. Rev. Lett.* **109**, 176803 (2012).
- C. Wickles, W. Belzig, *Phys. Rev. B* **86**, 035151 (2012).
- T. Yokoyama, S. Murakami, *Physica E* (2013).
- G. J. Ferreira, D. Loss, *Phys. Rev. Lett.* **111**, 106802 (2013).
- P. Wei et al., *Phys. Rev. Lett.* **110**, 186807 (2013).
- J. S. Moodera, X. Hao, G. A. Gibson, R. Meserve, *Phys. Rev. Lett.* **61**, 637–640 (1988).
- D. Ghosh, M. De, S. K. De, *Phys. Rev. B* **70**, 115211 (2004).
- D. O'Mahony et al., *Thin Solid Films* **488**, 200–203 (2005).
- Y. Xia et al., *Nat. Phys.* **5**, 398–402 (2009).
- Y. Zhang et al., *Nat. Phys.* **6**, 584 (2010).
- J. G. Analytis et al., *Nat. Phys.* **6**, 960–964 (2010).
- Y. H. Wang et al., *Phys. Rev. Lett.* **107**, 207602 (2011).
- Q. I. Yang et al., *Phys. Rev. B* **88**, 081407 (2013).
- K. C. Nowack et al., *Nat. Mater.* **12**, 787–791 (2013).
- E. M. Spanton et al., *Phys. Rev. Lett.* **113**, 026804 (2014).
- B. W. Gardner et al., *Rev. Sci. Instrum.* **72**, 2361 (2001).
- J. R. Kirtley et al., Advanced sensors for scanning SQUID microscopy, *Proceedings of the 14th International Superconducting Electronics Conference (ISEC)*, 2013.
- M. E. Huber et al., *IEEE Trans. Appl. Supercond.* **11**, 4048–4053 (2001).
- It is possible to induce CES with in-plane magnetization, but the effect may be very weak in Bi_2Se_3 (41) because of the small warping effect (23).
- See the supplementary materials on Science Online.
- A. Yuzin, A. Burkov, *Phys. Rev. B* **83**, 195413 (2011).
- J. G. Checkelsky, Y. S. Hor, R. J. Cava, N. P. Ong, *Phys. Rev. Lett.* **106**, 196801 (2011).
- D. Yoshioka, *The Quantum Hall Effect* (Springer, Berlin, 2002).
- A. T. Lee, M. J. Han, K. Park, *Phys. Rev. B* **90**, 155103 (2014).
- V. Men'shov, V. Tugushev, S. Ereemeev, P. Echenique, E. Chulkov, *Phys. Rev. B* **88**, 224401 (2013).
- J. Checkelsky, J. T. Ye, Y. Onose, Y. Iwasa, Y. Tokura, *Nat. Phys.* **8**, 729–733 (2012).
- Y. Tserkovnyak, D. Loss, *Phys. Rev. Lett.* **108**, 187201 (2012).
- A. R. Mellnik et al., *Nature* **511**, 449–451 (2014).
- R. Hammer, W. Potz, *Phys. Rev. B* **88**, 235119 (2013).
- C.-X. Liu et al., *Phys. Rev. B* **81**, 041307 (2010).

ACKNOWLEDGMENTS

These measurements were supported by the Center for Function Accelerated nanoMaterial Engineering (FAME), one of six centers of STARnet, a Semiconductor Research Corporation program sponsored by the Microelectronics Advanced Research Corp. (MARCO) and the Defense Advanced Research Projects Agency (DARPA). Preliminary measurements and analysis were supported by the Department of Energy (DOE), Office of Science, Basic Energy Sciences, Materials Sciences and Engineering Division, under contract DE-AC02-76SF00515. The SQUID microscope and sensors were developed with support from NSF-NSEC 0830228 and NSF IMR-MIP 0957616. Y.H.W. is partially supported by the

Urbanek Fellowship of the Department of Applied Physics at Stanford University. For sample preparation, F.K., P.J.-H., and J.S.M. acknowledge support by the Massachusetts Institute of Technology's Materials Research Science and Engineering Center (MRSEC) through the MRSEC Program of the National Science Foundation under award DMR-0819762. Partial support for sample development was provided by NSF (DMR-1207469), ONR (N00014-13-1-0301) (F.K. and J.S.M.), and by the DOE, Basic Energy Sciences Office, Division of Materials Sciences and Engineering, under award no. DE-SC0006418 (F.K. and P.J.-H.). We are grateful for the assistance from G. Gibson, M. Ketchen, and M. Huber on developing the SQUID sensors and from I. Sochnikov, E. Spanton, J. Palmstrom, and K. C. Nowack on the measurement, as well as for stimulating discussions with S.-C. Zhang, X.-L. Qi, J. Wang, D. Goldhaber-Gordon, and B. I. Halperin.

SUPPLEMENTARY MATERIALS

www.sciencemag.org/content/349/6251/948/suppl/DC1
Materials and Methods
Supplementary Text
Figs. S1 to S12
Reference (42)

21 October 2014; accepted 29 July 2015
Published online 13 August 2015
10.1126/science.aaa0508

QUANTUM MECHANICS

Quantum squeezing of motion in a mechanical resonator

E. E. Wollman,^{1*} C. U. Lei,^{1*} A. J. Weinstein,^{1*} J. Suh,² A. Kronwald,³ F. Marquardt,^{3,4} A. A. Clerk,⁵ K. C. Schwab^{1†}

According to quantum mechanics, a harmonic oscillator can never be completely at rest. Even in the ground state, its position will always have fluctuations, called the zero-point motion. Although the zero-point fluctuations are unavoidable, they can be manipulated. Using microwave frequency radiation pressure, we have manipulated the thermal fluctuations of a micrometer-scale mechanical resonator to produce a stationary quadrature-squeezed state with a minimum variance of 0.80 times that of the ground state. We also performed phase-sensitive, back-action evading measurements of a thermal state squeezed to 1.09 times the zero-point level. Our results are relevant to the quantum engineering of states of matter at large length scales, the study of decoherence of large quantum systems, and for the realization of ultrasensitive sensing of force and motion.

In the quantum ground state, a mechanical resonator has position fluctuations divided equally between its two motional quadratures, \hat{X}_1 and \hat{X}_2 , which are defined as the slowly varying envelopes of the position: $\hat{x} = \hat{X}_1 \cos(\omega_m t) + \hat{X}_2 \sin(\omega_m t)$. Additionally, the ground-state fluctuations minimize the uncertainty relation given by the quadratures' nonzero commutator: $\langle \Delta \hat{X}_1^2 \rangle \langle \Delta \hat{X}_2^2 \rangle \geq \frac{1}{4} |\langle [\hat{X}_1, \hat{X}_2] \rangle|^2 = \frac{1}{4} \hbar^2$,

where $x_{zp} = \sqrt{\hbar/2m\omega_m}$ is the amplitude of the zero-point fluctuations. Given this uncertainty relation, it is, in principle, possible to squeeze the zero-point noise such that fluctuations in one quadrature are reduced below the zero-point level at the expense of increasing noise in the orthogonal quadrature. More generally, other noncommuting observable pairs can be squeezed, and squeezed states have been created and detected in such varied systems as optical (*1*) and microwave (*2*) modes, the motion of trapped ions (*3*), and spin states in an ensemble of cold atoms (*4*). Transient quantum squeezing has also been created and observed in the motion of molecular nuclei (*5*) and of terahertz-frequency phonons in an atomic lattice on picosecond time scales (*6*). Here, we demonstrate steady-state squeezing of a micrometer-scale mechanical resonator by implementing a reservoir-engineering scheme (*7*) that is closely

¹Applied Physics, California Institute of Technology, Pasadena, CA 91125, USA. ²Korea Research Institute of Standards and Science, Daejeon 305-340, Republic of Korea. ³Friedrich-Alexander-Universität Erlangen-Nürnberg, Staudtstraße 7, D-91058 Erlangen, Germany. ⁴Max Planck Institute for the Science of Light, Günther-Scharowsky-Straße 1/Bau 24, D-91058 Erlangen, Germany. ⁵Department of Physics, McGill University, Montreal, Quebec, H3A 2T8, Canada.

*These authors contributed equally to this work. †Corresponding author. E-mail: schwab@caltech.edu

related to the approach recently used to produce quantum squeezed states in the motion of trapped ions (8).

A major challenge for quantum squeezing of a radio-frequency mechanical mode is that, even at a temperature of 10 mK, the thermal occupation and corresponding position fluctuations are far larger than the quantum zero-point fluctuations. $\Delta\hat{x}^2$ is approximately 100 times x_{zp}^2 for a 4 MHz resonator; quantum squeezing can only be accomplished by first overcoming this large thermal contribution. In contrast, optical modes are found in the quantum ground state at room temperature. Squeezing of mechanical fluctuations was first demonstrated far outside the quantum regime by parametrically modulating the mechan-

ical spring constant (9). Because parametric methods are limited to 3 dB of steady-state squeezing, the occupation factor of the mechanical mode must be well below one phonon to achieve squeezing below the zero-point fluctuations. There are many theoretical proposals for surpassing the 3-dB limit to produce quantum squeezing via coupling to a qubit (10), measurement plus feedback (11), injection of squeezed light (12), or strong optical pulses (13). Experimentally, improvement over the 3-dB limit has been realized with modified parametric techniques (14–16). Squeezing below the zero-point fluctuations, however, has been an outstanding problem.

Squeezing via reservoir engineering (7, 17) has advantages over other methods, because it creates

a system in which the mechanics relaxes into a steady-state squeezed state without the fast measurements and control necessary for feedback. The scheme consists of applying two pump tones to an optical or microwave cavity parametrically coupled to a mechanical resonator. The pumps are detuned from the cavity frequency ω_c by the mechanical frequency $\pm\omega_m$, with the red-detuned pump at a higher power than the blue-detuned pump (Fig. 1A). This is a similar set-up to one used for a back-action evading (BAE) measurement of a single quadrature (18), but with excess red-detuned power. The squeezing effect of the drives can be understood as a damping of both quadratures by the excess red-detuned power, similar to that of sideband cooling (19), but with less back-action noise added to \hat{X}_1 than the zero-point noise associated with the damping. By optimizing the pump power ratio, it is possible to produce arbitrarily large amounts of subzero-point squeezing (i.e., >3 dB) if the coupling between the mechanics and the squeezed reservoir sufficiently dominates the mechanical dissipation rate (7).

The effects of both damping and back-action on the amount of squeezing can be seen in the equations for the quadrature fluctuations of the system described above. Here, we take the cavity (mechanics) to be coupled to a bath with thermal occupation n_c^{th} (n_m^{th}) at a rate κ (γ_m). For optical systems, n_c^{th} is usually indistinguishable from 0, but for microwave systems, a nonzero n_c^{th} is commonly observed at high pump powers (20, 21). The presence of the pumps at $\omega_{\pm} = \omega_c \pm \omega_m$ generates coherent intracavity photon occupations n_p^{\pm} , which are proportional to both the pump power applied at the input of the system and the pump power measured at the output of the measurement chain. The cavity and mechanics are coupled at a single-photon coupling rate $g_0 = \frac{d\omega_c}{dx} x_{zp}$. We also define the enhanced optomechanical coupling rates for the blue and red pumps as $G_{\pm} = g_0 \sqrt{n_p^{\pm}}$ and the effective optomechanical coupling rate as $\mathcal{G} = \sqrt{G_-^2 - G_+^2}$.

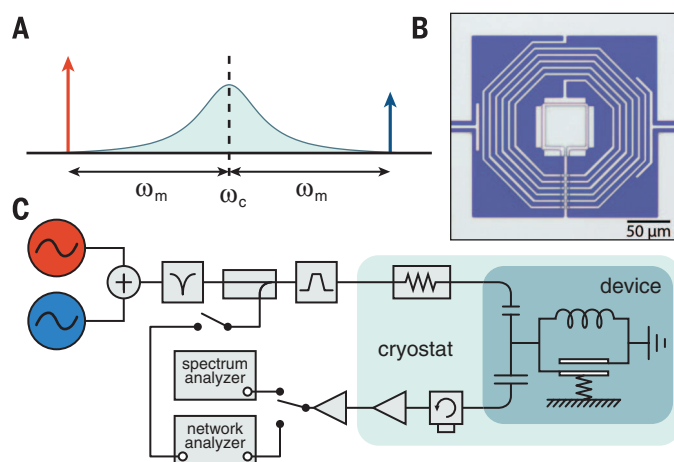


Fig. 1. Measurement setup and device. (A) Schematic showing frequencies of squeezing drive tones relative to the cavity frequency. (B) Optical micrograph of a typical device. Gray regions are aluminum, and blue regions are the exposed silicon substrate. The center square is a parallel-plate capacitor with a top plate that has a mechanical degree of freedom. The capacitor is surrounded by a spiral inductor, and coupling capacitors on the left and right provide input and output coupling to the device. (C) Microwave circuit diagram for squeezing measurements. The red- and blue-detuned tones are filtered at room temperature and attenuated at low temperatures so that they are shot-noise limited at the device. The device is thermally connected to the mixing plate of a dilution refrigerator. Signals are amplified and then measured with a spectrum analyzer or network analyzer.

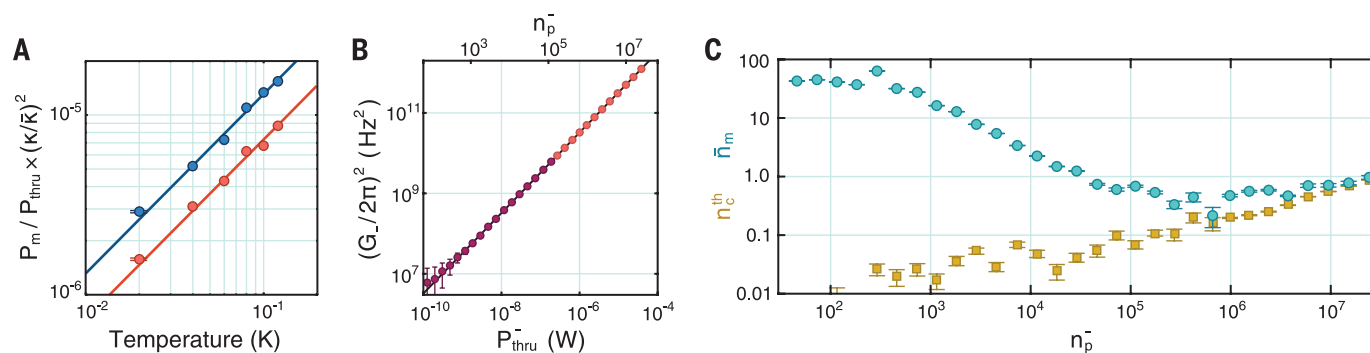


Fig. 2. Calibrations and characterization. (A) We measure the integrated mechanical sideband power (P_m) of a weak red-detuned (red) or blue-detuned (blue) pump and normalize by the measured pump power (P_{thru}). This ratio is proportional to the thermal occupation of the mechanics times g_0^2 . The difference in slopes is due to the difference in microwave transmission at ω_- and ω_+ . (B) Enhanced coupling rate calibration for a red-detuned drive. Purple circles, weak-driving regime in which the mechanical suscepti-

bility is a simple Lorentzian; black line, fit to the weak-driving regime damping versus power; red circles, strong-driving regime in which the mechanical linewidth becomes comparable to the cavity linewidth and G_- must be extracted using a full model. (C) Characterization of sideband cooling in the presence of a red-detuned drive. Turquoise circles, cooled mechanical occupation; yellow squares, cavity thermal occupation. The mechanical occupation is limited by heating of the cavity bath.

The linearized interaction Hamiltonian for this system is given by

$$\hat{H} = -\hbar\hat{a}^\dagger(G_+\hat{b}^\dagger + G_-\hat{b} + G_+\hat{b}e^{-2i\omega_m t} + G_-\hat{b}^\dagger e^{2i\omega_m t}) + \text{H.c.} \quad (1)$$

where \hat{a}^\dagger is the cavity photon creation operator and \hat{b}^\dagger is the mechanical phonon creation operator. In the good-cavity limit ($\omega_m \gg \kappa$), and when $\kappa \gg \gamma_m$, the quadrature fluctuations are then given by

$$\langle \Delta \hat{X}_{1,2}^2 \rangle = x_{zp}^2 \left\{ \frac{\gamma_m}{\kappa} \frac{(4\mathcal{G}^2 + \kappa^2)}{(4\mathcal{G}^2 + \gamma_m \kappa)} (2n_m^{th} + 1) + \frac{4(G_- \mp G_+)^2}{(4\mathcal{G}^2 + \gamma_m \kappa)} (2n_c^{th} + 1) \right\} \quad (2)$$

For both $\langle \Delta \hat{X}_1^2 \rangle$ and $\langle \Delta \hat{X}_2^2 \rangle$, the first term is proportional to $2n_m^{th} + 1$ and has a prefactor that is less than 1 for all $\mathcal{G} > 0$. This term represents the damping of both quadratures due to the excess red-detuned power. The second term is proportional to $2n_c^{th} + 1$ and is due to the back-action from the microwave field. We see that the back-action is reduced for $\langle \Delta \hat{X}_1^2 \rangle$ and increased for $\langle \Delta \hat{X}_2^2 \rangle$ relative to $\frac{4\mathcal{G}^2}{(4\mathcal{G}^2 + \gamma_m \kappa)} (2n_c^{th} + 1)$, the amount of back-action we would normally associate with the net damping rate set by \mathcal{G} . This reduction for \hat{X}_1 makes it possible to reduce $\langle \Delta \hat{X}_1^2 \rangle$ below x_{zp}^2 .

It is important to note that the quadrature variances depend on the thermal occupations of both the mechanical and cavity baths, which can both be heated by the applied pump power. These thermal occupations are also evident in the noise spectrum of photons leaving the cavity. For our two-port device measured in transmission, the output spectrum derived from the Hamiltonian in Eq. 1 has the form

$$\bar{S}_{VV}[\omega] = S_0 + \kappa_{out} \kappa \frac{(\gamma_m/2)^2 + (\omega - \omega_c)^2}{|f[\omega - \omega_c]|^2} n_c^{th} + \kappa_{out} \gamma_m \frac{G_-^2 n_m^{th} + G_+^2 (n_m^{th} + 1)}{|f[\omega - \omega_c]|^2} \quad (3)$$

where $f[\omega] = \mathcal{G}^2 + (\gamma_m/2 - i\omega)(\kappa/2 - i\omega)$, κ_{out} is the coupling through the output port of our device, and S_0 is the noise floor of our measurement system. To determine the state of the mechanics, we follow an approach analogous to that used for mechanical cooling measurements in the presence of heated baths (22): We fit the output noise spectrum in the presence of the squeezing tones to extract the bath occupations and then infer the quadrature variances for a mechanical resonator coupled to these baths.

Our device consists of a mechanical resonator of frequency $\omega_m = 2\pi \times 3.6$ MHz coupled capacitively to a microwave lumped-element resonator with frequency $\omega_c = 2\pi \times 6.23$ GHz, similar to the device used in (22) (Fig. 1B). The bare mechanical linewidth is $\gamma_m = 2\pi \times 3$ Hz at

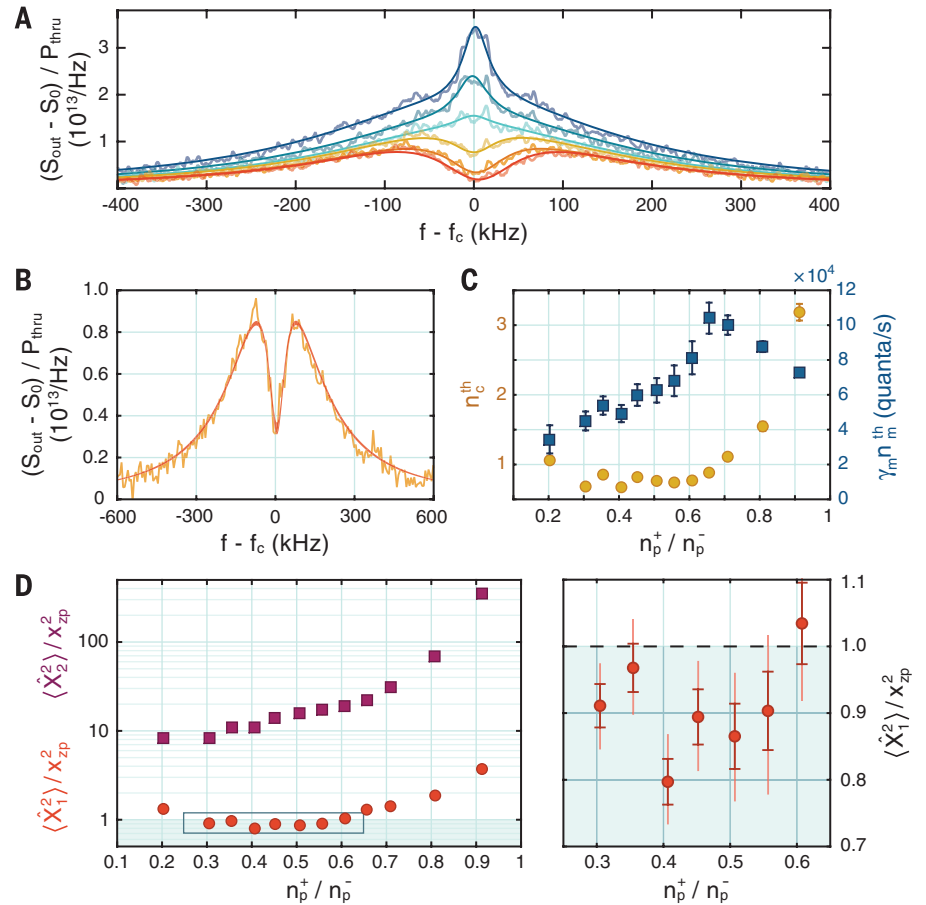


Fig. 3. Squeezing measurements. (A) Background-subtracted output spectra normalized by the measured red-detuned pump power at blue/red pump power ratios of 0.3, 0.4, 0.5, 0.6, 0.65, and 0.7, from red to blue. Darker lines indicate fits. All spectra are taken at the total power of $n_p^+ + n_p^- = 1.76 \times 10^7$. As the ratio decreases, the damping increases, broadening the mechanical linewidth and causing the mechanical noise to go from a peak to a dip due to noise squashing. (B) Close-up of spectrum and fit at $n_p^+/n_p^- = 0.4$. The thickness of the fit line corresponds to the 95% confidence bounds on the fit. (C) Values of n_c^{th} (yellow circles) and $\gamma_m n_m^{th}$ (blue squares) obtained from Bayesian analysis of the spectra. (D) (Left) Calculated quadrature noise for $\langle \Delta \hat{X}_1^2 \rangle$ (red circles) and $\langle \Delta \hat{X}_2^2 \rangle$ (purple squares). The shaded region indicates subzero-point squeezing. (Right) Close-up of the boxed area showing data with \hat{X}_1 fluctuations below the zero-point level. Dark and light red error bars represent the standard deviation and 95% confidence intervals, respectively. The lowest point has $\langle \Delta \hat{X}_1^2 \rangle / x_{zp}^2 = 0.797 \pm 0.034$. The fit for this point is shown in (B).

10 mK, and the cavity linewidth is $\kappa = 2\pi \times 450$ kHz. The optomechanical coupling rate is $g_0 = 2\pi \times 36$ Hz, and the zero-point fluctuations have an amplitude of $x_{zp} \sim 2.3$ fm. Our measurement setup is shown in Fig. 1C. Either we can measure the output noise spectrum of the system (spectral response) or we can sweep a small probe tone through the cavity to measure the complex transmission (driven response). We first calibrate the normalized spectral power at the output of our system using known thermal occupations to find g_0 (Fig. 2A). We then cool our sample temperature to 10 mK, giving an initial thermal occupation of $n_m^{th} \sim 50$ quanta. We calibrate the enhanced optomechanical coupling rate, G_- , to the output power of a red-detuned pump by measuring the total mechanical linewidth, $\gamma_{tot} = \gamma_m + 4\mathcal{G}^2/\kappa$, from the driven response

of the mechanics for linewidths much smaller than κ (Fig. 2B). As we increase the pump power further, the mechanical linewidth becomes comparable to the cavity bandwidth, and a strong-coupling model of the system is needed to fit the driven response. Fits with this model are in excellent agreement to the low-power calibrations, so we see that the device is well behaved and performs linearly over a broad range of pump powers (Fig. 2B). This agreement also confirms that the dynamics of our system are well described by the linearized Hamiltonian in Eq. 1 in the limit of no blue-detuned power. As we increase the red-detuned pump power, the mechanics becomes more strongly coupled to the cold cavity bath, reaching a minimum occupation of 0.22 ± 0.08 quanta (Fig. 2C). The blue-detuned coupling rate, G_+ , is also calibrated to the measured

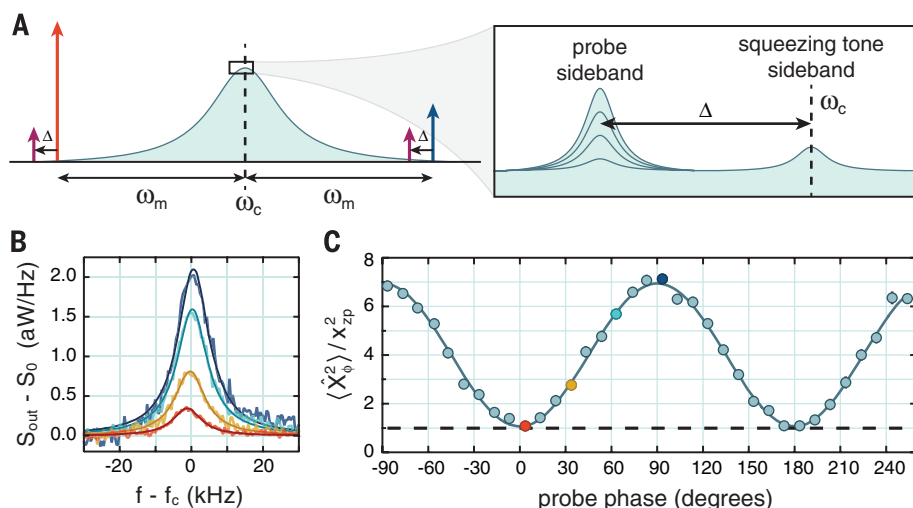


Fig. 4. BAE measurement of squeezing. (A) Schematic of pump and probe tone configuration, showing the sideband spectra for different probe phases. (B) Measured BAE probe sideband spectra for different probe phases with $n_p^- = 16 \times 10^6$, $n_p^- = 3.2 \times 10^6$, and each $n_p^{probe} = 0.95 \times 10^6$. (C) Quadrature variance as a function of phase, as obtained from the calibrated sideband area. The spectra shown in (B) are highlighted in their corresponding color. The zero-point variance is indicated with a dashed black line.

output power using the G_- calibration and a measurement of the output gain at ω_+ versus ω_- (23).

To squeeze the mechanical motion, a red-detuned pump is applied at $\omega_c - \omega_m$ and a weaker, blue-detuned pump is applied at $\omega_c + \omega_m$, such that their sidebands overlap at the cavity frequency, as described above. We then measure the output spectrum in the lab frame at different pump power ratios and fit a spectral model to the background-subtracted output spectrum normalized by the measured pump power (Fig. 3A). The spectral model includes “bad-cavity” effects that arise when $\omega_m \not\ll \kappa$ and does not assume that the pumps are aligned at precisely $\omega_c \pm \omega_m$. For our device, the former correction is small, because $\kappa/\omega_m \sim 0.1$. In the absence of these effects, the model reduces to Eq. 3. Because we determine G_- and G_+ from our calibrations and measure κ to high precision with a driven response, the only unknown parameters are n_c^{th} and $\gamma_m n_m^{th}$. For parameter estimation, we use a Bayesian analysis that systematically incorporates both the uncertainty from nonlinear fitting and the uncertainty in the independent calibration measurements. Given the observed data and our knowledge of the system Hamiltonian, we directly sample the posterior probability distribution of all system parameters. We then use this distribution to extract estimators for the bath occupations, n_c^{th} and $\gamma_m n_m^{th}$, and for the mechanical quadrature occupations ($\Delta \hat{X}_1^2$) and ($\Delta \hat{X}_2^2$) (23). The extracted bath occupations are plotted in Fig. 3C, and the quadrature variances are shown in Fig. 3D. We find that, at our lowest point, we are squeezed to $0.80 \pm 0.03 x_{zp}^2$, or 1.0 ± 0.2 dB below the zero-point fluctuations. The spectral fit for this point is shown in Fig. 3B.

To directly measure the fluctuations of a single quadrature, it is possible to introduce a set of weak back-action evading tones in addition to the

squeezing tones (24) (Fig. 4A). This type of back-action evading measurement has the advantage that thermal cavity noise does not affect the measured fluctuations. In order for the presence of the probe tones not to interfere with the measured mechanical quadrature, the probe sideband must be separated from the squeezing sideband by many mechanical linewidths. For this device, where the mechanical linewidth at optimal squeezing is $\sim 15\%$ of the cavity linewidth, such a separation would place the probe sideband outside the cavity bandwidth, appreciably decreasing the probe gain and leading to unrealistic measurement times. However, we have implemented such a measurement scheme using a similar device with a larger cavity bandwidth, $\kappa = 2\pi \times 860$ kHz, and narrower mechanical linewidth, $\gamma_{tot} = 2\pi \times 10$ kHz (Fig. 4B). As is shown in Fig. 4C, the phase-dependent BAE measurement shows the expected squeezed thermal state produced by the two squeezing pumps, with minimum fluctuations of $1.09 \pm 0.06 x_{zp}^2$, limited in a similar way as the first device by heating. This measurement demonstrates the quadrature squeezing produced by imbalanced pumps at $\omega_c \pm \omega_m$, as described by the theory.

Although a squeezed thermal state always has a positive Wigner function, when the fluctuations in one quadrature are reduced below the zero-point level, the squeezed state no longer has a well-behaved P representation—that is, it cannot be represented as an incoherent mixture of coherent states (25). For this reason, a quantum squeezed state is considered a nonclassical state. It is a current goal to study the nonclassical behavior in larger and larger systems, and recent progress in the field of opto- and electromechanics has resulted in the generation of mechanical Fock states (26), entanglement between photons and phonons (27), and obser-

vation of the mechanical zero-point fluctuations (28); quantum squeezing in a micrometer-scale mechanical resonator is an important addition to this list.

REFERENCES AND NOTES

1. R. E. Slusher, L. W. Hollberg, B. Yurke, J. C. Mertz, J. F. Valley, *Phys. Rev. Lett.* **55**, 2409–2412 (1985).
2. B. Yurke et al., *Phys. Rev. Lett.* **60**, 764–767 (1988).
3. D. M. Meekhof, C. Monroe, B. E. King, W. M. Itano, D. J. Wineland, *Phys. Rev. Lett.* **76**, 1796–1799 (1996).
4. J. Hald, J. L. Sørensen, C. Schori, E. S. Polzik, *Phys. Rev. Lett.* **83**, 1319–1322 (1999).
5. T. J. Dunn, J. N. Sweetser, I. A. Walmsley, C. Radzewicz, *Phys. Rev. Lett.* **70**, 3388–3391 (1993).
6. G. A. Garrett, A. G. Rojo, A. K. Sood, J. F. Whitaker, R. Merlin, *Science* **275**, 1638–1640 (1997).
7. A. Kronwald, F. Marquardt, A. A. Clerk, *Phys. Rev. A* **88**, 063833 (2013).
8. D. Kienzler et al., *Science* **347**, 53–56 (2015).
9. D. Rugar, P. Grütter, *Phys. Rev. Lett.* **67**, 699–702 (1991).
10. P. Rabl, A. Shnirman, P. Zoller, *Phys. Rev. B* **70**, 205304 (2004).
11. R. Ruskov, K. C. Schwab, A. N. Korotkov, *Phys. Rev. B* **71**, 235407 (2005).
12. K. Jähne et al., *Phys. Rev. A* **79**, 063819 (2009).
13. M. R. Vanner et al., *Proc. Natl. Acad. Sci. U.S.A.* **108**, 16182–16187 (2011).
14. A. Szorkovszky, G. A. Brawley, A. C. Doherty, W. P. Bowen, *Phys. Rev. Lett.* **110**, 184301 (2013).
15. A. Vinante, P. Falferi, *Phys. Rev. Lett.* **111**, 207203 (2013).
16. A. Pontin et al., *Phys. Rev. Lett.* **112**, 023601 (2014).
17. J. I. Cirac, A. S. Parkins, R. Blatt, P. Zoller, *Phys. Rev. Lett.* **70**, 556–559 (1993).
18. V. B. Braginsky, Y. I. Vorontsov, K. S. Thorne, *Science* **209**, 547–557 (1980).
19. F. Marquardt, J. P. Chen, A. A. Clerk, S. M. Girvin, *Phys. Rev. Lett.* **99**, 093902 (2007).
20. J. Gao et al., *Appl. Phys. Lett.* **92**, 152505 (2008).
21. J. Suh, A. J. Weinstein, K. C. Schwab, *Appl. Phys. Lett.* **103**, 052604 (2013).
22. J. D. Teufel et al., *Nature* **475**, 359–363 (2011).
23. Materials and methods are available as supplementary materials on Science Online.
24. J. Suh et al., *Science* **344**, 1262–1265 (2014).
25. M. S. Kim, F. A. M. de Oliveira, P. L. Knight, *Phys. Rev. A* **40**, 2494–2503 (1989).
26. A. D. O’Connell et al., *Nature* **464**, 697–703 (2010).
27. T. A. Palomaki, J. D. Teufel, R. W. Simmonds, K. W. Lehnert, *Science* **342**, 710–713 (2013).
28. F. Lecocq, J. D. Teufel, J. Aumentado, R. W. Simmonds, *Nat. Phys.* **11**, 635–639 (2015).

ACKNOWLEDGMENTS

This work is supported by funding provided by the Institute for Quantum Information and Matter, an NSF Physics Frontiers Center with support of the Gordon and Betty Moore Foundation (NSF-IQIM 1125565), by the Defense Advanced Research Projects Agency (DARPA-QUANTUM HR0011-10-1-0066), by the NSF (NSF-DMR 1052647 and NSF-EEC 0832819), and by the Semiconductor Research Corporation (SRC) and Defense Advanced Research Project Agency (DARPA) through STARnet Center for Function Accelerated nanoMaterial Engineering (FAME). A.A.C., F.M., and A.K. acknowledge support from the DARPA ORCHID program through a grant from AFOSR, F.M. and A.K. from ITN cQOM and the ERC OPTOMECH, and A.A.C. from NSERC.

SUPPLEMENTARY MATERIALS

www.sciencemag.org/content/349/6251/952/suppl/DC1
Materials and Methods
Figs. S1 to S5
References (29–32)

7 May 2015; accepted 28 July 2015
10.1126/science.aac5138

NANOPARTICLES

Production of amorphous nanoparticles by supersonic spray-drying with a microfluidic nebulator

Esther Amstad,^{1,2} Manesh Gopinadhan,³ Christian Holtze,⁴ Chinedum O. Osuji,³ Michael P. Brenner,¹ Frans Spaepen,¹ David A. Weitz^{1,5*}

Amorphous nanoparticles (a-NPs) have physicochemical properties distinctly different from those of the corresponding bulk crystals; for example, their solubility is much higher. However, many materials have a high propensity to crystallize and are difficult to formulate in an amorphous structure without stabilizers. We fabricated a microfluidic nebulator that can produce amorphous NPs from a wide range of materials, even including pure table salt (NaCl). By using supersonic air flow, the nebulator produces drops that are so small that they dry before crystal nuclei can form. The small size of the resulting spray-dried a-NPs limits the probability of crystal nucleation in any given particle during storage. The kinetic stability of the a-NPs—on the order of months—is advantageous for hydrophobic drug molecules.

The properties of nanoparticles (NPs) can differ greatly from those of their bulk counterparts, and for materials that are normally crystalline, even greater differences can be achieved by making amorphous NPs (a-NPs). For example, the solubility of a given material can be greatly enhanced even when its crystalline counterpart is very poorly soluble (*1*). Many materials have a very high propensity to crystallize, so it is challenging to produce amor-

phous structures in widely applicable ways. Inorganic materials that can be evaporated into the gas phase can form a-NPs via aggregation into amorphous clusters (*2, 3*). In addition, some metals can be processed into a-NPs by rapidly cooling drops composed of melts (*4, 5*). However, the majority of inorganic materials cannot be processed in this manner, and even fewer organic materials can be so processed. Instead, the most common route to process organic ma-

terials into NPs is through precipitation from solution (*6–9*).

For materials with a high propensity to crystallize, crystallization is typically much faster than termination of the precipitation reaction, and the resultant NPs are crystalline. a-NP production thus requires the addition of crystallization inhibitors (*10*), which must be carefully chosen for each crystallization-prone material. In some specific cases, the solution can be rapidly cooled to freezing, followed by lyophilization of the resulting particles (*11, 12*). Alternatively, the solution can be formed into drops through spray-drying (*13–15*). In this case, NPs start to form when the solute concentration exceeds its saturation concentration (*16, 17*). However, the rate of crystallization is typically still much faster than the rate of NP growth, and crystallization inhibitors are still required to create a-NPs. Nearly half of all drug compounds are hydrophobic (*1*), and formulating them as a-NPs would increase their bioavailability (*18*), solubility (*1*), and dissolution rates (*19*).

We show how to produce a-NPs from a range of materials without the use of any crystallization inhibitors. Our process uses a microfluidic

¹School of Engineering and Applied Sciences, Harvard University, Cambridge, MA, USA. ²Institute of Materials, Ecole Polytechnique Fédérale de Lausanne, Lausanne, Switzerland. ³Department of Chemical and Environmental Engineering, Yale University, New Haven, CT, USA. ⁴BASF SE, D-67056 Ludwigshafen, Germany. ⁵Department of Physics, Harvard University, Cambridge, MA, USA.

*Corresponding author. E-mail: weitz@seas.harvard.edu

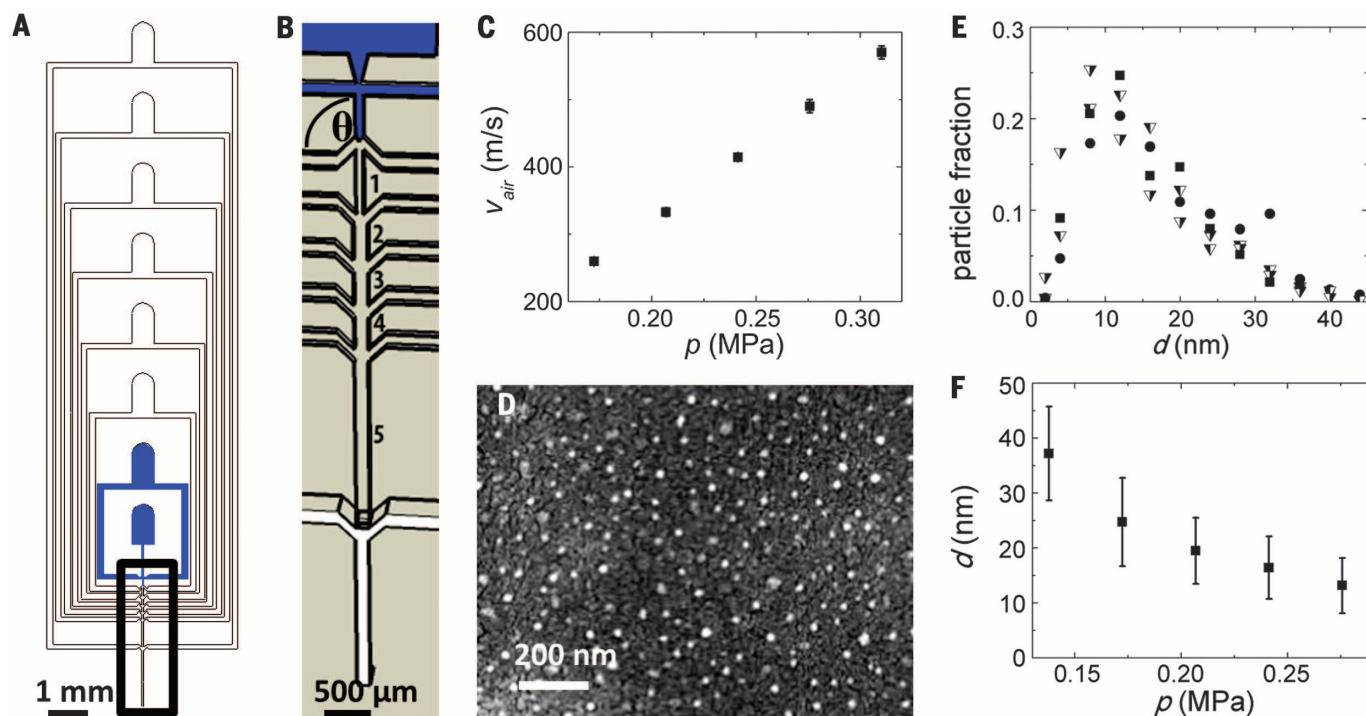


Fig. 1. The microfluidic nebulator. (A and B) Overview (A) and close-up (B) of a microfluidic nebulator. Liquids are injected through blue inlets; air is introduced through white inlets. (C) Air velocity at outlet as a function of pressure applied to all air inlets; error bars indicate the variance of air velocities measured in different devices. (D) SEM micrograph of spray-dried fenofibrate NPs. (E) Size distribution of fenofibrate (■), clotrimazole (●), danazol (▼), and estradiol (▼) NPs. (F) Size of fenofibrate NPs as a function of air pressure; error bars indicate the size distribution of NPs produced in different batches.

nebulator—a spray drier that enables supersonic air speeds to be achieved at moderate pressures. Liquids are nebulized into very small drops whose dimensions limit the size of the resultant spray-dried NPs. The very rapid evaporation of the solvent creates a kinetically arrested glass in the evaporating drop and prevents formation of crystal nuclei. The nebulator can produce a-NPs from both organic and inorganic materials, including materials with a very high propensity to crystallize, such as table salt (NaCl). The small size of these a-NPs (<15 nm) results in exceptionally high stability against crystallization, with most a-NPs maintaining that state under ambient conditions and at room temperature for at least 7 months.

We fabricated the nebulator from poly(dimethyl siloxane) (PDMS) using soft lithography (20). A main fluid-inlet channel is intersected by a pair of inlets for an additional fluid so that two fluid streams can mix if it is necessary to initiate chemical reactions prior to drop formation. The nebulator also has six air inlets (Fig. 1, A and B). The last junction is three-dimensional (3D), with a small inlet opening into a channel of larger dimensions (Fig. 1B) (21). We sliced the end of the main channel to make the final outlet (15). The same pressure was applied to each of the air inlets; the device can reliably sustain inlet pressures up to 0.28 MPa (~2.8 atm) before the PDMS bonding fails. The velocity of the air at the outlet scales with the inlet pressure (Fig. 1C).

To demonstrate the operation of the nebulator, we used a generic hydrophobic organic drug,

fenofibrate, which has a high propensity for crystallization. We dissolved fenofibrate in ethanol (5 mg/ml) and injected this solution into the first fluid inlet at a flow rate of 1 ml/hour. We inverted the direction of the first pair of air inlets to inject the air in the opposite direction to the ethanol flow (Fig. 1B). Because ethanol strongly wets the channel walls, thin homogeneous ethanol films were formed and flowed along the four channel walls. These films were detached from the walls at the 3D junction, where they broke into very small drops whose diameter must be similar to the film thickness. The drops began to dry through evaporation as they exited the device, forming NPs that were collected on a substrate placed 10 cm from the outlet.

Remarkably, NPs with an average diameter of 14 nm were produced with an inlet pressure of 0.28 MPa (Fig. 1D and fig. S1). Drug particles produced with commercially available spray-dry instruments typically have diameters greater than 350 nm (14, 22–26). We also produced NPs from other hydrophobic drugs, including clotrimazole, estradiol, and danazol, with similar size distributions (Fig. 1E). The thickness of the liquid film produced in the nebulator scaled inversely with applied air pressure, so the NP size decreased roughly inversely with increasing air pressure (Fig. 1F). This relation suggests that NPs as small as 1 nm could be produced with an inlet air pressure of 0.54 MPa.

The smallest-sized fenofibrate NPs (14 nm) were always amorphous, as indicated by the lack of any lattice plane in the high-resolution trans-

mission electron microscope (HRTEM) image and the absence of distinct diffraction peaks in its Fourier transform (Fig. 2A), as well as the absence of any peaks in x-ray diffraction (XRD) (Fig. 2B, top trace). By contrast, crystalline NPs (c-NPs) formed when spray-dried in the presence of Pluronic F127, which acted as a heterogeneous nucleant. These c-NPs had clear diffraction peaks (fig. S2, top trace) (27), which also validates the use of XRD to determine the structure of our spray-dried NPs. Fenofibrate has a glass transition temperature T_g of -20°C (28) and a melting temperature T_m of 80°C (29), so fenofibrate a-NPs must be undercooled liquids at room temperature. Similar amorphous structures were observed for small NPs formed from all other drugs tested (figs. S3 and S4); however, the others are glasses, as they all have T_g above room temperature.

We argue that a-NPs form as a result of this production route. Fenofibrate crystals can nucleate as soon as the solvent in the drop has evaporated sufficiently for the solute concentration to exceed its saturation value. Once a crystal nucleus is formed, crystal growth should transform the entire a-NP. Thus, formation of a-NPs can occur only if crystal nucleation is inhibited. We calculated the number of crystal nuclei that form in a drop as it evaporates, N , using classical nucleation theory under isothermal conditions (17, 27). As the solvent evaporates, the solute concentration becomes very high and the resultant nucleation rate is large. Even drops as small as 100 nm, which produce the 14-nm NPs, should yield c-NPs.

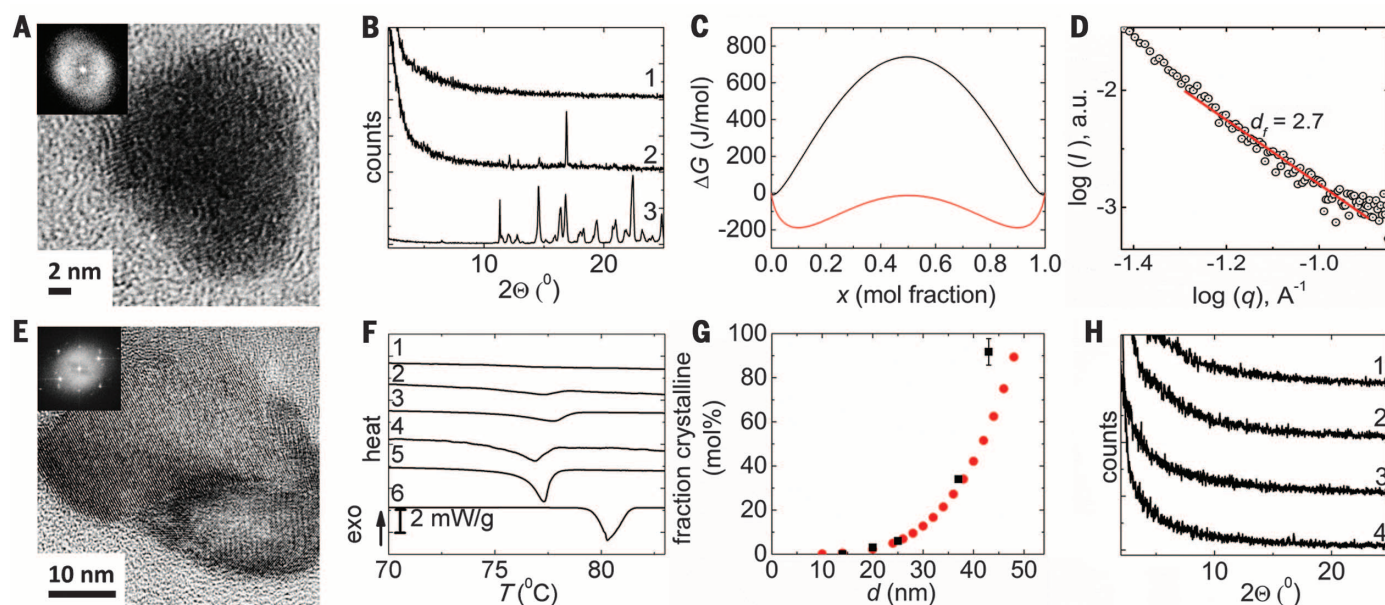


Fig. 2. Structure of spray-dried fenofibrate NPs. (A) HRTEM micrograph of fenofibrate spray-dried at 0.28 MPa, with the Fourier transform in the inset. (B) XRD spectra of fenofibrate spray-dried with inlet air pressures of (1) 0.28 MPa and (2) 0.14 MPa; crystalline fenofibrate (3) is shown as a reference. (C) Free energy of formation of fenofibrate-ethanol solution, ΔG , at room temperature (red curve) and -70°C (black curve). (D) SAXS data of fenofibrate NPs with the power-law fit (solid line). (E) TEM image of fenofibrate spray-dried at 0.14 MPa, with the Fourier trans-

formation in the inset. (F) DSC traces of fenofibrate NPs produced at (1) 0.28 MPa, (2) 0.21 MPa, (3) 0.17 MPa, (4) 0.14 MPa, and (5) 0.12 MPa; crystalline fenofibrate (6) is shown as a reference. (G) Fraction of c-NPs measured by integrating the melting peaks of the DSC traces (■) and calculated (●) as a function of their diameter; the error bars indicate the variance between particles produced in different batches. (H) XRD traces of fenofibrate NPs stored at (1) room temperature for 7 months, (2) 40°C for 6 months, (3) 65°C for 2 months, and (4) 65°C for 3 months.

The calculation of the nucleation rate assumes a homogeneous distribution of fenofibrate in the evaporating solvent.

However, if there is an attractive interaction between the solute molecules, they can undergo spinodal decomposition more rapidly than crystals nucleate, leading to high spatial heterogeneity. To determine whether there is an attractive interaction between fenofibrate molecules, we compute the difference in the Gibbs free energy between the individual components and the solution, ΔG , as a function of the solution composition (27). It has two minima, implying that this solution phase separates, as indicated by the red curve in Fig. 2C. The low concentration in the solute-poor phase will decrease the rate of crystal nucleation. The high concentration in the solute-rich phase will increase the rate of crystallization, but the viscosity will also increase, thus also reducing the rate of crystal nucleation.

We estimate that the rate of crystallization at room temperature would still result in c-NPs. However, the drop is also subjected to evaporative cooling: It decreases the drop temperature to a new steady-state value, determined by the balance of evaporative cooling and heat transferred from the air to the drop. Because of the rapid air flow, the boundary layers at the surface of the drop for both molecular transport and heat diffusion are very thin, resulting in both rapid evaporation and rapid heat transport. We estimate the new temperature to be $T = -70^\circ\text{C}$ (27). At this temperature, the solute-rich phase contains only 1 mol% of solvent, as shown by the black curve in Fig. 2C. Hence, the viscosity of the solute-rich phase is further increased by the increased solute concentration and the reduced temperature; this decreases the mobility of fenofibrate molecules and thus the rate of crystal nucleation.

Similarly, the reduced temperature decreases the nucleation rate in the solute-poor phase by reducing the solute mobility, but to a smaller extent. If the drop is sufficiently small, it will evaporate faster than crystal nuclei can form; thus, the NPs will remain amorphous. We postulate that the origin of the amorphous structure is kinetic arrest of the solute molecules into a glassy state. This mechanism, which involves a rapid increase in solute concentration accompanied by a decrease in temperature, is fundamentally different from the formation of conventional glasses, where the formation of crystal nuclei is kinetically suppressed only through a fast reduction in temperature. Intriguingly, the glass formation inside drops is similar to that observed for attractive colloidal particles that undergo kinetic arrest (30–32).

To test our postulate, we investigated the morphology of the NPs. The structure of a kinetically arrested glassy phase formed by spinodal decomposition should be highly tenuous, and remnants of this irregularity may persist even after the drop fully dries. We used small-angle x-ray scattering (SAXS) to investigate the structure of 14-nm fenofibrate NPs at scattering vectors, q , corresponding to length scales smaller than the particle

size. We observe a power-law dependence of the scattered intensity, $I(q) \propto q^{-d_f}$, consistent with a fractal structure having a fractal dimension $d_f = 2.7$ (Fig. 2D). Thus, the structure of the NPs is highly irregular, consistent with formation from spinodal decomposition (33).

Further validation of our postulate comes from the formation of larger drops, which take longer to dry and hence allow more time for nuclei to form. When we seeded a small crystal of fenofibrate in a supercooled liquid of pure fenofibrate, formed by spray-drying, it grew very rapidly. Thus, even if only a single crystal nucleation event occurred inside an evaporating drop, the entire particle would crystallize upon warming. Indeed, some 40-nm-diameter NPs were fully crystalline, as shown by HRTEM (Fig. 2E), by XRD (Fig. 2B, middle trace), and by the appearance of a melting peak measured with differential scanning calorimetry (DSC) (Fig. 2F, second thermogram), albeit at a lower temperature than observed for bulk melting.

To quantify the percentage of c-NPs, we determined the crystalline fraction as a function of NP size by integrating the area of the DSC melting peaks shown in Fig. 2F. The fraction of c-NPs increased with increasing NP size (Fig. 2G, black squares). For comparison, we predicted the crystalline fraction by calculating N as a function of NP size and found excellent agreement with experiment (Fig. 2G).

One of the major obstacles to the use of the amorphous structure for drugs is the high pro-

pensity toward crystallization during storage (34). Surprisingly, although the 14-nm fenofibrate a-NPs are undercooled liquids that are either deposited as monolayers or coated with a polymer to prevent aggregation, they remained amorphous even when stored for 7 months at room temperature under ambient conditions, as shown by XRD (Fig. 2H, first curve), and for at least 6 months if stored under ambient conditions at 40°C (Fig. 2H, second curve). Moreover, fenofibrate NPs remained amorphous for up to 2 months if stored even at 65°C (Fig. 2H, third curve) and only began to crystallize after 3 months, as indicated by the small XRD diffraction peaks at $2\theta = 16.3^\circ$ and 16.8° (Fig. 2H, fourth curve). We attribute this exceptionally high stability to the small NP size. If compartmentalized into many small NPs, crystal growth is kinetically restricted, as a large number of nuclei must form to fully crystallize the sample.

We also used the microfluidic nebulator to formulate inorganic a-NPs. For example, we formed CaCO_3 NPs exploiting the two liquid inlets to co-inject one aqueous solution containing 5 mM CaCl_2 and another containing 5 mM Na_2CO_3 . As soon as the two solutions were combined, nuclei of CaCO_3 could start to precipitate from the supersaturated solution. Water does not wet the PDMS walls. Nevertheless, we could use the same device design to operate the nebulator in the dripping regime, where drops of water are formed at the first inlet. The air from the first inlet must reverse its flow direction to enter the main

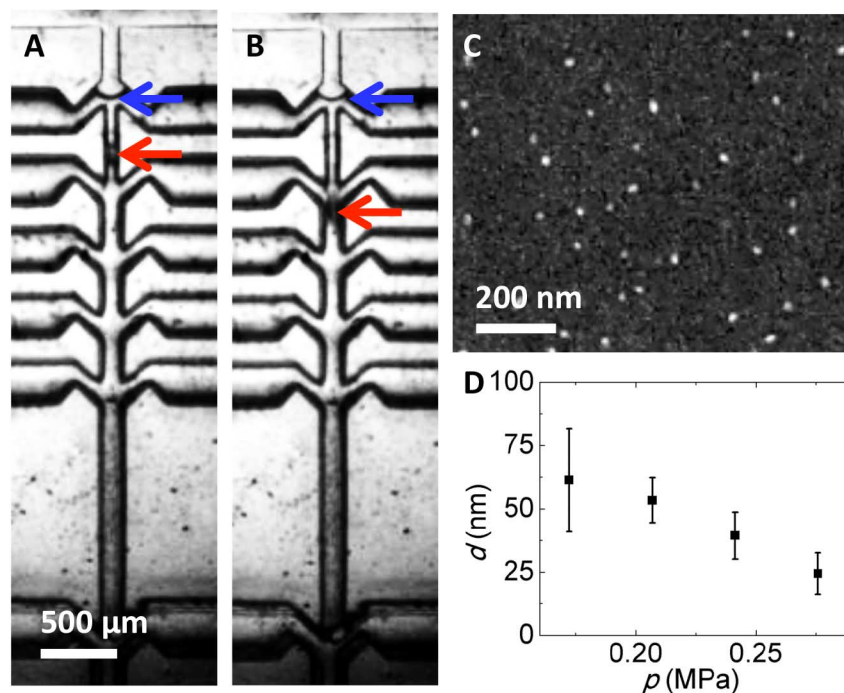


Fig. 3. Operation of the nebulator using a nonwetting fluid. (A and B) Optical micrographs of the nebulator operated with water, taken 120 μs (A) and 280 μs (B) after the drop pinched off. Red arrows point to the drops, blue arrows to the stagnation point of the air velocity v_x . (C) SEM image of spray-dried CaCO_3 NPs. (D) Size of CaCO_3 NPs as function of the air pressure; error bars indicate the size distribution of NPs produced in different batches.

channel. This configuration created a stagnation point where the component of the air velocity in the direction of the main channel, v_z , equals zero; this produced a stationary instability and dripping (Fig. 3, A and B, and movie S1). The size of these drops was similar to the channel dimension. Thus, the distance between the drop surface and the channel wall, l , was small, and the local shear stress, $\tau = \mu(dv/l)$, was very high; here, μ is the viscosity of air. This large shear stress overcame the Laplace pressure of the primary drop, breaking it into much smaller drops whose radius r was determined by the balance of the shear stress and the Laplace pressure $\mu(dv/l) = \gamma/r$; here, γ is the surface tension.

To estimate a lower limit for τ , we determined an upper limit of l using microscope images and determined dv by measuring the velocity at the outlet and calculating the velocity profile inside the device (27). The resultant shear stress was very large and produced drops as small as 400 nm in diameter, which would lead to 30-nm NPs. Consistent with this calculation, the size of the spray-dried CaCO_3 NPs measured from scanning electron microscopy (SEM) images is 20 nm (Fig. 3C). The NP size increased with decreasing pressure applied to the air inlet (Fig. 3D), in accord with our calculations. These CaCO_3 NPs were chemically homogeneous, as determined by electron-dispersive spectroscopy (EDS) (fig. S5). For NPs with diameters less than 20 nm, there was no evidence of

crystallinity revealed by HRTEM (Fig. 4A). By contrast, NPs exceeding 40 nm contained multiple crystal nuclei embedded in an amorphous matrix. In this case, crystal growth was much slower than for fenofibrate, and we could visualize intermediate stages of the crystallization where crystalline regions coexist with amorphous ones (Fig. 4B). If the NPs were sufficiently small, the nebulator could make a-NPs from inorganic materials with a greater propensity to crystallize, such as BaSO_4 and iron oxide, as shown in the HRTEM images in fig. S6, A and B, respectively.

A common material with a very high propensity to crystallize is table salt, NaCl. Amorphous NaCl has not been reported, although small amorphous clusters have been predicted by molecular dynamics simulations (35). Remarkably, the nebulator could produce a-NPs of NaCl if their diameter was below 15 nm, as indicated in HRTEM images and the corresponding Fourier transform in Fig. 4C and the bottom XRD spectrum in Fig. 4E. Moreover, x-ray photoelectron spectroscopy (XPS) showed that the binding energy of the Na 1s peak was shifted toward lower energies, indicating that the nearest neighbors of the Na ions are farther apart, or on average less electronegative, than the nearest neighbors of Na contained in the NaCl structure (Fig. 4F, bottom spectrum). Moreover, the Cl 1s peak was broadened, indicating that the distances of the nearest neighbors

of the Cl ions vary (fig. S7, bottom spectrum). Larger NaCl NPs were crystalline, as indicated by the HRTEM micrograph in Fig. 4D, the (220) reflection at $2\theta = 45.5^\circ$ in the middle XRD trace in Fig. 4E, and the unchanged binding energies of the Na 1s and Cl 1s peaks measured with XPS and shown respectively in the second spectra in Fig. 4F and fig. S7. The only materials with which we have been unable to form a-NPs are Au, Ag, and Pt.

The production rate of a single nebulizer is limited by its scale; thus, to make more useful quantities of material, the nebulators must be scaled up in number. We operated three nebulators in parallel with common inlets and increased throughput to 15 mg of material per hour, which is sufficient for laboratory-scale tests such as drug bioavailability. Hydrodynamic coupling between devices did not compromise their performance when operated in parallel, so further scale-up in the number of coupled nebulators should be feasible.

REFERENCES AND NOTES

- Y. Kawabata, K. Wada, M. Nakatani, S. Yamada, S. Onoue, *Int. J. Pharm.* **420**, 1–10 (2011).
- A. H. Tavakoli et al., *J. Phys. Chem. C* **117**, 17123–17130 (2013).
- L. Landström, J. Kokavecz, J. Lu, P. Heszler, *J. Appl. Phys.* **95**, 4408 (2004).
- Y. W. Kim, H. M. Lin, T. F. Kelly, *Acta Metall.* **37**, 247–255 (1989).
- A. L. Greer, *Nat. Mater.* **14**, 542–546 (2015).
- P. Guo, T. M. Hsu, Y. Zhao, C. R. Martin, R. N. Zare, *Nanomedicine* **8**, 333–341 (2013).
- L. Yu, C. Li, Y. Le, J.-F. Chen, H. Zou, *Mater. Chem. Phys.* **130**, 361–366 (2011).
- W.-Z. Zhu et al., *Int. J. Pharm.* **395**, 260–265 (2010).
- R. S. Dhumal, S. V. Biradar, S. Yamamura, A. R. Paradkar, P. York, *Eur. J. Pharm. Biopharm.* **70**, 109–115 (2008).
- M. E. Matteucci, M. A. Hotze, K. P. Johnston, R. O. Williams 3rd, *Langmuir* **22**, 8951–8959 (2006).
- W. Yang et al., *Int. J. Pharm.* **361**, 177–188 (2008).
- K. A. Overhoff et al., *Eur. J. Pharm. Biopharm.* **65**, 57–67 (2007).
- J.-S. Kim et al., *Int. J. Pharm.* **359**, 211–219 (2008).
- S. N. Harsha et al., *Drug Design Dev. Ther.* **9**, 273–282 (2015).
- J. Thiele et al., *Lab Chip* **11**, 2362–2368 (2011).
- M. E. Matteucci et al., *Mol. Pharm.* **4**, 782–793 (2007).
- K. F. Kelton, A. L. Greer, *Nucleation in Condensed Matter Applications in Materials and Biology* (Elsevier, New York, 2010).
- B. C. Hancock, M. Parks, *Pharm. Res.* **17**, 397–404 (2000).
- F. Kesiosoglou, S. Panmai, Y. Wu, *Adv. Drug Deliv. Rev.* **59**, 631–644 (2007).
- Y. N. Xia, G. M. Whitesides, *Annu. Rev. Mater. Sci.* **28**, 153–184 (1998).
- A. Rotem, A. R. Abate, A. S. Utada, V. Van Steijn, D. A. Weitz, *Lab Chip* **12**, 4263–4268 (2012).
- S. Harsha, *Drug Design Dev. Ther.* **7**, 1027–1033 (2013).
- C. Arpagaus, *Dry. Technol.* **30**, 1113–1121 (2012).
- K. Bürki, I. Jeon, C. Arpagaus, G. Betz, *Int. J. Pharm.* **408**, 248–256 (2011).
- X. Li, N. Anton, C. Arpagaus, F. Belleiteix, T. F. Vandamme, *J. Control. Release* **147**, 304–310 (2010).
- V. Martena, R. Censi, E. Hoti, L. Malaj, P. Di Martino, *J. Nanopart. Res.* **14**, 934 (2012).
- See supplementary materials on Science Online.
- Y. C. Ng, Z. Yang, W. J. McAuley, S. Qi, *Eur. J. Pharm. Biopharm.* **84**, 555–565 (2013).
- D. Law et al., *J. Pharm. Sci.* **92**, 505–515 (2003).
- P. J. Lu et al., *Nature* **453**, 499–503 (2008).

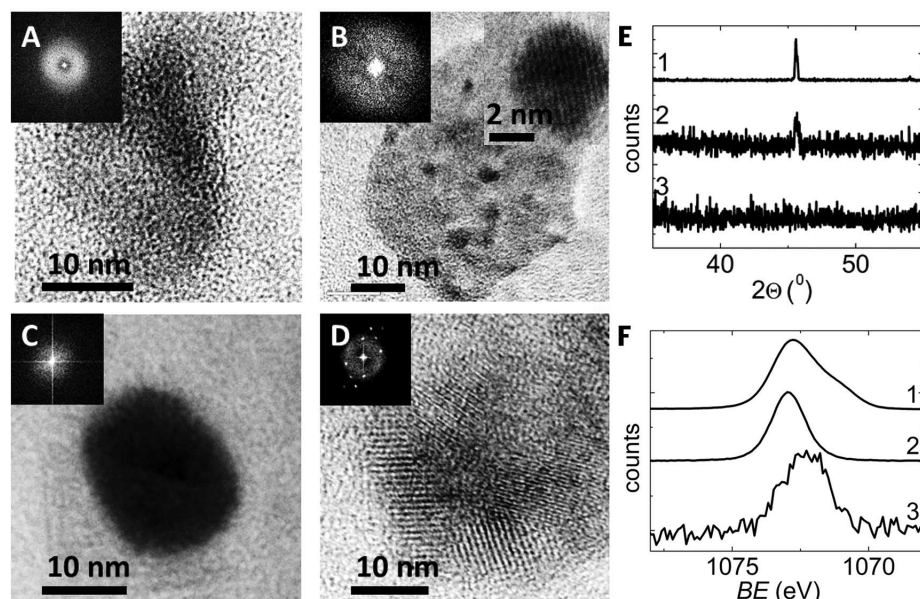


Fig. 4. Structure of spray-dried inorganic NPs. (A and B) HRTEM images, with Fourier transform insets, of CaCO_3 NPs produced at air inlet pressures of 0.28 MPa (A) and 0.21 MPa (B). The inset in (B) is a HRTEM of one of the dark spots shown in the main image, showing small amounts of crystal formation for this NP size. (C and D) HRTEM images of NaCl NPs spray-dried from aqueous solutions initially containing 4 mM NaCl (C) and 40 mM NaCl (D); the insets show their Fourier transforms. (E) XRD traces of (1) c-NaCl produced by slowly evaporating an aqueous solution containing 40 mM NaCl, (2) spray-dried NaCl NPs produced from a solution containing 40 mM NaCl, and (3) spray-dried NaCl NPs produced from a solution containing 4 mM NaCl. (F) XPS spectra of the Na 1s peak of (1) crystalline reference NaCl, (2) NaCl NPs spray-dried from a solution initially containing 40 mM NaCl, and (3) NaCl NPs spray-dried from a solution initially containing 4 mM NaCl.

31. V. Trappe, V. Prasad, L. Cipelletti, P. N. Segre, D. A. Weitz, *Nature* **411**, 772–775 (2001).
32. A. J. Liu, S. R. Nagel, *Nature* **396**, 21–22 (1998).
33. J. H. Page et al., *Phys. Rev. E* **52**, 2763–2777 (1995).
34. R. Laitinen, K. Löbmann, C. J. Strachan, H. Grohman, T. Rades, *Int. J. Pharm.* **453**, 65–79 (2013).
35. I. G. Nahtigal, I. M. Svishchev, *J. Phys. Chem. B* **113**, 14681–14688 (2009).

ACKNOWLEDGMENTS

We acknowledge support from BASF SE, NSF grants DMR-1310266 and DMS-1411694, and Harvard MRSEC grant

DMR-1420570. M.P.B. is an investigator of the Simons Foundation. Part of this work was performed at the Center for Nanoscale Systems (CNS), a member of the National Nanotechnology Infrastructure Network, supported by NSF award no. ECS-0335765. CNS is part of Harvard University. We thank D. C. Bell for acquiring the EDS images and L. R. Arriaga and D. M. Aubrecht for helpful discussions. Patent applications have been filed to cover the nebulator device (PCT/US2013/060522) and the production of a-NPs (PCT/US2014/062785). Additional data discussed in the main text are available in the supplementary materials. E.A. conducted the experiments; M.G. performed the SAXS experiments and analysis; E.A., F.S., and D.A.W. did the calculations and wrote the paper;

and all the authors contributed to the design and analysis of the experiments.

SUPPLEMENTARY MATERIALS

www.sciencemag.org/content/349/6251/956/suppl/DC1
Materials and Methods
Supplementary Text
Figs. S1 to S8
Movie S1
References (36, 37)

5 July 2015; accepted 31 July 2015
10.1126/science.aac9582

ORGANIC CHEMISTRY

Iron-catalyzed intermolecular [2+2] cycloadditions of unactivated alkenes

Jordan M. Hoyt, Valerie A. Schmidt, Aaron M. Tondreau, Paul J. Chirik*

Cycloadditions, such as the [4+2] Diels-Alder reaction to form six-membered rings, are among the most powerful and widely used methods in synthetic chemistry. The analogous [2+2] alkene cycloaddition to synthesize cyclobutanes is kinetically accessible by photochemical methods, but the substrate scope and functional group tolerance are limited. Here, we report iron-catalyzed intermolecular [2+2] cycloaddition of unactivated alkenes and cross cycloaddition of alkenes and dienes as regio- and stereoselective routes to cyclobutanes. Through rational ligand design, development of this base metal-catalyzed method expands the chemical space accessible from abundant hydrocarbon feedstocks.

Cycloaddition reactions as exemplified by the venerable [4+2] Diels-Alder reaction are among the most powerful in organic chemistry, providing an atom-economical method for the synthesis of six-membered rings (1). Despite their widespread utility and applications, these reactions require the use of activated substrates and are often ineffective for unactivated alkene coupling partners. Pure hydrocarbons are the principal feedstocks of the chemical industry, serving as essential precursors to fuels, films, liquid crystal displays, materials, and medicines (2). Among these, ethylene and propylene are the most abundant and are produced in 130 and 85 million metric tons annually, respectively, serving principally as monomers for the multibillion-dollar polyolefins industry (3, 4). Ethylene is also selectively trimerized and tetramerized on large scale rendering 1-hexene and 1-octene commodity alkenes (5), motivating the development of new cycloaddition methods that incorporate these fundamental industrial building blocks.

Although analogous [2+2] cycloadditions to prepare cyclobutanes are thermodynamically favorable and could be similarly transformative in synthesis, the exploration of the chemical space of four-membered carbocycles has been substantially hindered by the lack of selective methods

for their synthesis (6). One challenge in realizing a practical method is overcoming the high kinetic barrier imparted by the thermal constraints of orbital symmetry (7). The use of activated alkenes (8) and substrates that have the appropriate redox potentials to interact with photocatalysts (9, 10) have been described that overcome these challenges, and examples with high degrees of regio- and stereoselectivity have recently been reported (11, 12). Unactivated alkenes, such as those available in vast excess from shale gas reserves and biorenewable sources, are currently outside the scope of these methods (13). Although theoretical methods predict the photochemical feasibility of such cycloadditions (7), photodimerization of unactivated alkenes, typically conducted in the presence of copper catalysts, is limited to selected cyclic alkenes and often yields mixtures of products, highlighting the potential utility of alternative methods for cyclobutane synthesis (14).

Transition metal catalysis offers the prospect of promoting the [2+2] cycloaddition of unactivated alkenes by virtue of valence d-orbitals and low-energy pathways to metallacyclic intermediates (15). Nickel-phosphine combinations have been reported for the synthesis of cyclobutanes from dienes and unactivated alkenes, although both yields and selectivities are not synthetically useful (8). Related examples with Ti, Mn, and Fe have also been described and suffer from the same limitations in yield and selectivity (8). Examples of more-selective alkene [2+2] cycloadditions with

stoichiometric Mg, allyl chloride, and an Al reagent in the presence of Zr and Pd additives have also been reported (16).

Our group has found that iron and cobalt complexes bearing redox-active pyridine(diimine) ligands, which undergo reversible one-electron transfer with the transition metal, promote the intramolecular [2+2] cycloadditions of α,ω -dienes to yield the corresponding bicyclo[2.3.0]heptanes (Fig. 1A) (17–19). These base metal-catalyzed reactions proceed with unactivated dienes at ambient temperature, and mechanistic studies support reductive elimination from metallacyclic intermediates as the key C–C bond-forming step. In both iron (18) and cobalt (19) examples, the redox active pyridine(diimine) adopts its one-electron-reduced form, resulting in a more-oxidized metal center, and likely facilitates the directional, cyclobutane-forming $C(sp^3)-C(sp^3)$ reductive elimination.

The identification of selective, intermolecular variants of the base metal-catalyzed [2+2] cycloaddition is key to the development of a more broadly useful method compatible with abundant, unactivated alkenes. With the first-generation iron precatalyst, $(^{iPr}PDI)Fe(N_2)$ [^{iPr}PDI = 2,6-(2,6- $^{iPr}_2C_6H_3-N=CMe)_2C_5H_3N$, iPr is an isopropyl group, and Me is a methyl group], addition of common unfunctionalized terminal alkenes, such as propylene or 1-hexene, resulted in formation of a stoichiometric quantity of the corresponding alkane, arising from transfer hydrogenation from one of the isopropyl aryl groups on the iron catalyst (20). New approaches to catalyst design were therefore necessary to promote C–C bond formation via an iron metallacycle followed by $C(sp^3)-C(sp^3)$ reductive elimination. Here, we report that iron precatalysts attained through rational ligand design enable the regio- and stereochemically controlled synthesis of 1,2- and 1,3-disubstituted cyclobutanes by thermal [2+2] cycloaddition.

In an attempt to prevent transfer dehydrogenation, we synthesized an iron precatalyst lacking β -hydrogens on the aryl substituents, $[(^{Me}PDI)Fe(N_2)]_2(\mu-N_2)$, and observed catalytic turnover with propylene to produce a 2:1 mixture of 2,3-dimethylbutene and *trans*-1,2-dimethylcyclobutane. It is likely these products derive from a common iron metallacyclic intermediate, where β -hydrogen elimination followed by C–H reductive elimination yields the “tail-to-tail” dimerization product—a precursor to an

Department of Chemistry, Princeton University, Princeton, NJ 08544, USA.

*Corresponding author. E-mail: pchirik@princeton.edu

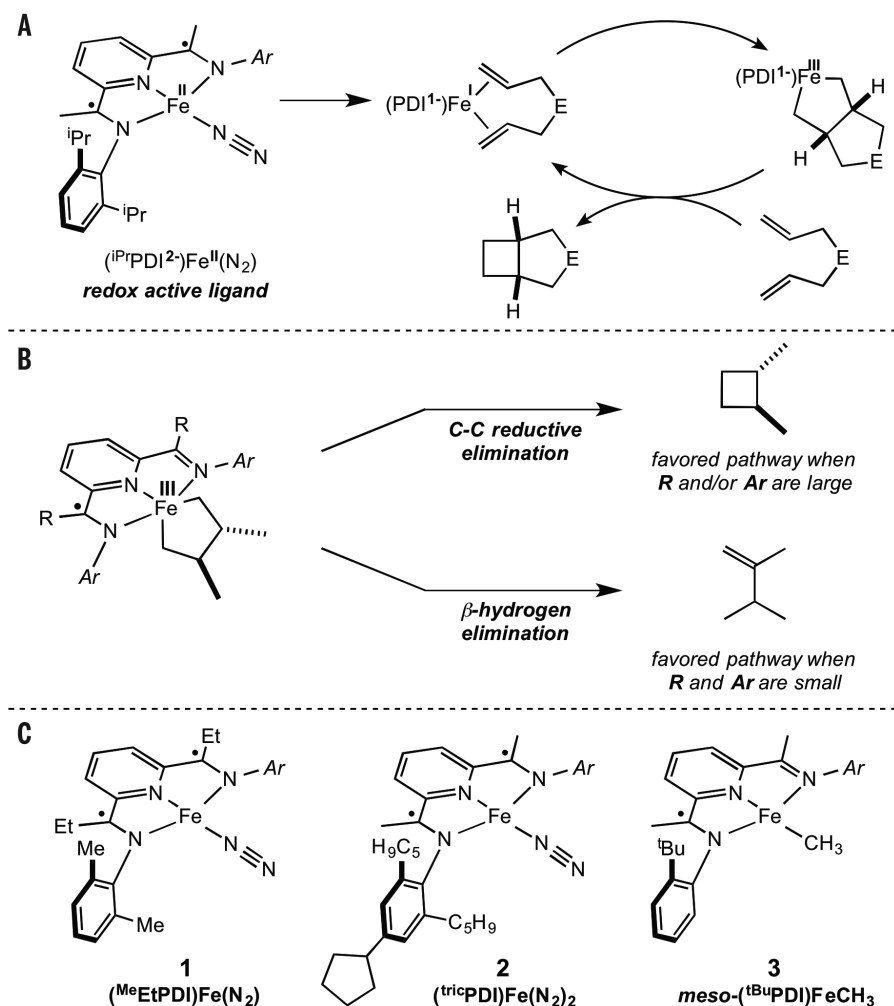
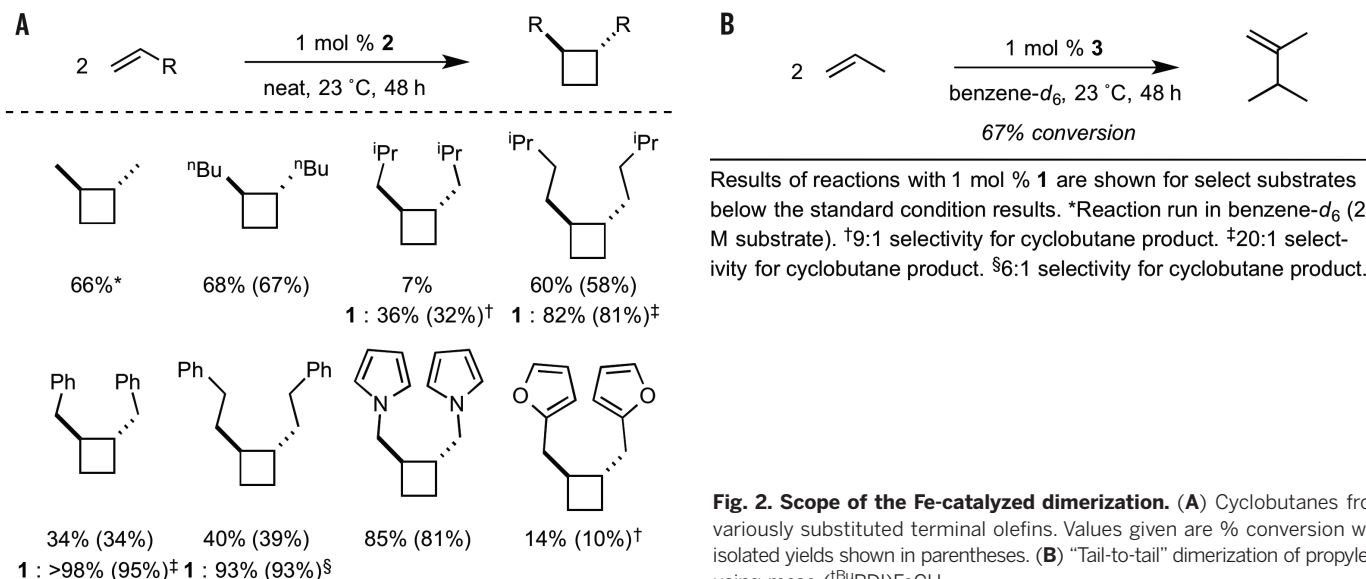


Fig. 1. Catalyst development. (A) Intramolecular $[(iPrPDI)Fe(N_2)]$ -catalyzed [2+2] cycloadditions of unactivated olefins. E=CH₂, N-alkyl, aryl, C(CO₂Et)₂. (B) (PDI)Fe-metallacycle model that allows for control over product distribution. R, methyl or ethyl groups. (C) (PDI)Fe compounds used in this study of intermolecular [2+2] alkene cycloadditions. The dots in the chemical structures represent electrons on the ligand.

important fuel additive used to boost octane ratings (21). Although selectivity for 2,3-dimethylbutene has been previously observed in nickel catalysis and is used industrially, such reactivity has not been observed previously with iron (10).

These observations inspired the catalyst design strategies illustrated in Fig. 1. Two sites of ligand modifications were explored with the goal of promoting reductive elimination over β -hydrogen elimination chemistry. Replacement of the imine methyl groups with ethyl substituents (**1**, Fig. 1C) was explored to prevent imine dissociation, a process that opens a coordination site for β -hydrogen elimination. The second modification installed cyclopentyl in place of isopropyl groups on the aryl rings (**2**, Fig. 1C). The cyclic substituents are constrained to minimize transfer dehydrogenation but remain sufficiently large to promote C-C reductive elimination.

Both **1** and **2** are effective precatalysts for the intermolecular [2+2] cycloaddition of unactivated alkenes. The reactions proceeded efficiently at ambient temperature and in neat substrate, obviating the need for solvent or separations. In each case, the cycloaddition product was identified as the *trans*-1,2-disubstituted cyclobutane, with selectivity resulting from preferential reductive elimination from the metallacycle where the alkyl substituents are distal from the iron (Fig. 1B). As presented in Fig. 2, the cyclopentyl-substituted catalyst **2** proved to be highly selective, forming exclusively cyclobutane products. The commodity terminal alkenes, propylene and 1-hexene, underwent efficient [2+2] cycloaddition over the course of 48 hours at 23°C. Only product and starting alkene were detected during the course of the reactions. The Fe-catalyzed cycloaddition was sensitive to alkene substitution on the allylic position indicated by decreased conversion with 4-methyl-1-pentene and allylbenzene. Improved activity, albeit with slightly reduced



selectivity, was observed with **1**; allyl- and 1-butenyl benzene resulted in the formation of their corresponding cyclobutanes in high yields. Consistent with cobalt-catalyzed intramolecular [2+2] cycloadditions (19), the reduced steric profile of the methyl (**1**) versus cyclopentyl (**2**) aryl substituents facilitates substrate coordination and metallacycle formation.

To demonstrate the scalability of the method, we conducted the cyclodimerization of allylbenzene on a 3.0-g scale with 1 mol % (mol %) of **1** and produced *trans*-1,2-dibenzylcyclobutane in 93% isolated yield. Catalytic cycloaddition was also explored with air-stable iron precursors by using in situ activation methods as described previously (17). Stirring neat allylbenzene in the presence of 5 mol % of (^{Me}EtPDI)FeCl₂ (Et, ethyl group) activated with 10 mol % NaBEt₃H produced 97% conversion of the alkene over the course of 48 hours. The product mixture contained 62% of the desired 1,2-*trans*-dibenzylcyclobutane product along with 4% hydrovinylation product and 31% *trans*-β-methyl styrene arising from alkene isomerization. These results highlight the improved catalytic performance associated with the isolated iron dinitrogen precatalysts.

Further support for the selectivity model presented in Fig. 1B was provided by the dimerization of propylene to 2,3-dimethylbutene with more open iron catalysts designed to promote β-hydrogen elimination. Because of the synthetic inaccessibility of the corresponding iron dinitrogen complex, we explored *meso*-(^{tBu}PDI)FeCH₃ (**3**) (tBu, *tert*-butyl group) (Fig. 2B). Stirring a benzene-*d*₆ solution of propylene and 1 mol % of **3** resulted in exclusive formation of 2,3-dimethylbutene in 67% conversion over the course of 48 hours at 23°C. Monitoring the catalytic reaction by ¹H nuclear magnetic resonance (NMR) spectroscopy revealed formation of small amounts of methane and ethane, likely resulting from Fe-CH₃ homolysis ensuing from catalyst activation en route to the intermediate metallacycle that undergoes preferential β-hydrogen elimination.

The success of iron-catalyzed [2+2] cycloaddition of unactivated alkenes prompted investigation into a more-general method for the heterodimerization of abundant dienes and alkenes to value-added cyclobutanes containing alkene substituents available for further elaboration. Iron-catalyzed cycloaddition of 1,3-butadiene and ethylene with 5 mol % (^{Me}PDI)Fe(N₂) to yield vinyl cyclobutane has been reported (22) and produced no evidence for six-membered ring products arising from competing Diels-Alder chemistry (23). We have since found that, in the presence of 5 mol % of (^{Me}PDI)Fe(N₂), [2+2] cycloaddition of butadiene with propylene resulted in >98% conversion to 1-methyl-3-vinylcyclobutane as a 67:33 mix of *cis*:*trans* diastereomers (Fig. 3A). As reported previously (22), this specific iron catalyst loses selectivity for [2+2] cycloaddition upon introduction of a substitution on

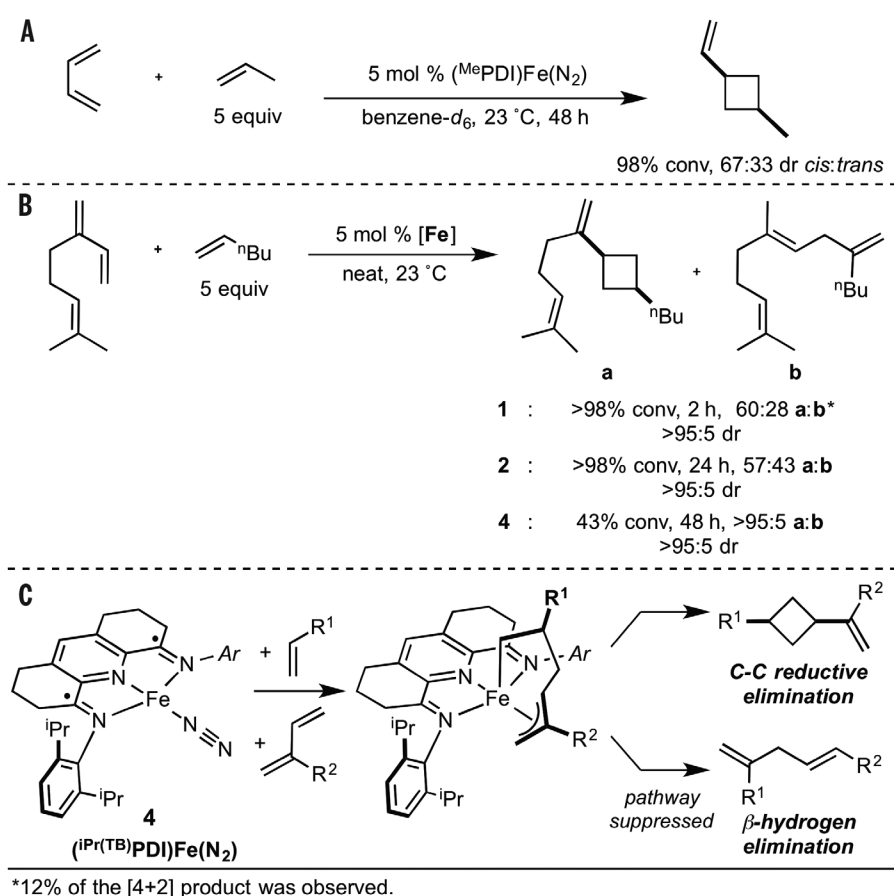


Fig. 3. Expanding from homodimerization to heterocoupling. (A) Single-step, Fe-catalyzed 3-methyl-1-vinylcyclobutane synthesis from commodity chemicals. (B) Catalyst effects on the [2+2] cycloaddition of myrcene and 1-hexene. (C) Fe-alkyl-allyl intermediate en route to 1,3-disubstituted cyclobutanes.

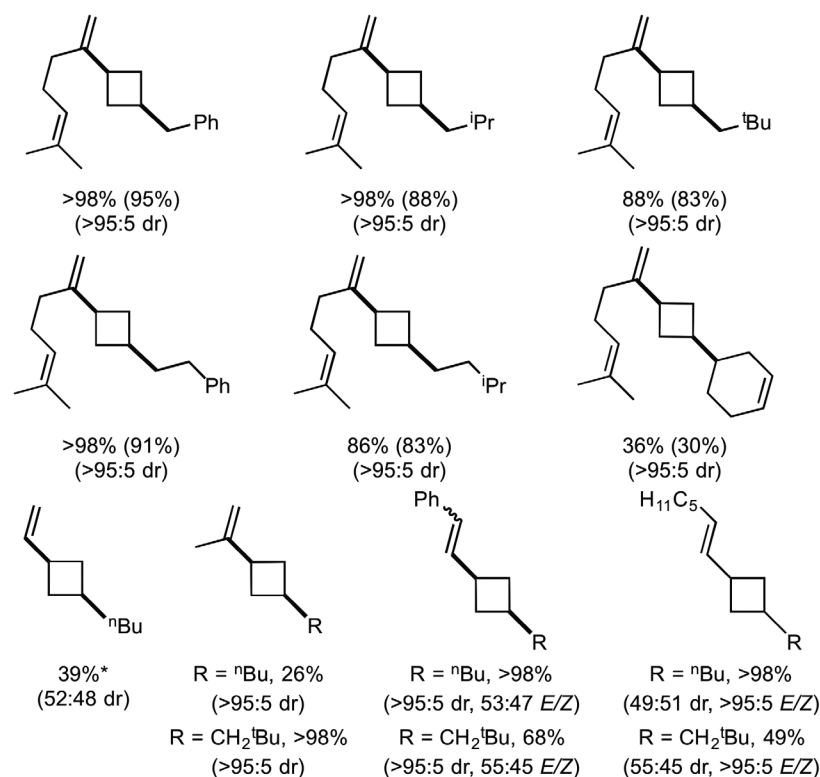
the diene component. For example, addition of ethylene or propylene to isoprene preferentially formed hydrovinylation products arising from β-hydrogen elimination over cyclobutane products.

To overcome this limitation, we explored the catalyst design strategies described for alkene [2+2] cycloaddition to increase the cyclization selectivity of diene-alkene reactions. Myrcene, a naturally occurring terpene found as an essential oil in bay, cannabis, parsley, and hops (24), was used as a representative diene for reaction discovery. Control experiments wherein neat myrcene was stirred at 23°C with 1 mol % of **1** or **2** resulted in [2+2] homodimerization to yield 46 and 74% of the 1,3-disubstituted cyclobutane product, respectively. Complex mixtures of unidentified organic products account for the mass balance of the reaction or material. The 1,3-disubstituted product was obtained with both catalysts, demonstrating preference for iron alkyl-allyl type metallacycle formation from diene coordination-insertion (22).

Evaluation of cross diene-alkene [2+2] cycloadditions were conducted with myrcene

and 1-hexene—two liquid substrates that are abundant bio- and fossil hydrocarbon resources, respectively (Fig. 3B). A 1:5 ratio of diene to alkene was used in all catalytic experiments to suppress diene homodimerization. Unfortunately with both **1** and **2**, only slight excesses (1.4:1 and 1.3:1, respectively) of the desired cyclobutane products were observed, demonstrating that the strategy used to suppress β-hydrogen elimination and favor C-C bond formation in terminal alkene [2+2] cycloaddition does not translate into diene-alkene chemistry.

A more-rigid catalyst design feature was therefore introduced to favor reductive elimination and suppress hydrovinylation chemistry (Fig. 3C). An iron dinitrogen precatalyst was used in which the imine substituents were covalently attached to the central pyridine, preventing formation of an open coordination site for β-hydrogen elimination (18). This approach proved successful, because stirring a 1:5 mixture of myrcene:1-hexene in the presence of 5 mol % of **4** resulted in exclusive (>20:1) selectivity for *cis*-1,3-disubstituted cyclobutane product (Fig. 3B).



*Run with 5 mol % ($^{\text{Me}}\text{PDI}$)Fe(N_2).

Fig. 4. Scope of the Fe-catalyzed diene- α -olefin cycloaddition. Values reported are % conversion with isolated yields shown in parentheses. Standard conditions were as follows: 5 mol % **4**, 1 equiv diene, 5 equiv olefin, 23°C for 48 hours. The reaction with butadiene and ethylene was conducted with 5 mol % ($^{\text{Me}}\text{PDI}$)Fe(N_2) dr is diastereomeric ratio as determined by means of ^1H NMR.

With an optimized iron precatalyst structure identified, the scope of the diene-alkene cross [2+2] cycloaddition was evaluated (Fig. 4). By using myrcene as the diene partner, we observed highly regio- and diastereoselective ($>95:5$) cycloaddition to form *cis*-1,3-disubstituted cyclobutanes with various terminal alkenes, including 1-hexene, allyl benzene, 4-methyl-1-pentene, 4,4-dimethyl-1-pentene, and 4-phenyl-1-butene. Introduction of a cyclohexenyl substituent onto the alkene coupling partner resulted in reduced yields but maintained high selectivity, likely because of the steric inhibition for forming the intermediate metallacycle. In each of these examples, good to excellent conversions and isolated yields were obtained. Products from diene or alkene homodimerization were not observed, demonstrating a highly selective iron-catalyzed regioselective route to stereodefined cyclobutanes with alkenyl substituents. The cross [2+2] cycloaddition of myrcene and 4,4-dimethylpentene was also effective with 5 mol % ($^{\text{Me}}\text{PDI}$)Fe(N_2), an iron catalyst precursor more straightforward to prepare than **4** and hence easily obtained in larger quantities. With this precatalyst, the cross cycloaddition was conducted on a 7.0-mmol scale of myrcene and

yielded 1.57 g (96% isolated yield) of the *cis*-1,3-disubstituted cyclobutane. Despite the excess of 4,4-dimethylpentene used in the reaction, 83% of this olefin was recovered by vacuum transfer of the volatile components from the crude reaction mixture. The cyclobutane product was then isolated by simple filtration through a short plug of silica and, after rinsing with hexanes, was obtained as an analytically pure material.

Variations in the diene partner were also tolerated, including the use of commodity hydrocarbons (Fig. 4). With butadiene:1-hexene, high 1,3-regioselectivity was maintained with reduction in diastereoselectivity, likely because of reduced steric interactions between the smaller substituents on the alkyl-allyl metallacycle and the supporting pyridine(diimine) ligand. Introduction of a methyl substituent as in isoprene returned the diastereoselectivity to $>95:5$. Terminal phenyl and pentyl substituents were also well tolerated on the diene partner; efficient cross [2+2] cycloaddition of 1-phenyl-1,3-butadiene and 1,3-nonadiene with 1-hexene and 4,4-dimethyl-1-pentene was observed (Fig. 4).

The iron precatalysts used in this work were ineffective for [2+2] cycloadditions in-

volving more functionalized alkenes, such as 4-bromo-1-butene, trimethylsilyloxypropene, and 2-butenyl-6-methylpyridine. The understanding of how ligand design affects the reactivity of intermediate metallacycles en route to cyclobutane formation provides important insight for the synthesis of the next generation of base metal catalysts to expand the scope of the reaction.

REFERENCES AND NOTES

- F. Fringuelli, A. Taticchi, *The Diels-Alder Reaction: Selected Practical Methods* (Wiley, Chichester, UK, 2002).
- S. Matar, L. F. Hatch, *Chemistry of Petrochemical Processes* (Gulf Professional, Boston, ed. 2, 1991).
- H. Zimmerman, R. Walzl, *Ullmann's Encyclopedia of Industrial Chemistry: Ethylene* (Wiley, Chichester, UK, 2009).
- H. Zimmerman, R. Walzl, *Ullmann's Encyclopedia of Industrial Chemistry: Propylene* (Wiley, Chichester, UK, 2009).
- D. S. McGuinness, *Chem. Rev.* **111**, 2321–2341 (2011).
- Z. Rappoport, J. F. Liebman, in *The Chemistry of Cyclobutanes* (Wiley, Chichester, UK, 2005), pp. 281–355.
- R. B. Woodward, R. Hoffmann, *Angew. Chem. Int. Ed. Engl.* **8**, 781–853 (1969).
- P. Heimbach, *Angew. Chem. Int. Ed. Engl.* **12**, 975–989 (1973).
- J. D. Winkler, C. M. Bowen, F. Liotta, *Chem. Rev.* **95**, 2003–2020 (1995).
- E. Lee-Ruff, G. Madenova, *Chem. Rev.* **103**, 1449–1484 (2003).
- R. Brimiouille, T. Bach, *Science* **342**, 840–843 (2013).
- J. Du, K. L. Skubi, D. M. Schultz, T. P. Yoon, *Science* **344**, 392–396 (2014).
- T. Bach, A. Spiegel, *Eur. J. Org. Chem.* **2002**, 645–654 (2002).
- R. G. Salomon, K. Folting, W. E. Streib, J. K. Kochi, *J. Am. Chem. Soc.* **96**, 1145–1152 (1974).
- J. P. Collman, L. S. Hegedus, J. R. Norton, R. G. Finke, in *Principles and Applications of Organotransition Metal Chemistry* (University Science Books, Mill Valley, USA, 1987), pp. 495–499.
- U. M. Dzhemilev, A. G. Ibragimov, M. N. Azhgaliev, A. P. Zolotarev, R. R. Muslukhov, *Russ. Chem. Bull.* **43**, 252–254 (1994).
- M. W. Bouwkamp, A. C. Bowman, E. Lobkovsky, P. J. Chirik, *J. Am. Chem. Soc.* **128**, 13340–13341 (2006).
- J. M. Hoyt, K. T. Sylvester, S. P. Semproni, P. J. Chirik, *J. Am. Chem. Soc.* **135**, 4862–4877 (2013).
- V. A. Schmidt, J. M. Hoyt, G. W. Margulieux, P. J. Chirik, *J. Am. Chem. Soc.* **137**, 7903–7914 (2015).
- R. J. Trovitch, E. Lobkovsky, P. J. Chirik, *J. Am. Chem. Soc.* **130**, 11631–11640 (2008).
- D. S. J. Jones, P. R. Pujadó, in *Handbook of Petroleum Processing* (Springer, Dordrecht, Netherlands 2006), pp. 389–399.
- S. K. Russell, E. Lobkovsky, P. J. Chirik, *J. Am. Chem. Soc.* **133**, 8858–8861 (2011).
- O. Diels, K. Alder, *Justus Liebigs Ann. Chem.* **460**, 98–122 (1928).
- A. Behr, L. Johnen, *ChemSusChem* **2**, 1072–1095 (2009).

ACKNOWLEDGMENTS

Financial support was provided by Firmenich, V.A.S. thanks the NIH for a Ruth L. Kirschstein National Research Award (F32 GM109594).

SUPPLEMENTARY MATERIALS

www.sciencemag.org/content/349/6251/960/suppl/DC1
Materials and Methods
Fig. S1
Tables S1 and S2
References (25–38)

5 June 2015; accepted 23 July 2015
10.1126/science.aac7440

This copy is for your personal, non-commercial use only.

If you wish to distribute this article to others, you can order high-quality copies for your colleagues, clients, or customers by [clicking here](#).

Permission to republish or repurpose articles or portions of articles can be obtained by following the guidelines [here](#).

The following resources related to this article are available online at www.sciencemag.org (this information is current as of September 1, 2015):

Updated information and services, including high-resolution figures, can be found in the online version of this article at:

<http://www.sciencemag.org/content/349/6251/960.full.html>

Supporting Online Material can be found at:

<http://www.sciencemag.org/content/suppl/2015/08/26/349.6251.960.DC1.html>

A list of selected additional articles on the Science Web sites **related to this article** can be found at:

<http://www.sciencemag.org/content/349/6251/960.full.html#related>

This article **cites 31 articles**, 2 of which can be accessed free:

<http://www.sciencemag.org/content/349/6251/960.full.html#ref-list-1>

This article has been **cited by** 1 articles hosted by HighWire Press; see:

<http://www.sciencemag.org/content/349/6251/960.full.html#related-urls>

This article appears in the following **subject collections**:

Chemistry

<http://www.sciencemag.org/cgi/collection/chemistry>

SEXUAL SELECTION

Irrationality in mate choice revealed by túngara frogs

Amanda M. Lea^{1*} and Michael J. Ryan^{1,2}

Mate choice models derive from traditional microeconomic decision theory and assume that individuals maximize their Darwinian fitness by making economically rational decisions. Rational choices exhibit regularity, whereby the relative strength of preferences between options remains stable when additional options are presented. We tested female frogs with three simulated males who differed in relative call attractiveness and call rate. In binary choice tests, females' preferences favored stimulus caller B over caller A; however, with the addition of an inferior "decoy" C, females reversed their preferences and chose A over B. These results show that the relative valuation of mates is not independent of inferior alternatives in the choice set and therefore cannot be explained with the rational choice models currently used in sexual selection theory.

Evolutionary theory is tightly linked to traditional decision theory, which predicts consumer behavior by assuming individuals' decisions will lead to outcomes that maximize the chooser's subjective utility, in terms of satisfaction or benefit (1, 2). A rational individual is one who makes choices that obey the simple mathematical axioms of transitivity (if $A > B$ and $B > C$, then $A > C$) and regularity (if $A > B$ in the absence of C, then $A > B$ in the presence of C). The simple nature of rational models is intuitively attractive; however, there has been much recent debate as to how valuable they are in predicting actual behavior (3–5). Human behavior commonly deviates from what is predicted by rational choice models, with individuals making seemingly sub-optimal decisions regardless of outcome importance. One well-known violation of regularity is the "decoy effect" (6–8). For example, while shopping for a used vehicle, the buyer may value both low price and fuel efficiency. Of the two vehicles considered, one has a higher price tag but also better efficiency (A), whereas the second has a lower price but also lower efficiency (B). The buyer decides that he or she values lower prices over higher efficiency and so chooses B. At this point, the salesperson mentions that there is a third vehicle (C), which also has good fuel efficiency but a much higher price than both A and B. This causes the buyer to reconsider, despite no interest in the higher-priced vehicle. To the salesperson's delight, the buyer ultimately chooses A, spending more money for better fuel efficiency. This irrational behavior has been produced by the decoy effect.

Mate choice is one of the most important decisions an animal makes. In many species, these critical decisions occur in dynamic social environments (such as leks) containing multiple potential mates with complex traits. Comparable to human consumers maximizing utility, we expect animals to maximize their Darwinian fitness by making

rational mate choices. The preference function concept, central to sexual selection theory (9), assumes that mate choice rules obey formal rationality (2, 7). The results of the scant empirical studies that have tested this assumption were either inconclusive (2) or failed to reject the axioms of transitivity (10) and regularity (11). Thus, we designed a study to address the axiom of regularity using a decoy paradigm (6–8). We hypothesized that females exhibit decoy effects similar to those commonly observed in humans,

whereby the probability of choosing stimulus A over B is dependent on the presence of the inferior third option C [$P(A|B) \neq P(A|B,C)$].

Mate choice behavior in our subject, the túngara frog (*Physalaemus pustulosus*), has been thoroughly studied for three decades (12). Males form lek-like aggregations and produce advertisement calls to attract females. Females exhibit a highly stereotyped and robust phonotactic response to speakers broadcasting stimuli that mimic male advertisement calls. Females generally prefer "static" call characteristics such as low dominant frequency and longer call durations, which are largely replicable within individuals, in addition to faster call rates, which change dynamically with the social conditions. For the current study (13), potential mates were represented by three acoustic stimuli (A, B, C) varying in two traits under selection by females: (i) static attractiveness [dimension 1 (DIM-1)] and (ii) call rate (DIM-2). The subjective values of each of these independent traits were determined by the actual measured preferences of 78 females from the same population in preliminary choice trials, which were completed before beginning our decoy experiments (Fig. 1, A and B; fig. S1; and tables S1 and S2). To represent variation in static attractiveness, we chose three natural male call variants from a previous study that demonstrated the range of multidimensional acoustic variation present in our study population (13, 14). Static attractiveness and call rate were inversely combined to

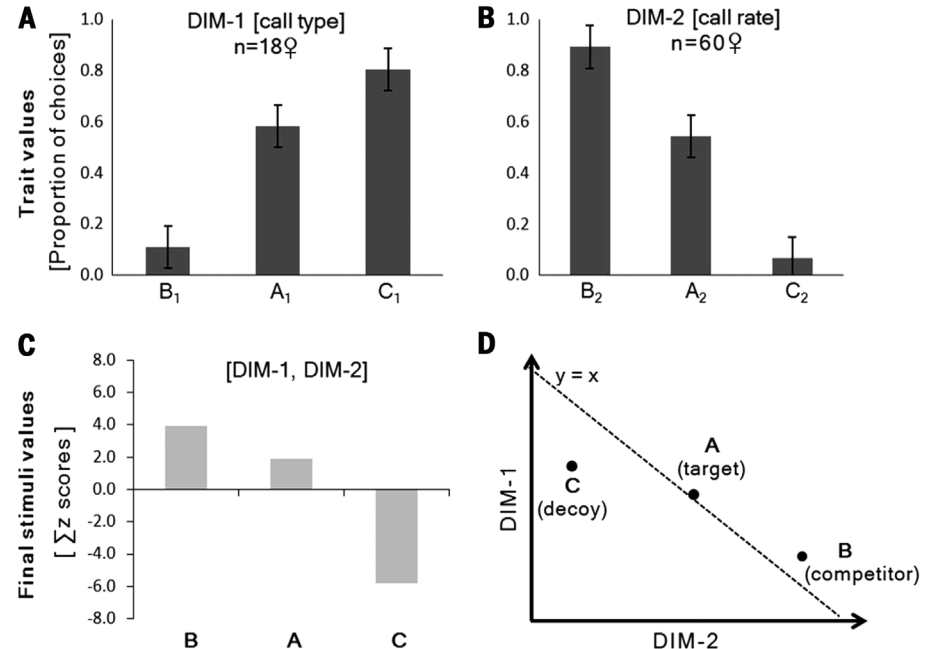


Fig. 1. Independent valuation of call traits. (A) Static attractiveness (DIM-1) is a composite trait of acoustic characters inherent to a given natural call variant (B_1 , A_1 , C_1). (B) Calls were presented at three different call rates (DIM-2): $C_2 = 1/4$, $A_2 = 1/2$, $B_2 = 1/1$ (in calls per second). Females' relative preferences for the three variants of each trait were measured in preliminary phonotaxis trials: (A_1 , B_1), (B_1 , C_1), (A_1 , C_1). The trait value is the proportion of females' choices out of the total possible. Each stimulus variant (e.g., A_1) was presented in two of the three pairwise tests; thus the sum of proportions for the three stimuli was 1.50, whereas the maximum possible for a given stimulus is 1.0. Error bars indicate \pm SE of the binomial distribution. (C and D) Differences in DIM-2 are discriminated more by females than differences in DIM-1, leading to an asymmetric relation among final stimuli (A, B, C) in total value, as calculated by the sum of binomial z ratios for each trait.

¹Department of Integrative Biology, The University of Texas, Austin, TX 78712, USA. ²Smithsonian Tropical Research Institute, Apartado 0843-03092, Balboa, Ancón, Republic of Panama. *Corresponding author. E-mail: alea@utexas.edu

produce an inferior decoy stimulus (C) among the final three stimuli (Fig. 1, C and D). We then measured females' relative mate preferences for each set of paired calls [(A, B), (A, C), and (B, C)] and for the trinary choice set (A, B, C). Based on compromise effects in other decoy experiments, we predicted that the relative preference for the intermediate stimulus A (target), with respect to the highest-value stimulus (competitor), will increase when C (decoy) is present.

In experiment one, we tested 40 females repeatedly on each of the four choice sets, using a grouped-speaker configuration that allowed females to choose the decoy option during the trinary test (Fig. 2A). Experiment two was identical to experiment one, with the important exception that during the trinary test, the decoy stimulus was broadcast from a speaker directly above the females' starting position to make it perceptible but inaccessible (Fig. 2B). The influence of unavailable decoys, referred to as the phantom decoy effect (15), has been shown to shift preferences toward the asymmetrically dominated target; thus, the prediction is the same as in experiment one. This experimental design also makes it possible to avoid complications potentially arising from the relative spatial positions of the speakers, such as a preference for centrally positioned males. Eighty females completed both the binary (A, B) and trinary (A, B; in the presence of C) choice sets. Fifty of these 80 females were also tested with the two additional binary tests [(A, C) and

(B, C)] to verify the inferior status of stimulus C in this configuration (experiment two).

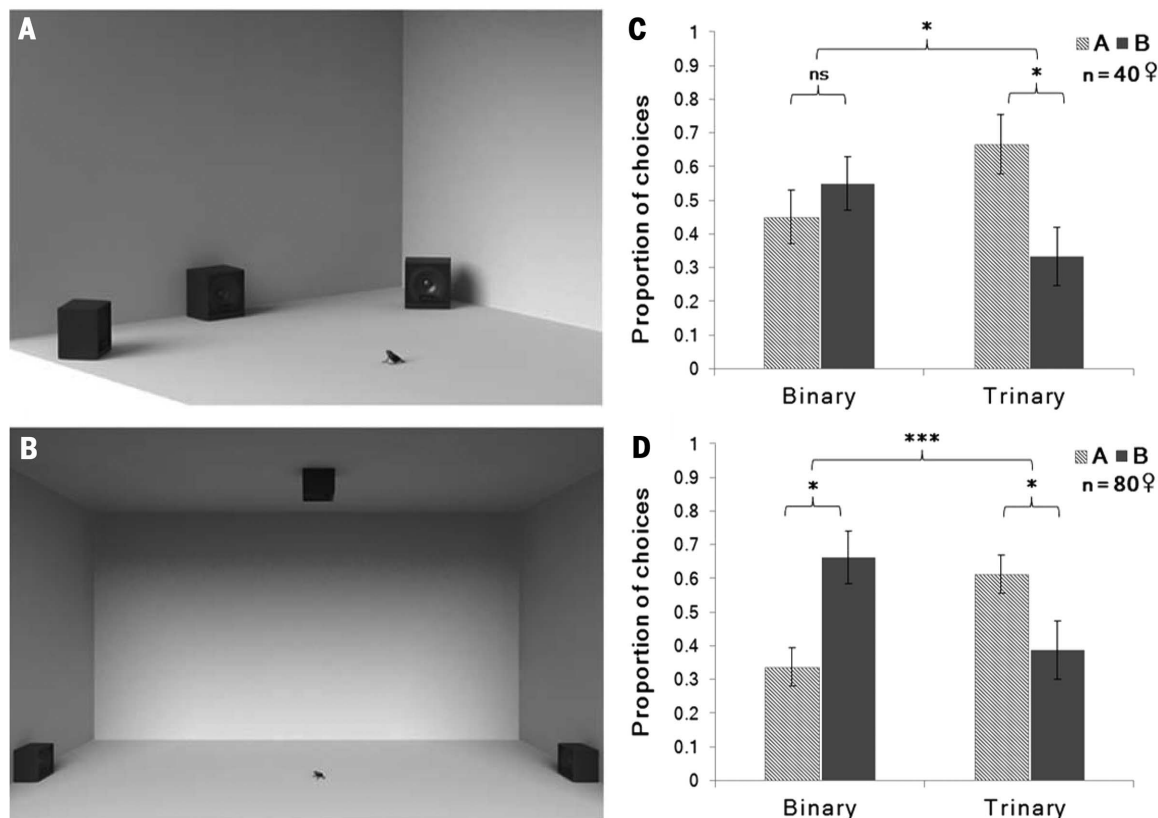
Results were consistent in both experiments. As predicted by independent trait valuation of the three stimuli (Fig. 1, C and D), stimulus C (decoy) was inferior to both A and B in all tests [experiment one: $C < B$, $P = 0.007$; $C < A$, $P < 0.001$; $P(C, \text{trinary}) = 0.175$, $P = 0.042$; all $n = 40$ females; experiment two: $C < A$, $P < 0.001$; $C < B$, $P = 0.034$, all $n = 50$]. In all binary tests, but not the trinary tests, the preferred stimulus in the pair was that with the fastest call rate [DIM-2] (Fig. 2, C and D). In the trinary tests, females were significantly more likely to choose the intermediate target A in the presence of the decoy regardless of the availability of the decoy as an option (Fig. 2, C and D). Female túngara frogs reversed their preferences in the presence of an irrelevant alternative in two separate experiments and thus violate a key assumption of mate choice models derived from decision theory.

In decision theory, predictions are based on the expected outcomes of individual behavior, and no assumptions are made about the underlying cognitive processes. Given the similarity of our results to systematic biases exhibited by human consumers, mate choice models might benefit from behavioral economics insights that employ psychological concepts such as perceptual biases or limited cognitive resources to explain irrational choices. Economic rationality does not account for reference dependence, which

is inherent to perceptual systems during rapid comparative evaluations (16, 17). In socially complex situations such as frog choruses, rational decisions could be time-consuming, potentially resulting in lost mating opportunities or the risk of further exposure to predators. Decision rules might evolve to include loss aversion (4, 18, 19), mitigating the risk of costly errors, which are more likely when there are extreme alternatives and in uncertain environments. Such heuristics could lead to stabilizing selection on male traits and maintenance of genetic variation. Moreover, as human consumers are susceptible to manipulation by salespeople, context-dependent choice rules may make female frogs vulnerable to behavioral exploitation by competing males; for instance, if males are selective of their nearest neighbors (20, 21).

Although it is clear that female choice patterns do not coincide with the consistent valuation predicted by traditional models in sexual selection, it is far from clear whether perfect formal rationality is mutually compatible with optimal evolutionary fitness (22–24). Closer inspection is required to determine whether inconsistencies revealed by decoy effects are, in fact, suboptimal in the context of fitness maximization. Variation of female mate choice in different social contexts might reflect adaptations for using additional sources of information (25), resulting in the expression of more complex but predictable choice patterns.

Fig. 2. Mate preference reversal for two stimuli (A, B) with the addition of an inferior decoy option (C). (A) Experiment one: The decoy was available as a third option in the trinary test. (B) Experiment two: The decoy was broadcast from a ceiling speaker and so was perceptible but unavailable. (C and D) Relative preferences were dependent on the presentation of the decoy in both experiments. Experiment one: binary ($n = 40$ females) versus trinary ($n = 33$, excludes choices to stimulus C), $\chi^2 = 3.765$, $P < 0.05$; experiment two: binary versus trinary ($n = 77$, excludes no choice data), $\chi^2 = 14.700$, $P < 0.001$. Error bars indicate \pm SE of the binomial distribution. ns, not significant. *, $P < 0.05$; ***, $P < 0.001$.



Growing empirical evidence suggests we lack a coherent understanding of the decision rules governing mate choice. Rational choice models have proven fruitful for static or otherwise simple selection scenarios, and yet may prove inadequate for generating accurate predictions of how sexually selected male traits evolve by female mate choice in the socially dynamic sexual marketplace. Further elucidating complex but predictable mate choice patterns would generate valuable insight into the evolution of decision-making and the coevolutionary processes of sexual selection.

REFERENCES AND NOTES

- W. S. Cooper, *Psychol. Rev.* **94**, 395–411 (1987).
- M. Kirkpatrick, A. S. Rand, M. J. Ryan, *Anim. Behav.* **71**, 1215–1225 (2006).
- M. H. Birnbaum, J. N. Patton, M. K. Lott, *Organ. Behav. Hum. Decis. Process.* **77**, 44–83 (1999).
- D. Kahneman, A. Tversky, *Econometrica* **47**, 263–291 (1979).
- A. Tversky, *Psychol. Rev.* **76**, 31–48 (1969).
- K. Tsetsos, M. Usher, N. Chater, *Psychol. Rev.* **117**, 1275–1293 (2010).
- M. Bateson, S. D. Healy, *Trends Ecol. Evol.* **20**, 659–664 (2005).
- D. Ariely, T. S. Wallsten, *Organ. Behav. Hum. Decis. Process.* **63**, 223–232 (1995).
- M. Andersson, L. W. Simmons, *Trends Ecol. Evol.* **21**, 296–302 (2006).
- F. X. Dechaume-Moncharmont, M. Freychet, S. Motreuil, F. Cézilly, *Front. Zool.* **10**, 69 (2013).
- L. T. Reaney, *Anim. Behav.* **77**, 139–143 (2009).
- M. J. Ryan, in *In Light of Evolution, Essays from the Laboratory and Field*, J. B. Losos, Ed. (Roberts and Company, Greenwood Village, CO, 2011), pp. 185–203.
- Materials and methods are available as supplementary materials on Science Online.
- M. J. Ryan, A. S. Rand, *Evolution* **57**, 2608–2618 (2003).
- J. C. Pettibone, D. H. Wedell, *J. Behav. Decis. Making* **20**, 323–341 (2007).
- D. Kahneman, *Am. Econ. Rev.* **93**, 1449–1475 (2003).
- K. L. Akre, H. E. Farris, A. M. Lea, R. A. Page, M. J. Ryan, *Science* **333**, 751–752 (2011).
- B. Marsh, A. Kacelnik, *Proc. Natl. Acad. Sci. U.S.A.* **99**, 3352–3355 (2002).
- H. A. Orr, *Evolution* **61**, 2997–3000 (2007).
- S. Candler, C. L. Hayes, M. D. Jennions, P. R. Y. Backwell, *Behav. Ecol.* **24**, 730–733 (2013).
- C. Gasparini, G. Serena, A. Pilastro, *Proc. R. Soc. B* **280**, 20123072 (2013).
- P. C. Trimmer, *Proc. R. Soc. B* **280**, 20130858 (2013).
- W. S. Cooper, *Biol. Philos.* **4**, 457–481 (1989).
- A. W. Schulz, *Philos. Soc. Sci.* **43**, 46–72 (2013).
- M. D. Jennions, M. Petrie, *Biol. Rev. Camb. Philos. Soc.* **72**, 283–327 (1997).

ACKNOWLEDGMENTS

We thank the Autoridad Nacional del Ambiente for permission to do field work in Panama; the Smithsonian Tropical Research Institute for logistical support; M. Still, S. Beckett, and A. Smejdir for assistance; and M. Jennions and an anonymous reviewer for helpful suggestions on the manuscript. M.J.R. thanks M. Bateson for early conversations on decoys. This study was supported by NSF Integrative Organismal Systems grant 1120031 to M.J.R., R. Taylor, and R. Page and an NSF Predoctoral Fellowship to A.M.L. Procedures were approved by the Institutional Animal Care and Use Committees at The University of Texas at Austin and the Smithsonian Tropical Research Institute (AUP 2011-0825-2014-02). Experimental data are provided in the supplementary materials.

SUPPLEMENTARY MATERIALS

www.sciencemag.org/content/349/6251/964/suppl/DC1

Materials and Methods

Fig. S1

Tables S1 and S2

References (26–28)

Additional Data Table S1

27 March 2015; accepted 3 August 2015

10.1126/science.aab2012

LIFE HISTORY

Age-related mortality explains life history strategies of tropical and temperate songbirds

Thomas E. Martin

Life history theory attempts to explain why species differ in offspring number and quality, growth rate, and parental effort. I show that unappreciated interactions of these traits in response to age-related mortality risk challenge traditional perspectives and explain life history evolution in songbirds. Counter to a long-standing paradigm, tropical songbirds grow at similar overall rates to temperate species but grow wings relatively faster. These growth tactics are favored by predation risk, both in and after leaving the nest, and are facilitated by greater provisioning of individual offspring by parents. Increased provisioning of individual offspring depends on partitioning effort among fewer young because of constraints on effort from adult and nest mortality. These growth and provisioning responses to mortality risk finally explain the conundrum of small clutch sizes of tropical birds.

Life history strategies of virtually all taxa vary along a slow-fast gradient. Slow strategies are characterized by slow growth, low total parental effort for fewer offspring but high effort per offspring [i.e., high parental investment (1)], and long life (2). Fast strategies are characterized by the opposite (2). This slow-fast gradient is particularly well defined for songbirds of different latitudes, with tropical songbirds typically on the slow end and northern temperate birds falling toward the fast end (3–7). An extensive body of work and theory has attempted to explain the drivers of this pattern of life history variation, yet no consensus has emerged (8–13).

An early perspective on latitudinal variation in life history strategies proposed that stable tropical environments allow habitats to become “saturated” with individuals, thereby favoring slow life history strategies that improve competitive abilities (10, 11). Yet the life history traits of coexisting tropical songbird species can vary as much or even more (5, 14) than those of temperate species, and this variation is difficult to explain by the simple argument that competition is greater in the tropics. Other hypotheses invoking latitudinal differences in food limitation or nest predation have also failed to explain latitudinal variation (4–6). Differences in parental effort within and among latitudes have been addressed in part by classic theories based on age-specific or season-specific mortality [e.g., (8, 9, 12, 13)]. However, an explanation is lacking for why effort may be partitioned among differing numbers of young and how this integrates with enigmatic growth strategies among species and latitudes. In short, the causes of variation in growth strategies, parental provisioning rates, and clutch size within and among latitudes remain unclear.

Here, I provide a conceptual framework for within- and across-latitude variation in life history strategies based on mortality risk across life stages (Fig. 1). I base this on empirical evidence from extensive field studies of 20 to 30 coexisting songbird species in each of three locations: north temperate Arizona, USA, and tropical Malaysia and Venezuela.

An initial enigma is presented by the slow growth of tropical songbirds. Predation causes the vast majority of mortality for songbird offspring in the nest (nestlings) (15). Higher risk of nest predation favors faster growth (Fig. 2A and table S1A) in order to reduce time in the nest (nestling period) and exposure to nest predators (Fig. 1) (5, 16). Yet tropical birds exhibit slower growth rates than temperate species for similar or even higher nest predation rates (Fig. 2A and table S1A), which has been perceived as a paradox (9). Moreover, this paradox was reinforced by the inability of an assumed longevity benefit to explain the slower growth of tropical birds (17).

This apparent paradox may reflect the way that growth rates have been viewed and estimated. Traditional growth rate estimates (5, 7, 17) provide estimates of peak growth (18). Slower peak growth rates of tropical birds have been implicitly assumed to reflect slower overall growth. Yet nestling periods of tropical species are 2 to 6 days shorter for the same peak growth rates (K_1) as temperate species (Fig. 2B and table S1B). If slower peak growth reflects slower overall growth, it should cause tropical offspring to leave the nest (fledge) at smaller relative sizes and earlier developmental states relative to temperate species (Fig. 3A, dashed versus yellow curves). Yet reduced development at fledging increases subsequent mortality (19). Tropical species might minimize such costs by extending the nestling period, but that increases nest predation risk (16) and is not reflected by the relationship of nestling period with peak growth rates (Fig. 2B). I suggest that this conundrum can be resolved by considering a

U.S. Geological Survey, Montana Cooperative Wildlife Research Unit, University of Montana, Missoula, MT 59812, USA.

E-mail: tom.martin@umontana.edu

heretofore unrecognized possibility that tropical birds use an alternative growth trajectory. Specifically, tropical birds exhibit slower peak growth rates but faster growth at later ages, thereby achieving a relative size similar to that of tem-

perate species without extending the nestling period (solid black versus yellow curves in Fig. 3A).

A pair of wren (Troglodytidae) species illustrates common differences in tropical-temperate

growth trajectories. Growth is faster in the temperate species at early ages (the yellow curve in Fig. 3B rises faster). However, the faster growth of the tropical wren at later ages allows it to achieve the same relative body mass as the temperate wren in the same amount of time (Fig. 3B). These differences are illustrated more clearly by calculating instantaneous growth rates over the nestling period (Fig. 3C). A series of tropical and temperate species paired by phylogeny shows that growth rates are higher for temperate species than for their tropical relatives in the early nestling period through peak growth (yellow above black curves in Fig. 3, C to I). The lower peak rates of tropical species (Fig. 3, C to I) reflect the paradigm of slow growth in the tropics (5, 7, 17). However, growth rates of tropical species also consistently exceed temperate species after their peak (black above yellow curves in Fig. 3, C to I). The growth trajectory of tropical birds allows them to often achieve a similar average growth rate over the entire nestling period (K_{avg} ; Fig. 3, C to G) and similar relative size at fledging as temperate relatives without extending the nestling period (e.g., Fig. 3B). Indeed, relative body mass at fledging does not differ between tropical and temperate birds for the same nestling period (Fig. 4A and table S2A). The ability to achieve similar fledging mass without increasing the length of the nestling period is critical because it means that tropical birds do not increase their risk of nest predation through longer nestling periods. Of course, in some cases, tropical species grow slower overall and extend the nestling period (Fig. 3, H and I), but these generally are species with lower nest predation risk (Fig. 2A).

The lower peak but more sustained growth of many tropical birds (Fig. 3) may be important for aiding wing growth and flight capabilities after fledging (Fig. 1). Enhanced locomotor performance aids escape from predators across taxa (20, 21) and can result from slower and steadier mass growth (22), as is typical of tropical birds (Fig. 3). Partially developed wings can help offspring to escape predators (23)—commonly the primary source of fledgling mortality in songbirds (19)—and longer, more developed wings increase fledglings' ability to evade predators (19, 24). Longer wings can be achieved through longer nestling periods (19, 24), but that increases nest predation risk (16) and creates a trade-off in predation risk between nestling and fledgling stages (Fig. 1). This trade-off can be resolved by a growth strategy (i.e., lower peak, more sustained growth) that allows enhanced wing growth without lengthening the time in the nest and exposed to nest predators. Indeed, tropical birds exhibit faster wing growth (Fig. 4B and table S2B), allowing them to fledge with longer wings than temperate birds for the same nestling period (Fig. 4C and table S2C). Thus, relative to temperate birds, tropical species enhance growth of a locomotor trait that can reduce mortality risk after leaving the nest (19, 24) without increasing mortality risk in the nest.

Given the survival advantage that more developed wings provide fledglings (19, 24), we might

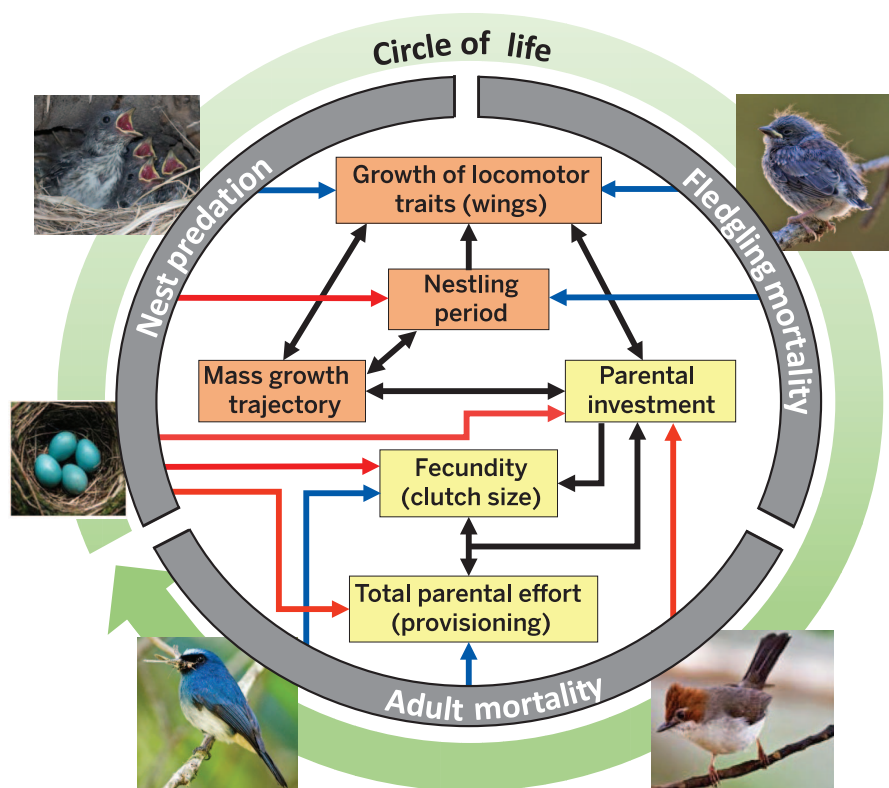


Fig. 1. Conceptual framework for life history strategies. Over the circle of life, mortality risk varies across life stages (gray ring) and exerts selection on growth strategies (orange boxes) and parental strategies (yellow boxes). Blue arrows reflect positive selection; red arrows reflect negative selection; black arrows reflect the influence of life history traits on each other. Nest and fledgling predation exert opposing selection on length of the nestling period. Fledgling predation risk favors longer nestling development to enhance locomotor traits (i.e., longer wings), but longer periods increase nest predation risk. Increased parental investment and steady mass growth allow enhanced wing growth without extending the length of the nestling period and increasing predation risk. Parental investment is a function of total parental effort (total provisioning rate) partitioned among young, where total parental effort is a result of adult and nest mortality. The higher parental investment that facilitates the longer wings favored in tropical birds is achieved by small clutch sizes.

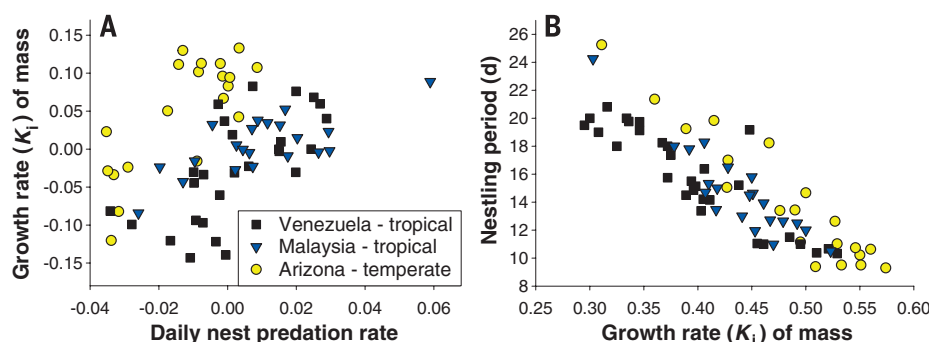


Fig. 2. Growth and nest predation on three continents. (A) Peak growth rate is faster in species with higher nest predation risk but is slower in tropical species with the same level of risk as temperate species, while controlling for mass (table S1A). Growth rate is the conventional peak rate of growth, K_1 (see Fig. 3A). (B) Nestling period covaries with growth rate, but tropical species have shorter nestling periods for the same growth rate as temperate species (table S1B).

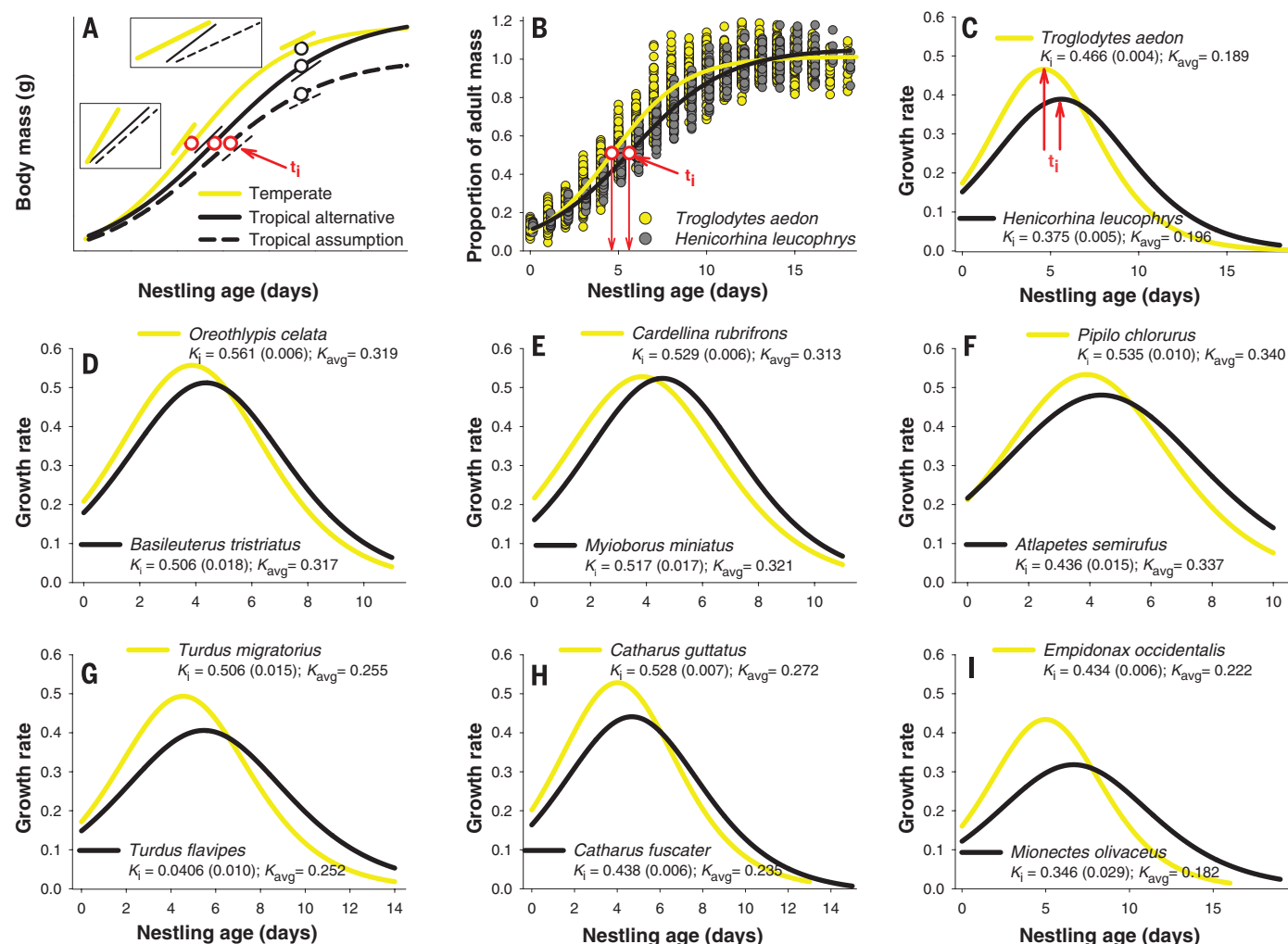


Fig. 3. Differences in growth trajectories of body mass of tropical versus temperate songbirds. (A) Conceptual characterization of possible growth trajectories [see also (18)]. Growth rate is estimated as the instantaneous slope (K_i depicted by the small lines) on the growth curve. The small lines representing slopes of differing growth trajectories are exaggerated in the boxes at two ages to illustrate the differences. Traditionally, estimates are made at the time (t_i) of the inflection point (red circles) where growth switches from accelerating to decelerating, which represents peak growth rate. However, growth rate may also differ at the late nestling stage (black circles). Tropical birds are assumed to have slower growth throughout the nestling period (dashed black curve), where slopes are shallower than for temperate birds (yellow curve) at both ages.

expect temperate birds to produce wings of comparable size. However, increased rates of energetically expensive wing growth may depend not only on a slower, more sustained growth strategy, but also on increased energy availability (Fig. 1) (25). The field data show that higher provisioning (food delivery) rates per offspring explain longer relative wing sizes within and across latitudes (Fig. 4D and table S2D). Thus, greater parental investment, commonly observed in tropical birds (4–6), can have critical fitness benefits through effects on offspring quality manifested by wing development and its consequences for survival of young after leaving the nest.

The reason that tropical and temperate species do not provision individual offspring at similar

rates arises in part from constraints of age-related mortality on provisioning effort (Fig. 1). Life history theory predicts that adult and offspring mortality should constrain parental effort (4, 5, 9, 12, 13). Indeed, variation in parental effort, reflected by total provisioning rate of all offspring, is explained by nest predation risk and adult mortality across species and latitudes (Fig. 4, E and F, and table S3A). Adult mortality is commonly lower for tropical birds (3, 17) and therefore is associated with lower overall provisioning rates (Fig. 4F).

The only way that tropical birds can increase provisioning rates per offspring, given mortality constraints on total provisioning, is through reduced clutch size. The smaller clutch size of trop-

ical birds indeed allows increased provisioning per offspring (Fig. 4G and table S3B), which enables growth of longer wings (Fig. 4D) to enhance fledgling survival (19, 24) without extending the nestling period and increasing nest predation risk. The small clutch sizes of tropical birds have puzzled scientists for more than half a century, and these results finally explain it as an integrated function of growth and parental provisioning strategies in response to age-related mortality risk.

Temperate birds may not increase parental investment to enhance wing growth as much as tropical birds because of greater adult and juvenile (independent young after the fledging stage) mortality. Mortality rates of juvenile songbirds to the

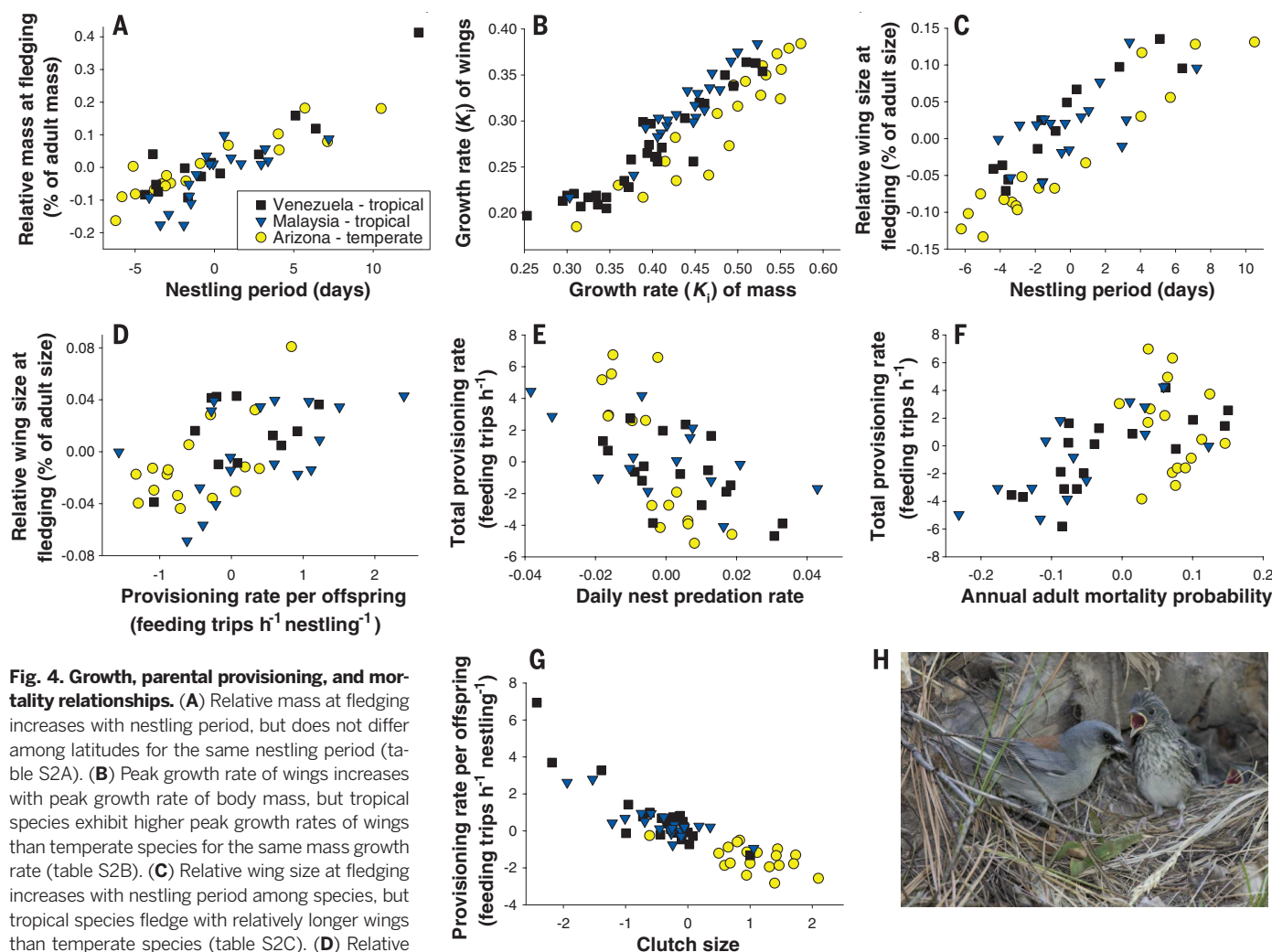


Fig. 4. Growth, parental provisioning, and mortality relationships. (A) Relative mass at fledging increases with nestling period, but does not differ among latitudes for the same nestling period (table S2A). (B) Peak growth rate of wings increases with peak growth rate of body mass, but tropical species exhibit higher peak growth rates of wings than temperate species for the same mass growth rate (table S2B). (C) Relative wing size at fledging increases with nestling period among species, but tropical species fledge with relatively longer wings than temperate species (table S2C). (D) Relative wing size at fledging increases with provisioning rate per offspring while controlling for other factors (table S2D). (E and F) Total provisioning rate decreases with nest predation risk (E) and increases with annual adult mortality probability (F) across species controlled for each other and other factors (table S3A). (G) Provisioning rate per offspring decreases with increasing clutch size, controlled for mass and total provisioning rate (table S3B). (H) A *Junco hyemalis* young taking its first steps to leave the nest and begging for food from its parent.

next breeding season, as well as adult mortality rates, are commonly higher in temperate than in tropical songbird species (3, 17, 26, 27). When adult and juvenile mortality are high, selection can favor a strategy of more, but lower-quality, young (2, 11–13). This hypothesis fits the patterns here because an increase in the number of offspring in the temperate zone comes at the expense of parental investment (Fig. 4G), and reduced parental investment produces lower-quality young, as reflected by shorter wing length (Fig. 4D). In short, temperate songbirds produce more young of lower quality, which is adaptive given their higher juvenile and adult mortality rates.

Mortality risk during different life stages can explain variation in the life history strategies of songbirds across latitudes (Fig. 1). Adult and offspring mortality have been theorized to influence parental effort across taxa (2, 9, 12, 13), and total provisioning rate (which reflects parental effort) is well explained by adult mortality and

nest predation risk in songbirds (Fig. 4, E and F). Consideration of mortality risk after leaving the nest (fledgling mortality) adds to our understanding of latitudinal variation in songbird life histories. In particular, seemingly paradoxical slower peak growth of tropical birds in the face of nest predation risk makes sense once their more sustained growth is recognized. The lower peak and sustained growth resolves the putative predation cost in the nest while allowing enhanced wing growth and survival after leaving the nest. Increased parental provisioning per offspring, achieved through reduced clutch size (Fig. 4G), further enhances wing growth (Fig. 4D) to benefit fledgling survival. Ultimately, selection by nest predation on growth rate and nestling period places constraints on the developmental stage at fledging (Fig. 2) (19) and creates a trade-off with subsequent fledgling survival. However, shifts in growth, fecundity, and parental provisioning strategies help to resolve this trade-off (Fig. 1). This interaction in mortality risk among

life stages, considered together with the interactions among life history traits (Fig. 1), is a basis for greater understanding of latitudinal variation in life history strategies.

REFERENCES AND NOTES

1. R. L. Trivers, in *Sexual Selection and the Descent of Man, 1871–1971*, B. Campbell, Ed. (Aldine-Atherton, Chicago, 1972), pp. 136–179.
2. S. C. Stearns, *Q. Rev. Biol.* **51**, 3–47 (1976).
3. B. K. Sandercock, S. R. Beissinger, S. H. Stoleson, R. R. Melland, C. R. Hughes, *Ecology* **81**, 1351–1370 (2000).
4. T. E. Martin, P. R. Martin, C. R. Olson, B. J. Heidinger, J. J. Fontaine, *Science* **287**, 1482–1485 (2000).
5. T. E. Martin *et al.*, *Evolution* **65**, 1607–1622 (2011).
6. S. A. Gill, T. M. Haggerty, *J. Avian Biol.* **43**, 461–471 (2012).
7. R. E. Ricklefs, *Ibis* **110**, 419–451 (1968).
8. N. P. Ashmole, *Ibis* **103**, 458–473 (1963).
9. T. E. Martin, *J. Avian Biol.* **27**, 263–272 (1996).
10. T. Dobzhansky, *Am. Sci.* **38**, 209–221 (1950).
11. R. H. MacArthur, E. O. Wilson, *The Theory of Island Biogeography* (Princeton Univ. Press, Princeton, NJ, 1967).
12. R. Law, *Am. Nat.* **114**, 399–417 (1979).
13. G. C. Williams, *Am. Nat.* **100**, 687–690 (1966).
14. T. E. Martin, *Proc. Natl. Acad. Sci. U.S.A.* **105**, 9268–9271 (2008).

15. T. E. Martin, *Ecol. Monogr.* **65**, 101–127 (1995).
16. V. Remé, T. E. Martin, *Evolution* **56**, 2505–2518 (2002).
17. T. E. Martin, J. C. Oteyza, A. E. Mitchell, A. L. Potticary, P. Lloyd, *Am. Nat.* **185**, 380–389 (2015).
18. Z. Wang *et al.*, *Evolution* **68**, 81–91 (2014).
19. T. E. Martin, *Am. Nat.* **183**, 313–324 (2014).
20. T. B. Watkins, *Physiol. Zool.* **69**, 154–167 (1996).
21. D. B. Miles, *Evol. Ecol. Res.* **6**, 63–75 (2004).
22. K. O. Perez, S. B. Munch, *Funct. Ecol.* **10.1111/1365-2435.12343** (2014).
23. K. P. Dial, R. J. Randall, T. R. Dial, *Bioscience* **56**, 437–445 (2006).
24. K. W. Morrison, J. M. Hipfner, C. Gjerdrum, D. J. Green, *Condor* **111**, 433–441 (2009).
25. R. D. Dawson, C. C. Lawrie, E. L. O'Brien, *Oecologia* **144**, 499–507 (2005).
26. B. E. Sæther, *Ornis Scand.* **20**, 13–21 (1989).
27. C. E. Tarwater, R. E. Ricklefs, J. D. Maddox, J. D. Brawn, *Ecology* **92**, 1271–1281 (2011).

ACKNOWLEDGMENTS

I thank J. Maron, F. S. Dobson, two anonymous reviewers, and my graduate students for helpful comments; Z. Wang for providing initial R-code for growth analyses; Sabah Parks and the Sabah Biodiversity Centre in Malaysia; and C. Bosque, INPARQUES, and Fonacit in Venezuela. This work was supported by NSF grants DEB-1241041 and IOS-1349178 and by the U.S. Geological Survey Climate Change Research Program, and was conducted under auspices of University

of Montana IACUC no. 059-10TMMCWU. Any use of trade, firm, or product names is for descriptive purposes only and does not imply endorsement by the U.S. Government. Data are available in Dryad: DOI 10.5061/dryad.2m15n; data files: Life_history_data.

SUPPLEMENTARY MATERIALS

www.sciencemag.org/content/349/6251/966/suppl/DC1
Materials and Methods
Supplementary Text
Fig. S1
Tables S1 to S3
References (28–42)

2 May 2015; accepted 29 July 2015
10.1126/science.aad1173

FUNGAL SYMBIONTS

Global assessment of arbuscular mycorrhizal fungus diversity reveals very low endemism

J. Davison,^{1,*†} M. Moora,^{1,*†} M. Öpik,^{1,*†} A. Adholeya,² L. Ainsaar,¹ A. Bâ,³ S. Burla,² A. G. Diedhiou,⁴ I. Hiiesalu,^{1,5} T. Jairus,¹ N. C. Johnson,⁶ A. Kane,⁴ K. Koorem,^{1,7} M. Kochar,⁸ C. Ndiaye,⁴ M. Pärtel,¹ Ü. Reier,¹ Ü. Saks,¹ R. Singh,⁸ M. Vasar,¹ M. Zobel^{1,*}

The global biogeography of microorganisms remains largely unknown, in contrast to the well-studied diversity patterns of macroorganisms. We used arbuscular mycorrhizal (AM) fungus DNA from 1014 plant-root samples collected worldwide to determine the global distribution of these plant symbionts. We found that AM fungal communities reflected local environmental conditions and the spatial distance between sites. However, despite AM fungi apparently possessing limited dispersal ability, we found 93% of taxa on multiple continents and 34% on all six continents surveyed. This contrasts with the high spatial turnover of other fungal taxa and with the endemism displayed by plants at the global scale. We suggest that the biogeography of AM fungi is driven by unexpectedly efficient dispersal, probably via both abiotic and biotic vectors, including humans.

The arbuscular mycorrhizal (AM) fungi (phylum Glomeromycota) are an ancient but species-poor group of root symbionts whose origin coincided with the first appearance of land plants (1). The AM symbiosis involves ~80% of land plants and ~250 morphologically defined or 350 to 1000 molecularly defined AM

fungi (2, 3). The relationship typically allows the fungus to receive plant-synthesized carbon, while conferring the plant with an increased capacity for nutrient capture and improved tolerance of drought and pathogens (4). At a wider scale, the symbiosis influences plant-plant interactions and the structure of plant communities, and thus it can affect agricultural production and the conservation and restoration of ecosystems (5). Because many AM fungi are unculturable, identification of AM fungal taxa in the environment is principally dependent on DNA-based methods; these asexual organisms are classified into approximately species-level taxonomic units using clustering or sequence-matching algorithms (6). The recent rapid development of DNA sequencing technology is allowing detection of increasing numbers of AM fungi and other microorganisms in environmental samples and enabling their responses to local and regional environmental gradients to be recorded (7–9). However, knowledge about global AM fungal diversity is piecemeal. This is partly because most classification approaches generate operational taxonomic units (OTUs) that cannot be readily compared between different studies or study areas (2, 10). Additionally, the communities of AM fungi present in many geographic regions, biomes, and ecosystems remain entirely unstudied (11, 12).

Although empirical data concerning AM fungal dispersal are limited, the process is believed to be mostly local and mediated by invertebrates (4, 13), with some evidence of small mammals, water, and human activities (e.g., agricultural practices) dispersing propagules farther (14–16). As yet, there is no direct evidence of efficient long-distance dispersal (13, 17). Hence, extensive global sampling of AM fungal diversity should reveal high endemism and similar responses to environmental conditions as those shown to drive local-scale diversity (7, 8). We used high-throughput sequencing of environmental samples to survey AM fungal diversity and distribution in natural ecosystems worldwide. We examined the contributions of environmental conditions, spatial distance between plots, paleogeographic history, and plant-host identity on AM fungal diversity at local to global scales.

We collected 1014 individual root samples from vegetation plots worldwide and identified DNA-based AM fungal taxa ["virtual taxa" (VT), after (10)] in plant roots by using 454 sequencing. VT are phylogenetically defined sequence groups that exhibit a taxonomic resolution similar to that of morphological species, or above that resolution in some AM fungal families (17). As in traditional binomial nomenclature, the VT classification applies consistent principles to taxonomic assignments across data sets and provides comparability between studies. We used 912,515 quality-filtered AM fungal reads, representing 836 samples, 161 plant species, and 67 plots, for further analysis (Fig. 1A, fig. S1, tables S1 to S3, and database S1). We recorded 236 (68%) of the 348 currently known AM fungal VT and identified a further 10 taxa that were previously undescribed (fig. S2). Ninety-three percent of recorded VT were present on more than one continent, and one-third (34%) were present on all six sampled continents. Furthermore, 90% of VT were found in more than one climatic zone, and 79% were found in both forests and grasslands (the two most widely sampled ecosystems) (Fig. 1B). We added published data on AM fungal VT distribution from the MaarjaAM database (10) to create a comprehensive data set containing all available VT records. We compared this data set with the distribution of plants (the AM fungus host organisms) for which global data are available at the family (18) but not the species level. The mean fractions of the AM fungal taxon pool found on individual continents (57%) and of shared

¹Institute of Ecology and Earth Sciences, University of Tartu, Lai 40, Tartu 51005, Estonia. ²Centre for Mycorrhizal Research, The Energy and Resources Institute (TERI), India Habitat Centre, Lodhi Road, New Delhi 110 003, India. ³Laboratoire des Symbioses Tropicales et Méditerranéennes, Unité Mixte de Recherche 113, Laboratoire de Biologie et Physiologie Végétales, Faculté des Sciences Exactes et Naturelles, Université des Antilles, BP 592, 97159, Pointe-à-Pitre, Guadeloupe (French West Indies). ⁴Laboratoire Commun de Microbiologie de l'Institut de Recherche pour le Développement–Institut Sénégalais de Recherches Agricoles–Université Cheikh Anta Diop (UCAD), Département de Biologie Végétale, UCAD, BP 5005 Dakar, Sénégal. ⁵Institute of Botany, Czech Academy of Sciences, Dukelska 135, 379 01 Trebon, Czech Republic. ⁶School of Earth Sciences and Environmental Sustainability, Northern Arizona University, Flagstaff, AZ 86011-5694, USA. ⁷Netherlands Institute of Ecology, Droevendaalsesteeg 10, 6708 PB Wageningen, Netherlands. ⁸TERI-Deakin Nano Biotechnology Centre, Biotechnology and Management of Bioresources Division, TERI, India Habitat Centre, Lodhi Road, New Delhi 110 003, India.

*Corresponding author. E-mail: john.davison@ut.ee (J.D.); mari.moora@ut.ee (M.M.); maarja.opik@ut.ee (M.O.); martin.zobel@ut.ee (M.Z.) †These authors contributed equally to this work.

VT recorded from pairs of continents (56%) were similar to the respective values for plant families (59% in both cases) (Fig. 1, C and D). Using available data on plant species diversity, we estimated that the mean proportion of plant species shared

between pairs of continents is at least an order of magnitude lower (~4%) (Fig. 1, C and D).

Cosmopolitan organismal distribution may occur if speciation events representing the origins of extant taxa happened before major continental

reconfigurations (i.e., ancient vicariance); it may also occur as a result of efficient global dispersal (16). Where ancient vicariance is the primary driver, taxa with an origination time after putative vicariance events should display restricted distributions. We used distribution data for AM fungal VT, along with a dated phylogenetic tree reconstructed using small subunit ribosomal RNA (SSU rRNA) gene sequence data, to show that most VT had origination times after the major continental shifts occurred; in addition, we found that the collective descendant taxa of all but the most recent ancestral nodes are globally distributed (Fig. 2 and figs. S3 and S4). Though it was derived from a fossil-calibrated single-gene analysis, this pattern strongly suggests that the wide distribution of AM fungal VT is driven by efficient recent dispersal rather than by ancient vicariance. Integrating this finding with the current understanding of AM fungal ecology requires a reassessment of potential dispersal mechanisms. First, the frequency of long-distance dispersal events mediated by known agents, including wind (13, 19) and human activities (16), may have been underestimated owing to a lack of empirical data. Second, overlooked dispersal agents might be responsible for substantial propagule transport. For example, although there is no quantitative evidence concerning dispersal in seawater or via birds (20), these agents might explain the abundance of AM fungi on oceanic islands (21). Third, rare dispersal events, such as powerful dust storms, may strongly influence distribution patterns, because AM fungal propagules exhibit high viability. Given that AM fungal spores are generally large and demonstrate high survival rates in harsh environmental conditions (4, 22), they might form a propagule bank that can efficiently exploit favorable conditions even if these are encountered infrequently, analogous to large-seeded plants (23) and sporocarp-forming ectomycorrhizal fungi (24).

To disentangle the effects on AM fungal communities of biotic and abiotic ecosystem components and of spatial processes, we partitioned variation in AM fungal richness and community composition between sets of variables related to paleogeography, spatial distance between plots, environment, and plant host (figs. S5 to S7 and tables S4 to S6). We found that the richness of AM fungal communities in individual plant roots or vegetation plots varied in relation to spatial distance and environmental gradients (Fig. 3A and fig. S8), consistent with existing evidence (3, 7, 8). However, our data showed that the taxon richness (alpha diversity) of AM fungal communities decreases with latitude (Fig. 3E), a pattern that is widespread in macroorganisms (25) but is not observed among ectomycorrhizal fungi (12, 26) or other soil microbes (27). Environmental variables explained slightly more of the variation in plot and sample richness than spatial distance did, but most variation was explained by the intersection of these variable sets (i.e., environmental gradients that exhibit a spatial lag, such as temperature) (table S4). AM fungal community richness was consistently higher in grasslands than in forests (Fig. 3E), whereas the converse was true of the local taxon

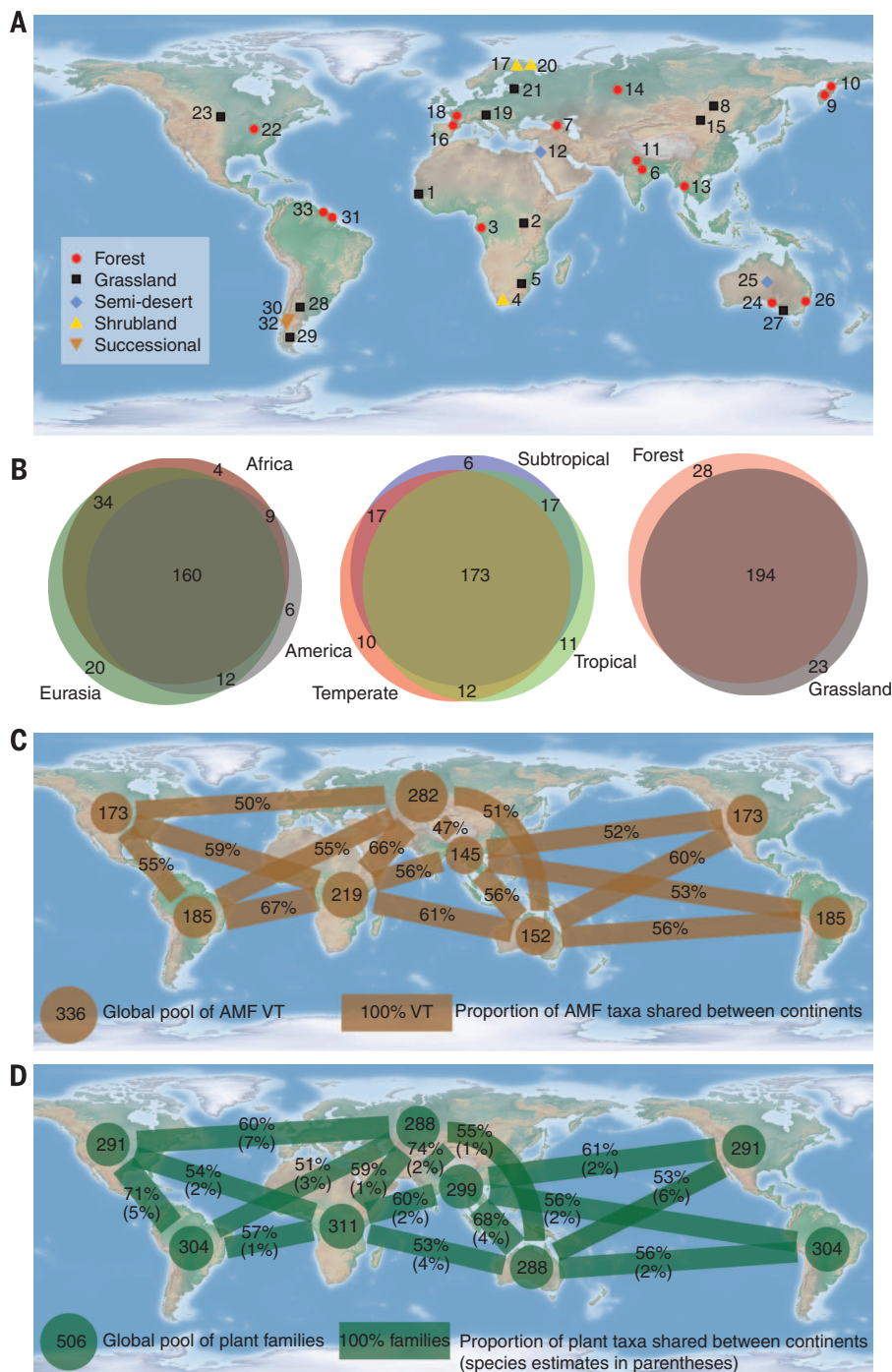


Fig. 1. Global biogeography in AM fungi and plants. (A) Sampled sites (table S1). (B) Venn diagrams (using relevant subsets of the full data set) showing the sharing of AM fungal VT between continents, biomes, and ecosystems. (C) Counts of VT and (D) plant families found on each continent (circles) and the percentages shared between different continents (lines). The areas of circles and thicknesses of lines are respectively proportional to the fraction of the global taxon pool represented and the fraction of taxa shared between pairs of continents. Shared-species estimates for continent pairs are shown in parentheses in (D). (C) also includes distribution data from the MaarjAM database of published SSU rRNA gene sequences (10) for AM fungal VT with at least one known geographic point of origin.

turnover rate (beta diversity) (Fig. 3F), and the total richness (gamma diversity) recorded in the two habitats was similar (Fig. 1B). Thus, despite grassland biomes having originated during the Eocene (making them an order of magnitude younger than the first AM fungi) (28), they have become a favorable habitat for AM fungi. Vascular plants exhibit a similar pattern: Higher small-scale richness is observed in grasslands (29), but total richness is higher in forests (30).

Spatial distance explained at least as much plot-level variation in community composition as did environmental variables (Fig. 3, B and C; table S6). The role of local-scale dispersal limitation in structuring AM fungal communities has previously been recognized (7); here, we provide empirical evidence of distance decay on a global scale. Sample-level community composition was additionally explained by paleogeographic history and host-plant phylogeny, though the explanatory power of these variable sets was very low (Fig. 3C). Although the idea that AM fungal community composition contains a paleogeographic signature has previously been proposed (31), our analysis represents the first empirical evidence to support this theory. The best-fitting predictor variables related to the plant host suggested that AM fungal community composition responds to the coarsest-scale differences in plant phylogeny (fig. S6). Previous research (32) found that AM fungal community structure converges as the phylogenetic distance between host plants increases; our study demonstrates the converse pattern.

Because biogeographic analyses are highly dependent on taxonomic resolution (33), we repeated our analyses using a second widely used approach for sequence identification: *de novo* clustering of OTUs at 97% sequence similarity (figs. S1 and S9). The recorded degree of endemism among OTUs (fig. S10) was higher than that of VT and plant families, but it was approximately an order of magnitude lower than that estimated for plant species (Fig. 1D). Variations in AM fungal richness and community composition were similar across the two approaches used for sequence identification (fig. S11) [similar findings are presented in (34)]. Furthermore, rarefaction, as a means of standardizing the sequencing effort between samples, made a negligible difference to the results of community richness and composition analyses (fig. S11).

We have demonstrated for an important terrestrial microbial group that local environmental conditions and spatial configurations determine the composition of communities. AM fungal taxa are known to differ in their habitat preferences (35) and responses to local environmental gradients (7–9), and unfavorable environmental conditions are a likely factor limiting within-region dispersal of AM fungal taxa with particular ecological requirements (8, 35). This bears a warning message, because progressive habitat loss and fragmentation of landscapes might result in a situation where human-induced dispersal barriers, such as agricultural systems with few potential

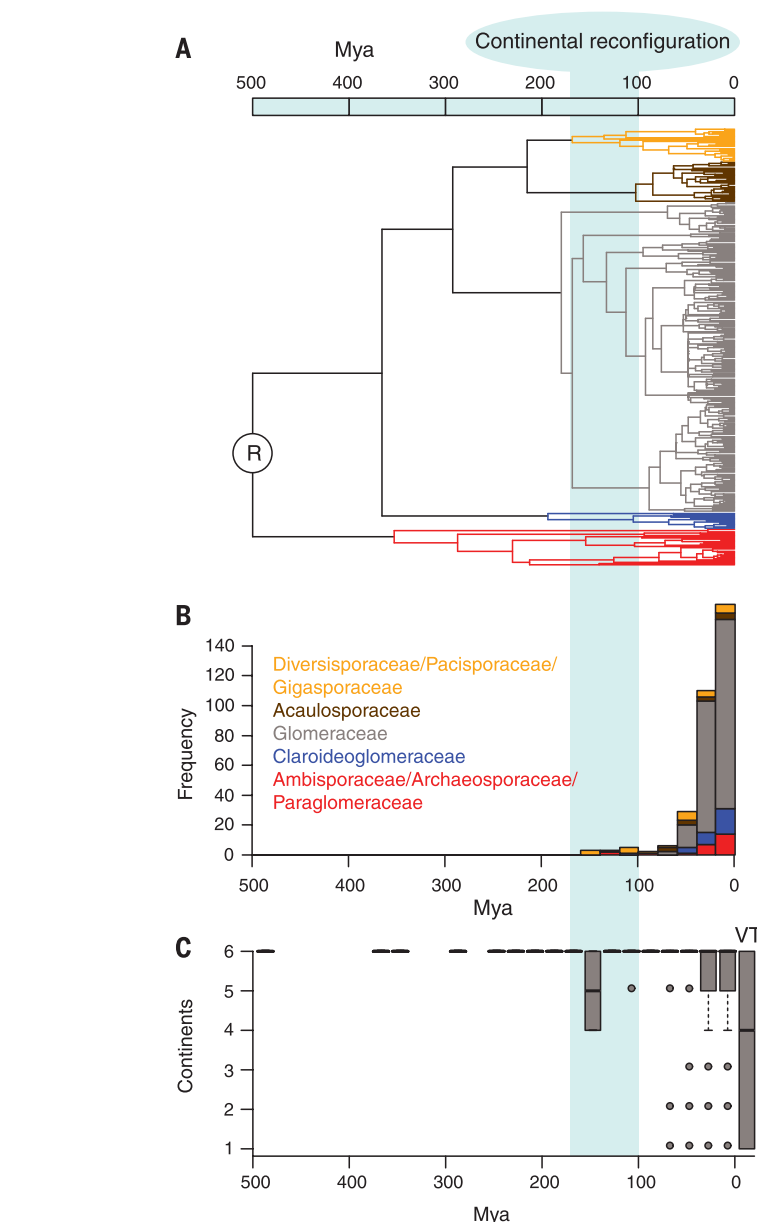


Fig. 2. Phylogeny-based analysis of AM fungal distribution. (A) Bayesian phylogenetic tree of AM fungi, with family groupings shown in different colors. Tree tips represent VT type (i.e., representative) sequences. (B) Mean ages of nodes immediately ancestral to VT, as estimates of VT origination times. (C) Number of continents occupied by the descendant taxa of internal tree nodes (i.e., ancestral taxa). The median (central bar), quartiles (gray box), ranges excluding outliers (whiskers), and outliers (points) of the continental distributions are shown for nodes over 20-million-year increments. The right-most boxplot shows the continental distribution of tree tips (VT). VT distribution was determined using data from this study and from the MaarjAM database (10) for VT with at least one known geographic point of origin. Timing was derived by using a relaxed clock analysis with fossil calibration of the root [R in (A)] at 505 million years ago (Mya). The vertical blue band across panels shows the timing of continental reconfiguration events, according to (40).

mutualist partners, inhibit the arrival of symbiotic fungi that are necessary for ecosystem functioning and service provision. We showed that the cosmopolitan distribution pattern of AM fungal taxa contrasts with that of their host plants at the species level, whereas the host plants exhibit a similar pattern at a taxonomic rank several levels higher (28). At a continental scale, this pattern

also contrasts with the high spatial turnover of some microbial organisms, including fungi (36, 37), but it resembles observed patterns for certain bacteria (38). We propose that earlier reports of patchily distributed AM fungal taxa at the continental or global scales may have been related to low sampling effort (11) and/or the collation of methodologically diverse data (3, 10). We suggest

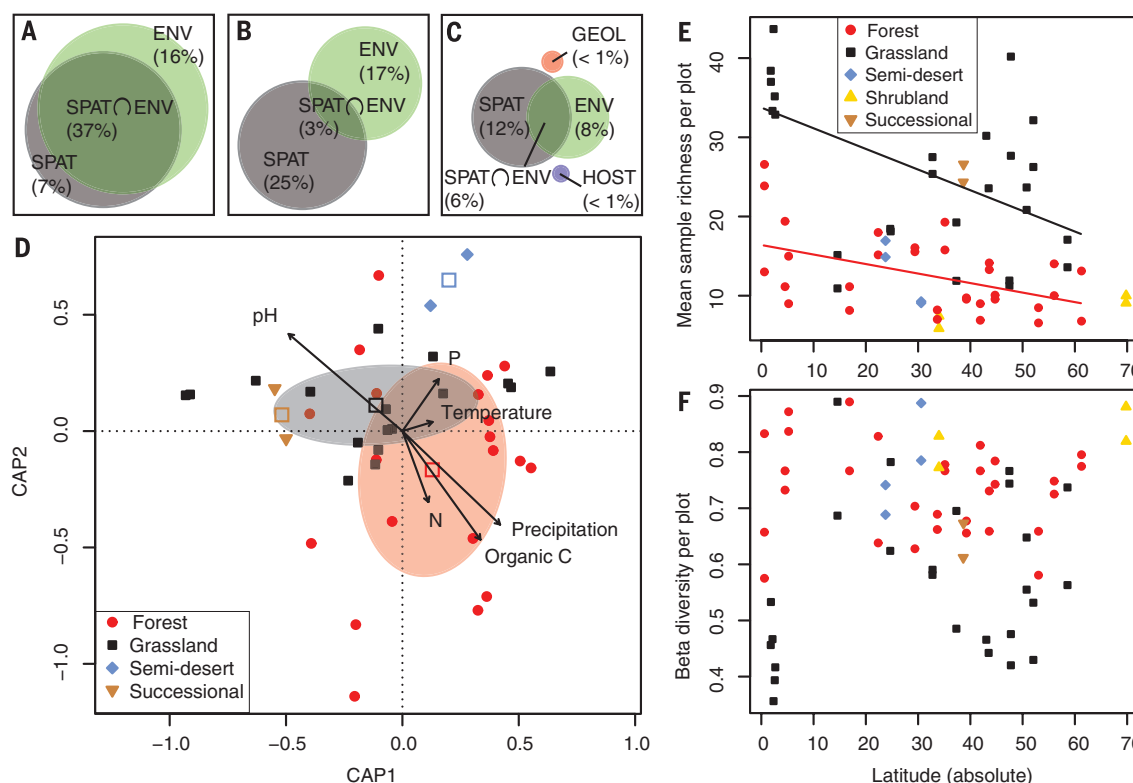


Fig. 3. Variation in AM fungal community richness and composition related to paleogeography (GEOL), spatial distance (SPAT), environment (ENV), and plant host (HOST). (A) Richness per plot. (B) Qualitative community composition per plot. (C) Qualitative community composition per sample. (D) Spatially constrained, distance-based redundancy analysis of plot-based qualitative community composition. Ecosystem centroids (open squares) and dispersions (ellipses, 1 SD around forest and grassland centroids) are shown. Arrows indicate the direction of the maximum change in environmental variables.

(E) Alpha diversity (mean sample richness) per plot (absolute latitude: $F = 11.5$, $P = 0.002$; ecosystem: $F = 30.9$, $P < 0.001$; interaction: $F = 1.4$, $P = 0.25$). Only forest and grassland plots were analyzed. Lines are model-predicted values of richness at a range of latitudes. (F) Beta diversity (mean Sørensen index between sample pairs) per plot (absolute latitude: $F = 0.7$, $P = 0.40$; ecosystem: $F = 23.7$, $P < 0.001$; interaction: $F = 2.4$, $P = 0.14$). In (A) through (C), n indicates the intersection of variable sets and is shown when $>1\%$; the size of each component is proportional to the fraction of the variation explained.

that addressing both global and local dispersal of AM fungi and the role of dispersal agents such as birds, large mammals (including humans), wind, surface water, and seawater can illuminate the processes governing AM fungal diversity patterns. Along with a better understanding of the functional attributes of cosmopolitan taxa throughout their ranges (39), such information will not only enhance our understanding of microbial biogeography but will also facilitate ecosystem restoration and sustainable agriculture.

REFERENCES AND NOTES

- P. Bonfante, A. Genre, *Trends Plant Sci.* **13**, 492–498 (2008).
- M. Öpik, J. Davison, M. Moora, M. Zobel, *Botany* **92**, 135–147 (2014).
- S. N. Kivlin, C. V. Hawkes, K. K. Treseder, *Soil Biol. Biochem.* **43**, 2294–2303 (2011).
- S. E. Smith, D. J. Read, *Mycorrhizal Symbiosis* (Academic Press, Amsterdam, ed. 3, 2008).
- M. G. A. van der Heijden, R. D. Bardgett, N. M. van Straalen, *Ecol. Lett.* **11**, 296–310 (2008).
- H. M. Bik et al., *Trends Ecol. Evol.* **27**, 233–243 (2012).
- A. J. Dumbrell, M. Nelson, T. Helgason, C. Dytham, A. H. Fitter, *ISME J.* **4**, 337–345 (2010).
- C. Hazard et al., *ISME J.* **7**, 498–508 (2013).
- Y. Lekberg, J. Meadow, J. R. Rohr, D. Redecker, C. A. Zabinski, *Ecology* **92**, 1292–1302 (2011).
- M. Öpik et al., *New Phytol.* **188**, 223–241 (2010).
- M. Öpik et al., *Mycorrhiza* **23**, 411–430 (2013).
- L. Tedersoo et al., *Science* **346**, 1256688 (2014).
- C. Egan, D. W. Li, J. N. Klironomos, *Fungal Ecol.* **12**, 26–31 (2014).
- S. A. Mangan, G. H. Adler, *Oecologia* **131**, 587–597 (2002).
- M. J. Harner, N. Opitz, K. Geluso, K. Tockner, M. C. Rillig, *Aquat. Sci.* **73**, 35–42 (2011).
- S. Rosendahl, P. McGee, J. B. Morton, *Mol. Ecol.* **18**, 4316–4329 (2009).
- S. N. Kivlin, G. C. Winston, M. L. Goulden, K. K. Treseder, *Fungal Ecol.* **12**, 14–25 (2014).
- V. H. Heywood, R. K. Brummitt, A. Culham, O. Seberg, *Flowering Plant Families of the World* (Kew Publishing, Richmond, UK, 2007).
- N. J. Warner, M. F. Allen, J. A. MacMahon, *Mycologia* **79**, 721–730 (1987).
- W. D. McIlveen, H. Cole Jr., *Can. J. Bot.* **54**, 1486–1489 (1976).
- R. E. Koske, J. N. Gemma, *Am. J. Bot.* **77**, 466–474 (1990).
- S. Varga, C. Finozzi, M. Vestberg, M.-M. Kytöviita, *Mycorrhiza* **25**, 335–343 (2015).
- J. Metz et al., *J. Ecol.* **98**, 697–704 (2010).
- S. I. Glassman et al., *New Phytol.* **205**, 1619–1631 (2015).
- H. Hillebrand, *Am. Nat.* **163**, 192–211 (2004).
- L. Tedersoo et al., *Mol. Ecol.* **21**, 4160–4170 (2012).
- R. D. Bardgett, W. H. van der Putten, *Nature* **515**, 505–511 (2014).
- G. J. Bredenkamp, F. Spada, E. Kazmierczak, *Plant Ecol.* **163**, 209–229 (2002).
- J. B. Wilson, R. K. Peet, J. Dengler, M. Pärtel, *J. Veg. Sci.* **23**, 796–802 (2012).
- G. Kier et al., *J. Biogeogr.* **32**, 1107–1116 (2005).
- J. B. Morton, S. P. Bentivenga, J. D. Bever, *Can. J. Bot.* **73**, 25–32 (1995).
- S. D. Veresoglou, M. Rillig, *Plant Soil* **377**, 395–406 (2014).
- C. A. Hanson, J. A. Fuhrman, M. C. Horner-Devine, J. B. H. Martiny, *Nat. Rev. Microbiol.* **10**, 497–506 (2012).
- Y. Lekberg, S. M. Gibbons, S. Rosendahl, *New Phytol.* **202**, 1101–1104 (2014).
- T. Helgason, A. H. Fitter, *J. Exp. Bot.* **60**, 2465–2480 (2009).
- A. Meiser, M. Bálint, I. Schmitt, *New Phytol.* **201**, 623–635 (2014).
- J. M. Talbot et al., *Proc. Natl. Acad. Sci. U.S.A.* **111**, 6341–6346 (2014).
- J. B. H. Martiny, J. A. Eisen, K. Penn, S. D. Allison, M. C. Horner-Devine, *Proc. Natl. Acad. Sci. U.S.A.* **108**, 7850–7854 (2011).
- P. L. Chagnon, R. L. Bradley, H. Maherali, J. N. Klironomos, *Trends Plant Sci.* **18**, 484–491 (2013).
- A. Schettino, C. R. Scotese, *Geophys. J. Int.* **163**, 727–759 (2005).

ACKNOWLEDGMENTS

This research was funded by grants from the Estonian Science Foundation (9050 and 9157), the Estonian Research council (IUT-20-28 and IUT-20-29), the European Regional Development Fund (Frontiers in Biodiversity Research Centre of Excellence), and the U.S. NSF (DEB-0842327 to N.C.J.). We are grateful to colleagues who offered local support and contributed to fieldwork: J. D. Bever, C. Birnbaum, H. Bruelheide, J. J. Cantero, J. Cole, E. Corcket, M. Diallo, K. J. Esler, E. Facelli, J. M. Facelli, L. Götzenberger, R. Johnson, J. M. Kalwij, A. Koppel, M. E. Leal, J. Liira, E. Louisanna, E. Marcon, E. Mayemba, H. Moora, J. Morgan, V. Neshataeva, J. Paal, A. K. Pandey, C. Phosri, J. N. Price, S. Pölme, J. Propster, G. Sharma, K. Shukla, R. Singh, H. Schimann, M. Semchenko, G. Sharma, R. Singh, S. Sitawan, K. Sukla, A. Zobel, E. Vanatoa, and W. Wei. We thank I. A. Dickie for useful comments on the manuscript. All the raw and filtered data are available either in the supplementary materials or from the European Nucleotide Archive (raw data: data set PRJEB9764; representative read set: accession numbers LN615280–LN623520).

SUPPLEMENTARY MATERIALS

www.sciencemag.org/content/349/6251/970/suppl/DC1
Materials and Methods
Figs. S1 to S11
Tables S1 to S6
Database S1
References (41–84)

16 March 2015; accepted 29 July 2015
10.1126/science.aab1161

This copy is for your personal, non-commercial use only.

If you wish to distribute this article to others, you can order high-quality copies for your colleagues, clients, or customers by [clicking here](#).

Permission to republish or repurpose articles or portions of articles can be obtained by following the guidelines [here](#).

The following resources related to this article are available online at www.sciencemag.org (this information is current as of September 3, 2015):

Updated information and services, including high-resolution figures, can be found in the online version of this article at:

<http://www.sciencemag.org/content/349/6251/970.full.html>

Supporting Online Material can be found at:

<http://www.sciencemag.org/content/suppl/2015/08/26/349.6251.970.DC1.html>

This article **cites 76 articles**, 21 of which can be accessed free:

<http://www.sciencemag.org/content/349/6251/970.full.html#ref-list-1>

This article appears in the following **subject collections**:

Ecology

<http://www.sciencemag.org/cgi/collection/ecology>

NEURONAL DEVELOPMENT

Glycerophospholipid regulation of modality-specific sensory axon guidance in the spinal cord

Adam T. Guy,¹ Yasuko Nagatsuka,¹ Noriko Ooashi,¹ Mariko Inoue,¹ Asuka Nakata,¹ Peter Greimel,^{1,2} Asuka Inoue,^{3,4} Takuji Nabetani,¹ Akiho Murayama,⁵ Kunihiro Ohta,⁵ Yukishige Ito,⁶ Junken Aoki,^{3,7} Yoshio Hirabayashi,^{1*} Hiroyuki Kamiguchi^{1*}

Glycerophospholipids, the structural components of cell membranes, have not been considered to be spatial cues for intercellular signaling because of their ubiquitous distribution. We identified lyso-phosphatidyl- β -D-glucoside (LysoPtdGlc), a hydrophilic glycerophospholipid, and demonstrated its role in modality-specific repulsive guidance of spinal cord sensory axons. LysoPtdGlc is locally synthesized and released by radial glia in a patterned spatial distribution to regulate the targeting of nociceptive but not proprioceptive central axon projections. Library screening identified the G protein-coupled receptor GPR55 as a high-affinity receptor for LysoPtdGlc, and GPR55 deletion or LysoPtdGlc loss of function in vivo caused the misallocation of nociceptive axons into proprioceptive zones. These findings show that LysoPtdGlc/GPR55 is a lipid-based signaling system in glia-neuron communication for neural development.

During nervous system development, axon-guiding proteins play major roles in network formation, but lipids may also be a family of intercellular guidance cues because of their abundance and diversity in nervous tissue (1, 2). Phosphatidyl- β -D-glucoside [PtdGlc [2-O-arachidoyl-1-O-(1-stearoyl)-sn-glycer-3-yl]- β -D-glucopyranosyl phosphate; fig. S1A] is a membrane glycerophospholipid (3) that is localized to radial glia and nascent astrocytes (4, 5). We showed that PtdGlc and its hydrolytic derivative lyso-phosphatidyl- β -D-glucoside (LysoPtdGlc; fig. S1A) occur in a patterned distribution in the developing spinal cord and mediate glia-neuron communication to guide nociceptive afferent axons.

Nanoliquid chromatography/tandem mass spectrometry detected PtdGlc in proliferative glia isolated from spinal cords of stage (st.) 34 chick embryos (fig. S1, B and C). Their conditioned medium contained water-soluble LysoPtdGlc (fig. S1, D and E) but not PtdGlc, which suggests that PtdGlc can be hydrolyzed in glial membranes and released as LysoPtdGlc. We double-stained

glial cultures with DIM21, an antibody to PtdGlc (6, 7), and EAP3, an antibody to transitin, a marker of radial glia (8). 94.1% of cultured glia were labeled positive for PtdGlc, and of these cells, 91.1% coexpressed PtdGlc and transitin (fig. S1, F and G). In spinal cord sections, PtdGlc is distinct from cells

labeled with the neuronal marker NeuN, whereas it colocalizes with transitin (fig. S2). Because these data suggested that spinal cord radial glia produce PtdGlc and can release LysoPtdGlc into the extracellular environment, we examined a role for these glycerophospholipids in spinal cord development.

Dorsal root ganglion (DRG) axons of different sensory modalities elongate through a common tract, the dorsal root, but segregate as they elongate in the spinal cord (fig. S3). Then these axons bifurcate and extend in the white matter both rostrally and caudally (9), with nociceptive afferents positioned laterally and proprioceptive afferents occupying a more dorsomedial position, the primordial dorsal funiculus (10) (fig. S4A). To examine this initial segregation process, we observed the spatiotemporal relationship between PtdGlc-positive radial glia and DRG afferents. We labeled transverse sections with DIM21 and antibody to either TrkA or TrkC to stain nerve growth factor (NGF)-responsive nociceptive or neurotrophin-3 (NT-3)-responsive proprioceptive axons (Fig. 1). At st. 28, DIM21 labels PtdGlc in cell bodies lining the dorsal midline as well as the primordial dorsal funiculus that receives the pial processes of PtdGlc-positive cells (Fig. 1A). TrkA-expressing axon terminals are localized to the primordial dorsal root entry zone (DREZ), whereas those expressing TrkC extend into the PtdGlc-positive primordial dorsal funiculus. At st. 34, PtdGlc is abundant in the dorsomedial spinal cord, colocalizing with TrkC but not TrkA (Fig. 1B). We used mass spectrometry to quantify

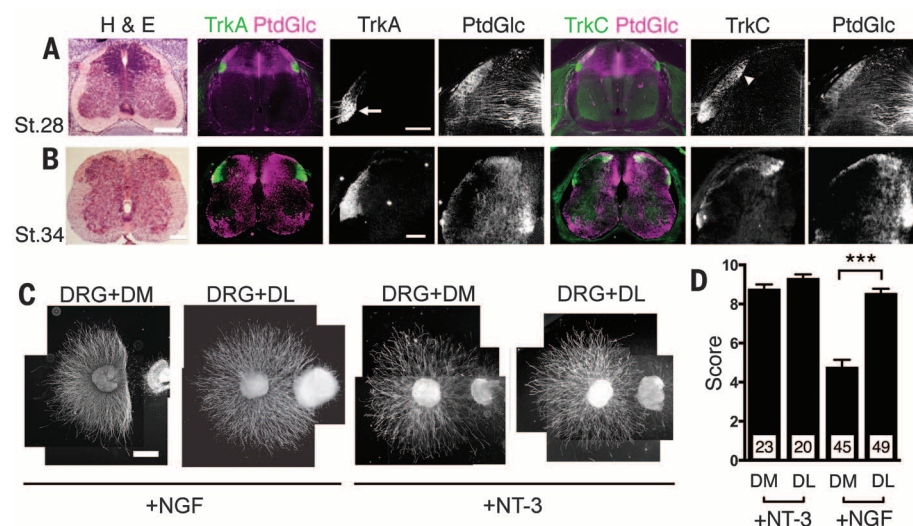


Fig. 1. Intraspinal localization of PtdGlc and chemorepulsive activity toward DRG afferents. (A and B) Transverse sections of st. 28 (A) and st. 34 (B) chick lumbar spinal cord with hematoxylin and eosin (H & E) stain (scale bar, 100 μ m), double immunofluorescence of PtdGlc and either TrkA or TrkC, and grayscale images showing the unilateral dorsal cord from green/magenta merges at higher magnification (scale bar, 50 μ m). The arrow and arrowhead indicate the dorsal root entry zone (DREZ) and the primordial dorsal funiculus, respectively. (C) Collagen gel explant assay. Dorsomedial (DM) or dorsolateral (DL) st. 34 spinal cord explants were cocultured with a DRG explant enriched for either TrkA or TrkC neurons by adding NGF or NT-3 to the medium, respectively. DRG axons were visualized with antibody to β -tubulin. Images are composites of three or four photomicrographs. Scale bar, 500 μ m. (D) Explants were scored using a scale of 0 to 10, with 0 representing the greatest chemorepulsion (see the supplementary methods for the scoring protocol). Bars represent mean chemorepulsion score \pm SEM, and numbers in boxes represent cultures per group. *** $P < 0.001$; Kruskal-Wallis test.

¹RIKEN Brain Science Institute, 2-1 Hirosawa, Wako, Saitama 351-0198, Japan. ²Lipid Biology Laboratory, RIKEN, 2-1 Hirosawa, Wako, Saitama 351-0198, Japan. ³Graduate School of Pharmaceutical Sciences, Tohoku University, 6-3 Aoba, Sendai, Miyagi 980-8578, Japan. ⁴Japan Science and Technology Agency, Precursory Research for Embryonic Science and Technology (PRESTO), 4-1-8 Honcho, Kawaguchi, Saitama 332-0012, Japan. ⁵Department of Life Sciences, Graduate School of Arts and Sciences, University of Tokyo, 3-8-1 Komaba, Meguro, Tokyo 153-8902, Japan. ⁶Synthetic Cellular Chemistry Laboratory, RIKEN, 2-1 Hirosawa, Wako, Saitama 351-0198, Japan. ⁷Japan Agency for Medical Research and Development, Core Research for Evolutional Science and Technology (AMED-CREST), 1-7-1 Otemachi, Chiyoda, Tokyo 100-0004, Japan.

*Corresponding author. E-mail: kamiguchi@brain.riken.jp (H.K.); hirabaya@riken.jp (Y.H.)

LysoPtdGlc in spinal cord subregions (fig. S5). At st. 34, LysoPtdGlc was undetectable in the dorso-lateral spinal cord, whereas approximately 7.4 μ M LysoPtdGlc was present in the dorsomedial cord (see supplementary methods for the protocol),

indicating that LysoPtdGlc codistributes with PtdGlc in this area. The demarcation of the TrkA and PtdGlc domains compared to the colocalization of TrkC with PtdGlc at all stages observed (fig. S4) led us to hypothesize that PtdGlc or its

derivative LysoPtdGlc has a repulsive effect that is specific to nociceptive afferents.

To assess the repulsive activity of the dorso-medial cord, we cocultured one DRG explant and one spinal cord subregion explant dissected from

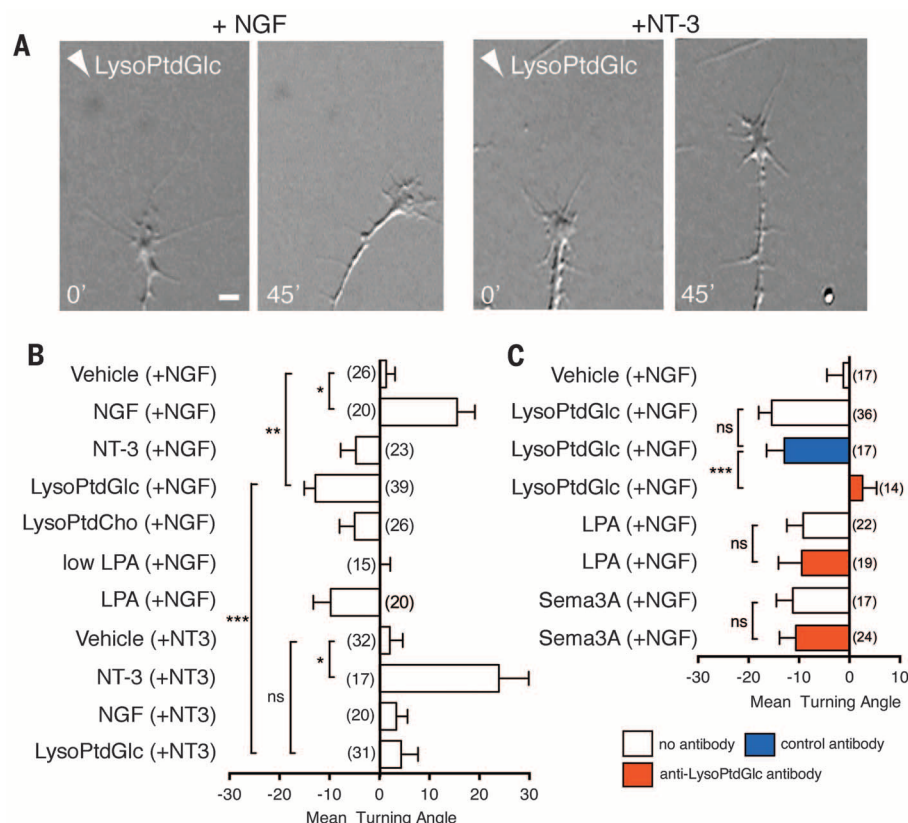
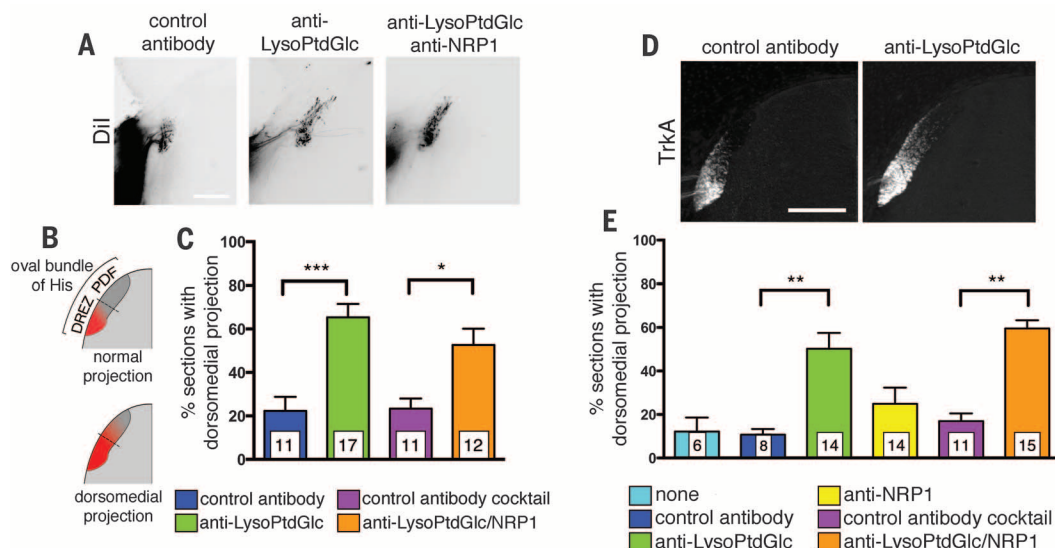


Fig. 2. LysoPtdGlc repels NGF-responsive but not NT-3-responsive DRG axons. (A) Dissociated st. 36 chick DRG neurons were cultured with either NGF or NT-3 and exposed to a concentration gradient of purified LysoPtdGlc. The number in each panel indicates minutes after initiation, and the arrowhead shows the direction of LysoPtdGlc gradient; scale bar, 10 μ m. (B) Quantification of axon turning angle. Bars represent mean turning angle \pm SEM with positive and negative values indicating attraction and repulsion, respectively. Numbers in parentheses are growth cones tested per group. The y-axis labels indicate the lipid or neurotrophin added to the culture medium. Abbreviations and in-pipette concentrations used are as follows: LysoPtdGlc (purified; 1 μ M); LysoPtdCho, lysophosphatidylcholine (1 μ M); low LPA (1 μ M); LPA (20 μ M); NGF (50 μ g/ml); NT-3 (50 μ g/ml). *** P < 0.001, ** P < 0.01, * P < 0.05; Kruskal-Wallis test. (C) Antibody to LysoPtdGlc blocked the chemorepulsive turning of NGF-responsive st. 28 DRG axons induced by LysoPtdGlc. Bars represent mean turning angle \pm SEM. Numbers in parentheses are growth cones tested per group. In-pipette concentrations used are as follows: LysoPtdGlc (synthetic; 10 μ M); LPA (20 μ M); Sema3A (10 μ g/ml). *** P < 0.001; Kruskal-Wallis test.

Fig. 3. LysoPtdGlc regulates nociceptive afferent projections in developing spinal cord.

Injection of function-blocking antibody into the spinal cord in ovo attenuated LysoPtdGlc signaling.

(A) Transverse lumbar spinal cord sections showing unilateral Dil-labeled putative nociceptive afferents in embryos injected with control antibody, anti-LysoPtdGlc, or a cocktail of anti-LysoPtdGlc and anti-NRP1. Scale bar, 75 μ m. (B) Method of evaluating normal and dorsomedial projection phenotypes. The dorsolateral white matter known as the oval bundle of His is composed of the DREZ and the primordial dorsal funiculus (PDF). For quantification, the oval bundle of His was divided into dorsal and ventral halves as indicated by the broken line. Sections showing Dil- or TrkA antibody-labeled afferents only in the ventral half were considered normal, whereas those showing positive labeling in the dorsal half were classed as dorsomedial projections. (C) Quantification of dorsomedial projection of Dil-labeled afferents after antibody injection. (D) TrkA immunofluorescence in control antibody or anti-LysoPtdGlc-injected spinal cords. Scale bar, 50 μ m. (E) Quantification of TrkA⁺ dorso-medial projection after antibody injection. [(C) and (E)] Bars represent mean percentage \pm SEM of sections showing dorsomedial projection of all embryos in each test group. Numbers within each bar indicate the number of embryos examined per group. *** P < 0.001, ** P < 0.01, * P < 0.05; Kruskal-Wallis test.



Sections showing Dil- or TrkA antibody-labeled afferents only in the ventral half were considered normal, whereas those showing positive labeling in the dorsal half were classed as dorsomedial projections. (C) Quantification of dorsomedial projection of Dil-labeled afferents after antibody injection. (D) TrkA immunofluorescence in control antibody or anti-LysoPtdGlc-injected spinal cords. Scale bar, 50 μ m. (E) Quantification of TrkA⁺ dorso-medial projection after antibody injection. [(C) and (E)] Bars represent mean percentage \pm SEM of sections showing dorsomedial projection of all embryos in each test group. Numbers within each bar indicate the number of embryos examined per group. *** P < 0.001, ** P < 0.01, * P < 0.05; Kruskal-Wallis test.

st. 34 embryos in a collagen matrix, with either NGF or NT-3 added to the culture medium (Fig. 1, C and D) to enrich explants with NGF- or NT-3-responsive neurons (11). Explants of dorsomedial, but not dorsolateral, cord repelled NGF-responsive axons. NT-3-responsive axons did not display a chemorepulsive response to spinal cord explants of either subregion.

To test whether LysoPtdGlc alone is sufficient for the chemorepulsion, we prepared dissociated cultures of st. 28 or 36 DRG neurons and quantified growth cone turning responses to a concentration gradient of LysoPtdGlc in the culture medium (Fig. 2). DRG neurons that had been maintained with bath-applied NGF or NT-3 showed attractive responses to a gradient of NGF or NT-3, respectively, but not to a gradient of the opposite neurotrophin (Fig. 2B), indicating that we could selectively subject NGF- or NT-3-responsive neurons to this assay. PtdGlc purified from embryonic brain tissue (4) was hydrolyzed *in vitro* to produce LysoPtdGlc, and a gradient of LysoPtdGlc chemorepelled NGF-responsive but not NT-3-responsive axons (Fig. 2, A and B). In this assay, the LysoPtdGlc concentration near the growth cone was approximately 0.1% of in-pipette concentration (12), or 1 nM. The same concentration of lysophosphatidic acid (LPA) did not repel NGF-responsive axons (low LPA in Fig. 2B), excluding the possibility that LysoPtdGlc was chemorepulsive after being hydrolyzed to LPA in the medium. We synthesized LysoPtdGlc (fig. S6 and supplementary text) to avoid the possibility of contaminants in brain-

derived preparations and found that synthetic LysoPtdGlc also repelled NGF-responsive but not NT-3-responsive axons (fig. S7). Lysophosphatidylcholine, a structurally related lysophospholipid, did not induce axon turning (Fig. 2B).

Using the Autonomously Diversifying Library System (13) we raised a function-blocking antibody to LysoPtdGlc that exhibited negligible binding to PtdGlc or other lipids tested (fig. S8). This antibody abolished the repulsive turning of NGF-responsive axons induced by LysoPtdGlc, but not that by LPA or semaphorin 3A (Sema3A) (Fig. 2C), and attenuated the chemorepulsive activity of dorsomedial spinal cord explants toward NGF-responsive DRG axons (fig. S9).

We injected anti-LysoPtdGlc into the spinal cord *in ovo*, either alone or as a cocktail with anti-neuropilin-1 (NRP-1). Antibody-injected embryos were fixed at st. 28 and phenotyped by labeling nociceptive afferents by 1,1'-dioctadecyl-3,3,3',3'-tetramethylindocarbocyanine perchlorate (DiI) injection into the dorsomedial DRG (14) (fig. S10). Whereas DiI-labeled nociceptive afferents were confined to the DREZ in control embryos, these afferents showed dorsomedial projection into the primordial dorsal funiculus after injection of anti-LysoPtdGlc alone or a cocktail of the two antibodies (Fig. 3, A to C). This guidance error of nociceptive afferents was also confirmed by TrkA immunofluorescence (Fig. 3, D and E) and quantitative pixel analysis (fig. S11). Anti-LysoPtdGlc injection alone induced guidance errors (Fig. 3, C and E), most likely because Sema3A is absent from the lateral spinal cord

(15) and may not participate in nociceptive axon guidance in the oval bundle of His. Antibody injection did not affect PtdGlc or TrkC domains (figs. S11 and S12). These results indicate that LysoPtdGlc-mediated chemorepulsion prevents TrkA-positive nociceptive axons from entering the primordial dorsal funiculus.

We next searched for a receptor and downstream signals that mediate axon repulsive responses to LysoPtdGlc. We found that CT04, an inhibitor of Rho guanosine triphosphatases (16), or Y-27632, an inhibitor of Rho-associated protein kinase (17), abolished LysoPtdGlc-induced repulsion in NGF-responsive neurons (fig. S13A). Because Rho can be activated downstream of $G_{\alpha_{12/13}}$ (18), we used targeted inhibitory $G_{\alpha_{12/13}}$ C-terminal peptides (19) and found that $G_{\alpha_{13}}$ mediates LysoPtdGlc-induced chemorepulsion (fig. S13B).

We conducted screening to identify a G protein-coupled receptor (GPCR) mediating LysoPtdGlc, using the transforming growth factor- α (TGF- α) shedding assay (20). Of 115 GPCRs tested, only GPR55 responded to LysoPtdGlc (fig. S14). The half-maximal effective concentration (EC_{50}) of LysoPtdGlc was 16 nM (fig. S15). Although GPR55 has been reported as a receptor for lysophosphatidylinositol (LysoPtdIns) (21), the EC_{50} of LysoPtdIns was 110 nM (fig. S15B), indicating that LysoPtdGlc is the more potent ligand. $G_{\alpha_{12}}$ and $G_{\alpha_{13}}$ knockdown abolished the LysoPtdGlc-induced TGF- α response, which could be rescued by a chimeric G_{α} protein that consisted of a G_{α_q} backbone with the $G_{\alpha_{13}}$ C-terminal sequence

Fig. 4. GPR55 is a receptor for LysoPtdGlc-mediated axon guidance. (A) LysoPtdGlc chemorepels NGF-responsive DRG axons of wild-type (WT) but not *Gpr55*^{-/-} mice. The number in the panels indicates minutes after initiation, and the arrowheads show the direction of the gradient; scale bar, 10 μ m. (B) Quantified turning responses of WT or *Gpr55*^{-/-} axons to gradients of LysoPtdGlc, LPA, LysoPtdIns, or Sema3A. NGF or NT-3 was added to the culture medium as indicated in parentheses. Bars represent mean turning angle \pm SEM; numbers in parentheses indicate growth cones tested. ** $P < 0.01$; one-way analysis of variance with Tukey's post-test. (C) TrkA immunofluorescence in WT or *Gpr55*^{-/-} mouse lumbar spinal cord. Solid circles indicate the midline; scale bar, 200 μ m. (D) Method of evaluating TrkA immunofluorescence. Gray-shaded area represents the TrkA⁺ domain, and the broken line indicates the midline. If the TrkA⁺ domain in the medial quarter (MQ) of the spinal cord was equal to or greater in thickness than the TrkA⁺ domain in the DREZ (arrowheads), the section was classified as a dorsomedial projection. (E) Quantification of TrkA⁺ dorsomedial afferent projection in WT and *Gpr55*^{-/-} mice. Bars represent mean percentage \pm SEM of sections showing dorsomedial projection of all embryos in each test group. Numbers within each bar indicate the number of embryos examined per group. * $P < 0.05$; *t* test.

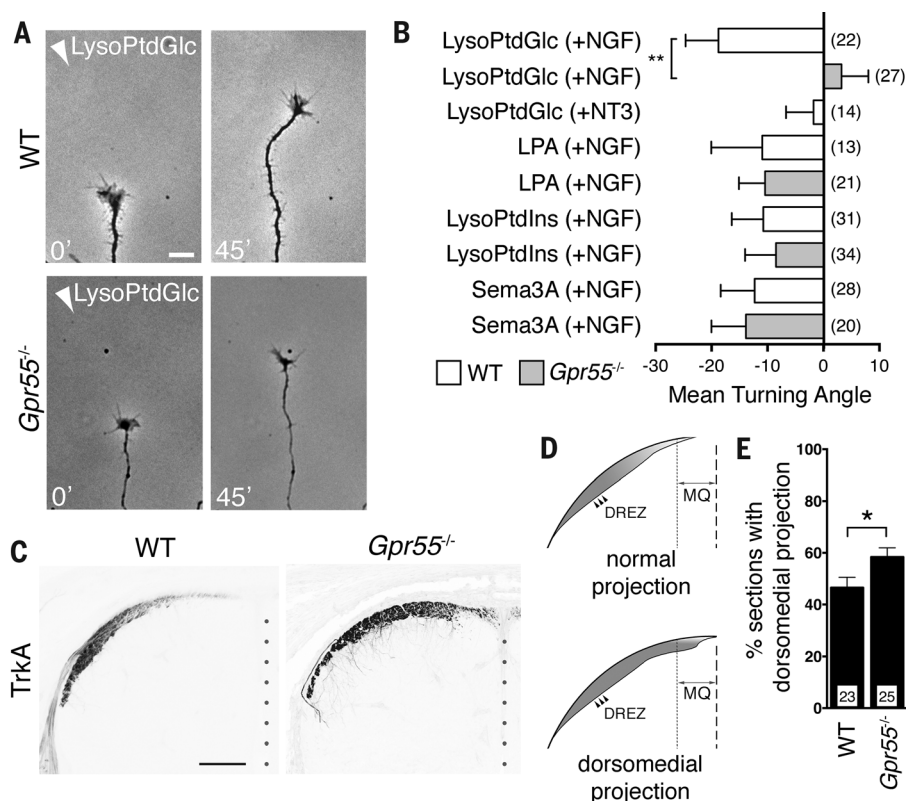


(fig. S16), indicating that LysoPtdGlc signals through $G\alpha_{13}$ -coupled GPR55.

After confirming GPR55 expression in DRG neurons by polymerase chain reaction (fig. S17), we used a *Gpr55* knockout mouse (22) to test whether GPR55 mediates repulsive axon responses to LysoPtdGlc. In vitro, LysoPtdGlc did not affect the directional growth of NT-3-responsive axons but chemorepelled NGF-responsive axons in a GPR55-dependent manner (Fig. 4, A and B). Although it has been reported that LysoPtdIns induces neurite retraction through GPR55 (23), LysoPtdIns chemorepelled *Gpr55*^{-/-} axons (Fig. 4B), indicating that LysoPtdIns can signal through GPR55-independent pathways as reported (24). To examine *Gpr55* function in vivo, we labeled nociceptive afferents in the spinal cord of embryonic day 14.0 wild-type or *Gpr55*^{-/-} mice with TrkA antibody (Fig. 4C) or DiI (fig. S18). Nociceptive afferents were localized mostly to the PtdGlc-sparse DREZ in the wild type, but displayed dorsomedial projection in *Gpr55*^{-/-} mice (Fig. 4, C to E) to where PtdGlc is concentrated and normally TrkC⁺ afferents predominate (fig. S20). These data indicate that *Gpr55* deletion in the mouse causes nociceptive afferent projection errors analogous to those induced by LysoPtdGlc loss of function in the chick. Thus, we demonstrated a mechanism for a diffusible glycerophospholipid that mediates glia-neuron intercellular communication to guide nociceptive axons in the central nervous system. This lipid-mediated guidance may underlie the role of GPR55 in nociception in vivo (25).

REFERENCES AND NOTES

1. L. Strohlic, A. Dwivedy, F. P. van Horck, J. Falk, C. E. Holt, *Development* **135**, 333–342 (2008).
2. P. Berghuis et al., *Science* **316**, 1212–1216 (2007).
3. Y. Nagatsuka et al., *Proc. Natl. Acad. Sci. U.S.A.* **100**, 7454–7459 (2003).
4. Y. Nagatsuka et al., *Biochemistry* **45**, 8742–8750 (2006).
5. M. O. Kinoshita et al., *Biochem. J.* **419**, 565–575 (2009).
6. Y. Yamazaki et al., *J. Immunol. Methods* **311**, 106–116 (2006).
7. P. Greimel, M. Lapeyre, Y. Nagatsuka, Y. Hirabayashi, Y. Ito, *Bioorg. Med. Chem.* **16**, 7210–7217 (2008).
8. G. J. Cole, J. A. Lee, *Brain Res. Dev. Brain Res.* **101**, 225–238 (1997).
9. A. L. Eide, J. C. Glover, *J. Comp. Neurol.* **353**, 247–259 (1995).
10. S. Ozaki, W. D. Snider, *J. Comp. Neurol.* **380**, 215–229 (1997).
11. R. H. Friedel, H. Schnürch, J. Stubbusch, Y. A. Barde, *Proc. Natl. Acad. Sci. U.S.A.* **94**, 12670–12675 (1997).
12. A. M. Lohof, M. Quillan, Y. Dan, M. M. Poo, *J. Neurosci.* **12**, 1253–1261 (1992).
13. H. Seo et al., *Nat. Biotechnol.* **23**, 731–735 (2005).
14. J. T. Rifkin, V. J. Todd, L. W. Anderson, F. Lefcort, *Dev. Biol.* **227**, 465–480 (2000).
15. S. Y. Fu, K. Sharma, Y. Luo, J. A. Raper, E. Frank, *J. Neurobiol.* **45**, 227–236 (2000).
16. K. Aktories, A. Hall, *Trends Pharmacol. Sci.* **10**, 415–418 (1989).
17. M. Uehata et al., *Nature* **389**, 990–994 (1997).
18. O. Kranenburg et al., *Mol. Biol. Cell* **10**, 1851–1857 (1999).
19. A. Gilchrist, M. Bünemann, A. Li, M. M. Hosey, H. E. Hamm, *J. Biol. Chem.* **274**, 6610–6616 (1999).
20. A. Inoue et al., *Nat. Methods* **9**, 1021–1029 (2012).
21. S. Oka, K. Nakajima, A. Yamashita, S. Kishimoto, T. Sugiyama, *Biochem. Biophys. Res. Commun.* **362**, 928–934 (2007).
22. E. Pérez-Gómez et al., *Oncogene* **32**, 2534–2542 (2013).
23. Y. Obara, S. Ueno, Y. Yanagihata, N. Nakahata, *PLOS ONE* **6**, e24284 (2011).
24. A. Bondarenko et al., *Br. J. Pharmacol.* **161**, 308–320 (2010).
25. P. C. Staton et al., *Pain* **139**, 225–236 (2008).

ACKNOWLEDGMENTS

We thank Y. Shinoda, Y. Osaka, A. Shuto, H. Akiyama, and E. Stoeckli for technical assistance; S. Higashiyama, J. Miyazaki, and F. Lefcort for reagents; and C. Yokoyama for critical reading of the manuscript. Funding for this research was provided by Japan Society for the Promotion of Science Foreign Postdoctoral Fellowships (A.T.G. and P.G.), AMED-CREST (J.A.), PRESTO (A.I.), the Mizutani Foundation for Glycoscience (P.G.), a Naito Foundation Subsidy for Promotion of Specific Research Projects (Y.H.), the Platform for Dynamic Approaches to Living System (K.O. and A.M.), and a Ministry of Education, Culture, Sports, Science and Technology (MEXT) Grant-in-Aid for Scientific

Research (22116001 to J.A.) and for Scientific Research on Innovative Areas (23114003 to K.O. and A.M., 24110519 to Y.H., and 21200009 to H.K.). All reagents in this study are available from H.K. or Y.H. under a materials transfer agreement with RIKEN. The authors declare the following financial interests: Y.H., H.K., K.O., A.M., and RIKEN have a patent issued (20130142813) relating to the production of anti-LysoPtdGlc, and K.O. is an executive director of Chiome Bioscience Inc. The supplemental material contains additional data.

SUPPLEMENTARY MATERIALS

www.sciencemag.org/content/349/6251/974/suppl/DC1
Materials and Methods
Additional Author Notes
Supplementary Text
Figs. S1 to S28
References (26–49)

15 April 2015; accepted 21 July 2015
10.1126/science.aab3516

DNA RECOMBINATION

Base triplet stepping by the Rad51/RecA family of recombinases

Ja Yil Lee,¹ Tsuyoshi Terakawa,^{1,2*} Zhi Qi,^{1*} Justin B. Steinfeld,¹ Sy Redding,^{3†} YoungHo Kwon,⁴ William A. Gaines,⁴ Weixing Zhao,⁴ Patrick Sung,⁴ Eric C. Greene^{1,5‡}

DNA strand exchange plays a central role in genetic recombination across all kingdoms of life, but the physical basis for these reactions remains poorly defined. Using single-molecule imaging, we found that bacterial RecA and eukaryotic Rad51 and Dmc1 all stabilize strand exchange intermediates in precise three-nucleotide steps. Each step coincides with an energetic signature (0.3 $k_B T$) that is conserved from bacteria to humans. Triplet recognition is strictly dependent on correct Watson-Crick pairing. Rad51, RecA, and Dmc1 can all step over mismatches, but only Dmc1 can stabilize mismatched triplets. This finding provides insight into why eukaryotes have evolved a meiosis-specific recombinase. We propose that canonical Watson-Crick base triplets serve as the fundamental unit of pairing interactions during DNA recombination.

Homologous recombination enables the exchange of genetic information between DNA molecules and is a driving force in evolution. During homologous recombination, a presynaptic single-stranded DNA (ssDNA) is paired with the complementary strand of a homologous double-stranded DNA (dsDNA), resulting in displacement of the noncomplementary strand (1). This strand exchange reaction plays essential roles in double-strand DNA break (DSB) repair (1, 2), the rescue of stalled or collapsed replication forks (2, 3), chromosomal rearrangements (2), horizontal gene transfer (4, 5), and meiosis (6, 7). These reactions are promoted by the Rad51/

RecA family of DNA recombinases, which are adenosine triphosphate (ATP)-dependent proteins that form helical filaments on DNA (1, 8). Crystal structures of RecA-ssDNA presynaptic complexes and RecA-dsDNA postsynaptic complexes reveal that the DNA is organized into near B-form base triplets separated by ~7.1 to 8.4 Å between adjacent triplets (Fig. 1A) (9, 10); for brevity, we refer to these nucleic acids as RS-DNA (Rad51/RecA-stretched DNA).

We previously developed single-molecule methods to study DNA recombination by total internal reflection fluorescence microscopy (TIRFM) (11). Using this approach, we showed that presynaptic complexes search for homology by sampling dsDNA for ≥8-nucleotide (nt) tracts of microhomology and rapidly reject sequences with ≤7 nt of microhomology (11). We have also reported that strand exchange by *Saccharomyces cerevisiae* Rad51 (ScRad51) occurs in 3-nt steps, presumably reflecting the base triplet organization of RS-DNA (Fig. 1, A and B) (11), and 3-nt stepping has also been proposed for bacterial RecA (12). Here, we sought to determine the underlying principles that contribute to base triplet stepping and establish how

¹Department of Biochemistry and Molecular Biophysics, Columbia University, New York, NY, USA. ²Department of Biophysics, Kyoto University, Sakyo, Kyoto, Japan.

³Department of Chemistry, Columbia University, New York, NY, USA. ⁴Department of Molecular Biophysics and Biochemistry, Yale University School of Medicine, New Haven, CT, USA. ⁵Howard Hughes Medical Institute, Columbia University, New York, NY, USA.

*These authors contributed equally to this work. †Present address: Department of Biochemistry and Biophysics, University of California, San Francisco, CA, USA. ‡Corresponding author. E-mail: ecg2108@cumc.columbia.edu

these principles influence the mechanism and fidelity of DNA recombination. To address these questions, we assembled presynaptic complexes on ssDNA curtains (Fig. 1C and fig. S1) using one of four different recombinases: *Escherichia coli* RecA (EcRecA) (1); ScRad51 or human Rad51 (hRad51), eukaryotic orthologs of RecA (2); or *S. cerevisiae* Dmc1 (ScDmc1), which is specialized for meiotic recombination (fig. S2) (6, 13).

For visualization of strand exchange intermediates, 70–base pair (bp) Atto565-dsDNA substrates were briefly incubated with the presynaptic complexes and unbound dsDNA was flushed away. Complexes were visualized by TIRFM (Fig. 1, C and D), and dissociation rates were obtained from the survival probabilities of the bound Atto565-dsDNA (fig. S3). The dsDNA substrates bore 8- to 15-nt tracts of microhomology targeted to two different regions of the presynaptic ssDNA (Fig. 2A, fig. S1B, fig. S4A, and table S1) (11). The dissociation rates for both sets of substrates scaled with microhomology length for each of the recombinases. In each instance, pronounced changes in dissociation rates coincided with recognition of the 9th, 12th, and 15th nucleotides, and similar results were observed in reactions with the nonhydrolyzable ATP analogs adenyllyl imidodi-

phosphate (AMP-PNP) and adenosine 5′-O-(3-thiotriphosphate) (ATPγS) (Fig. 2 and fig. S4). These binding patterns demonstrate that 3-nt stepping is a broadly conserved feature of the Rad51/RecA family of DNA recombinases.

Comparison of reactions with EcRecA, ScRad51, hRad51, and ScDmc1 revealed that the free energy change ($\Delta\Delta G^\ddagger$) associated with the binding of each base triplet was similar for all recombinases (Fig. 2 and fig. S4), corresponding to $0.30 \pm 0.14 k_B T$ (mean \pm SD) for completion of a single triplet step (fig. S5). This result supports the conclusion that the free energy changes associated with triplet steps during DNA recombination are broadly conserved. In addition, reactions with AMP-PNP or ATPγS revealed no appreciable shift in the free energy change associated with each triplet step (Fig. 2 and fig. S4). Thus, the physical determinants governing the energetics of strand exchange have been retained during the evolution of the Rad51/RecA gene family.

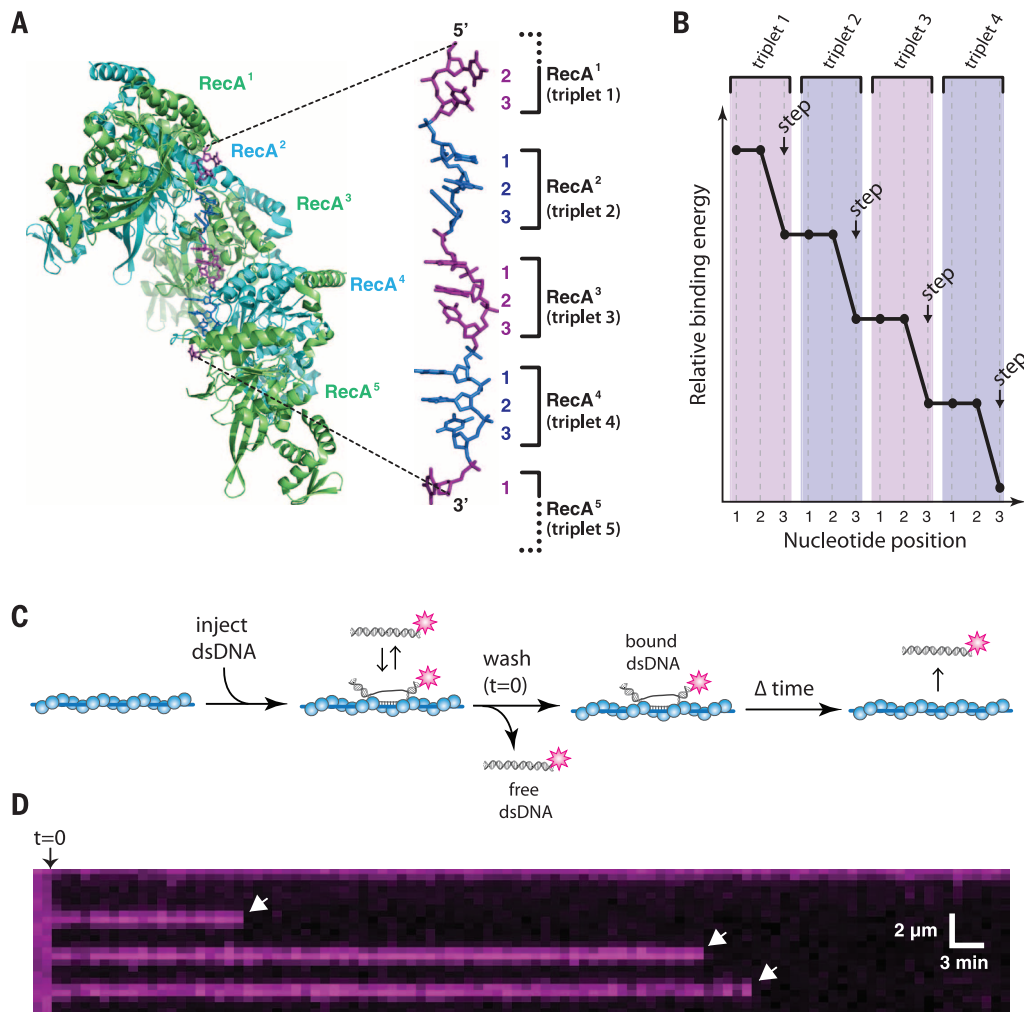
Whereas base stacking dominates the stability of B-DNA (14), stacking interactions are disrupted in RS-DNA, which suggests that the structure of RS-DNA may enhance the fidelity of recombination by relying more on correct Watson-Crick pairing. Therefore, we next asked whether

noncomplementary bases affect individual strand exchange steps (Fig. 3A). These experiments demonstrated that a single mismatch anywhere within a base triplet completely abolishes recognition of the entire triplet (Fig. 3B and fig. S6). All noncomplementary nucleotides abolished triplet recognition regardless of mismatch identity, and this high level of discrimination was conserved across the Rad51/RecA family (Fig. 3B and fig. S6). In addition, reactions with ATPγS or AMP-PNP revealed that ATP hydrolysis played no discernible role in mismatch discrimination at the level of a single triplet step (Fig. 3B and fig. S6, C and F).

We next sought to determine whether strand exchange could progress beyond a mismatch (Fig. 3C and fig. S7A). Extending the length of homology by just a single triplet allowed each recombinase to step past the mismatches, as evidenced by the corresponding reduction in binding free energy (Fig. 3D and fig. S7B). When EcRecA, ScRad51, or hRad51 stepped over a mismatched triplet, the mismatched triplets did not contribute to the binding free energy of the resulting intermediates. This conclusion is based on the observation that the corresponding reduction in binding free energy was comparable to

Fig. 1. Structure of the presynaptic complex and experimental overview.

(A) Structure of the RecA-ssDNA filament highlighting the base triplet organization of the presynaptic RS-ssDNA (9). (B) Cartoon illustration of base triplet stepping for *S. cerevisiae* Rad51. Quantized reductions in binding energy are proposed to coincide with the third base of each triplet. (C) Experimental outline for measuring the survival probability of fluorescently tagged dsDNA oligonucleotides bound to the presynaptic complex. (D) Example of a kymograph showing the binding of single Atto565-dsDNA molecules to a ScRad51 presynaptic complex. White arrowheads highlight individual dsDNA dissociation events.



products reflecting a second rather than a third strand exchange step (Fig. 3D and fig. S7B). This result supports a model in which these internal mismatch-bearing triplets remain destabilized (Fig. 3E). In contrast, when ScDmc1 stepped over a mismatched triplet, the stability of the resulting intermediates was comparable to expectations for completion of both the second and the third strand exchange steps (Fig. 3D and fig. S7B). The simplest interpretation of this result is that in reactions with ScDmc1, the internal mismatched triplet was either partially or fully paired with presynaptic ssDNA (Fig. 3E). To determine whether the ability to stabilize mismatched triplets is a conserved feature of the Dmc1 lineage, we next performed experiments using human Dmc1 (hDmc1). Like the other recombinases, hDmc1 strand exchange intermediates were stabilized in 3-nt steps, triplet recognition coincided with a change in free energy of $\sim 0.3 k_B T$, and mismatches abolished triplet recognition (fig. S8, A to D). Like ScDmc1, hDmc1 is able to step over mismatches, and also stabilizes the mismatched triplets (fig. S8, E and F). Although Rad51, RecA, and Dmc1 can all step over mismatches, the ability to stabilize mismatched triplets embedded within longer tracts of homology is only conserved within the Dmc1 lineage.

It is not known why eukaryotes have evolved two recombinases. Rad51 is expressed ubiquitously, but Dmc1 is present only during meiosis (6, 13). A fundamental difference between mitotic and meiotic recombination is the choice of template used to direct DSB repair (6, 7, 15). Mitotic recombination is biased toward use of the identical sister chromatid to ensure accurate repair. Meiotic recombination favors use of the homolog, yielding crossovers and increasing genome diversity through reshuffling of parental alleles and meiotic gene conversion (6, 7, 15). The mechanisms that direct template choice remain poorly defined (6, 7, 15). Our findings reveal that Dmc1 can stabilize mismatches, which may play a role in guiding template choice. For example, the inability of Rad51 to stabilize mismatches could help bias mitotic recombination toward use of the sister chromatid by disfavoring interhomolog recombination. This bias may be enforced through mismatch repair (MMR) anti-recombination activity (16, 17), which could selectively disrupt mismatched intermediates arising from any attempts by Rad51 to promote interhomolog recombination. Conversely, the ability of Dmc1 to stabilize mismatches may allow recombination between polymorphic maternal and paternal alleles during meiosis by masking mismatched intermedi-

ates from premature dissolution by the MMR machinery. Dissociation of Dmc1 upon completion of strand invasion would then allow efficient gene conversion through MMR-mediated repair of the mismatched heteroduplex.

We next sought a quantitative explanation for why strand exchange takes place in 3-nt steps. Given our findings, it is conceivable that base-pairing transitions within the interior of the presynaptic complexes are governed primarily by the thermodynamic characteristics of RS-DNA. Concordant with this view is the finding that the complementary strand within the RecA-dsDNA postsynaptic complex is held in place mainly by Watson-Crick hydrogen bonds (9). However, the thermodynamic properties of RS-DNA cannot be experimentally accessed outside the context of Rad51/RecA nucleoprotein filaments. As an alternative, we used Monte Carlo and molecular dynamics simulations to explore how extension of every third phosphodiester bond may alter the melting and annealing transitions of RS-DNA. These simulations used a coarse-grained model that recapitulates structural, thermodynamic, and mechanical characteristics of DNA (18). Although more complex in silico models can be envisaged, such models would require further assumptions that could only serve to confuse the general

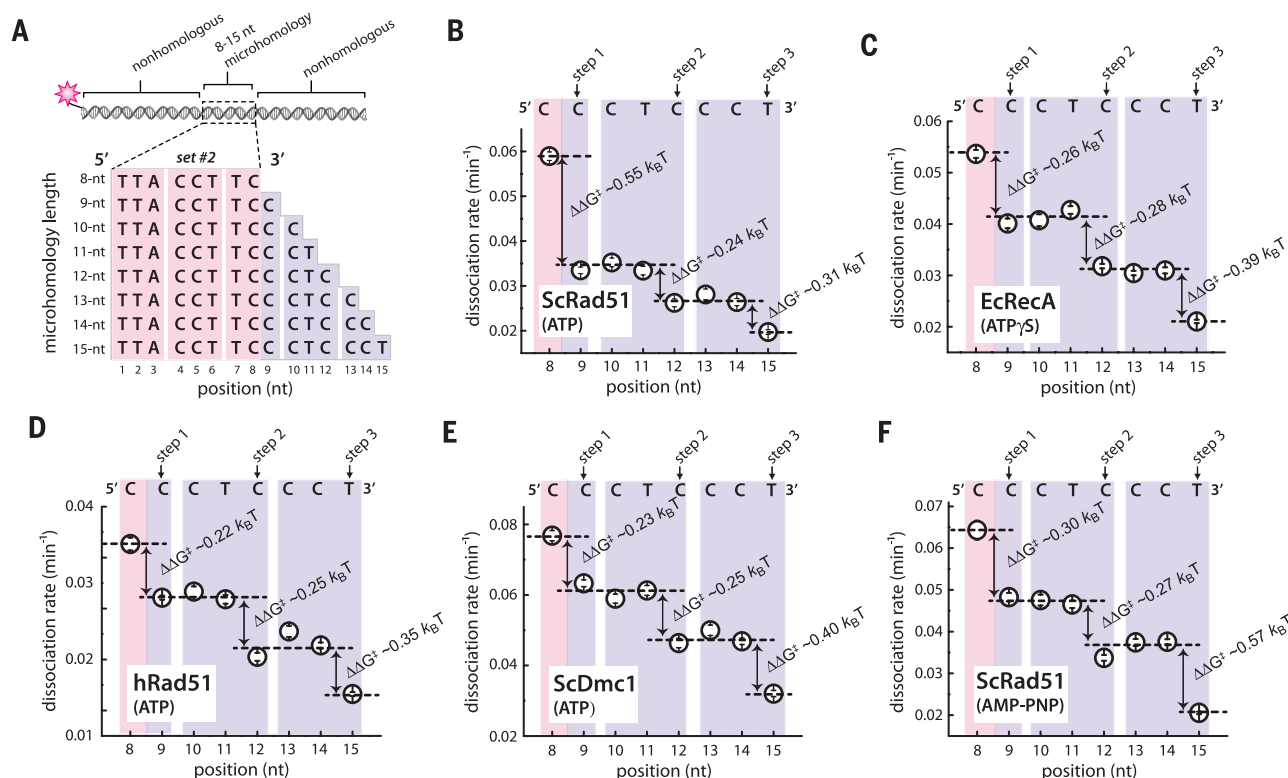
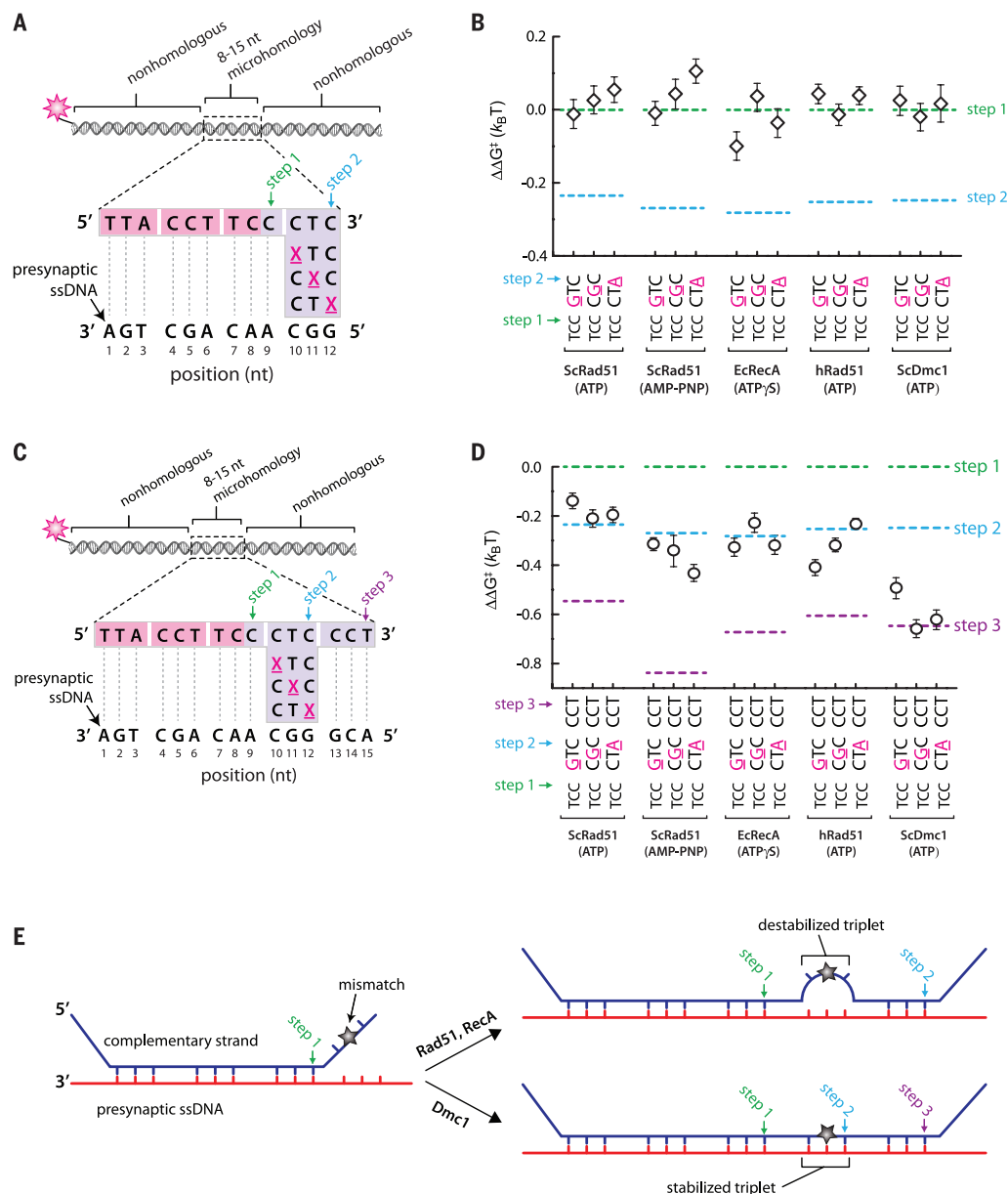


Fig. 2. Conservation of base triplet stepping among Rad51/RecA family members. (A) Schematic of the 70-bp dsDNA substrates (set #2; see table S1). All substrates contain an internal 8- to 15-nt tract of microhomology (as indicated) flanked by nonhomologous sequence. (B) Atto565-dsDNA dissociation rates (mean \pm SD) for ScRad51 plus ATP. (C) EcRecA plus ATP γ S. (D) hRad51 plus ATP. (E) ScDmc1 plus ATP. (F) ScRad51 plus AMP-PNP. In (B) to (F), each data point was calculated from an average of ~ 150

molecules ($N = 70$ to 250); the color-coded shading highlights each base triplet; magenta shading indicates the minimum 8 nt necessary for binding; purple shading corresponds to additional homologous nucleotides; arrows indicate stepwise reductions in dissociation rates coincident with recognition of the third base of each triplet; dashed lines report the mean rate for each step; and the free energy changes ($\Delta\Delta G^\ddagger$) associated with each triplet step are indicated.

Fig. 3. Effects of mismatches on base triplet recognition. (A) Schematic highlighting the design of dsDNA substrates (set #2; see table S3) bearing mismatched bases within the fourth nucleotide triplet, corresponding to the second strand exchange step; each mismatch position is highlighted as an underlined magenta X. (B) Mismatch substrate binding for ScRad51, EcRecA, hRad51, and ScDmc1, as indicated. All indicated $\Delta\Delta G^\ddagger$ values are relative to the step 1 binding data for the substrate bearing 9 nt of microhomology (see Fig. 2); each data point was calculated from an average of ~150 molecules. The green and blue dashed lines correspond to data obtained for non-mismatched substrates with each of the four different recombinases (see Fig. 2, B to F). (C) Substrate design (set #2; see table S4) for testing whether Rad51/RecA is capable of stepping over a mismatched triplet. (D) Triplet binding data illustrating how base mismatches within the fourth triplet affect recognition of the fifth triplet. (E) Schematic highlighting the different models predicted for mismatched substrates in reactions with RecA and Rad51 versus Dmc1.



argument that the physical architecture of RS-DNA itself may be sufficient to define some mechanistic attributes of strand exchange.

Monte Carlo simulations reveal that RS-DNA annealing is highly unfavorable because of the energetic penalty associated with extension of the complementary ssDNA strand (fig. S9A). However, annealing becomes favorable when the incoming homologous ssDNA strand is constrained into base triplets to mimic the effect of the recombinases (fig. S9A). This result agrees with the expectation that Rad51/RecA must locally stretch the incoming homologous DNA to more closely conform to the extended configuration of the presynaptic RS-ssDNA (9, 10, 19). Moreover, the free energy profiles for RS-DNA reveal pronounced energetic barriers with 3-nt periodicity (fig. S9A). Molecular dynamics simulations confirm that B-DNA annealing and melting transitions occur

in 1-bp increments; consistent with a 1-bp zipper mechanism (18), the lifetimes of pairing intermediates are largely independent of nucleotide position (Fig. 4, A to C, and fig. S9, B and D). In contrast, the annealing and melting transitions for RS-DNA occur in 3-nt steps (Fig. 4, D to F, and fig. S9, C and D), and partially paired RS-DNA triplets are highly transient relative to fully paired triplets (Fig. 4E and fig. S9D). These simulations reveal that partially paired RS-DNA triplets are not stable, which recapitulates a key feature of our experimental data—base triplet stepping—even though the model intentionally omits any detailed contributions of the proteins or amino acid side chains other than to stretch the DNA strands into an RS-DNA configuration. Together, the simulations and experimental work suggest that canonical Watson-Crick base triplets act as the fundamental pairing unit within RS-DNA.

RecA, Rad51, and Dmc1 differ in many structural, functional, and mechanistic details; they each interact with different accessory factors; and they are adapted for diverse biological functions (1, 2, 6). Our work reveals that despite these differences, unifying mechanistic principles underlie the process of strand exchange: Rad51/RecA family members all stabilize strand exchange intermediates in 3-nt steps; each step coincides with a broadly conserved energetic signature; and a single mismatch can abolish recognition of an entire base triplet. We also show that RecA, Rad51, and Dmc1 can all step over mismatches, but only Dmc1 can stabilize mismatched triplets; this distinction likely reflects the role of Dmc1 in promoting strand exchange between polymorphic alleles during meiosis. Our findings support a model in which a primary role of the Rad51/RecA family members during strand exchange is to establish the

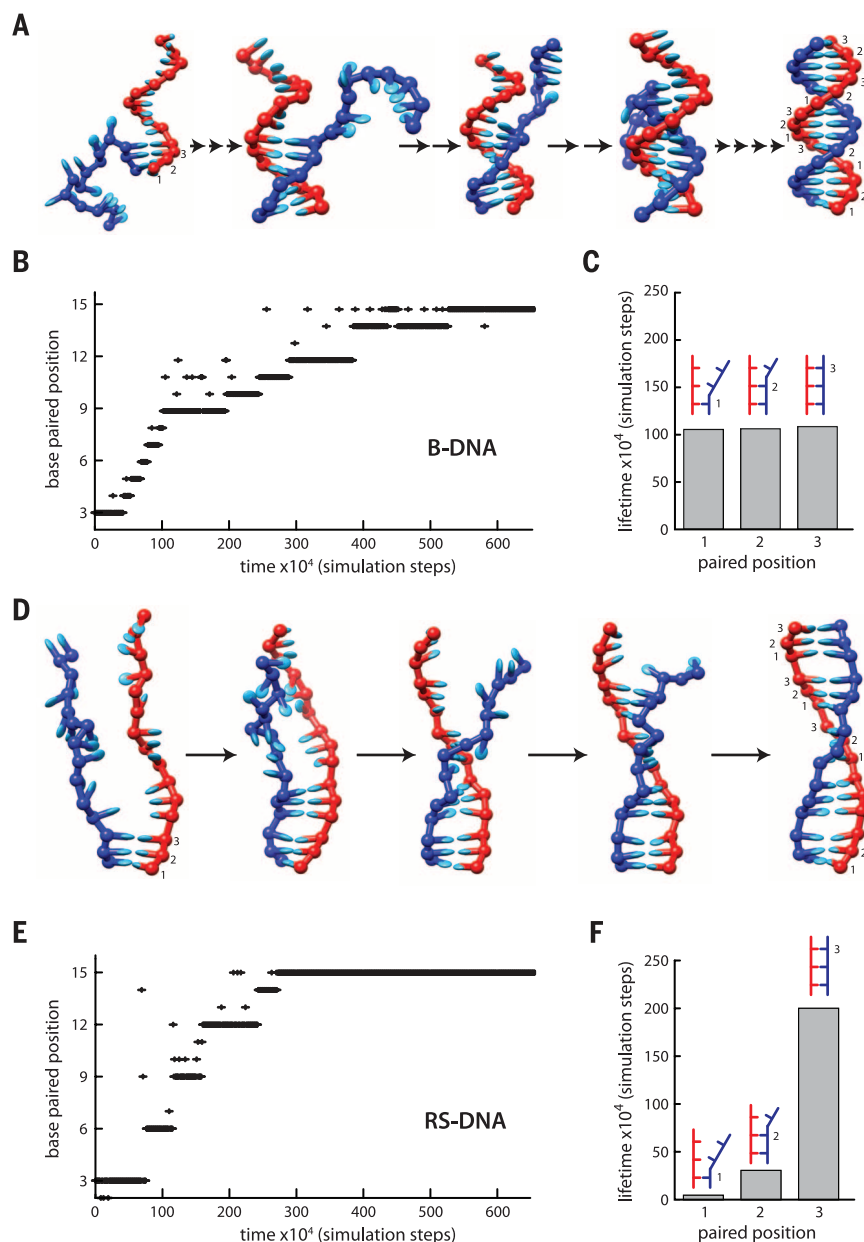


Fig. 4. RS-DNA governs triplet stepping during strand exchange. (A) Molecular dynamics snapshots of B-DNA annealing intermediates. Paired bases are numbered 1 to 3 for comparison to RS-DNA triplets. (B) Sample annealing trajectory for B-DNA. (C) Lifetimes of B-DNA intermediates calculated from 50 separate simulation runs (5×10^8 simulation steps total). (D) Molecular dynamics snapshots of RS-DNA. (E) Sample annealing trajectory for RS-DNA. (F) Lifetimes of RS-DNA intermediates calculated from 50 separate simulation runs (5×10^8 simulation steps total). In (A) and (D), the number of arrows between each image corresponds to the number of steps necessary to reach the depicted state. The y axes in (B) and (E) denote the position of the most distal paired base relative to the pre-annealed end of the DNA. The data in (C) and (F) do not include the terminal triplets.

structure of RS-DNA, whereas the mechanism, energetics, and fidelity of the base-pairing transitions that take place during recombination are all governed by the physical architecture of RS-DNA itself. We propose that RS-DNA was selected at least ~ 2 billion years ago by an ancestral recombinase as the most energetically favorable solution for allowing efficient exchange of genetic information between related DNA molecules.

REFERENCES AND NOTES

- P. R. Bianco, R. B. Tracy, S. C. Kowalczykowski, *Front. Biosci.* **3**, D570–D603 (1998).
- L. S. Symington, R. Rothstein, M. Lisby, *Genetics* **198**, 795–835 (2014).
- M. M. Cox *et al.*, *Nature* **404**, 37–41 (2000).
- C. Fraser, W. P. Hanage, B. G. Spratt, *Science* **315**, 476–480 (2007).
- P. J. Keeling, J. D. Palmer, *Nat. Rev. Genet.* **9**, 605–618 (2008).
- M. S. Brown, D. K. Bishop, *Cold Spring Harb. Perspect. Biol.* **10**, 1101/cshperspect.a016659 (2014).
- M. J. Neale, S. Keeney, *Nature* **442**, 153–158 (2006).
- S. D. Sheridan *et al.*, *Nucleic Acids Res.* **36**, 4057–4066 (2008).
- Z. Chen, H. Yang, N. P. Pavletich, *Nature* **453**, 489–4 (2008).
- S. C. Kowalczykowski, *Nature* **453**, 463–466 (2008).
- Z. Qi *et al.*, *Cell* **160**, 856–869 (2015).
- K. Ragnathan, C. Joo, T. Ha, *Structure* **19**, 1064–1073 (2011).
- D. K. Bishop, D. Park, L. Xu, N. Kleckner, *Cell* **69**, 439–456 (1992).
- P. Yakovchuk, E. Protopanova, M. D. Frank-Kamenetskii, *Nucleic Acids Res.* **34**, 564–574 (2006).
- E. M. Selva, L. New, G. F. Crouse, R. S. Lahue, *Genetics* **139**, 1175–1188 (1995).
- E. Evans, N. Sugawara, J. E. Haber, E. Alani, *Mol. Cell* **5**, 789–799 (2000).
- W. Chen, S. Jinks-Robertson, *Genetics* **151**, 1299–1313 (1999).
- J. P. Doye *et al.*, *Phys. Chem. Chem. Phys.* **15**, 20395–20414 (2013).
- C. Danilowicz *et al.*, *Nucleic Acids Res.* **42**, 526–533 (2014).

ACKNOWLEDGMENTS

We thank R. Rothstein, L. Symington, H. Klein, M. Lichten, M. Gottesman, J. Dworkin, D. Duzdevich, and other members of the Greene and Sung laboratories for comments on the manuscript. Supported by NIH grants GM074739 (E.C.G.), RO1ES015252 (P.S.), and CA146940 (E.C.G. and P.S.); NSF grant MCB-1154511 (E.C.G.); and a Japan Society for the Promotion of Science fellowship (T.T.). E.C.G. is an HHMI Early Career Scientist. The data described in this manuscript are archived in the laboratory of E.C.G. in the Department of Biochemistry and Molecular Biophysics, Columbia University.

SUPPLEMENTARY MATERIALS

www.sciencemag.org/content/349/6251/977/suppl/DC1
Materials and Methods
Figs. S1 to S9
Tables S1 to S4
References (20–33)

1 April 2015; accepted 31 July 2015
10.1126/science.aab2666

This copy is for your personal, non-commercial use only.

If you wish to distribute this article to others, you can order high-quality copies for your colleagues, clients, or customers by [clicking here](#).

Permission to republish or repurpose articles or portions of articles can be obtained by following the guidelines [here](#).

The following resources related to this article are available online at www.sciencemag.org (this information is current as of September 2, 2015):

Updated information and services, including high-resolution figures, can be found in the online version of this article at:

<http://www.sciencemag.org/content/349/6251/977.full.html>

Supporting Online Material can be found at:

<http://www.sciencemag.org/content/suppl/2015/08/26/349.6251.977.DC1.html>

This article **cites 33 articles**, 11 of which can be accessed free:

<http://www.sciencemag.org/content/349/6251/977.full.html#ref-list-1>

This article appears in the following **subject collections**:

Genetics

<http://www.sciencemag.org/cgi/collection/genetics>

Molecular Biology

http://www.sciencemag.org/cgi/collection/molec_biol

HEART DISEASE

Titin mutations in iPS cells define sarcomere insufficiency as a cause of dilated cardiomyopathy

John T. Hinson,^{1*†} Anant Chopra,^{2,3†} Navid Nafissi,⁴ William J. Polacheck,^{2,3} Craig C. Benson,⁵ Sandra Swist,⁶ Joshua Gorham,⁴ Luhan Yang,^{3,4} Sebastian Schafer,⁷ Calvin C. Sheng,⁴ Alireza Haghighi,^{1,4,8} Jason Homsy,⁴ Norbert Hubner,^{7,9} George Church,^{3,4} Stuart A. Cook,^{10,11} Wolfgang A. Linke,⁶ Christopher S. Chen,^{2,3†} J. G. Seidman,^{4,†} Christine E. Seidman^{1,4,8*†}

Human mutations that truncate the massive sarcomere protein titin [TTN-truncating variants (TTNtvs)] are the most common genetic cause for dilated cardiomyopathy (DCM), a major cause of heart failure and premature death. Here we show that cardiac microtissues engineered from human induced pluripotent stem (iPS) cells are a powerful system for evaluating the pathogenicity of titin gene variants. We found that certain missense mutations, like TTNtvs, diminish contractile performance and are pathogenic. By combining functional analyses with RNA sequencing, we explain why truncations in the A-band domain of TTN cause DCM, whereas truncations in the I band are better tolerated. Finally, we demonstrate that mutant titin protein in iPS cell-derived cardiomyocytes results in sarcomere insufficiency, impaired responses to mechanical and β -adrenergic stress, and attenuated growth factor and cell signaling activation. Our findings indicate that titin mutations cause DCM by disrupting critical linkages between sarcomerogenesis and adaptive remodeling.

Dilated cardiomyopathy (DCM) is characterized by progressive left ventricular dilation; systolic dysfunction; and, ultimately, heart failure. Occurring in 1 of 250 adults (1), DCM arises from underlying cardiovascular conditions or as a primary genetic disorder. We recently identified dominant mutations that truncate the sarcomere protein titin [TTN-truncating variants (TTNtvs)] as the most common genetic cause of DCM, occurring in ~20% of familial or sporadic cases (2).

TTN is a massive protein that spans half of the sarcomere (1 μ m) and includes >34,000 amino acids within four functionally distinct segments (Fig. 1A): (i) an N-terminus that is anchored at

the Z disk; (ii) a distensible I band (~1 MD) composed of repeating immunoglobulin-like domains and disordered regions; (iii) an inextensible, thick filament-binding A band (~2 MD); and (iv) a carboxyl M band with a kinase domain. TTNtvs have been identified in each protein segment, but TTNtvs in DCM patients are markedly enriched in the A band (2, 3). In addition, numerous rare missense variants in TTN have been identified, most with unknown medical importance (2, 3). Both TTN's size and a general incomplete knowledge of the protein's function in cardiomyocyte biology have hindered traditional approaches for elucidating why some TTN mutations produce clinical phenotypes. To address this, we harnessed recent advances in stem cell reprogramming (4), gene editing (5), and tissue engineering (6) to produce human cardiac microtissue (CMT) models of TTNtvs.

We generated human induced pluripotent stem cell-derived cardiomyocytes (iPS-CMs) from patients (labeled with "p" preceding genotype) (see supplementary materials and methods). Cryopreserved blood samples from one unaffected and three DCM patients with dominant TTN mutations (Fig. 1A and table S1A) were reprogrammed, and high-quality iPS cell clones (fig. S1, A to C) were expanded, differentiated (7), and enriched by metabolic selection (8) to achieve cultures with >90% iPS-CMs (fig. S2, A to C). We produced iPS-CMs with two A-band TTNtvs (pA22352fs^{+/-} or pP22582fs^{+/-}) and a missense mutation (pW976R^{+/-}) within the Z/I junction that cosegregated with DCM in a large family (9). Single-cell assays of contractile function on microarray post detectors (mPADS) (10) showed no

significant difference between wild-type (WT) and TTNtv iPS-CMs (fig. S2D). Because three-dimensional (3D) CMTs (Fig. 1B) better recapitulate native cardiomyocyte architecture and mechanics, improving sarcomere alignment, expression of contractile proteins, and iPS-CMs maturity (6, 11, 12), we assessed the contractile function of iPS-CMTs containing WT or mutant iPS-CMs. We observed minor variation in contractile function between biological replicates of CMTs or between CMTs made from independent clones from the same patient (fig. S2, E and F). However, CMTs expressing either A-band TTNtv or W976R^{+/-} variants exhibited less than half the contractile force (Fig. 1, C and D, and movies S1 to S6) or the stress (force normalized to tissue area) (fig. S2I) generated by pWTs, and function did not improve over time (fig. S2G). As static force was similar in pWT and pP22582fs^{+/-} CMTs (fig. S2H), we conclude that the contractile deficits observed in mutant CMTs are not due to non-myocyte factors. In addition, the comparable force deficits observed in CMTs with both A-band TTNtvs and the Z/I junction missense mutation demonstrate that W976R^{+/-} is a pathogenic TTN missense mutation.

To ensure that the observed functional abnormalities did not reflect background genetic differences in patient-derived iPS-CMs, we also introduced TTNtvs into an independent, isogenic iPS cell using scarless, CRISPR (clustered regularly interspaced short palindromic repeats)/CAS9 technology (5) to target the I- or A-band exons (Fig. 1A and table S1B). Mutant isogenic iPS cell lines (labeled with "c" preceding genotype) were differentiated into iPS-CMs and incorporated into CMTs. cN22577fs^{+/-} creates an A-band TTNtv in exon 322 (similar to patient-derived pP22582fs^{+/-}) (Fig. 1A). cN22577fs^{+/-} CMTs had significantly reduced contractile force (2.19 μ N) compared with isogenic cWT-CMTs (Fig. 1E) ($P < 0.003$), but not to the extent observed in pA22352fs^{+/-} or pP22582fs^{+/-} CMTs (0.767 and 1.001 μ N, respectively; $P < 0.02$). Tissue stress was similarly reduced in TTNtv CMTs compared to WT CMTs (fig. S2J). These data confirm that A-band TTNtvs markedly reduced contractile function in both patient-derived and isogenic CMTs and raise the possibility that the genetic background can modify the functional severity of TTNtvs.

Premature protein truncation at any location within a molecule is generally assumed to result in loss of function and comparable deleterious consequences. However, I-band TTNtvs have been identified in healthy individuals and in the general population without DCM (2, 3). Two models have been proposed to explain this dichotomy: (i) Alternative splicing excludes I-band exons from most mature TTN transcripts and thereby reduces the functional consequences of I-band TTNtvs, whereas the inclusion of A-band exons with TTNtvs is deleterious. (ii) A-band TTNtv transcripts produce longer, stable mutant proteins with dominant negative effects on sarcomere biology. To distinguish these models, we compared the functional consequences of isogenic

¹Division of Cardiovascular Medicine, Brigham and Women's Hospital, Boston, MA 02115, USA. ²Department of Biomedical Engineering, Boston University, Boston, MA 02215, USA.

³The Wyss Institute for Biologically Inspired Engineering at Harvard University, Boston, MA 02115, USA. ⁴Department of Genetics, Harvard Medical School, Boston, MA 02115, USA.

⁵Division of Cardiovascular Medicine, Beth Israel Deaconess Medical Center, Boston, MA 02215, USA. ⁶Department of Cardiovascular Physiology, Ruhr University Bochum, MA 3/56 D-44780, Bochum, Germany. ⁷Cardiovascular and Metabolic Sciences, Max Delbrück Center for Molecular Medicine, Berlin, Germany. ⁸Howard Hughes Medical Institute, Chevy Chase, MD 20815, USA. ⁹DZHK (German Center for Cardiovascular Research), Partner Site Berlin, Berlin, Germany. ¹⁰National Institute for Health Research (NIHR) Biomedical Research Unit in Cardiovascular Disease at Royal Brompton and Harefield National Health Service (NHS) Foundation Trust, Imperial College London, London, UK. ¹¹National Heart Centre and Duke-National University, Singapore, Singapore.

*Corresponding author. E-mail: jthinson@partners.org (J.T.H.); cseidman@genetics.med.harvard.edu (C.E.S.) †These authors contributed equally to this work. ‡These authors contributed equally to this work.

heterozygous (*cV6382fs*^{+/-}) and homozygous (*cV6382fs*^{-/-}) I-band TTNts in exon 66 to A-band TTNts (*cN22577fs*^{+/-}, *cN22577fs*^{-/-}, *cT33520fs*^{+/-}). We used RNA sequencing (RNA-seq) analyses to assess TTN RNA splicing in iPS-CMs and to compare our findings with normal adult left ventricle (LV) tissue. TTN transcripts from iPS-CMs incorporated more I-band exons than did adult LV tissue (fig. S3, A and B). More than 80% of iPS-CM TTN transcripts included exon 66, five times more than adult LV (in which 18% of TTN transcripts contained exon 66).

cV6382fs^{+/-} CMTs had markedly impaired force generation, similar to the deficits observed in isogenic CMTs with A-band *cN22577fs*^{+/-} or patient-derived CMTs with A-band *pP22582fs*^{+/-} (Fig. 1, D and E). Functional comparisons of CMTs with homozygous TTNts in the I or A band were also similar. Homozygous A-band CMTs (*cN22577fs*^{-/-} and *cT33520fs*^{-/-}) produced no force, whereas homozygous I-band CMTs (*cV6382fs*^{-/-}) generated small but demonstrable force (0.472 μ N), presumably due to 18% of TTN transcripts that excluded exon 66 and the TTNtv (fig. S3A). On the basis of these functional and RNA-seq data, we suggest that alternative exon splicing is the predomi-

nant mechanism for reduced penetrance of I-band TTNts.

As TTN is responsible for sensing and responding to myocardial stresses (13), we posited that TTNtv mutants would exhibit aberrant stress responses. To model low and high mechanical load, we assessed contractile performance of pWT and *pP22582fs*^{+/-} CMTs grown on flexible (0.2 μ N/ μ m) and rigid (0.45 μ N/ μ m) cantilevers (Fig. 1F). *pP22582fs*^{+/-} CMTs produced less force than pWT CMTs at low load. At higher load, pWT CMTs produced a twofold increase in force, greater than four times that produced by *pP22582fs*^{+/-} CMTs. In response to isoproterenol treatment to mimic β -adrenergic stimulation, force and beating rate were increased in pWT CMTs, but *pP22582fs*^{+/-} CMTs had markedly blunted responses (Fig. 1, G and H). Together, these data demonstrate that TTNts had both basal and stress-induced inotropic and chronotropic deficits that are expected to impair cardiac adaptation to increased mechanical load and β -adrenergic signaling.

We considered whether A-band TTNts affected the organization of the sarcomere, where TTN is localized, which could cause or contribute to functional defects. Using antibodies to TTN

(9D10 recognizes the N-terminus of TTNts) (Fig. 2A) and α -actinin (Fig. 2, B and C), we identified well-formed parallel arrays of repeating sarcomeres in myofibrils from WT iPS-CMs. *pP22582fs*^{+/-} iPS-CMs had fewer myofibrils and abnormal, irregular sarcomeres, a phenotype that was even more pronounced in homozygous *cT33520fs*^{-/-} iPS-CMs (Fig. 2, A and D, and fig. S4A). Sarcomere disorganization was observed regardless of whether the iPS-CMs were aligned on micro-patterned lines (Fig. 2B) or 3D CMTs (Fig. 2C). In addition, sarcomere length was shorter in *pP22582fs*^{+/-} CMTs compared with pWT CMTs (Fig. 2E), indicating both a quantitative and qualitative defect in sarcomerogenesis. Analogous to these results, LV tissue from the patient with the *P22582fs*^{+/-} mutation showed disorganized myofibrils compared with control tissue (Fig. 2, G and H, and fig. S4B).

To determine whether sarcomere deficits reflected insufficient TTN levels, we performed RNA-seq (14) and protein analyses. CWT and *cN22577fs*^{+/-} iPS-CMs showed comparable levels of TTN transcripts [fragments per kilobase of transcript per million mapped reads (FPKM)] and similar patterns of TTN splicing (fig. S3, B

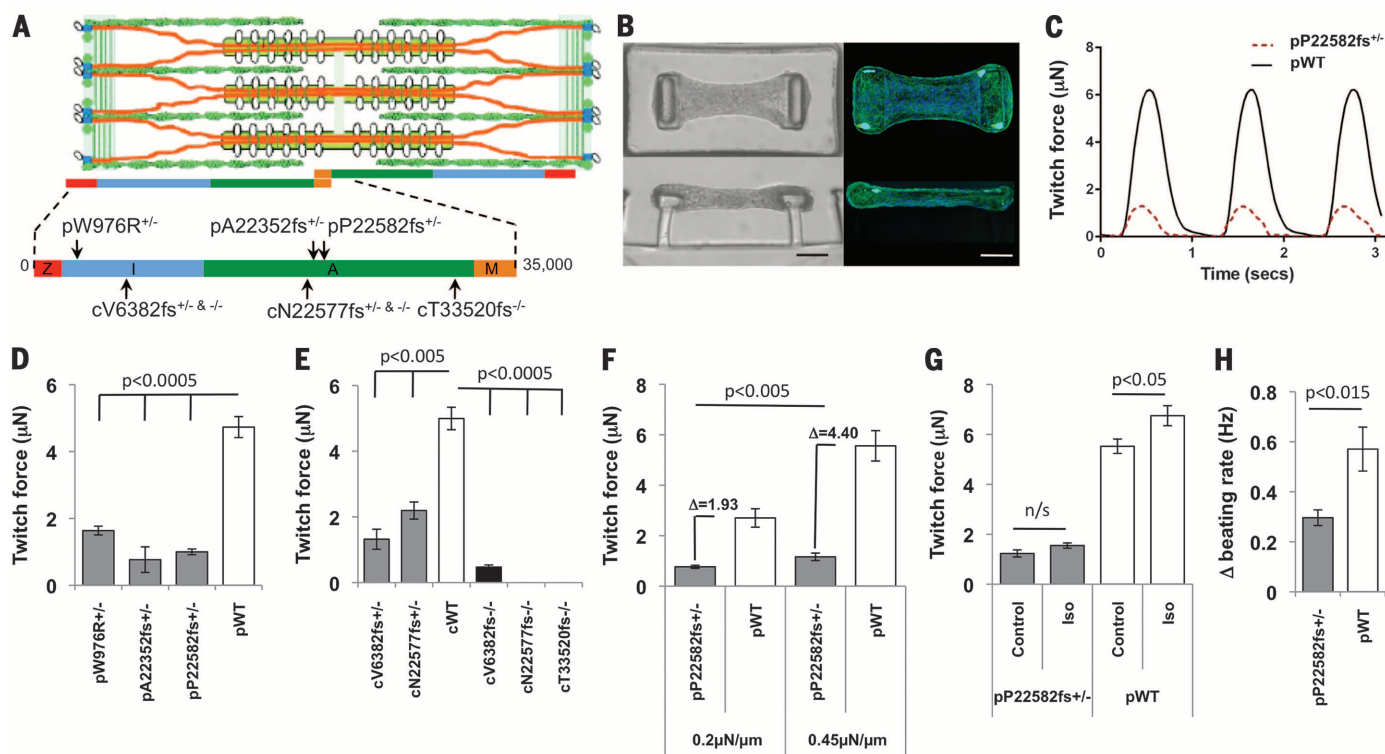


Fig. 1. Engineered iPS-CM microtissues with TTN mutations have impaired intrinsic contractility and responses to stress. (A) Schematic of the cardiac sarcomere with TTN (orange), thick filaments (gold rods with white globular heads), and thin filaments (green, coiled ovals). TTN protein segments (Z disc, red; I band, blue; A band, green; M band, gold) are shown with locations of human (p, patient-derived; c, CRISPR/CAS9-derived) mutations marked. (B) Images [bright field (left) and fluorescent (right); green, phalloidin Alexa Fluor 488; blue, 4',6-diamidino-2-phenylindole (DAPI)] of iPS-CMT suspended between two polydimethylsiloxane pillars from top-down (upper) and side (lower) views. Scale bar, 50 μ m. (C) Representative force tracing of pWT (black) and *pP22582fs*^{+/-}

(red) CMT over three twitch cycles. (D) Mean force of *pW976R*^{+/-}, *pA22352fs*^{+/-}, and *pP22582fs*^{+/-} iPS-CMTs compared with pWT iPS-CMTs ($N = 5$). (E) Mean force produced by isogenic iPS-CMTs with heterozygous or homozygous I-band (*cV6382fs*) or A-band (*cN22577fs*) TTNts ($N > 4$ CMTs). (F) Mean force produced by pWT and *pP22582fs*^{+/-} CMTs in response to increased pillar stiffness (0.2 to 0.45 μ N/ μ m; $N > 11$ CMTs). Difference (Δ) in force generation between *pP22582fs*^{+/-} and pWT measured at low and high stiffness. (G) Isoproterenol-induced force ($N > 5$) and (H) spontaneous beating rate ($N > 5$, in hertz) in *pP22582fs*^{+/-} versus pWT CMTs ($N > 5$). Significance was assessed by Student's t test [(D) to (H)]; data are means \pm SEM (error bars) [(D) to (H)].

and C). RNA-seq (table S1D) and Sanger sequencing of reverse transcriptase polymerase chain reaction products (fig. S5) demonstrated equal amounts of mutant and WT transcripts. Consistent with RNA-seq data, protein gels of iPS-CM extracts showed expression of the larger fetal TTN isoforms, which include more I-band exons than the adult TTN isoforms (Fig. 2F). We next sought to identify truncated TTN protein (Fig. 2F and fig. S6, A to I) in protein lysates from iPS-CMs with an A-band (pP22582fs^{+/-}, pA22353fs^{+/-}) or I-band [pS6394fs^{+/-} (benign variant)] TTNtv. Both iPS-CMs and adult LV contained N2BA (~3300 to 3700 kD) and N2B TTN isoforms (~3000 kD); however, iPS-CM lysates also contained the larger fetal N2BA isoforms (~3700 kD). In addition, a smaller fragment (~2500 kD) was present in pP22582fs^{+/-} iPS-CM

extracts, but not in pWT (Fig. 2F), pA22353fs^{+/-}, or pS6394fs^{+/-} iPS-CMs (fig. S6, B and C). This smaller fragment reacted with TTN T12 antibody and, on the basis of size and immunoreactivity, is probably a stable truncated TTN protein. Given both the detection of mutant TTNtv protein and the paucity of sarcomeres in heterozygous pP22582fs^{+/-} and homozygous cT33520fs^{-/-} iPS-CMs (Fig. 2, A to C), we deduced that TTNtv protein, even if stable within CMs, is unable to promote sarcomerogenesis.

RNA-seq analyses of cWT, cN22577fs^{+/-}, and cN22577fs^{-/-} iPS-CMs also indicated that TTNtv affected CM signaling and RNA expression. The significantly altered transcripts in iPS-CMs with TTNtv (Fig. 3A and table S1C) suggested increased activity of three critical upstream microRNA (miRNA) regulators: miR-124 (15), miR-16

(16), and miR-1 (17). Consistent with this prediction, cN22577fs^{+/-} and cN22577fs^{-/-} iPS-CMs had diminished expression of miR-124 targets (15), including lower MYH7:MYH6 transcript and protein ratios (Fig. 3, B and C, and fig. S6, J and K) and reduced atrial (NPPA) and brain (NPPB) natriuretic peptide transcript levels compared with WT iPS-CMs (Fig. 3, B and C).

Pathway analysis of RNA-seq data on cN22577fs^{+/-} and cN22577fs^{-/-} compared with WT iPS-CMs (fig. S3E) also implied diminished activation of factors regulating growth [transforming growth factor- β 1 (TGF β 1), vascular endothelial growth factor (VEGF), hepatocyte growth factor (HGF), epidermal growth factor (EGF), and basic fibroblast growth factor (FGF2)], responses to hypoxia [hypoxia-inducible factor 1 (HIF1A) and EPAS1 or HIF2A], and mitogen-activated protein kinases

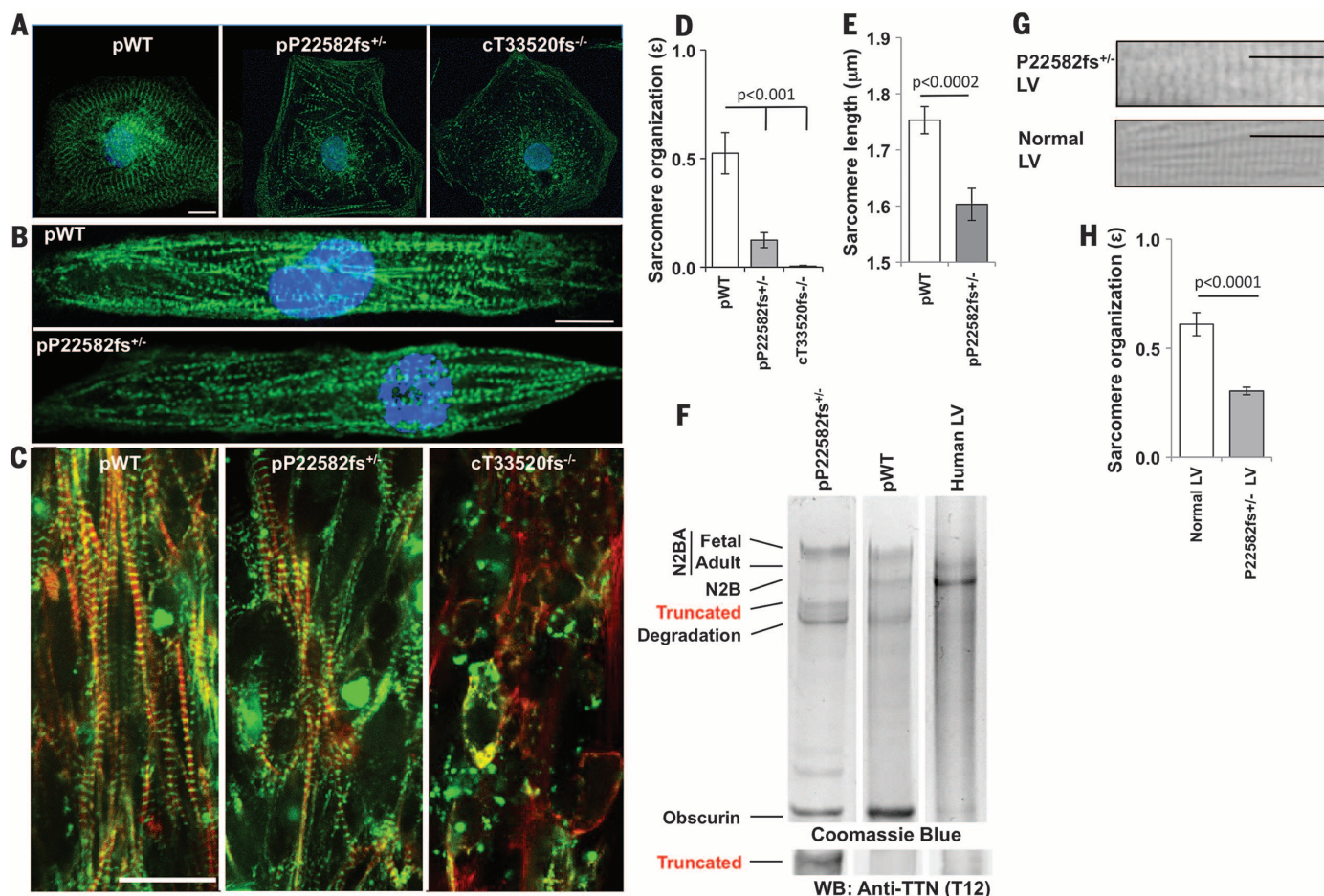


Fig. 2. Sarcomere abnormalities in TTNtv iPS-CMs. (A) pWT, pP22582fs^{+/-}, and cT33520fs^{-/-} iPS-CMs stained with TTN specific antibody (9D10, green) and nuclei (DAPI, blue). Magnification, 40 \times ; scale bar, 20 μ m. (B) pWT and pP22582fs^{+/-} iPS-CMs were patterned on 25- μ m-by-25- μ m grids and stained for Z discs (α -actinin A, green) and nuclei (DAPI, blue). Magnification, 40 \times ; scale bar, 20 μ m. (C) pWT, pP22582fs^{+/-}, and cT33520fs^{-/-} CMTs stained for α -actinin A (green) and F-actin (red). Magnification, 40 \times ; scale bar, 20 μ m. (D) Sarcomere organization (ϵ) quantified by 2D fast Fourier transform (FFT) analysis of pWT, pP22582fs^{+/-}, and cT33520fs^{-/-} iPS-CMs ($N > 5$ per genotype). (E) Sarcomere length (in micrometers) measured by intensity profiles of α -actinin in pWT and pP22582fs^{+/-} iPS-CMs ($N > 22$). (F) Protein electropherograms of

lysates from pP22582fs^{+/-} and pWT iPS-CMs and human LV stained with Coomassie Blue (for additional blots, see fig. S6). Sizes of TTN isoforms and fragments are as follows: N2BA fetal, ~3700 kD; N2BA adult, ~3300 kD; N2B, ~3000kD; TTNtv, ~2500 kD; degraded TTN, ~1800 to 2200 kD. Obscurin size is ~700 kD. Western blots (WB) were probed with N-terminal TTN antibody (T12 in fig. S6). TTNtv protein (~2500 kD) was detected in pP22582fs^{+/-} iPS-CMs. (G) Representative micrographs of hematoxylin-and-eosin-stained tissue from the LV of control and P22582fs^{+/-} patients. Scale bars, 20 μ m. (H) Sarcomere organization quantified by FFT analysis of LV tissue from control and P22582fs^{+/-} patients ($n > 15$ regions per genotype). Significance was assessed by Student's t test [(D), (E), and (H)]; data are means \pm SEM (error bars) [(D), (E), and (H)].

(MAPKs) [MAPK kinase kinase (MEK) and extracellular signal-regulated kinase (ERK)]. Quantification of transcripts, proteins, and phosphorylation levels confirmed that TTNtv iPS-CMs exhibited significant attenuation (all $P < 0.01$) in the levels or phosphorylation of TGF β , VEGF, MAPKs, and AKT (Fig. 3, D to H) but not HGF, EGF, or FGF2 (fig. S3E). To determine whether these signaling deficits contributed to force deficits, we pretreated pP22582fs $^{+/-}$ and pW976R $^{+/-}$ iPS-CMs with VEGF (50 ng/ml) or TGF- β (0.5 ng/ml) for 4 days before studying CMTs. In contrast to the failed augmentation in response to mechanical load (Fig. 1F)

or β -adrenergic stimulation (Fig. 1G), supplementation with VEGF, but not TGF- β (fig. S3F), improved force production in pP22582fs $^{+/-}$ and pW976R $^{+/-}$ CMTs (Fig. 3I).

Coupled with engineered biomimetic culture systems, the use of patient-derived or gene-editing technologies to produce iPS-CMs provides robust functional genomic insights. Our studies of iPS-CM with different TTN mutations revealed that some missense variants like TTNtv are pathogenic, whereas comparisons of contractile function in patient-derived and isogenic CMTs implied a role for genetic modifiers in clinical

manifestations of TTNtv. We found that both I- and A-band TTNtv can cause substantial contractile deficits but that alternative exon splicing (fig. S3, A and B) mitigates the pathogenicity of I-band TTNtv. Additional factors—such as iPS-CMs not fully recapitulating the cell biology of adult cardiomyocytes and CMT tissues lacking in vivo compensatory responses—may also account for different degrees of contractile deficits in iPS-CMTs and human hearts with TTNtv. Surprisingly, some TTNtv produced stable truncated protein, but this mutant peptide failed to assemble with other contractile proteins into

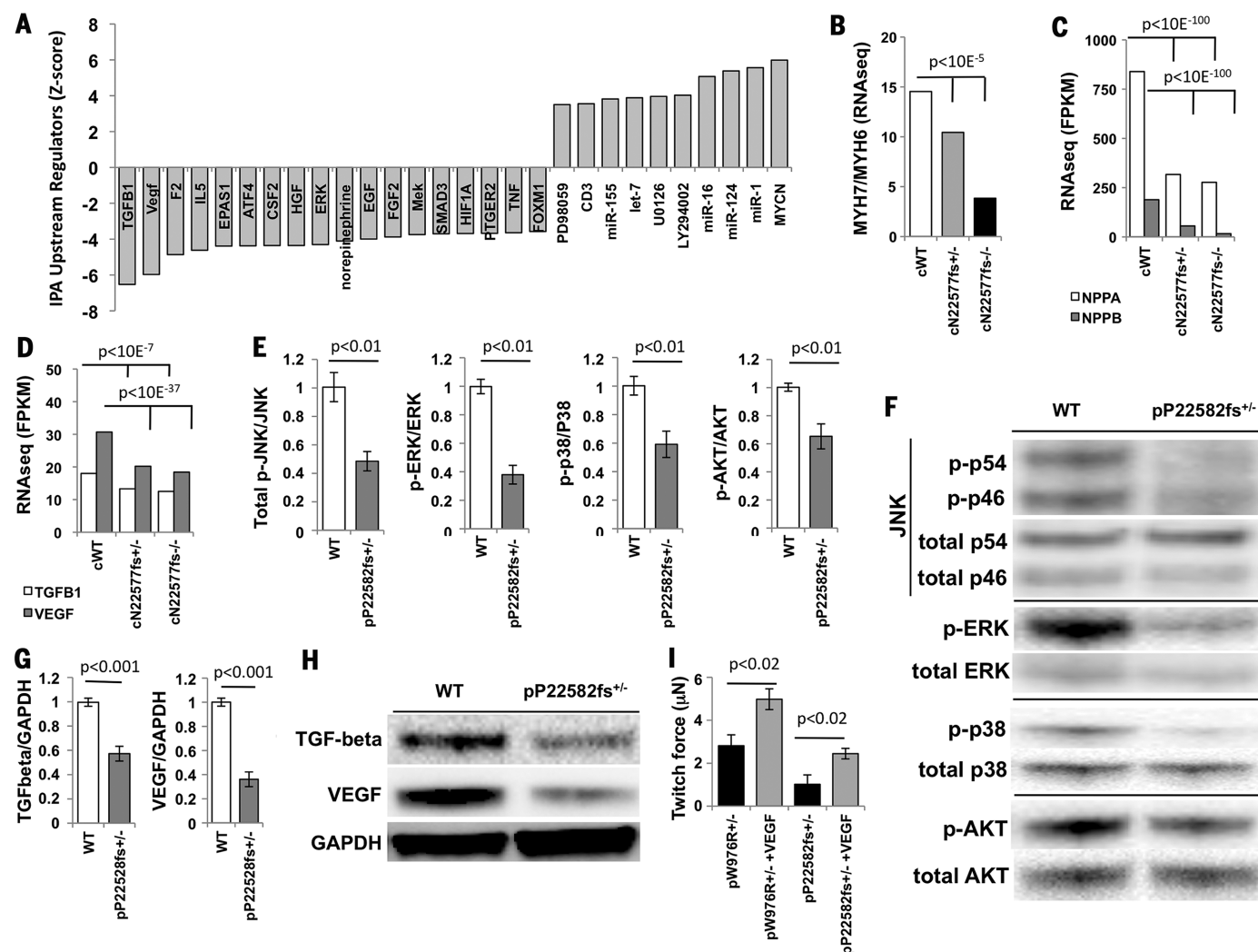


Fig. 3. TTN regulates iPS-CM signaling and RNA expression. (A) Upstream transcriptional regulators were identified by Ingenuity pathway analysis (IPA) of differentially regulated genes (normalized ratio >1.2 and <0.8 and $P < 0.01$) (table S1C) using RNA-seq from cWT, cN22577fs $^{+/-}$, and cN22577fs $^{-/-}$ iPS-CMs. Data are plotted as z score of enrichment (z score cutoff: ≥ 3.5 and ≤ -3.5). (B to D) Comparison of cWT, cN22577fs $^{+/-}$, and cN22577fs $^{-/-}$ iPS-CMs normalized expression (FPKM) of (B) β (MYH7) and α (MYH6) myosin heavy-chain ratios; (C) atrial (NPPA) and brain natriuretic (NPPB) peptides; and (D) TGF- β 1 and VEGF-A in cWT, cN22577fs $^{+/-}$, and cN22577fs $^{-/-}$ iPS-CMs. (E) Densitometry of Western blots ($N \geq 4$ lanes) of pWT and pP22582fs $^{+/-}$ lysates, normalized for protein loading and probed with antibodies to phosphorylated c-Jun N-

terminal kinase (JNK) (p46, p54), ERK, p38, and AKT. (F) Representative Western blots of pWT and pP22582fs $^{+/-}$ iPS-CMs lysates probed for (p-)JNK (T183/Y185), p-ERK(T202/Y204), p-p38(T180/Y182), and p-AKT(T308), as well as total JNK, ERK, p38, and AKT. (G) Densitometry of Western blots ($N \geq 4$ lanes) normalized to protein loading of TGF- β 1-3 and VEGF. (H) Representative lanes from Western blots from pWT and pP22582fs $^{+/-}$ iPS-CMs probed for TGF- β 1, TGF- β 2, TGF- β 3, VEGF, and glyceraldehyde-3-phosphate dehydrogenase (GAPDH). (I) Mean twitch force (in microneurons) generated by pP22582fs $^{+/-}$ iPS-CMTs pretreated with 50 ng/ml VEGF ($N > 4$ CMTs). Significance was assessed by Bayesian P values [(B) to (D)] or Student's t test [(E), (G), and (I)]; data are means \pm SEM (error bars) [(E), (G), and (I)].

well-organized functional sarcomeres. The resultant sarcomere insufficiency (fig. S7) caused both profound baseline contractile deficits and attenuated signaling that limited cardiomyocyte reserve in response to mechanical and adrenergic stress, parameters that are critical to DCM pathogenesis. The consequences of TTN truncation are markedly different from the effects of truncating mutations in another sarcomere protein, myosin-binding protein C (MYBPC); truncation of MYBPC causes enhanced contractile power (18). Our findings also suggest potential therapeutic targets for TTNts, including strategies to enhance TTN gene expression, diminish miRNAs that inhibit sarcomerogenesis (15, 19), or stimulate cardiomyocyte signals that improve function (20).

REFERENCES AND NOTES

1. R. E. Hershbarger, D. J. Hedges, A. Morales, *Nat. Rev. Cardiol.* **10**, 531–547 (2013).
2. D. S. Herman et al., *N. Engl. J. Med.* **366**, 619–628 (2012).
3. A. M. Roberts et al., *Sci. Transl. Med.* **7**, 270ra6 (2015).
4. Y. H. Loh et al., *Cell Stem Cell* **7**, 15–19 (2010).
5. P. Mali et al., *Science* **339**, 823–826 (2013).
6. T. Boudou et al., *Tissue Eng. Part A* **18**, 910–919 (2012).
7. X. Lian et al., *Nat. Protoc.* **8**, 162–175 (2013).
8. S. Tohyama et al., *Cell Stem Cell* **12**, 127–137 (2013).
9. B. Gerull et al., *Nat. Genet.* **30**, 201–204 (2002).
10. J. L. Tan et al., *Proc. Natl. Acad. Sci. U.S.A.* **100**, 1484–1489 (2003).
11. N. Thavandiran et al., *Proc. Natl. Acad. Sci. U.S.A.* **110**, E4698–E4707 (2013).
12. D. Zhang et al., *Biomaterials* **34**, 5813–5820 (2013).
13. W. A. Linke, *Cardiovasc. Res.* **77**, 637–648 (2008).
14. D. C. Christodoulou, J. M. Gorham, D. S. Herman, J. G. Seidman, *Curr. Protoc. Mol. Biol.* **4**, 4.12 (2011).
15. B. Cai et al., *Stem Cells* **30**, 1746–1755 (2012).
16. J. L. Liu et al., *Life Sci.* **90**, 1020–1026 (2012).
17. S. Ikeda et al., *Mol. Cell. Biol.* **29**, 2193–2204 (2009).
18. F. S. Korte, K. S. McDonald, S. P. Harris, R. L. Moss, *Circ. Res.* **93**, 752–758 (2003).
19. E. van Rooij, E. N. Olson, *Nat. Rev. Drug Discov.* **11**, 860–872 (2012).
20. L. Zentilin et al., *FASEB J.* **24**, 1467–1478 (2010).

ACKNOWLEDGMENTS

We thank M. von Frieling-Salewsky for titin gels and Innolign Biomedical for CMTs. This work was supported in part by grants from the LaDue Fellowship (J.T.H., J.H.), the American Heart Association (A.C.), the Sarnoff Foundation (N.N., C.C.S.), the Leducq Foundation (S.A.C., N.H., S.S., J.G.S., C.E.S.), the German Research Foundation [W.A.L. (SFB 1002 TPB3)], the NIH [L.Y. and G.C. (HG005550), C.C.S. (EB017103 and HL115553), C.C.B. (HL007374), J.T.H. (HL125807), C.E.S., and J.G.S.], the NIHR Cardiovascular Biomedical Research Unit of Royal Brompton and Harefield NHS Foundation Trust (S.A.C.), the RESBio Technology Resource for Polymeric Biomaterials (C.S.C.), and Howard Hughes Medical Institute (C.E.S., A.H.). C.E.S. and J.G.S. are cofounders of and own shares in Myokardia Inc., a company that is developing therapeutics for cardiomyopathies. C.S.C. is a cofounder of and owns equity in Innolign Biomedical, a company that is developing an organ-on-chip platform (based on the device used in this study) for measuring forces of cardiac microtissues. S.A.C. is a paid consultant for Illumina, Inc.

SUPPLEMENTARY MATERIALS

www.sciencemag.org/content/349/6251/982/suppl/DC1
Materials and Methods
Figs. S1 to S7
Table S1
References (21–34)
Movies S1 to S6

22 December 2014; accepted 30 July 2015
10.1126/science.aaa5458

SYNTHETIC BIOLOGY

Emergent genetic oscillations in a synthetic microbial consortium

Ye Chen,^{1*} Jae Kyoung Kim,^{2,3*} Andrew J. Hirning,¹
Krešimir Josić,^{4,5} Matthew R. Bennett^{1,6†}

A challenge of synthetic biology is the creation of cooperative microbial systems that exhibit population-level behaviors. Such systems use cellular signaling mechanisms to regulate gene expression across multiple cell types. We describe the construction of a synthetic microbial consortium consisting of two distinct cell types—an “activator” strain and a “repressor” strain. These strains produced two orthogonal cell-signaling molecules that regulate gene expression within a synthetic circuit spanning both strains. The two strains generated emergent, population-level oscillations only when cultured together. Certain network topologies of the two-strain circuit were better at maintaining robust oscillations than others. The ability to program population-level dynamics through the genetic engineering of multiple cooperative strains points the way toward engineering complex synthetic tissues and organs with multiple cell types.

Most synthetic gene circuits have been constructed to operate within single, isogenic cellular populations (1–4). However, synthetic microbial consortia could provide a means of engineering population-level phenotypes that are difficult to obtain with single strains (5). Indeed, several synthetic systems have been constructed to exhibit population-level phenotypes (6–9), including synthetic predator-prey systems (10), multicellular computers (11), and spatio-temporal pattern generators (12, 13). We constructed two genetically distinct populations of *Escherichia coli* to create a bacterial consortium that exhibits robust, synchronized transcriptional oscillations that are absent if either strain is grown in isolation. Specifically, we used two different bacterial quorum-sensing systems to construct an “activator” strain and a “repressor” strain that respectively increase and decrease gene expression in both strains. When cultured together in a microfluidic device, the two strains form coupled positive and negative feedback loops at the population level, akin to the circuit topology (i.e., how regulatory components within a circuit regulate each other) of a synthetic dual-feedback oscillator that operates within a single strain (14, 15). We used a combination of mathematical modeling and targeted genetic perturbations to better understand the roles of circuit topology and regulatory promoter strengths in generating and maintaining oscillations. The dual-feedback topology was robust to changes in promoter

strengths and fluctuations in the population ratio of the two strains.

The two synthetic strains in our system were constructed to enzymatically produce and transcriptionally respond to intercellular signaling molecules (Fig. 1A). The activator strain produces C4-homoserine lactone (C4-HSL) (16), a signaling molecule that increases transcription of target genes within the synthetic circuits of both strains. The repressor strain produces 3-OHC14-HSL (17), which decreases transcription in both strains through a synthetic transcriptional inverter (18, 19) mediated by the repressor LacI. These two signaling mechanisms jointly create coupled positive and negative feedback loops at the population level when the two strains are grown together (Fig. 1B). Additionally, each strain, when active, produces the enzyme AiiA, which degrades both signaling molecules, resulting in another layer of negative feedback.

To observe the dynamics of the synthetic consortium, we used a custom-designed microfluidic device in conjunction with time-lapse fluorescence microscopy to observe the two strains as they grew together in a small chamber in which the diffusion time of the HSLs was small (see supplementary materials) (20). Each strain contained a gene encoding a spectrally distinct fluorescent reporter (*cfp*, cyan fluorescent protein, in the activator; *yfp*, yellow fluorescent protein, in the repressor), driven by promoters that respond to both positive and negative signals in the network (Fig. 1A). After an initial transient time, synchronous, in-phase oscillations emerged in the fluorescent reporters of both strains (Fig. 1, C and D). Neither strain oscillated when cultured in isolation (fig. S1). Oscillations had a period of ~2 hours and persisted throughout the experiments (usually more than 14 hours).

The circuit topology of our synthetic consortium consisted of linked positive and negative feedback loops, similar to the topologies of many naturally occurring biological oscillators (21, 22).

¹Department of Biosciences, Rice University, Houston, TX 77005, USA. ²Department of Mathematical Sciences, Korea Advanced Institute of Science and Technology, Daejeon 305-701, Korea. ³Mathematical Biosciences Institute, The Ohio State University, Columbus, OH 43210, USA. ⁴Department of Mathematics, University of Houston, Houston, TX 77204, USA. ⁵Department of Biology and Biochemistry, University of Houston, Houston, TX 77204, USA. ⁶Institute of Biosciences and Bioengineering, Rice University, Houston, TX 77005, USA.

*These authors contributed equally to this work. †Corresponding author. E-mail: matthew.bennett@rice.edu

However, a single negative feedback loop is sufficient to generate rhythms (14, 23). Therefore, we tested whether the additional feedback loops in our system were necessary for oscillations. We eliminated either the extra positive or extra negative feedback loop, or both simultaneously. To eliminate the extra positive feedback loop, we created a variant activator strain in which the hybrid promoter $P_{rhI/lac-S}$ was replaced with P_{lac} . We eliminated the additional negative feedback loop by constructing a variant repressor strain without *lacI*. By combining one of the two variant activator strains with one of the two variant repressor strains, we generated consortia with four different topologies (fig. S2): P_2N_2 (containing both additional feedback loops), P_2N_1 (lacking the additional negative feedback loop), P_1N_2 (lacking the additional positive feedback loop), and P_1N_1 (lacking both additional feedback loops). Each topology still contained the negative feedback loop mediated by AiiA.

Each of the topologies described above generated rhythms if and only if both strains were present, confirming that additional feedback loops are not required for oscillations. Further, the oscillations were robust to fluctuations in the population ratio of the two strains in the microfluidic trap (Fig. 2, A to D). In contrast to the effect in a single-strain oscillator (14), removing the additional positive feedback loop lengthened the period in P_1N_2 and P_1N_1 (Fig. 2E). Furthermore, P_1N_2 and P_1N_1 generated double-peaked activator oscillations, in contrast to the single-peaked oscillations generated by P_2N_2 and P_2N_1 .

To understand the behaviors of the different topologies, we developed a mathematical model (24, 25) to simulate the intra- and extracellular dynamics of the key proteins and molecules (see supplementary materials and table S1). In our model, most of the parameters (32 of 40) were either obtained from the literature or by measurement of promoter activity under various conditions (fig. S3 and table S1). The unknown parameters were randomly and independently sampled from uniform distributions covering biologically realistic ranges (see supplementary materials). We obtained 10,000 parameter sets that led to oscillations in four different versions of our model, corresponding to the different network topologies. Of these 10,000 parameter sets, 1506 resulted in rhythms with approximately correct periods (100 to 250 min) for all topologies (fig. S4). More than 40% of these sets gave rise to double-peaked oscillations in the activator strain for both P_1N_2 and P_1N_1 , but not P_2N_2 and P_2N_1 , matching experimental observations (Fig. 2, C and D, and fig. S5, A to D). In simulations, the periods of P_1N_2 and P_1N_1 were longer when activator oscillations displayed double peaks (Fig. 2F). This indicates that the double peaks and period lengthening of P_1N_2 and P_1N_1 observed in experiments (Fig. 2, C to F) are related. Specifically, the model suggests that both the double peaks and period lengthening of P_1N_2 and P_1N_1 are caused by competition between RhlI and CFP for ClpXP-mediated proteolysis in the activator strain (26, 27).

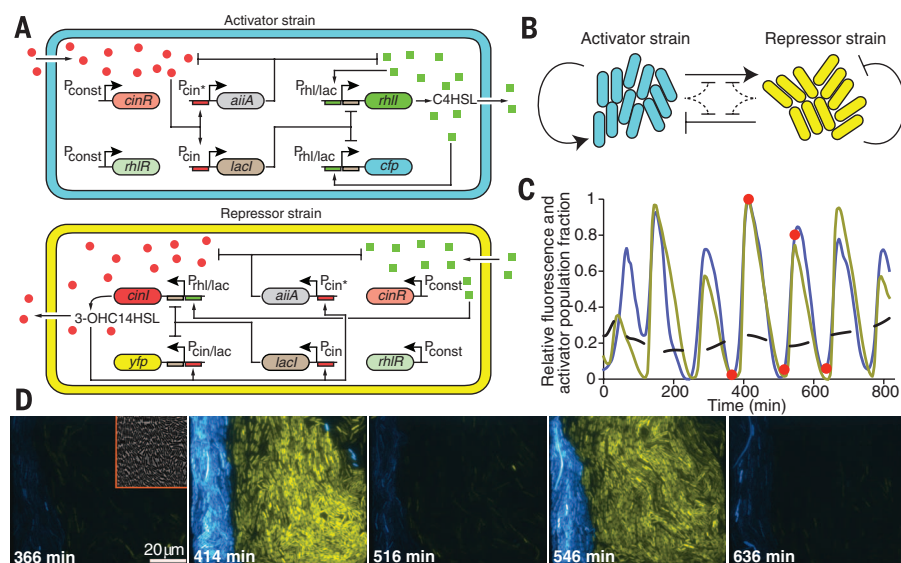


Fig. 1. The synthetic microbial consortium oscillator. (A) Circuit diagrams of the activator (top) and repressor (bottom) strains. In the activator strain, transcription of *rhIR* and *cfp* are regulated by separate copies of the hybrid promoter, $P_{rhI/lac}$, which is up-regulated by C4-HSL and down-regulated by LacI. In the repressor strain, *cinI* is driven by the hybrid promoter $P_{rhI/lac}$ and *yfp* is regulated by the hybrid promoter $P_{cin/lac}$, which is up-regulated by 3-OHC14-HSL and down-regulated by LacI. Both strains contain constitutively expressed copies of *cinR* and *rhIR*, which encode transcription factors that respond to the HSLs to regulate their respective promoters, and *allA* and *lacI* driven by 3-OHC14-HSL-responsive promoters. (B) Global topology of the dual-feedback consortium oscillator. The activator strain up-regulates genes in both strains. The repressor strain down-regulates genes in both strains. AiiA down-regulates signaling (dashed lines, omitted in Figs. 2 and 3 and figs. S2 and S7 for simplicity). (C) Representative time series of activator (blue) and repressor fluorescence (yellow), and activator population fraction (black, ratio of the area of activator cells to the area of the entire population of cells, as measured in pixels) for the consortium depicted in (A). Relative fluorescence values are the population average relative to the maximum after background subtraction. (D) Five images of the consortium from time points indicated by red dots in (C).

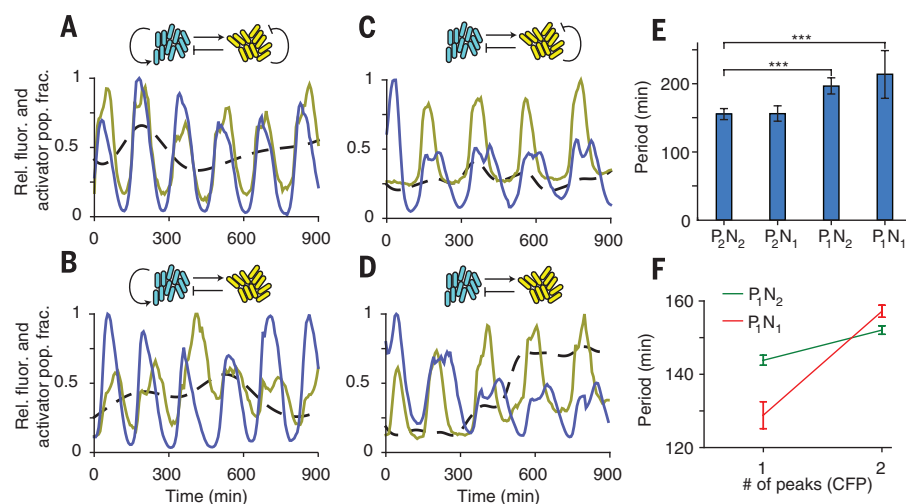


Fig. 2. Dynamics of consortia with various topologies. (A to D) P_2N_2 (A) and P_2N_1 (B) generate rhythms with shorter periods than P_1N_2 (C) and P_1N_1 (D). The CFP rhythms in the activator strain of P_1N_2 (C) and P_1N_1 (D) exhibited double peaks, in contrast to P_2N_2 (A) and P_2N_1 (B). Here, each line style is the same as in Fig. 1C. (E) Experimentally measured periods for each topology. The periods of P_1N_2 ($P < 10^{-11}$) and P_1N_1 ($P < 10^{-6}$) were not the same as that of P_2N_2 (t test with Bonferroni correction). Error bars are mean \pm SD; from left to right, the number of measured periods was $N = 19, 21, 15, 14$. (F) The mean period (\pm SEM) of simulated oscillations with parameter sets leading to either single or double peaks in CFP oscillations among the 1506 parameter sets described in the main text. The periods in P_1N_2 and P_1N_1 were longer when CFP oscillations exhibited double peaks.

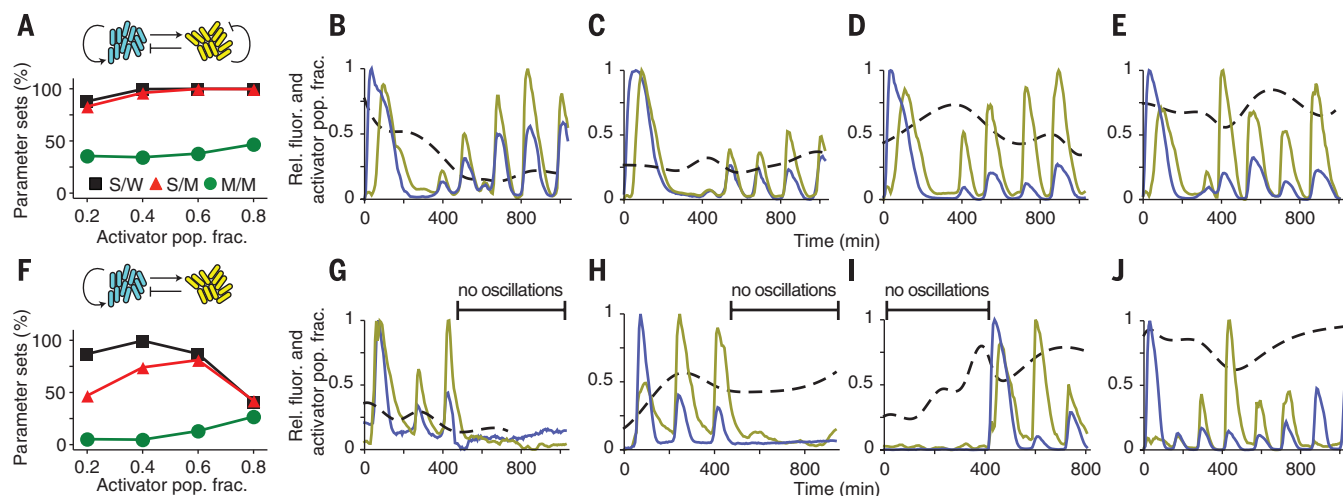


Fig. 3. Additional negative feedback increases robustness. (A) Percentage of the 1506 parameter sets (fig. S4) that led to oscillations in the model as a function of percentage of activator strain in the P_2N_2 consortium. Shown are the results for three different combinations of promoter strengths. S/W: $P_{rhI/lac-s}$ and $P_{rhI/lac-w}$ promoters in activator and repressor strains, respectively. S/M: $P_{rhI/lac-s}$ promoter in activator and $P_{rhI/lac-m}$ promoter in repressor. M/M: $P_{rhI/lac-m}$ promoters in both strains. (B to E) Example trajectories for the P_2N_2 topology

with $P_{rhI/lac-m}$ promoters in both activator and repressor strains with different activator population fractions. (F) Percentage of the 1506 parameter sets that led to oscillations in the model as a function of percentage of activator strain in the P_2N_1 consortium. Symbols are the same as in (A). Results for P_1N_2 and P_1N_1 are given in fig. S6. (G to J) Example trajectories for the P_2N_1 topology with the M/M promoter configuration showing occasional loss of oscillations.

We investigated how the additional feedback loops affect the robustness of oscillations, as theoretically additional feedback can increase the robustness of genetic oscillators (21, 22). We were interested in two types of perturbations: (i) variations in the population ratio of the two strains, and (ii) different promoter strengths within the circuit. Perturbations in the population ratio of the two strains arose naturally from variations in growth of the two strains within the microfluidic device. To perturb the promoter strengths within the circuits, we altered the $P_{rhI/lac}$ promoters used to drive *cinI* in the repressor strain and *rhII* in the activator strain to have different expression strengths (see supplementary materials). The original activator strain contained a strong promoter, $P_{rhI/lac-s}$, and the repressor strain a weaker promoter, $P_{rhI/lac-w}$. Gene expression from the strong promoter was approximately 15 times that of the weak promoter. We also created a medium promoter, $P_{rhI/lac-m}$, which was approximately 10 times as strong as the weak promoter (fig. S3).

To examine how changes to the promoter strengths and fluctuations in the population ratio affected oscillations in the mathematical model, we used the 1506 parameter sets described above and systematically altered the parameters governing promoter activities and the population ratio (fig. S3 and table S1). We then calculated the percentage of parameter sets that still led to oscillations in the four different topologies (fig. S6). The mathematical model predicted that P_2N_2 and P_1N_2 show similar robustness (i.e., the percentage of parameter sets leading to oscillations after perturbation was similar) and that both are more robust than P_2N_1 and P_1N_1 (Fig. 3, A and F, and fig. S6). Hence, the model predicts that the addition of a negative feedback loop, but not a positive feedback loop, has a pivotal role in

generating robust rhythms because it tightly regulates repressor concentration (fig. S6) (22, 28). Thus, for different promoter-strength combinations, the P_2N_2 oscillator is expected to be more robust to differences in population ratio than P_2N_1 (Fig. 3, A and F). To test this prediction, we constructed P_2N_2 and P_2N_1 using the medium promoter, $P_{rhI/lac-m}$, for both strains. P_2N_2 oscillated over a wide range of population ratios, whereas P_2N_1 occasionally stopped oscillating when the activator population fraction was low (Fig. 3).

We also explored other configurations of promoter strengths within the four topologies. When the promoter driving *cinI* in the repressor strain was changed from $P_{rhI/lac-w}$ to $P_{rhI/lac-m}$ (and $P_{rhI/lac-s}$ was kept in the activator), all topologies still generated oscillations (fig. S7, A to D). However, P_1N_2 and P_1N_1 showed rhythms with a much shorter period than those of P_2N_2 and P_2N_1 (fig. S7, C and D). Furthermore, oscillations in the repressor strain were robust even though activator strain oscillations in P_1N_2 and P_1N_1 were low and unstable.

To understand why the P_1N_2 and P_1N_1 topologies exhibited strong and short-period repressor oscillations even in the absence of strong activator oscillations, we again turned to the mathematical model. Our simulations matched experimental data when $P_{rhI/lac-m}$ was used in the repressor strain in the P_1N_2 and P_1N_1 topologies (fig. S8, A and B). The model predicted that when $P_{rhI/lac-m}$ is used in P_1N_2 and P_1N_1 , the mechanism responsible for generating oscillations is an intracellular negative feedback loop mediated by AiiA in the repressor strain and not the intercellular transcriptional negative feedback loop between the two strains (fig. S8). Essentially, the feedback loop mediated by AiiA in the repressor strain has a shorter delay time than the tran-

scriptional loop between the strains, and hence the period becomes shorter (29).

Our results show that engineering dynamic population-level phenotypes in synthetic microbial consortia is possible with multiple intercellular signaling mechanisms. Because the population ratio within a consortium can fluctuate, it is important to engineer synthetic circuits that are robust to such perturbations. Overall, our synthetic microbial consortia provide a platform for testing the relation between population-level dynamics and genetic-level regulation.

REFERENCES AND NOTES

1. T. S. Gardner, C. R. Cantor, J. J. Collins, *Nature* **403**, 339–342 (2000).
2. M. B. Elowitz, S. Leibler, *Nature* **403**, 335–338 (2000).
3. A. Levskaya et al., *Nature* **438**, 441–442 (2005).
4. T. Danino, O. Mondragón-Palomino, L. Tsimring, J. Hasty, *Nature* **463**, 326–330 (2010).
5. K. Brenner, L. You, F. H. Arnold, *Trends Biotechnol.* **26**, 483–489 (2008).
6. L. You, R. S. Cox 3rd, R. Weiss, F. H. Arnold, *Nature* **428**, 868–871 (2004).
7. K. Brenner, D. K. Karig, R. Weiss, F. H. Arnold, *Proc. Natl. Acad. Sci. U.S.A.* **104**, 17300–17304 (2007).
8. W. Shou, S. Ram, J. M. G. Vilar, *Proc. Natl. Acad. Sci. U.S.A.* **104**, 1877–1882 (2007).
9. N. Marchand, C. H. Collins, *Biotechnol. Bioeng.* **110**, 3003–3012 (2013).
10. F. K. Balagaddé et al., *Mol. Syst. Biol.* **4**, 187 (2008).
11. A. Tamsir, J. J. Tabor, C. A. Voigt, *Nature* **469**, 212–215 (2011).
12. S. Basu, R. Mehreja, S. Thiberge, M. T. Chen, R. Weiss, *Proc. Natl. Acad. Sci. U.S.A.* **101**, 6355–6360 (2004).
13. S. Basu, Y. Gerchman, C. H. Collins, F. H. Arnold, R. Weiss, *Nature* **434**, 1130–1134 (2005).
14. J. Stricker et al., *Nature* **456**, 516–519 (2008).
15. F. Hussain et al., *Proc. Natl. Acad. Sci. U.S.A.* **111**, 972–977 (2014).
16. E. C. Pesci, J. P. Pearson, P. C. Seed, B. H. Iglewski, *J. Bacteriol.* **179**, 3127–3132 (1997).
17. J. K. Lithgow et al., *Mol. Microbiol.* **37**, 81–97 (2000).
18. Y. Yokobayashi, R. Weiss, F. H. Arnold, *Proc. Natl. Acad. Sci. U.S.A.* **99**, 16587–16591 (2002).

19. J. J. Tabor *et al.*, *Cell* **137**, 1272–1281 (2009).
20. M. R. Bennett, J. Hasty, *Nat. Rev. Genet.* **10**, 628–638 (2009).
21. T. Y. Tsai *et al.*, *Science* **321**, 126–129 (2008).
22. J. K. Kim, D. B. Forger, *Mol. Syst. Biol.* **8**, 630 (2012).
23. B. Novák, J. J. Tyson, *Nat. Rev. Mol. Cell Biol.* **9**, 981–991 (2008).
24. E. L. O'Brien, E. Van Itallie, M. R. Bennett, *Math. Biosci.* **236**, 1–15 (2012).
25. F. Naqib *et al.*, *Phys. Rev. E Stat. Nonlin. Soft Matter Phys.* **85**, 046210 (2012).
26. W. H. Mather, N. A. Cookson, J. Hasty, L. S. Tsimring, R. J. Williams, *Biophys. J.* **99**, 3172–3181 (2010).
27. A. Prindle *et al.*, *Nature* **508**, 387–391 (2014).
28. H. Cho *et al.*, *Nature* **485**, 123–127 (2012).
29. W. Mather, M. R. Bennett, J. Hasty, L. S. Tsimring, *Phys. Rev. Lett.* **102**, 068105 (2009).

ACKNOWLEDGMENTS

This work was funded by the National Institutes of Health, through the joint NSF–National Institute of General Medical Sciences Mathematical Biology Program grant R01GM104974 (M.R.B. and K.J.), the Robert A. Welch Foundation grant C-1729 (M.R.B.), the Hamill Foundation (M.R.B.), NSF grant DMS-0931642 to the Mathematical Biosciences Institute (J.K.K.), and the China Scholarship Council (Y.C.). M.R.B., Y.C., K.J., and J.K.K. conceived and designed the study. Y.C. performed the experiments and analyzed the data. A.J.H. designed and fabricated the microfluidic devices. J.K.K. performed the computational modeling and

analyzed simulations. M.R.B. supervised the project. All authors wrote the manuscript. The mathematical model and experimental data are archived in the BioModels Database at www.ebi.ac.uk/biomodels-main/MODEL1505050000.

SUPPLEMENTARY MATERIALS

www.sciencemag.org/content/349/6251/986/suppl/DC1
Materials and Methods
Figs. S1 to S10
Table S1
Movie S1
References (30–52)

26 November 2014; accepted 2 July 2015
10.1126/science.aaa3794

MUCOSAL IMMUNOLOGY

The microbiota regulates type 2 immunity through ROR γ ⁺ T cells

Caspar Ohnmacht,^{1,*†} Joo-Hong Park,^{1,*} Sascha Cording,¹ James B. Wing,² Koji Atarashi,^{3,4} Yuuki Obata,⁵ Valérie Gaboriau-Routhiau,^{6,7,8} Rute Marques,^{1,†} Sophie Dulauroy,¹ Maria Fedoseeva,⁹ Meinrad Busslinger,¹⁰ Nadine Cerf-Bensussan,^{6,7} Ivo G. Boneca,^{11,12} David Voehringer,¹³ Koji Hase,⁵ Kenya Honda,^{3,14} Shimon Sakaguchi,^{2,15} Gérard Eberl^{1§}

Changes to the symbiotic microbiota early in life, or the absence of it, can lead to exacerbated type 2 immunity and allergic inflammations. Although it is unclear how the microbiota regulates type 2 immunity, it is a strong inducer of proinflammatory T helper 17 (T_H17) cells and regulatory T cells (T_{regs}) in the intestine. Here, we report that microbiota-induced T_{regs} express the nuclear hormone receptor ROR γ t and differentiate along a pathway that also leads to T_H17 cells. In the absence of ROR γ t⁺ T_{regs}, T_H2-driven defense against helminths is more efficient, whereas T_H2-associated pathology is exacerbated. Thus, the microbiota regulates type 2 responses through the induction of type 3 ROR γ t⁺ T_{regs} and T_H17 cells and acts as a key factor in balancing immune responses at mucosal surfaces.

Allergic reactions are on the rise in industrialized nations, paralleling a decrease in the incidence of infectious diseases (1, 2). The hygiene hypothesis proposes that exposure to pathogens reduces the risk of allergy, a notion that may be extended to exposure to the symbiotic microbiota. In support of this hypothesis, germfree mice, devoid of microorganisms, develop increased susceptibility to allergy (3–6). Furthermore, a developmental time window during childhood determines such susceptibility (1, 2). Mice treated early with antibiotics, which deeply affect the microbiota, develop an increased susceptibility to allergy (7) that can last into adulthood (8), an effect also found in mice that remain germfree until weaning (9).

The mechanism by which the microbiota regulates type 2 responses remains unclear. A direct effect of microbiota on type 2 cells, such as T helper 2 (T_H2) cells and innate lymphoid cells (ILC2), has not been documented. In contrast, symbionts are necessary for the differentiation of T_H17 cells that produce interleukin (IL)–17 and IL–22 (10), cytokines involved in homeostasis and defense of mucosal surfaces, and a subset of intestinal regulatory T cells (T_{regs}) (11). Intriguingly, the absence of extrathymically generated T_{regs}

leads to spontaneous type 2 pathologies at mucosal sites (12). As intestinal T_{regs} recognize bacterial antigens (11), the microbiota may regulate type 2 responses through the induction of extrathymically generated T_{regs}.

The nuclear hormone receptor ROR γ t is a key transcription factor for the differentiation of T_H17 cells and ILC3s (13, 14). In addition, a substantial fraction of ROR γ t⁺ T cells residing in the lamina propria of the small intestine does not express IL–17, but rather IL–10, the T_{reg} marker FoxP3 (a transcription factor), and has regulatory functions (15). Furthermore, the generation of such ROR γ t⁺ T_{regs} requires the microbiota (16). Using reporter mice for the expression of ROR γ t and Foxp3, we found that a majority of ROR γ t⁺ T cells in the colon of adult mice expressed Foxp3, and, reciprocally, a majority of colon T_{regs} expressed ROR γ t (Fig. 1A). The frequency of ROR γ t⁺ T_{regs} increased with age, representing most intestinal T_{regs} in 1-year-old mice (fig. S1A). These cells were not found in the thymus (fig. S1B) and did not express Helios or Neuropilin-1, markers of thymically derived T_{regs} (17, 18), in contrast to conventional ROR γ t⁺ T_{regs} (Fig. 1B and fig. S1C). In the colon, most Helios⁺ T_{regs} were absent in ROR γ t-deficient mice (Fig. 1B). ROR γ t⁺ T_{regs} also

expressed an activated CD44^{high} CD62L^{low} phenotype, as well as increased levels of ICOS, CTLA-4, and the nucleotidases CD39 and CD73 (fig. S1C), altogether indicating robust regulatory functions. Another major subset of intestinal T_{regs} expresses Gata3, responds to IL–33, and is involved in the regulation of effector T cells during inflammation (19, 20). Gata3⁺ T_{regs} were distinct from ROR γ t⁺ T_{regs} and expressed Helios, as well as lower levels of IL–10 (fig. S2).

ROR γ t⁺ T_{regs} were profoundly reduced in germ-free or antibiotic-treated mice, whereas Helios⁺ and Gata3⁺ T_{regs} were unaffected (Fig. 1C and fig. S3). Recolonization of germfree mice with a specific pathogen-free (SPF) microbiota restored normal numbers of ROR γ t⁺ T_{regs} (fig. S4). Furthermore, a consortium of symbionts composed of 17 *Clostridia* species efficiently induces the generation of T_{regs} expressing IL–10 in the colon (21), the majority of which expressed ROR γ t (Fig. 1D). The microbiota has been shown to induce the generation of intestinal T_{regs} through short-chain fatty acids (SCFA) (22, 23) and antigen (11). We found that the SCFA butyrate induced an increase

¹Institut Pasteur, Microenvironment and Immunity Unit, 75724 Paris, France. ²Laboratory of Experimental Immunology, Immunology Frontier Research Center, Osaka University, Suita 565-0871, Japan. ³RIKEN Center for Integrative Medical Sciences (IMS-RCMI), Yokohama, Kanagawa 230-0045, Japan. ⁴PRESTO, Japan Science and Technology Agency, Saitama 332-0012, Japan. ⁵The Institute of Medical Science, The University of Tokyo, Tokyo 108-8639, Japan. ⁶INSERM, U1163, Laboratory of Intestinal Immunity, Paris, France. ⁷Université Paris Descartes–Sorbonne Paris Cité and Institut Imagine, Paris, France. ⁸INRA Micalis UMR1319, Jouy-en-Josas, France. ⁹Center of Allergy and Environment (ZAUM), Technische Universität und Helmholtz Zentrum München, Munich, Germany. ¹⁰Research Institute of Molecular Pathology, Vienna Biocenter, 1030 Vienna, Austria. ¹¹Institut Pasteur, Biology and Genetics of Bacterial Cell Wall, 75724 Paris, France. ¹²INSERM, Groupe Avenir, 75015 Paris, France. ¹³Department of Infection Biology at the Institute of Clinical Microbiology, Immunology and Hygiene, University Clinic Erlangen and Friedrich-Alexander University Erlangen-Nuremberg, 91054 Erlangen, Germany. ¹⁴CREST, Japan Science and Technology Agency, 4-1-8 Honcho Kawaguchi, Saitama 332-0012, Japan. ¹⁵Department of Experimental Pathology, Institute for Frontier Medical Sciences, Kyoto University, Kyoto 606-8507, Japan.

*These authors contributed equally to this work. †Present address: Center of Allergy and Environment (ZAUM), Technische Universität und Helmholtz Zentrum München, Munich, Germany. ‡Present address: INSERM, U1163, Laboratory of Intestinal Immunity, and Université Paris Descartes–Sorbonne Paris Cité and Institut Imagine, Paris, France. §Corresponding author. E-mail: gerard.eberl@pasteur.fr

mainly in ROR γ ⁺ T_{regs} (fig. S5). The generation of ROR γ ⁺ T_{regs} was dependent on dendritic cells (DCs) and major histocompatibility complex (MHC) class II (Fig. 1E) and induced by oral antigen (ovalbumin) in transferred naïve CD4⁺ T cells expressing the OT-II transgenic T cell receptor specific for that antigen (Fig. 1F). Altogether, these data show that ROR γ ⁺ T_{regs} are induced by microbiota and oral antigen, and that microbiota-induced intestinal T_{regs} express ROR γ .

T_H17 cells are efficiently induced by the pathobiont segmented filamentous bacteria (SFB) that forms colonies on epithelial cells of the small intestine

(24, 25) and by cytokine signaling pathways involving the transcription factor Stat3 (26). Surprisingly, ROR γ ⁺ T_{regs} differentiated following similar pathways. ROR γ ⁺ T_{regs} were efficiently induced by SFB in the small intestine, even though more T_H17 cells were induced in these conditions (Fig. 2A). Furthermore, similar to T_H17 cells, innate receptors of the Toll-like receptor and NOD-like receptor families were not involved (fig. S6). In contrast, mice deficient for IL-6 or the p19 subunit of IL-23 (encoded by *Il23a*), both involved in the induction of T_H17 cells (27, 28), developed significantly less ROR γ ⁺ T_{regs} (Fig. 2B), whereas

Gata3⁺ T_{regs} were increased (fig. S7). In accordance with the fact that both cytokines signal through the transcription factor Stat3, similar results were obtained in mice that lack expression of Stat3 in T_{regs} or ROR γ ⁺ cells (Fig. 2B).

If T_H17 cells and ROR γ ⁺ T_{regs} are induced through similar pathways, how then is the development to T_H17 cells or ROR γ ⁺ T_{regs} regulated? In cell cultures, the vitamin A metabolite retinoic acid (RA) promotes the generation of T_{regs} (29) and of ROR γ ⁺ T_{regs} (15) rather than of T_H17 cells. We now find that feeding mice with vitamin A-deficient food, or treating mice with

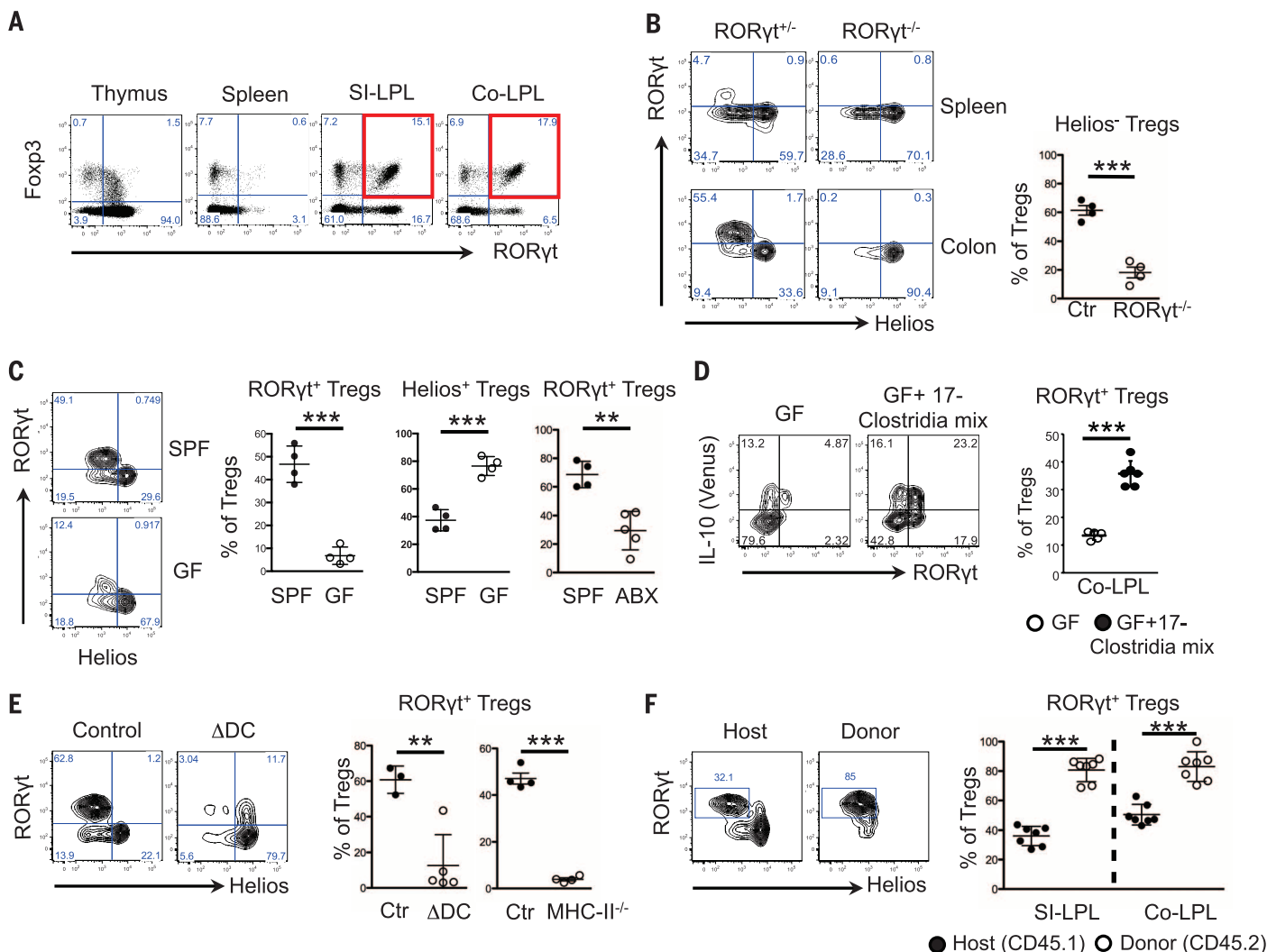


Fig. 1. A majority of colon ROR γ ⁺ T cells are microbiota-induced ROR γ ⁺ T_{regs}. (A) Expression of Foxp3 and ROR γ by CD4⁺ T cells in double reporter mice. SI, small intestine; Co, colon; LPL, lamina propria lymphocytes. (B) Expression of Helios and ROR γ by T_{regs} (FoxP3⁺ CD4⁺ T cells) from spleen and colon lamina propria of littermate control (left) and ROR γ -deficient mice (right). Right, frequency of colon Helios⁺ T_{regs}. *n* = 4 mice per group. (C) Expression of ROR γ and Helios by T_{regs} in the colon of SPF or germfree (GF) mice and frequencies of ROR γ ⁺ Helios⁺ T_{regs} (left) and Helios⁺ T_{regs} (middle) in SPF and germfree mice; *n* = 4 mice per group. Right, frequency of ROR γ ⁺ T_{regs} in the colon of SPF mice or mice treated from birth with a cocktail of antibiotics; *n* ≥ 4. (D) Expression of ROR γ and IL-10 by T_{regs} and frequency of ROR γ ⁺ T_{regs} in the colon of germfree mice (left) or mice recolonized for 3 weeks with a con-

sortium of 17 strains of *Clostridia* (right); *n* ≥ 4 mice per group. (E) Expression of ROR γ and Helios by colonic T_{regs} (left) and frequency of ROR γ ⁺ T_{regs} (middle) in *Cd11c*^{Cre} × *Rosa26*^{Dta} (Δ DC) and littermate control mice, *n* ≥ 3 mice per group. Right, frequencies of ROR γ ⁺ T_{regs} in colon of control or MHC class II-deficient mice; *n* = 4. (F) Naïve CD4⁺ T cells were isolated from CD45.2⁺ OT-II Rag2^{-/-} mice and adoptively transferred into CD45.1⁺ congenic mice and subsequently fed for 7 days with 1.5% chicken ovalbumin in the drinking water. Expression of ROR γ and Helios in small intestine T_{regs} (left) and frequency of ROR γ ⁺ T_{regs} in small intestine and colon (right) in host (CD45.1) and donor (CD45.2) cells; *n* = 7 mice. Data are representative of at least two independent experiments. Error bars, mean ± 1 SD; ns, not significant; **P* < 0.05; ***P* < 0.01; ****P* < 0.001, as calculated by Student's *t* test.

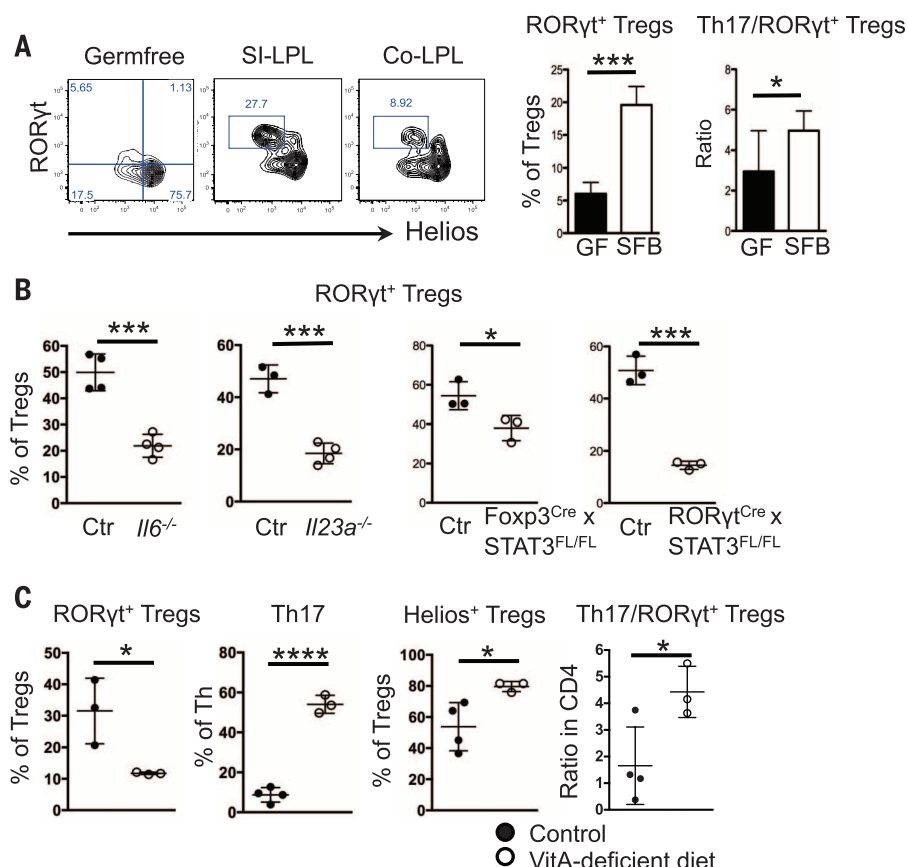


Fig. 2. A proinflammatory pathway plus retinoic acid induce RORγt⁺ T_{regs}. (A) Expression of RORγt and Helios by T_{regs} in germfree mice and germfree mice recolonized for 3 weeks with SFB. Histograms show frequencies of RORγt⁺ T_{regs} and ratio of Th17 cells versus RORγt⁺ T_{regs}; $n \geq 4$ mice per group. (B) Frequencies of (Helios⁺) RORγt⁺ T_{regs} in colon of *Il6*^{-/-}, *Il23a*^{-/-}, *Fcpx3*^{Cre} x *Stat3*^{FL/FL}, *RORγt*^{Cre} x *Stat3*^{FL/FL}, and littermate control mice; $n \geq 3$ mice per group. (C) Frequencies of RORγt⁺ T_{regs}, Th17 cells, Helios⁺ T_{regs}, and ratio of Th17 cells versus RORγt⁺ T_{regs} in colon of mice fed a control diet or a vitamin A-deficient diet from birth for 10 weeks; $n \geq 3$ mice per group. Data are representative of at least two independent experiments. Error bars, mean \pm 1 SD; * $P < 0.05$; *** $P < 0.001$, as calculated by Student's *t* test.

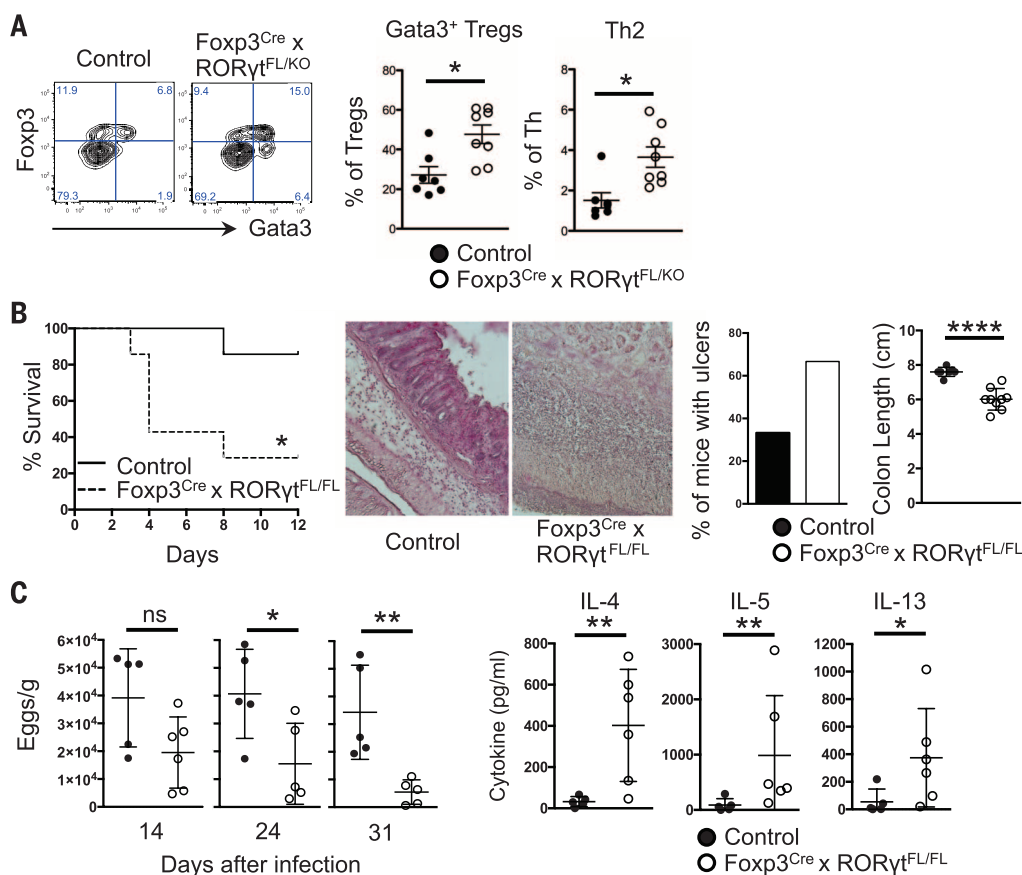


Fig. 3. RORγt⁺ T_{regs} regulate type 2 immune responses. (A) Expression of Foxp3 and Gata3 by small intestine CD4⁺ T cells (left), and frequency of Gata3⁺ T_{regs} (middle) and Gata3⁺ non-T_{regs} CD4⁺ T cells (right) in *Fcpx3*^{Cre} x *Rorc*(γt)^{FL/KO} mice; $n = 7$ mice per group. (B) Survival curve (left) of littermate control mice (straight line) or *Fcpx3*^{Cre} x *Rorc*(γt)^{FL/FL} mice (hatched line) treated with oxazolone; $n = 7$ mice per group. Periodic acid-Schiff staining of colons from the corresponding mice and ratio of mice with ulcers (middle) and length of colons 3 days after oxazolone challenge (right). (C) Egg burden 14, 24, and 31 days after infection with *H. polygyrus* and production of type 2 cytokines by T cells isolated from mesenteric lymph nodes 21 days after infection in control mice (filled symbols) or *Fcpx3*^{Cre} x *Rorc*(γt)^{FL/FL} mice (open symbols); $n \geq 5$ mice per group. Data are representative of at least two independent experiments. Error bars, \pm 1 SD; ns, not significant; * $P < 0.05$; ** $P < 0.01$; **** $P < 0.0001$, as calculated by Student's *t* test or Mann-Whitney test.

an inhibitor of the RA receptor (RARI), prevented the development of ROR γ t⁺ T_{regs} but not of Helios⁺ T_{regs} or T_H17 cells (Fig. 2C and fig. S8). RA also promotes the expansion of ILC3s over ILC2s (30) and the maturation of fetal ILC3s through RAR-mediated regulation of the *Rorc* locus encoding ROR γ t (31). Thus, vitamin A metabolism promotes the development of ROR γ t⁺ cells and type 3 immunity, yet favors the development of ROR γ t⁺ T_{regs} over T_H17 cells, presumably to limit the number of proinflammatory cells present in the healthy intestine.

We next assessed whether ROR γ t⁺ T_{regs} regulate type 2 responses. Mice that lack only ROR γ t⁺ T_{regs} were generated through a conditional knockout of *Rorc* in Foxp3⁺ cells. Such *Foxp3*^{Cre} × *Rorc*(γ t)^{FL} mice developed increased frequencies of Gata3⁺ T cells and Gata3⁺ T_{regs} (Fig. 3A), and, as a consequence, T cells produced higher amounts of the type 2 cytokines IL-4 and IL-5 (fig. S9A). These mice developed a more severe and lethal form of oxazolone-induced colitis, a model of ulcerative colitis dependent on the type 2 cytokines IL-4 (32) and IL-13 (33), as compared with their wild-type littermates (Fig. 3B). In contrast, they were more resistant to infection by the helminth *Heligmosomoides polygyrus*, because they produced higher levels of IL-4, IL-5, and IL-13 during the infection (Fig. 3C). T_H17 cells contributed to the control of type 2 responses, because a more pronounced increase in T_H2 cells was observed in full ROR γ t-deficient mice (fig.

S9B). Furthermore, ROR γ t-deficient mice expressed high levels of immunoglobulin E (IgE) (fig. S9C), a hallmark of type 2 immunity, at levels sometimes similar to those found in germfree mice (3). In contrast, *Foxp3*^{Cre} × *Rorc*(γ t)^{FL} mice did not develop increased T_H17 or T_H1 responses, even during acute intestinal inflammation induced by sodium dextran sulfate (fig. S10). These data are in agreement with the spontaneous type 2 pathologies observed in mice lacking extrathymically generated T_{regs} (12) and indicate that microbiota regulate type 2 responses through ROR γ t⁺ T_{regs} and more generally ROR γ t⁺ T cells.

What are the mechanisms by which ROR γ t⁺ T_{regs} regulate type 2 immunity? We find that both cell-intrinsic and cell-extrinsic mechanisms of regulation are involved. Naïve OT-II⁺ CD4⁺ T cells developed into ROR γ t⁺ T_{regs} when transferred into mice fed ovalbumin (Fig. 1F), whereas a majority of them developed into Gata3⁺ T_{regs} when cells deficient in ROR γ t were transferred (Fig. 4A and fig. S11A). However, host T_{regs} were not affected, showing that a loss in ROR γ t affects T_{regs} only through a cell-intrinsic pathway. In contrast, the transfer of ROR γ t-deficient OT-II⁺ cells affected the generation of both donor and host T_H2 cells, but not T_H17 cells, showing that ROR γ t⁺ T_{regs} regulate T_H2 cells also through a cell-extrinsic pathway. Furthermore, in ROR γ t⁺ T_{regs} that lacked Stat3, the expression of Gata3 was deregulated, and thus both transcription factors were coexpressed (Fig. 4B). This is in accord-

ance with earlier data showing that IL-23 blocks the IL-33-mediated accumulation of Gata3⁺ T_{regs} (20), and, conversely, that the absence of Gata3 leads to the expansion of ROR γ t⁺ T_{regs} (19, 34). This cross-inhibition may act directly, as Foxp3 binds to Gata3, Stat3 (35), and ROR γ t (15, 36), and Gata3 binds to the *Rorc* promoter (19). In contrast, the expression levels of Gata3 remained unchanged in Stat3-deficient T_H17 cells (fig. S11B).

We next investigated the mechanisms of the cell-extrinsic regulation of T_H2 cells by ROR γ t⁺ T_{regs}. Because ROR γ t⁺ T_{regs} express high levels of IL-10 (Fig. 1D and fig. S2B) (15), we assessed whether ROR γ t⁺ T_{regs} regulate T_H2 cells through IL-10, the receptor of which activates Stat3 (37). However, IL-10-deficient mice showed massive expansion of T_H17 cells but no expansion of Gata3⁺ T cells (fig. S12). ROR γ t⁺ T_{regs} also express high levels of CTLA4 (fig. S1C), shown to regulate the expression of CD80 and CD86 on DCs (38). As a consequence, the expression of both CD80 and CD86 by intestinal DCs was increased in *Foxp3*^{Cre} × *Rorc*(γ t)^{FL} mice (Fig. 4C). Furthermore, in mice that lack CTLA4 expression in T_{regs}, Gata3⁺ T cells were significantly expanded in the intestine, whereas T_H1 and T_H17 cells were not (Fig. 4D), and serum levels of IgE were increased (38). These data indicate that ROR γ t⁺ T_{regs} regulate coactivator functions of DCs through CTLA4 and thereby regulate the generation of T_H2 cells in the intestine. Finally, ROR γ t⁺ T_{regs} express high levels of interferon regulatory factor

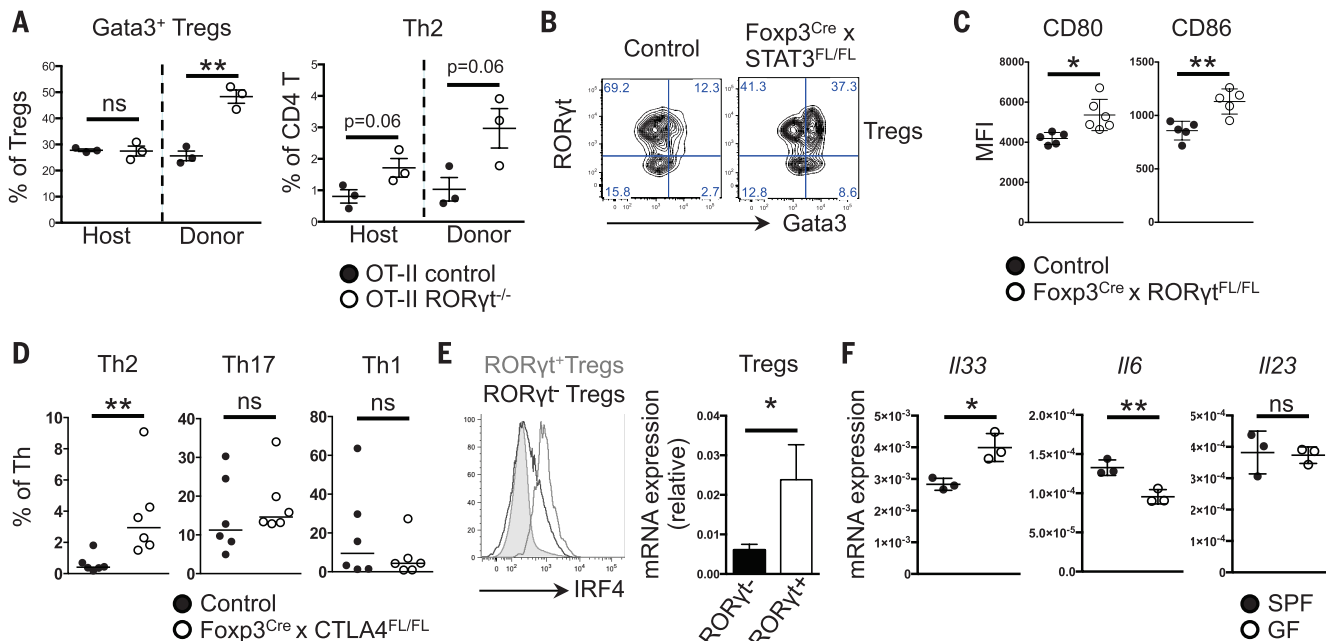


Fig. 4. Mechanisms of regulation by ROR γ t⁺ T_{regs}. (A) Naïve CD4⁺ T cells were isolated from CD45.2⁺ OT-II wild-type or CD45.2⁺ OT-II ROR γ t^{-/-} mice, adoptively transferred into CD45.1⁺ congenic mice, and subsequently fed for 7 days with 1.5% chicken ovalbumin. Frequency of Gata3⁺ T_{regs} and T_H2 cells in the small intestine in host (CD45.1) and donor (CD45.2) cells; *n* = 3 mice. (B) Expression of ROR γ t and Gata3 by T_{regs} in colon of littermate control mice and of *Foxp3*^{Cre} × *Stat3*^{FL/FL} mice. (C) Mean fluorescence intensity (MFI) of CD80 and CD86 on colon DCs; *n* ≥ 5 mice per group. (D) Frequency of Gata3⁺, ROR γ t⁺, or T-bet⁺ (a marker for T_H1 cells) non-T_{reg} CD4⁺ T cells in

littermate control mice (filled symbols) or *Foxp3*^{Cre} × *CTLA4*^{FL/FL} mice (open symbols); *n* = 6 mice per group. (E) Expression of IRF4 protein and transcripts by ROR γ t⁺ T_{regs} and ROR γ t⁻ T_{regs} (gray filled histogram represents effector T cells); *n* = 3 mice (left) or in triplicates (right). (F) Expression of transcripts for IL-33, IL-6, and IL-23 in the ileum of SPF and germfree mice, as determined by quantitative reverse transcriptase polymerase chain reaction; *n* = 3 mice per group. Data are representative of at least two independent experiments. Error bars, ± 1 SD; ns, not significant; **P* < 0.05 [0.06 in (A)]; ***P* < 0.01, as calculated by Student's *t* test or Mann-Whitney test.

4 (IRF4) (Fig. 4E), which endows T_{regs} with the ability to suppress T_H2 responses (39).

Type 2 responses are proposed to perform “housekeeping” repair functions co-opted for defense against large parasites (40). In germfree mice, type 2 immunity is exacerbated (3–6), possibly as a consequence of deregulated repair responses. In accordance with this view, expression of the type 2 cytokine IL-33 by epithelial cells is increased in germfree mice (Fig. 4F and fig. S11C). IL-33 promotes the accumulation and function of microbiota-independent (fig. S3) Gata3⁺ T_{regs} which express high levels of amphiregulin, an epidermal growth factor receptor ligand involved in tissue repair (20). In contrast, the microbiota induces type 3 responses through cytokines such as IL-6 and IL-23 (Fig. 4F) and thereby suppresses the default type 2 responses (Fig. 3 and fig. S13).

A model of the immune system may therefore be proposed in which type 1, 2, and 3 responses, induced by intracellular threats, tissue injury, and extracellular threats, respectively, establish a healthy equilibrium. In that model, T_{reg} subsets are part of each type of responses and play an essential role in balancing the number of effectors that are generated during steady state, infection, or injury. As we have evolved and developed in the presence of microbes, an absence of microbes leads to a loss in type 1 (41) and type 3 responses and, therefore, to deregulated type 2 responses associated with profibrotic and proallergic pathologies (42). A similar mechanism may account for the increase, in industrialized nations, of autoimmune pathologies associated with type 3 immunity (1).

REFERENCES AND NOTES

- J. F. Bach, *N. Engl. J. Med.* **347**, 911–920 (2002).
- G. Priault, C. Nagler-Anderson, *Immunol. Rev.* **206**, 204–218 (2005).
- J. Cahenzli, Y. Köller, M. Wyss, M. B. Geuking, K. D. McCoy, *Cell Host Microbe* **14**, 559–570 (2013).
- K. D. McCoy et al., *Immunity* **24**, 329–339 (2006).
- T. Herbst et al., *Am. J. Respir. Crit. Care Med.* **184**, 198–205 (2011).
- D. A. Hill et al., *Nat. Med.* **18**, 538–546 (2012).
- M. E. Bashir, S. Louie, H. N. Shi, C. Nagler-Anderson, *J. Immunol.* **172**, 6978–6987 (2004).
- S. L. Russell et al., *EMBO Rep.* **13**, 440–447 (2012).
- T. Olszak et al., *Science* **336**, 489–493 (2012).
- I. I. Ivanov et al., *Cell Host Microbe* **4**, 337–349 (2008).
- K. Lathrop et al., *Nature* **478**, 250–254 (2011).
- S. Z. Josefowicz et al., *Nature* **482**, 395–399 (2012).
- I. I. Ivanov et al., *Cell* **126**, 1121–1133 (2006).
- G. Eberl et al., *Nat. Immunol.* **5**, 64–73 (2004).
- M. Lochner et al., *J. Exp. Med.* **205**, 1381–1393 (2008).
- M. Lochner et al., *J. Immunol.* **186**, 1531–1537 (2011).
- A. M. Thornton et al., *J. Immunol.* **184**, 3433–3441 (2010).
- J. M. Weiss et al., *J. Exp. Med.* **209**, 1723–1742, S1 (2012).
- E. A. Wohlfert et al., *J. Clin. Invest.* **121**, 4503–4515 (2011).
- C. Schiering et al., *Nature* **513**, 564–568 (2014).
- K. Atarashi et al., *Science* **331**, 337–341 (2011).
- Y. Furusawa et al., *Nature* **504**, 446–450 (2013).
- P. M. Smith et al., *Science* **341**, 569–573 (2013).
- V. Gaboriau-Routhiau et al., *Immunity* **31**, 677–689 (2009).
- I. I. Ivanov et al., *Cell* **139**, 485–498 (2009).
- C. T. Weaver, R. D. Hattori, P. R. Mangan, L. E. Harrington, *Annu. Rev. Immunol.* **25**, 821–852 (2007).
- E. Bettelli et al., *Nature* **441**, 235–238 (2006).
- C. L. Langrish et al., *J. Exp. Med.* **201**, 233–240 (2005).
- D. Mucida et al., *Science* **317**, 256–260 (2007).
- S. P. Spencer et al., *Science* **343**, 432–437 (2014).
- S. A. van de Pavert et al., *Nature* **508**, 123–127 (2014).
- M. Boirivant, I. J. Fuss, A. Chu, W. Strober, *J. Exp. Med.* **188**, 1929–1939 (1998).

- F. Heller, I. J. Fuss, E. E. Nieuwenhuis, R. S. Blumberg, W. Strober, *Immunity* **17**, 629–638 (2002).
- F. Yu, S. Sharma, J. Edwards, L. Feigenbaum, J. Zhu, *Nat. Immunol.* **16**, 197–206 (2014).
- D. Rudra et al., *Nat. Immunol.* **13**, 1010–1019 (2012).
- L. Zhou et al., *Nature* **453**, 236–240 (2008).
- H. Yasukawa et al., *Nat. Immunol.* **4**, 551–556 (2003).
- K. Wing et al., *Science* **322**, 271–275 (2008).
- Y. Zheng et al., *Nature* **458**, 351–356 (2009).
- J. E. Allen, T. E. Sutherland, *Semin. Immunol.* **26**, 329–340 (2014).
- E. Kernbauer, Y. Ding, K. Cadwell, *Nature* **516**, 94–98 (2014).
- T. A. Wynn, *J. Pathol.* **214**, 199–210 (2008).

ACKNOWLEDGMENTS

We thank B. Ryffel for providing the *Il23a*^{−/−} mice, I. Förster for the *Stat3*^{FL/FL} mice, and C. Leclerc for *Il10*^{−/−} mice. We thank L. Polomack for technical assistance and the members of the Microenvironment and Immunity Unit for discussion and support. The data presented in this manuscript are tabulated in the main paper and in the supplementary materials. This work was supported by the Institut Pasteur, grants from the Agence

Nationale de la Recherche (ANR 11 BSV3 020 01), the Fondation de la Recherche Médicale (DEq. 2010318246), the Fondation Simone e Cino Del Duca from the Institut de France, and an Excellence Grant from the European Commission (MEXT-CT-2006-042374). This study has received funding from the French government's Investissement d'Avenir program, Laboratoire d'Excellence “Integrative Biology of Emerging Infectious Diseases” (grant no. ANR-10-LABX-62-IBED). C.O. was supported by a European Molecular Biology Organization fellowship, S.C. by a Marie Curie intra-European fellowship from the European Union, J.B.W. by Japan Society for the Promotion of Science Young Scientist B grant 15K19129, and M.B. by Boehringer Ingelheim.

SUPPLEMENTARY MATERIALS

www.sciencemag.org/content/349/6251/989/suppl/DC1
Materials and Methods
Figs. S1 to S13
References (43–53)

16 January 2015; accepted 23 June 2015
Published online 9 July 2015
10.1126/science.aac4263

MUCOSAL IMMUNOLOGY

Individual intestinal symbionts induce a distinct population of ROR γ ⁺ regulatory T cells

Esen Sefik,¹ Naama Geva-Zatorsky,¹ Sungwhan Oh,¹ Liza Konnikova,³ David Zemmour,¹ Abigail Manson McGuire,⁴ Dalia Burzyn,^{1*} Adriana Ortiz-Lopez,¹ Mercedes Lobera,⁵ Jianfei Yang,⁵ Shomir Ghosh,⁵ Ashlee Earl,⁴ Scott B. Snapper,³ Ray Jupp,⁶ Dennis Kasper,¹ Diane Mathis,^{1,2,†} Christophe Benoist^{1,2,†}

T regulatory cells that express the transcription factor Foxp3 (Foxp3⁺ T_{regs}) promote tissue homeostasis in several settings. We now report that symbiotic members of the human gut microbiota induce a distinct T_{reg} population in the mouse colon, which constrains immunoinflammatory responses. This induction—which we find to map to a broad, but specific, array of individual bacterial species—requires the transcription factor Ror γ , paradoxically, in that Ror γ is thought to antagonize FoxP3 and to promote T helper 17 (T_H17) cell differentiation. Ror γ 's transcriptional footprint differs in colonic T_{regs} and T_H17 cells and controls important effector molecules. Ror γ , and the T_{regs} that express it, contribute substantially to regulating colonic T_H17/T_H17 inflammation. Thus, the marked context-specificity of Ror γ results in very different outcomes even in closely related cell types.

FoxP3 regulatory T (Foxp3⁺ T_{reg}) cells are essential regulators of immunologic homeostasis and responses (1). Beyond their well-described role in regulating the activity of other immunocytes, T_{regs} located in parenchymal tissues control other, nonimmunological, processes. These “tissue T_{regs} ” include those that reside in visceral adipose tissue and regulate metabolic paramet-

ters (2, 3) and those that help channel inflammatory and regenerative events in injured muscle (4). The activities, transcriptomes, and T cell receptor (TCR) repertoires of these tissue T_{regs} are distinct from their counterparts in secondary lymphoid organs.

Another essential and specific population of tissue T_{regs} resides in the lamina propria (LP) of the digestive tract, in particular in the colon, where these cells modulate responses to commensal microbes [reviewed in (5)]. Colonic T_{regs} are an unusual population that has provoked some contradictory observations. TCRs expressed by colonic T_{regs} show marked reactivity against microbial antigens that seem to be important drivers of their differentiation and/or expansion (6, 7). Many of them appear to arise by conversion from FoxP3[−] conventional CD4⁺ T cells (T_{conv}) (6, 7), although arguments for a

¹Division of Immunology, Department of Microbiology and Immunobiology, Harvard Medical School, Boston, MA 02115, USA.

²Evergrande Center for Immunologic Diseases, Harvard Medical School and Brigham and Women's Hospital, Boston, MA 02115, USA. ³Division of Gastroenterology and Hepatology, Brigham and Women's Hospital, Boston, MA 02115, USA, and Department of Medicine, Harvard Medical School, Boston, MA 02115, USA. ⁴Broad Institute of MIT and Harvard, Cambridge, MA 02142, USA.

⁵Tempo Pharmaceuticals, a GSK Company, Cambridge, MA 02139, USA. ⁶UCB Pharma, Slough, Berkshire, UK.

*Present address: Jounce Therapeutics, Inc., Cambridge, MA 02138, USA.

†Corresponding author. E-mail: cbdm@hms.harvard.edu (D.M.); C.B.)

thymic origin have been made (7). Many colonic T_{regs} express marker profiles (Helios⁺ and Nr1⁺) that differ from T_{regs} of thymic origin [reviewed in (8)], although the importance of these markers has been questioned (5, 8). Accordingly, most studies have found a decreased abundance of colonic T_{regs} in germ-free (GF) mice [reviewed in (5)], and colonization of GF mice by pools of microbes [Schadler's flora (9) or *Clostridia* combinations (10, 11)] elicited the differentiation or expansion of Helios⁺ Nr1⁺ colonic T_{regs} . The abil-

ity of single microbes to induce colonic T_{regs} has been more controversial, and the need for complex combinations (10, 11) has been questioned (12).

The transcriptomes of tissue-resident T_{regs} adapt to their location, most strikingly in terms of transcription factors (TFs) (13), and we searched for such elements in colonic T_{regs} . Comparison of transcriptomes of highly purified CD4⁺ FoxP3⁺ T_{regs} [from *Foxp3*^{ires-gfp} reporter mice (14)] from colon or spleen uncovered 933 differential transcripts [at a fold change >2 and false discovery

rate (FDR) <0.1] [Fig. 1A (top), fig. S1A, and table S1]. These encompassed important signaling and effector pathways (*Icos*, *Gzmb*, *Lag3*, *Areg*, and *Il1rl1*) [Fig. 1A (top) and table S1], shared in a patchwork manner by other tissue T_{regs} . Yet ~39% (at a colon-specific bias of >1.5-fold) had preferential expression in colonic T_{regs} (including *Il10*, *Ctla4*, *Havcr2*, *Ccl20*, *Jak2*, and *Fosl2*) [Fig. 1A (bottom) and table S2]. GeneOntology analysis revealed no enriched function or pathway, except for a high proportion of TFs, including *Ahr*, *Epa1*,

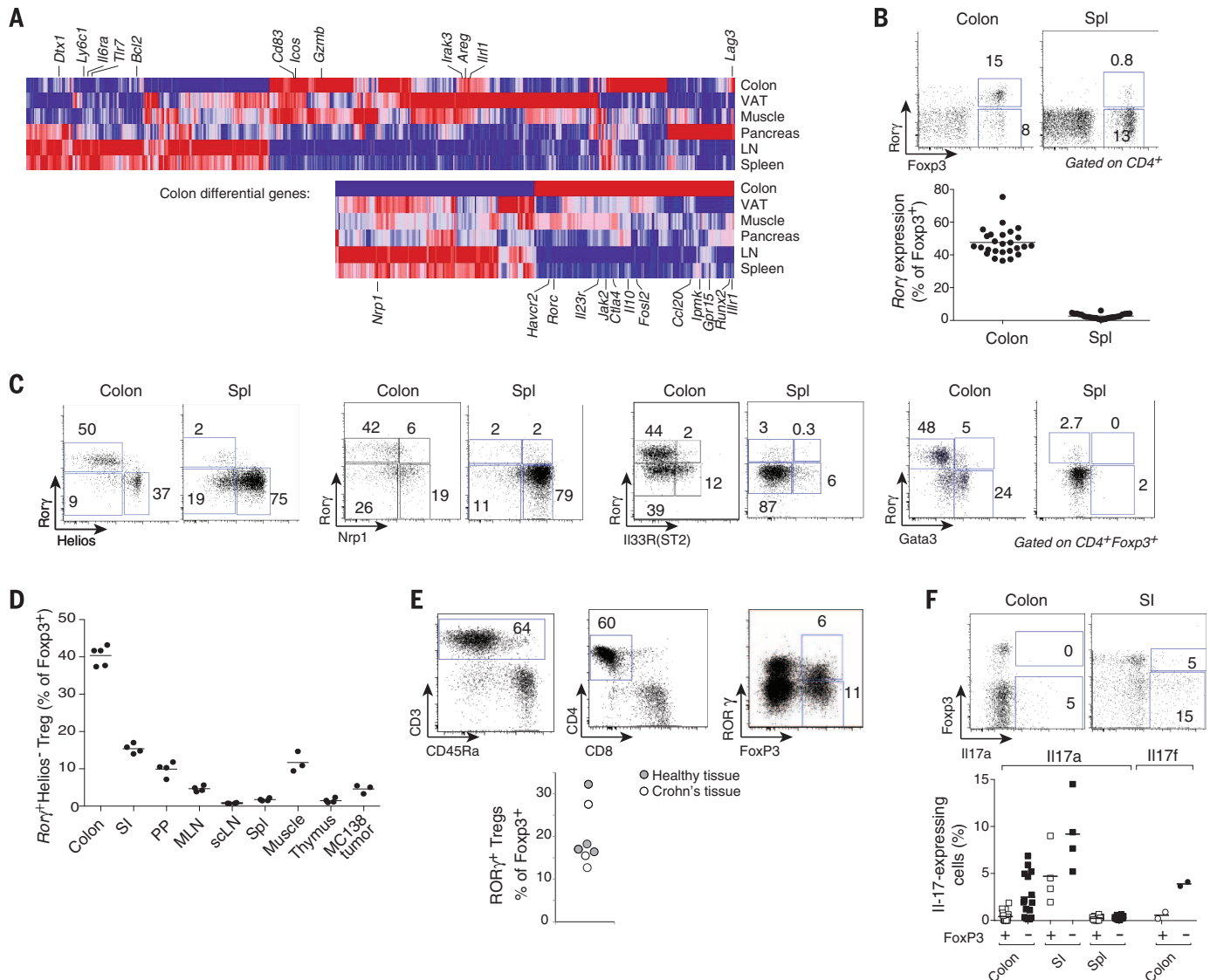


Fig. 1. Rorγ, encoded by Rorc, is preferentially expressed in colonic T_{regs} .

Gene expression profiles from purified T_{reg} cells of various origins. (A) Transcripts that are enriched in tissue and colonic T_{regs} . (Top) Transcripts differentially represented in tissue versus splenic T_{regs} (at a fold change >2). VAT, visceral adipose tissue. (Bottom) Transcripts that are most biased in colonic T_{regs} (fold change >1.5 versus any other tissue T_{reg}). Means of at least two duplicates. (B) Representative flow cytometry plots of CD4⁺ T cells and a compilation of frequencies (bottom) of Rorγ⁺ Helios⁺ T_{regs} within the FoxP3⁺ CD4⁺ TCRβ⁺ population. Each point is an individual mouse. Data are representative of more than three independent experiments. (C) Representative Rorγ versus Helios, Nr1, IL-33R, or Gata3 plots for colon or spleen FoxP3⁺ CD4⁺ TCRβ⁺ T_{regs} (see fig. S2 for quantification). (D) Frequencies of Rorγ⁺ Helios⁺ T_{regs} among FoxP3⁺ CD4⁺ TCRβ⁺

cells of different tissues (SI, small intestinal lamina propria; PP, Peyer's patches; MLN, mesenteric LNs; scLN, subcutaneous LNs; spleen, Spl). Each point is an individual mouse. Data pooled from at least two independent experiments. (E) Flow cytometry analysis of human colon biopsies and frequencies of human Rorγ⁺ T_{regs} within the FOXP3⁺ CD4⁺ CD8⁺ CD3⁺ CD45⁺ population. Healthy tissue samples were endoscopically determined normal areas from chronic constipation or irritable bowel syndrome patients; inflamed tissue was from Crohn's lesions. Each point is an individual patient. Data pooled from five independent experiments. (F) IL-17a (after phorbol 12-myristate 13-acetate + ionomycin activation and intracellular staining) or IL-17f (reporter in *Il17f*^{flp} mice) expression among FoxP3⁺ T_{reg} or FoxP3⁺ T_{conv} mice. Each point is an individual mouse. Data are representative of three independent experiments.

Heyl, *Bcl6*, *Npas2*, *Nr1d1*, and *Maf*. To our surprise, the most differential of these TFs proved to be *Rorc* (encodes Ror γ) (fig. S1B). Ror γ controls many aspects of immunocyte differentiation (15) but is perhaps best known as the key regulator of interleukin-17 (IL-17)-producing CD4⁺ T cells (T_H17), and as a reciprocal antagonist of FoxP3 during in vitro differentiation in which CD4⁺FoxP3⁺ T_{reg} and T_H17 represent alternative cell fates [reviewed in (16)].

Cytometry confirmed that many colonic CD4⁺FoxP3⁺ T_{reg} express Ror γ (40 to 60% in C57BL/6J or other inbred mouse strains) (Fig. 1B and fig. S2A), a phenotype largely absent in spleen or lymph node (LN) and among FoxP3⁺ cells induced in vitro. Helios and Nrp1, described as markers of thymus-derived T_{reg} [reviewed in (8)], were absent on colonic Ror γ ⁺ T_{reg} (Fig. 1C); this absence demarcated three distinct subsets of colonic T_{reg}s with Ror γ ⁺ representing the majority of Helios[−] cells (Fig. 1C and fig. S2, B and C). Consistent with the RNA data, Ror γ ⁺ T_{reg}s were also detected in low proportions in the small intestine (SI) and regenerating muscle (Fig. 1D and fig. S2D). In keeping with a recent report (17), Ror γ ⁺ T_{reg}s were distinct from those expressing the IL-33 receptor, most of which were Helios⁺ (Fig. 1D and fig. S2, B, C, E, and F), and from Gata3^{hi} T_{reg}s

(18), which also belong to the Helios⁺ T_{reg} subset (Fig. 1D and fig. S2, B and C).

We asked whether ROR γ is also expressed by colonic T_{reg}s in humans, by staining cells from healthy or inflamed (Crohn's) colon biopsies. Ror γ ⁺ T_{reg}s were indeed detected at comparable levels in both contexts (Fig. 1E).

Rare T_{reg}s expressing IL-17 and Ror γ have been observed during chronic inflammation or cancer, usually being Helios^{hi} [reviewed in (19)]. We tested IL-17 production in colonic Ror γ ⁺ T_{reg}s. Although IL-17-expressing T_{reg}s could be detected in the SI LP, colonic Ror γ ⁺ T_{reg}s did not secrete detectable IL-17a or f (Fig. 1F).

The properties of this dominant colonic Ror γ ⁺Helios[−] T_{reg} population suggested a link to the gut microbiota. Indeed, GF mice had a lower proportion of Ror γ ⁺ T_{reg}s than their conventionally raised specific pathogen-free (SPF) counterparts (Fig. 2A). During normal maturation in the mouse, Ror γ ⁺ T_{reg}s appeared between 15 and 25 days of age (Fig. 2B), coincident with the changes in the gut microbiota that accompany the transition to solid food. Note that Ror γ ⁺ T_{reg}s appeared a few days after Ror γ [−]Helios[−] T_{reg}s. Antibiotic treatment strongly affected Ror γ ⁺ T_{reg}s (Fig. 2C), a large reduction followed a broad-spectrum antibiotic combination, whereas individual antibi-

otics had less or no effect, which suggested the contribution of several microbes. As the reported impacts of various microbial species on total colonic T_{reg}s have differed (10, 12), we took advantage of a panel of mice generated in a large-scale screen in which GF mice were colonized with a single species from a panel of 22 bacterial species from the human gastrointestinal tract (table S3). A number of microbes elicited colonic Ror γ ⁺ T_{reg}s, with a gradient of responses and, for some, at frequencies comparable with those of SPF mice (Fig. 2D). This restoration of Ror γ ⁺ T_{reg}s was independent of bacterial load and not accompanied by inflammation (fig. S3). Bacteria able to induce Ror γ ⁺ T_{reg} (and colonic FoxP3⁺ T_{reg}s more generally) belonged to several phyla and genera and were not restricted to *Clostridiaceae* (10, 11). Segmented filamentous bacteria (SFB)—which are classic inducers of Ror γ -dependent T_H17 cells (20) and which elicit IL-17-producing T_{reg}s in the SI (21)—were only mediocre inducers of colonic Ror γ ⁺ T_{reg}s which reinforced the distinction between the cell populations. We noticed diversity within the *Bacteroides* genus and assessed a wider *Bacteroides* panel (fig. S4A and table S3). Here again, a range of colonic Ror γ ⁺ T_{reg}s was observed. This distribution did not relate to the *Bacteroides* phylogeny for these strains, and there was no unique correlation

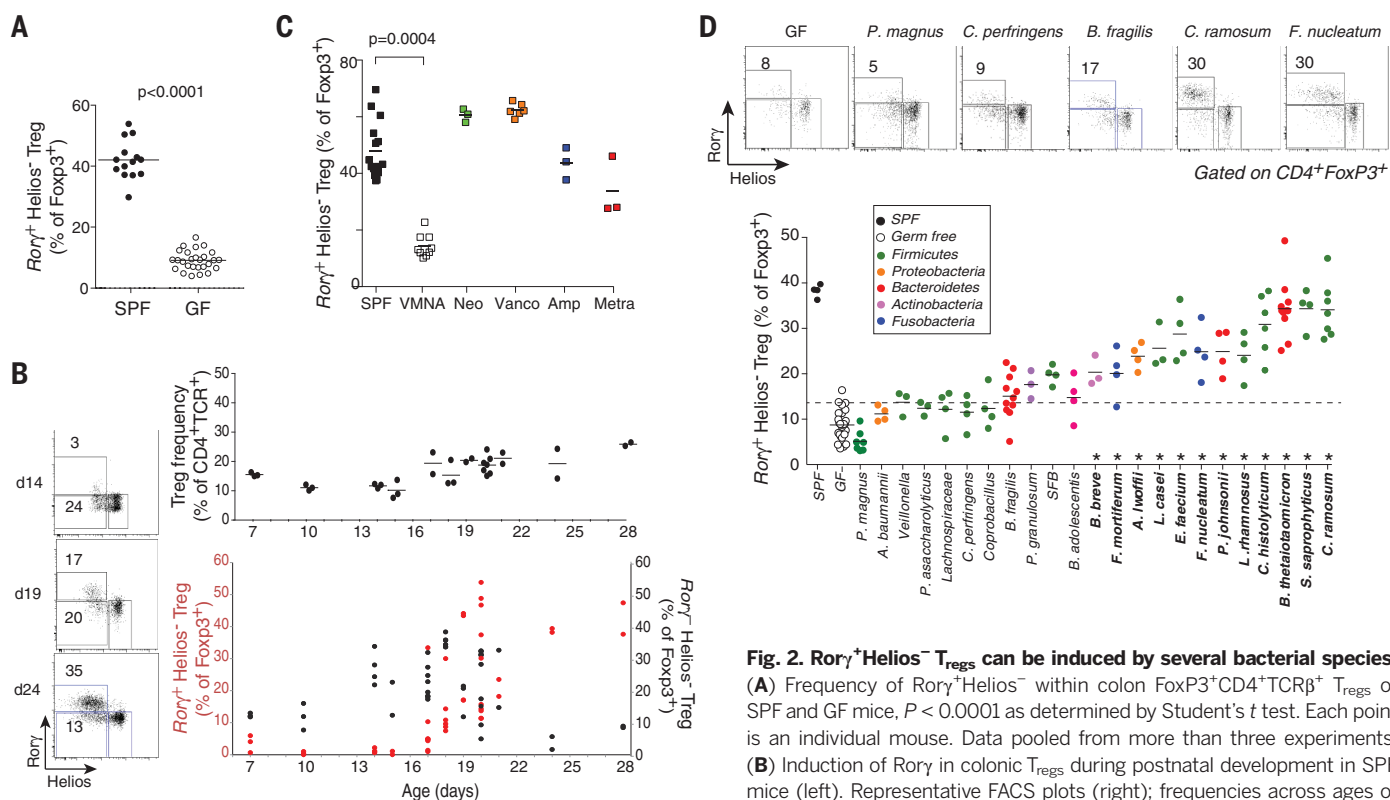


Fig. 2. Ror γ ⁺Helios[−] T_{reg}s can be induced by several bacterial species.

(A) Frequency of Ror γ ⁺Helios[−] within colon FoxP3⁺CD4⁺TCR β ⁺ T_{reg}s of SPF and GF mice, $P < 0.0001$ as determined by Student's t test. Each point is an individual mouse. Data pooled from more than three experiments. (B) Induction of Ror γ in colonic T_{reg}s during postnatal development in SPF mice (left). Representative FACS plots (right); frequencies across ages of FoxP3⁺ T_{reg}s within CD4⁺TCR β ⁺ cells, as well as Ror γ ⁺Helios[−] (red) and

Ror γ [−]Helios[−] (black) cells within T_{reg}s. Each point is an individual mouse. Data pooled from four or more experiments. (C) SPF mice were treated with single antibiotics (abbreviations for neomycin, vancomycin, ampicillin, metronidazole) or all four (VMNA) antibiotics for 4 weeks. Frequency of colonic Ror γ ⁺Helios[−] T_{reg}s within the FoxP3⁺CD4⁺TCR β ⁺ population. $P = 0.0004$, Bonferroni-corrected Student's t test. Each point is an individual mouse. Data pooled from two experiments. (D) GF mice were colonized with single bacterial species, and colonic T_{reg}s were analyzed after 2 weeks (top). Representative plots and frequencies of Ror γ ⁺Helios[−] within FoxP3⁺CD4⁺TCR β ⁺ T_{reg}s, color-coded per phyla (bottom). Each point is an individual mouse. Data are representative one to three experiments for each microbe. *Different from GF at an FDR of <0.05.

between T_{reg} -inducing ability and gene content (fig. S4B). Colonic $Rory^+$ T_{regs} did not appear immediately after GF colonization but only after a few days, again after $Rory^-$ Helios $^-$ cells (fig. S4C).

Several reports have suggested that short-chain fatty acids (SCFAs) promote increased colonic T_{regs} (22–24). To test their relevance to $Rory^+$ T_{regs} , SCFAs were quantified by liquid chromatography–mass spectrometry (LC-MS) in cecal content of monocolonized mice. No significant correlation was observed between any SCFA and $Rory^+$ T_{reg} frequency or to other T_{reg} parameters (fig. S5, A and B, and table S4). In addition, we could not reproduce previously reported effects of oral or rectal SCFA administration (fig. S5, C and D). Although SCFA combinatorial effects or intercolony variation cannot be ruled out, SCFAs cannot alone explain the microbial impact on colonic T_{regs} observed here.

To integrate our observations with intercellular pathways that influence intestinal T cells, we measured the relative abundance of $Rory^+$

T_{regs} in mice lacking receptors for key cytokines and alarmins. Signaling through IL-23, IL-1, or IL-33 receptors was not required to sustain $Rory^+$ T_{regs} , nor was IL-10 (fig. S6, A to D). In fact, only the Helios $^+$ population expanded after IL-33 administration (fig. S6E).

We then asked what transcripts $Rory$ controls in $Rory^+$ T_{regs} and whether $Rory$ is necessary to specify this particular T_{reg} lineage. We compared transcriptomes of $Rory^+$ and $Rory^-$ colonic T_{regs} (sorted from $Foxp3^{Thy1.1} \times Rorc^{gfp}$ intercrossed mice). $Rory^+$ cells were enriched in some, but not all, transcripts of the colonic T_{reg} signature, notably *Il23r*, *Cxcr3*, *Tbx21*, and *Havcr2* (Fig. 3A), as validated at the protein level, including the unexpected CXCR3 (Fig. 3B). Conversely, *Il1r1* (encodes IL-33R), *Nrp1*, and *Ikzf2* were underrepresented in $Rory^+$ T_{regs} .

To further delineate the transcriptional signature of $Rory$ in T_{reg} cells, RNA sequencing profiles were generated from $Nrp1^-$ cells of $Foxp3\text{-}cre$. $Rorc^{fl/fl}$ mice, which have a T_{reg} -selective deletion

of *Rorc* (fig. S7A), or paired wild-type (WT) littermates. Differentially expressed genes were related to the $Rory$ -dependent signature in conventional T_H17 cells (defined from a comparison of SI CD4 $^+$ T cells of mice colonized, or not, with SFB) (Fig. 3C and table S5). Part of the classic T_H17 signature was unrelated to $Rory$ in colonic T_{regs} (blue in Fig. 3C) or *Il1r1* or the canonical T_H17 cytokines *Il17a/f* and *Il22*; some were shared (*Rorc* itself, *Il23r*); and a third segment was controlled by $Rory$ in $Nrp1^-$ colonic T_{regs} but not in T_H17 cells (*Havcr2*, *Irak3*, and *Il1rn*). Thus, the transcriptional footprint of $Rory$ is context-dependent in different T cells.

Next, we explored whether $Rory$ contributes to colonic T_{reg} homeostasis. First, mice were treated for 3 weeks with a pharmacologic $Rory$ antagonist (25), which reduces SI T_H17 levels. This treatment partially decreased both the total frequency of colonic FoxP3 $^+$ cells and their $Rory^+$ component (Fig. 3D). Second, $Foxp3\text{-}cre$. $Rorc^{fl/fl}$ mice—which have no systemic T_{reg} deficiency or *scurfy*-like

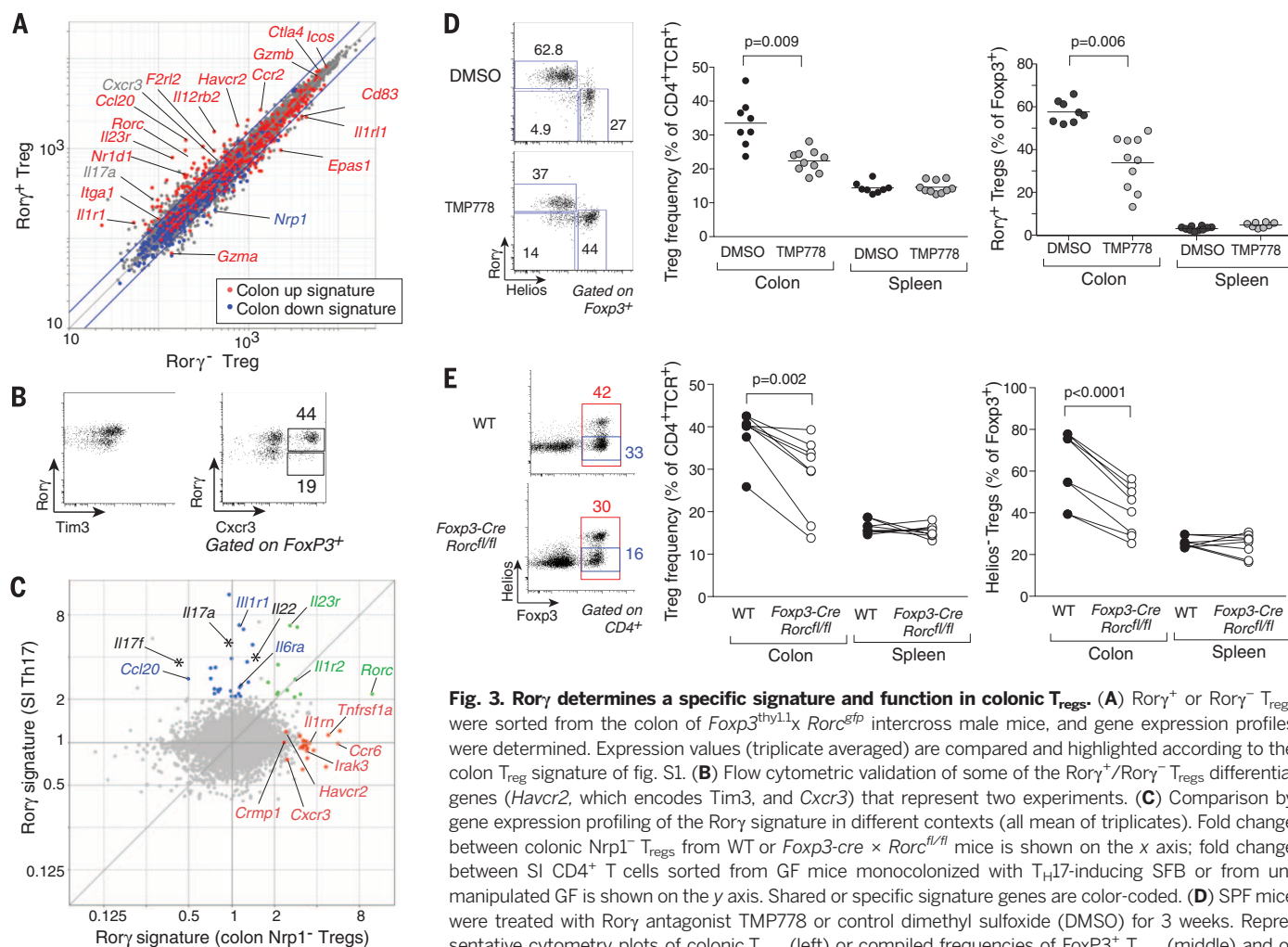


Fig. 3. *Rory* determines a specific signature and function in colonic T_{regs} . (A) $Rory^+$ or $Rory^-$ T_{regs} were sorted from the colon of $Foxp3^{Thy1.1} \times Rorc^{gfp}$ intercross male mice, and gene expression profiles were determined. Expression values (triplicate averaged) are compared and highlighted according to the colon T_{reg} signature of fig. S1. (B) Flow cytometric validation of some of the $Rory^+$ / $Rory^-$ T_{regs} differential genes (*Havcr2*, which encodes *Tim3*, and *Cxcr3*) that represent two experiments. (C) Comparison by gene expression profiling of the $Rory$ signature in different contexts (all mean of triplicates). Fold change between colonic $Nrp1^-$ T_{regs} from WT or $Foxp3\text{-}cre \times Rorc^{fl/fl}$ mice is shown on the x axis; fold change between SI CD4 $^+$ T cells sorted from GF mice monocolonized with T_H17 -inducing SFB or from unmanipulated GF is shown on the y axis. Shared or specific signature genes are color-coded. (D) SPF mice were treated with $Rory$ antagonist TMP778 or control dimethyl sulfoxide (DMSO) for 3 weeks. Representative cytometry plots of colonic T_{regs} (left) or compiled frequencies of FoxP3 $^+$ T_{regs} (middle) and of $Rory^+$ Helios $^-$ (right) within FoxP3 $^+$ CD4 $^+$ TCR $^+$ T_{regs} ($P = 0.009$ as determined by Student's t test). (E) Analysis of $Rory$ -deficient T_{regs} from $Foxp3\text{-}cre \times Rorc^{fl/fl}$ mice or control ($Foxp3\text{-}cre$. $Rorc^{+/+}$) littermates. Cytometry plots of colonic T_{regs} (left) or compiled frequencies of FoxP3 $^+$ T_{regs} (middle) and of $Rory^+$ Helios $^-$ (right) within FoxP3 $^+$ CD4 $^+$ TCR $^+$ T_{regs} (P values were determined by paired Student's t test). Each point is an individual mouse. Data are representative of more than three independent experiments.

Each point is an individual mouse. Data are representative of two or more independent experiments. Cytometry plots of colonic T_{regs} (left) or compiled frequencies of FoxP3 $^+$ T_{regs} (middle) and of $Rory^+$ Helios $^-$ (right) within FoxP3 $^+$ CD4 $^+$ TCR $^+$ T_{regs} (P values were determined by paired Student's t test). Each point is an individual mouse. Data are representative of more than three independent experiments.

pathology nor any change in FoxP3 intensity—showed a reduced frequency of colonic T_{regs}, and, more specifically, of Helios⁺ T_{regs}; the proportion of Helios⁺ Gata3⁺ T_{regs} was correspondingly increased (Fig. 3E and fig. S7B).

We noted that the loss of Rorγ⁺ T_{regs} in *Foxp3-cre.Rorc^{fl/fl}* mice led to increased production of IL-17 and interferon-γ (IFN-γ) but not T_H2 cytokines like IL-5 or IL-13, by T_{conv} cells in colons of otherwise unchallenged mice (Fig. 4A), which suggested a decreased ability of colonic T_{regs} lacking Rorγ to regulate inflammatory responses. We thus assessed *Foxp3-cre.Rorc^{fl/fl}* mice in the trinitrobenzenesulfonic acid (TNBS)-induced colitis model and found an exacerbation of disease severity, in colitis score and histopathology (Fig. 4, B and C). Furthermore, after TNBS challenge of GF mice monocolonized with different microbes, the frequency of Rorγ⁺ T_{regs} correlated with the colitis score (Fig. 4D). These results imply a non-redundant role for Rorγ and Rorγ⁺ T_{regs} in colonic homeostasis.

Thus, Rorγ contributes unexpectedly but in an important way to the T_{reg} response to commensal microbes. This role contrasts with the accepted dichotomy between FoxP3 and Rorγ, a notion stemming mainly from their antagonism

in vitro (14, 26–28); perhaps this relation has been overinterpreted. There had been indications that the two TFs are not incompatible (19), but the present data suggest a collaborative transcriptional impact, consistent with the overlap between their chromatin-binding sites (29). The context-specificity of Rorγ's transcriptional footprint is in line with its broad involvement in many immunological and nonimmunological processes (organogenesis, circadian rhythm, and lipid metabolism) (15, 30). Rorγ-dependent *IL23R* expression in T_{regs} also raises the intriguing speculation that human *IL23R* genetic variants associated with inflammatory bowel disease (31) might involve balancing effects in effector and regulatory T cells.

Rorγ⁺ T_{regs} form the majority of the Helios⁺ T_{regs} that differentiate locally in response to antigens of commensal microbes in the gut (6) and do not respond to the alarmin IL-33, in contrast to Gata3⁺ Helios⁺ cells that expand during tissue damage (17, 18). Mutually exclusive expression of Gata3 and Rorγ in colonic T_{regs} suggests that they may distinguish T_{reg} responses to symbiotic (Rorγ) versus aggressive (Gata3) microbes. Contrary to expectations, many individual microbes proved able to elicit Rorγ⁺ and Helios⁺ T_{regs}, a property not restricted to *Clostridiaceae* (10). The graded range

suggests that several mechanisms may be involved. The molecular mediator of Rorγ⁺ T_{reg} induction remains elusive but is unlikely to be SCFAs alone. Rorγ⁺ induction must follow different routes in T_H17 versus colonic T_{regs}, because the best Rorγ⁺ T_{reg} inducers do not affect SI T_H17 and vice versa.

In conclusion, these studies show Rorγ as a uniquely microbe-responsive factor induced in two different cellular contexts, in response to different microbes, with distinct transcriptional consequences, and with diametrically opposite functional outcomes.

REFERENCES AND NOTES

- S. Z. Josefowicz, L. F. Lu, A. Y. Rudensky, *Annu. Rev. Immunol.* **30**, 531–564 (2012).
- M. Feuerer et al., *Nat. Med.* **15**, 930–939 (2009).
- D. Cipolletta et al., *Nature* **486**, 549–553 (2012).
- D. Burzyn et al., *Cell* **155**, 1282–1295 (2013).
- T. L. Ai, B. D. Solomon, C. S. Hsieh, *Immunol. Rev.* **259**, 60–74 (2014).
- S. K. Lathrop et al., *Nature* **478**, 250–254 (2011).
- A. Cebula et al., *Nature* **497**, 258–262 (2013).
- A. M. Bilate, J. J. Lafaille, *Annu. Rev. Immunol.* **30**, 733–758 (2012).
- M. B. Geuking et al., *Immunity* **34**, 794–806 (2011).
- K. Atarashi et al., *Science* **331**, 337–341 (2011).
- K. Atarashi et al., *Nature* **500**, 232–236 (2013).
- J. J. Faith, P. P. Ahern, V. K. Ridaura, J. Cheng, J. I. Gordon, *Sci. Transl. Med.* **6**, 220ra11 (2014).
- D. Burzyn, C. Benoist, D. Mathis, *Nat. Immunol.* **14**, 1007–1013 (2013).
- E. Bettelli et al., *Nature* **441**, 235–238 (2006).
- D. J. Cua, C. M. Tato, *Nat. Rev. Immunol.* **10**, 479–489 (2010).
- T. Korn, E. Bettelli, M. Oukka, V. K. Kuchroo, *Annu. Rev. Immunol.* **27**, 485–517 (2009).
- C. Schiering et al., *Nature* **513**, 564–568 (2014).
- E. A. Wohlfert et al., *J. Clin. Invest.* **121**, 4503–4515 (2011).
- R. Du, H. Zhao, F. Yan, H. Li, J. Leukoc. Biol. **96**, 39–48 (2014).
- I. I. Ivanov et al., *Cell* **139**, 485–498 (2009).
- M. Lochner et al., *J. Immunol.* **186**, 1531–1537 (2011).
- N. Arpaia et al., *Nature* **504**, 451–455 (2013).
- Y. Furusawa et al., *Nature* **504**, 446–450 (2013).
- P. M. Smith et al., *Science* **341**, 569–573 (2013).
- J. Skepner et al., *J. Immunol.* **192**, 2564–2575 (2014).
- L. Zhou et al., *Nature* **453**, 236–240 (2008).
- X. O. Yang et al., *Immunity* **29**, 44–56 (2008).
- D. Mucida et al., *Science* **317**, 256–260 (2007).
- S. Xiao et al., *Immunity* **40**, 477–489 (2014).
- A. M. Jetten, *Nucl. Recept. Signal.* **7**, e003 (2009).
- C. Abraham, J. H. Cho, *Annu. Rev. Med.* **60**, 97–110 (2009).

ACKNOWLEDGMENTS

We thank A. Onderdonk, C. Dong, A. Rudensky, R. Lee, V. Kuchroo, and L. Bry for microbial and mouse strains and S. Edwards, A. T. Sherpa, K. Hattori, K. Rothamel, and R. Cruse for help with mice or profiling. TMP778 is available to academic investigators from G.S.K. under a material transfer agreement that does not unduly affect or prohibit publication. The data are tabulated in supplementary materials and deposited at the National Center for Biotechnology Information, NIH, Gene Expression Omnibus (GSE68009). E.S., N.G.-Z., D.K., D.M., C.B., and Harvard Medical School have filed a provisional patent application related to work presented in this paper. This work was supported by NIH R01-AI151530 and R56-AI110630 and the J.P.B. Foundation (D.M. and C.B.); a Sponsored Research Agreement from UCB Pharma (D.M., C.B., D.K., and A.E.); the Helmsley Charitable Trust and the Wolpew Family Chair in the Center for Inflammatory Bowel Disease Treatment and Research (S.B.S.). E.S. and D.Z. were supported by fellowships from the Boehringer Ingelheim Fonds, N.G.-Z. by the Human Frontier Science Program and European Molecular Biology Organization (ALTF 251-2011) fellowships and the Weizmann—National Postdoctoral Award for Advancing Women in Science.

SUPPLEMENTARY MATERIALS

www.sciencemag.org/content/349/6251/993/suppl/DC1

Materials and Methods

Figs. S1 to S6

Tables S1 to S5

References (32–58)

17 February 2015; accepted 22 July 2015
Published online 13 August 2015

10.1126/science.aaa9420

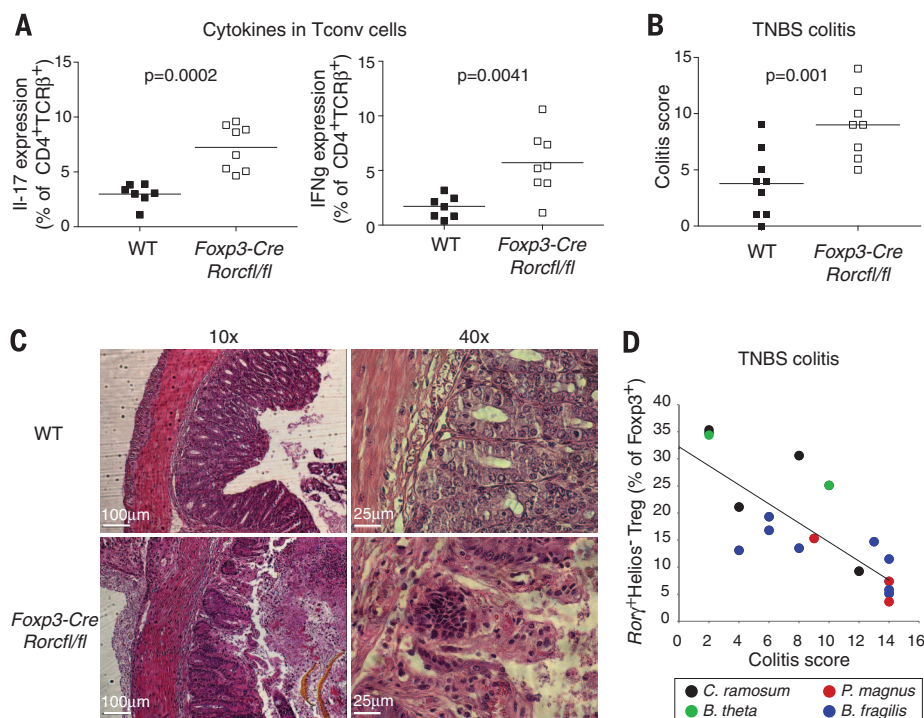


Fig. 4. Rorγ⁺ T_{regs} control gut inflammation. (A) Frequency of IL-17a and IFN-γ expression in Foxp3⁺ CD4⁺ T_{conv} cells from *Foxp3-cre × Rorc^{fl/fl}* mice and control *Foxp3-cre × Rorc^{+/+}* littermates at steady state; *P* values determined by paired Student's *t* test. Each point is an individual mouse. Data are representative of three or more independent experiments. (B and C) Colitis score (B) and histology (C) of *Foxp3-cre × Rorc^{fl/fl}* mice and control *Foxp3-cre × Rorc^{+/+}* littermates challenged with TNBS, calculated on the basis of weight loss, histologic score, and other physical parameters; *P* value as determined by paired Student's *t* test. Each point is an individual mouse. Data representative of more than three independent experiments. (D) Correlation between TNBS-colitis score (*x* axis) with frequency of Rorγ⁺ Helios⁻ T_{regs} within colonic T_{regs} in GF mice monocolonized for 2 weeks with bacteria that elicit different levels of Rorγ⁺ Helios⁻ T_{regs} before TNBS colitis induction. *B. theta*, *B. theta*Δ*toam*. Pearson's correlation coefficient *r* = 0.82, *P* < 0.0001. Each point is an individual mouse. Data pooled from four experiments.

1ST YEAR IN
PHOENIX



2016 **MRS**® SPRING MEETING & EXHIBIT
March 28–April 1, 2016 | **Phoenix, Arizona**

CALL FOR PAPERS

Abstract Submission Opens
September 15, 2015

Abstract Submission Deadline
October 15, 2015

CHARACTERIZATION AND MODELING OF MATERIALS

- CM1 New Frontiers in Aberration Corrected Transmission Electron Microscopy
- CM2 Quantitative Tomography for Materials Research
- CM3 Mechanics and Tribology at the Nanoscale—*In Situ* and *In Silico* Investigations
- CM4 Verification, Validation and Uncertainty Quantification in Multiscale Materials Simulation

ENERGY AND ENVIRONMENT

- EE1 Emerging Materials and Phenomena for Solar Energy Conversion
- EE2 Advancements in Solar Fuels Generation—Materials, Devices and Systems
- EE3 Materials and Devices for Full Spectrum Solar Energy Harvesting
- EE4 Electrode Materials and Electrolytes for Lithium and Sodium Ion Batteries
- EE5 Next-Generation Electrical Energy Storage Chemistries
- EE6 Research Frontiers on Liquid-Solid Interfaces in Electrochemical Energy Storage and Conversion Systems
- EE7 Mechanics of Energy Storage and Conversion—Batteries, Thermoelectrics and Fuel Cells
- EE8 Grid-Scale Energy Storage
- EE9 Hydrogen and Fuel Cell Technologies for Transportation—Materials, Systems and Infrastructure
- EE10 Recent Advances in Materials for Carbon Capture
- EE11 Caloric Materials for Renewable Energy Applications
- EE12 Radiation Damage in Materials—A Grand Multiscale Challenge
- EE13 Actinides—Fundamental Science, Applications and Technology
- EE14 Titanium Oxides—From Fundamental Understanding to Applications
- EE15 Materials for Sustainable Development—Integrated Approaches

ELECTRONICS AND PHOTONICS

- EP1 Organic Excitonic Systems and Devices
- EP2 Silicon Carbide—Substrates, Epitaxy, Devices, Circuits and Graphene
- EP3 Perovskite-Based Photovoltaics and Optoelectronic Devices
- EP4 Emerging Silicon Science and Technology
- EP5 Metal Oxide Hetero-Interfaces in Hybrid Electronic Platforms
- EP6 Integration of Heterovalent Semiconductors and Devices
- EP7 Material and Device Frontiers for Integrated Photonics
- EP8 Resonant Optics—Fundamentals and Applications
- EP9 Materials and Processes for Nonlinear Optics
- EP10 Optoelectronic Devices of Two-Dimensional (2D) Materials
- EP11 Novel Materials for End-of-Roadmap Devices in Logic, Power and Memory
- EP12 Materials Frontiers in Semiconductor Advanced Packaging
- EP13 Tailoring Superconductors—Materials and Devices from Basic Science to Applications
- EP14 Materials for Next-Generation Displays
- EP15 Diamond Power Electronic Devices

MATERIALS DESIGN

- MD1 Materials, Interfaces and Devices by Design
- MD2 Tuning Properties by Elastic Strain Engineering—from Modeling to Making and Measuring
- MD3 Functional Oxide Heterostructures by Design
- MD4 Phase-Change Materials and Applications
- MD5 Fundamentals of Organic Semiconductors—Synthesis, Morphology, Devices and Theory
- MD6 Electronic Textiles
- MD7 Advances in Lanthanide Materials for Imaging, Sensing, Optoelectronics and Recovery/Recycling
- MD8 Multiscale Behavior of Materials in Extreme Environments
- MD9 Magnetic Materials—From Fundamentals to Applications
- MD10 Micro-Assembly Technologies

NANOTECHNOLOGY

- NT1 Functional Nanostructures and Metamaterials for Solar Energy and Novel Optical Phenomena
- NT2 Oxide and Chalcogenide-Based Thin Films and Nanostructures for Electronics and Energy Applications
- NT3 Carbon Nanofluidics
- NT4 Emerging Non-Graphene 2D Materials
- NT5 Nanodiamonds—Fundamentals and Applications
- NT6 Colloidal Nanoparticles—From Synthesis to Applications
- NT7 Nanoparticle Characterization and Removal
- NT8 Silicon Nanostructures—Doping, Interface Effects and Sensing

SOFT MATERIALS AND BIOMATERIALS

- SM1 Liquid Crystalline Materials—Displays and Beyond
- SM2 Bioinspired Dynamic Materials—Synthesis, Engineering and Applications
- SM3 Soft Materials for Compliant and Bioinspired Electronics
- SM4 Engineering Biointerfaces with Nanomaterials
- SM5 Surfaces and Interfaces for Biomaterials
- SM6 Transient and Biologically-Inspired Electronics
- SM7 Future Healthcare Needs through Biomaterials, Bioengineering and the Cellular Building Block
- SM8 Bioinspired Metal Nanoparticles—Synthesis, Properties and Application
- SM9 Structure and Properties of Biological Materials and Bioinspired Designs
- SM10 Biofabrication-Based Biomaterials and Tissues

www.mrs.org/spring2016

Meeting Chairs

Christopher A. Bower X-Celeprint Ltd.
Andrew M. Minor University of California, Berkeley
Lawrence Berkeley National Laboratory
Roger Narayan UNC/NCSU Joint Department
of Biomedical Engineering
Izabela Szlufarska University of Wisconsin-Madison
Osamu Ueda Kanazawa Institute of Technology

Don't Miss These Future MRS Meetings!

2016 MRS Fall Meeting & Exhibit
November 27 – December 2, 2016
Boston, Massachusetts

2017 MRS Spring Meeting & Exhibit
April 17 – 21, 2017
Phoenix, Arizona

MRS MATERIALS RESEARCH SOCIETY®
Advancing materials. Improving the quality of life.

506 Keystone Drive • Warrendale, PA 15086-7573
Tel 724.779.3003 • Fax 724.779.8313
info@mrs.org • www.mrs.org

Two Faculty Career Features

THERE'S A SCIENCE TO REACHING SCIENTISTS.

September 18, 2015

Reserve ads by September 1
Ads accepted until September 14

October 9, 2015

Reserve ads by September 22
Ads accepted until October 5



For recruitment in science, there's only one

Science

Special packages
available when
you advertise in
both features

Hiring faculty? Whatever your timing, we've got two special features for your **Faculty ads** this fall! The September 18 feature covers strategies and resources to build teaching skills. The October 9 feature offers strategies for moving into academia from other industries.

What makes *Science* the best choice for recruiting?

- Read and respected by 570,400 readers around the globe
- 60% of our weekly readers work in academia and 67% are Ph.D.s. *Science* connects you with more scientists in academia than any other publication
- Your ad dollars support AAAS and its programs, which strengthens the global scientific community.

Why choose these faculty features for your advertisement?

- Relevant ads lead off the career section with special Faculty banner
- September 18 issue will be distributed at the Biotechnica Meeting in Hanover, Germany, 6–8 October.

Expand your exposure. Post your print ad online to benefit from:

- Link on the job board homepage directly to Faculty jobs
- Dedicated landing page for faculty positions
- Additional marketing driving relevant job seekers to the job board.

SCIENCECAREERS.ORG

ScienceCareers

FROM THE JOURNAL SCIENCE  AAAS

To book your ad: advertise@sciencecareers.org

The Americas
202-326-6582

Japan
+81-3-3219-5777

Europe/RoW
+44 (0) 1223-326500

China/Korea/Singapore/Taiwan
+86-186-0082-9345

JOIN AAAS

Get instant access to *Science*. Support all of the sciences.



The American Association for the Advancement of Science (AAAS) is a non-profit community that is open to everyone, from Nobel laureates to high school students. Ours is a global membership of over 120,000 people who believe in the power of science to make the world a better place.

From the moment you join, you get immediate access to everything that AAAS's award-winning journal *Science* has to offer, including:

- 51 weeks of home delivery of *Science*;
- Instant online retrieval of every *Science* article ever published, from today, dating back to 1880;
- Anytime, anywhere access via the *Science* mobile site and apps for Android, iPad, and iPhone devices;
- Members-only newsletters; and more.

As a member, you are also making a critical contribution to AAAS's efforts to provide a public voice for all of science. With public skepticism about science increasing, and public funding for research more uncertain than ever, this work has never been more important.

AAAS is hard at work promoting science in government offices, in schools, and in the public commons all around the world—with programs like AAAS Senior Scientists and Engineers, which brings volunteer scientists into public school classrooms, or our sweeping petition drives calling for the preservation of federal R&D funding.

Visit promo.aaas.org/joinaaas and join today. Together we can make a difference.



Grete Lundbeck European Brain Research Foundation

Call for Nominations for

THE BRAIN PRIZE

THE PRIZE OF €1 MILLION WILL BE AWARDED IN COPENHAGEN JULY 2016

Nominations by 15 September 2015

Nominations will be reviewed by the Selection Committee:

HUDA AKIL, USA

ANDERS BJÖRKLUND, SWEDEN, VICE-CHAIRMAN

COLIN BLAKEMORE, UNITED KINGDOM, CHAIRMAN

JOSEPH COYLE, USA

TOM JESSELL, USA

RANGA R. KRISHNAN, SINGAPORE

PHILIP SCHELTENS, THE NETHERLANDS

IRENE TRACEY, UNITED KINGDOM

FOR THE NOMINATION FORM AND DETAILS OF THE NOMINATION PROCEDURE, PLEASE VISIT:

WWW.THEBRAINPRIZE.ORG

Prize Winners 2015

Winfried Denk, Max Planck Institute of Neurobiology, Germany, Arthur Konnerth, Technical University Munich, Germany,

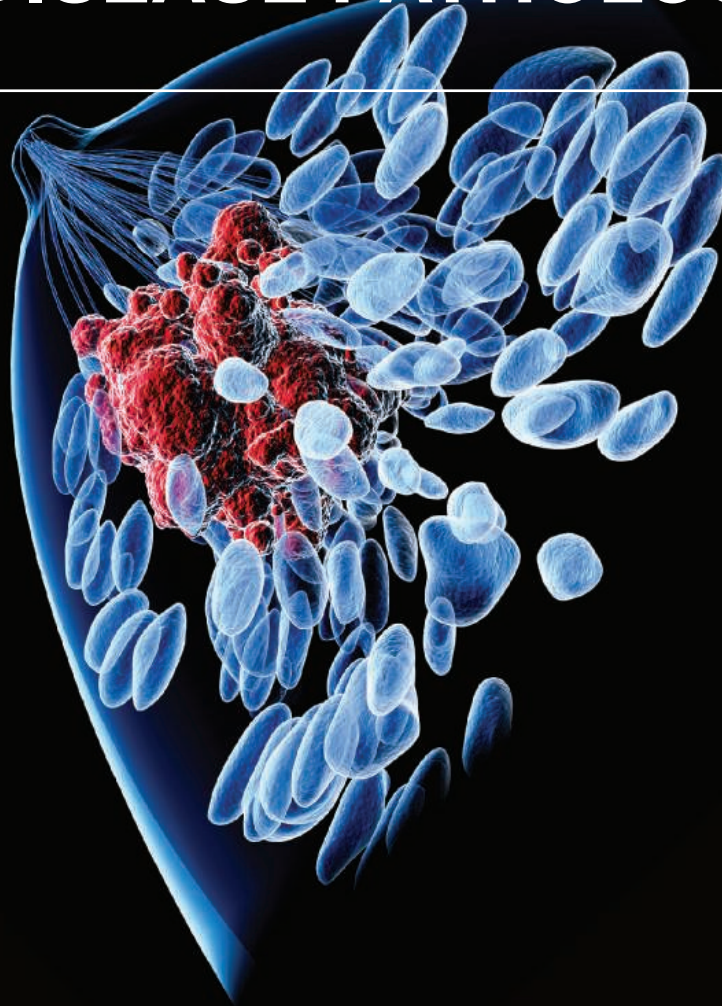
Karel Svoboda, Janelia Research Campus, HHMI, USA, David W. Tank, Princeton University, USA

GRETE LUNDBECK
EUROPEAN
BRAIN RESEARCH
FOUNDATION

THE
BRAIN
PRIZE

The Brain Prize recognizes and rewards outstanding contributions to European neuroscience, from basic to clinical

DOES YOUR LAB SEEK TO UNDERSTAND MECHANISMS OF DRUG RESISTANCE OR DISEASE PATHOLOGY?

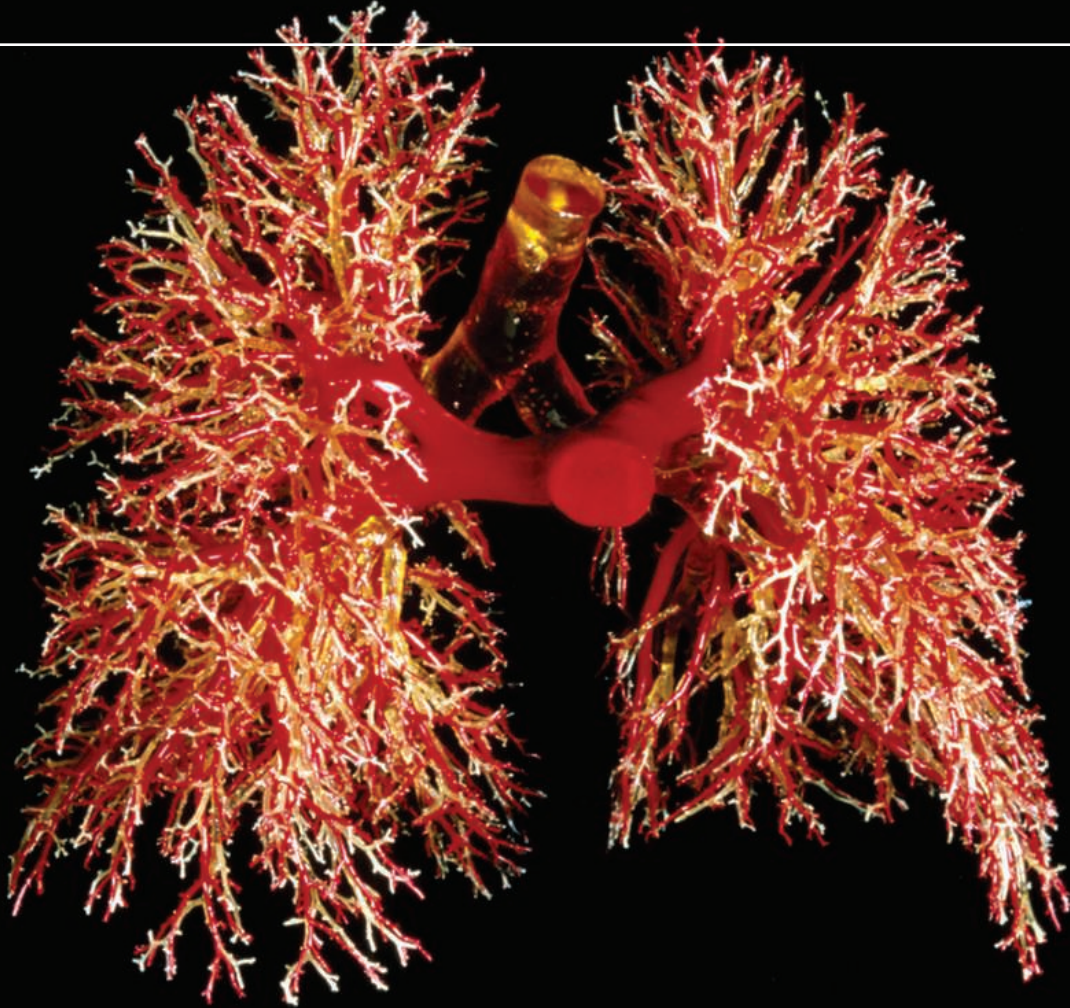


Leslie K. Ferrarelli, "Focus Issue: Refining the War on Cancer", *Sci. Signal.* 7, 318eg2 (2014). Image: Raycat/iStockphoto

Science Signaling | AAAS
CELL SIGNALING IN PHYSIOLOGY AND DISEASE

Find out more about the scope of the journal and submit your research today!
ScienceSignaling.org

WILL YOUR RESEARCH LEAD TO BETTER LIVES FOR PATIENTS?



Gopinath Sutendra and Evangelos D. Michelakis, "Pulmonary Arterial Hypertension: Challenges in Translational Research and a Vision for Change", *Sci. Transl. Med.* 5, 208sr5 (2013) Credit: Science Source

Science Translational Medicine |  AAAS

INTEGRATING SCIENCE, ENGINEERING, AND MEDICINE

Find out more about the scope of the journal and submit your research today!

ScienceTranslationalMedicine.org



Lab Management System

The NuGenesis Lab Management System is a unique and powerful alternative to a traditional laboratory information management system with advances that enable deeper insight into scientific challenges, accelerated decision-making, better business results, and compliance with government regulations. The NuGenesis Lab Management System offers high-impact functionality. New advances include NuGenesis SampleShare, an optional, secure webclient for sample submissions and results management; NuGenesis Stability, a complete stability protocol management and testing solution to facilitate a consistent regimented workflow across lab operations; NuGenesis Connectors, a bidirectional link between lab systems and business applications; and Paradigm Scientific Search, a fully integrated scientific search solution for text, documents, and science objects. Uniquely combining data, workflow, and sample management capabilities to support the entire product lifecycle from discovery through manufacturing, the NuGenesis Lab Management System is a user-centric platform that encompasses a scientific data management system, electronic laboratory notebook, and laboratory execution system.

Waters Corporation

For info: 800-252-4752

www.waters.com/nugenesis

SFE Bio-Botanical Extraction System

A new 10 L extraction vessel is now available for the SFE Bio-Botanical Extraction System (BBES), a multivessel supercritical fluid extraction (SFE) system that rapidly fractionates and extracts large quantities of desired components from a multitude of botanical matrices. The BBES functions as a bulk-scale, high-pressure separator for collecting extracted compounds. The 10 L vessel doubles current capacity and can be acquired as an add-on to installed systems. Furthermore, a new computer-controlled automation module that allows the SFE BBES to extract the high-quality product in less time with even less manual intervention is expected to be available soon. The new automation module will provide greater flexibility for unattended operation through seamless transition between the first and second extractions without user intervention, thereby extending uninterrupted operation even further. The SFE BBES uses supercritical CO₂ as its mobile phase, which has been shown to be a safer alternative to organic solvents or hydrocarbons (butane).

Waters Corporation

For info: 800-252-4752

www.waters.com



Conical Tubes

With the introduction of the two 15 mL and 50 mL screw cap tubes, Eppendorf Tubes now cover the entire volume range from 0.5 mL to 50 mL. The newly designed screw caps provide not only optimal sealing properties, but with their grooved and multisurface side-contour, they simultaneously ensure a secure, slip-free grip. The optimized handling features further facilitate safe opening and closing of the tubes via convenient one-handed operation. The Eppendorf Conical Tubes are further characterized by an expanded purity grade: they are not only sterile and pyrogen-free, but they are also free from DNases and RNases as well as human and bacterial DNA. These features make them ideally suited for cell biology applications in a sterile environment, which rely on freedom from contaminations with DNA. The highest level of manufacturing precision and robustness ensures smooth performance of these tubes in laboratory instruments such as centrifuges or thermomixers.

Eppendorf

For info: 800-645-3050

www.eppendorf.com/conicals

Heat-Stabilization System

The Denator Stabilizer heat-stabilization system preserves lipids at close to in vivo levels. To preserve lipids in a reliable manner prior to mass spectrometry-based analysis is pivotal to accurately quantify and identify potential biomarkers and perform disease research. Lipids play several key roles in biological systems including storing energy, cell signaling, and acting as components of cell membranes. However, it is often difficult to quantify accurate levels of lipids in tissue samples due to post-sampling changes that cause substantial variations in detected lipid levels during sample preparation. Denator's Stabilizer system has been shown to stop degradation and other post-sampling changes immediately and permanently. This ensures a stable sample from the moment of excision until the point of analysis, which increases the accuracy and quality of analytical results. By using heat stabilization, scientists are able to drastically improve the consistency of sample quality and discover new, biologically relevant information without needing to use inhibitors.

Denator AB

For info: +46-(0)-70-771-59-67

www.denator.com

Xeno-Free and Endotoxin-Free Human Cytokines

A complete new range of commonly used human cytokines and growth factors is now available. Unlike most other commercially available cytokine products, ActiveMax cytokines are

expressed exclusively in human cells under strict animal-free and xeno-free conditions. Therefore, they are uniquely suitable for human cell culture and assay development. Endotoxin and other nonhuman components can provoke an immune response in human systems. These contaminations are significant complicating factors for human cell culture experiments, in particular those relevant to human cell therapy or other clinical applications. ActiveMax cytokines are exclusively produced in a serum-free, animal component-free, and chemically defined cell culture system. These cytokines are absolutely xeno-free, and have an endotoxin level of less than 1.0 Ehrlich unit per microgram. The bulk production of ActiveMax cytokines relies entirely on the human cellular machinery provided by the HEK293 cells, and therefore retains their authentic posttranslational processing, which translates into high bioactivity and stability.

AMS Biotechnology

For info: +44-(0)-1235-828200

www.amsbio.com/activemax-cytokines.aspx

Electronically submit your new product description or product literature information! Go to www.sciencemag.org/products/newproducts.dtl for more information.

Newly offered instrumentation, apparatus, and laboratory materials of interest to researchers in all disciplines in academic, industrial, and governmental organizations are featured in this space. Emphasis is given to purpose, chief characteristics, and availability of products and materials. Endorsement by *Science* or AAAS of any products or materials mentioned is not implied. Additional information may be obtained from the manufacturer or supplier.

want new technologies?

antibodies

apoptosis

biomarkers

cancer

cytometry

data

diseases

DNA

epigenetics

genomics

immunotherapies

medicine

microbiomics

microfluidics

microscopy

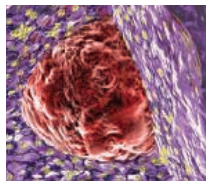
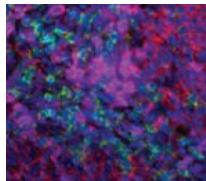
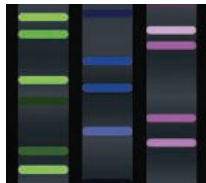
neuroscience

proteomics

sequencing

toxicology

transcriptomics



watch our **webinars**

Learn about the latest breakthroughs, new technologies, and ground-breaking research in a variety of fields. Our expert speakers explain their quality research to you and answer questions submitted by live viewers.

VIEW NOW!

webinar.sciencemag.org

Science
AAAS

Brought to you by the *Science*/AAAS
Custom Publishing Office



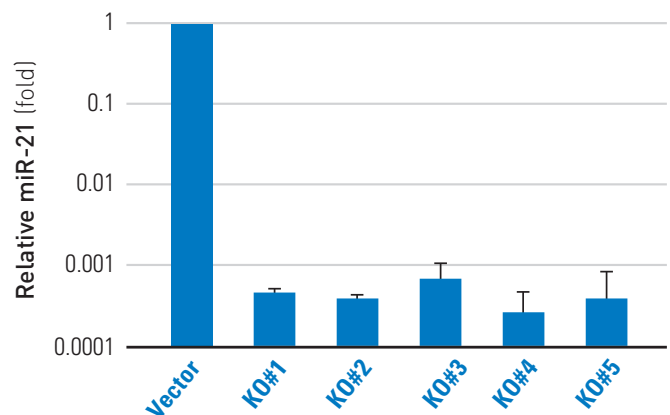
@SciMagWebinars

CATALYZING CHANGE

GENOME ENGINEERING WITH CRISPR/CAS9

Because experience matters, we think your best choice for CRISPR/Cas9 products and services is System Biosciences (SBI). We've been in the CRISPR/Cas9 business longer than any other commercial vendor on the market, giving us an edge when it comes to direct experience with this game-changing technology. Delivering easy-to-use systems and high-quality construct and cell engineering services, SBI is a smart choice for genome engineering. Learn more at:

www.systembio.com/cas9-smartnuclease



Efficient miRNA knockout using Cas9 SmartNuclease results in high rate of bi-allelic mutation (7/34 clones).



System Biosciences
Harnessing innovation to drive discoveries



There's only one **Science**

Science Careers Advertising

For full advertising details, go to ScienceCareers.org and click For Employers, or call one of our representatives.

Tracy Holmes

Worldwide Associate Director
Science Careers
Phone: +44 (0) 1223 326525

THE AMERICAS

E-mail: advertise@sciencecareers.org
Fax: +1 (202) 289 6742

Tina Burks

Phone: +1 (202) 326 6577

Nancy Toema

Phone: +1 (202) 326 6578

Online Job Posting Questions

Phone: +1 (202) 312 6375

EUROPE / INDIA / AUSTRALIA / NEW ZEALAND / REST OF WORLD

E-mail: ads@science-int.co.uk

Fax: +44 (0) 1223 326532

Sarah Lelarge

Phone: +44 (0) 1223 326527

Kelly Grace

Phone: +44 (0) 1223 326528

Online Job Posting Questions

Phone: +44 (0) 1223 326528

JAPAN

Katsuyoshi Fukamizu (Tokyo)

E-mail: kfukamizu@aaas.org
Phone: +81 3 3219 5777

Hiroyuki Mashiki (Kyoto)

E-mail: hmashiki@aaas.org
Phone: +81 75 823 1109

CHINA / KOREA / SINGAPORE / TAIWAN / THAILAND

Ruolei Wu

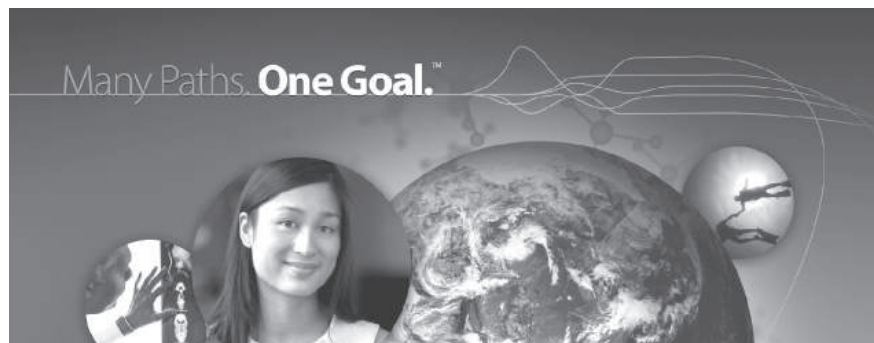
Phone: +86 186 0082 9345
E-mail: rwu@aaas.org

All ads submitted for publication must comply with applicable U.S. and non-U.S. laws. *Science* reserves the right to refuse any advertisement at its sole discretion for any reason, including without limitation for offensive language or inappropriate content, and all advertising is subject to publisher approval. *Science* encourages our readers to alert us to any ads that they feel may be discriminatory or offensive.

ScienceCareers

FROM THE JOURNAL SCIENCE AAAS

ScienceCareers.org



Pfizer Worldwide Research and Development Postdoctoral Program

At Pfizer, postdocs are trained in the art and science of drug discovery, and work side-by-side with scientists who are expert in cutting-edge biology, disease mechanisms, drug delivery and mechanisms of action, and the engineering of novel therapeutic proteins, vaccines, and nucleic acids. Areas of scientific focus include cardiovascular and metabolic diseases, clinical research, comparative medicine, drug safety, biotherapeutics/protein engineering, inflammation and immunology, human exploratory biology, medicinal chemistry, neuroscience and pain, oncology, pharmacology, and vaccines, among several others.

We recruit highly motivated Ph.D. recipients with an outstanding record of scientific productivity and a passion for ground-breaking, fast-paced research that facilitates the development of innovative therapies for human diseases. Our program promotes dissemination of research through publications and participation in scientific meetings, provides opportunities for collaboration with leading academic labs and industry consortia, and offers exceptional professional development training and networking opportunities.

To explore our program and research, visit us online at:
www.pfizercareers.com/student-programs/postdoc



Working together for a healthier world™

www.pfizercareers.com

SANFORD RESEARCH



The Sanford Children's Health Research Center (SCHRC) (www.sanfordresearch.org/researchcenters/childrenshealth/) at Sanford Research located in Sioux Falls, South Dakota has multiple full time positions available for **postdoctoral fellows**.

The mission of the SCHRC is to conduct basic, translational, and clinical pediatric research. This highly interactive and collaborative center is housed in a unique research facility with state-of-the-art resources and equipment. Interdisciplinary approaches are used to understand the underlying basis of a wide array of congenital defects and childhood diseases. Areas of interest include rare diseases, pediatric cancers, neurological disorders, developmental disorders, and genetic and environmental effects on childhood health and disease. In addition, a major initiative within the center is the Sanford Project, which aims to better understand, treat, and cure Type I Diabetes. Researchers within the center have expertise in a wide range of disciplines, including molecular biology, cell biology, developmental biology, biochemistry, neuroscience, immunology, and genetics. In addition to diverse research interests and cutting-edge facilities, Sanford Research has a dynamic career development program for postdoctoral fellows that includes professional development workshops, career seminars, and an annual Postdoctoral Symposium. In addition, there are teaching opportunities for postdoctoral fellows in courses offered to regional graduate students doing their dissertation research at Sanford Research.

The Postdoctoral Fellow will carry out independent scientific research including complex laboratory testing, experiments and analysis. The successful candidate will write technical summaries and co-author articles for publication, as well as present formal presentations of research results. The individual will work under the broad direction of the principal investigator.

These opportunities will effectively prepare the individual for a wide range of career options in the sciences. The Postdoctoral Fellow position requires a PhD in a clinical, health or life science field or MD with sufficient publication history. Previous relevant experience is preferred. To view a full job description and apply, visit <http://www.sanfordresearch.org/careers/>.

EOE/AA

abbvie



IT'S ABOUT THE APPLIED RESEARCH AND FOCUSING ON WHAT'S REALLY IMPORTANT.

Through dynamic collaboration, AbbVie's Postdoctoral Program empowers researchers to make new discoveries, advance leading-edge science and deliver patient-centric solutions.



To learn more, visit:
careers.abbvie.com

PEOPLE. PASSION. POSSIBILITIES.

online @sciencecareers.org

ScienceCareers

FEATURED EMPLOYER



Transitioning fields between a Ph.D. and postdoc

It takes guts to pursue a career in science and even more to switch fields midstream. Executing a disciplinary change between the Ph.D. and postdoc appointment requires thoughtful analysis, research, and due diligence. You have to demonstrate to your new colleagues how your expertise can be a potential boon for their research group, and you have to gain an understanding of the new field and its culture and language. For researchers who have the fortitude to start over in a new discipline and can effectively market their abilities, changing fields can lead to a career homerun. **By Alaina G. Levine**

Amir Erez is a theoretical physicist who yearned to change the world. “People would ask what I do and I had trouble explaining what impact my condensed matter research could have on our lives,” he says. As a grad student at Ben Gurion University in Israel, he had the chance to work on a collaborative project at Princeton University for a few months when he heard that a biophysics professor from his alma mater was on sabbatical at Memorial Sloan Kettering Cancer Center (MSKCC), about an hour away in Manhattan. He reached out to the scientist and the two hit it off, remained in contact, and 2 years later, Erez suggested that he work with him, under a fellowship from the Human Frontier Science Program, an international nonprofit that support postdocs who move into the life sciences from other disciplines. Now a

postdoc at MSKCC, Erez uses techniques from the physics of complex systems to study the dynamics of immune response in the context of cancer. “Suddenly I could ground my research in the real world and not just keep it in the Ivory Tower,” he notes.

The decision to change fields is not always about personal preference. Some professionals do so to ensure their employability. **Maria Patterson** had been concerned about the narrowing career opportunities for astronomers who wanted to remain in academia. “I knew it was a rough road ahead,” she says, where less than 10% of astronomy postdocs land tenure-track positions in the field. So she began looking at other vocations, including data science. As a graduate student, she was accepted into a fellowship program that exposed her to big data problems, and it was during this experience that she met her future principal investigator (PI), a computational biologist, with whom she began corresponding and discussing potential collaborative projects. She ended up at the University of Chicago in the Center for Data Intensive Science, Knapp Center for Biomedical Discovery, where she currently uses her expertise in spatial analyses to mine electronic medical records for patterns of geospatial clusters of disease. She describes her move as enjoyable as she now uses her skills in novel ways. “In astronomy, as you move up, the topics become very narrow and if I had an impact it would be small and only a few people would know about it,” she says. “But in medicine, the research has the potential to have a great impact on a lot of people.”

Other scientists discover and delve into new disciplines while trying to solve the classic “two-body problem,” in which two academics who have a personal relationship must job search at the same time. Such was the case with **Shaun McCullough**, a postdoc at the Environmental Protection Agency (EPA). When his wife landed a post in Research Triangle Park (RTP), North Carolina, he became the “trailing spouse” and cast a wide net to find a job in the region. Educated in biochemistry and molecular genetics, McCullough found a home in the Clinical Research Branch of the EPA’s Environmental Public Health Division in RTP,

where he conducts both clinical and in vitro cell-based research in toxicology. It wasn’t what he expected to do when he originally chose the life sciences, but he finds his research to be extremely rewarding since toxicology “is constantly evolving to emphasize a broader range of sub-specialties in molecular biology,” he notes. “It needs emissaries from these different fields to work together to find novel and creative ways to answer critical and pressing questions in the field. This need has created opportunities for someone like me, to apply my skills in epigenetics *continued*>



Shaun McCullough

Upcoming Features

Faculty—September 18 ■ *Regional Focus: China—October 2* ■ *Faculty—October 9*

AAAS SCIENCE & TECHNOLOGY POLICY FELLOWSHIPS

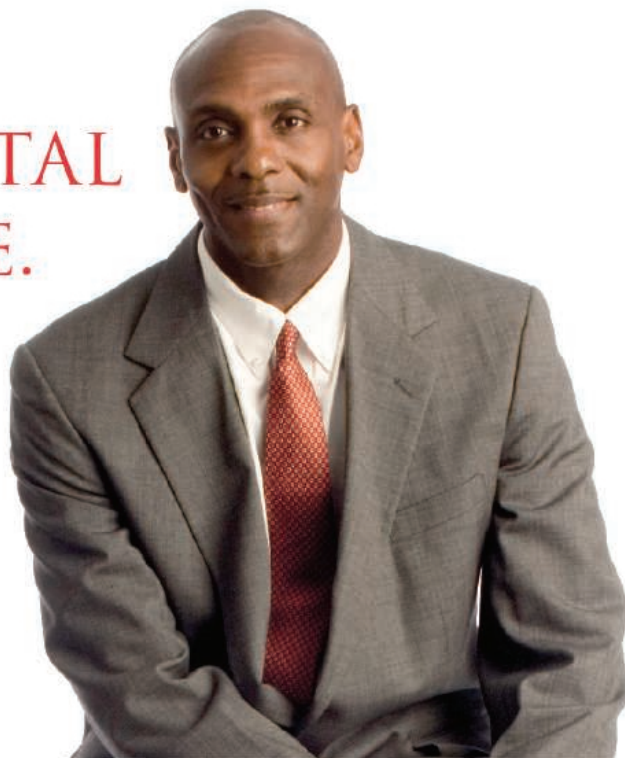


"I facilitated an agency knowledge management strategy."



I HAD A
MONUMENTAL
EXPERIENCE.
YOU CAN
TOO.

— Garrick Louis, PhD, Engineering & Public Policy; Executive Branch Fellow, Environmental Protection Agency



MAKE A DIFFERENCE.
TRANSFORM YOUR CAREER.

Apply your scientific analysis and technical knowledge to inform policy through assignments in the Legislative, Executive and Judicial Branches.

Stipends from
\$75,000 to
\$100,000.
Applications due
November 1.

aaas.org/stpf/science3



Enhancing Policy, Transforming Careers

SCIENCE & TECHNOLOGY
POLICY FELLOWSHIPS



“I used to communicate using quantitative information and theoretically rigorous approaches but during my postdoc I had to deal with more qualitative information and empirical approaches.”

— Diego Fazi



and molecular biology to solving the next generation of problems facing this field.”

Noting differences between fields

As you adjust to a new discipline, there are many challenges to be met. One major difference in any new field is how the experts think about problem-solving. Each field has its own research approaches, which you have to learn quickly when transitioning areas. This requires an abundance of reading papers, speaking with experts, learning techniques, and shadowing colleagues. “The first few months into my postdoc, the only thing I wanted to do was sleep, because it was so much to learn and incredibly mentally exhausting,” says **Elizabeth George**, a postdoc at the Max Planck Institute for Extraterrestrial Physics near Munich, Germany, who migrated from cosmology with the cosmic microwave background (CMB) to infrared astronomy.

The cultural differences between disciplines can be surprising, even if the science seems to overlap. George’s culture shock manifested as she realized the different approaches to solving scientific problems in astrophysics versus astronomy. “Infrared astronomy is much more traditional astronomy, where you look at objects and try to understand what you are seeing,” she says. “But in CMB cosmology, you start with a model of the universe and only measure one thing—the cosmic microwave background radiation—and try to fit your data to the model.”

In making her transition, Patterson noticed a difference in how data itself is perceived and handled in different subjects. Astronomers are very open with their results, and since astronomical data is shared often, it has a uniform format, no matter the source. But in medicine, the tables are completely turned: data is sensitive and since it is drawn from medical records, there is much more concern over who has access to what. Additionally, “people don’t want to share their data as much, because it is valuable for commercial purposes,” she notes.

Moving from a lab-based science to one that involves patients requires nimbleness and flexibility. “I had never

worked with humans before,” says McCullough. “As a molecular biologist, I worked with cells in a dish. They didn’t talk, and they didn’t have to be informed” about the nature and risks of the studies. But in investigating how environmental factors contribute to disease, he had to learn a new protocol and ensure that the subjects understood everything that was taking place. When **Ewan Cameron**, an astronomer-turned-epidemiologist, “jumped ship” (as he puts it) to become a senior computational statistician in the spatial ecology and epidemiology group in the Department of Zoology at the University of Oxford, he not only began working with human subjects but he also had to learn how to collaborate with nonscientists, such as policy makers and representatives of nongovernmental organizations and nonprofits.

With any disciplinary switch, there’s usually a new language to master. “The jargon barrier can be quite formidable,” notes Erez. “I’m 8 months in to my postdoc, and I’m just beginning to know the right jargon for my neck of the woods, and what the right questions are to ask.”

Diego Fazi, a theoretical physicist who migrated to renewable energy via a postdoc at Argonne National Laboratory (ANL), had to adapt to variances in the manner in which professionals share information. “I used to communicate using quantitative information and theoretically rigorous approaches,” he says, but “during my postdoc I had to deal with more qualitative information and empirical approaches.”

Day-to-day differences can also pop up, especially for those who switch from theoretical to experimental fields. Both Erez and Fazi had never done wet lab work. “Before I came here, I was a theorist with clean hands,” says Erez. Adds Fazi: “I had to learn basic chemical techniques, such as making a solution and setting up an experimental apparatus.”

And of course, “when you switch fields, you incur a time penalty,” notes Erez. “It takes time to settle into a new field,” to learn its nuances and then be able to be productive enough to publish. Adds George: “Changing disciplines feels like you are starting grad school all over again, except that you are a much better learner.” It took her 6 months to “start feeling productive, and to be able to begin asking questions that pushed knowledge forward and were as useful to my colleagues as they were to me.” Erez recommends giving yourself a break as you ramp up your knowledge. “Don’t expect to be as productive in your first year as you would have if you stayed in the same field,” he says.

Making the switch

Whether your switch seems radically different, like physics to immunology, or something seemingly more related, like astrophysics to astronomy, it is important to be ready to market your talents and show what you can offer a new field based on your background. This is especially crucial given the fact that as you transition, you are not necessarily going to be acknowledged for your research reputation, as George **continued>**

WASHINGTON RESEARCH FOUNDATION INNOVATION POSTDOCTORAL FELLOWSHIPS

Protein Design

Learn protein design methods and apply them to problems in medicine, materials, computer science, and energy.



Data Science

Join a new generation of researchers in advancing data-intensive discovery in the physical, life, and social sciences.



Clean Energy

Transform clean energy delivery by focusing on advanced solar materials, energy storage, and smart grid integration.



Neuroengineering

Perform cutting-edge research at the interface between neuroscience, engineering, computing, and mathematics.



Exceptional candidates of outstanding talent and achievement are invited to apply.

Applications are accepted twice a year, with due dates on January 15 and July 15.

Fellowships provide two years of funding including salary and a budget for research expenses.

Co-funding between Institutes is possible. Research will be conducted in Seattle.

<http://wrf.washington.edu>



COMMIT TO DISCOVERY THROUGH THE POSTDOCTORAL FELLOWSHIP PROGRAM

The Morgridge Institute for Research, a private research institute affiliated with the University of Wisconsin – Madison, is now seeking candidates for our postdoctoral fellowship program. This program provides a unique opportunity to be part of dynamic, innovative, and interdisciplinary research teams and learn from investigators at the forefront of discovery in the following research areas:

Bioethics and Law
Bioinformatics
High Throughput Computing
Imaging Informatics
Metabolism
Multiscale Imaging
Regenerative Biology
Statistics
Virology

For more information about this program, please visit: <https://morgridge.org/postdoc-fellows/>

Inquiries welcome.

The Morgridge Institute for Research promotes and supports a diverse and inclusive environment.



The Argonne Named Fellowship Program

Argonne National Laboratory is accepting applications for the 2016 Named Fellowship. Argonne awards these special fellowships internationally on an annual basis to outstanding doctoral-level scientists and engineers who are at early points in promising careers. The fellowships are named after scientific and technical luminaries who have been associated with Argonne and its predecessors, and the University of Chicago, since the 1940's.

Candidates for these fellowships must display superb ability in scientific or engineering research, and must show definite promise of becoming outstanding leaders in their fields. Fellowships may be renewed up to three years. The 2016 fellowship carries a highly competitive salary with an additional allocation research support and travel. The deadline for submission of application materials is **October 14, 2015**.

Applicants should identify an Argonne staff member to sponsor the nomination. The sponsor could be someone who is already familiar with your research work and accomplishments through previous collaborations or professional societies. If you have not yet identified an Argonne sponsor, visit the detailed websites of the various research efforts at www.anl.gov/science.

Applications must be submitted online through: <http://www.anl.gov/careers/apply-job>. Correspondence and supporting letters of recommendation should be submitted to Named-Postdoc@anl.gov.

For more information visit the Types of Appointments page at www.anl.gov/postdocs or by contacting the Postdoctoral Program Coordinator, Kristene Henne at khenne@anl.gov.

Argonne is an Equal Opportunity Employer and we value diversity in our workforce. Argonne is a U.S. Department of Energy laboratory managed by UChicago Argonne, LLC.

Featured Participants

Argonne National
Laboratory
www.anl.gov

Environmental Protection
Agency
www.epa.gov

Human Frontier Science
Program
www.hfsp.org

Los Alamos National
Laboratory
www.lanl.gov

Max Planck Institute for
Extraterrestrial Physics
www.mpe.mpg.de/2169/en

Memorial Sloan Kettering
Cancer Center
www.mskcc.org

University of Chicago
www.uchicago.edu

University of Missouri
www.missouri.edu

University of Oxford
www.ox.ac.uk

discovered as she plotted her move. “In my new discipline, I am a completely unknown quantity. People haven’t read my papers,” she says. To land a postdoc, she pitched her PI that her experience in building and deploying astronomical instruments, unusual for an astrophysicist, could serve as an asset for the new research group.

“Start as early as possible in your planning,” says Erez. Many scientists who change fields launch their career plan in grad school. For example, Patterson took classes in Python and programming. Erez attended biophysics talks at physics conferences as well as on his campus, and engrossed himself in papers and books that focused on his newfound subject.

Your grad school mentor might be helpful too, if you can present your switch as an advantage to them to advance their own research interests. In doing so, “you might find that your advisor is inclined to send you to a conference in the field you are interested in,” says **Eric Brown**, acting deputy division leader of the Materials Science and Technology Division at Los Alamos National Laboratory, whose doctorate is in physics. Furthermore, he recommends leveraging the resources offered by the professional association of your new field. “Many science societies issue reports on demographics, career paths, and employment statistics,” he says, which can be invaluable in the career planning process.

As you transition, you have to establish a connection between your past and your desired future. “Those bridges, of taking what you learned from one area and applying it to another, need to be visible,” says **Jason Cooley**, who switched from biology to biochemistry and then eventually found his way to the chemistry department of the University of Missouri as a solution to his own two-body problem. He equates it to telling a story with a narrative that explains the natural progression of how you got to where you are today. Without it, “people will think that if you get bored, you will jump somewhere else,”



Ewan Cameron had to learn how to collaborate with nonscientists, such as policy makers and representatives of nongovernmental organizations and nonprofits.

he adds. In George’s case, her narrative showcased her desire to build high-quality scientific instruments, which she had demonstrated as a grad student and which she planned to do as a postdoc.

No matter your story, your publications are your “scientific currency,” so “before you move, write a paper that relates, even in a tangential way, to your future field,” urges **Joel Cavallo**, a postdoc in psychiatry with a dual appointment as a fellow in the Program of Clinical Pharmacology and Pharmacogenomics at the University of Chicago. As he completed grad school in neuroscience and psychology, Cavallo authored an article on the erasure of associative memories in a sea slug. Because maladaptive learning and associative memories can play a role in mental disorders, this work helped show his dedication to his desired discipline of psychiatry.

Getting the appointment

It’s not surprising that, despite your best intentions, it can be difficult to change fields, especially right after grad school. “It wasn’t easy to get a postdoc because most biologist PIs wanted someone with experience in biology,” admits Erez. He was lucky to have found a mentor who appreciated his background in physical science and had experienced a similar transition into the field. “I needed a PI who had a good background in biophysics because otherwise it would be very difficult to communicate, since I didn’t speak the language of biology and he wouldn’t have spoken the language of physics.”

But as more STEM fields become interdisciplinary, sources say that there will be growing opportunities for innovators who can understand and unite multiple universes. Brown notes that it is becoming more common for early career scientists to switch subjects between the Ph.D. and postdoc, as “it’s an opportunity to jump into something that is new and fresh and exciting,” he says. And having the capacity to connect seemingly disparate fields can hold other advantages. Indeed, Fazi, who recently leveraged his postdoc into a full time position at ANL as a technology innovation strategist with a focus on green tech, says that changing course for him “gave me more perspective in science,” he says. “I came out a more complete scientist with more cards to play.”

Alaina G. Levine is a science writer based in Tucson, AZ.

DOI: 10.1126/science.opms.r1500156



Postdoctoral Professional Master's Program

The Postdoctoral Professional Masters in bioscience management (PPM) is a 9-month program designed to help PhD scientists and engineers acquire the business, regulatory, and management skills needed to secure rewarding careers in the life sciences industry, or embark on entrepreneurial ventures.

The program curriculum focuses on the unique business environment in the life sciences and includes:

- Participation on an industry-sponsored Team Master's Project (TMP) with 3-5 people
- Business/Regulatory coursework
- Advanced industry sector-specific electives
- Networking opportunities with industry leaders and alumni

KGI also offers a 5-course *Certificate in Bioscience Management* that can be completed on-campus or online. The required coursework for the certificate constitutes the core one-third of the PPM program so that PhDs may begin pursuit of the PPM while still completing their academic research.

For more information please visit:

<http://www.kgi.edu/ppm>
and

<http://www.kgi.edu/certificate-bioscience-management>



Postdoctoral Position in BioPharmaceutical Industry

Alexion is a global biopharmaceutical company focused on developing and delivering life-transforming therapies for patients with devastating and rare disorders. Alexion developed and commercializes Soliris® (eculizumab), the first and only approved complement inhibitor to treat patients with paroxysmal nocturnal hemoglobinuria (PNH) and atypical hemolytic uremic syndrome (aHUS), two life-threatening ultra-rare disorders. Alexion is also establishing a premier global metabolic rare disease franchise with the development of two late-stage therapies, Strensiq™ (asfotase alfa) for hypophosphatasia (HPP) and Kanuma™ (sebelipase alfa) for Lysosomal Acid Lipase Deficiency (LAL-D). In addition, Alexion is advancing the most robust rare disease pipeline in the biotech industry, with highly innovative product candidates in multiple therapeutic areas.

We are seeking highly motivated candidates with a demonstrated ability to deliver significant results to join our R&D Postdoctoral Program. Three postdoctoral positions are currently available for recent Ph.Ds. to work on innovative research questions to facilitate drug discovery, including: (1) discovery and engineering of proteins for tissue specific targeting, (2) identification and characterization of antibodies for brain blood barrier penetration, and (3) elucidation of the mechanisms of uptake of biotherapeutics to mitochondria. Two positions are available in Cheshire/New Haven, CT, and one in Cambridge, MA. Please refer to <http://alexionpharma.com/careers/job-opportunities> for detailed descriptions of open postdoctoral opportunities.

Individuals applying for this program must be authorized to work in the United States for any employer. Alexion will not provide visa sponsorship for this program.

D E Shaw Research

Postdoctoral Fellowships at D. E. Shaw Research

D. E. Shaw Research is seeking postdoctoral fellows of exceptional ability to join our New York-based team. This is a unique opportunity to develop and work with transformative technology in a dynamic, interdisciplinary environment. Candidates should have expertise in computational chemistry, biology, or physics, or in a relevant area of computer science or applied mathematics.

Relevant areas of experience might include the study of allosteric interactions or other conformational changes in biological molecules, structure prediction or design for proteins or RNA, the study of protein-protein or protein-nucleic acid interactions, force field development using quantum-chemical data or comparison with experimental data, or development and implementation of new methodologies. Specific knowledge of any of these areas is less critical, however, than outstanding intellectual ability, unusually strong research skills, and a history of innovation and accomplishment. We are committed to fostering a stimulating, rewarding, and flexible work environment, and we are prepared to offer above-market compensation to candidates of truly exceptional ability.

D. E. Shaw Research is an independent research group that is pursuing an ambitious, long-term strategy aimed at fundamentally transforming the process of drug discovery. We have developed a special-purpose supercomputer capable of executing molecular dynamics (MD) simulations orders of magnitude faster than was previously possible. Our current projects include investigations of proteins and other biomedically relevant macromolecules as well as the development of computational chemistry methods to enable more accurate and effective MD simulations.

To submit an application, please email your CV to:
ScienceCareers@DEShawResearch.com

D. E. Shaw Research does not discriminate in employment matters on the basis of race, color, religion, gender, pregnancy, national origin, age, military service eligibility, veteran status, sexual orientation, marital status, disability, or any other protected class.

The National Academies of
SCIENCES • ENGINEERING • MEDICINE

Graduate, Postdoctoral, and Senior Research Awards
offered for research at
US federal laboratories and affiliated institutions

Opportunities for research in all areas of science and engineering

- Awards for independent research at over 100 participating laboratory locations
- 12-month awards renewable for up to 3 years
- Annual stipend \$45,000 to \$80,000 for recent PhD recipients and higher for additional experience. Graduate entry level stipend is \$30,000 and higher for additional experience
- Relocation, professional travel, and health insurance
- Annual application submission deadlines February 1, May 1, August 1, November 1
- Open to international applicants

Detailed program information, including instructions on how to apply online can be found on the NRC website at:

www.nationalacademies.org/rap

Applicants must contact Adviser(s) at the lab(s) prior to application deadline to discuss research interests and funding opportunities.

Questions should be directed to the:

NRC Research Associateship Programs

TEL: 202-334-2760; EMAIL: rap@nas.edu

Qualified applicants will be reviewed without regard to race, religion, color, age, sex or national origin.



The International Post-Doc Initiative (IPODI) is part of the gender equality strategy of the Technische Universität Berlin and aims at increasing the number of female researchers in leadership positions. The IPODI Fellowship Programme is open to outstanding female researchers of all nationalities and from all fields of research represented at the TU Berlin. IPODI Fellows will find excellent research conditions in one of the seven faculties of the TU Berlin. IPODI awards

Seven Incoming Postdoctoral Fellowships
(salary in the range of E 13/14 TV-L).

IPODI Fellows will receive:

- A two-year employment contract with salaries equal to those of the Marie Curie Programme for experienced researchers, including social security and health insurance as well as pension coverage,
- A yearly travel allowance,
- A monthly contribution to research costs,
- The opportunity for professional training in career development and research management.

For further information see www.ipodi.tu-berlin.de or contact the IPODI Office (application@ipodi.de).

Researchers returning from periods of international mobility (researching outside Germany), intersectoral mobility (working in the private sector) or non-academic mobility (e.g. after parental leave) are especially encouraged to apply.

Application deadline: 15 October 2015

IPODI is co-funded by the European Union (Marie Curie Co-funding of Regional, National, and International Programmes) and awards a total of 21+2 fellowships in three internationally open selection rounds.



STOWERS INSTITUTE[®]
FOR MEDICAL RESEARCH

Postdoctoral Research Associate

The Zeitlinger lab at the Stowers Institute for Medical Research has an opening for a postdoctoral researcher to work on the development of a high-resolution ChIP-seq technique to map transcription factor binding sites in sparse cell types. The technique can be applied to a developmental system of choice as proof-of-principle (e.g. early mouse embryos or stem cells).

The project builds on a recent lab publication: "ChIP-nexus enables improved detection of *in vivo* transcription factor binding footprints" *Nature Biotechnology* **33**:395–401 (2015).

Qualified candidates will have a doctorate degree in biology, a strong background in transcription, developmental biology or genomics, and the ability to lead a project both independently and collaboratively in a team-oriented environment. Experience in chromatin immunoprecipitation (ChIP) and genomic data analysis (UNIX, R) is a plus.

To apply, please submit a cover letter with a short summary of interests, a CV, and the contact information of 2-3 references to Julia Zeitlinger at jbz@stowers.org. The position is available immediately until filled.

The **Stowers Institute for Medical Research** in Kansas City, Missouri is a non-profit, basic biomedical research organization dedicated to improving human health by studying the fundamental processes of life (visit www.stowers.org). Founded and endowed by Jim and Virginia Stowers, the Institute is home to over 20 independent research programs and more than a dozen technology-development and core facilities. Kansas City is an emerging metropolitan city in the Midwest with a high quality of living and affordability (visit www.visitkc.com).



STOWERS INSTITUTE[®]
FOR MEDICAL RESEARCH

Postdoctoral Research Associate

The Halfmann lab at the Stowers Institute for Medical Research has two openings for postdoctoral researchers to explore the cellular and evolutionary implications of protein aggregation and phase partitioning in living organisms.

The projects will build on recent discoveries in yeast (Holmes et al. *Cell*; 2013;**153**:153-165) and mammalian systems (Cai et al. *Cell*; 2014;**156**:1207-1222) that suggest wide-ranging roles for prions and other self-templated protein assemblies in regulating the flow of information through cellular networks.

Qualified candidates will have a doctorate degree in biology and possess the ability to work both independently and collaboratively in a team-oriented environment. Experience in protein biochemistry and cell biology are desired.

To apply, please submit a cover letter that includes a short summary of interests, a CV, and the contact information of 2-3 professional references to **Randal Halfmann** at rhn@stowers.org. The positions are available immediately until filled.

The **Stowers Institute for Medical Research** in Kansas City, Missouri is a non-profit, basic biomedical research organization dedicated to improving human health by studying the fundamental processes of life (visit www.stowers.org). Founded and endowed by Jim and Virginia Stowers, the Institute is home to over 20 independent research programs and more than a dozen technology-development and core facilities. Kansas City is an emerging metropolitan city in the Midwest with a high quality of living and affordability (visit www.visitkc.com).

M UNIVERSITY OF MICHIGAN

A POSTDOCTORAL RESEARCH FELLOW position is available at the University of Michigan, Ann Arbor. This position benefits from outstanding interdisciplinary intellectual support from the Department of Periodontics and Oral Medicine, School of Dentistry; Department of Otolaryngology, School of Medicine; Translational Oncology Program in the Michigan Comprehensive Cancer Center; and the Distributed Health Technology program. We are seeking a highly self-motivated research scientist with a recent Ph.D. degree and a background in the area of cancer biology, immunology, molecular biology, or cell biology. The candidate will participate in innovative projects with clear translational significance. Individuals with expertise in cell signaling, lentivirus-based technique, and cancer mouse models are strongly encouraged to apply. Interested candidates should submit a cover letter with a brief description of past research experiences and career goals, an up-to-date curriculum vitae, and contact information of three referees to **Dr. Yu Lei** (e-mail: leiyuleo@umich.edu).

POSTDOCTORAL RESEARCH FELLOW

DESCRIPTION: The Optoelectronic Components and Materials Group, www.umich.edu/~ocm, at the University of Michigan is seeking a **POSTDOCTORAL RESEARCH FELLOW** with expertise in organic thin films for use in electroluminescence and other photonic devices. Qualifications should include hands-on, in-depth experience with the design, vacuum deposition, device fabrication, analysis and characterization of active optical components such as OLEDs, solar cells, detectors, etc. Successful candidates should be able to work on independent research projects, as well as lead larger teams of graduate students. Maintaining large laboratory facilities and infrastructure is an important part of the job.

REQUIREMENTS: Prospective candidates must have a Ph.D. in electrical engineering, materials science, chemical engineering, physics or associated field. Salary level commensurate with experience.

TO APPLY: Please send your resume and cover letter to Professor Stephen Forrest at e-mail: emruff@umich.edu. Review of applications will be accepted until the position is filled.

The University of Michigan is an Affirmative Action, Equal Opportunity Employer with an Active Dual-Career Assistance Program. The College of Engineering is especially interested in candidates who contribute, through their research, teaching, and/or service, to the diversity and excellence of the academic community.

Host-pathogen interactions in tuberculosis

We have recently discovered TNT as the first toxin of *Mycobacterium tuberculosis* (PNAS 111, 6750; Nat. Struct. Mol. Biol.; website: <http://goo.gl/IQFYzZ>). In this project we will examine the role of TNT in TB pathogenesis, its unusual secretion mechanism and the molecular pathway that leads to TNT-induced host cell death. This project is supported by a new NIH grant.

University of Alabama at Birmingham is an excellent research institution in an affordable city with many cultural and outdoor attractions (website: <http://goo.gl/fcHnDH>).

Applicants should submit their curriculum vitae and their three top publications as a single pdf file and the contact information of three potential referees to Michael Niederweis (e-mail: mnieder@uab.edu).

Drug Abuse Research Postdoctoral Fellowships for Non-U.S. Citizens

M.D. or Ph.D. and 2 years' research experience required

Fellowships provide 12 months of training with a NIDA grantee in the United States

Any non-U.S. researcher may apply for the:

INVEST and INVEST/CTN Fellowships

- INVEST Fellows work with any U.S. NIDA grantee
- INVEST/CTN Fellows work with a NIDA grantee affiliated with one of the NIDA Clinical Trials Network Regional Research and Training Centers in the United States

Researchers from specific countries may apply for the:

U.S.-Mexico Drug Abuse Prevention Research Fellowship

- Mexican scientists work with a NIDA grantee conducting drug abuse prevention research in the United States

NIDA-Inserm Postdoctoral Drug Abuse Research Fellowship

- French scientists work with a U.S. NIDA grantee conducting research on specific topics in the United States

ANNUAL APPLICATION DEADLINE: APRIL 1

ip@nida.nih.gov or
drugabuse.gov/international/fellowships



National Institute
on Drug Abuse



Notre Dame Institute for
ADVANCED STUDY

Call for Fellows for 2016-2017

Residential & Graduate Student Fellowships

Application deadline: October 15, 2015

**Congratulations to Jessica Hellmann,
NDIAS Alumna, on being named
Director of the Institute on the
Environment (U of Minn.)**

ndias.nd.edu



**TENURE TRACK/TENURED POSITIONS
CENTER FOR RNA BIOLOGY**

The Center for RNA Biology (<http://www.urmc.rochester.edu/rna-biology/>), directed by Lynne E. Maquat, PhD, and David H. Mathews, MD, PhD, invites applications for a tenure-track position at the **ASSISTANT, ASSOCIATE or FULL PROFESSOR** level. We are seeking outstanding candidates holding a PhD and/or an MD degree(s) and at least two years of post-doctoral training with research interests in any area of RNA biology. Emphasis is being placed on the study of mammalian-cell RNA-protein interactions and function, possibly using large-scale transcriptomic and proteomic approaches. Successful applicants are expected to develop independent, externally funded research programs and to contribute toward graduate- and medical-school teaching. The University of Rochester Medical Center and the adjacent College of Arts, Sciences and Engineering are part of a world-class life sciences research campus, providing excellent opportunities for interactions and collaborations, and offer an outstanding research environment with established strengths in RNA Biology. Center for RNA Biology members have expertise in post-transcriptional processing and regulation, genome stability, structural and functional characterization of molecular interactions, computational biology, biophysical chemistry and disease-associated RNA metabolism. Studies encompass rRNA, pre-mRNA, mRNA, tRNA, lncRNA, miRNA and piRNA in humans, model organisms and pathogens.

Applicants should forward a PDF file with their cover letter, CV, descriptions of research accomplishments and future research plans [and arrange for three letters of reference to be sent] to Coryn Herrema, Director, Executive and Senior Faculty Recruitment at Coryn_Herrema@URMC.Rochester.edu and also apply on line at www.rochester.edu/jobopp, job number **190621**.

The University of Rochester has a strong commitment to principles of diversity and, in that spirit, actively encourages applications from groups underrepresented in higher education.



**LINDA CRNIC
INSTITUTE**
FOR DOWN SYNDROME™

Sie Foundation Postdoctoral Fellowship

The University of Colorado-Boulder, the BioFrontiers Institute, and the Linda Crnic Institute for Down Syndrome seek courageous and innovative postdoctoral fellows to ameliorate cognitive, cardiovascular, neurodegenerative or other ill effects of trisomy 21 in affected children. Possible approaches include working with people with Down syndrome, mouse or other animal models of Down syndrome, or cell lines trisomic for chromosome 21. This should be considered an opportunity to apply modern techniques, such as next generation sequencing, induced pluripotent stem cells, or advanced techniques in proteomics, to aid in understanding a very complex syndrome coming from a known but poorly understood genetic alteration, an extra copy of the smallest human chromosome.

Sie Fellows may work in any laboratory on the Boulder campus, and will interact with the entire Boulder bioscience community and with Dr. Tom Blumenthal and colleagues at the Crnic Institute at the CU Anschutz Medical Campus in Denver. Sie Fellows will be awarded salaries of \$55 -70,000, depending on field, experience and qualifications, as well as substantial research budgets, and will be encouraged to take the project with them when they start their independent faculty positions.

Applicants should have a Ph.D. and/or M.D. degree and no more than three years of prior postdoctoral experience. Applications should include C.V. and a letter describing their interest in Down syndrome research. Applicants should email these materials no later than **January 15, 2016** to **Angela Kirkpatrick** (angela.kirkpatrick@ucdenver.edu) with a subject line of Sie Foundation Postdoctoral Fellowship and should have three letters of recommendation sent directly to the same address.

Download the *Science Careers* jobs app from Science



Get a job on the go.

Search thousands of scientific jobs in academia, industry, and government from around the globe. The seamless application process includes linking you directly to job postings from your customized push notifications.

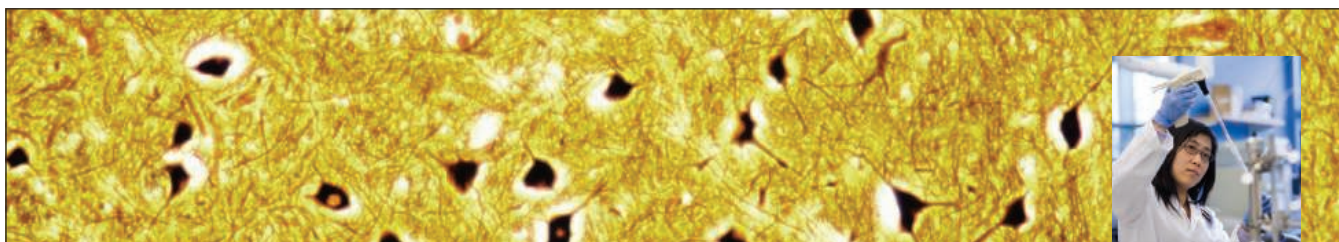


Scan this code to download app or visit apps.sciencemag.org for information.

Science Careers

FROM THE JOURNAL SCIENCE AAAS

ScienceCareers.org



Explore the Amgen Difference

At Our Expanded Facilities in Cambridge and South San Francisco

If you're seeking a career where you can truly make a difference in the lives of others, a career where you can work at the absolute forefront of biotechnology with the top minds in the field, you'll find it at Amgen.

Amgen is committed to unlocking the potential of biology for patients suffering from serious illnesses by discovering, developing, manufacturing and delivering innovative human therapeutics. This approach begins by using tools like advanced human genetics to unravel the complexities of disease and understand the fundamentals of human biology.

Amgen focuses on areas of high unmet medical need and leverages its biologics manufacturing expertise to strive for solutions that improve health outcomes and dramatically improve people's lives. A biotechnology pioneer since 1980, Amgen has grown to be one of the world's leading independent biotechnology companies, has reached millions of patients around the world and is developing a pipeline of medicines with breakaway potential.

Amgen is a biotechnology pioneer with a mission to serve patients. If you're ready for your next step, join us at one of our expanded facilities in **Cambridge, MA** or **South San Francisco, CA**.



www.amgen.com/careers

Amgen is an Equal Opportunity employer and will consider all qualified applicants for employment without regard to race, color, religion, sex, sexual orientation, gender identity, national origin, protected veteran status or disability status.

M UNIVERSITY OF MICHIGAN

BIOLOGICAL SCIENCES SCHOLARS PROGRAM For Junior, Tenure-Track Faculty

The University of Michigan Medical School announces recruitment for the Biological Sciences Scholars Program (BSSP) to enhance the institution's strengths in the biological and biomedical research areas.

Now entering its 17th year, the BSSP has led recruitment of outstanding scientists pursuing research in genetics, microbiology, immunology, virology, structural biology, biochemistry, molecular pharmacology, stem cell biology, cancer biology, physiology, cell and developmental biology, bioinformatics, and the neurosciences. The Program seeks individuals with PhD, MD, or MD/PhD degrees, at least two years of postdoctoral research experience, and who have not previously held a faculty position. Candidates will show evidence of superlative scientific accomplishment and scholarly promise. Successful candidates will be expected to establish a vigorous, externally-funded research program, and to become leaders in departmental and program activities, including teaching at the medical, graduate, and/or undergraduate levels. Primary departmental affiliation(s) will be determined by the applicant's qualifications and by relevance of the applicant's research program to departmental initiatives and themes. All faculty recruited via the BSSP will be appointed at the Assistant Professor level.

APPLICATION INSTRUCTIONS: Please apply to the Scholars Program through the BSSP website at: <http://bssp.med.umich.edu>. A curriculum vitae (including bibliography), a three page research plan, an NIH biosketch, and three original letters of support should all be submitted through the BSSP website. More information about the Scholars Program, instructions for applicants and those submitting letters of recommendation, and how to contact us is located on the BSSP web site: <http://bssp.med.umich.edu>. The deadline for applications is **Friday, October 16, 2015**.

The University of Michigan is an Affirmative Action/Equal Opportunity Employer.



東北林業大學

2015~2017 High-level Talent Introduction Announcement of Northeast Forestry University

Established in 1952 and located in Harbin – beautiful “Ice City”, Northeast Forestry University is in national “211 Project” directly under the Ministry of Education of the People’s Republic of China and key construction projects of “Advantage Discipline Innovation Platform”. It is a multidisciplinary university integrating agriculture, science, industry, economics, management, culture, law, medicine and art with forestry science as advantage and forestry engineering as specialty. To further improve the overall level of teaching staff and achieve a research university with international view, we are hereby looking for talents sincerely and mainly introducing excellent domestic and foreign talents with important complementary and supporting functions for the construction of subjects and talent team.

I. Subject Areas for Recruitment:

Agriculture, General Computing, Computer Science, Information Science and Technology, Architecture, Planning, Cell & Molecular Biology, Bioinformatics, Ecology, Genetics, Microbiology & Virology, Plant Science, Zoology & Animal Science, Civil Engineering & Construction, Electrical & Electronics Engineering, Materials Science, Mechanical Engineering, Polymer Science & Technology, Veterinary Medicine, Business, Economics, Finance, and Accounting, Analytical Chemistry, Chemical Engineering, Inorganic Chemistry, Organic Chemistry, Physical Chemistry, Botany.

II. Recruitment Plan

1. Leading Talents or Teams: to introduce leading talents or teams with international advanced level and competitive capacity in distinctive preponderant disciplines of the university and national key disciplines.
2. Distinguished Young Scholars: distinguished domestic and foreign young scholars have published high cited academic paper in the top-level publication of related field, with the potential to be selected into talent projects such as Thousands of People Plan, National Science Fund for Distinguished Young Scholars, Thousand Youth Talents Plan and Tens of Thousands of People Plan, or personnel with academic title of associate professor in overseas famous colleges and universities and above or personnel equivalent to the level of researchers in overseas famous research institutes; age under 40, and 45 for the excellences.
3. Excellent Young Scholars: excellent domestic and foreign young scholars have published high cited academic paper in the top-level publication of related secondary discipline, with the potential to be selected into talent projects such as Provincial Science Fund for Distinguished Young Scholars, Longjiang Scholars and Provincial Excellent Young and Middle-aged Experts; age under 35, and 40 for the excellences.
4. Young Backbone: domestic and foreign young backbone have published high cited academic paper in the top-level publication of related secondary discipline, with the ability of winning National Science Foundation of China and Philosophy and Social

Science Foundation of China and great development potential in academy and scientific research; age: under 35.

5. Excellent Young Teachers: doctors with strong ability of teaching and scientific research; age: under 35.

III. Treatment

1. Leading Talents: appointed to the post of professor;
 2. Distinguished Young Scholars: appointed to the post of professor;
 3. Excellent Young Scholars: appointed to the post of professor or associate professor;
 4. Young Backbone: appointed to the post of associate professor or lecturer;
- The university will provide salary standard, scientific research start-up fund and house purchase subsidies according to the level of talent introduction.

IV. Further Details and Contact Information

Please check the following links for more details about the recruitment plan:

http://202.118.223.214:8081/hire/hireNetPortal/search_zp_position.do?b_login=login

For official website, please check:

<http://www.nefu.edu.cn>

Contact Person:

Mr. Zhang Chunlei (Tel: +86-451-82190165)

Mr. Li Guoliang or Ni Songyuan (+86-451-82190494, 82192070)

Email: nefugee@nefu.edu.cn



南京工業大學

NANJING UNIVERSITY
OF TECHNOLOGY

海外领军人才招聘

Overseas Talents Recruitment

Nanjing Tech University, with a history of more than one hundred years, is a multidisciplinary university with a particular strength in engineering.

Aiming at excellence and innovation, Nanjing Tech University is set to become a first-class research university with a global vision. We are now seeking outstanding academic and research leaders in the following and related fields: Basic disciplines from within the Physical Sciences; Cutting edge disciplines from within the Life Sciences; Applied disciplines from within the Information Sciences; Humanities represented by Management Science.

Applicants should have a Ph.D. with at least 3-years research experience from leading universities or institutes. Candidates should demonstrate an internationally recognized research record and outstanding achievements. Successful candidates are expected to develop vigorous research programs and lead an independent research team. Successful candidates will be provided with a competitive relocation fee and salary package, generous start-up funds and spacious laboratories.

Interested candidates should visit <http://rczyb.njtech.edu.cn> for application details.

Phone: Ms. Wang +86-25-58139148.

E-mail: job@njtech.edu.cn



Faculty Positions available at Hohai University, Nanjing, China

Hohai University invites applications for faculty positions at the assistant, associate, or full professor level in the area of engineering, science, economics, management, liberal arts, and law. Applicants should have a doctoral degree from a prestigious university. For the complete job announcements and directions on how to apply, visit: rsc.hhu.edu.cn or contact the Department of human resource at 86-25-83786205.

Hohai University, founded in 1915, wins its worldwide reputation on the research of Water Science& Civil Engineering&Environment Engineering. It is a National key university of China, and among the universities of the National “211 Project” and Innovation Bases of the National “985 Project”. Hohai University aims to be a research oriented university.



杭州电子科技大学
HANGZHOU DIANZI UNIVERSITY

Faculty Positions Available at Hangzhou Dianzi University

About HDU:

Hangzhou Dianzi University (HDU), located in Hangzhou, a well-known city for its history and culture, is one of the advanced universities in Zhejiang Province, China. There are more than 28000 full-time students and over 2200 faculty and staffs in campus, 1 academician of the developing country, 5 sharing academicians, 2 young middle-aged outstanding experts, 5 distinguished experts of the "Thousand-talent Project" awarded by the Organization Department of the Central Committee of the CPC, 3 of New Century's Talent Project, 4 holders of the National Outstanding Youth Fund, 10 of the New Century's Excellent Talents Project supported by the Ministry of Education, 4 of National Outstanding Teachers and a large number of famous scholars and middle-aged experts with profound academic accomplishments. HDU has developed into a significant institution for its personnel training, scientific research and community service, and holds the lead among the universities in Zhejiang Province in every aspect as the school scale, the education level, the teaching quality and efficiency in school management.

HDU website: <http://www.hdu.edu.cn>

Vacancies:

Mechanical Engineering, Electric Engineering, Marine Equipment & Technology, Control Theory & Control Engineering, Biomedical Engineering, Instrument Science & Technology, Electronic Science & Technology, Computer Application Technology, Information & Communication Engineering, Economics, Business Administration, Material & Environmental Engineering, Digital Media, Artistic Designing, Journalism, Law, Mathematics, Physics, English Language and Literature and so on. (Link Recruitment of Personnel Department of HDU for further Information).

Qualifications:

Applicants with PHD degree from prestigious domestic and overseas universities; Professors or assistant professors/researchers of the equivalent titles, having been working at overseas prestigious universities or research institutes.

Salary, Benefits and Support:

Successful applicant will be offered a competitive package, including sufficient laboratory space, startup funding and competitive salary commensurate with experience, in addition to a housing allowance, and other employee benefits. HDU is recruiting overseas talents all year around. Applicants may refer to the recruitment in our website <http://renshi.hdu.edu.cn> for further information. For those exceptionally qualified talents, the salary could be negotiated in person.

Contact:

So appreciated for interested individuals sending curriculum vitae by e-mail to rsc@hdu.edu.cn. Or contact us by telephone 86-(0)571-86915031, fax 86-(0)571-86915029.

Website: <http://renshi.hdu.edu.cn>



上海大学
Shanghai University

2015 Shanghai University Overseas Job Fair (SUOJF 2015)

Time: 14:00-18:00, Saturday, 10 October, 2015

Venue: Grand Horizon Room, Covel Commons, University of California, Los Angeles

Address: 330 De Neve Drive, Los Angeles, USA

Shanghai Municipality is devoted to establishing the city into both an innovation center of science and technology and a professional hub of global innovation. In order to fulfill its role, Shanghai University has been actively recruiting overseas elites and planning its Overseas Job Fair in 2015.

【University Profile】

Shanghai University is co-sponsored by China's Ministry of Education and Shanghai Municipal Government. It is listed as a national university of "211" project. Shanghai University has 27 schools/colleges and 2 independent departments with 4 national key disciplines, 11 provincial key disciplines, and 6 disciplines ranked among top 1% of ESI. Currently 12,181 graduate students and 23,036 undergraduate students are studying at Shanghai University.

Shanghai University places a great emphasis on the strategy of recruiting elite professionals. It now has 8 academicians, 577 professors and 924 associate professors, and the university is inviting more outstanding academic and research scholars in the related fields to join the family.

【Recruitment of Global Talents】

1. Schools & Colleges: Materials Genome Institute, School of Materials Science and Engineering, School of Sociology and Political Science, Shanghai Film School (School of Film and Television Art & Technology), College of Fine Arts, College of Science, School of Communication and Information Engineering, School of Computer Engineering and Science, School of Mechatronic Engineering and Automation, School of Environmental and Chemical Engineering, School of Liberal Arts, School of Social Sciences, School of Economics, School of Management, etc.

2. Requirements: Professors with outstanding academic achievements and international reputation; associate professors, heads of R&D departments of top multi-national corporations; assistant professors, post-doctors, PhD holders from prestigious overseas universities.

Level	Background Requirement	Job Description	Remuneration
Tier One	Professors with outstanding academic achievements and international reputation	Establish world-class research platforms, undertake national key research projects, carry out high-end international cooperation, apply for being recruited in China's "1,000-Talent Plan", the professorship of Yangtze River Scholar, etc.	Annual salary: RMB 0.8-1.5 million Housing subsidy: RMB 1.5-2.3 million Research fund: RMB 1-5 million
Tier Two	Associate professors, heads of R&D departments of top multi-national corporations	Lead the related disciplines, undertake national key research projects, carry out high-end international cooperation, apply for being recruited in China's "1,000-Talent Plan" meant for young researchers, National Science Fund for Distinguished Young Scholars, and Shanghai "1,000-Talent Plan", etc.	Annual salary: RMB 0.5-1 million Housing subsidy: RMB 1.3-1.8 million Research fund: RMB 1-2 million
Tier Three	Assistant professors, post-doctors, PhD holders from prestigious overseas universities	Apply for and undertake national research projects, publish quality research papers, apply for the professorship of Oriental Scholar (including Young Oriental Scholar), etc.	Annual salary: RMB 0.2-0.5 million Housing subsidy: RMB 0.2-0.8 million Research fund: RMB 0.3-1.5 million

【Application】

If you are interested in joining Shanghai University or attending this Job Fair, please register on <http://en.shu.edu.cn/Default.aspx?tabid=23926>. You can also send your C.V. to shucareer@oa.shu.edu.cn. We will contact you via your email address.

【Contact Detail】

International Office & Human Resources Office, Shanghai University:
Tel: +86-21-66136672; +86-21-66133029;
Mobile: +86-18221784505;
Fax: +86-21-66743200; Email: shucareer@oa.shu.edu.cn

High-level Talents Online Job Fair 2015



The second action of 2015

will be held on october 18th, from 7AM to 24PM
in Shanghai

Recruitment requirements:

Scholars and doctors with working experience and graduating doctors domestic and overseas

Please send your curriculum vitae to:

acabridge@gmail.com

chisa.add@gmail.com

chisa_yang@163.com

For more information, please check the following web sites

<http://www.edu.cn/cv>

http://www.chisa.edu.cn/zt/yczt/network_video/index.html

Tenure-Track Faculty Position Department of Microbiology and Physiological Systems

The Department of Microbiology and Physiological Systems at the University of Massachusetts Medical School (<http://www.umassmed.edu/>) invites applications for a **tenure-track faculty position** at the rank of **ASSISTANT PROFESSOR**. Depending on qualifications, candidates may be proposed for a more senior appointment at the rank of **ASSOCIATE** or **FULL PROFESSOR**. The Department is seeking candidates who use cross-disciplinary or systems-level approaches to solve problems in bacterial or viral infection including, but not limited to: molecular mechanisms of pathogenesis; cell biology of infection; analysis of complex microbial communities and their impact on the host; and host responses and adaptation to infection. Candidates will be expected to develop and maintain an innovative, externally funded research program. We offer generous support and a collaborative environment with opportunities for both basic and translational research. The position will be highly competitive with regard to start-up funds and salary. Review of applications will begin on September 1, 2015, and continue until the position is filled.

Applicants should submit a cover letter explaining their interest in the Department, a curriculum vitae that includes honors and publications, and a succinct research plan to <https://academicjobsonline.org/ajob/jobs/5742>. To expedite the review process, applicants should invite three individuals who are familiar with their work and potential for success to upload recommendation letters at the same web address.

UMass Medical School is committed to being an equal opportunity and affirmative action employer and recognizes the power of a diverse community. We encourage applications from protected veterans, individuals with disabilities and those with varied experiences, perspectives and backgrounds to consider UMass Medical School as their employer of choice.

Assistant/Associate Professor in Pharmacology

The Department of Pharmaceutical Sciences at North Dakota State University invites applications for a tenure-track faculty position at the rank of Assistant/Associate Professor, with appointment beginning on or after August 15, 2016. Candidates must hold a doctoral degree in pharmacology, physiology, or closely related field, have at least two years of postdoctoral experience with a strong record of scholarship, and possess good interpersonal skills and effective written and oral communication skills. Preference will be given to applicants with training and research expertise in areas that complement existing departmental strengths in cancer and cardiovascular research. The successful candidate will be expected to establish an externally funded research program, teach and mentor graduate students, and participate in team-taught pharmacology courses offered to pharmacy students.

A highly competitive salary and a start-up package commensurate with qualifications and experience are available. The Department of Pharmaceutical Sciences has the mission of teaching pharmacy students how basic science is applied to Pharmacy. In addition to teaching professional (Pharm.D.) students, the department has M.S., Ph.D. and Pharm. D./Ph.D. programs and participates in a multidisciplinary Ph.D. program in Cellular and Molecular Biology. Currently, there are twelve research-active faculty, 30 Ph.D. graduate students, and 8 Post-doctoral Fellows/Research Associates in the department. All department faculty are funded by extramural sources such as NIH, NSF, American Heart Association, and pharmaceutical industries. The department also participates on an NIH-funded COBRE grant with the Department of Chemistry. Additional information concerning the department, the university, and Fargo can be obtained at www.ndsu.edu/pharmacy. Review of applications will begin on **October 31st, 2015**, applications will be accepted until the position is filled. Submit electronically a curriculum vitae, description of research interests and future plans, statement of teaching philosophy and methods, and names and contact information of three references to: <http://jobs.ndsu.edu/postings/6686>. For further information please contact: **Dr. Bin Guo**, Department of Pharmaceutical Sciences, e-mail: Bin.Guo@ndsu.edu or **701-231-5164**.

NDSU is an Equal Opportunity Institution. Women and traditionally underrepresented groups are encouraged to apply.



TENURE-TRACK PROFESSOR Harvard University Faculty of Arts and Sciences Cambridge, MA Department of Chemistry & Chemical Biology

Position Description: The Department of Chemistry & Chemical Biology seeks to appoint a tenure-track assistant professor in the open field of chemistry and chemical biology. The appointment is expected to begin on July 1, 2016. The tenure-track professor will be responsible for teaching at the undergraduate and graduate levels.

Basic Qualifications: Doctorate or terminal degree in chemistry or related discipline required by the time the appointment begins.

Additional Qualifications: Demonstrated excellence in teaching is desired.

Special Instructions: Please submit the following materials through the ARIeS portal (<http://academicpositions.harvard.edu/postings/6320>). Applications must be submitted no later than **October 15, 2015**.

1. Cover letter
2. Curriculum Vitae
3. Teaching statement (describing teaching approach and philosophy)
4. Outline of future research plans
5. Names and contact information of 3-5 references (three letters of recommendation are required, and the application is complete only when all three letters have been submitted)
6. List of publications

Contact Information: Helen Schwickrath, Search Administrator, Department of Chemistry & Chemical Biology, Faculty of Arts and Sciences, Harvard University, 12 Oxford St., Cambridge, MA 02138. Phone: (617) 496-8190; Helen@chemistry.harvard.edu

Harvard is an Equal Opportunity Employer and all qualified applicants will receive consideration for employment without regard to race, color, religion, sex, sexual orientation, gender identity, national origin, disability status, protected veteran status, or any other characteristic protected by law.

TENURE-TRACK POSITION IN GENOMICS KECK SCIENCE DEPARTMENT CLAREMONT McKENNA, PITZER, AND SCRIPPS COLLEGES

The Keck Science Department invites applications for a tenure-track appointment in biology at the Assistant Professor level to begin July 2016. The department, which houses the biology, chemistry, and physics faculty for Claremont McKenna, Pitzer, and Scripps Colleges (three of the five undergraduate Claremont Colleges), offers innovative and interdisciplinary programs in the natural sciences and prides itself on its small class sizes and emphasis on hands-on, investigative learning by students in both classroom and research laboratory settings. The colleges are located near Los Angeles, surrounded by other colleges and universities.

Strong candidates will be committed to excellence in teaching and will develop a vibrant research program that fully engages undergraduate students. Of particular interest are candidates who use genomics-based approaches with an empirical, laboratory component to address important problems in, but not limited to, molecular/cellular biology, plant biology, microbiology, or evolutionary biology. Teaching responsibilities include an upper division course in genomics with bioinformatics, Introductory Biology (cell/molecular), and other courses in the candidate's field. A Ph.D. degree, post-doctoral experience, and a record of scholarly publication are required.

Please apply online at https://webapps.cmc.edu/jobs/faculty/faculty_opening_detail.php?PostingID=14028. Uploaded materials should include (1) a cover letter, (2) a curriculum vitae, (3) a statement of teaching philosophy, (4) a description of proposed research with equipment needs, (5) a diversity statement (one page) outlining the applicant's philosophy for fostering a learning environment that is inclusive of all students. Please also ensure that three letters of recommendation are uploaded. Inquiries about the position should be directed to Dr. Emily Wiley at ewiley@kecksci.claremont.edu. Additional information about the department may be found at www.kecksci.claremont.edu. Review of applications will begin **September 21, 2015**, and the position will remain open until filled.

In a continuing effort to enrich its academic environment and provide equal educational and employment opportunities, The Claremont Colleges actively encourage applications from women and members of historically under-represented social groups in higher education. The Claremont Colleges are an Equal Opportunity Employer.



Tenure Track Assistant Professor Position, Virology Department of Cell Biology and Molecular Genetics

The Department of Cell Biology and Molecular Genetics at the University of Maryland College Park is seeking to fill a tenure-track faculty position at the level of Assistant Professor in the area of Virology using animal or plant systems.

The successful candidate will be expected to maintain a cutting-edge externally funded research program in the area of virology that synergizes with existing core groups in the molecular and cellular biological sciences at UMD. Areas of synergy include molecular genetics, genomics and gene regulation, RNA structure and function, immunology and pathogenesis, cell biology and plant biology. The appointed candidate will also participate in undergraduate and graduate teaching. Applicants must have a doctorate degree, an outstanding publication record, and a commitment to excellence in teaching.

The University of Maryland, College Park is the flagship campus of the University System of Maryland. Close proximity to Washington DC, Baltimore, and the Maryland Biotechnology Corridor facilitates interactions with an extraordinary range of major research institutions such as NIH, NIST, FDA, USDA and JCVI, in addition to providing a rich cultural environment.

Applications should be submitted electronically to <http://ejobs.umd.edu/postings/35061> and addressed to Dr. Jeffrey DeStefano, chair of the faculty search committee. Applications should consist of a single PDF file containing (1) a cover letter, (2) curriculum vitae, (3) summary of research plans (maximum two pages) and teaching philosophy (one page), and (4) contact information for at least three references. Complete applications should be received by **October 15, 2015**, but will be accepted until the position is filled.

The University of Maryland is an Affirmative Action/Equal Opportunity Employer. Women and members of underrepresented groups are especially encouraged to apply.

Dartmouth

Faculty Position in Neuroscience Department of Biological Sciences Hanover, NH USA

The Department of Biological Sciences at **Dartmouth** invites applications for a full time, tenure-track position in **Neuroscience** at the Assistant, Associate, or Full Professor rank. We seek highly qualified candidates using cellular, biophysical, and/or computational approaches to address outstanding research questions at the molecular, cellular, developmental and/or circuit levels of neurobiology. The successful candidate will be expected to direct an independent research program that will attract extramural funding, provide research training for graduate and undergraduate students, and teach at the undergraduate and graduate levels. The successful candidate will join a larger neuroscience community at Dartmouth including faculty in the departments of Physiology and Neurobiology, Biochemistry, and Psychological and Brain Sciences as well as in the Thayer School of Engineering. Department members participate in the Molecular and Cellular Biology graduate program and the Neuroscience division of the Program in Experimental and Molecular Medicine. Both programs are shared with the Geisel School of Medicine at Dartmouth. Application materials should include a cover letter, curriculum vitae, three representative publications, statements of research and teaching interests, and at least three confidential letters of reference. Please upload application materials electronically to: apply.interfolio.com/30645.

Application review will begin on **October 1, 2015** and continue until the position is filled. The following links provide further information about the department <http://biology.dartmouth.edu/> and graduate programs <http://www.dartmouth.edu/~mcb/>; <https://geiselmed.dartmouth.edu/pemml/>.

Dartmouth College combines a commitment to innovative scholarship with dedication to excellent teaching. One of the most diverse institutions of higher education in New England, Dartmouth College is an Equal Opportunity/Affirmative Action Employer; has a strong commitment to diversity, and in that spirit encourages applications from all individuals regardless of gender, race, religion, color, national origin, sexual orientation, age, disability, or veteran status.



OPEN FACULTY POSITIONS INSTITUTE OF MOLECULAR BIOLOGY ACADEMIA SINICA, TAIWAN, ROC

One tenure-track faculty position is open for a highly qualified individual to establish independent research programs in **all disciplines of molecular and cellular biology**. Applicants should hold a Ph.D. degree or its equivalent, with appropriate postdoctoral research experience. The successful recruit will be appointed at the levels of **Assistant, Associate, or Full Research Fellows** (equivalent to academic ranks of Assistant, Associate and Full Professors at universities), and receive a generous multi-year start-up package, followed by annual intramural support.

The Institute of Molecular Biology at Academia Sinica (<http://www.imb.sinica.edu.tw/en>) provides an active and stimulating research environment, is well supported by both extramural and long-term intramural funding, and features several core facilities (imaging, microarray, Next Generation Sequencing, RNAi, electrophysiology, FACS, bioinformatics and mouse facilities) that provide state-of-the-art resources and key technical expertise to the Institute's research community. Recent research works were published in top journals such as Science, Nature, and Cell. Currently two Ph.D. programs, with one recruiting international students, are formally affiliated with the Institute. English is the official language for regular seminars and most of the lectures at the Institute, and proficiency in Chinese language is not a prerequisite for application.

Applicants should send their Curriculum Vitae, a description of past research accomplishments and future research plans, and arrange for three letters of recommendation to be sent directly to:

Dr. Soo-Chen Cheng, Director
c/o Ms. Vivi Chiang
Institute of Molecular Biology,
Academia Sinica
Taipei, Taiwan 11529, ROC

The selection process will start on **December 15, 2015** until the positions are filled. Further information can be obtained from Ms. Vivi Chiang at vivi@imb.sinica.edu.tw



Managing Director – Center for Sustainable Nanotechnology PVL 83199

The Department of Chemistry of the University of Wisconsin-Madison is recruiting for a Managing Director in the Center for Sustainable Nanotechnology (CSN.) The Director works with the Center Director and the CSN Executive Committee and is responsible for actively directing and coordinating scientific research and additional integrative activities at multiple institutions to achieve the center's goals. A Ph.D. in Chemistry or related field experience is required. This is a full-time position with an anticipated beginning date of October 1, 2015. There will be a minimum twelve-month evaluation period. Specific duties of the Director may include: Overseeing general operation of the center; establishing and implementing center-wide policies and procedures that will maximize the effectiveness of the center's scientific objectives and associated integrative activities; oversee center-wide finances (including multiple sub-contracts) and develop financial plans for the center; ensure that Center programs and activities are compliant with federal/state regulations; interface directly with federal agency personnel to meet reporting requirements and to communicate the center's scientific progress and objectives. This will include identifying high-impact scientific results and translating into language appropriate for program managers and policymakers.

For additional information, please go to: http://www.ohr.wisc.edu/Weblisting/External/PVLSummary.aspx?pv1_num=83199. Additional information on the Center for Sustainable Nanotechnology is available at <http://susnano.chem.wisc.edu>. Please submit a letter of interest, curriculum vitae and 3 references referring to **PVL 83199** to **Dennis Reece at the Department of Chemistry, University of Wisconsin-Madison, 1101 University Ave., Madison, Wisconsin 53706-1322**. To guarantee full consideration, all materials must be received by **September 15, 2015**.

The University of Wisconsin is an Equal Opportunity and Affirmative Action Employer; applications from qualified women and minority candidates are encouraged. Unless confidentiality is requested in writing, information regarding the identity of the applicant must be released on request and there are deadlines for disclosure. Finalists cannot be guaranteed confidentiality. A background check may be required prior to employment.

POSITIONS OPEN

ASSISTANT PROFESSOR in Complex Systems

The Center for the Study of Complex Systems (CSCS) at the University of Michigan invites applications for a tenure-track position of Assistant Professor of Complex Systems. Candidates at a more senior-level will also be considered. The appointment will begin September 1, 2016. This is a University-year appointment. Information about the Center can be found at website: <http://www.lsa.umich.edu/cscs>.

Required Qualifications: Candidates must have a demonstrated research agenda focusing on complex systems. This may involve theoretical or applied research on complexity, including (but not limited to) mathematical and computational models in areas such as networks, computation, emergence, large events and robustness or applications where complexity lies at the core such as quantitative modeling of social systems, soft condensed matter physics, evolutionary or ecological dynamics, epidemiology and disease transmission, artificial life, neuroscience, and cognition. Preference will be given to candidates with a track record of working across disciplines.

How to Apply: All application materials must be uploaded onto this website: <https://complexsystems-lsa.applicantstack.com/x/apply/a2guio5y9cxc>

The position is based in CSCS but will be a joint appointment with another department. In the cover letter, candidates should identify one or more partner departments at the University of Michigan suitable for such a joint appointment. Applicants must submit: a current curriculum vitae, statement of current and future research plans, a statement of teaching philosophy and experience, evidence of teaching excellence (if any) and one writing sample. At least three letters of recommendation are required and must be uploaded onto the same website. Applications will be reviewed starting October 1, 2015. Applications will be accepted until the position is filled.

Women and minority candidates are encouraged to apply. The University of Michigan is an equal opportunity/affirmative action employer and is supportive of the needs of dual career couples.

ASSISTANT PROFESSOR ANALYTICAL, PHYSICAL OR BIOPHYSICAL CHEMISTRY CALIFORNIA STATE UNIVERSITY EAST BAY

The California State University, East Bay (CSUEB) Department of Chemistry & Biochemistry invites applications for a tenure track **ASSISTANT PROFESSOR** position in Analytical, Physical or Biophysical Chemistry (#16-17 CHEM-ANALYTICS/PHYS/BIOPHYS-TT) for the 2016-2017 academic year. The successful candidate must have extensive training in chemistry and a strong commitment to teaching. Applicants are expected to establish an externally funded research program appropriate for undergraduate and M.S. students pursuing a chemistry curriculum. Teaching responsibilities may include introductory and advanced lecture and laboratory courses such as basic chemistry, general chemistry, quantitative analysis, environmental chemistry and advanced topics in specific areas. A Ph.D. is required; postdoctoral research and teaching experience in chemistry are preferred. Applicants must submit, via regular mail, hard copies of a cover letter specifying the position number, a curriculum vitae, a one-page statement of teaching philosophy, a brief research plan (3 pages max.), and undergraduate and graduate transcripts to Dr. Ann McPartland, Chair, Department of Chemistry and Biochemistry, California State University, East Bay, Hayward, CA 94542. Applicants must also submit the cover letter and curriculum vitae electronically at website: https://cmsweb.csueastbay.edu/psp/HEBPRD/EMPLOYEE/HRMS/c/HRS_HRAM.HRS_CE.GBL and arrange to have three letters of recommendation sent to Dr. McPartland via US mail or electronically to e-mail chemistry.search_15-16@csueastbay.edu. Review of applications will begin September 30, 2015 and continue until the position is filled.

CSUEB, an Equal Opportunity Employer, is committed to the principles of diversity in employment.

POSITIONS OPEN

CHEMICAL BIOLOGY FACULTY POSITION Boston College Chemistry Department

The Chemistry Department of Boston College invites applications for a tenure-track position to be effective in the fall of 2016. Applicants will be evaluated based on their potential to establish a prominent and well-funded research program and to excel in teaching at the graduate and undergraduate levels. Successful applicants will join a department of approximately 120 doctoral students, 30 postdoctoral fellows, 200 undergraduate majors, and an internationally recognized faculty.

Assistant Professor in the area of Chemical Biology requires a Ph.D. in Chemistry or related areas; postdoctoral experience is desirable but not required. The candidate is expected to have published in top refereed journals and demonstrated the ability to perform outstanding independent research.

Interested applicants must submit a cover letter (which includes the names of three references), a graphical executive summary of research plans (one page), curriculum vitae, a summary of research plans (eight pages maximum), a statement of teaching philosophy and arrange to have three letters of reference submitted via the online faculty application at website: <http://apply.interfolio.com/30499>.

All application materials must be submitted electronically on or prior to October 15, 2015.

Boston College, a university of eight schools and colleges, is an Equal Opportunity Employer and supports Affirmative Action.

FACULTY POSITION

The Department of Molecular & Cellular Physiology invites applications for a tenure track position at the level of Assistant Professor. Successful applicants will be expected to develop an independent, nationally funded research program and to contribute to the education mission of the Department. Research areas are open, but preference will be given to individuals with an interest and record of achievement in the cardiovascular sciences. Information about the departmental research focus is available at website: <http://www.shreveportphysiology.com>. A generous startup package and appropriate space will be offered. Applicants should have a Doctoral degree and relevant postdoctoral experience. Applications will be reviewed as they are received until the position is filled. Send curriculum vitae and names of three references to: D. Neil Granger, PhD, Boyd Professor & Head, Department of Molecular & Cellular Physiology, LSU Health Sciences Center, 1501 Kings Highway, Shreveport, Louisiana, 71130-3932, FAX:318-675-6005, e-mail: dgrang@lsuhsc.edu.

Louisiana State University Health Science Center – Shreveport is an Equal Opportunity Employer and all qualified applicants will receive consideration for employment without regard to race, color, religion, sex, national origin, disability status, protected veteran status, or any other characteristic protected by law.

PRINCETON UNIVERSITY DEPARTMENT OF CHEMISTRY ASSISTANT PROFESSOR

The Department of Chemistry at Princeton University invites applications for a tenure-track assistant professor position in all areas of chemistry. We seek a faculty member who will create a climate that embraces excellence and diversity with a strong commitment to research and teaching that will enhance the work of the department and attract and retain a diverse student body. We strongly encourage applications from members of all underrepresented groups. Candidates are expected to have completed the Ph.D. in chemistry or a related field at the time of appointment. Applicants should submit a description of research interests, curriculum vitae, a list of publications, and contact information for three referees online at website: https://jobs.princeton.edu/applicants/jsp/shared/position/JobDetails_css.jsp. The deadline for applications is October 15, 2015.

Princeton University is an Equal Opportunity Employer. All qualified applicants will receive consideration for employment without regard to race, color, religion, sex, national origin, disability status, protected veteran status, or any other characteristic protected by law. This position is subject to the University's background check policy.

AWARDS

ROSENSTIEL AWARD

The Department of Marine Biology and Ecology at the University of Miami seeks nominations for the Rosenstiel Award. This award was created by the Rosenstiel Foundation to recognize outstanding contributions to marine science including oceanographically relevant aspects of atmospheric science and fundamental developments in ocean engineering. It is given annually by the Rosenstiel School of Marine and Atmospheric Sciences at the University of Miami to honor a scientist in the formative years of their careers. In order to accommodate the various disciplines on which ocean science is based, the award is presented on a rotating basis for achievements in six broad disciplinary areas: meteorology and physical oceanography; marine geology and geophysics, marine and atmospheric chemistry; marine biology and ecology; applied marine physics and marine affairs and policy. This year the award will be made in the general area of Marine Biology and Ecology. The general areas of interest include physiology, genetics, genomics, proteomics, ecology, behavior, population dynamics, connectivity, toxicology and conservation science in a marine field. Further information on the award can be found at our website <http://www.rsmas.miami.edu/about-rsmas/rosenstiel-award/>. Please forward your nominations by October 1, 2015 to Chris Langdon, e-mail: clangdon@rsmas.miami.edu University of Miami, 4600 Rickenbacker Causeway, Miami, FL 33149.

POSITIONS OPEN

Clarkson University seeks an excellent teacher and productive researcher to fill a tenure-track position in bioinformatics at the rank of Assistant Professor beginning with the 2016-17 academic year. For additional information about this position and to apply on-line, see website: <http://www.clarkson.edu/hr>. Applications should be received by 1 October 2015 for full consideration.

An Equal Opportunity/Affirmative Action Employer, Clarkson actively seeks and encourages applications from minorities, women and people with disabilities.

Advance
your career
with expert
advice from
Science
Careers.



Download Free Career
Advice Booklets!

ScienceCareers.org/booklets



Science Careers

FROM THE JOURNAL SCIENCE ■ AAAS

M | MEDICAL SCHOOL

UNIVERSITY OF MICHIGAN

Faculty Positions Department of Pharmacology

The Department of Pharmacology at the University of Michigan Medical School invites applications for two tenured/tenure-track positions at the **ASSISTANT, ASSOCIATE** or **FULL PROFESSOR** level. We are seeking outstanding individuals with research experience and interests that augment current department initiatives in the areas of **G protein-coupled receptors or Pharmacogenomics**. Qualifications include a Ph.D. in Pharmacology or a related discipline and/or a M.D. degree, and for those applying above the level of Assistant Professor, a strong record of nationally competitive external funding, a sustained record of excellent research productivity, and an outstanding national reputation in their field of interest. Physician-Scientists are encouraged to apply, as joint appointments are available with clinical departments. Applicants will be expected to maintain extramural funding, participate in the teaching of medical, graduate, and undergraduate courses, and to support and mentor graduate students and postdoctoral fellows. An attractive startup package including excellent laboratory space and generous funding is available. Salary will be commensurate with experience.

The successful candidates will join a dynamic, diverse, and collaborative department with new leadership in a Top 10 Medical School in a university setting with superb opportunities for continuing career development. The quality of life in Ann Arbor is outstanding. The combination of a large, major research university with a diverse, safe, family-oriented community make Ann Arbor an ideal environment for work-life balance. Ann Arbor offers an outstanding combination of sports, recreation, and cultural events.

Applicants should send a cover letter stating the position and subject area for which they are applying and the names and contact information of three referees, their *curriculum vitae*, a three-page summary of their research program and future research plans, and information related to past and current teaching experience as a single PDF file to jdani@umich.edu. Address all correspondence to: **Dr. John Traynor, Chair, Pharmacology Faculty Search Committee, Department of Pharmacology, The University of Michigan Medical School, 1150 West Medical Center Dr., Ann Arbor, MI 48109-5632.**

Review of applications will begin on **October 1, 2015**, and will continue until both positions are filled.

*The University of Michigan is an Affirmative Action/Equal Opportunity Employer.
Applications from qualified women, minorities and/or disabled individuals are encouraged.*

Williams

Cell and Molecular Biologist/ Biochemist Tenure -Track Faculty Position Biology Department

The Biology Department at Williams College, a premier liberal arts college with a long-standing tradition of excellence in the sciences, invites applications for a tenure-track position at the rank of Assistant Professor, to begin July 2016. We are especially interested in candidates who can contribute to the intellectual vibrancy and diversity of the academic community through their research, teaching, and service, and who are committed to working effectively with a broadly diverse student population.

We seek a biochemist or molecular biologist whose research interests in protein structure and function emphasize protein complexes and networks. The candidate's research should incorporate state-of-the-art methods and address questions of broad biological significance to cells, organisms and evolution. The successful candidate will teach upper level courses in his or her area of specialty, a metabolic biochemistry course, and contribute to our introductory course in cellular and molecular biology. This individual will advise undergraduates in research and participate in interdisciplinary programs in Biochemistry & Molecular Biology, and/or Bioinformatics, Genomics & Proteomics. Normally, faculty members teach one course and two associated laboratory sections (or the equivalent) each semester.

A dynamic research program that is attractive to extramural funding agencies and involves talented undergraduates is expected. Start-up funds and internal funding for research are available. A Ph.D., postdoctoral experience, and a strong research record are required. We anticipate the appointment at the beginning assistant professor level, although a more senior appointment may be possible under special circumstances.

All applications should be submitted through Interfolio at <http://apply.interfolio.com/30712>. Email and paper applications will not be accepted. Through Interfolio submit: a letter of application addressed to **Professor Joan Edwards** (Chair, Biology Department), a curriculum vitae, concise statements of teaching and research plans, and three current letters of recommendation. All offers of employment are contingent upon completion of a background check <http://faculty.williams.edu/prospective-faculty/background-check-policy/>. Application deadline is **October 23, 2015**.

Williams College is a coeducational liberal arts institution located in the Berkshire Hills of western Massachusetts. The College has built its reputation on outstanding teaching and scholarship and on the academic excellence of its approximately 2,000 students. Please visit the Williams College website (<http://www.williams.edu>). Beyond meeting fully its legal obligations for non-discrimination, Williams College is committed to building a diverse and inclusive community where members from all backgrounds can live, learn, and thrive.

Two Faculty Career Features

THERE'S A SCIENCE TO REACHING SCIENTISTS.

September 18, 2015

Reserve ads by September 1
Ads accepted until September 14

October 9, 2015

Reserve ads by September 22
Ads accepted until October 5

For recruitment in science, there's only one **Science**

Why choose these faculty features for your advertisement?

- Relevant ads lead off the career section with special Faculty banner
- September 18 issue will be distributed at the Biotechnica Meeting in Hanover, Germany, 6-8 October.



SCIENCECAREERS.ORG

**Science
Careers**
MAAAS

To book your ad: advertise@sciencecareers.org

The Americas
202-326-6582

Europe/RoW
+44 (0) 1223-326500

Japan

+81-3-3219-5777

China/Korea/Singapore/Taiwan
+86-186-0082-9345

By Joan W. Bennett

The fungi that ate my house

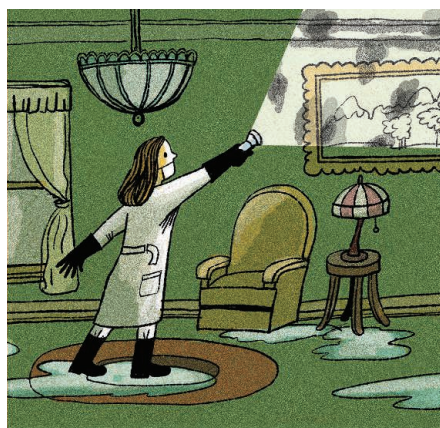
Ten years ago, I was a professor of cell and molecular biology at Tulane University in New Orleans, Louisiana. I was riding high on a series of recent academic honors for my work studying toxicogenic molds and was looking forward to spending a sabbatical leave at The Institute for Genomic Research, now the J. Craig Venter Institute, in Maryland. Then, in August 2005, just a few weeks before I was to leave on sabbatical, Hurricane Katrina nearly destroyed my university and my city. The storm upended my comfortable life and unexpectedly sent me down a new research trajectory.

The weeks after Hurricane Katrina were some of the worst of my life. My family and I had safely evacuated to New Jersey, where we had friends who could house us, but our home had been flooded and our city devastated. I suffered acute insomnia, heightened by the fact that I knew too much about mold metabolism. Fungi, the life forms that had fascinated me since childhood, secrete digestive enzymes into the environment, often turning their substrates to slime, and then reabsorb the breakdown products. They are nature's great recyclers. I hated knowing that molds were recycling the contents of my waterlogged home.

More than a month after Hurricane Katrina, we flew back to New Orleans to survey the damage. When we unlocked our front door, we were greeted with fungal anarchy. Molds were growing on everything: rugs, curtains, wall-paper, upholstered furniture, and—worst of all—some of my most treasured books. The odor was overpowering.

Before my return to New Orleans, I figured I might salvage something from the loss of my home if I turned it into a living laboratory. I visited Jim White, a mycologist friend at Rutgers University in New Jersey, who equipped me to sample the molds in my flooded home. I traveled with a suitcase full of sterile swabs, masks, gloves, and 10 sleeves of petri dishes filled with growth media. As I sampled my house, wearing gloves and a mask, I started to feel sick. I had to take several breaks and go outside. I began to empathize with people who claimed to have gotten sick from indoor mold exposure, a controversial condition sometimes called “sick building syndrome.” I vowed that if I ever got a functioning lab again, I would study the volatile compounds that were causing the odious smell in my house.

Later that fall, Rutgers invited me to finish my sabbatical leave there. The hurricane had kept me from my original



“As I sampled my house, wearing gloves and a mask, I started to feel sick.”

sabbatical plans, and all of the microbial cultures in my Tulane laboratory had died during the weeks without power after the storm, so it was an attractive offer. Several months later, I agreed to stay on at Rutgers as founder and associate vice president of the Office for the Promotion of Women in Science, Engineering, and Mathematics.

During my first years at Rutgers, I worked on issues related to women in science while reinventing my research career. In my new laboratory, as I had promised myself after Hurricane Katrina, my team adapted genetic models to study the possible physiological effects of fungal volatile organic compounds (VOCs). We found that several common fungal VOCs are neurotoxic in a *Drosophila* (fruit fly) model. Somewhat surprisingly, we also found that the VOCs from the most common fungus isolated from my flooded home, a *Trichoderma* species, can make the plant *Arabidopsis* and tomatoes grow better. Although I haven't been able to demonstrate that the gases from molds contribute to sick building syndrome, I have been able to show that they have many profound physiological effects.

I don't recommend experiencing a devastating hurricane and losing your home as a way to revitalize your research. Nevertheless, my science has kept me focused on future possibilities rather than on past losses. The Hurricane Katrina catastrophe has led me to what may be the best science that I have ever done. ■

Joan W. Bennett is a distinguished professor of plant biology and pathology and senior faculty adviser to the Office for the Promotion of Women in Science, Engineering, and Mathematics at Rutgers University, New Brunswick, in New Jersey. For more on life and careers, visit sciencecareers.org. Send your story to SciCareerEditor@aaas.org.